SEISMICITY AND STRUCTURE OF THE OROZCO TRANSFORM FAULT

from

OCEAN BOTTOM SEISMIC OBSERVATIONS

by

Anne Martine Trehu

B.A., Princeton University, Princeton, New Jersey
(1975)

SUBMITTED IN PARTIAL FULFILLMENT
OF THE REQUIREMENTS FOR THE DEGREE OF
DOCTOR OF PHILOSOPHY

at the

MASSACHUSETTS INSTITUTE OF TECHNOLOGY
and the
WOODS HOLE OCEANOGRAPHIC INSTITUTION

February, 1982

Signature of Author .....
Department of Earth and Planetary Sciences, Massachusetts Institute of Technology and the Joint Program in Oceanography, Massachusetts Institute of Technology / Woods Hole Oceanographic Institution, January, 1982.

Certified by .....
Thesis Co-supervisor

Certified by .....
Thesis Co-supervisor

Accepted by .....
Chairman, Joint Oceanography Committee in the Earth Sciences, Massachusetts Institute of Technology / Woods Hole Oceanographic Institution

SEISMICITY AND STRUCTURE OF THE OROZCO TRANSFORM FAULT from OCEAN BOTTOM SEISMIC OBSERVATIONS

by

Anne Martine Trehu

Submitted to the Department of Earth and Planetary Sciences
Massachusetts Institute of Technology
and
the Department of Geology and Geophysics
Woods Hole Oceanographic Institution
on January 25, 1982,
in partial fulfillment of the requirements
for the degree of Doctor of Philosophy.

ABSTRACT

In this thesis, seismic waves generated by sources ranging from 2.7 kg shots of TNT to magnitude 5 earthquakes are studied in order to determine the seismic activity and crustal structure of the Orozco transform fault. Most of the data were collected by a network of 29 ocean bottom seismometers (OBS) and hydrophones (OBH) which were deployed as part of project ROSE (Rivera Ocean Seismic Experiment). Additional information is provided by magnetic anomaly and bathymetric data collected during and prior to ROSE and by teleseismic earthquakes recorded by the WWSSN (Worldwide Seismic Station Network).

In Chapter II, the tectonic setting, bathymetry and teleseismic history of the Orozco Fracture Zone are summarized. Covering an area of 90 x 90 km which includes ridges and troughs trending both parallel and perpendicular to the present spreading direction (approximately east-west), the bathymetry of the transform portion of the fracture zone does not resemble that of other transform faults which have been studied in detail. A detailed study of one of the largest teleseismic earthquakes (m_b=5.1) indicates right lateral strike-slip faulting with a strike parallel to the present spreading direction and a focal depth of less than 5 km. The moment sum from teleseismic earthquakes suggests an average fault width of at most a few kilometers. Because the teleseismic earthquake locations are too imprecise to define the present plate boundary and the magnetic anomaly data are too sparse to resolve the recent tectonic history, more questions are raised than are answered by the results in this chapter. These questions provide the focus for the study of the ROSE data.

Chapter III contains an examination of the transfer function between seafloor motion and data recorded by the MIT OBS. The response of the recording system is determined and the coupling of the OBS to the seafloor during tests at two nearshore sites is analysed. Applying these results to the ROSE data, we conclude that the ground motion in the absence of the instrument can be adequately determined for at least one of the MIT OBS deployed during ROSE.

Hypocentral parameters for 70 earthquakes, calculated for an assumed laterally homogeneous velocity structure which was adapted from the results of several refraction surveys in the area, are presented in Chapter IV. Because of the large number of stations in the ROSE network, the epicentral locations, focal depths and source mechanisms are determined with a precision unprecedented in marine microseismic work. Relative to the assumed model, most horizontal errors are less than ±1 km; vertical errors are somewhat larger. All epicenters are within the transform region of the Orozco Fracture Zone. About half of the epicenters define a narrow line of activity parallel to the spreading direction and situated along a deep topographic trough which forms the northern boundary of the transform zone (region 1). Most well determined depths are very shallow ($\leq$4km) and no shallowing of activity is observed as the rise-transform intersection is approached. In fact, the deepest depths (4-10km) are for earthquakes within 10 km of the intersection; these apparent depth differences are supported by the waveforms recorded at the MIT OBS. First motion polarities for all but two of the earthquakes in region 1 are compatible with right lateral strike-slip faulting along a nearly vertical plane striking parallel to the spreading direction. Another zone of activity is observed in the central part of the transform (region 2). The apparent horizontal and vertical distribution of activity is more scattered than for the first group and the first motion radiation patterns of these events do not appear to be compatible with any known fault mechanism. No difference can be resolved between the stress drops or b values in the two regions.

In Chapter V, lateral variations in the crustal structure within the transform region are determined and the effect of these structures on the results of the previous chapter is evaluated. Several data sources provide information on different aspects of the crustal structure. Incident angles and azimuths of body waves from shots and earthquakes measured at one of the MIT OBS show systematic deflections from the angles expected for a laterally homogeneous structure. The effect of various factors on the observed angles and azimuths is discussed and it is concluded that at least some of the deflection reflects regional

lateral velocity heterogeneity. Structures which can explain the observations are found by tracing rays through three dimensional velocity grids. High velocities are inferred at upper mantle depths beneath a shallow, north-south trending ridge to the west of the OBS, suggesting that the crust under the ridge is no thicker, and perhaps thinner, than the surrounding crust. Observations from sources in region 2 suggest the presence of a low velocity zone in the central transform between the sources and the receiver. That the presence of such a body provides answers to several of the questions raised in Chapter IV about the hypocenters and mechanisms of earthquakes in region 2 is circumstantial evidence supporting this model. These proposed structures do not significantly affect the hypocenters and fault plane solutions for sources in region 1. The crustal velocity structure beneath the north-south trending ridges in the central transform and outside of the transform zone is determined by travel time and amplitude modeling of the data from several lines of small shots recorded at WHOI OBH. Outside of the transform zone, a velocity-depth structure typical of oceanic crust throughout the world oceans is found from three unreversed profiles: a 1 to 2 km thick layer in which the velocity increases from about 3 to 6.7 km/sec overlies a 4 to 4.5 km thick layer with a nearly constant velocity of 6.8 km/sec. A reversed profile over one of the north-south trending ridges, on the other hand, indicates an anomalous velocity structure with a gradient of 0.5 sec^{-1} throughout most of the crust (from 5.25 km/sec to 7.15 km/sec over 3.5 km). A decrease in the gradient at the base of the crust to about 0.1 sec^{-1} and a thin, higher gradient layer in the upper few hundred meters are also required to fit the travel time and amplitude data. A total crustal thickness of about 5.4 km is obtained. An upper mantle velocity of 8.0 to 8.13 km/sec throughout much of the transform zone is determined from travel times of large shots of TNT recorded at MIT and WHOI instruments. "Relocations" of the large shots relative to the velocity model assumed in Chapter IV support the conclusion from the ray tracing that results from region 2 may be systematically biased because of lateral velocity heterogeneity whereas results from region 1 are not affected.

In the last chapter, the results on crustal structure and seismicity are combined in order to define the present plate boundary and to speculate on the history of the present configuration.

Thesis advisors: Dr. S.C. Solomon, Associate Professor of Geophysics at the Massachusetts Institute of Technology

Dr. G.M. Purdy, Associate Scientist at the Woods Hole Oceanographic Institution

ACKNOWLEDGEMENTS

Many people have contributed to the mental, physical and emotional realization of this thesis.

I would first like to express my appreciation for the guidance and encouragement provided by my thesis advisors, Drs. Sean Solomon and Mike Purdy, and I hope to continue discussions with them in the future. The other members of my committee - Drs. Kei Aki, Henry Dick and John Ewing - were also very helpful.

I must also thank Jeremy Duschenes, Tim Barash and Paul Mattaboni for developing the tool of my trade (i.e., the MIT OBS) and for being patient when confronted by my engineering ignorance.

Michel Bouchon, Tom Fitch, Mike Purdy, Ralph Stephen and Cliff Thurber were generous with their computer programs; I hope that, in return, my programs will be useful to those following me. Dickie Allison and Steve Gildea were always ready to help when the WHOI and MIT computers tried to assert their independence.

Kim Klitgord, Bill Prothero, and Jean Francheteau provided preprints and unpublished data.

Debby Roecker and Jake Pierson shielded me from the bureaucratic babble, and Tonia Fardis saw that my bills were paid. Dorothy Frank typed the manuscript; her agility on the word processor is astonishing.

The "Falafel King" has supplied nutrients and cartoons at the "Off the Wall" have provided an occasional escape

during the last few months.

Sylvie LeDouaran, Rob Stewart, Brian Tucker, John Crowe, Helene Lyon-Caen, Claude Jaupart, Olga Levshin, Jean Andrews, Arthur Cheng, Bernard Celerier, Jeremy Henderson, Ken Tubman,, Qiming Wang, Debby and Steve Roecker, Danielle and Bernard Chouet, and many others have been - and, I trust, will continue to be - companions, confidents, consultants, critics sounding boards, tennis partners, etc.

Heartfelt thanks are extended to John Nábělek for being all of the above.

Reflecting on the past, I thank Dr. Jason Morgan for channelling a passing enthusiasm for paleo-anthropology into a longer-term interest in geophysics by offering me the opportunity spend a month at sea (with three hours on the Galapagos Islands). Dr. John Sclater introduced me to Woods Hole.

Finally, I thank the Rivera Fracture Zone for providing the name for project ROSE. Although "that which we call a rose, by any other name would smell as sweet," project OOSE was certainly more appealing with the name of ROSE; moreover, I prefer the paintings of Diego Rivera to those of Jose Orozco.

A National Science Foundation three year graduate fellowship gave me the opportunity to browse freely within the department before deciding on a thesis topic. This research was supported by the Office of Naval Research, under contracts N 00014-75-C-0291 and N 00014-80-C-0273.

This thesis is dedicated to the memory of my mother,
Cecily Supnick Trehu.

Her determination to do her best
- with thought, humour and consideration towards others -
will always inspire me.

TABLE OF CONTENTS

CHAPTER I

INTRODUCTION

Understanding the process of creation of crust and lithosphere at mid-ocean ridges is a major goal of marine geophysics, and answers are being sought through several different and complementary approaches. Seismic refraction and reflection data provide information on crustal structure and how it changes with age, and additional constraints are imposed by other geophysical methods such as gravity and heat flow. Petrologic studies attempt to trace the temporal and spatial path of magma as it is emplaced. The most direct signal of present tectonic processes, however, is earthquake activity. The distribution of activity in time and space and the source parameters of the earthquakes along spreading centers and transform faults contain information on the forces active in the spreading process, and the maximum depth of activity constrains the thermal structure by determining the temperature sensitive transition between brittle and ductile behavior of the rock.

In the past few years, a number of research groups have independently been using ocean bottom seismometers (OBS) and hydrophones (OBH) to study crustal structure and seismicity of mid-ocean ridges and transform faults. Refraction studies have indicated regional heterogeneity as well as systematic changes in the crustal structure as a function of age (e.g., Houtz and Ewing, 1976; Orcutt et al., 1976; Lewis and Snydsman, 1979; Detrick and Purdy, 1980; McClain and Lewis,

1980; Spudich and Orcutt, 1980; Purdy, 1982a).

Microearthquake surveys have been conducted with OBS and free-floating sonobuoys to associate microearthquake hypocenters with tectonic features, determine earthquake source parameters, and use shear waves from earthquake sources to study the shear wave velocity structure of the crust (e.g., Francis and Porter, 1973; Reid et al., 1973; Reid and Macdonald, 1973; Spindel et al., 1974; Macdonald and Mudie, 1974; Prothero et al., 1976; Reichle et al., 1976; Reichle and Reid, 1977; Reid et al., 1977; Solomon et al., 1977; Francis et al., 1977, 1978; Lilwall et al., 1977, 1978, 1980, 1981; Johnson and Jones, 1978; Jones and Johnson, 1978; Reid and Prothero, 1981; Rowlett, 1981). A few general conclusions from these microearthquake surveys are that transform faults have a higher level of seismic activity than spreading centers, that the activity of fracture zones is restricted to the active transform zone, that most earthquakes occur at depths less than about 8 km with, at several sites, a concentration of activity around 7 km, and that earthquake swarms are associated with spreading centers. Because all such previous studies have been conducted with at most a few stations, the epicentral location capability of the arrays has generally been limited and the focal depth resolution poor. The detailed relationship between epicenter location and specific physiographic features has therefore not been resolved.

Several years ago, the marine seismological community decided that a joint experiment assembling instruments from many research groups would produce data of a quality unattainable by any single group. The result of this consensus was project ROSE (Rivera Ocean Seismic Experiment, Ewing, 1982). As indicated by its name, project ROSE was originally planned for the Rivera Fracture Zone which forms the plate boundary between the Pacific, Cocos and Rivera plates. This site had been chosen for the experiment because of its known high level of seismic activity (Reid, 1976). Moreover, the bathymetry of the area was already well charted, facilitating the design of an optimal configuration for the OBS array. Project ROSE, however, became a victim of the vagaries of international diplomacy and, on the eve of the expedition, permission to conduct the experiment within the territorial waters of Mexico was not granted. The experiment was therefore moved to the next closest major fracture zone, the Orozco, about which next-to-nothing was known.

Field work for Project ROSE consisted of two phases during January to March 1979 (Figure 1.1). During Phase I (active phase), seismic refraction lines were shot both parallel and perpendicular to isochrons on 0 to 4 m.y. old seafloor near the East Pacific Rise at 11° to 13° N. Phase II (passive phase) was primarily a survey of microearthquake activity on the Orozco transform fault and adjacent rise axis areas. Several refraction experiments were also conducted to provide additional constraints on the velocity structure.

Groups from 12 institutions (the University of California at San Diego and at Santa Barbara, University of Hawaii, Instituto Oceanographico at Manzanillo, Lamont-Doherty Geological Observatory, Massachusetts Institute of Technology, Naval Ocean Research and Development Activity, Naval Research Laboratory, Oregon State University, University of Texas, University of Washington, and Woods Hole Oceanographic Institution) participated in the field work which was conducted from five research vessels (R/V Robert Conrad, R/V Kana Keoki, R/V Thomas Thompson, USNS De Steiguer, USNS Hayes). A total of 67 ocean bottom seismometers and hydrophones as well as several hydrophone arrays were deployed. A centralized data exchange system was established so that all the data from the experiment would be accessible to the participants and, eventually, the entire scientific community.

The main objective of this thesis is to determine the active tectonic regime of the Orozco transform fault as reflected by the seismic activity, and the primary data are the microearthquakes recorded by the ROSE network during Phase II. Because determination of earthquake source parameters and tectonic processes cannot be decoupled from the crustal structure, several data sets, from both natural and artificial sources, are also studied in an attempt to constrain the velocity structure of the crust and upper mantle throughout the transform zone.

In Chapter II, the tectonic setting and teleseismic history of the Orozco Fracture Zone are summarized. This chapter also contains a study of the source mechanism of one of the largest teleseismic events recorded from the fracture zone (m_b = 5.1). The transform region covers a 90 x 90 km area which includes ridges and troughs trending both parallel and perpendicular to the spreading direction. Because teleseismic earthquake locations are too imprecise to define the present plate boundary and magnetic anomaly data are too sparse to resolve the recent tectonic history, more questions are raised than are answered.

Chapter III contains an examination of the transfer function between seafloor motion and the data recorded by the MIT OBS. This study applies to the MIT OBS in general and is a prerequisite to the further study of the waveforms recorded by these instruments. It is important because the three-component, digitally recording MIT OBS with an externally deployed geophone package has the potential of recording data of a quality heretofore unattained with deep-sea OBS.

Chapter IV presents the earthquake locations calculated from travel times submitted by the different groups participating in the experiment. Fault plane solutions and seismic moments of some of the larger events are also presented. Project ROSE is unprecedented in the large number of ocean bottom stations deployed; the epicentral locations, focal depths, and source mechanisms are therefore unusually

well constrained and clearly define the active plate boundary. All calculations in this chapter are relative to a laterally homogeneous velocity structure; several observations, however, suggest the presence of lateral heterogeneity.

In Chapter V, several independent data sets are used to look at various aspects of the velocity structure in the transform zone. Incidence angles and azimuths of body waves from both shots and earthquakes show systematic deflections from the angles expected for a simple layered structure, thus signaling the presence of lateral velocity gradients. Structures which could explain these observations are examined by tracing rays through three-dimensional velocity models. Refraction profiles recorded by WHOI OBH are analyzed using both travel time inversion and synthetic seismogram techniques and a significant departure from "normal oceanic crust" is found to be correlated with topographic highs. Travel times from large shots recorded by the MIT and WHOI instruments are used to determine the upper mantle velocity. The effects of the inferred lateral velocity variations on the hypocenters and fault plane solutions of the previous chapter are discussed.

The last chapter summarizes the major points of the thesis.

FIGURE CAPTIONS

1.1 Geographic location of project ROSE.

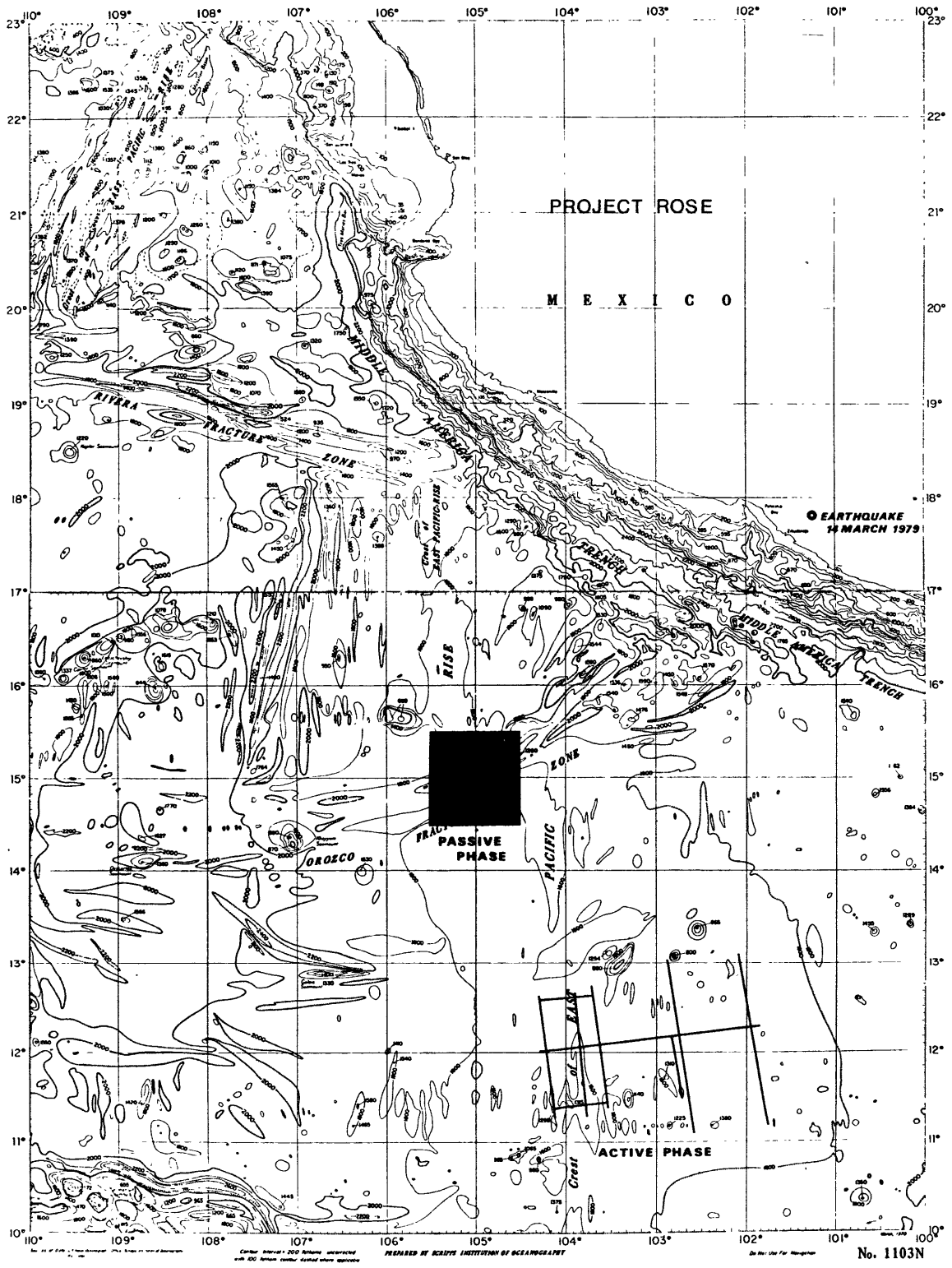
PROJECT ROSE
M E X I C O
EARTHQUAKE
14 MARCH 1979
PASSIVE
PHASE
ACTIVE PHASE
RIVERA
FRACTURE
ZONE
MIDDLE
AMERICA
TRENCH
RISE
OROZCO
PACIFIC
EAST
Crest
of
EAST PACIFIC RISE
No. 1103N

figure 1.1

CHAPTER II

TECTONICS AND TELESEISMIC HISTORY OF THE OROZCO FRACTURE ZONE

In this chapter, the tectonic history of the Orozco Fracture Zone is summarized, the bathymetry of the transform zone is examined, and the historic record of teleseismic earthquakes is compiled. The interpretation of the tectonic history is drawn primarily from Klitgord and Mammerickx (1982) and points out the changing configuration of the plate tectonic boundaries in the eastern Pacific Ocean during the past several million years. The detailed bathymetry of the transform zone suggests a complicated tectonic regime, but teleseismic earthquake locations are too imprecise to define the location of the active plate boundary over the past tens of years.

2.1 TECTONIC HISTORY OF THE OROZCO FRACTURE ZONE

At the present time, the Orozco transform fault* offsets the East Pacific Rise left laterally by approximately 90 km. The local spreading rate is 93 mm/yr (full rate) with an azimuth of N80°E. The pole of rotation is at 37.15° N, 107.88°

---

* Note: In accordance with commonly accepted nomenclature, the term "fracture zone" will be used throughout this thesis to refer to the entire physiographic feature and the term "transform fault" will be reserved for that portion of the fracture zone which links the two branches of the spreading center. According to the theory of rigid plate tectonics, seismic activity should be restricted to the transform fault zone.

with an angular rate of 2.21°/my (Klitgord and Mammerickx, 1982). This pole was determined from the width of the central anomaly along the Pacific-Cocos boundary and thus represents motion over the past 700,000 years. It is very similar to that obtained by Minster and Jordan (1978) (38.72° N, 107.39° W, 2.2°/my) from a data set containing spreading rates, fracture zone trends and earthquake slip vectors. The present maximum age contrast across the transform is less than 2 m.y.

Figure 2.1 places the Orozco Fracture Zone within the tectonic framework of the central eastern Pacific and shows the age of the seafloor as determined from magnetic anomalies. Because of the proximity to the pole of rotation, the spreading rate along the East Pacific Rise increases rapidly from north to south, the fracture zone exhibits a pronounced curvature, and the magnetic anomalies fan away from the axis.

The large scale topographic manifestation of the fracture zone belies its currently modest offset and is a reflection of its past tectonic role. Klitgord and Mammerickx (1982) have interpreted the complex bathymetric and magnetic patterns to the west of the present rise axis to be traces of an extinct spreading center. On the basis of this interpretation, a series of eastward jumps and reorientations of the spreading center are thought to have occurred in the past 15 m.y.; several other investigators had previously identified portions of this fossil system (e.g., Sclater et al., 1971; Handschumacher, 1976). The tectonic history proposed by Klitgord and Mammerickx is summarized in Figure 2.2.

According to their scenario, the Orozco Fracture Zone was the Rivera-Cocos plate boundary from the time of anomaly 5 through anomaly 3.

2.2 PHYSIOGRAPHIC DESCRIPTION OF THE OROZCO TRANSFORM FAULT

Most transform faults which have been studied in detail fall into one of two classifications on the basis of topography. The simplest are those which have a single well defined trough, often flanked by one or two narrow, shallow ridges running parallel to the trough (e.g., Vema Fracture Zone-Eittreim and Ewing, 1975; Oceanographer Fracture Zone-Fox et al., 1976; Kane Fracture Zone-Detrick and Purdy, 1980). More complicated transforms show two parallel troughs connected by a median ridge perpendicular to the troughs which in several cases has been identified to be a small spreading segment (e.g., Rivera Fracture Zone-Reid, 1976; Siqueiros Fracture Zone-Crane, 1976; Tamayo Fracture Zone-Kastens et al., 1979; CYAMEX scientific team, 1981; Gibbs Fracture Zone-Searle, 1981).

The topography of the Orozco transform fault (Figure 2.3) cannot be readily placed in either category. The transform fault is characterized by a 90 x 90 km zone in which the depth ranges from shallower than 1800m to deeper than 4000m. Figure 2.4 schematically illustrates the major topographic features and defines the nomenclature used to refer to these features throughout this thesis. A deep, narrow east-west trending trough forms the northern boundary of the transform (trough

A). The central part is characterized by two broad, shallow north-south trending ridges separated by a trough (ridges α and β and trough C). This system extends to the south parallel to the present axis of the East Pacific Rise. Ridge β is bisected by a northwest-southeast trending trough which joins the southern branch of the East Pacific Rise (trough B); the extensions of ridges α and β to the north of trough C are distinguished by α' and β'. Regions 1 and 2 refer to seismic groupings discussed in Chapter IV. In an attempt to determine whether ridges α and β and trough C represent a short spreading segment with an axial valley and flanking highs, topographic and magnetic anomaly profiles were collected across these features. The track lines (oriented approximately perpendicular to the East Pacific Rise) are displayed in figure 2.5a, bathymetric profiles are shown in figure 2.5b, and magnetic anomaly profiles are shown in figure 2.5c. Unfortunately, the existence of ridges α and β and trough C was not known when the experiment was being conducted and few bathymetric and magnetic survey lines were long enough or oriented appropriately to address this question.

Comparing bathymetric profiles A and B to G, I, K and L, we see that to the north of the transform the topography is very rough and shallow; to the south, the East Pacific Rise shows the low amplitude topography characteristic of a fast spreading rate (Shih, 1979). The anomalously shallow depth to the north of the transform continues to about 16°N where the East Pacific Rise resumes a "normal" profile (Klitgord and

Mammerickx, 1982). Profiles D and E show the transition from the rough topography of ridges α and β, which resembles that of profiles A and B, to the smooth crust recently formed at the East Pacific Rise. A narrow trough can also be noted at the boundary between the two types of crust. Similar troughs were found by Klitgord and Mammerickx (1982) to the west of the East Pacific Rise at the boundary between different age crust formed at different spreading centers.

In Figure 2.5c, profile K appears to show symmetric magnetic anomalies from the central anomaly through what is tentatively identified as anomaly 2. The central anomaly through anomaly 2 are also seen in profiles H and L, on the east and west flanks of the East Pacific Rise, respectively; on H, however, the distance between 1 and 2 is much less than on K. Profiles E and F extend onto ridge β. On profile F, anomaly J can also be clearly identified, implying that ridge β was formed along the present East Pacific Rise crest. Because of possible navigation errors, however, profile F might actually be further south. On profile E, the polarity reversal defining the edge of the central anomaly is not clear and identification of anomaly J is uncertain. A profile extending further to the west would be required to make a definitive identification.

Several SEABEAM lines have also been recorded across the Orozco Fracture Zone and East Pacific Rise in this area (J. Francheteau, personal communication, 1981). With SEABEAM, a contour map approximately 2 km wide is obtained directly from

a single line. Ideally, the region of interest is covered by parallel, overlapping lines; interpretation of a single line is limited. We can, however, observe lineations in the topography if a few directions are dominant. The location of the lines and the observed lineations are shown in Figure 2.6. Where no direction is indicated, no predominant lineations were observed. The shaded areas are regions of unusually smooth topography. The most striking features are the scarps parallel to the spreading axis in crust formed along the East Pacific Rise. Along profile A, a single scarp can be traced for at least 10 km. From these observations we can identify crust formed at relatively undisturbed portions of the spreading center. Features trending 80° to 90° NE are observed in trough A and at the eastern end of trough B. Few systematic trends are observed over ridges α, α', β and β' or in the old fracture zone.

These data are incorporated into the map of Klitgord and Mammerickx (1982) in Figure 2.7. The dotted lines indicate the location of data used in constructing this map. The additional data are denoted by dashed lines. Between the Orozco Fracture Zone and 14°N, we note a pronounced asymmetry in the magnetic anomalies since the time of anomaly 2. This pattern suggests an eastward shift of the spreading center. The offset of the central anomaly along offset B and the progressive rapproachment of J and 2 to the east are constrained by lines H and M. The interpretation of symmetric anomalies along profile K in figure 2.5c is not consistant

with this pattern which predicts that the distance from anomaly J to anomaly 2 should be less toward the east than toward the west. The interpretation of a complete central anomaly along profile E must also be questioned; what appears to be the eastern edge of the central anomaly may actually be anomaly J or 2. Without more data to the east and west along profiles K and E, we cannot determine which interpretation is correct. A few minor changes in the map which are imposed by the data presented above are marked by arrows: Profile E indicates that anomaly J should not be explicitly extended so far north and the lineations observed in the SEABEAM data suggest that the trace of the old fracture zone to the east of the present transform zone should be further north. These changes do not contradict any data from which Fig. 2.1 was originally constructed.

Questions that arise from this figure are: Where is the trace of the active plate boundary as defined by the seismicity and is it a narrow or a diffuse zone? What is the origin of ridges α and β and do they represent current or relict tectonic features? What is the recent history of the present plate tectonic configuration of the transform zone? These questions will be addressed directly or indirectly throughout this thesis.

2.3 TELESEISMIC HISTORY OF THE OROZCO FRACTURE ZONE

All earthquakes listed in the NOAA earthquake data file (1838-1963) or the ISC bulletin (1964-1979) with epicenters between 13° N and 17° N and 103° W and 107°W are compiled in Table 2.1. Most of these epicenters, especially since the inception of the WWSSN, actually fall between 14° N and 16° N, 104° W and 106° W and are clearly associated with the Orozco Fracture Zone. That several of the others were probably also associated with the Orozco Fracture Zone is suggested by calculated locations between 13° N and 14° N or 16° N and 17° N for events that appear to be foreshocks or aftershocks of Orozco Fracture Zone events (e.g., September 24, 1965; May 24, 1974). Note, also, that two of the largest events ever recorded from the Orozco (m_b=5.1) occurred in October, 1978, approximately four months before the ROSE experiment. No teleseismic earthquakes were detected during ROSE.

The epicenters from Table 2.1 are plotted in Figure 2.8. Although many are aligned along a general east-west trend in the northern part of the transform, the epicenters are quite scattered. Because most of these events were located using only a few readings from a narrow azimuthal range, the calculated locations probably have errors of tens of kilometers and are not accurate enough to delineate the active plate boundary. No particular pattern of temporal migration along the transform can be discerned for the period 1961-78, nor are any conspicuous quiet zones observed (Figure 2.9).

Figure 2.10 is a plot of log(N) vs. m_b where N is the number of earthquakes with magnitude greater than or equal to m_b. Two curves are shown: the first includes all events in Table 2.1 since 1964; the other includes only those events located between 15° N and 16° N, 104° W and 106° W. For $m_b < 4.2$, both curves level off suggesting incomplete sampling of the seismicity; for $m_b > 4.2$ the b values* are 1.40 ± .09 and 1.15 ± .09, respectively. The value of 1.15 is similar to that found by Francis (1968) for other transform faults and the value of 1.4 is intermediate between the b value for spreading centers (1.7) and that for transforms. High b values, reflecting an abundance of small events, are generally associated with low stress volcanic environments (Wyss, 1973). A possible explanation for the lower b value observed with the restricted data set is that two populations of earthquakes are being sampled, one with a high b value and scattered locations and the other with epicenters along trough A (Figure 2.4) and a lower b value. Alternatively, the difference is probably at least partly due to an increasing degree of mislocation for smaller events. Extrapolating from the curves in figure 2.10 implies 20 to 225 events per day with $m_b > 1$.

The maximum magnitude observed (m_b=5.1) since 1964 is also rather modest and probably does not represent slip along the entire transform during a single event. Only two pre-WWSSN magnitude determinations are available from the

---

* Defined by $\log(N) = c - b \cdot m_b$ where N is the number of events with magnitude $\geq m_b$ and c and b are constants.

literature: a magnitude of 6.0 for an event in 1931 (Gutenberg and Richter, 1954) and a magnitude of 6.2 for an event in 1955 (Rothe, 1969). These magnitude values are not directly comparable to m_b but are probably similar to M_S determined from 20 second surface waves recorded on the WWSSN long period seismometers (Geller and Kanamori, 1977). The relationship between m_b and M_S has been found to vary with geographic province (Liebermann and Pomeroy, 1969). From Tsai (1969), $M_S \simeq 1.64m_b - 3.35$ for 14 earthquakes along East Pacific Rise transform faults ($5 \leq m_b \leq 7$) ; Reichle (1975) found $M_S \simeq 1.69m_b - 3.49$ for earthquakes in the Gulf of California ($4 \leq m_b \leq 5.5$). In the magnitude range $4.2 < m_b < 5.1$ these two relations yield essentially the same M_S for a given m_b. For $M_S=6.0$, $m_b=5.6$ from Reichle (1975) or $m_b=5.7$ from Tsai (1969) indicating that the Orozco Fracture Zone may have been the site of larger earthquakes in the recent past.

A more fundamental measure of earthquake size than magnitude is the seismic moment (Aki, 1966):

$$M_o = \mu L w d \qquad (2.1)$$

where μ is the shear modulus, L is the fault length, w is fault width, and d is the displacement. The moment can be measured from the excitation of long period waves (wavelength >> dimensions of source). Seismic moments were estimated by combining the $m_b - M_S$ relation of Reichle (1975) with the $M_S - M_o$ relation determined empirically by Brune (1968) for

earthquakes in the Imperial Valley of California ($\log(M_0) = M_S + 19.2$) and which should apply for $M_S \leq 6$ (Aki,1972). Burr and Solomon (1978) found that this M_0-M_S relationship agreed with data from oceanic transform fault earthquakes for which M_0 had been determined independently. Combining the m_b - M_S and M_0 - M_S relations gives:

$$\log(M_0) = 1.69m_b + 15.71 \qquad (2.2a)$$

$$N = AM_0^B \qquad (2.2b)$$

where $A=10^{(c+15.71b)/1.69}$ and $B=b/1.69$. Errors related to these estimates have been discussed by Brune (1968) and Reid (1976) and may be as large as a factor of 5 for individual events. For the January 31, 1975 event ($m_b=5.1$), however, equation 2.2a indicates a moment of 2.1×10^{24} dyne-cm which agrees well with the double couple moment of 2.3×10^{24} dyne-cm obtained from an inversion of the surface wave data as described below. Figure 2.11 shows the cumulative moment from 1964 to 1979 as estimated from equation 2.2. We can see a quiet period from 1968 to 1973 and an apparent sharp increase in the moment rate from 1974 to 1978. Most of this is due to the three $m_b=5.1$ events of 1975 and 1978. With our small data sample, a mistake in the magnitude of even one event (not unheard of in the ISC bulletin) would affect the slope of the curve considerably.

Given the length of the transform fault and the spreading rate, we can estimate the width of the seismic zone from the sums of the moments of all earthquakes during a time period

long enough to represent movement along the entire fault and assuming that all slip is seismic (Brune, 1968):

$$W = \Sigma M_0/(\mu LVT) \tag{2.3}$$

where V is slip rate, T is the time period over which the sum is taken, L is transform length and W is width. Evidence as to whether the period from 1964 to 1979 is adequate for this estimate is ambiguous. The scattering of earthquake epicenters throughout the transform zone and a level of activity showing several peaks during the period of observation suggest that the transform has been active along its entire length, whereas the change in the moment rate with time and the recording of earthquakes with magnitudes > 5.1 prior to 1964 suggest that one full cycle of activity may not yet be complete.

For all events in Table 2.1 since 1964 with $m_b \geq 4.2$, the moment rate is 0.94×10^{24} dyne-cm/yr; for only those events between 15° N and 16° N, 104° W and 106° W, it is 0.75×10^{24} dyne-cm/yr. We can estimate the fraction r of total moment due to events with $m_b < 4.2$ ($M_0 < 2.45 \times 10^{22}$) from the observed b value following Reid (1976) (see also Wyss, 1973). The total moment due to earthquakes with $M_1 \leq M_0 \leq M_2$ is:

$$\sum M_0 = \int_{N(M_2)}^{N(M_1)} M_0 dN = \int_{M_1}^{M_2} BAM_0^{-B} dM_0 \tag{2.4a}$$

and the fraction of the total moment due to earthquakes with $M_0 \leq M_1$ is:

$$r < \int_0^{M_1} / \left(\int_{M_1}^{M_2} + \int_0^{M_1}\right) = (M_1/M_2)^{(1-B)} \qquad (2.4b)$$

where M_1 is the smallest moment included in the sum, M_2 is the largest, and B is the slope of log(N) vs. log(M_0) (assuming that B is a constant not equal to 1). For b=1.4, B = 0.83 and r = 0.40 giving a total moment rate of 1.32×10^{24} dyne-cm/yr. The assumption of a constant B may not, however, be valid. In chapter 4.8, B=0.5 is found for the microearthquakes located during ROSE ($M_0 < 10^{22}$) ; this implies r=0.1 and a moment rate of 1.17×10^{24} dyne-cm/yr. Adding the 1931 and 1955 events to the moment sum (moments of 15.8×10^{24} and 25.1×10^{24} dyne-cm) and taking T from 1931 to 1979, a moment rate of 1.27 dyne-cm/yr is obtained.

For V=9.3 cm/yr, L=92 km (the total logitudinal distance between the north and south branches of the East Pacific Rise), and $\mu=3.3 \times 10^{11}$ dyne/cm^2, we obtain an effective fault width of only 0.43 to 0.48 km. Similar studies by Brune (1968), Reichle (1975), Reid (1976) and Burr and Solomon (1978) found widths of 0.04 to 6.5 km for most oceanic transform faults. The possible error on the moment rate determination has already been discussed. A related error source is the spreading rate which was determined from magnetic anomaly data (Klitgord and Mammerickx, 1982) and represents an average over 700,000 years (the width of the central anomaly). This slip rate may not be applicable for a time scale measured in decades. The value of μ assumed is appropriate for most oceanic rocks but is twice that

appropriate for hydrated serpentinite (μ=1.6 x 10^{11} dyne/cm^2) which may be a major component of fracture zone crust (Christensen, 1972). Considering these various errors, the estimate of 0.47 km for the width of the seismic zone may be in error by as much as an order of magnitude and does not necessarily indicate a major component of aseismic slip. It does indicate, however, that the average width of the seismic zone is at most a few kilometers.

2.4 SOURCE MECHANISM OF THE JANUARY 31, 1975 EARTHQUAKE

Figure 2.12 shows the fault plane solution from first motion polarities for the m_b=5.1 earthquake of January 31, 1975. Although the dip of the nodal planes is not well constrained, the solution clearly is compatible with right lateral strike-slip motion along a fault striking 75°-80° NE. In order to determine the depth and moment of the event, data from the vertical component of the Rayleigh wave were inverted to obtain the source moment tensor (Gilbert, 1970; McCowan, 1976; Mendiguren, 1977; Patton, 1980). The technique employed here has been described in detail in the paper by Trehu et al. (1981), included in this thesis as Appendix I. The stations used in the surface wave analysis are listed in Table 2.2 and displayed in Figure 2.13. The azimuthal distribution is poor, with stations available over a range of only 154° in azimuth, and many of the earthquake-station paths cross several complicated structural provinces at highly oblique angles. This results in multipathing and focusing of

surface wave energy which distorts the observed amplitude and phase radiation patterns so that the corrections described in Appendix I do not retrieve the true source radiation pattern. Moving window analysis of the data (Landisman et al., 1969) revealed that data from stations in the eastern United States were indeed contaminated, especially for periods less than about 30 seconds. Samples of data are shown in Figure 2.14.

Input data for the inversion are the real and imaginary parts of the source spectrum as functions of azimuth and period. For a given depth, the moment tensor components can be retrieved by a one-step linear inversion. Depth is determined by performing the inversion at a series of depths and choosing that which produces the smallest residual. Because of the behavior of the excitation functions with depth and frequency, most of the resolving power of the inversion resides in the real part of the spectrum.

As discussed in Appendix I, a major drawback in applying the moment tensor inversion technique to a single isolated event is the requirement that phase velocities along the earthquake-station path be known very precisely in order to obtain the source phase from the observed phase. Moreoever, for a very shallow source the behavior of the excitation functions for the vertical component Rayleigh wave as a function of depth and period is such that any errors in the data will be magnified in the M_{xy} and M_{xz} components of the moment tensor which are obtained from the imaginary part of the spectrum (see Appendix I for a more detailed discussion of

the resolving power of the inversion). For very shallow sources, when faced by imperfect data, it may be necessary to constrain the imaginary part of the source spectrum to be zero; this is equivalent to constraining the principal axes of the moment tensor to be either horizontal or vertical corresponding to a double couple fault mechanism of either pure dip-slip with a dip of 45° or vertical strike-slip. The source phase radiation patterns of these mechanisms are illustrated in Figure 2.15.

Since all previous detailed studies of transform fault earthquakes have indicated very shallow source depths (e.g. Tsai, 1969; Weidner and Aki, 1973), we began by assuming that the earthquake of January 31, 1975 was probably also very shallow and inverted the amplitude radiation pattern assuming a vertical, right lateral strike-slip fault. Stations in the northeast quadrant were assigned an initial phase of 0.5 cycles and stations in the southeast quadrant a phase of 0.0 cycles. Whether the phase at station TUC, which falls on a nodal plane of the fault plane solution, is 0.0 or 0.5 cycles does not affect the solution significantly. Figure 2.16 shows the residuals as a function of depth and indicates a shallow source at 0 to 7 km below sea floor. In this case, the additional work of correcting the observed phase back to the source would probably not improve the resolution of the moment tensor components.

The results of the inversion at a depth of 3 km below sea floor are displayed in Table 2.3. The orientation of the axes

for solutions at depths in the neighborhood of 3 km is stable, with scalar moment increasing gradually with depth as expected. The orientation of the axes indicates right lateral strike slip along a plane with a strike of about N 76° E. Note, however, the large non-double component in the solution and the apparently very good resolution of the moment tensor components. This is probably an artifact induced by noise in the data combined with poor azimuthal distribution. Figure 2.17 shows the fit of the solution to the data. The amplitudes in the northeast quandrant are systematically greater and more scattered than those in the southeast quandrant. Although this could be due to a dip of the fault plane and/or a dip-slip component in the source, we have already seen from the moving window analysis that these stations also appear to be more contaminated by structural effects along the path. The offset of the sinusoidal curve fit to the data is manifested as a non-double component in the solution when the solution is constrained to have vertical and horizontal axes. Were data available from a broader range of azimuths, the "fit" to the data would appear less good unless the noise had the same azimuthal variation as the source radiation pattern. (See Romanowicz, 1982, for a detailed study of the effects of various noise sources on the moment tensor inversion.) Because of the poor distribution of data and the apparent shallow source depth, no significance can be attributed to the presence of a non-double couple component in the source.

To further constrain the source depth would require extending the analysis to shorter period data which would further reduce the azimuthal distribution of data. In Figure 2.18 the amplitude spectrum of the Rayleigh wave to periods of 10 seconds at station QUI is compared to spectra calculated by Tsai (1969) for a vertical strike-slip fault at various depths in an oceanic model. Several other South American stations showed similar spectra. This figure indicates that the source was probably shallower than about 3-5 km. Because of uncertainties in water depth, attenuation along the path, and a possible dip-slip component in the source, the depth can not be determined more precisely. In general, higher frequency body waves are more appropriate for studying details of the source mechanism such as depth and fault dimensions; for this event, however, the body wave amplitudes were too small to justify modeling by synthetic seismograms.

2.5 SUMMARY

The bathymetric and magnetic anomaly patterns of the central eastern Pacific indicate a number of reorganizations of the plate boundaries in the past 15 million years and the bathymetry of the Orozco Fracture Zone probably reflects this history. Unfortunately, the available magnetic anomaly data are inadequate for reconstructing the detailed history of the fracture zone for the last few million years. The present transform zone is a 90 km x 90 km square of dramatic topography with features trending both parallel and

perpendicular to the spreading direction. The current zone of transform activity is not clearly delineated in the bathymetry and epicenters of teleseismically recorded earthquakes are too scattered to constrain the locus of seismic activity. The moment sum for teleseismic earthquakes from 1964 to 1979 indicates an average width of the seismic zone of only 0.47 km, but this estimate may be in error by up to an order of magnitude. A detailed study of the body and surface waves from one of the larger of these earthquakes (m_b = 5.1) indicates right-lateral strike-slip motion along a nearly vertical fault plane with a strike of about N75°E and a focal depth of less than 5 km.

TABLE 2.1

Teleseismic Earthquakes in the Orozco Fracture Zone*

year	origin time mon	day	hr	min	sec	lat. (°)	long. (°)	depth (km)	m_b	number of stations
1931	1	25	12	34	24	15	105	0	6.0	-
1932	8	24	3	40	6	17	104	0	-	-
1933	5	8	18	1	6	17	103	0	-	-
1934	2	14	22	18	12	17	106	0	-	-
1934	6	22	18	33	30	17	106	0	-	-
1934	8	28	11	23	0	17	106	0	-	-
1935	9	10	7	5	12	17	107	0	-	-
1936	12	25	20	3	54	16	105	0	-	-
1937	2	22	1	18	24	17	104	0	-	-
1937	12	22	3	37	12	17	107	0	-	-
1952	7	15	19	3	35	13.8	104.6	0	-	-
1954	5	12	5	11	34	15.5	106.3	0	-	-
1954	5	12	8	7	40	15.5	106.3	0	-	-
1955	1	20	3	48	52	15.5	104.4	0	6.2	-
1955	2	1	14	11	47	15.6	103.1	0	-	-
1956	4	25	17	2	14	13.0	103.2	0	-	-
1961	7	3	12	15	27	15.3	104.6	25	-	-
1961	12	8	7	57	53	15.3	104.7	33	-	-
1962	3	5	1	50	59	16.8	105.0	33	-	13
1962	6	29	22	35	21	15.3	105.2	33	-	12
1963	5	23	18	21	18	14.5	105.2	33	-	10
1964	3	23	6	12	31	16.6	105.1	33	3.9	11
1964	4	10	10	00	42	16.5	104.6	33	3.7	8
1964	7	27	06	27	53	16.8	104.9	33	3.9	5
1965	4	13	20	43	02	15.4	104.7	33	4.2	19
1965	4	13	22	37	21	15.4	104.7	33	4.3	12
1965	9	24	3	9	28	14.2	106.3	33	3.8	9
1965	9	24	3	33	45	15.4	105.5	33	4.5	22
1965	9	24	3	57	20	14.4	105.3	33	4.0	9
1966	1	17	6	12	11	15.6	104.5	33	4.2	14
1966	3	11	1	32	32	15.4	104.5	53	4.8	38
1966	3	11	9	49	38	15.6	104.3	33	4.6	46
1966	6	16	8	59	35	15.6	104.4	33	4.2	19
1966	6	16	10	14	11	15.6	104.2	33	4.4	41
1966	10	13	2	38	02	15.2	105.6	33	4.2	20
1967	9	25	9	49	41	15.6	105.0	33	4.0	20
1968	1	20	21	41	10	16.2	105.3	51	4.8	66
1968	11	23	4	20	29	15.2	105.4	33	4.3	26
1970	2	3	08	59	36	14.2	105.1	33	4.0	4
1970	6	3	18	35	34	15.0	104.9	33	4.3	9
1970	6	3	20	57	15	15.8	104.7	33	4.3	32
1970	7	27	2	12	07	13.5	104.9	33	4.1	4
1970	10	26	5	41	17	14.8	105.1	33	4.2	4
1972	12	15	02	21	04	14.7	104.4	0	4.0	9

TABLE 2.1 (cont'd.)

year	origin time mon	day	hr	min	sec	lat. (°)	long. (°)	depth (km)	m_b	number of stations
1973	3	8	21	16	06	16.7	104.5	33	4.0	10
1973	4	9	05	25	36	16.0	105.2	0	4.0	4
1973	6	10	12	39	19	14.4	105.4	33	4.3	10
1973	11	8	22	52	20	16.9	106.1	0	4.3	9
1973	12	14	7	5	15	15.2	105.6	0	4.4	10
1973	12	20	14	05	37	16.4	105.8	0	4.4	6
1974	3	31	7	42	00	14.7	105.7	33	4.5	12
1974	5	24	11	33	8	15.3	104.9	33	4.2	17
1974	5	24	12	26	18	13.4	105.5	0	4.2	4
1974	5	30	3	30	48	15.2	105.0	33	4.2	17
1974	8	13	8	51	37	15.5	105.0	0	-	4
1974	12	14	17	29	35	15.6	105.4	0	4.6	10
1975	1	31	16	14	32	15.4	104.8	44	5.1	41
1975	1	31	18	51	58	15.6	104.6	110±21	4.4	13
1975	9	30	6	4	53	14.7	105.0	33	4.5	7
1975	10	23	12	6	24	15.6	104.4	33	4.4	7
1976	3	14	20	13	56	14.9	104.7	33	4.7	34
1976	4	7	23	49	20	14.1	104.0	24	-	6
1976	8	30	9	42	52	15.2	104.4	33	4.6	16
1976	12	2	11	19	53	16.5	104.2	33	-	-
1977	2	3	3	0	41	14.6	104.1	33	-	-
1977	8	13	0	16	41	15.1	104.7	33	4.6	13
1978	7	17	05	50	57	16.3	103.0	33	4.5	12
1978	9	7	3	46	45	14.9	105.9	33	4.6	9
1978	9	7	5	55	52	15.4	105.3	33	4.7	10
1978	10	13	9	5	45	15.0	104.8	33	4.5	9
1978	10	22	14	7	1	15.3	104.5	38±8.5	5.1	112
1978	10	22	14	17	15	15.4	104.5	33	5.1	83
1979	3	14	14	5	2	15.7	104.6	0	-	6
1979	6	23	09	10	52	16.1	104.5	44	4.3	15

* Earthquake parameters are from the NOAA Earthquake Data File for events before 1964 and are from the Regional Catalogue of Earthquakes of the International Seismological Center for events since 1964. The magnitudes for the 1931 and 1955 events are from Gutenberg and Richter (1954) and Rothé (1969) respectively (see text).

TABLE 2.2 Stations Used in the Surface Wave Analysis of the January 31, 1975 Earthquake on the Orozco Fracture Zone.

Station	Azimuth (degrees)	Distance (degrees)	Period (seconds)
ALQ	-4.2	19.6	22-50
ATL	42.1	25.8	30-50
BHP	101.6	25.4	22-50
BLA	40.2	30.7	30-50
BOG	106.3	32.0	26-50
CAR	92.8	37.1	22-50
GIE	137.0	21.5	22-50
JCT	16.0	15.7	22-50
LPS	92.0	15.1	22-50
LUB	7.7	18.4	22-50
OGD	39.6	36.6	30-50
OXF	33.2	23.6	30-50
QUI	118.4	30.2	22-50
TUC	-17.0	17.8	22-50

TABLE 2.3 Results of the Moment Tensor Inversion for the January 31, 1975 Event for a Depth of 3 km Below Sea Floor

	(a)	(b)	(c)
	moment tensor components ($\times 10^{24}$ dyne-cm)		
M_{xx}	-1.27±0.07	-1.25±2.23	-1.18±0.07
M_{xy}	2.92±0.07	2.92±0.15	3.08±0.08
M_{yy}	1.96±0.07	1.98±2.17	1.76±0.07
M_{xz}	---	---	---
M_{yz}	---	---	---
M_{zz}	-0.69±0.06	-0.60±10.3	-0.59±0.06
	eigenvalues ($\times 10^{24}$ dyne-cm)		
Tension	3.68±.09	3.70±1.72	3.71±0.09
Intermediate	-0.69±.06	-0.60±10.30	-0.59±0.06
Compression	-2.99±.09	-2.97±1.75	-3.12±0.09
	eigenvectors (strike/dip)		
Tension	31/0	31/0	32/0
Intermediate	0/180	0/180	0/180
Compression	-59/0	-59/0	-58/0
	components of source (percent)		
Double couple	63	62	68
CLVD	37	34	32
Explosion	-	4	-
	double couple scalar moment ($\times 10^{24}$ dyne-cm)		
	2.3	2.3	2.5

a) initial phase at TUC = π radians; $\Sigma M_{ii} = 0$.
b) initial phase at TUC = π radians.
c) initial phase at TUC = 0 radians; $\Sigma M_{ii} = 0$.

FIGURE CAPTIONS

2.1 Tectonics of the eastern Pacific (from Klitgord and Mammerickx, 1982).

2.2 Plates and plate boundaries for the eastern equatorial Pacific (from Klitgord and Mammerickx, 1982).

2.3 Offset of the East Pacific Rise by the Orozco Fracture Zone (Mammerickx, 1980). Contours are in corrected meters; the contour interval is 100m. The axis of the East Pacific Rise to the north and south of the fracture zone is at longitudes of 105°20'W and 104°20'W, respectively.

2.4 Schematic map pointing out the major topographic features in the Orozco Fracture Zone and defining the nomenclature used throughout this thesis. The 3000 km contour from Figure 2.3 is included. The location of the rise axis was determined from magnetic anomalies (Klitgord and Mammerickx, 1982).

2.5 a. Track lines for bathymetric and magnetic anomaly profiles displayed in Figure 2.5b and c. Most profiles were collected by the R/V Conrad or R/V Kana Keoki during ROSE; profiles F, H and J are from Klitgord and Mammerickx (1982).

b. Bathymetric profiles across the East Pacific Rise. The horizontal line on the profiles indicates a depth of 3 km. The arrows mark the location of the axial anomaly. The location of the axis to the north of the Orozco Fracture Zone, 105°N20'W, was determined by extrapolation from profiles in Klitgord and Mammerickx (1982).

c. Magnetic anomaly profiles across the East Pacific Rise. The horizontal line indicates 0γ. The arrows mark the location of the axial anomaly. The central anomaly, "J" anomaly and anomaly "2" are also indicated.

2.6 Dominant lineations observed on the SEABEAM profiles across the Orozco Fracture Zone and East Pacific Rise plotted along the track line.

2.7 Enlargement of Figure 2.1 in the neighborhood of the Orozco transform fault. Dotted lines show location of data from which Figure 2.1 was constructed; dashed lines indicate additional data discussed in text. Arrows show changes suggested by additional data.

2.8 Epicenters of teleseismically recorded earthquakes along the Orozco Fracture Zone for the period 1931 to 1979.

2.9 Longitude vs. time for teleseismically recorded earthquakes along the Orozco Fracture Zone. No systematic temporal or spatial pattern of activity can be resolved.

2.10 Plot of log(N) vs. m_b for Orozco Fracture Zone earthquakes. N is the number of earthquakes with magnitude $\geq m_b$. The solid dots correspond to the dataset of all earthquakes with epicenters between 14°N and 16°N, 104°W and 106°W; the open triangles correspond to earthquakes between 15°N and 16°N, as described in the text.

2.11 Cumulative moment vs. time for teleseismically recorded earthquakes on the Orozco Fracture Zone. The two curves correspond to the two data sets described in Figure 2.10.

2.12 Fault plane solution for the January 31, 1975, earthquake on the Orozco Fracture Zone. Filled circles represent compressional first arrivals; open circles represent dilitations.

2.13 WWSSN stations used for surface wave analysis of January 31, 1975, earthquake. The star represents the epicenter.

2.14 a. Examples of results of the moving window analysis. The letters and numbers represent steps of 1 dB in energy, normalized to the maximum energy (z) at each period. Contours are drawn at 2 dB and 4 dB down from maximum. The vertical lines indicate the period range used for the inversion. Note the loss of energy in the fundamental mode at periods shorter than about 28 seconds for station BLA.
b. Amplitude spectra for the stations in 2.14a.

2.15 Phase radiation pattern (in cycles) for a pure dip-slip fault with a dip of 45° or a vertical strike-slip fault. A factor of 0.125 cycles has been added to the initial phase which includes the effects of a Heaviside source-time function and the asymptotic expansion of the Hankel function (see Appendix I).

2.16 Residual vs. focal depth for the moment tensor inversion of the Rayleigh wave radiation pattern for the January 31, 1975 event.

2.17 Examples at several periods of the fit of the moment-tensor solution to the observed data for solution (a) in Table 2.3.

2.18 Amplitude spectrum at station QUI compared to spectra calculated for vertical strike-slip sources at several depths in an oceanic model. The calculated spectra are from Tsai (1969).

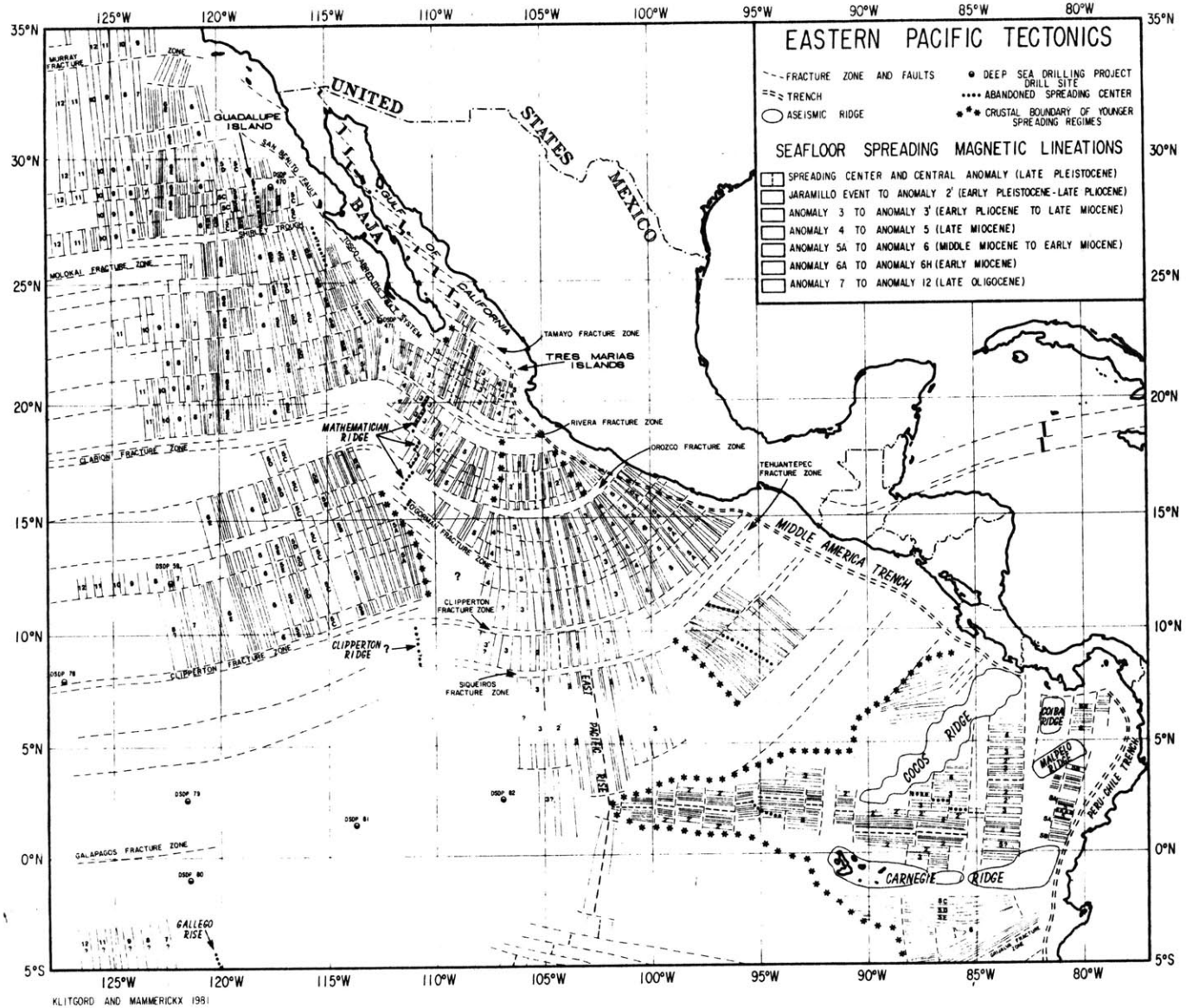
EASTERN PACIFIC TECTONICS
FRACTURE ZONE AND FAULTS
TRENCH
ASEISMIC RIDGE
DEEP SEA DRILLING PROJECT DRILL SITE
ABANDONED SPREADING CENTER
CRUSTAL BOUNDARY OF YOUNGER SPREADING REGIMES
SEAFLOOR SPREADING MAGNETIC LINEATIONS
SPREADING CENTER AND CENTRAL ANOMALY (LATE PLEISTOCENE)
JARAMILLO EVENT TO ANOMALY 2' (EARLY PLEISTOCENE-LATE PLIOCENE)
ANOMALY 3 TO ANOMALY 3' (EARLY PLIOCENE TO LATE MIOCENE)
ANOMALY 4 TO ANOMALY 5 (LATE MIOCENE)
ANOMALY 5A TO ANOMALY 6 (MIDDLE MIOCENE TO EARLY MIOCENE)
ANOMALY 6A TO ANOMALY 6H (EARLY MIOCENE)
ANOMALY 7 TO ANOMALY 12 (LATE OLIGOCENE)
UNITED STATES
MEXICO
GULF OF CALIFORNIA
BAJA
GUADALUPE ISLAND
TRES MARIAS ISLANDS
TAMAYO FRACTURE ZONE
RIVERA FRACTURE ZONE
OROZCO FRACTURE ZONE
TEHUANTEPEC FRACTURE ZONE
MATHEMATICIAN RIDGE
CLARION FRACTURE ZONE
CLIPPERTON FRACTURE ZONE
CLIPPERTON RIDGE
SIQUEIROS FRACTURE ZONE
MIDDLE AMERICA TRENCH
COCOS RIDGE
CARNEGIE RIDGE
GALAPAGOS FRACTURE ZONE
GALLEGO RISE
PERU-CHILE TRENCH
KLITGORD AND MAMMERICKX 1981

figure 2.1

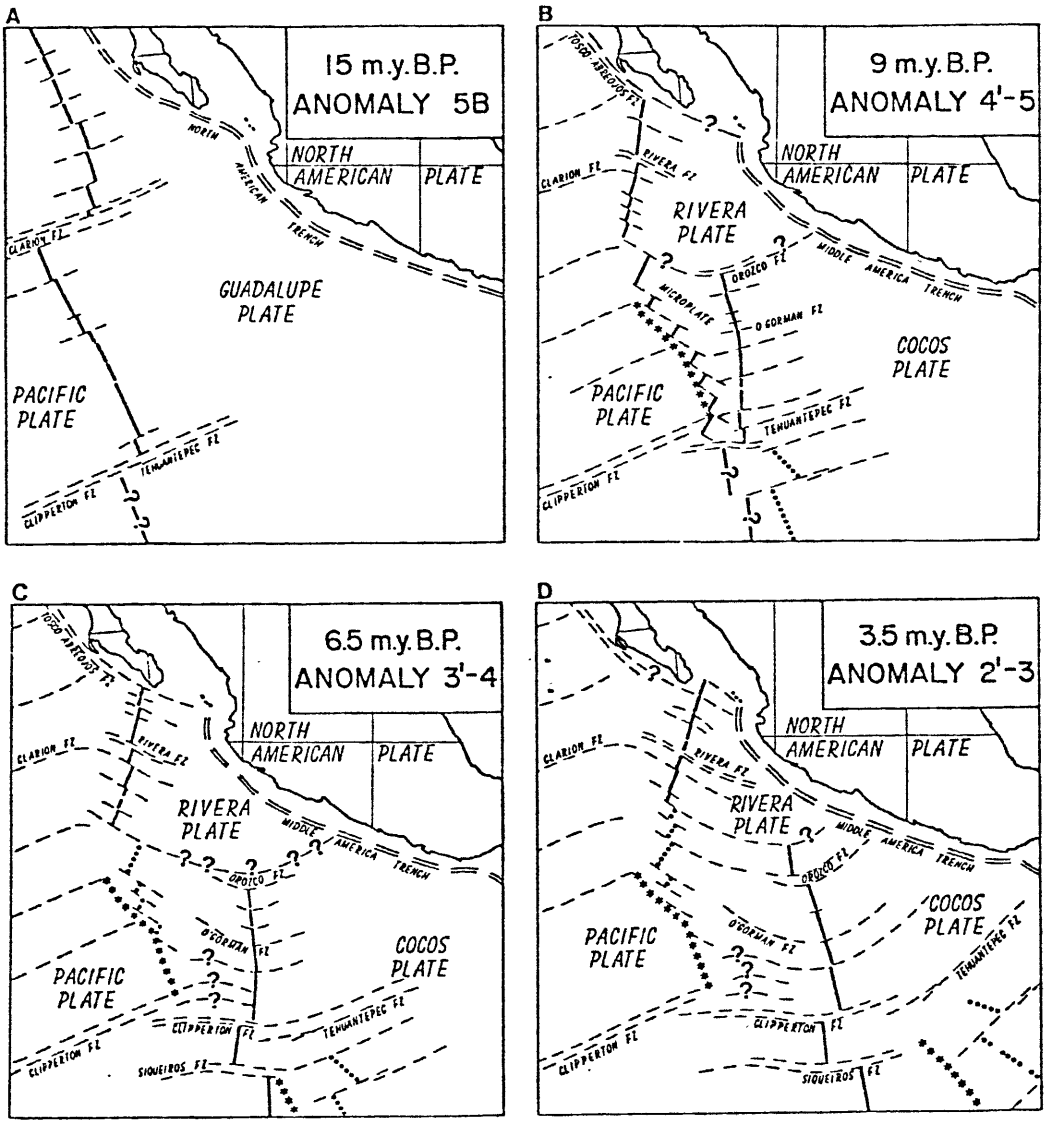
A
15 m.y.B.P.
ANOMALY 5B
NORTH AMERICAN PLATE
NORTH AMERICAN TRENCH
GUADALUPE PLATE
PACIFIC PLATE
CLARION FZ
TEHUANTEPEC FZ
CLIPPERTON FZ
B
9 m.y.B.P.
ANOMALY 4'-5
TOSCO-ABREOJOS FZ
CLARION FZ
RIVERA FZ
NORTH AMERICAN PLATE
RIVERA PLATE
OROZCO FZ
MIDDLE AMERICA TRENCH
MICROPLATE
O GORMAN FZ
COCOS PLATE
PACIFIC PLATE
TEHUANTEPEC FZ
CLIPPERTON FZ
C
6.5 m.y.B.P.
ANOMALY 3'-4
TOSCO-ABREOJOS FZ
CLARION FZ
RIVERA FZ
NORTH AMERICAN PLATE
RIVERA PLATE
MIDDLE AMERICA TRENCH
OROZCO FZ
O'GORMAN FZ
COCOS PLATE
PACIFIC PLATE
CLIPPERTON FZ
TEHUANTEPEC FZ
SIQUEIROS FZ
D
3.5 m.y.B.P.
ANOMALY 2'-3
CLARION FZ
RIVERA FZ
NORTH AMERICAN PLATE
RIVERA PLATE
MIDDLE AMERICA TRENCH
OROZCO FZ
COCOS PLATE
PACIFIC PLATE
O'GORMAN FZ
TEHUANTEPEC FZ
CLIPPERTON FZ
SIQUEIROS FZ

figure 2.2

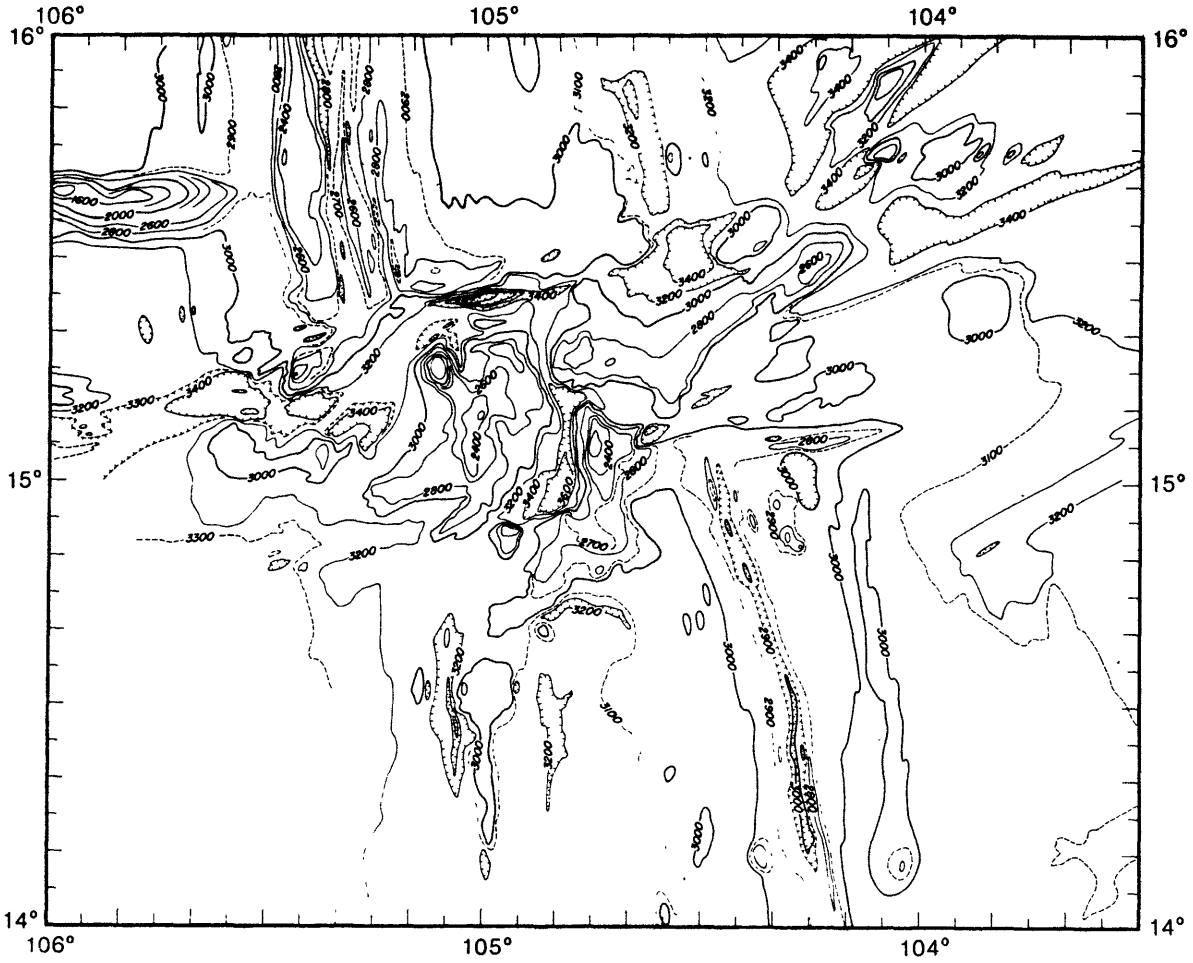
106°
105°
104°
16°
15°
14°
Offset of the East Pacific Rise by the Orozco Fracture Zone
April 1980
J.Mammerickx

figure 2.3

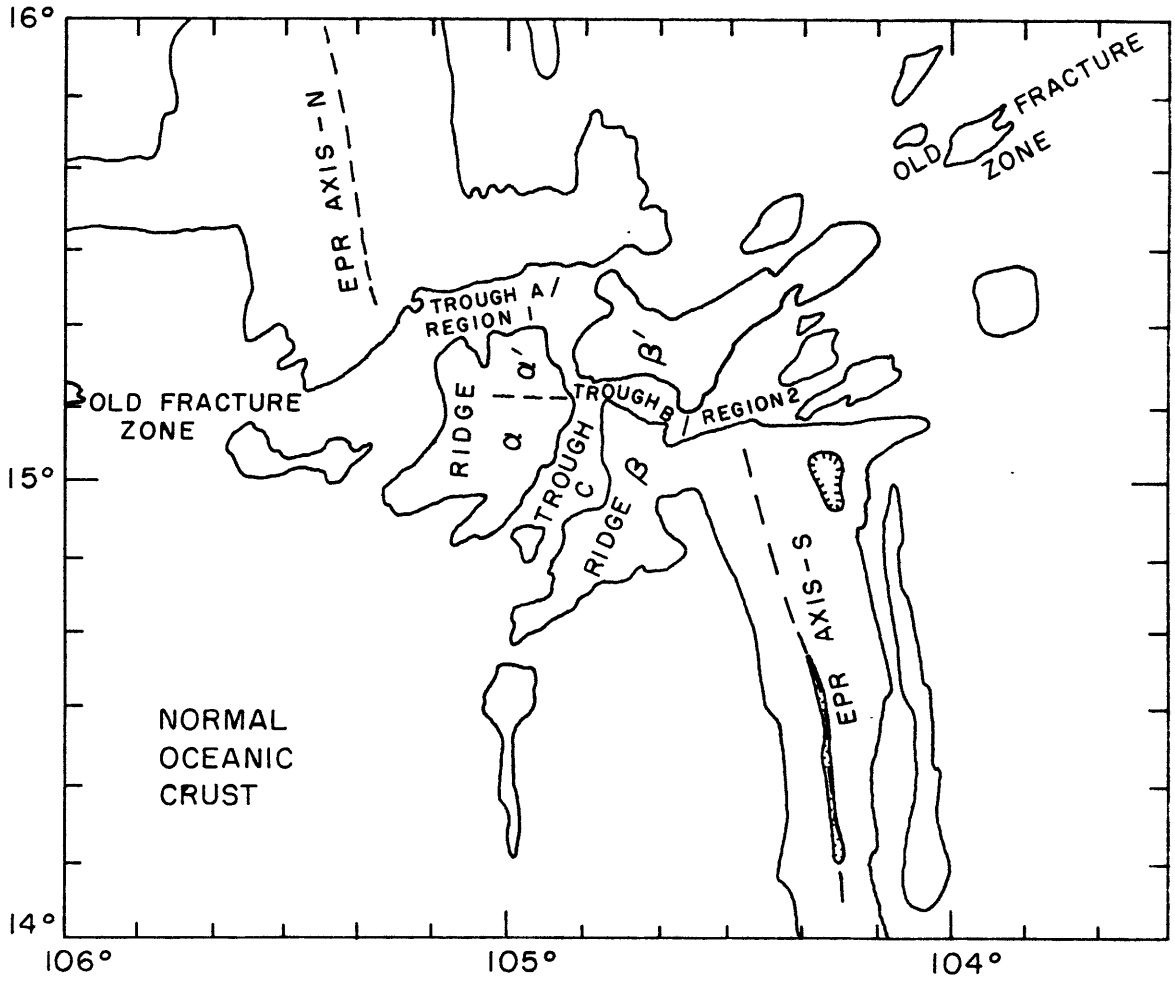
16°
15°
14°
106°
105°
104°
EPR AXIS-N
TROUGH A/
REGION 1
OLD FRACTURE
ZONE
OLD FRACTURE
ZONE
RIDGE α
α'
TROUGH B/ REGION 2
β'
TROUGH C
RIDGE β
EPR AXIS-S
NORMAL
OCEANIC
CRUST

figure 2.4

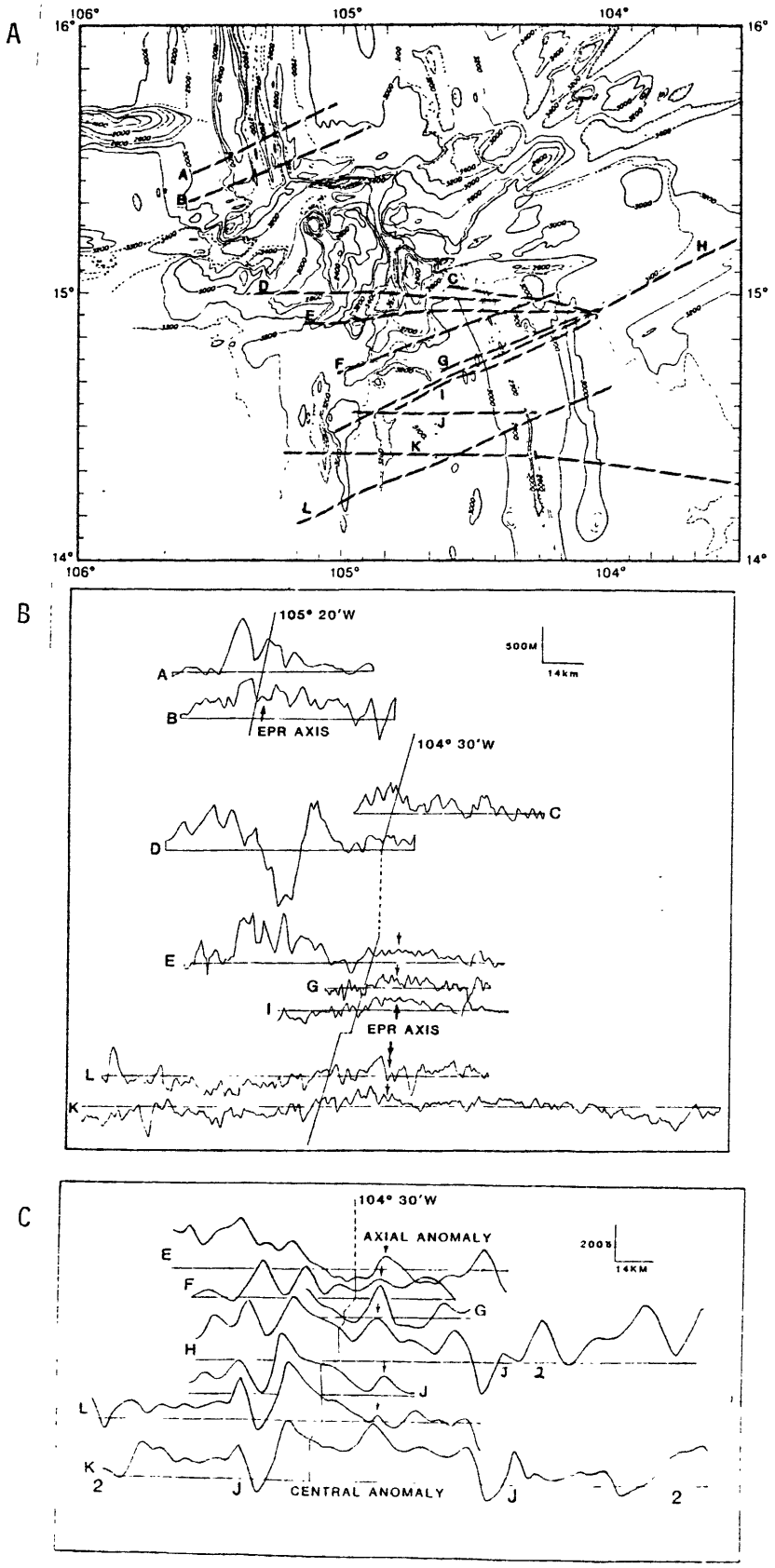
A
106°
105°
104°
16°
15°
14°
A
B
C
D
E
F
G
H
I
J
K
L
B
105° 20'W
500M
14km
A
B
EPR AXIS
104° 30'W
C
D
E
G
I
EPR AXIS
L
K
C
104° 30'W
AXIAL ANOMALY
200s
14KM
E
F
G
H
J
2
J
L
K
2
J
CENTRAL ANOMALY
J
2

figure 2.5

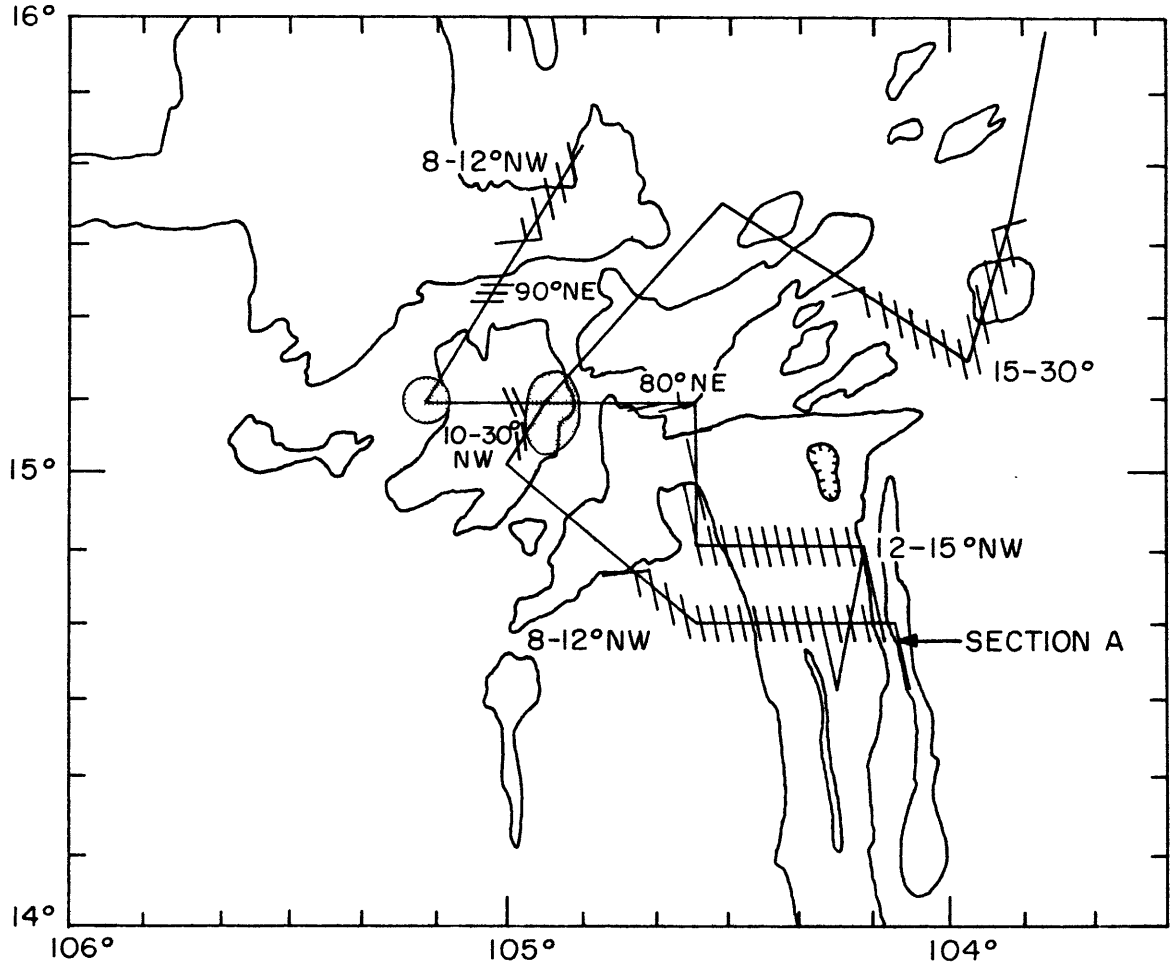
16°
15°
14°
106°
105°
104°
8-12°NW
90°NE
80°NE
15-30°
10-30°
NW
12-15°NW
8-12°NW
SECTION A

figure 2.6

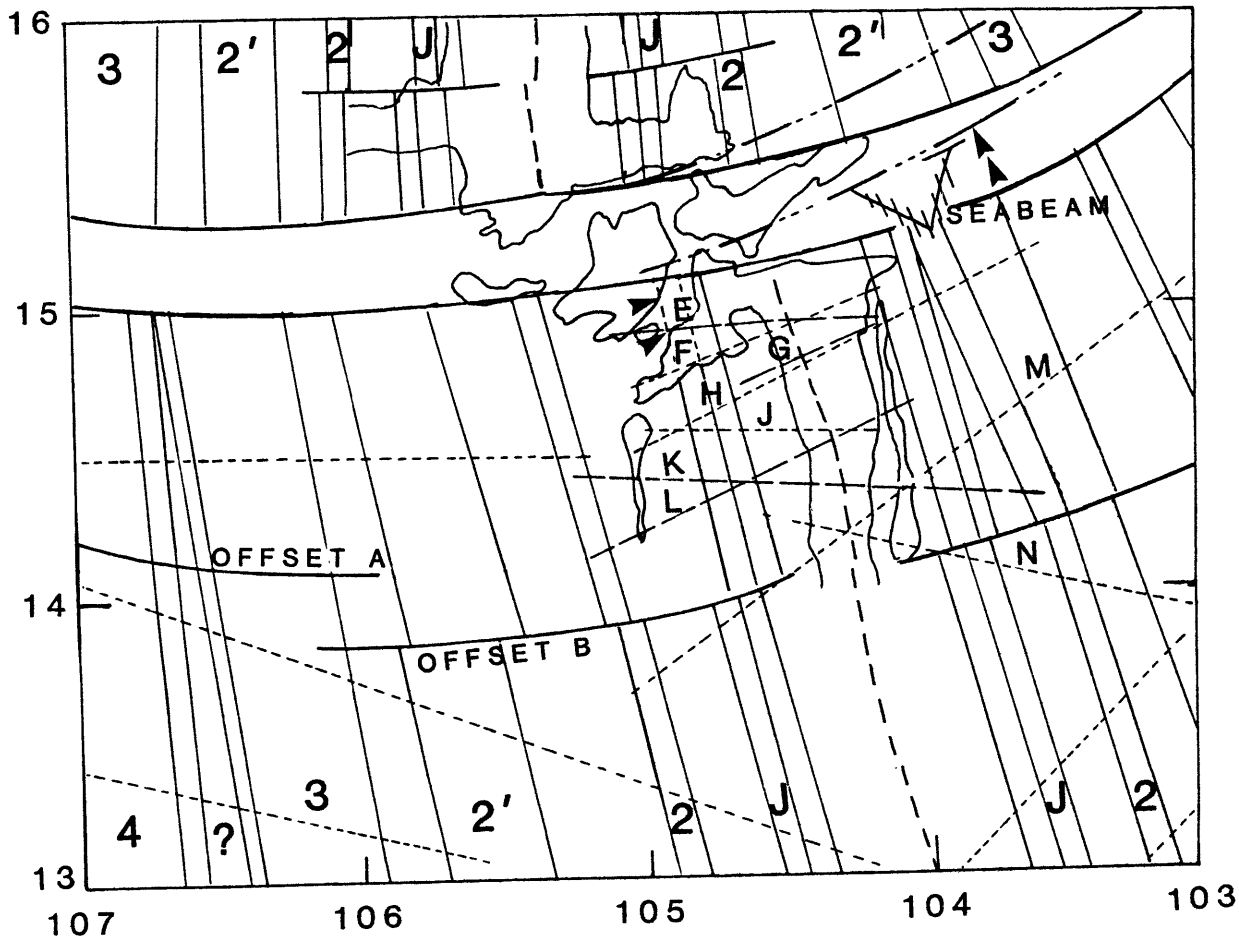
16
15
14
13
107
106
105
104
103
3
2'
2
J
J
2
2'
3
SEABEAM
E
F
G
H
J
K
L
M
N
OFFSET A
OFFSET B
4
?
3
2'
2
J
J
2

figure 2.7

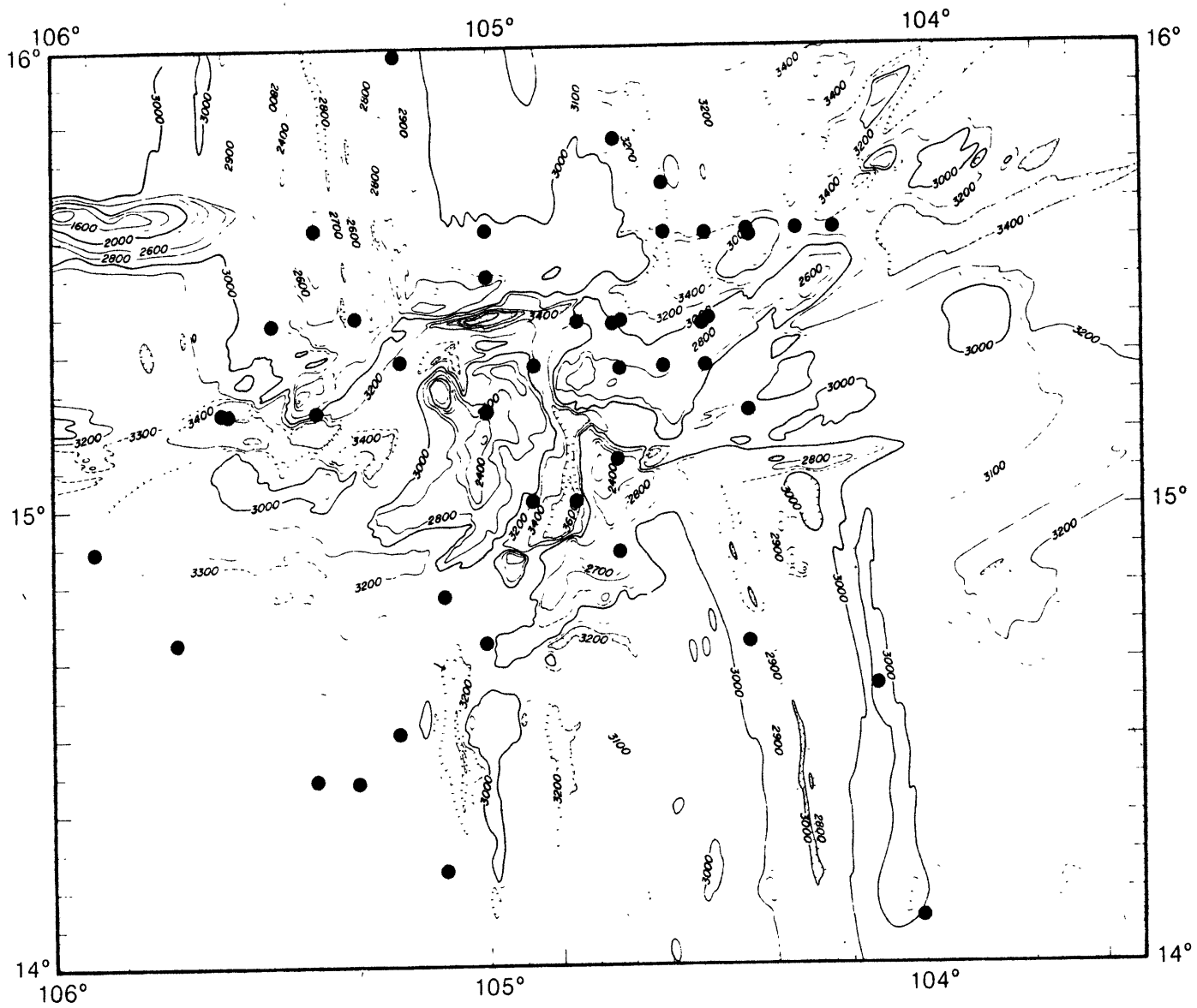

figure 2.8

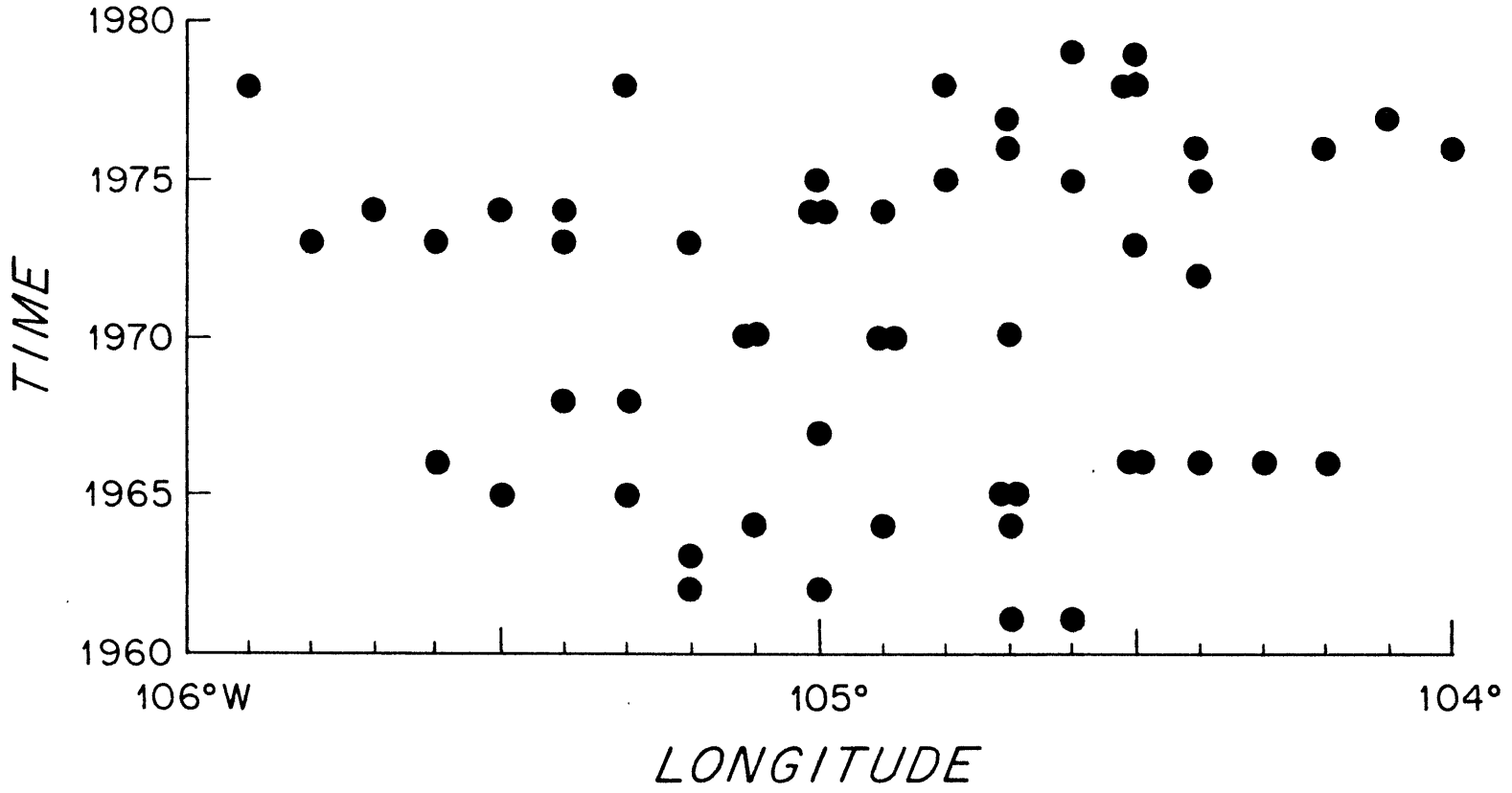

figure 2.9

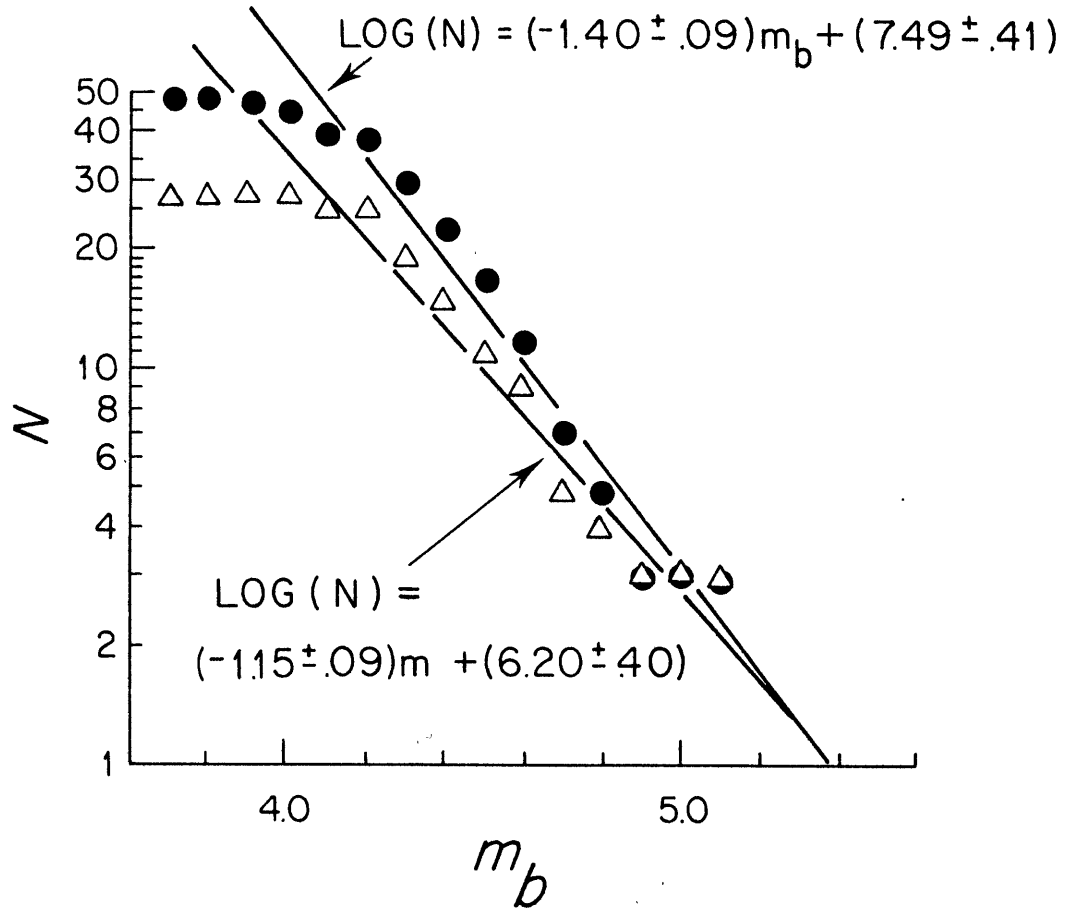
LOG (N) = (-1.40 ± .09)m_b + (7.49 ± .41)
50
40
30
20
10
8
6
4
2
1
N
LOG (N) =
(-1.15 ± .09)m + (6.20 ± .40)
4.0
5.0
m_b

figure 2.10

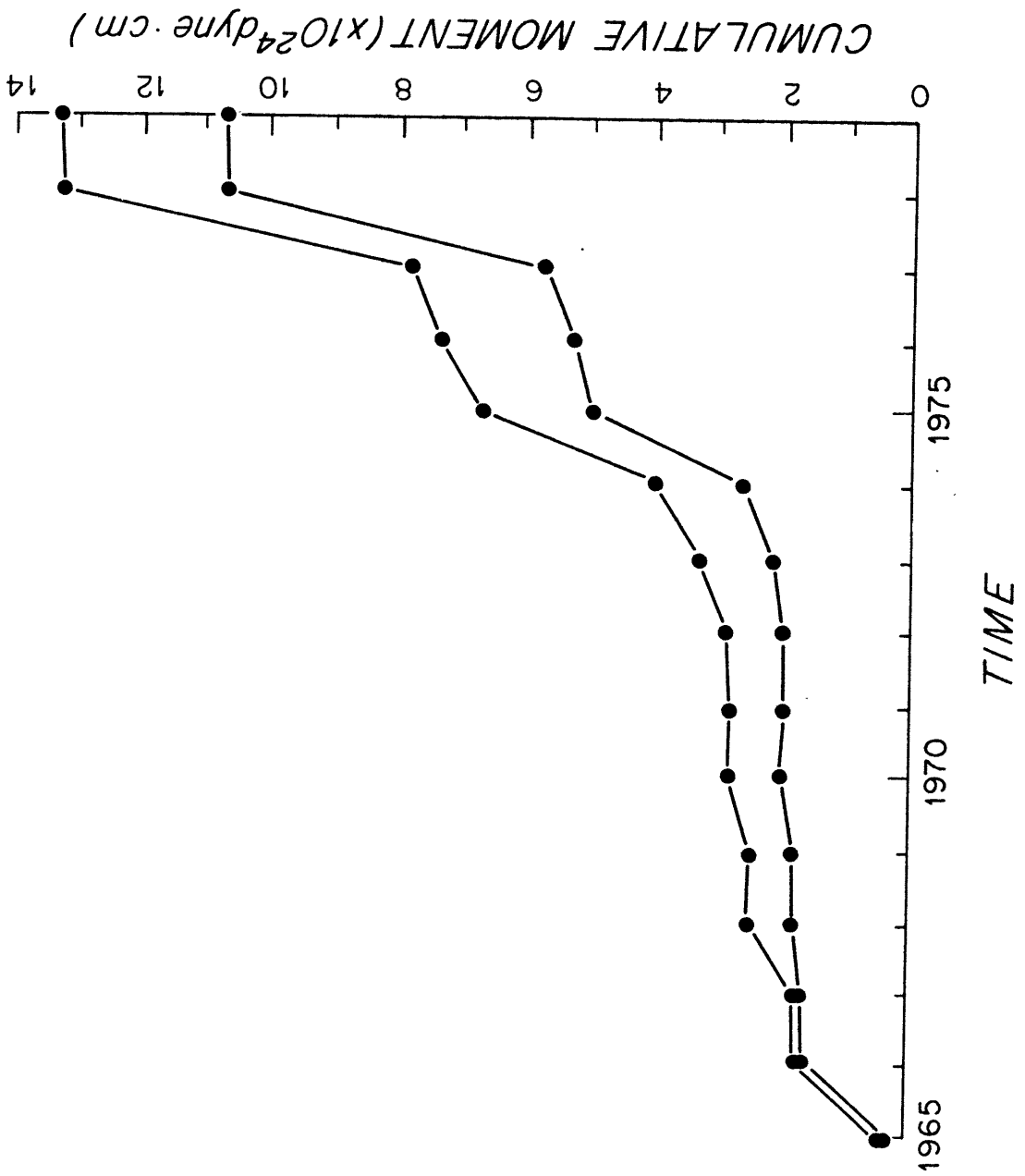
CUMULATIVE MOMENT (x10²⁴dyne·cm)
0
2
4
6
8
10
12
14
1965
1970
1975
TIME

figure 2.11

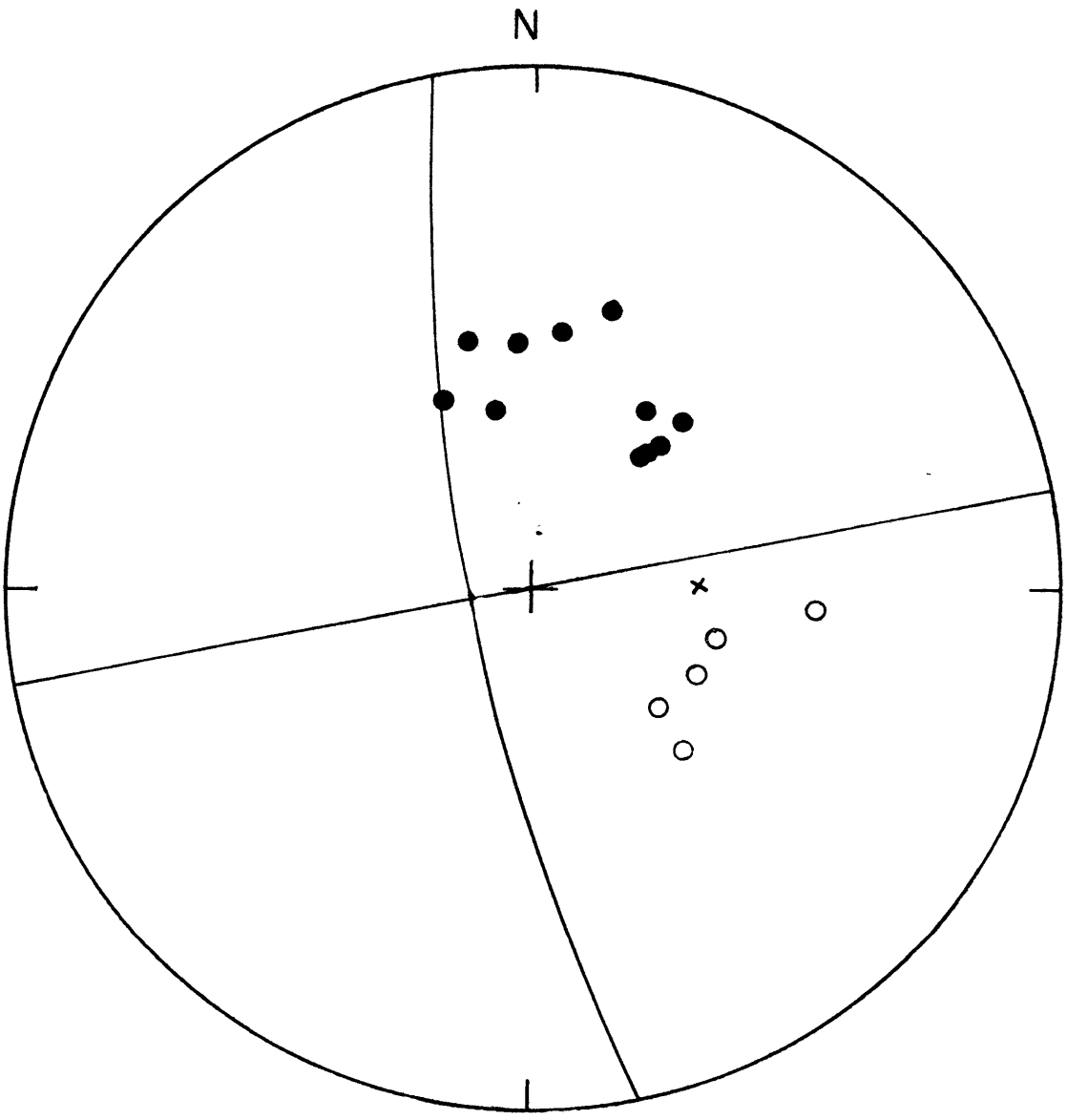

figure 2.12

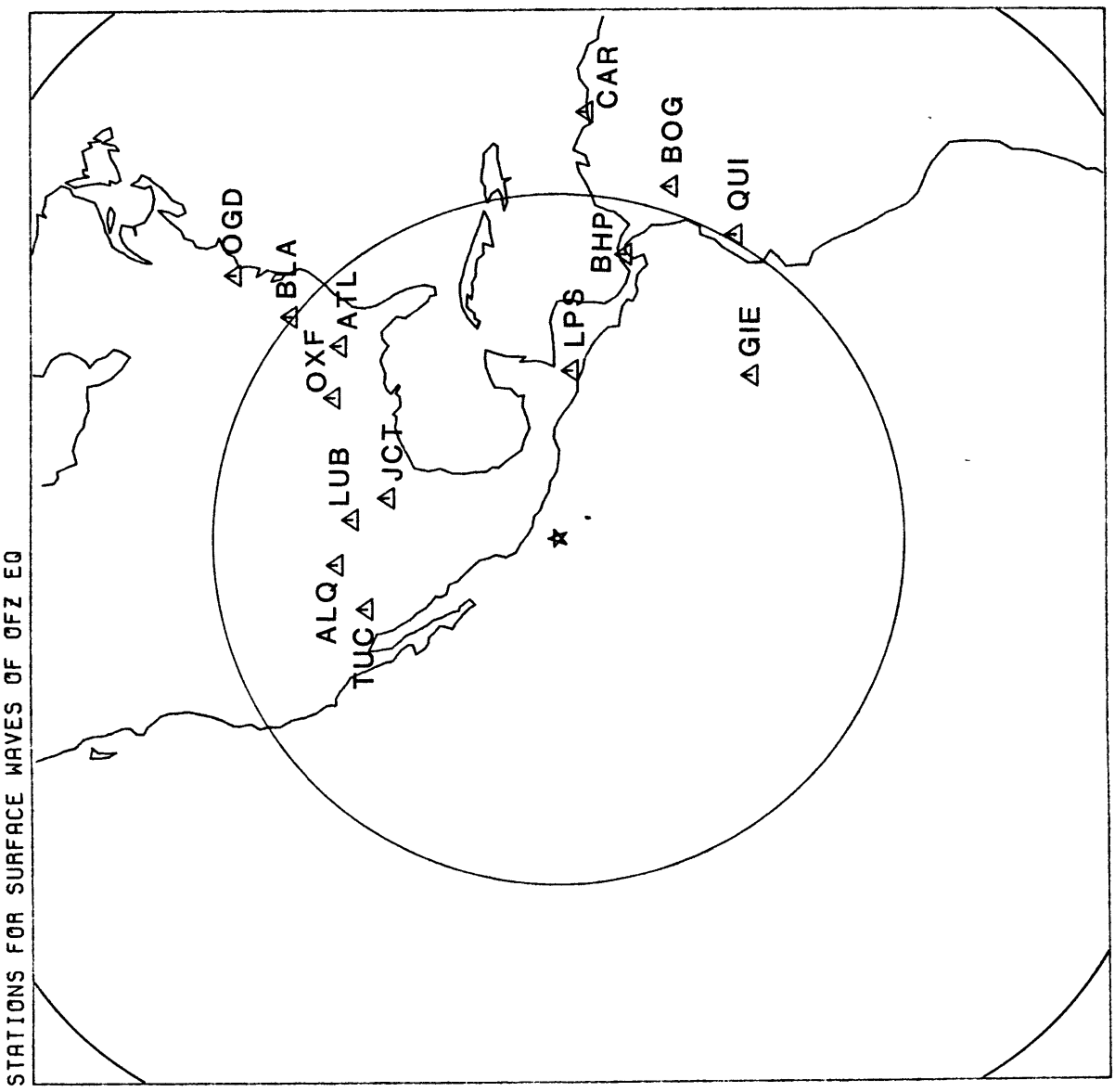
STATIONS FOR SURFACE WAVES OF OFZ EQ
OGD
BLA
ATL
OXF
LUB
JCT
ALQ
TUC
LPS
BHP
CAR
BOG
QUI
GIE

figure 2.13

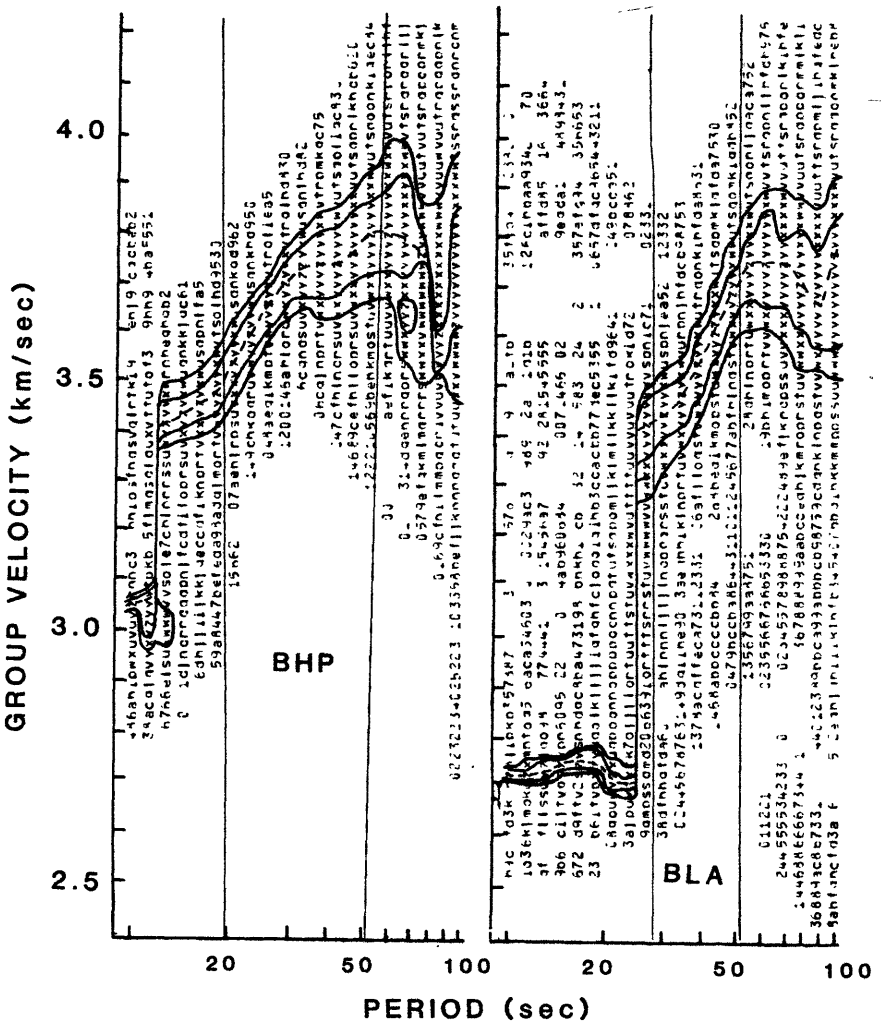
GROUP VELOCITY (km/sec)
4.0
3.5
3.0
2.5
BHP
BLA
20
50
100
20
50
100
PERIOD (sec)

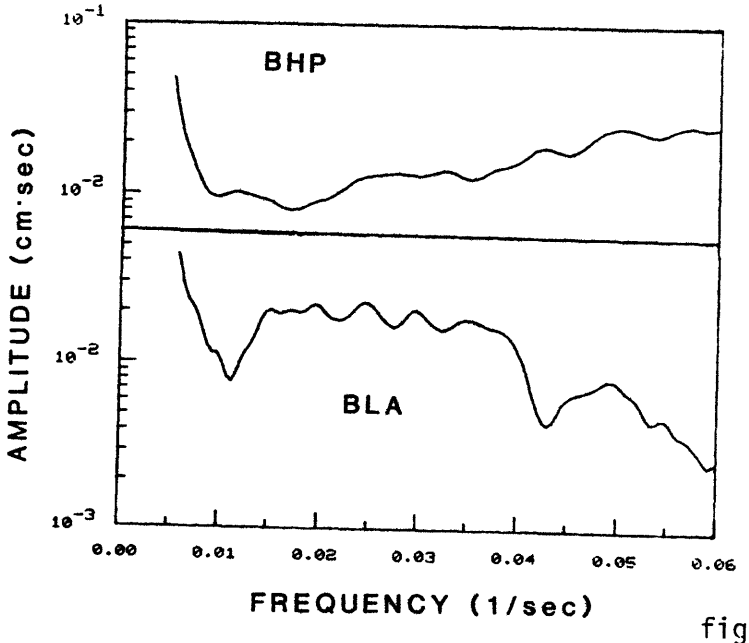
AMPLITUDE (cm·sec)
10^{-1}
10^{-2}
10^{-2}
10^{-3}
BHP
BLA
0.00
0.01
0.02
0.03
0.04
0.05
0.06
FREQUENCY (1/sec)

figure 2.14

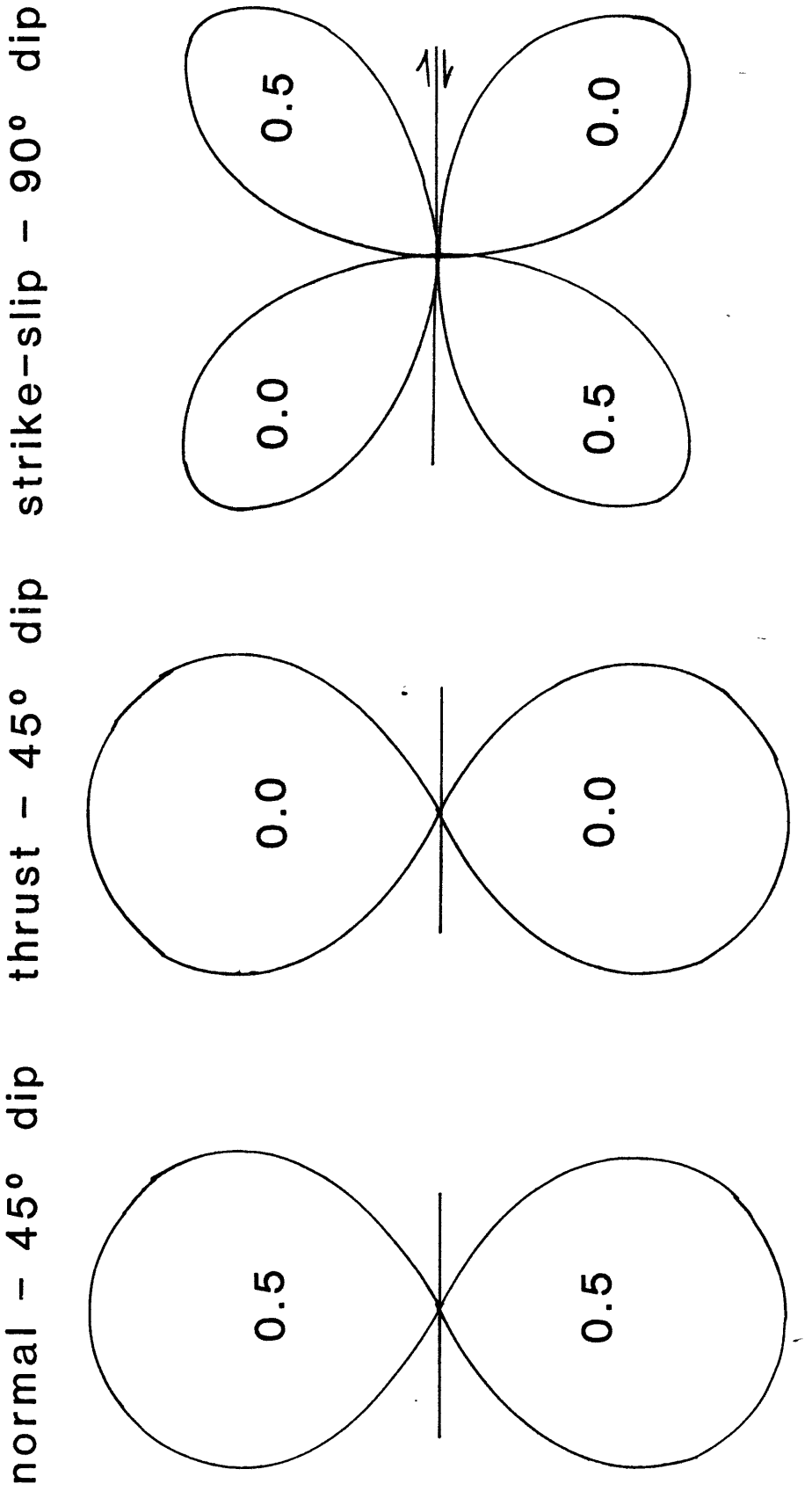
normal - 45° dip
thrust - 45° dip
strike-slip - 90° dip
0.5
0.5
0.0
0.0
0.0
0.0
0.5
0.5

figure 2.15

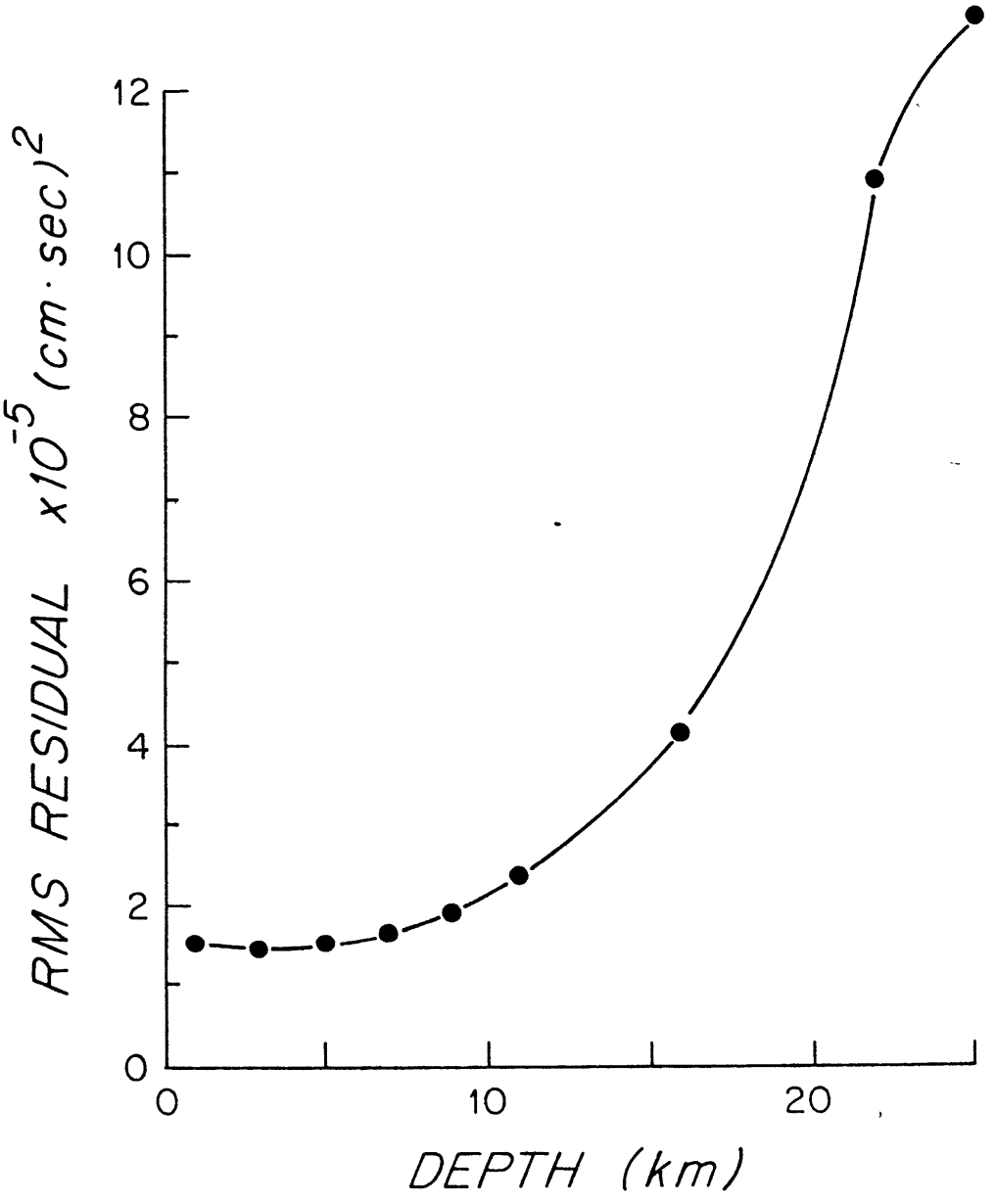

figure 2.16

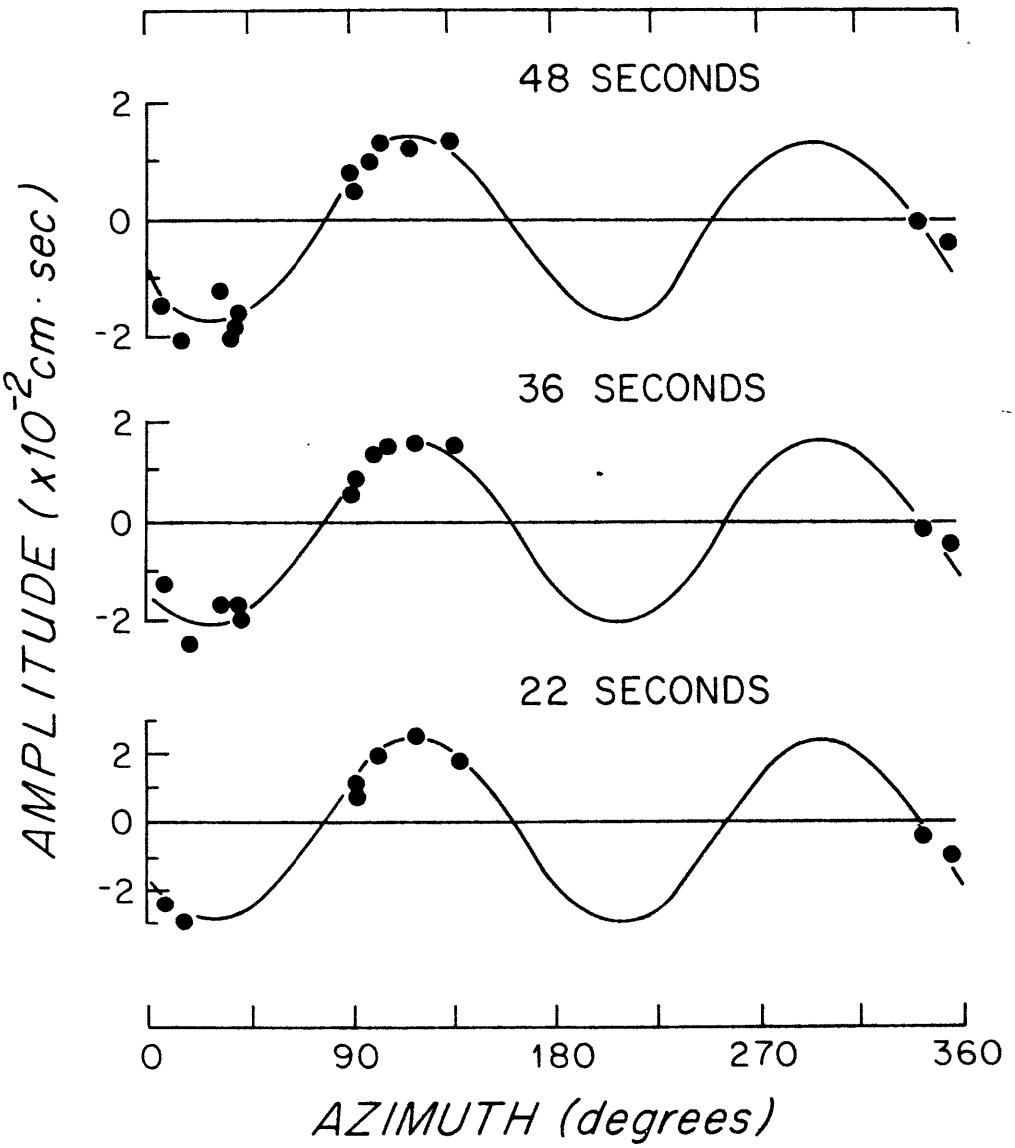
48 SECONDS
36 SECONDS
22 SECONDS
2
0
-2
AMPLITUDE (x10⁻² cm · sec)
0
90
180
270
360
AZIMUTH (degrees)

figure 2.17

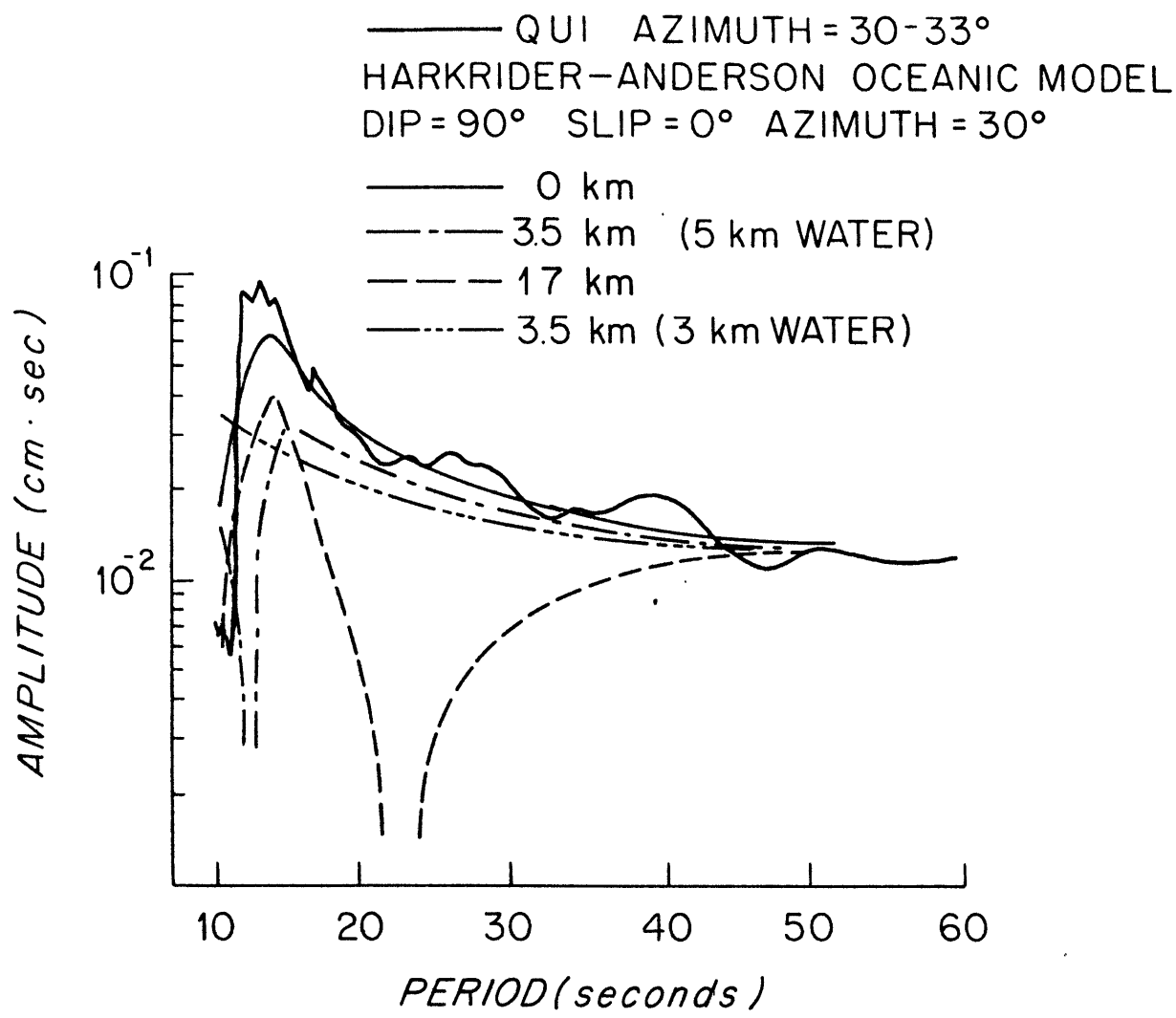
QUI AZIMUTH = 30-33°
HARKRIDER–ANDERSON OCEANIC MODEL
DIP = 90° SLIP = 0° AZIMUTH = 30°
0 km
3.5 km (5 km WATER)
17 km
3.5 km (3 km WATER)
AMPLITUDE (cm · sec)
10^{-1}
10^{-2}
10
20
30
40
50
60
PERIOD (seconds)

figure 2.18

CHAPTER III

RESPONSE OF THE MIT OBS

To interpret information about path and source effects which is contained in the waveforms recorded by an OBS, we must be able to describe the relationship between the signal and the motion of the ground. This has been limited by the lack of a model to characterize the coupling between sensed motion and the sea-floor motion in the absence of the OBS. Progress toward solution of this problem has recently been made by Sutton et al. (1981) and Zelikovitz and Prothero (1981), who adapted a model from the engineering literature (e.g., Richart et al., 1970) in which a structure sitting on sediment is represented as a mass-spring-dashpot system. This model satisfactorily explains the results of transient tests performed on OBS from different institutions during tests conducted at Lopez Island, Washington in preparation for ROSE.

In this chapter, we attempt to derive the total instrument response. We first briefly describe the MIT OBS. The response of the geophones and recording hardware is examined step by step. The coupling model is summarized and the results obtained for the MIT OBS at Lopez Island are compared to results from similar tests conducted at a dockside site at Woods Hole, Massachusetts. The model is then used to qualitatively explain differences in the character of the seismograms recorded by the MIT OBS during several deployments.

3.1 THE MIT OBS

The MIT OBS is a freefall, pop-up instrument designed primarily for microearthquake work and has been described by Mattaboni and Solomon (1977) and Duschenes et al. (1981). Its external design is shown schematically in Figure 3.1. The recording and timing electronics and power supply are housed in a cylindrical pressure vessel which sits vertically atop a circular base plate. Without the baseplate, the instrument package is buoyant; the baseplate serves as ballast and remains on the seafloor after recovery of the OBS. Attached to the main pressure case are three glass spheres providing buoyancy, two flashing lights and a radio transmitter with pressure sensitive switches to aid in locating the instrument during recovery, and an electromagnetic compass to orient the horizontal components relative to magnetic north. After a preset time interval, a motor driven mechanical latch releases the instrument from the baseplate and it floats to the surface.

To determine the instrument response of the MIT OBS, each stage of the recording process must be examined.

3.1.1 GEOPHONES

The ground motion sensors are three orthogonal 4.5 Hz geophones which are housed in a smaller cylindrical pressure vessel. This package is placed on the seafloor a few hours after deployment by means of a rigid arm attached to the main package (Duschenes et al., 1981) and a "lollipop" release

(Barash, 1981). After deployment, the arm springs back, decoupling the deployed package from the main package. To assure horizontal and vertical orientation of the geophones even if the package lands on an inclined surface, the geophones are mounted in a gimbal and the system is damped by submersion in viscous oil. This configuration can compensate for up to 30° of inclination of the package.

The deployed package represents a modification of the original instrument which was introduced to counteract several problems encountered when the geophones were housed in the main pressure vessel (Duschenes et al., 1981). In particular, this design modification greatly improved the signal to noise ratio of the data by decreasing resonances which appear to be excited by bottom currents and the mechanical operation of the tape recorder. The simple geometry of the deployed package, moreover, permits relatively rigorous application of the theoretical results on OBS-bottom coupling to actual data (section 3.2) and facilitates testing of alternate configurations for the baseplate. The major disadvantages of the deployed package are that it entails an additional underwater electrical connection and that the cable joining the two packages can become entangled on the sea floor. Although their importance is uncertain, these two factors increase the possibility of an instrument malfunction.

We have determined the response of the geophones from the theoretical response, with constants determined from the manufacturer's specifications, and have tested the geophones

individually to obtain an estimate of the variability. Theoretically, the response of a geophone to oscillatory ground motion is:

$$V/I = \frac{-A\omega^2}{\omega_r{}^2 - \omega^2 + 2b_t\omega\omega_r i} \qquad (3.1)$$

where V is the voltage output of the geophone; I is ground velocity (actually, the velocity of the geophone package, see 3.2); A is a constant gain; ω is angular frequency; ω_r is the natural resonant frequency of the geophone; and b_t is the damping expressed as a fraction of critical. Displacement response is obtained by multiplying by $i\omega$.

To determine b_t and A for the MIT OBS, we must consider the principle of the geophone circuit which is shown schematically in Figure 3.2 (from Aki and Richards, 1981). Use of such a circuit to measure ground motion was first introduced by Galitzin in 1914. Within a geophone, a magnetic field is set up by a magnet attached to the casing. Motion of the casing relative to the inertial mass m (which includes a coil of wire wrapped around a support and suspended from a spring with spring constant K) induces a current in the coil. The voltage across the coil is proportional to the velocity of the casing which is generally assumed to be rigidly coupled to the ground. In section 3.2 we will examine a way of parameterizing the transfer function between ground motion and case motion when this assumption does not hold.

For the geophones used during ROSE (Walker-Hall-Sears model Z-3CA), the natural resonant frequency $f_r(=\omega_r/2\pi)$ is 4.5Hz±0.5Hz and the damping b_o due to the resistance R_c of the geophone coil is 60%±10% of critical (manufacturer's specifications). The total damping is adjusted by changing the value of resistance R across the poles of the geophone:

$$b_t = b_o + G^2/[4\pi f_r m(R+R_c)10^{-7}] \qquad (3.2)$$

where G is the intrinsic sensitivity of the geophone ($G = B\ell$ where B is the average magnetic field strength and ℓ is the length of the wire) and m is the mass of the inertial element. From the manufacturers specifications for the Z-3CA geophone, G = 0.598 volts/cm/sec, m = 23 grams and R_c = 1060 ohms. (The factor 10^{-7} is a conversion factor relating volts and ohms to cgs units).

A response which is "maximally flat" for $\omega > \omega_c$ is achieved with $b_t = 1/\sqrt{2} = 0.707$ (see Figure 3.3) and is generally used for OBS geophones. Because of human error, M2 at ROSE and the external package at Lopez Island had R = 3800Ω resulting in b_t = 1.16. The other MIT OBS in ROSE (M1 and M2) were open circuit so that R was effectively ∞ and $b_t = b_o$ = 0.60. For reasons discussed in section 3.2, most of the data used for particle motion and spectral analysis were recorded by M2.

The constant A represents the gain of the geophone and is determined from:

$$A = GR/(R+R_c) \qquad (3.3)$$

For M2, A = 0.468 volts/cm/sec; for M1 and M3, A = G = 0.598 volts/cm/sec. The amplitude and phase responses of the geophones for several values of b_t are shown in Figure 3.3.

To obtain an idea of the variability among geophones with the same manufacturer's specifications, certain parameters were measured directly. The coil resistances for 11 Z-3CA geophones were all less than 1060Ω (Table 3.1) and the deviation was as much as 12%. By chance, the coil resistance of the three geophones in M2 ranged from 970-986Ω and were thus the same within 2%. Correcting G to 0.571 volts/cm/sec by assuming that the lower measured resistance reflects simply a proportionately shorter wire in the coil, and substituting R = 978Ω in equations 3.2 and 3.3 gives b_t = 1.12 and A = 0.454 volts/cm/sec for M2. The difference between the response calculated with these parameters and that calculated with b_t = 1.16 and A = 0.468 volts/cm/sec is less than the thickness of the line in Figure 3.3.

The frequency response was tested by shaking the geophones with a constant displacement amplitude over a sweep of frequencies. The displacement was produced by driving a piezoceramic cylinder to which the geophone was rigidly coupled with an oscillatory voltage. With a peak-to-peak voltage of approximately 600V, a peak displacement on the order of 10^{-3}cm can be produced. Because we have not calibrated the displacement of the peizoceramic cylinder exactly, we cannot calibrate the geophones exactly. We can, however, compare the variability among geophones. It must be

noted that repeated tests of a given geophone yielded essentially identical results. The results for the geophones used in M2 and M3 are shown in Figure 3.4. At low frequencies (~5 Hz), variability of up to 30% of total output can be observed. The three geophones used in M2, however, had very similar responses. The ringing at high frequencies was due to a vibration of the testing apparatus and not to the geophones. From these tests, we conclude that the response of the three channels of M2 is adequately represented by a single equation.

Similar tests were performed on the HS-1 4.5 Hz geophones manufactured by Geospace which had been used in the MIT OBS before ROSE and were readopted for subsequent expeditions. These geophones showed less variability and the measured coil resistances were closer to the manufacturer's specifications.

3.1.2 RECORDING SYSTEM

Figure 3.5 shows a simplified block diagram of the data recording system (from Mattaboni and Solomon, 1977). The signals from the three sensors are preamplified and low-pass filtered through an anti-aliasing filter with a cut-off frequency of 30 Hz. The signal from each channel is then passed through an automatic gain control circuit, a sample-and-hold circuit, and a 12 bit analogue to digital converter. The digital signal from each channel is loaded into a 2195-word memory which is equivalent to about 18.3 seconds of data at a sampling rate of 120 samples/sec. The 12 bit word length results in a resolution of over 66 dB for a

single event; combined with 8 bits of automatic gain control, this leads to a total dynamic range for the recording system of 108 dB.

The preamplified and filtered signal from the vertical component is simultaneously passed to the event detection circuitry which compares the output of a long term average of the rectified signal (time constant of 500 seconds) to a short term average (time constant of 1 second). When a set fraction of the short term average exceeds the long term average, the tape recorder is turned on and the contents of the memories are written on 9 track magnetic tape along with sync channel, timing, gain, and mission code. During an event, the gain and long-term average are frozen and data are recorded continuously for a period of 30 seconds after the long term average falls below the detection threshold. The logic of the detection circuitry has been described in detail by Ambuter and Solomon (1974). At a tape speed of 4.8 cm/sec, about seven hours of recording time are available, enough to record several hundred local events.

Timing signals are provided by a 5 MHz oscillator housed in a temperature controlled oven (Austron Sulzer model 1115). The manufacturer's rated timing stability of 1 part in 10^9 per day ($\sim 2 \times 10^{-5}$ sec/day) has been achieved to within nearly an order of magnitude in laboratory tests of the oscillators with respect to WWV standard time (Figure 3.6). These tests also confirm that, after letting the oscillator stabilize for several days, the drift rate is indeed linear as is assumed

when correcting field data. During ROSE I and II, total drifts corresponding to drift rates of ±2 to 23 x 10^{-3} sec/day were observed for different instruments. This increase in the drift may be due to the extremes of temperature encountered by the OBS on the trip to and from the sea floor, in which case this added drift component would not be linear. The timing error introduced by clock drift during ROSE was probably smaller for most instruments than that introduced by other sources such as instrument mislocation (see Chapters IV and V).

To retrieve ground motion from the recorded data, we must specify the response of the low-pass filters, the gain of the system and the digitizing interval. The low-pass filter is constructed from three identical cascaded circuits of a form illustrated in Figure 3.7. This configuration approximates a two-pole, low-pass Chebyshev filter with a cut-off frequency of 30 Hz and a passband ripple amplitude of 1 dB. The response of each circuit can be described by:

$$V_2/V_1 = Gb_0/(-\omega^2 + b_1 i\omega + b_0) \qquad (3.4)$$

$$b_0 = 1/(R_1 R_2 C_1 C)$$

$$b_1 = \frac{1}{R_2 C_1}(1-\mu) + \frac{1}{R_1 C} + \frac{1}{R_2 C}$$

$$G = \mu = 1 + R_4/R_3$$

where V_2 is the output voltage; V_1 is the input voltage; R_1, R_2, R_3, R_4, C_1 and C are the values of the circuit elements in ohms and farads, respectively; and ω is angular frequency.

For the MIT OBS, R_1 = 33kΩ, R_2 = 36kΩ, R_3 = 150kΩ, R_4 = 130kΩ, and $C = C_1$ = 0.15μf. Normalizing to $\omega_c = \sqrt{b_0} = 2 \cdot \pi \cdot 30.779$, this gives:

$$V_2/V_1 = [1.8776/(-(\omega/\omega_c)^2 + 1.1722(\omega/\omega_c)i + 1)]^3 \quad (3.5)$$

for the response of three identical filters in series. Additional amplifiers in the circuit lead to a total gain of approximately 680 for the maximum gain setting (including the preamplifier in the deployed package).

In Figure 3.8 the amplitude and phase response indicated by equation 3.5 is compared to the response of the MIT OBS analog circuit (filters and amplifiers) measured directly (Table 3.2). Amplitude responses have been normalized to 6.8 at 10 Hz. Once again, the three components of M2 have a very similar response.

The eight bits of automatic gain control add a factor of $V_{out} = V_{in} \cdot G/256$ where G is the gain represented by the 8 bits of automatic gain control. The data are then digitized at a rate of 120 samples/sec, and each digital unit equals 1.22 millivolts.

The complex spectrum of ground displacement $M(\omega)$ in cm·sec (actually, displacement of the geophone package) is thus related to the complex spectrum of the recorded seismogram $D(\omega)$ through:

$$M(\omega) = D(\omega) \cdot 0.0012[680(G/256)S(\omega)]^{-1} \quad (3.6)$$

where $S(\omega) = i\omega \cdot \frac{-A\omega^2}{(\omega_f^2 - \omega^2 + 2b_t\omega\omega_r i)} \cdot \frac{1}{(-(\omega/\omega_c)^2 + 1.1722(\omega/\omega_c)i + 1)^3}$

and A=0.468 volts/cm/sec, b_t=1.16 for M2; A=0.598 volts/cm/sec, b_t=0.60 for M1 and M3. The response of $S(\omega)$ for M2 and M3 is shown in Figure 3.9.

3.1.3 PLAYBACK

The format of the tape recorded in the OBS is not compatible with most computers and must be reformatted. The same tape recorder as that in the OBS is used to play back the data. As a first step, the data are reconverted to analogue form and played back on a strip chart recorder. These plots provide a guide to which data should be reformatted for further analysis.

Because the OBS tape does not contain any gaps within an event, an entire event must be read into the computer at once through a driver program written specifically for this purpose. An HP1000 computer was used to reformat the ROSE data. To store 60 seconds of data with 14 words/sample requires 100k words of storage. At the present time, the available memory on the HP1000 limits the length of an event to 60 seconds (a longer event can, of course, be reformatted as several overlapping events). The format of the tape recorded in the OBS includes much redundant information on timing because the full header (year, month, etc.) is attached

to each data sample. Since accurate timing is an essential component of the data, this provides a safeguard against temporary malfunctions during the experiment. During reformatting, the four data bits containing the seconds digit are monitored to confirm that each second does indeed contain 120 samples; if not, interpolated data points are inserted. After checking, the data are written to a second tape in a much condensed format where only the time of the first sample of an event and the seconds digit are explicitly saved. The ROSE data were reformatted a second time to correspond to the standardized ROSE format (LaTraille et al., 1982). The event headers in ROSE format contain the time of the first sample corrected for clock drift and for the 18.3 second lag of the OBS memory and include additional information on instrument characteristics, shot description, etc. In this form, the data can be plotted, filtered and otherwise analyzed to answer a variety of scientific questions.

3.2 COUPLING OF AN OBS TO THE SEAFLOOR

Data recorded by OBS are often very narrow band indicating some sort of resonance phenomenon. Several possible sources which have been identified are bottom currents (Duennebier et al., 1981), mechanical noise due to the instrument tape recorder, "fish bumps" (Buskirk et al., 1980), and the effect of the presence of the OBS on the motion of a soft sedimentary bottom. Although the development of the deployed package represented a major step in improving the

quality of the data recorded by the MIT OBS, even with the deployed package very monotonic data are sometimes collected. This suggests that, in some cases, a description of the interaction of the package with the seafloor must be included in $S(\omega)$ in equation 3.6.

3.2.1 THE MODEL

Recently, Sutton et al. (1981) and Zelikovitz and Prothero (1981) have independently adapted a model from the engineering literature (e.g. Richart et al., 1970) in which a structure sitting on sediment is represented as a mass-spring-dashpot system. Briefly, the system can be parameterized by a resonant frequency and a damping constant, both of which are functions of the instrument geometry and mass and of the physical properties of the underlying sediment. For the OBS situation, a coupling constant which includes the effect of instrument buoyancy multiplies the system forcing function (ground motion in the absence of the instrument), and a correction factor must be added to the mass of the instrument to compensate for the hydrodynamic force of the water when the water moves relative to the instrument. Near the resonant frequency, the OBS motion is amplified relative to the overall ground motion we wish to measure, and the amplification is determined by the damping of the system and the buoyancy of the instrument. At frequencies above the resonant frequency, the response is attenuated. It has also been shown that the response of a geophone-sediment system

calculated from wave theory for a mass sitting on an elastic half-space is essentially equivalent to this simple model (e.g. Lamer, 1969; Hoover and O'Brien, 1980).

Figure 3.10 illustrates the model. The equation of motion for this system is:

$$\ddot{x}+[d/M^*]\cdot\dot{x}+[K+(\rho_S-\rho_\omega)Ag]/M^*\cdot x = (M-Mw-Ms)/M^*\cdot\ddot{z} \qquad (3.7)$$

where M is the mass of the object, M_W and M_S are the average masses of water and sediment displaced by the object; ρ_ω and ρ_S are the density of water and sediment; $M^* = M + M_V$ where M_V is a term which compensates for the hydrodynamic forces resisting motion of the object through the water; K is the spring constant; d is damping; A is the area of the base; g is the gravitational constant; z is displacement of the seafloor; and x is displacement of the mass relative to the seafloor. Dots signify differentiation with respect to time.

Defining $C = (M - M_\omega - Ms)/M^*$ and $\omega_c^2 = [K + (\rho_S-\rho_\omega)Ag]/M^*$ this can be rewritten in the form:

$$\ddot{x} + 2D\omega_c\dot{y} + \omega_c^2 y = C\ddot{z} \qquad (3.8)$$

where D is the damping expressed as a fraction of critical. The position of the bottom of the OBS is i=z-x and the response spectrum is (Sutton et al., 1981):

$$I(\omega)/Z(\omega) = 1 - \frac{X(\omega)}{Z(\omega)} = 1 - \frac{-C(i\omega)^2}{(i\omega)^2+2D\omega_c\omega i+\omega_c^2} \qquad (3.9)$$

$$= (1-C)\,\frac{-\omega^2+2D/(1-C)\cdot\omega_c\omega_i+\omega^2{}_c/(1-C)}{\omega^2{}_c-\omega^2+2d\omega_c\omega i}$$

where X, I and Z represent the complex Fourier transforms of x, i and z. The amplitude response is illustrated in Figure 3.11 for several values of C and D.

Ignoring the mass of sediment displaced, C represents the effect of buoyancy (Sutton et al., 1981). In the dry land situation developed in the engineering literature, C = 1; when the OBS is neutrally buoyant ($M=M_W$), C=0 and the OBS moves exactly with the seafloor. Of course, in practice a neutrally buoyant instrument would be affected by the slightest current. To calculate C, M_W can be calculated from the known OBS dimensions and M_V can be estimated from analytic or laboratory determinations for simple geometric shapes (Byrd, 1978; Zelikovitz and Prothero, 1981). For horizontal motion or for the transient tests described in 3.2.2, C = 1.

The resonant frequency and damping of the system are related to the physical properties of the sediment; if the properties of the sediment are known, the coupling response is known and vice-versa. By calculating the full wave-theory response for a mass on an elastic half-space for a wide range of elastic parameters, Lysmer (1965) found that the effective spring constant and damping were independent of frequency.

For vertical motion and a circular base, $d \simeq [3.4R(1-\nu)]\cdot\sqrt{\rho_s \mu}$ and $K \simeq 4\mu R/(1-\nu)$ where R = radius of base and μ, ν and ρ_s are the shear modulus, Poisson's ratio and density of the sediment. These relations are valid if non-dimensional frequency $a = \omega R\sqrt{\rho/\mu}$ is less than 1, which holds for the MIT OBS situation where $\omega < 2\pi 30$, R = 20 cm, $\rho_s < 2$ gm/cm^3 and $\mu \sim 10^6$-10^8 dynes/cm^2. Similar relations can be obtained for horizontal, torsional, and rocking modes of motion (see Richart et al., 1970). Ignoring the effect of buoyancy on ω_c and D, we can express ω_c and D as:

$$\omega_c \simeq 2[\mu/(1-\nu)\cdot R/M^*]^{1/2} \qquad (3.10a)$$

$$D \simeq 0.85[\rho_s/(1-\nu)\cdot R^3/M^*]^{1/2} \qquad (3.10b)$$

3.2.2 RESULTS OF TRANSIENT TESTS

At the Lopez Island OBS intercomparison experiment in June, 1978 (Sutton et al., 1981), transient tests were conducted to measure the system responses of ocean bottom seismometers of a variety of designs. The underlying theory and experimental apparatus for the transient tests has been described by Sutton et al., (1981). A float attached to the instrument by an electromagnet is suddenly released, resulting in a step in force on the instrument. In a highly damped mass-spring-dashpot system, the instrument-mass will essentially experience a step in displacement and an impulse in velocity as the equilibrium position of the sediment-spring readjusts to the step in force. The spectrum of the velocity

response will therefore be flat for frequencies below the characteristic system frequency.

Sutton et al. (1981) and Zelikovitz and Prothero (1981) have demonstrated that the resonant frequencies and damping constants measured from these transient tests generally vary with (R/M^*) as predicted by the model (Figure 3.12). Unfortunately, many instruments showed a resonant frequency well within the range of interest for seismic data. Resonances at the frequencies determined from the transient tests can also be observed in records obtained from airgun and explosive shots (Johnson and McAlister, 1981).

One of the instruments which showed the most desirable response at Lopez Island was the MIT OBS with an external geophone package. The results of the transient tests are illustrated in Figure 3.13 and the amplitude spectra are shown in Figure 3.14. The spectra have been corrected for the velocity response of the geophones. At Lopez Island, one vertical and one horizontal component were recorded on land from the external package and one horizontal component was recorded from the main package. The response of the vertical component to a vertical transient shows a highly damped resonance at about 22 Hz with a flat response below this frequency. The response of the horizontal channel to a horizontal impulse shows a corner frequency at about 6-10 Hz which may reflect the horizontal mode of resonance. A secondary peak at 22 Hz is possibly a manifestation of the

vertical resonance. The vertical resonance at 22 Hz indicates a sediment shear modulus (equation 3.9) of about 5 x 10^6 dyne/cm^2 (Table 3.3).

During the vertical transient, a signal was sometimes observed on the horizontal component and vice versa (transients #233 and #234). These signals reflect both vertical and horizontal resonances, and the maximum amplitude is about 0.2 times the amplitude observed on the channel parallel to the force direction (Figure 3.14). Vertical transient #136, however, does not show any signal on the horizontal component. In practice, the vertical and horizontal transients are probably not purely vertical and horizontal.

Another noteworthy feature of Figure 3.13 is the signal observed on the horizontal component in the main package. The amplitude of this signal is approximately two orders of magnitude smaller than that for the signal on the external package. One of the often-stated objections to externally deployed packages is that the effect on the external package of the presence of the main package is not known. Although here the geometry is reversed and the situation is not directly analogous to a seismic wave incident on both packages from below, this observation provides a qualitative estimate of the importance of this effect. This problem deserves further study, both experimentally and theoretically.

During the tests at Woods Hole, only the response of the vertical component to a vertical transient was measured. The

test was performed on both the external package and the main package, but the two instruments were not deployed simultaneously.

The tests were originally designed to determine the effect of varying the diameter of the baseplate on the external package from 0.33m to 0.47m, thus changing the bearing pressure from 12.4 to 6.2 x 10^3 dyne/cm^2 (Duschenes et al., 1981). If we look at the relationship between the coupling parameters and the instrument geometry (equations 3.10a and b), however, we see that for a given site the ratio of R/M^* and not the bearing pressure determines the coupling parameters; the bearing pressure will act only indirectly by perhaps embedding the instrument into the bottom so that it feels the shear modulus of deeper sediment. For the range of R/M^* used in this experiment (Table 3.3), the correction factor M_V, which compensates for the hydrodynamic force of the water, increases so as to nearly counteract the increase in R even though the actual mass of the package M is not greatly increased. $(R/M^*)^{1/2}$ increases by only about 6% and we should not expect a significant difference in the resonant frequency for the different baseplates. The quantity $(R^3/M^*)^{1/2}$ changes by about 33%, so we might expect to see a difference in the system damping. M_V was determined by calculating the factor for a disk of radius R minus a disk of radius r and adding the factor for a cylinder of radius r and height h, where r and h are radius and height of the deployed geophone package (Byrd, 1978; Zelikovitz and Prothero, 1981).

The results of the tests at Woods Hole are shown in Figure 3.15. The amplitude spectra have again been corrected for the velocity response of the geophones. The spectra show a pronounced peak, unlike those from Lopez Island, and the shapes are similar to those of the theoretical spectra of Figure 3.11 for C = 0.8 and D = 0.08. Although only one example is shown for each baseplate, the tests were repeated four to ten times for each case and no significant differences could be observed.

The system resonance $f_r = \omega_c/(2\pi)$ and damping constant D for each case were determined by trial and error to be the pair which best removed the peak in the amplitude spectrum when the spectrum was corrected for the effect described by equation 3.9. Figure 3.16 illustrates this procedure. The results for different baseplates are listed in Table 3.3. No significant relationship between the coupling parameters and baseplate size could be determined. The shear modulus of the sediment indicated by the coupling resonance at 13 Hz is very low, approximately 1.5×10^6 dyne/cm^2.

The main instrument package shows a higher resonant frequency and damping than the external package. This suggests that, from the point of view of the coupling model, the configuration of the main package is preferable to that of the external package, at least at the Woods Hole site. In practice, however, the main package is susceptible to several additional noise sources which are avoided with the external package (Duschenes et al., 1981). The main package indicates

a sediment shear modulus which is an order of magnitude higher than that indicated by the external package.

Does the apparent difference between the shear moduli of the sediments at the two sites correspond to a difference in sediment type? At Lopez Island, 3 meters of soft, silty mud overlie a horizon (identified on seismic reflection profiles) which is probably a glacial deposit or hard siltstone. The density of the surficial sediment is approximately 1.57 g/cm^3 and the shear velocity in the top few meters, obtained from surface wave dispersion data, is approximately 20 m/sec (Tuthill and Lewis, 1981) giving a shear modulus of 6.3×10^6 $dynes/cm^2$. This value agrees well with that deduced from the transient tests.

The only data available from the Woods Hole site are from a core taken by the contractor who built the dock. Sediment strength is measured in units of "number of blows with a 140 lb hammer falling from a height of 30 inches needed to insert a 1 3/8 inch sampler 6 inches." At this site, the top 0.6 m of sediment consists of very soft, porous, black organic silt into which the sampler could be pushed by hand. This silt is underlain by 5.5 m of porous, medium-soft sand (10 blows per 6 in of sampler) followed by a meter of very dense, coarse-medium sand (46 blows per 6 in). The resonant frequency of the external package is probably determined by the top layer which must indeed have a very low shear modulus; the resonance of the main package is probably determined by the underlying layer. The presence of an interface just below

the surface may reflect energy back into the system, decreasing the damping as compared to the Lopez site. In the model, damping results from energy being radiated into an infinite elastic half-space in the form of seismic waves. That the elastic half-space assumption is so clearly violated at the Woods Hole site may also explain why we do not see the predicted variation in damping with baseplate size.

3.2.3 APPLICATION TO FIELD RESULTS

The results of this comparison of the response of the MIT OBS to transient tests at two different sites has implications which are both encouraging and discouraging for future OBS studies. They are discouraging because, even for the MIT OBS which showed a good response at Lopez Island, the characteristic system resonance is well within the frequency band of interest for very soft sediments which may sometimes be encountered in the marine environment. The results are nonetheless encouraging because they suggest that the mass-spring-dashpot model, which can be simply parameterized by a resonant frequency and a damping constant for each mode of motion, does indeed describe one of the major coupling problems which has plagued OBS studies.

Qualitatively applying this model to data collected by the MIT OBS during ROSE, one can observe both "well-coupled" and "poorly coupled" deployments. Figure 3.17 shows amplitude displacement spectra of S waves from several earthquakes recorded by M2 and M3 during ROSE II. At M2, we observe a wide range of spectral shapes. At M3, we consistently observe

a pronounced peak at about 6 Hz for these same events. Because the takeoff angles, azimuths and earthquake-station paths are similar for the two stations, this peak probably reflects an OBS coupling resonance at M3 rather than a source or path effect. Additional support for this inference is provided by the observation that incidence angles observed at M3 (see Chapter V) are nearly vertical for P waves and nearly horizontal for S waves, suggesting that M3 was sitting on very low velocity material. At M2, incidence angles ranging from about 45° to nearly vertical can be observed. During other deployments of the MIT deployed geophone package both previous and subsequent to ROSE, sites for which observed P waves have very steep incidence angles are correlated with narrow band data with a resonance in the range of 5 to 10 Hz; broad band data are associated with observed P-wave incidence angles which apparently vary with azimuth and distance to the source.

Some features of the resonance of M3 cannot be directly explained in terms of the simple mass-spring coupling resonance. In particular, we note consistently higher amplitudes on one of the horizontal components (H1), regardless of the azimuth from source to receiver. Apparent polarizations of the S waves measured during the first cycle of motion (see Chapter V) are also approximately in the direction of this component. The tests of the geophones and filters discussed in the previous section and the response of the horizontal components to the water wave from shots (see

Chapter V) do not indicate a systematically greater amplification on H1 for this instrument; any preferential amplification should occur on H2, according to the geophone tests. This apparent polarization of the S waves is therefore probably controlled by the detailed geometry of the sediment pond below M3. We also cannot resolve the several peaks which should correspond to the different modes of motion. Neglecting the effect of C and D which shift the resonant frequency somewhat from $\sqrt{K/M^*}$, the resonant frequency for horizontal motion should be approximately $(1-\nu)^{1/2}$ times the vertical resonant frequency. For an infinite half-space, D for horizontal and vertical motion are similar. In a real situation, however, the departure from the half-space assumption, which decreases the damping by reflecting energy back into the system, is usually quite different for the horizontal and vertical directions. Moreover C=1 for horizontal motion since the bouyancy force is vertical; C is approximately 0.3 for the MIT OBS for vertical motion. The resonant frequency for the rocking mode depends on the moment of inertia, and should be much less damped than vertical or horizontal motion. At M3, we see a single pronounced peak at 6-7 Hz for all events on all components. A second peak at 12-14 Hz may be seen in some cases and may represent a harmonic of the 6 Hz resonance. In later portions of the records beyond the S waves, a rocking mode with a very low damping can be observed. This mode also has a frequency of 6.5 Hz which appears as 13 Hz on the vertical channel.

One can also question the applicability of this model of OBS-sediment coupling for sites near spreading centers where bottom photographs indicate the absence of any sediment cover. Some of the "well-coupled" OBS may indeed be sitting directly on basement whereas the "poorly-coupled" OBS might be perched on a boulder and rocking. In the former case, the nature of the bottom just below the instrument is not important for interpreting the coupling response since no correction for coupling is needed in the frequency range of the observations. The observations of vertically incident P waves and delayed arrivals on the horizontal components and the consistent pattern of apparent azimuth of approach for water waves from explosive shots at sites which do show a coupling resonance suggest that low velocity sediments have probably been responsible for the resonance observed in past MIT OBS deployments.

In a very young tectonic environment where bottom photographs indicate that basement volcanics are exposed, the topography is very rough for wavelengths comparable to the radius of the baseplate of the MIT OBS. For an OBS that is freely thrown overboard to land on a smooth site several kilometers below the ship requires a certain element of luck. The most fruitful approach to an OBS network in such an environment is probably to deploy a large number of relatively simple, inexpensive instruments to provide arrival time readings and first motion polarities. A few sites where the bottom appears smooth as determined from underway reflection

data can then be carefully chosen for the emplacement of a few more complicated, three component instruments. These sites will probably usually have a continuous sediment cover.

For cases like M3 where the coupling resonance is in the dominant frequency range of the instrument and has a low damping, the presence of harmonics and the effects of detailed site geometry will probably not permit us to use the trial and error method described in Figure 3.16 to remove the effect of the coupling resonance accurately enough to confidently retrieve parameters of the displacement spectrum such as corner frequency, falloff rate, etc. The results of the transient tests and the qualitative extension of those results to past MIT OBS deployments, however, do suggest that the simple mass-spring-dashpot model provides a useful framework for understanding the factors involved in OBS-bottom coupling and for designing an instrument so that the effect of coupling resonance will be outside of the frequency range of interest for most environments. Additional controlled tests are needed to study the effect of instrument geometry on the coupling constants for sites on a range of sediment types with known physical properties and local structure. In situ tests to determine coupling parameters (Zelikovitz and Prothero, 1981) and surficial sediment properties for each deployment should also be very useful.

3.3 SUMMARY

The effect of instrument response can be removed from data recorded by the MIT OBS through equation 3.6 which describes the theoretical response of the geophones and recording system for specified values of the circuit elements. Tests on individual components of the OBS used during ROSE demonstrate that for instrument M2 variability among the components was negligible.

An important factor not included in equation 3.6 is the transfer function between seafloor motion in the absence of the OBS (the desired quantity) and the actual motion of the OBS package. The effect of the presence of the OBS package on seafloor motion can be described by a mass-spring-dashpot system. The system is parameterized by a resonant frequency and a damping constant which are functions of the instrument geometry and of the local sediment properties. Results of tests on the MIT OBS at two nearshore sites suggest that, for the range of sediment types encountered in the ocean, the resonant frequency for the MIT deployed geophone package will be above the frequency range of interest for many sediments ($\mu > 4.5 \times 10^6$ dynes/cm^2), but may be a problem for very soft sediments ($\mu \approx 1.5 \times 10^6$ dynes/cm^2). Of the two MIT OBS recording data during ROSE II, one instrument (M2) appears to have been well coupled whereas spectra for the other (M3) show a pronounced resonance peak.

TABLE 3.1 Measured Coil Resistances of Litton Z-3CA Geophones*

Geophone		Type	Coil Resistance
			Ω
1	M1	H1	939
2	M1	H2	1017
3	M2	V	986
4	M2	H2	970
5	M2	H1	981
6	M3	V	1025
7	M3	H2	1008
8	M3	H1	1042
9		H	938
10		H	1038
11		H	1037
12		H	1041
13		H	1039

*Manufacturer's specifications cite 1060Ω. Those geophones deployed in M1, M2 and M3 during ROSE are identified. The vertical geophone in M1 ruptured and was flooded by oil during ROSE II.

TABLE 3.2 Measured Frequency Response of the MIT OBS Analog Card for OBS Deployed During ROSE

a) Gain as a function of frequency - normalized to 6.8 at 10 Hz. Input signal was 100 mV peak to peak

frequency Hz	M1			M2			M3		
1.5	6.1	6.5	6.2	6.1	6.2	6.0	6.1	6.2	6.2
2	6.2	6.5	6.2	6.2	6.3	6.1	6.1	6.3	6.3
2.5	6.2	6.6	6.3	6.2	6.3	6.2	6.2	6.3	6.3
3	6.3	6.6	6.3	6.2	6.4	6.2	6.2	6.4	6.3
4	6.3	6.7	6.3	6.3	6.4	6.2	6.2	6.4	6.3
5	6.4	6.7	6.4	6.4	6.4	6.3	6.3	6.5	6.4
6	6.5	6.8	6.4	6.4	6.5	6.4	6.4	6.5	6.5
8	6.7	6.8	6.6	6.6	6.6	6.6	6.6	6.7	6.6
10	6.8	6.8	6.8	6.8	6.8	6.8	6.8	6.8	6.8
15	7.2	6.6	7.2	7.3	7.2	7.4	7.5	7.2	7.4
20	7.1	5.8	7.2	7.4	7.0	7.6	7.7	7.0	7.4
25	5.9	4.2	6.2	6.5	6.0	6.7	6.8	6.0	6.6
30	4.0	2.7	4.4	4.2	4.3	4.9	4.2	4.2	4.8
40	1.5	1.2	1.7	1.4	1.4	1.1	1.5	1.4	1.6
50	.62	.72	.76	.46	.42	.46	.42	.43	.48
60	.40	.70	.56	.15	.15	.15	.15	.15	.15
80	.02	.02	.03	.03	.03	.03	.03	.03	.03
100	.01	.01	.01	.01	.01	.01	.01	.01	.01

TABLE 3.2 (cont'd.)

b) Frequency (Hz) as a function of phase delay

phase delay degrees	M1			M2			M3		
0	1.6	1.3	1.6	1.5	1.6	1.6	1.4	1.7	1.6
90	12.6	10.6	12.8	13.2	12.8	13.4	13.4	12.8	13.4
180	21.7	19.1	22.0	22.6	22.4	22.7	22.4	22.3	22.7
270	30.0	27.3	30.4	31.0	31.2	31.2	30.6	31.1	31.4
360	42.2	39.5	42.7	43.2	43.5	43.2	42.1	43.7	43.7

TABLE 3.3. Summary of the results of vertical transient tests on the MIT OBS. R is the baseplate radius; M*, f_r and D were determined as described in the text; μ was calculated from equation (3.10a). The range of values for μ reflects the range $.33 < \nu < .49$.

Site	R(meters)	M*(kg)	f_r(Hz)	D	μ(x10^6 dynes/cm^2)
Lopez	0.205	31	22	>.25	4.5-5.9
WHOI	0.165	28	13	.10	1.4-1.9
	0.205	31	13	.10	1.3-1.7
	0.235	35	13	.12	1.3-1.7
	0.636	643	18	.16	17.-22.

FIGURE CAPTIONS

3.1 Schematic illustration of the MIT OBS capsule.

3.2 Schematic illustration of the moving coil, electromagnetic ground motion sensor (from Aki and Richards, 1980).

3.3 Velocity and phase response of the geophones in the MIT OBS. For a discussion of the parameters b_t and A, see the text.

3.4 Response of the individual geophones tested as described in the text. The three geophones in M2 are shown to have essentially the same response. Of the other geophones tested (Table 3.1), only those which gave a response which was noticeably different from the response for the three geophones in M2 are shown.

3.5 Block diagram of the data recording system. In the upper left are triaxial seismometers each of which is connected to a preamplifier and a low-pass filter. The vertical component waveform is applied to the automatic gain circuits. The X and Y component gains are slave-controlled from the vertical channel. The output of the gain circuit is applied to the analogue to digital converter through a sample and hold circuit. Digital data from the A/D are converted from parallel to serial form and delayed by the buffer memory for 18 seconds. Data are then recorded on magnetic tape via the tape head drivers. The data bus multiplexer accepts inputs from the automatic gain circuit, the real time clock, and the mission code switch. The resulting combined data are fed to the tape head drivers. The 5 MHz oscillator drives a divider chain which supplies one pulse per second to the real time clock and 1680 Hz to the control and timing circuits. The control and timing circuits provide fourteen phases to the multiplexer as well as timing for all of the digital functions. The event detector and logic control output is ANDED with the four-hour delay turn on. The resultant output controls the tape recorder. Delay data on inhibits the tape head drivers from applying the digital data to the tape for 2s. This allows the tape to come up to speed. The BCD switch sets the comparator to a future release time. When the real time clock reaches the BCD switch setting, a release signal is generated (from Mattaboni and Solomon, 1977).

3.6 Drift of the oscillators used for timing in the MIT OBS during ROSE measured at MIT several months after ROSE. Slopes of drift lines are in units of msec/day.

3.7 Circuit diagram for the filter described by equation 3.4.

3.8 Amplitude and phase response of the cascaded filters described by equation 3.5 (solid line). The dotted lines and the squares delimit the responses measured for the three components of M2. In Table 3.2, one can see that all but one channel (H1 in M1) is well described by equation 3.5.

3.9 Combined response of the geophones and filters for the MIT OBS. The total recording gain of 680 is included.

3.10 Schematic illustration of the spring-dashpot model for describing coupling of an OBS to the seafloor (from Sutton et al., 1981).

3.11 Amplitude response of the OBS-sediment system relative to ground motion in the absence of the OBS. The parameters are described in the text (from Sutton et al., 1981).

3.12 a. Observed resonant frequency as a function of $(R/M^*)^{1/2}\cdot(1-2D^2)^{1/2}$ for the OBS tested at Lopez Island. The lines represent a constant value of sediment shear modulus. Most of the instruments indicate a shear modulus of about 2.5×10^6 dynes/cm^2. The higher shear modulus felt by UWF can be attributed to the very high bearing pressure of this instrument; this may have caused it to be imbedded in the sediment where it felt a stiffer layer found at a depth of about 3 meters below sea floor (from Zelikovitz and Prothero, 1981).

b. Damping as a function of instrument geometry; $B = (1-\nu)/(4\rho_s)\cdot M^*/R^3$. The dashed line represents the theoretical damping for a half-space. In the model, damping results from the radiation of energy away from the mass. In the earth, we expect that some energy is reflected back into the system, decreasing the total damping. The expected trend as a function of instrument geometry can, nevertheless, be observed (from Zelikovitz and Prothero, 1981).

3.13 Results of transient tests on the MIT OBS external package at Lopez Island. The numbers on the left are the identification numbers from the Lopez catalogue; V and H indicate vertical and horizontal test, respectively. Trace a is the vertical component in the external package; b and c are the horizontal components in the external and main packages, respectively. The numbers on the right are the scaling factors relative to the trace from the component in the direction of the applied force.

3.14 Spectra of the traces shown in Figure 3.13. Scale on the left refers to test #233; scale on the right to #234.

3.15 Examples of transient tests performed at the Woods Hole site. 'Main' indicates main instrument package; 'lbp' indicates large base plate with radius 0.235 m; 'mbp' indicates medium base plate with radius 0.205 m; 'sbp' indicates small base plate with radius 0.165 m.

3.16 Example illustrating determination of f_r and D by removing the coupling effect described by equation 3.9. At frequencies above the resonant frequency, the spectrum does not fall off as rapidly as predicted by the model and a peak is observed in the corrected spectrum. The frequency of this peak is approximately double the resonant frequency for both the Lopez Island and Woods Hole results and probably represents a harmonic of the main resonance. The uncorrected spectrum is also shown for comparison. The best-fitting values for f_r and D are 13 Hz and 0.10, respectively. Other values for f_r and D are: (a) f_r = 12.5, D = 0.10; (b) f_r = 13.0, D = 0.12; (c) f_r = 13.0, D = 0.08; (d) f_r = 13.5, D = 0.10.

3.17 Amplitude spectra of S waves observed at M2 and M3 from several of the earthquakes located in Chapter IV. The spectra have been corrected for instrument response with equation 3.6. No correction for range or attenuation has been included. The solid line represents the vertical component; the dashed line, H1; the dash-dotted line, H2.

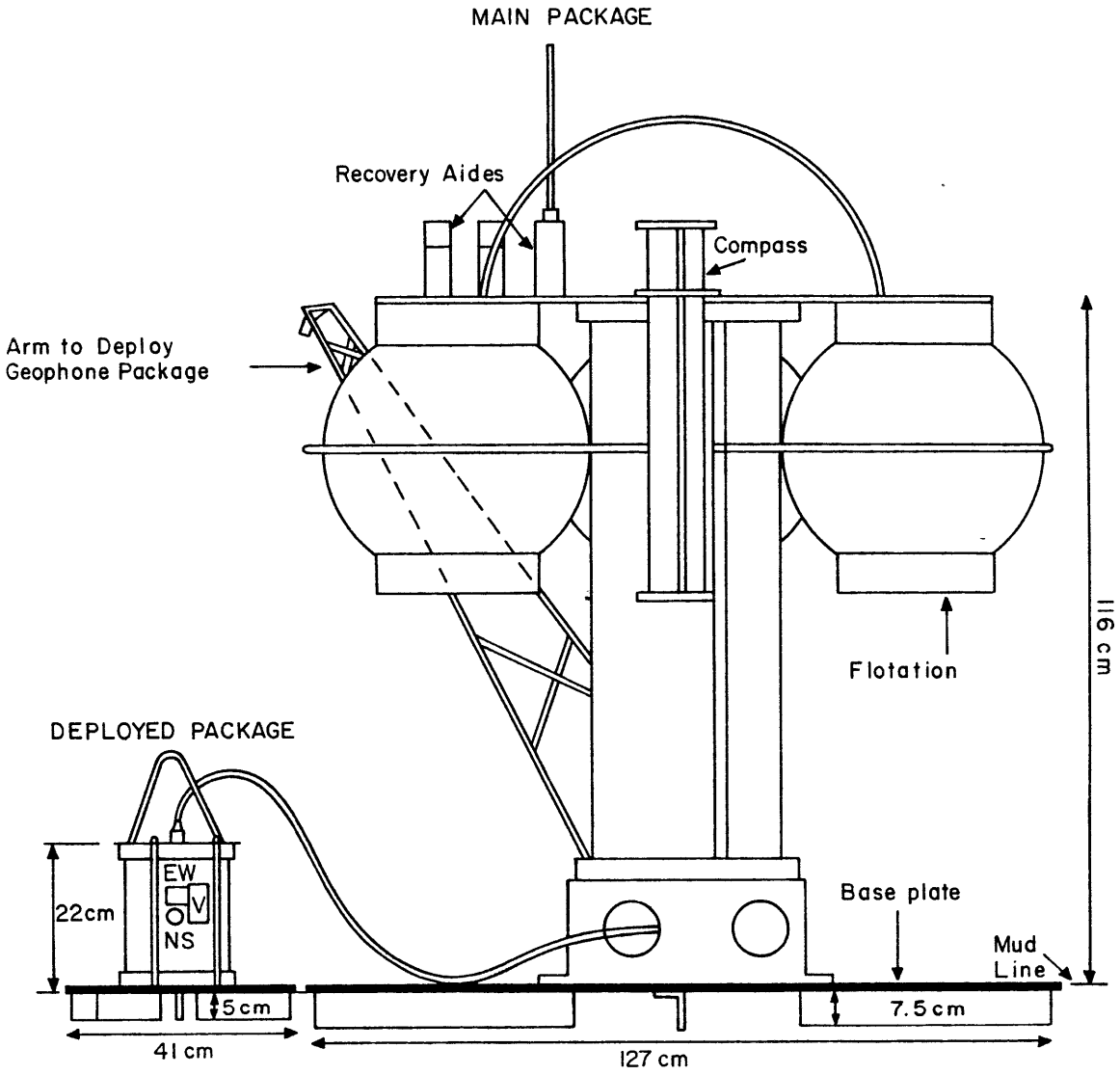
MAIN PACKAGE
Recovery Aides
Compass
Arm to Deploy
Geophone Package
Flotation
116 cm
DEPLOYED PACKAGE
22cm
EW
V
NS
Base plate
Mud
Line
5cm
7.5cm
41 cm
127 cm

figure 3.1

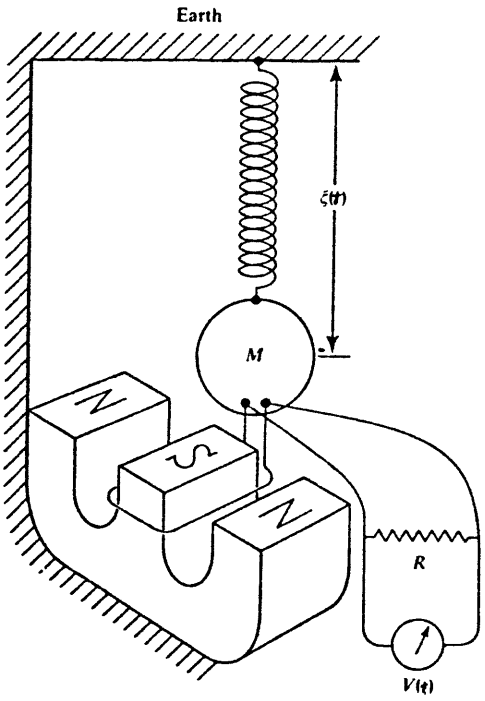

figure 3.2

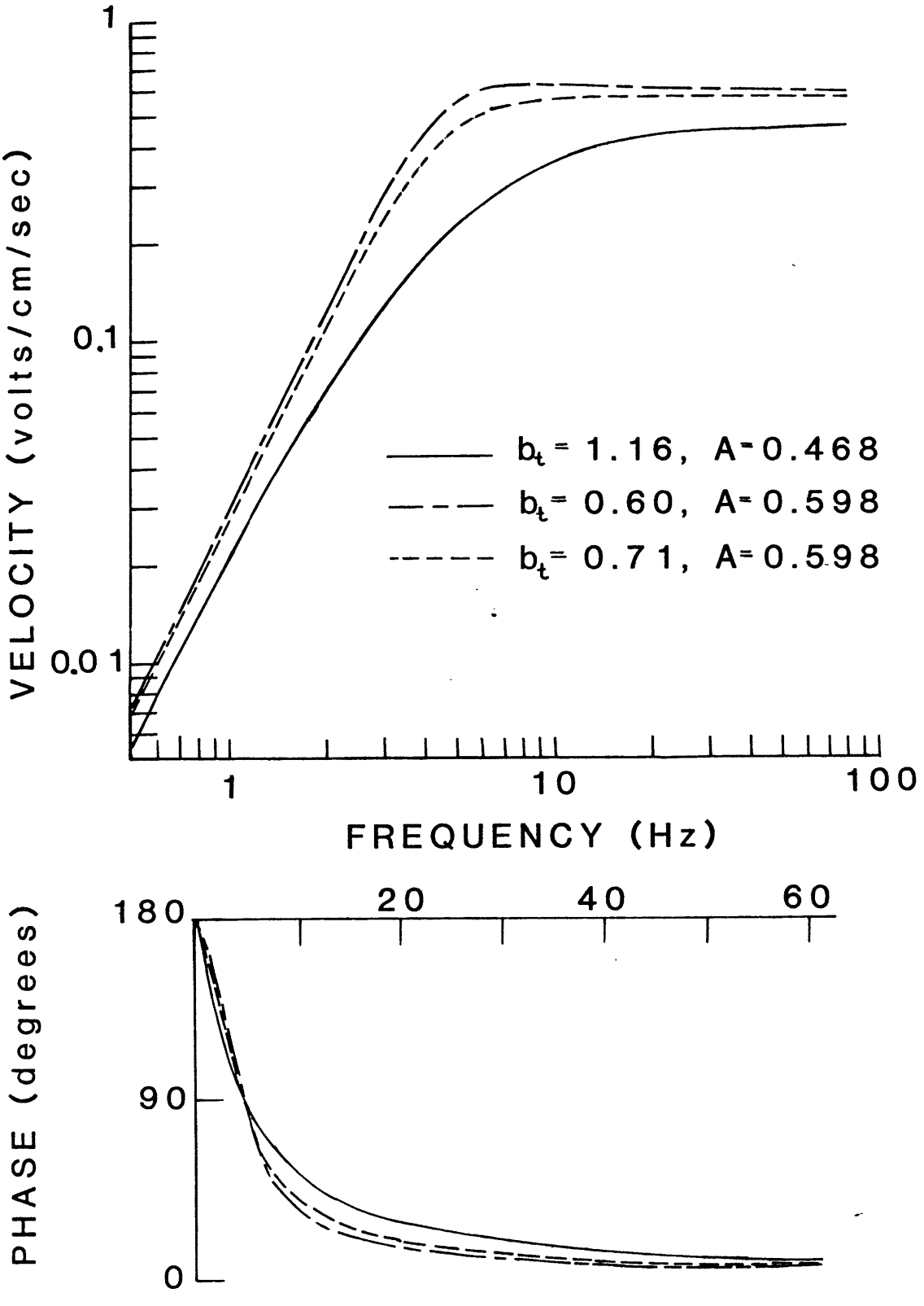
VELOCITY (volts/cm/sec)
1
0.1
0.01
1
10
100
FREQUENCY (Hz)
b_t = 1.16, A=0.468
b_t = 0.60, A=0.598
b_t = 0.71, A=0.598
PHASE (degrees)
180
90
0
20
40
60

figure 3.3

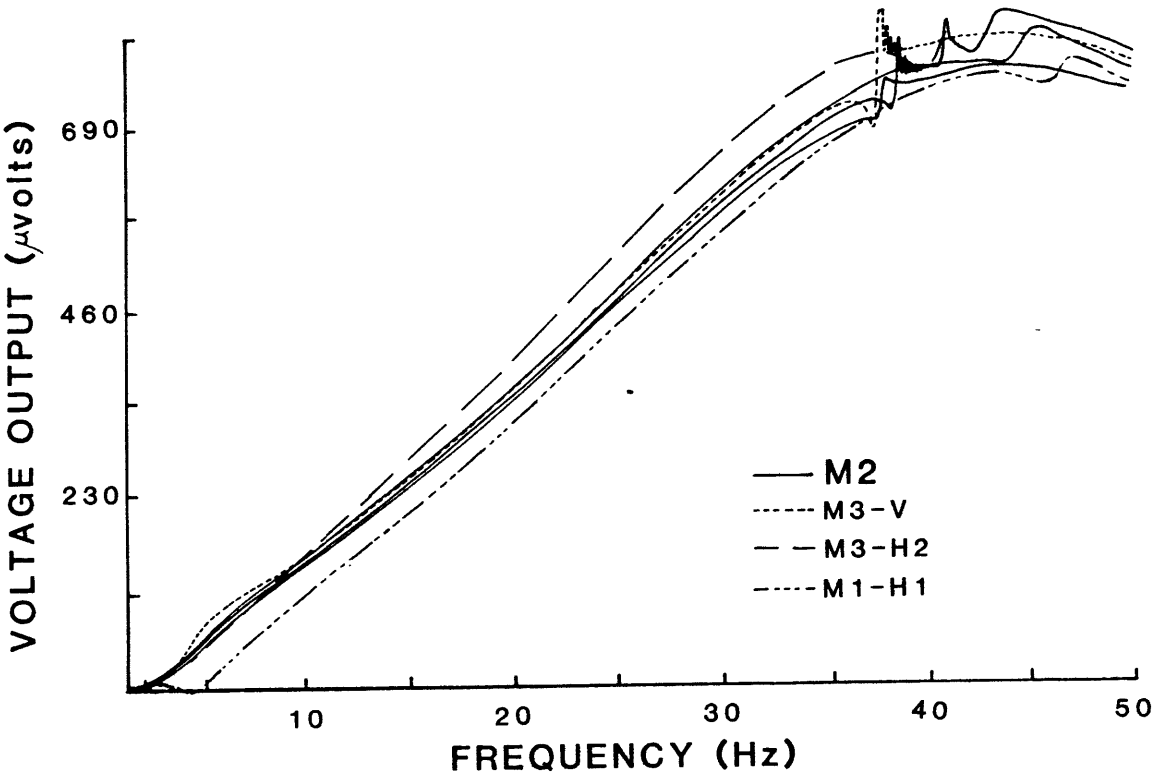
VOLTAGE OUTPUT (μvolts)
690
460
230
10
20
30
40
50
FREQUENCY (Hz)
M2
M3-V
M3-H2
M1-H1

figure 3.4

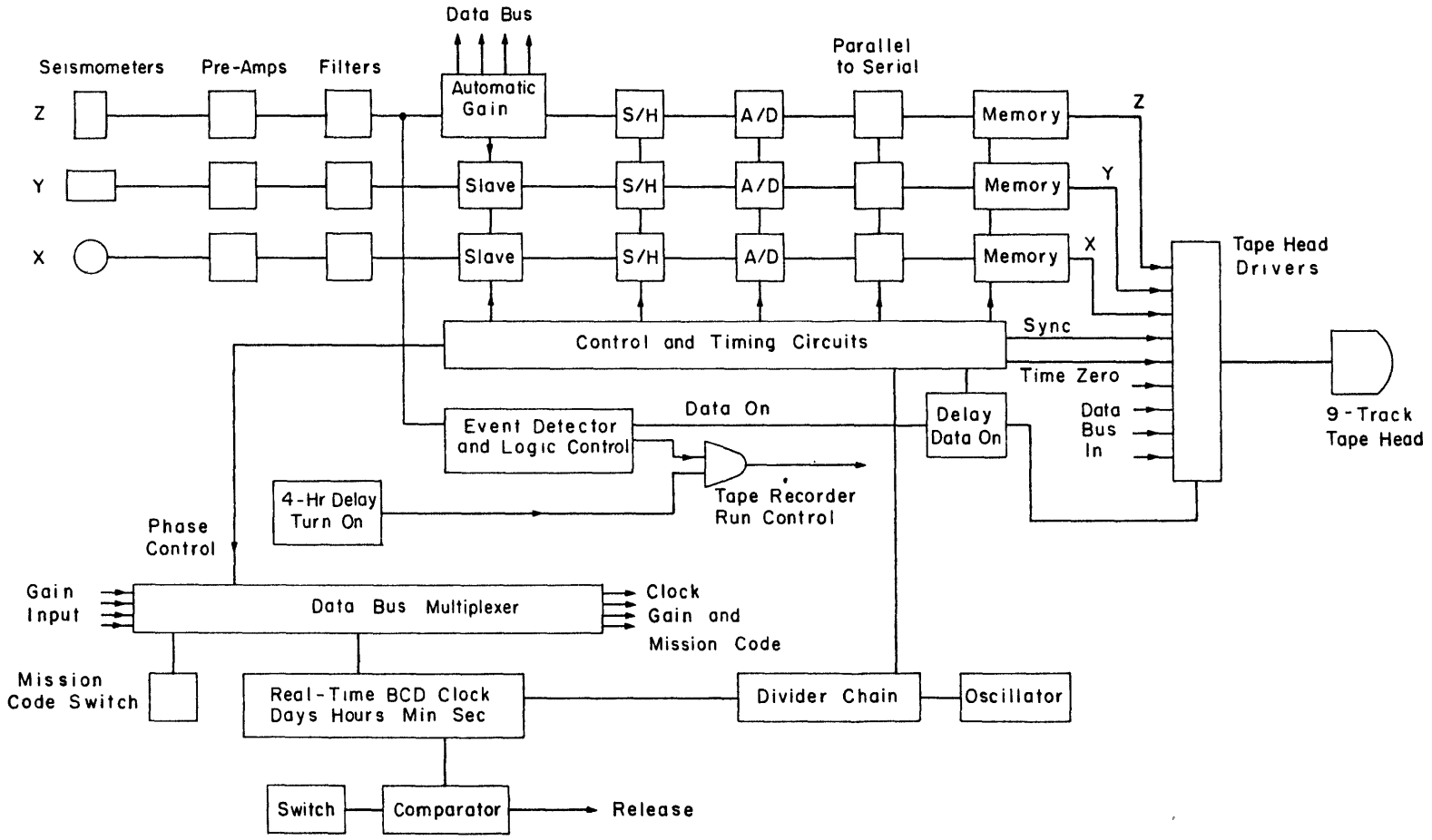
Data Bus
Seismometers
Pre-Amps
Filters
Automatic Gain
Parallel to Serial
Z
Y
X
Slave
Slave
S/H
A/D
Memory
Tape Head Drivers
Control and Timing Circuits
Sync
Time Zero
Data Bus In
Event Detector and Logic Control
Data On
Delay Data On
9-Track Tape Head
4-Hr Delay Turn On
Tape Recorder Run Control
Phase Control
Gain Input
Data Bus Multiplexer
Clock Gain and Mission Code
Mission Code Switch
Real-Time BCD Clock Days Hours Min Sec
Divider Chain
Oscillator
Switch
Comparator
Release

figure 3.5

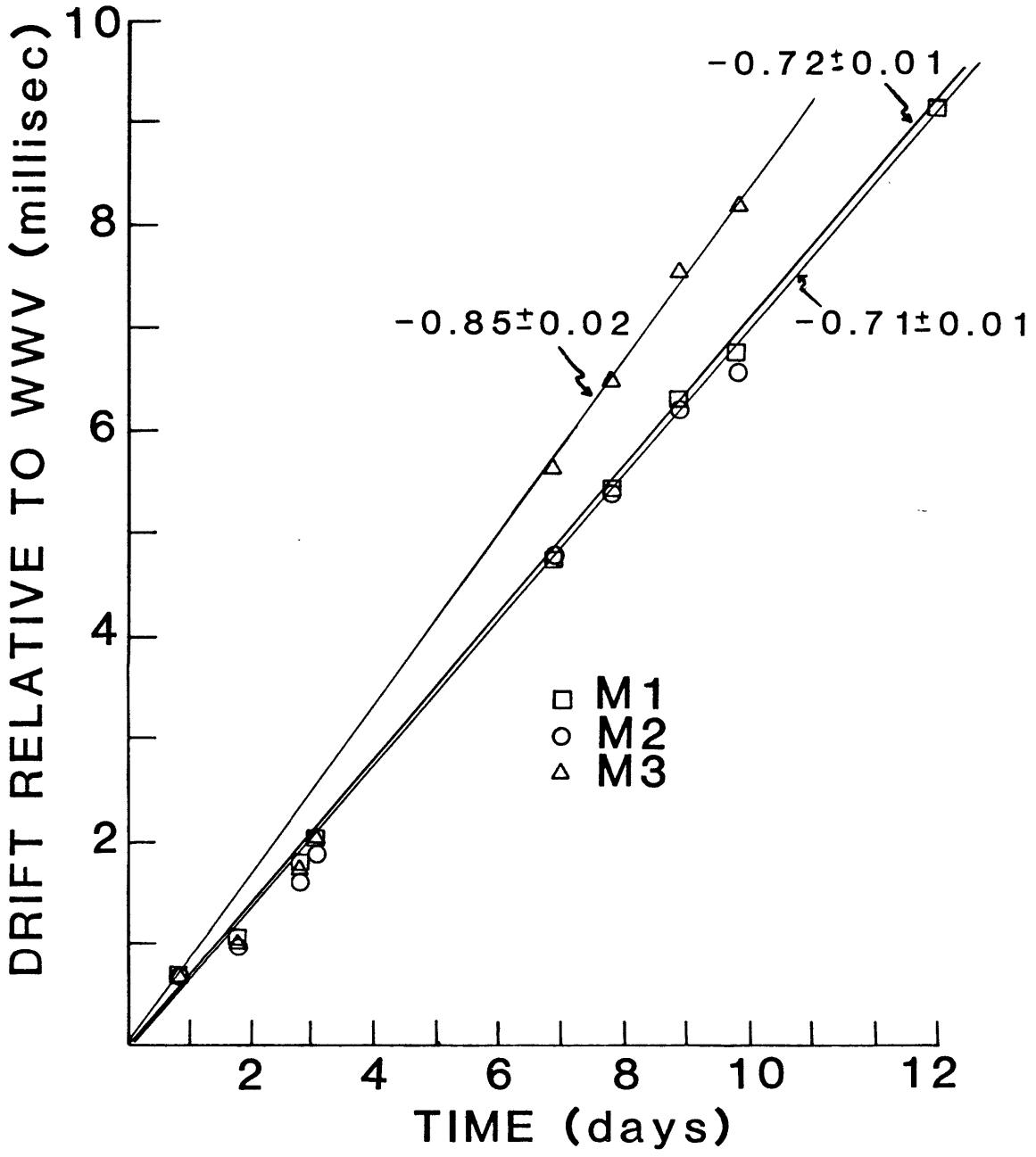
DRIFT RELATIVE TO WWV (millisec)
TIME (days)
-0.72±0.01
-0.85±0.02
-0.71±0.01
M1
M2
M3
2
4
6
8
10
12

figure 3.6

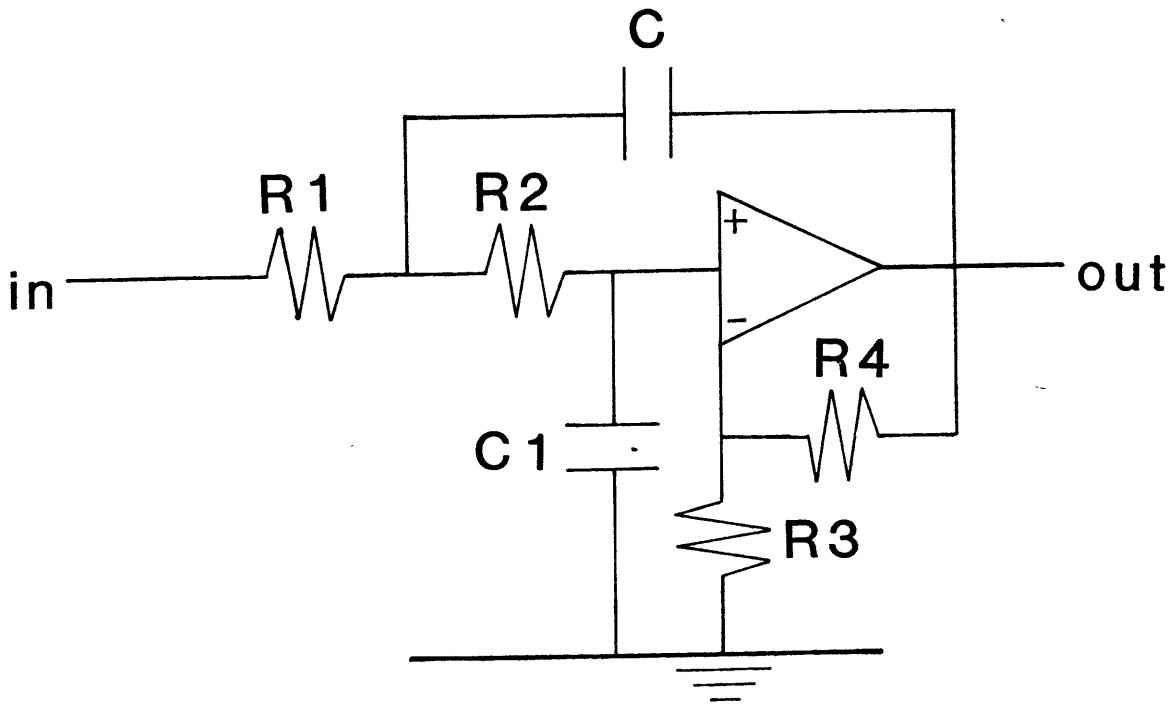

figure 3.7

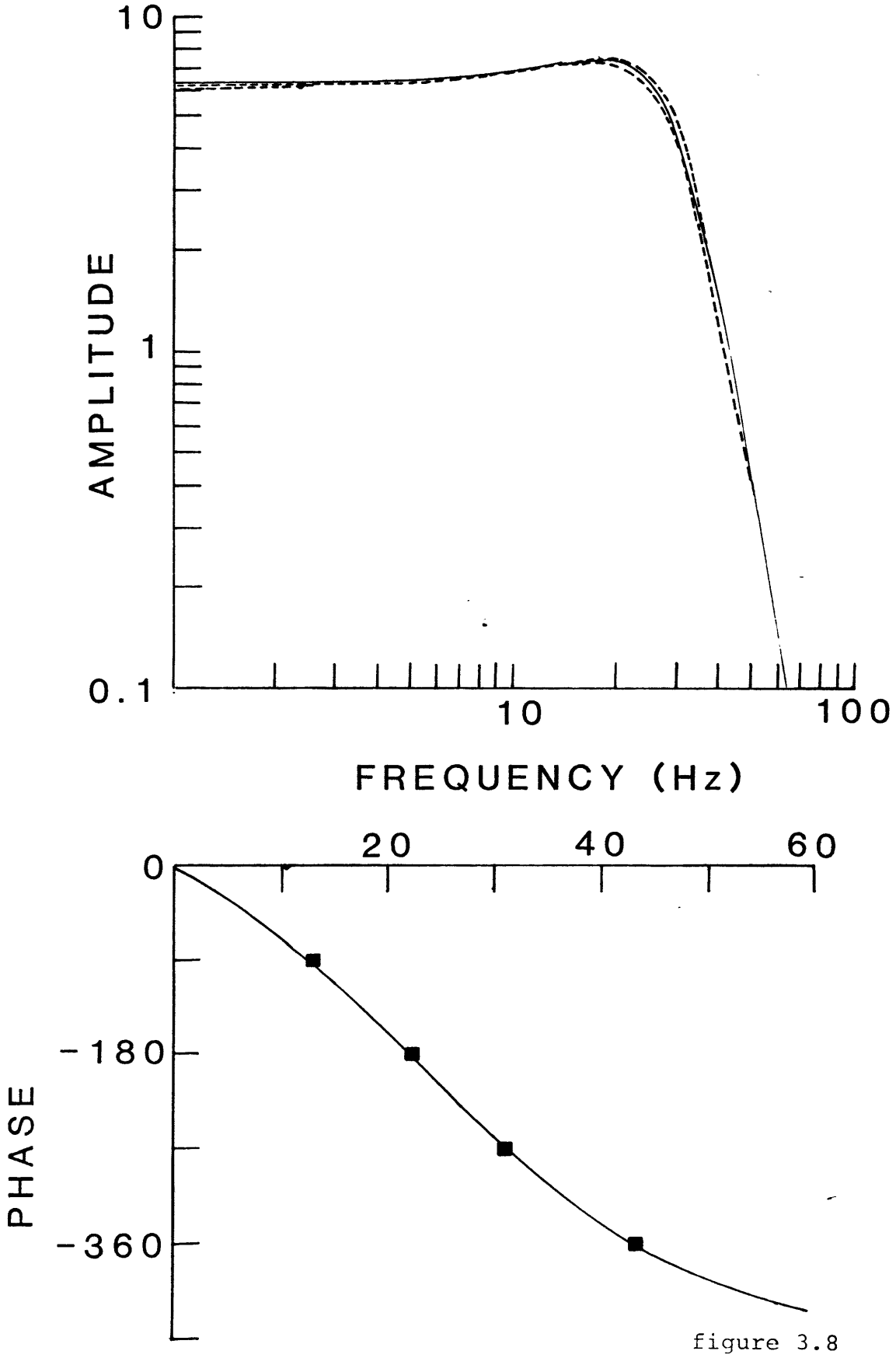

figure 3.8

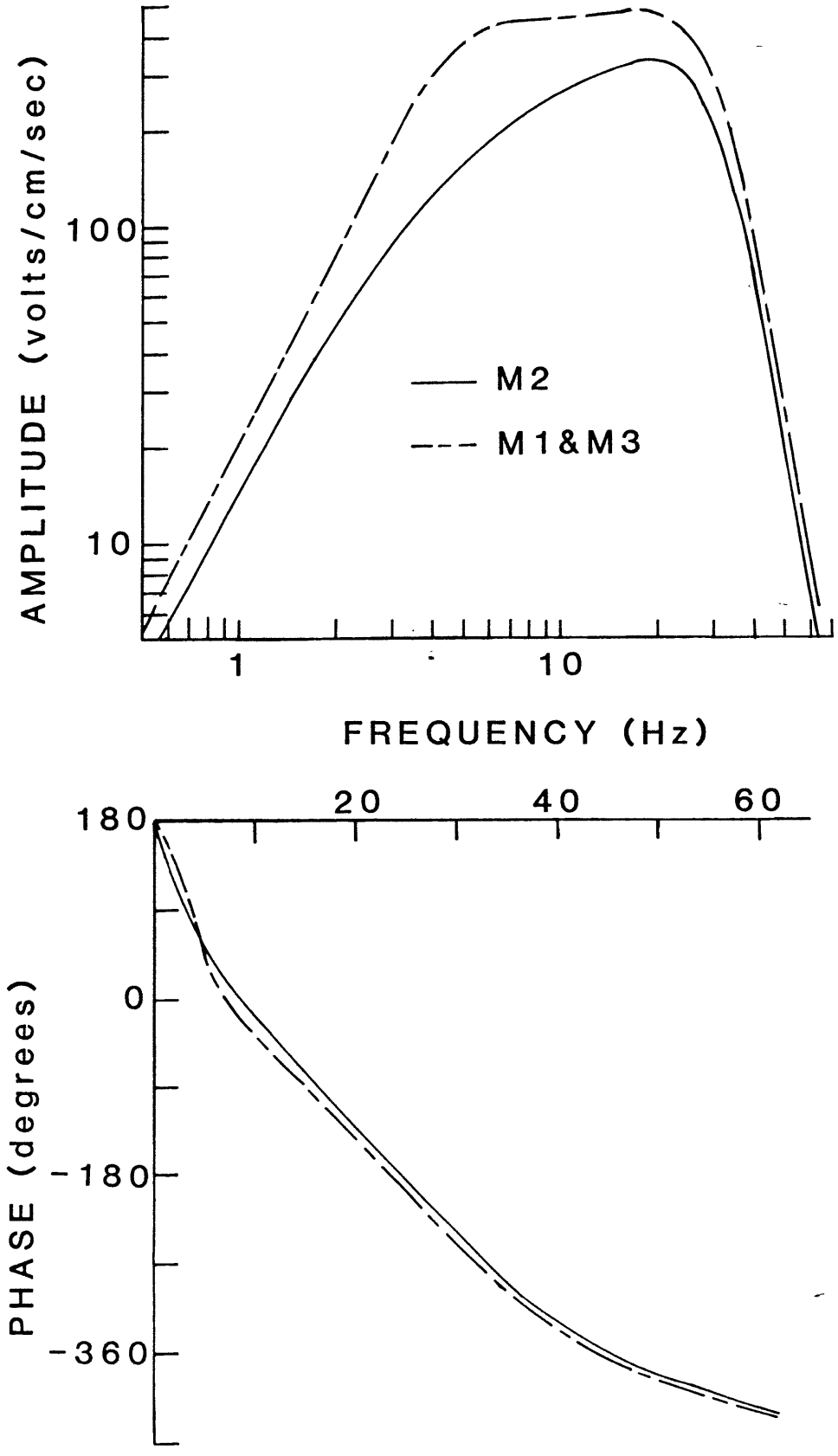
AMPLITUDE (volts/cm/sec)
100
10
M2
M1&M3
1
10
FREQUENCY (Hz)
20
40
60
180
0
-180
-360
PHASE (degrees)

figure 3.9

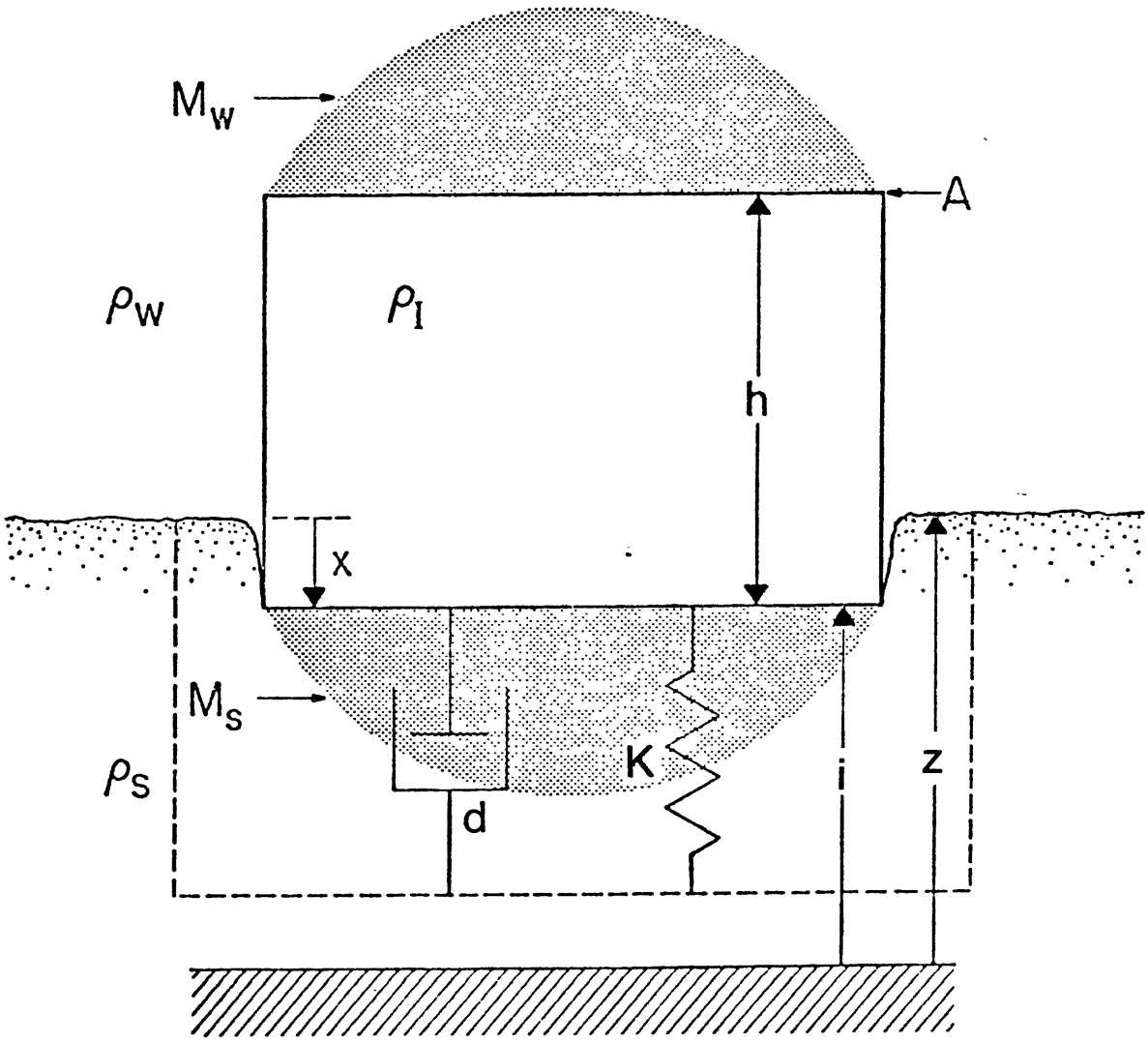

figure 3.10

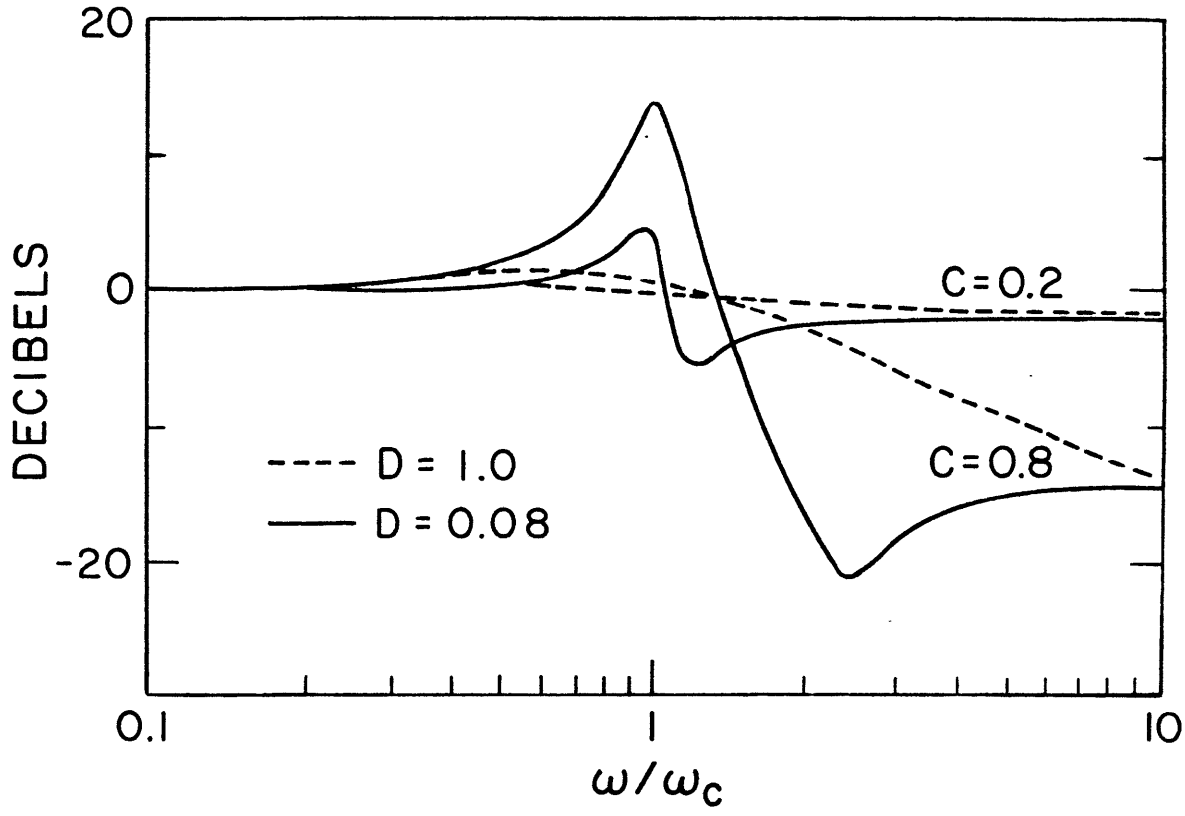

figure 3.11

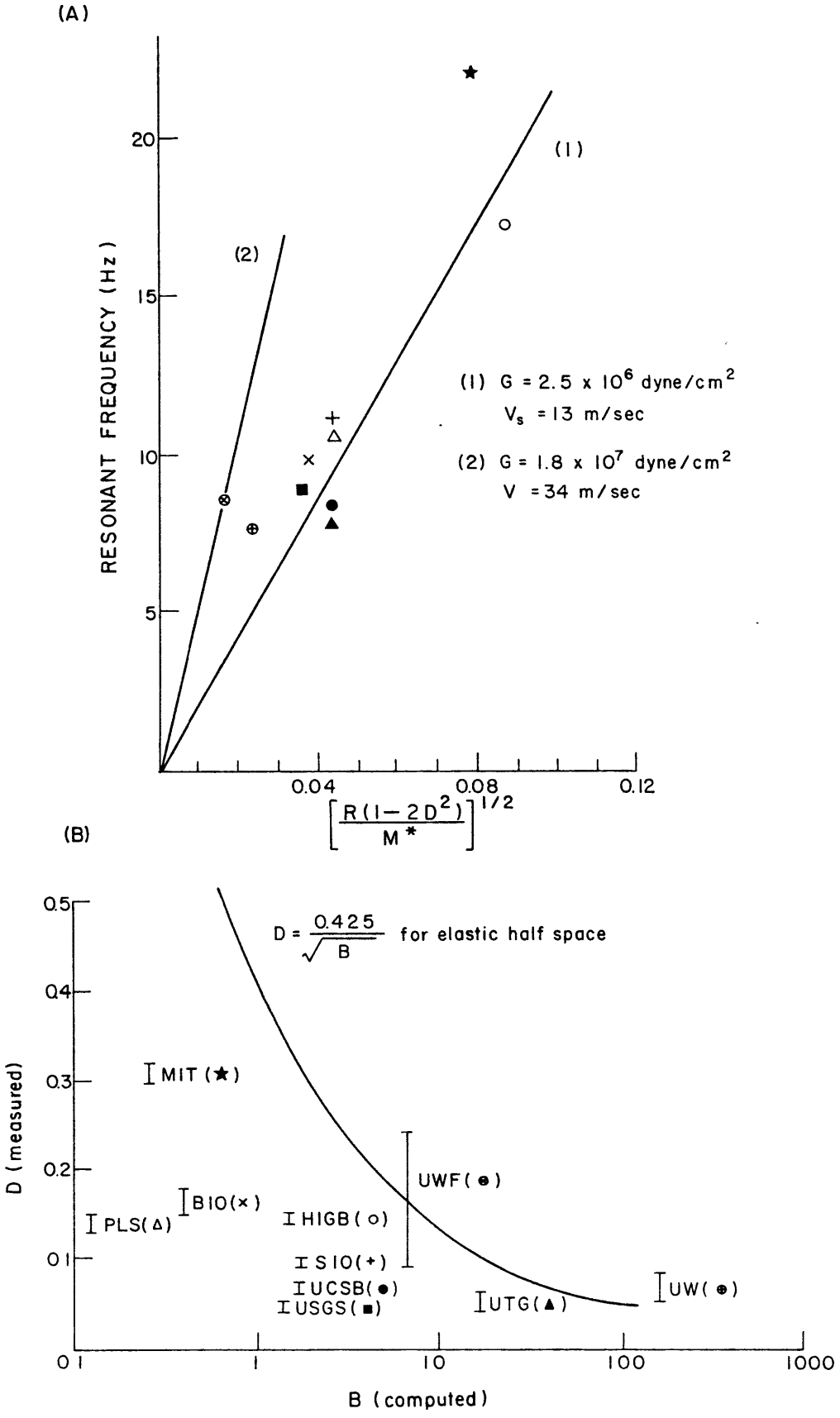
(A)
RESONANT FREQUENCY (Hz)
20
15
10
5
(1)
(2)
(1) G = 2.5 x 10^6 dyne/cm^2
Vs = 13 m/sec
(2) G = 1.8 x 10^7 dyne/cm^2
V = 34 m/sec
0.04
0.08
0.12
[R(1−2D^2)/M*]^1/2
(B)
D (measured)
0.5
0.4
0.3
0.2
0.1
D = 0.425/√B for elastic half space
MIT (★)
PLS(Δ)
BIO(×)
HIGB(○)
SIO(+)
UCSB(●)
USGS(■)
UWF(●)
UTG(▲)
UW(●)
0.1
1
10
100
1000
B (computed)

figure 3.12

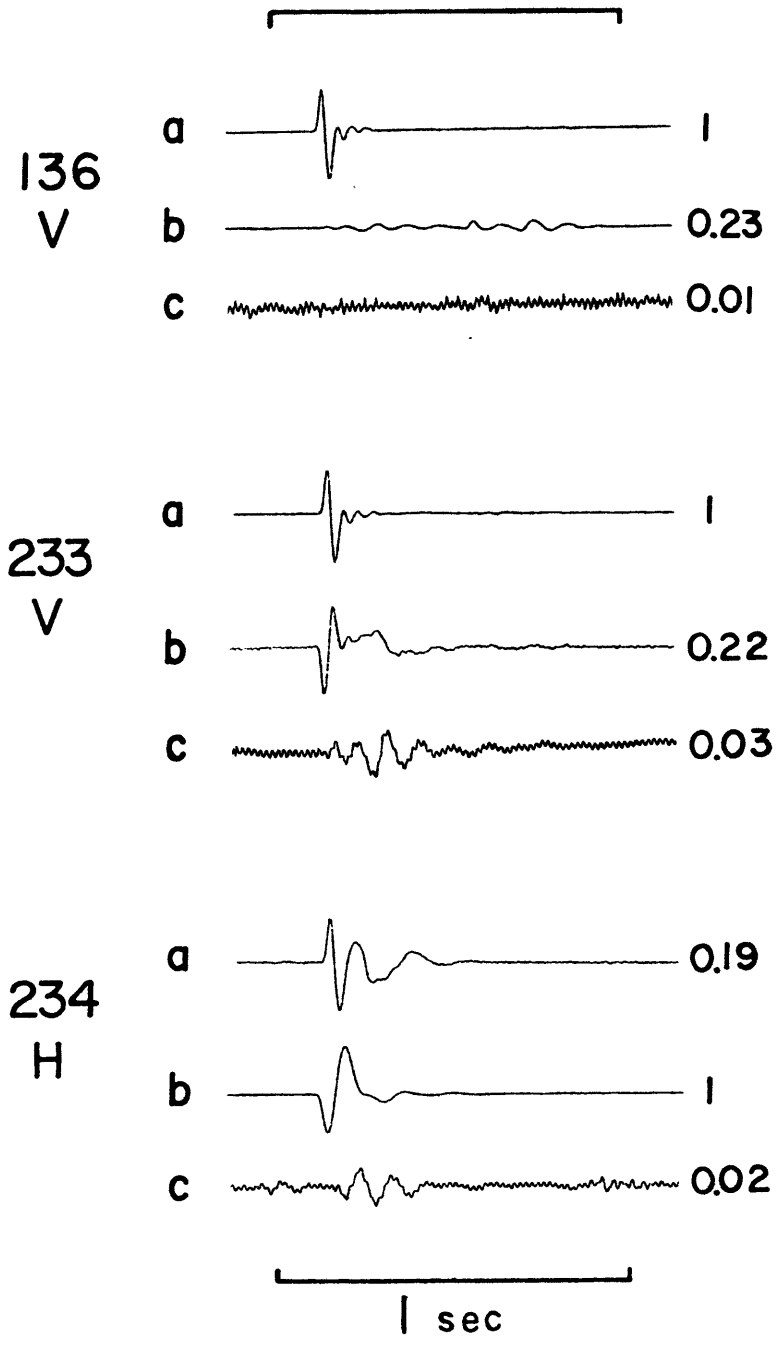

figure 3.13

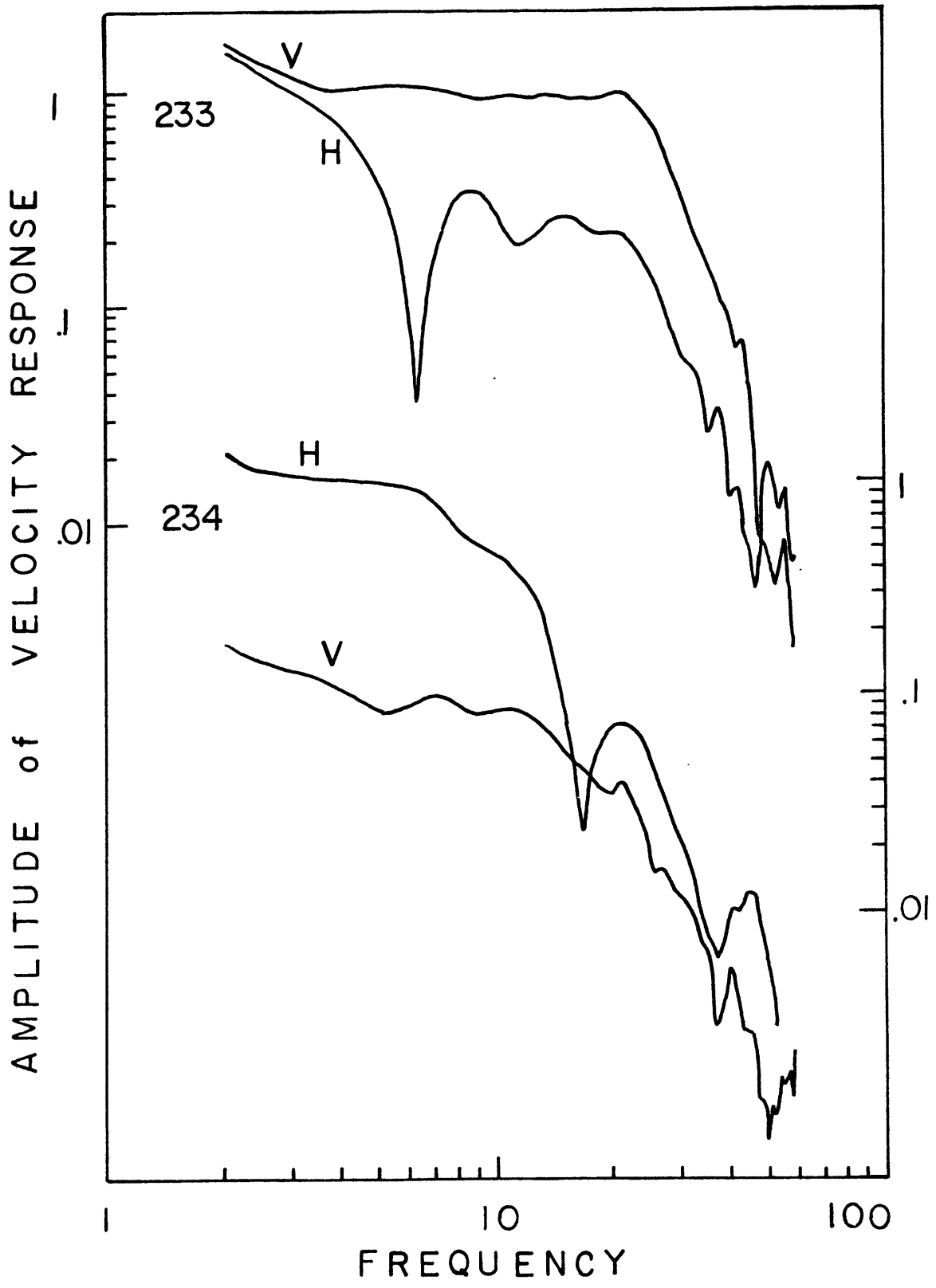
V
233
H
H
234
V
AMPLITUDE of VELOCITY RESPONSE
1
.1
.01
1
.1
.01
1
10
100
FREQUENCY

figure 3.14

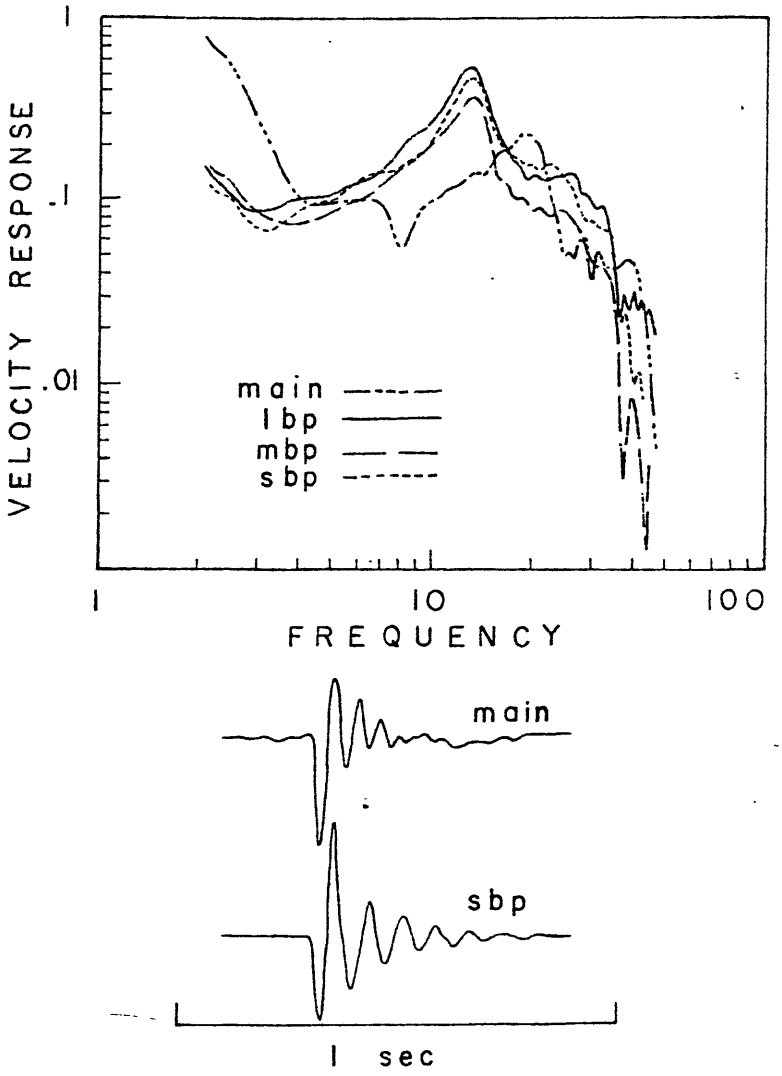

figure 3.15

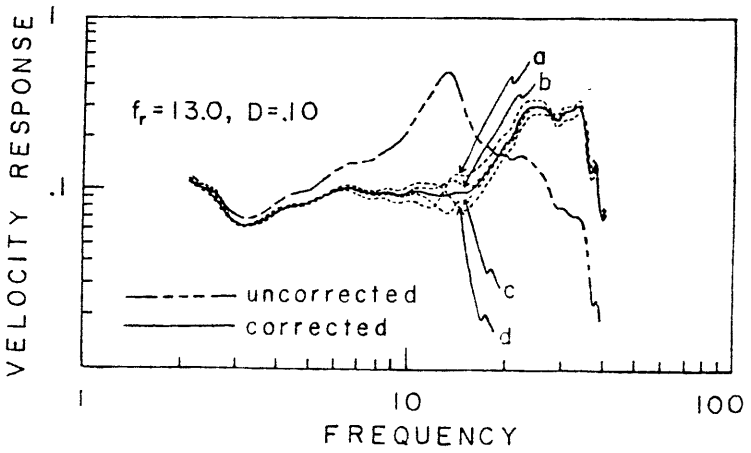

figure 3.16

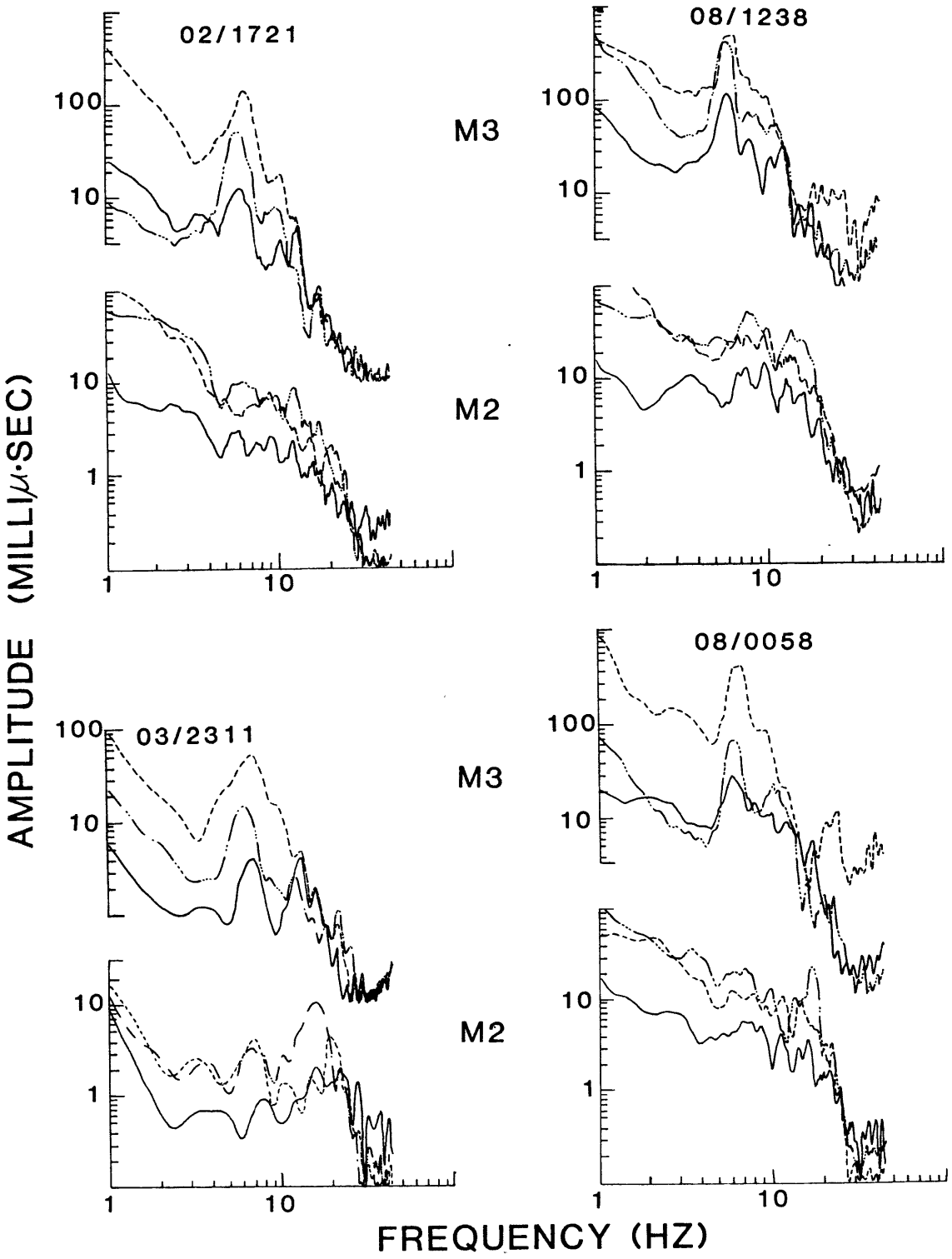
02/1721
08/1238
03/2311
08/0058
M3
M2
100
10
1
AMPLITUDE (MILLIμ·SEC)
FREQUENCY (HZ)

figure 3.17

CHAPTER IV

MICROEARTHQUAKE LOCATIONS AND SOURCE PARAMETERS

In this chapter, microearthquakes recorded in the Orozco Fracture Zone during the second phase of ROSE (ROSE II) are located. The primary data sources for this study are the arrival time readings reported by the various groups participating in the experiment. Fault plane solutions and moments for the larger events are also presented.

The results in this chapter are all relative to a laterally homogeneous velocity structure adapted from the results of several earlier refraction experiments in the region. In Chapter V, the velocity structure of the transform will be studied from data collected during ROSE II. Although lateral velocity variations are found, the major conclusions of this chapter are not changed and some of the questions raised here will be tentatively answered.

4.1 THE ROSE NETWORK

Forty-four OBS and OBH operated by nine institutions recorded data during the second phase of ROSE, and arrival times from 29 instruments were reported for the microearthquake locations. This data set includes nearly all of those stations deployed in the vicinity of features which were found to be seismically active and eventual inclusion of the data from additional stations will not increase significantly the number of locatable earthquakes or the precision of the calculated hypocenters.

The instruments varied from three component, digitally recording, event detecting seismometers to continuously recording, one-channel hydrophones. Table 4.1 summarizes the distinctive features of these instruments. Figure 4.1 shows the locations of the instruments with respect to the regional bathymetry; their geographic coordinates are listed in Table 4.2. Because the total recording time for the Woods Hole OBH is approximately 8 days, most of these instruments were retrieved and redeployed midway through ROSE II. Instrument SC1 released prematurely and was also redeployed.

The deployment pattern was designed so that each geographic alliance of groups would have a self-contained data set with which to work during the initial stage of data analysis. The University of California at Santa Barbara and at San Diego monitored the seismicity of the northern transform trough and the Woods Hole-M.I.T. group deployed a network in the central transform. A number of instruments were deployed outside the active transform in order to study the effect of propagation through the oceanic crust on earthquake generated waves, in particular shear waves. The asymmetry of the deployment pattern depicted in Figure 4.1 also reflects certain unscientific considerations such as the 200 mile limit of Mexican jurisdiction and the limited ship time available for deploying the network.

Figure 4.2 shows histograms of earthquake activity per 12 hour period reported by the instruments providing arrival time readings for this study and indicates the time period during

which each instrument was recording data. The histograms are stacked from top to bottom in order of decreasing latitude. The hatched area represents all events reported for the instrument whereas the solid area represents only those earthquakes located in this study and listed in Table 4.5. No arrival times from T13 were used for the locations because of a problem with the internal clock in the instrument. The great number of events reported by the Woods Hole instruments is partly an artifact of the method of defining an "event." For the continuously recording Woods Hole instruments, any discrete event with a maximum amplitude of at least twice the background noise level was counted; for many of these, it is impossible to pick a first arrival. For the other instruments, only those events whose arrival time had been determined were included. From this figure we can make a few preliminary inferences about the seismicity. We can see that several groups of earthquakes were detected throughout the network. Instruments SB1, SB2, SC1, SC2, T2, WH1 and WH7 also recorded many presumably very local events which were not recorded by enough instruments for a location to be calculated; UT14 also recorded many events but did not record many of those detected throughout the network (Ouchi et al., 1982).

4.2 LOCATION METHOD

The earthquake location problem was the first inverse problem studied in seismology and has been discussed by many authors. Thorough reviews are given by Stewart and Lee (1981) and Aki and Richards (1980). The non-linear nature of the problem is well known, as is its linear approximation in the form:

$$[A] \cdot x = b \tag{4.1}$$

where [A] is an nx4 matrix of the travel time derivatives for an assumed velocity model, x is a 4-dimensional vector of adjustments to an assumed hypocenter and origin time, and b is an n-dimensional vector of differences between the observed arrival times and those calculated for the assumed hypocenter. The solution is found by iterating until x becomes negligible as defined by a specified convergence criterion.

In this study, earthquakes were located using the computer program HYPOINVERSE developed at the USGS (Klein, 1978). HYPOINVERSE solves for x by doing a singular value decomposition of [A] and calculating the generalized inverse. The matrix [A] can be decomposed into:

$$[A] = [U][\Lambda][\tilde{V}] = [U_p][\Lambda_p][\tilde{V}_p]] \tag{4.2}$$

where [U] and [V] represent the eigenvectors of the "data space" and "model space", respectively, and [Λ] is a diagonal matrix of eigenvalues. A "~" indicates the transpose of the complex conjugate of the matrix. $[U_p] = [U]-[U_0]$ and $[V_p] = [V]-[V_0]$ contain the eigenvectors corresponding to non-zero

eigenvalues in $[\Lambda_p]$ and couple the data to the model; $[U_o]$ represents the discrepancy between the model and the data and $[V_o]$ represents elements of the model which cannot be determined from the data. The generalized inverse of [A] can be defined as:

$$[A_g]^{-1} = [V_p][\Lambda_p]^{-1}[\tilde{U}_p] \qquad (4.3)$$

For the (usually) overdetermined problem of hypocenter determination where $[V_o] = 0$ and $[U_o] \neq 0$, the generalized inverse is equivalent to the least squares solution classically used to locate earthquakes. The advantage of the singular value decomposition is that the resolution ($[V_p]\cdot[V_p]$), data importance ($[U_p]\cdot[U_p]$) and covariance ($\sigma_d^2\cdot[V_p]\cdot[\Lambda_p]^{-2}\cdot[Vp]$ where σ_d^2 = variance of data, assuming all data have same variance) matrices can be easily determined. Since the hypocenter location problem is usually overdetermined, the model is perfectly resolved. The data importance matrix represents the weight of each observation towards the solution and is useful for examining the effect of network geometry for individual events. The covariance matrix represents the errors in the solution due to the errors in the data but does not include the effect of errors in the assumed velocity model.

Sometimes, because of the geometry of the network relative to the source, the solution may actually be underdetermined even though more than 4 data are available. In this case, one of the eigenvalues of [A] is very small resulting in instability in $[\Lambda_p]^{-1}$ and $[\Lambda_p]^{-2}$. The

corresponding eigenvector indicates a direction in which the solution is poorly resolved. In practice, the largest component in this direction is usually depth. The singular value decomposition identifies this direction explicitly and hypocentral adjustments in this direction can be damped accordingly. For this study, an eigenvalue cutoff of 0.016 was found to be appropriate.

Another important feature of the location algorithm is that it assigns weights to the observed arrival times as a function of the residual from the previous iteration. This provision is useful for pointing out arrival time readings which are grossly in error such as in the case of a misidentification of phase. For the first iteration, P-wave arrival times were assigned a weight of 1. To compensate for larger arrival time reading errors combined with the inherently greater importance of these readings toward the solution, S-wave arrival times were weighted by a factor of 0.75.

A complete description of the location program is given by Klein (1978).

4.3 ARRIVAL TIME DATA

Arrival time readings reported by the various groups participating in ROSE were used to calculate the microearthquake locations. P wave arrival time readings were obtained from all stations. Errors in picking the arrival times were less than 0.04 seconds for most of the events and

most of the instruments. For the MIT OBS, arrival times could be picked with a precision of about 0.01 seconds for all but a few emergent events.

MIT, the University of California at San Diego and at Santa Barbara, and the University of Texas also reported S wave arrival times. On the MIT instruments, the S wave arrivals were picked by looking at the waveform recorded on three orthogonal components and are, in most cases, precise to within approximately 0.03 seconds. On the University of Texas and University of California at San Diego OBS, the S wave was picked from only a single vertical component. Although the University of California at Santa Barbara OBS is equipped with three orthogonal components, because of instrument malfunctions the S wave was picked from only a vertical and a single horizontal component (SB1) or one vertical component (SB2). Experience gained with the MIT data indicates that S wave picks from fewer than 3 components must be regarded with caution.

Figure 4.3 illustrates a few of the pitfalls of picking S arrival times with fewer than three orthogonal components. Figure 4.3a shows the seismograms from an event recorded by the MIT OBS. Because this instrument was located on low velocity material, P wave incidence angles are nearly vertical and S wave incidence angles are close to horizontal. Although an S wave can be observed on the vertical component, it is usually emergent and delayed by one or two cycles relative to the horizontal component. Moreover, on the example of figure

4.3a the S wave is polarized such that it is essentially parallel to one of the horizontal components and demonstrates the false economy of saving tape by recording only one horizontal component. In Figure 4.3b, the S wave arrival is well identified on both horizontal components. On the vertical component, however, a phase arrives considerably earlier which might be misidentified as S although its high frequency would argue against such an interpretation. This problem increases with range as refracted and converted phases become important in the seismogram (Kanasewich et al., 1973). Example 4.3b also illustrates an effect which again demonstrates the importance of having two horizontal components; a time difference of 0.12 seconds is observed between the arrival of SV on the radial component and SH on the transverse component. (The process of orienting the horizontal components will be discussed in Chapter V). Example 4.3c shows that even when the S wave arrival appears to be impulsive on the vertical channel, it may be considerably delayed relative to the arrival observed on the horizontal components.

Example 4.3a is the most extreme illustration from the MIT dataset of the above effects. Examples 4.3b and 4.3c, however, are representative of most of the data as can be seen in Appendix II which contains a catalogue of waveforms recorded from earthquakes in the Orozco Fracture Zone by the MIT OBS. Because of these effects, S wave arrivals read from fewer than three components were used only when their

inclusion permitted location of an event which had too few P wave arrival time readings.

All arrival times were corrected for the drift of the internal instrument clock during its time on the bottom relative to international standard time (WWV). For most of the instruments, the total drift over a period of a month was less than 0.25 seconds although a few instruments in ROSE had a total drift of a few seconds per month. A linear drift rate is usually assumed when making the correction. It is probable, however, that for clocks which are not encased in a temperature-controlled oven, much of the drift is due to temperature changes during trips to and from the ocean floor. The MIT OBS uses an oven encased 5 MHz oscillator rated to an accuracy of 1 part in 10^9 per day (Mattaboni and Solomon, 1977) and had an actual drift rate of approximately 6.5 msec/day during ROSE. For the network as a whole, errors due to errors in the clock drift correction are probably on the order of a few hundredths of a second.

The arrival time readings were also corrected to normalize all stations to the same water depth of 3000 meters by adding $\Delta h/V$ where Δh is the depth of the OBS minus 3000 meters and V is the crustal velocity. An average crustal P wave velocity of 6.5 km/sec was assumed in making this correction and S wave arrivals were corrected by assuming a ratio of P wave to S wave velocity of 1.75. This velocity is midway between an upper crustal velocity of 5 km/sec and a mantle velocity of 8 km/sec and represents a compromise

between attributing depth variations to either variations in the thickness of the upper crust or to deepening with age of a constant thickness crust. Both mechanisms are probably affecting this dataset. The depths of the instruments ranged from 2203 to 4068 meters with most between 2700 and 3350 meters - this corresponds to corrections to the P wave arrival times between 0.13 and -0.15 seconds with most between 0.05 and -0.06 seconds. The error in the correction due to errors in the instrument depth and in the velocity used for the correction is probably 0.01-0.03 seconds.

Errors in the geographical coordinates of the OBS due both to navigation errors and to lateral motion of the OBS during the trip through the water column may range up to a kilometer. The effect on the locations is similar to the error induced by differences between the assumed and actual velocity structure. These errors are not included in the "picking error" and will be discussed in section 4.5.

For the calculation of the covariance matrix, an effective "picking error" of 0.07 seconds was assumed.

4.4 VELOCITY MODEL FOR HYPOCENTER LOCATIONS

The assumption that the [A] matrix in equation 4.2 is known implies that the velocity structure is known. To locate the earthquakes recorded during ROSE, a P wave velocity structure of 9 homogeneous, flat layers was assumed which approximates a crust with velocity increasing rapidly from 4.4 to 5 km/sec in the first two kilometers and then gradually

increasing to a Moho velocity of 7.8 km/sec at a depth of 6.65 km (Table 4.3). This velocity structure was based on the results obtained from line 57 of Lewis and Snydsman (1979) on 0 to 0.4 million year old crust at 13.5°N and from line B of Orcutt et al. (1976) on 2.9 million year old crust at 9°N. Similar velocity-depth profiles were obtained independently from these two data sets and seemed appropriate for this study which involves crust of age 0 to 2 million years. Although several refraction lines along the axis of the East Pacific Rise have suggested the presence of a low velocity zone in the crust (e.g., Orcutt et al., 1976) or upper mantle (Bibee, 1981), the lateral extent of this low velocity zone must be limited to a few kilometers and was not included here. For the S wave velocity structure, a V_p/V_s ratio of 1.75 corresponding to a Poisson's ratio of 0.26 was assumed. The effect on the hypocenter calculations of varying the layered P-wave velocity structure or V_p/V_s will be discussed in section 4.5 and the effect of lateral velocity heterogeneity will be examined in Chapter V.

An attempt was made to constrain V_p/V_s directly from the observations by plotting (S2-S1) vs. (P2-P1) where P1 and S1 are the P and S wave arrival times at station 1, and P2 and S2 are the arrival times of the same event at station 2. For a laterally homogeneous medium with a constant V_p/V_s throughout, the data should define a line passing through the origin with a slope equal to V_p/V_s. The data are displayed in Figure 4.4 and the slopes and intercepts of lines determined by a

least-squares regression assuming all error to be in S are given in Table 4.4. Because of errors in the data, the lines were not constrained to pass through the origin.

Data sets 1, 2 and 3 give a slope of about 1.77 which corresponds to a Poisson's ratio ν of 0.27. This is similar to the values for V_p/V_s which are found from laboratory measurements on the type of rocks thought to make up the lower oceanic crust and upper mantle (Christensen and Salisbury, 1972, 1973, 1975). Data sets 4 and 5, however, indicate very low values of V_p/V_s. Both in situ experiments and laboratory measurements have observed Vp/Vs considerably greater than 1.77 (up to 2.05), and these observations have been explained in terms of cracking and weakening of the upper layer of oceanic basalt (Christensen and Salisbury, 1973; Francis, 1976) or serpentinization of peridotite (Christensen, 1972). No oceanic rock types, however, have V_p/V_s much lower than 1.70 (ν = 0.24) (Spudich and Orcutt, 1980) and a geologic process resulting in such a situation is difficult to envisage. Moreover, the intercepts are significantly different from zero, suggesting a systematic bias in the data.

Reexamining Figure 4.4, we see that the lower V_p/V_s ratio is determined by data with $\Delta P \geq 2$ seconds. If we divide datasets 4 and 5 into two subsets, we find that, with the exception of datset 4 which was determined from only 4 points, the slopes increase (Table 4.4b) and are no longer significantly different from 1.77. The data do not permit us

to determine whether this observation is due to a systematic mispicking of phases or to local velocity anomalies. For data set 4, $\Delta P > 2.1$ seconds corresponds to hypocenters in the central transform whereas $\Delta P < 2.1$ seconds corresponds to hypocenters in the northern transform. In section 4.6, a pronounced delay of S waves relative to P waves is observed at M2 and M3 for events in the central transform. This would also produce the result observed in Figure 4.4 and signals a structural cause. For data set 5, the difference corresponds to hypocenters near 105°12'W ($\Delta P < 2.1$) and 105°6'W ($\Delta P > 2.1$) along trough A. These two groups of earthquakes also appear to be distinguished by differences in focal depth (section 4.5.2) and the observation of Figure 4.4 may be due to either local velocity structure or to a systematic mispicking of phase.

4.5 HYPOCENTER LOCATIONS

The hypocentral parameters of earthquakes located during Phase II of ROSE are presented in Table 3.5. All events located with a root-mean-squared residual of less than 0.25 seconds are included. These 70 events represent 85% of the events for which four or more arrival time readings were available. Although data from 29 stations were reported, no event was reported by all stations. Thirteen events were located using at least 15 arrival time readings and most locations calculated from only four or five readings are supported by spatial and temporal association with a larger,

well-located earthquake. The number of stations reporting an event provides a crude measure of relative magnitude. Magnitude will be discussed further in section 4.8.

An initial hypocenter close to the station reporting the earliest arrival time was assumed. The locations were calculated twice, starting from initial depths of 5 and 12 km. For most events, the two initial hypocenters converged to the same solution. When two different depths were obtained, the solution giving the smaller residual was chosen; with only one exception (March 4 at 20h10m) this was the shallower depth. That this one exception is probably a spurious result will be discussed in 4.5.1.

Although most of the earthquakes were not detected by all of the instruments, the large number of instruments deployed during ROSE was useful for two reasons. Obviously, it extended the spatial extent of good hypocentral resolving power of the network compared to the much smaller networks of instruments used in earlier studies. Equally importantly, the large number of stations led to the detection of errors in data processing which might otherwise have been undetected and would have therefore led to erroneous locations. An examination of the residuals at each station for those events located using 18 or more arrivals revealed systematic trends which could be traced to errors in the clock drift correction for a few instruments. Small events located using only 4-6 arrival times including the erroneous data often seemed to be well located (as indicated by small root-mean-squared

residuals and covariance ellipses) when actually their locations were in error by several kilometers.

The calculated epicenters are superimposed on the local bathymetry in Figure (4.5). Unlike the teleseismic epicenters of Figure 2.6 most of the activity is localized in two regions and is clearly related to topographic features. Over half of the epicenters are aligned along trough A (Figure 2.4), subsequently referred to as region 1. The second concentration of activity is associated with the western end of trough B and ridge β', subsequently referred to as region 2. The epicenters are quite scattered, and some do not bear any obvious relationship to topography. Before discussing the implications of this pattern of seismicity, we must first examine the precision of the calculated locations with respect to the layered velocity model.

4.5.1 PRECISION OF THE LOCATIONS

The axes of the covariance matrix of the solution calculated by HYPOINVERSE define the 32% confidence ellipse of the solution to the linearized problem. The 95% confidence ellipse is obtained by multiplying the axis lengths by a factor of 2.4. Because the problem is not linear, these ellipses provide only a qualitative measure of the precision of the location. The projection of these axes (95% confidence level) onto horizontal and vertical planes through the hypocenter are listed in Table 4.5 as measures of the horizontal and vertical errors in the solution. Only the

larger of the two horizontal errors is listed. These formal errors suggest that most of the earthquake locations are precise to within one or two kilometers in the horizontal direction and point out those events for which one of the eigenvalues is less than the cutoff value, indicating that the geometry of the available data provides little constraint in that direction. In general, the poorly constrained direction is nearly vertical, corresponding to depth. Locations for several events near the northern ridge-transform intersection, however, have a zero eigenvalue corresponding approximately to latitude. These events were located using P and S arrival times at only two stations. Usually this leads to two possible epicenters. For these events, however, the two stations and the epicenter fall approximately on the same line and the two possible solutions degenerate to one.

Additional information for evaluating the precision is contained in the parameters "maximum azimuthal gap" and "distance to the closest station" which are also listed in Table 4.5. As can be seen in Figure 4.5, most of the earthquakes were along the perimeter of the network and the maximum azimuthal gap is sometimes quite large. Lilwall and Francis (1978) have demonstrated through numerical experiments that this does not necessarily imply poor resolution of the hypocenter, provided that the distance between the event and the closest station is "small." In fact, for a three or four station array with a station spacing of 10 km, the best depth and epicenter resolution is obtained for events just

outside the array near one of the instruments. A generally accepted rule of thumb for evaluating depth resolution is that the closest station to the event should be within a horizontal distance less than the focal depth.

The effects of errors in the assumed layered model were also examined empirically by perturbing parameters of the layered model and recalculating the locations. The latitude, longitude and depth of the new location were subtracted from the latitude, longitude and depth calculated with the model of Table 4.3 and the differences were plotted as histograms. Results from three alternate models are shown in Figure 4.6. In Figure 4.6a, the locations were recalculated with the crustal model of Table 3 and a V_p/V_s ratio of 1.78; in 4.6b, a model consisting of a single 6 km thick layer with a velocity of 6 km/sec overlying an 8 km/sec half-space was assumed; and in 4.6c the crust of Table 4.3 was modified by increasing the half-space velocity to 8 km/sec and decreasing the thickness of the 7.72 km/s layer to 0.5 km.

For all three cases, most latitude and longitude changes are less than 0.3 km and almost all are less than 1 km. All larger epicentral perturbations correspond to events for which HYPOINVERSE indicated poor depth control and for which the calculated depth changed by several kilometers when the model was perturbed.

The depths are more sensitive than the epicenters to changes in the model. In Figures 4.6a and 4.6c, most depth changes are within ±1 km; 4.6b shows a bit more scatter.

Increasing the Moho velocity (Figure 4.6c) systematically decreases the depths, and the velocity model of Figure 4.6b, which decreases the velocity in the lower crust, increases the depths. In most cases, relative depth differences among events are preserved. The change in the rms travel time residual is not significantly different from 0.0 for any of the models tested and we cannot resolve whether any of these models represents a more appropriate average velocity model than that of Table 4.3.

To summarize the results presented in this section, the errors indicated by HYPOINVERSE appear, in most cases, to be an accurate reflection of the precision of the locations with respect to a layered velocity model. For most events the calculated hypocenters are precise to within less than a kilometer horizontally and to within about 2 km vertically. Errors due to small changes in the assumed layered velocity structure are of the same order. The effect of possible lateral heterogeneity in the true velocity structure has not been considered here and will be discussed in Chapter V.

4.5.2 SEISMICITY OF REGION 1

Figure 4.7 shows the epicenters which were located along the northern trough and illustrates the temporal pattern of activity. Most of the earthquakes were clearly aligned along

the topographic trace of the trough.*

No earthquakes were recorded along the northern transform trough on February 27 and 28. During the first few days of March, earthquakes occurred near 105°W and from 105°10'W to the intersection of the transform with East Pacific Rise near 105°17'W. On March 5,6, and 7, only a few events were located and the epicenters are quite scattered. Unfortunately, most of the instruments deployed near the ridge-transform intersection were no longer recording data at this time and at least part of this scatter may result from poor station distribution. The cluster of earthquakes at 105°06'W on March 8 represents a mainshock-aftershock sequence along a section of the transform which did not show any seismic activity during the preceding week. The main shock of this sequence was the largest earthquake recorded during ROSE II. Within the sequence, an eastward progression of activity with time (with a few exceptions) can be observed (Figure 4.8). All

---

* Note: The bathymetric contours in Figure 4.7 and 4.14 were drawn by myself from the data collected by the R/V CONRAD and R/V KANA KEOKI during ROSE. Although, in general, the contours I determined were the same as those determined by Mammerickx (1980) from data collected previous to ROSE and including a subset of the ROSE data, a few differences can be observed, most notably in the position of the 3000 m contour at the intersection of the East Pacific Rise and trough A (Figure 2.4 and at the intersection of troughs B and C. I have preferred to use the Mammerickx (1980) map as a base map for several figures because of its better coverage of areas outside of the immediate vicinity of the ROSE II network and because of its more "professional" aspect. Because of my interest in the detailed tectonics of the transform, however, I reexamined the areas of discrepancy when the Mammerickx map became available and feel that, in the two areas mentioned, the contours I determined are a more accurate portrayal of the bathymetry.

epicenters could have occurred along a single 5 km long fault with a strike of N75°E.

Figure 4.9 is a vertical section of the earthquakes in region 1 projected onto an east-west striking plane. Most of the earthquakes appear to be shallower than about four kilometers. It has been predicted that the depth of the seismic zone in transform faults should decrease as the spreading center-transform intersection is approached because of the elevation of the isotherms predicted by thermal models of spreading centers. For a spreading rate of 9.3 cm/yr at a distance of 10 km from the rise crest, the 300° isotherm should be at a depth of less than 1 km and temperatures near the melting point should be encountered at a depth of 5 km, according to the model of Sleep (1975). This model does not include the effect of deep hydrothermal circulation or of cooling of the crust due to lateral conduction of heat into the older, colder crust on the other side of the transform. In Figure 4.9, we certainly do not see a shallowing of the activity as the ridge-transform intersection is approached. In fact, the deepest hypocenters are near 105°12'W and are within 10 km of the intersection. These events (March 2 at 13h00m and 17h21m and March 3 at 17h24m) were among the larger earthquakes recorded during ROSE and were located using readings from stations throughout the network. Unlike the sequence of March 8, they do not appear to represent a mainshock-aftershock sequence along a single fault.

This sequence of events at 105°12'W illustrates the importance of having a station at an epicentral distance less than one focal depth. Data from Scripps were not reported until after the initial locations had been calculated and interpreted (ROSE project scientists, 1981). Without SC2, the closest station was SB1 at a distance of about 15 km, and apparently well-constrained hypocentral depths of 12 to 15 km were obtained for these events. Figure 4.10 shows residuals for locations calculated for a series of fixed depths. The weighting of arrivals as a function of the residual during the previous iteration was suppressed so that all locations were calculated from the same dataset. For all events except that of March 2 at 16h45m, minima at depths ranging from 7 to 15 km are indicated when SC2 is not included in the dataset. These apparent depths were particularly puzzling because of the proximity of these events to the intersection of the transform with the East Pacific Rise. When SC2 is added to the dataset, the depths decrease and the minima in the residuals are very sharply defined. The travel time residual at most stations is not affected by the change in depth of the hypocenter. At SB1, however, the shallow depth induces a P-wave residual of 0.13 to 0.23 sec and an S wave residual of 0.83 seconds. These residuals may be indicative of significant departures of the true velocity structure from the assumed layered model. Depths for the earthquakes on March 8 are not changed significantly by the addition of data from SC1' which decreases the distance to the closest station from 9 to 3 km

(Figure 4.11).

Because of the large importance of SC2 on the solution, the effect of errors in the geographical coordinates of SC2 was examined by perturbing the location of SC2 by 0.5 minutes to the north, east, south, and west and recalculating the locations for the crustal structure of Table 4.3 and for a single 6 km/sec layer over an 8 cm/sec half-space, The results are displayed in Figure 4.12. In general, calculated depths decrease as the station moves away from the epicenter of the earthquakes and vice versa. For the single layer crustal model, the variation in depth among the events is decreased so that all events appear to be at approximately the same depth. Most epicentral perturbations are well within the indicated error and the relative position of the epicenters does not change.

The apparent depth difference between earthquakes near 105°6'W and 105°12'W is supported by the waveforms recorded on M2 and M3 (Fig. 4.13). For earthquakes near 105°12'W, the onset of the P wave is impulsive and the waveform is simple; for events near 105°6'W, the first arrival is a low amplitude, relatively long period phase, interpreted to be P_n, followed 0.35 to 0.38 seconds later by a larger amplitude, higher frequency arrival interpreted to be either the direct arrival or the wide angle reflection from the Moho. In fact, the P waveforms for events near 105°6'W are very similar to those observed from 500 lb shots of TNT at similar ranges, and the shots are known to be very shallow.

The differences between the P waveforms do not result from radiation pattern or path differences since the fault plane solutions (see section 4.7) and paths to M2 and M3 are similar for sources in the two groups; nor are the differences due to source strength since the moments of several events are also comparable (see section 4.8). The difference must therefore be attributed to differences in depth and/or in the crustal structure of the source region. In particular, the absence of a P_n arrival for earthquakes near 105°12'W indicates that the source was below the Moho, suggesting that the crust is very thin near the ridge-transform intersection. The upper mantle, moreover, must be cold enough to store elastic energy and fail seismically.

The arrival time difference between the P_n and the direct arrival for events near 105°6'W further constrains the source depth. This difference increases as the Moho is approached from above. For a crust with a thickness of 5.5 km and a velocity of 6.5 km/sec overlying an 8 km/sec upper mantle, at a range of 40 km the time difference increases from 0.16 to 0.55 seconds as depth increases from the surface to 3.5 kilometers. For a crustal velocity of 6.8 km/sec, the time difference increases from 0.05 to 0.37 seconds. The observed arrival time difference therefore suggests that the earthquakes of the sequence were all at a similar mid-crustal depth.

In Figure 4.2, it can be seen that several stations deployed near the trough recorded many more earthquakes than

could be located. Although the sensitivity of different instruments may not have been the same because of differences in both the gain of the recording electronics and the geologic parameters of the deployment site (see Chapter 3.2), examination of the arrival time difference between P and S waves at these stations provides additional insights into the temporal and spatial pattern of activity during the two weeks of the experiment (Figure 4.14). The solid circles represent earthquakes which were located and are listed in Table 4.5. Several of the larger, located events do not appear on Figure 4.14 because the P wave saturated the recording system and no S wave arrival could be picked. Most events for which no S wave arrival was reported in the arrival time list submitted to us were larger events, indicating that small events which were too close to the instrument for the S-P time difference to be resolved are not a major factor. For a constant velocity half-space, the arrival time difference is equal to $[(V_p/V_s-1)/V_p]\cdot D$, where D is the distance between the earthquake and the station and V_p and V_s are the P and S wave velocities, respectively. Assuming that these earthquakes occurred at shallow depths along the line defined by the located events, the observed S-P time differences correspond to two possible locations. The dashed lines at a constant S-P time for each instrument indicate the S-P time difference for a surface event located along the line defined by the epicenters assuming V_p = 6 cm/sec and V_p/V_s = 1.75. This figure shows that the seismic gap preceeding the March 8, 1214

sequence is reflected by the smallest events recorded. In particular, note that SB1 detected many events with a wide range of S-P times; only one had S-P<1.15 seconds which corresponds to a distance of approximately 9 km for a surface source or 7 km for a source at 5 km depth. SC3 (SC1' in Table 4.2) also lacks S-P times corresponding to the portion of the fault affected by the March 8 sequence; one or both ends of the fault beyond this section showed a fairly continuous level of activity before March 8 and then became quiet. SB2 and H517 (see Figure 4.2) detected very few events which were not detected by several other instruments.

4.5.3 SEISMICITY OF REGION 2

Figure 4.15 shows the seismicity of the central part of the Orozco transform fault. The note in the previous section referring to the contours on Figure 4.7 also applies to this figure. Because of the station distribution, hypocentral parameters in this region are less well determined than in region 1. Except for a continuously active area near 15°13'N, 104°47'W, no particular temporal pattern of activity can be observed and the epicenters do not show a clear lineation along topographic contours. The topography, moreover, suggests a series of small basins rather than a single well-defined trough. Trough C (Fig. 2.4), which runs parallel to the southern branch of the East Pacific Rise, was not the site of any located seismic activity during ROSE II.

Several earthquakes were located in region 2 outside of trough B. The hypocenters of the March 2 05h23m, March 4 14h59m and March 5 10h10m earthquakes were calculated from data recorded throughout the array and are well determined with respect to the assumed layered velocity model. Most of the others were located with only four or five arrival time readings and probably have errors larger than those indicated by HYPOINVERSE. In particular, the hypocenters of the March 2 events at 08h53m and 13h35m are indistinguishable from that of the March 3 23h11m event when they are relocated relative to the March 4 09h19m earthquake using a master event technique. These two events were located using data from H520 but no readings from WH1, and in section 4.4, where average residuals at individual stations are discussed, we will see that this would indeed bias the location. The station distribution was poor for determining hypocenters at the eastern end of the trough and the locations of these events are quite scattered. Four events were located near the site of instrument UT13. As previously mentioned, arrival times at this instrument could not be included in the dataset for the inversion. The observed arrival time difference between S and P at UT13, however, is not consistent with the calculated hypocenter. Assuming a surface source, the S-P arrival time difference at UT13 and UT14 places these events near either 15°11'N, 104°32' or 15°N, 104°33'W (Ouchi et al., 1982).

Figure 4.16 shows a vertical section of the hypocenters in region 2 projected on a north-south plane. The depths are

scattered from 0 to 15 km. Figure 4.17 shows residuals as a function of depth for the largest events. Although HYPOINVERSE placed the March 2 05h23m earthquakes at a depth of 11-13 km, we can see that this minimum in the residuals is probably not significant. Among the other events, some depth variation is suggested.

As previously mentioned, 15°13'N, 104°47'W was the site of recurrent activity during ROSE II. This activity includes both isolated events and sequences that resemble "swarms" rather than mainshock-aftershock activity. Relocating these earthquakes relative to the March 4, 09h19m event, these earthquakes appear to have been aligned in a north-south direction and some depth differences are indicated (Figure 4.18).

As previously mentioned, UT14 recorded a continuously high level of activity which was not detected throughout the network. The S-P arrival time difference for these events is shown in Figure 4.19. The S-P times of 3 to 4 seconds correspond primarily to events located near 15°12'N, 104°47'W. The many earthquakes with S-P times of 1.2 to 2.2 seconds represent the population of earthquakes which was not detected throughout the array. From a magnitude scale based on duration, Ouchi *et al.* (1982) have suggested that these events may also have a higher "b" value than those in either region I or in the region near 15°13'N, 104°47'W. Note, also, that no S-P times are observed which would indicate activity very near UT13; as previously noted, this contradicts several of the

calculated epicenters. At UT10 and 03, the shortest S-P times correspond to activity near 15°12'N, 104°47'W, confirming that trough C (Fig. 2.4) was seismically inactive during ROSE.

4.6 RESIDUALS AT INDIVIDUAL STATIONS

The travel time residuals observed at individual stations potentially contain information about local departures from the assumed velocity model. The residuals at each station from earthquakes in region 1 and region 2 were therefore separated into two groups to see if systematic differences could be observed. Each group was further subdivided into residuals from earthquakes located by at least 10 arrival time readings and residuals from events with fewer than 10 readings. This additional division was designed to determine whether locations calculated with only a few readings might be systematically biased relative to locations calculated from data from stations throughout the network.

The mean of the residuals, rms deviation of the mean, and number of events at each station for these four groups is presented in Table 4.6. The rms deviation of the average residuals at a given station reflects the random arrival time picking errors combined with variations in the source region anomaly for events within a group. The average rms deviation for P wave arrivals (excluding stations T14 and T4 for sources in region 2) is 0.067, indicating that the generalized "picking error" of 0.07 seconds used to calculate the covariance matrix of the solution is reasonable (Table 4.6b).

As expected, the rms deviation of the S wave residuals (0.12 seconds) is somewhat higher.

At many stations, the average residual is less than 0.10 seconds and no significant difference among the four groupings is observed. The residuals at several stations, however, deserve further discussion.

The marked increase in residuals at SB1 from the group of earthquakes near 15°23'N, 104°12'W when SC2 was added to the dataset has already been mentioned. For SB1, these earthquakes dominate the residual for "region 1, >10 readings" in Table 4.6. Not surprisingly, for earthquakes located with fewer than 10 readings this large residual is not observed. For the March 4, 18h56m and March 4, 09h42m earthquakes, the only other events recorded by both SB1 and SC2 and located with more than 10 readings, these large residuals were also not determined. We therefore cannot distinguish whether the residual at SB1 results from a very local structural effect and should not be included as a station correction when locating small earthquakes west of 105°12'W or whether it represents a more regional anomaly. Relocating these events with station corrections determined from the average residuals, however, does not significantly alter the pattern of seismicity described in 4.5.2.

WH1 and H520 both show a small average residual from earthquakes in region 1. For region 2, however, WH1 has a consistent residual of about -0.13 seconds and H520 has a residual of about +0.13. The distance between the two

stations is approximately 2.5 km according to the reported geographical coordinates. Although the relative delay of 0.26 seconds between H520 and WH1 might be due to a pronounced local P velocity anomaly between the two stations, a more likely cause is errors in the geographic coordinates of one or both instruments. Moving WH1 east by 0.5 minutes (approximately 1 km) and H520 west by the same distance eliminates these observed residuals without significantly changing the residual for events in region 1. The hypocentral parameters of earthquakes in neither region change and the rms residual for events in region 2 decreases (Figure 4.20).

At stations M2 and M3, the residual for both P and S waves is, in general, small for events in region 1. For events in region 2, a negative average residual is observed for the P wave at each station. We cannot determine whether this results from a structural anomaly or from errors in the instrument coordinates. This residual is not observed for the S wave arrivals, however, and thus indicates that S waves are delayed relative to P waves for events in region 2. This can result either from a very low S wave velocity in region 2 or from a true ray path from source to station which is actually about 10% longer than that calculated for the layered structure. That the S waves do not appear to be highly attenuated compared to the P waves argues against passage through a low velocity body caused by partial melting and supports the explanation of a longer ray path.

Assuming that the calculated locations are correct, for

those earthquakes located with more than 10 readings the travel times of S and P to M2 and M3 from earthquakes in region 1 indicate V_p/V_s ratios of 1.76±0.02 and 1.78±0.02, respectively. For earthquakes in region 2, a V_p/V_s ratio of 1.83±0.04 and 1.91±0.04 is indicated at M2 and M3, respectively. These average V_p/V_s ratios do not change when the locations are calculated from P wave arrival times only. In Table 4.4 and Figure 4.4 a V_p/V_s ratio of 1.78±0.22 was indicated for dataset 1. This previous result measured V_p/V_s in the region between the two stations since the sources and the stations were approximately aligned. The V_p/V_s ratio indicated by the residuals from the hypocenter locations reflects the average V_p/V_s along the earthquake-station path, implicitly localizing the cause of the V_p/V_s anomaly in the source region.

At T14, large average residuals with large rms deviations are observed for both P and S waves. This may be due at least partly to structural complexity in region 2. At WH5 and WH6, a positive residual is observed from region 1 and a negative residual from region 2 but we cannot determine whether this reflects instrument mislocation or structural heterogeneity. WH2 and L4 both show consistent residuals from both regions which probably reflect instrument mislocation or a timing error.

We had originally hoped to invert the travel time data from earthquakes and from large explosive shots to jointly determine the hypocenters and the velocity structure. The

possibility that at least some of the systematic velocity residuals are due to instrument mislocations would render such an exercise futile. Creager and Dorman (1980) have proposed a method to relocate the instruments relative to each other using the observed arrival time of the direct water wave from shots. If this source of error were thus removed, some lateral velocity heterogeneity might be resolvable. Because the seismic activity was localized in narrow zones and the distribution of shots (Figure 5.1) and receivers (Figure 4.1) is such that very few paths cross these zones, the velocity structure in regions of current tectonic activity where we might expect the largest anomalies would nonetheless be poorly resolved even if the station locations were known perfectly.

4.7 FIRST MOTION POLARITIES

First motion polarity determinations were available from the MIT, Woods Hole, University of California at Santa Barbara, University of Texas, and University of Hawaii instruments. Fault plane solutions were determined from the takeoff angles and azimuths calculated by HYPOINVERSE with respect to the layered model of Table 4.3. The uncertainty in the depth of several of the events results in a large uncertainty in the takeoff angle. When the calculated take off angle is between 90° and 100° (0° = vertical down), the observed polarity is plotted at the station azimuth with a takeoff angle of 90° rather than being rotated about the vertical by 180° (for lower hemisphere projections). This preserves a direct

indication of the azimuthal distribution of the data.

4.7.1 FAULT PLANE SOLUTIONS: REGION 1

Composite fault plane solutions of the earthquakes in region 1 are shown in Figure 4.21. The earthquakes have been divided into four groups: a) events west of 105°14'W; b) the sequence near 104°12'W discussed in 4.5.2; c) the March 8 mainshock-aftershock sequence; d) events east of 105°05'W. Of the 33 earthquakes included, all but two are compatible with right-lateral strike-slip motion along an east-west striking, nearly vertical fault plane. This determination is not affected by the uncertainty in the takeoff-angles. Although the fault strike for individual events is well-constrained only for the larger earthquakes for which many first motion polarity determinations are available, the data for smaller events are consistent with the solutions obtained for larger events. In many cases, this conclusion is also supported by similar waveforms for events related in time and space. In Figure 4.21c, most first motions observed at station H517 at an azimuth of 82° were compressional; the few dilatational first motions were all observed from small aftershocks and reflect either the difficulty of picking first motion polarities in near nodal directions or a slight change in strike or dip of the fault during the sequence.

Only two earthquakes in region 1 are not compatible with right lateral strike slip motion along an east-west plane. The earthquake of March 7 at 16h43m, which was the only event located with at least 10 arrival time readings that was not

located along the topographic trace of the fault, is compatible with east-west strike slip motion but in a left lateral sense. This solution is by no means well constrained and no tectonic interpretation is ventured.

One of the aftershocks of the March 8, 12h14m earthquake also does not fit the same pattern as the others and indicates either right lateral strike-slip motion on a shallow dipping fault or north-south normal faulting. The possible normal faulting interpretation is interesting because this event was also an exception to the general eastward progression of activity during the sequence (Figure 4.8) and might represent normal faulting in response to secondary stresses imposed by the main strike slip faulting.

4.7.2 FAULT PLANE SOLUTIONS: REGION 2

Unlike the solutions for region 1, those for region 2 do not display a straightforward pattern. Solutions for three of the larger events are compatible with right lateral strike slip motion although the solutions are not well-constrained (Figure 4.22a and b). Solutions representing 22 other events, however, cannot be so simply interpreted.

Figure 4.22c is a composite solution for the activity near 15°13'N, 104°47'W which includes four earthquakes which were located with at least 10 readings and a number of smaller events with waveforms similar to those of the larger events, suggesting a similar mechanism (Fig. 4.23). Regions of consistently observed dilatations or compressions are observed, with the only significant exception being that for

the March 4, 09h42m earthquake dilatations were observed at azimuths near 300° whereas compressions were observed for the other events. These "quadrants", however, cannot be separated by any configuration of orthogonal nodal planes. An east-west, right-lateral strike slip solution requires azimuthal deflections of up to 45° for take-off angles in the north-east quadrant.

Although many first motion polarity readings were available for the March 2 05h23m earthquake, the fault plane solution is very poorly constrained because of the uncertainty in the depth. Almost all first motions over a broad range of azimuths are compressional (Figure 4.22d). If the true take-off angles are indeed approximately horizontal, then normal faulting along an undetermined strike is suggested.

A composite solution for the events near 15°10'N, 104°49'W shows only compressional first motions (Figure 3.22e). The events of March 2 at 08h53m and 13h35m were plotted with take-off angle and azimuth calculated for March 3 at 23h11m because, as discussed in 4.5.2, the master event relocations indicated that the epicenters of the March 2 events were indistinguishable from that of the March 3 event. These observations are consistent with a north-south striking normal fault although this interpretation is poorly constrained.

All observed first motions were also compressional for the scattered events east of 104°45'W (Figure 4.21f). Because of the large uncertainties in these hypocenters, however, no

interpretation is attempted.

The first motions of earthquakes in region 2 show (very) tentative evidence for both normal faulting and strike-slip activity as well as for severe distortions of the azimuthal radiation pattern. In Chapter V, we shall see that incidence angles and azimuths observed at M2 from earthquakes and shots passing through this region are deflected from those expected for a laterally homogeneous structure. These observed first motion patterns will be reexamined in light of possible velocity anomalies inferred from the observations of incident angles.

4.8 EARTHQUAKE MOMENTS AND CORNER FREQUENCIES

Moments and corner frequencies were determined for earthquakes recorded on OBS M2. This includes all events located with more than 15 readings. For several sequences of earthquakes for which the waveforms were similar from event to event, moments of earthquakes too small to be detected by M2 were estimated from the amplitude observed on instruments M3 and SB2 relative to a larger event for which the moment had been determined from M2. The apparent moment of 500 lbs of TNT was also calculated.

The amplitude spectrum of the vertical component of the P and S waves was calculated and corrected for instrument response by equation 3.6 and for attenuation by a factor of $\exp(\pi fx/(cQ))$ where f = frequency, x = distance, c = phase velocity and Q^{-1} is the attenuation factor. Values of 6.5 km/sec and 3.7 km/sec were assumed for c_p and c_s,

respectively. Several workers have found that Q of S waves and coda waves decreases with frequency in the range 1 to 24 hz from about 800-1000 at high frequencies to less than 500 at 2 Hz (e.g., Rautian and Khalturin, 1978; Aki, 1980; Roecker, 1981). The rate of change varies strongly with depth and degree of tectonic complexity, suggesting that attenuation of S waves is due primarily to scattering. In this study, the data were not adequate for constraining Q directly and a constant Q of 500 was assumed.

Examples of seismograms and spectra are shown in Figure 4.24. The observed spectra, in general, have the shape predicted by most models of earthquake sources (Aki, 1967; Brune, 1970) showing a constant level for frequencies below a corner frequency f_c and falling off approximately as $(2\pi f)^{-2}$ for f greater than f_c. The observed low frequncy level and corner frequency are rather insensitive to the length of record transformed or the values for Q and c assumed. The spectrum of the P wave from a 500 lb. shot of TNT is shown for comparison and shows a broad peak at about 4 Hz which corresponds to the bubble pulse frequency of the source.

The moment was calculated from (Brune, 1970):

$$M_0 = \frac{4\pi\rho x c^3 \Omega_0}{K R_{\theta\phi}} \qquad (4.4)$$

where Ω_0 is the low frequency level of the spectral amplitude, ρ is density, $R_{\theta\phi}$ is the radiation pattern factor and K is the free surface correction. For earthquakes in

region 1, the fault plane solutions indicate that M2 was near a lobe in the radiation pattern, and for region 2 the fault plane solutions are indeterminate; $R_{\theta\phi}$ was therefore taken to be 1 in all cases.

For shots, the spectral level at the peak was picked for Ω_0, and an apparent moment of $4.3\pm1.0 \times 10^{19}$ was obtained from 5 shots at distances ranging from 7.4 to 34.8 km, assuming Q = 500. For Q = 1000, $M_0 = 3.0 \times 10^{19}$; for Q = 250, $M_0 = 5.2 \times 10^{19}$. Because the source is narrow band and Ω_0 is measured from a spectral peak, this moment value is somewhat larger than that which would be obtained for an earthquake releasing the same energy. This calculation does, however, give an idea of the error induced by our estimate of a constant Q and by the simplified linear relationship between distance x and moment in equation 4.4.

The moments and corner frequencies for the earthquakes are shown in Table 4.7. The moments are probably accurate to within a factor of 2 and the relative accuracy within a region is somewhat better; most of the corner frequency picks are precise to within ±2 Hz. Over 3 orders of magnitude are represented. The largest event, representing about half of the total moment released along the Orozco transform fault during ROSE II, is the March 8, 12h14m main shock. For region 1, P wave moments are about 30% smaller than the S wave moment; for region 2, the P wave moments are, in general, about twice the S wave moment. This may result from radiation pattern differences which were not accounted for.

The corner frequency can be related to source dimension r through the equation $r = K\beta/f_c$ where f_c is the corner frequency of the S wave and K is a factor which depends on the azimuth relative to the source and on a model of the faulting process (e.g., Brune, 1970; Madariaga, 1976; Brune et al., 1979). For most models and azimuths, $0.2<K<0.4$; r therefore ranges from several tens to several hundreds of meters for these events.

In Figure 4.25, the moments are plotted against corner frequency and against cumulative number of events with moment less than M_0. In Figure 4.25a lines of constant stress drop, calculated from the model of Brune (1970), are also shown. Stress drops range from about 1 to 20 bars and appear to increase with moment. No difference is observed between region 1 and region 2. These results are similar to those obtained by Prothero and Reid (1982) in the Rivera Fracture Zone and by Chouet et al. (1978) in the Stone Canyon area of the San Andreas fault. Chouet et al. (1978) found that the relationship between moment and corner frequency varied with geographic locality and related this to the scale length of heterogeneities on the fault plane.

No difference can be observed between the B values obtained for regions 1 and 2 (Fig. 4.25b). The B value of 0.5 is somewhat lower than that found in Chapter 2.3 from the teleseismic earthquakes.

4.9 SUMMARY

Seventy earthquakes have been located in the Orozco Fracture Zone, assuming a layered velocity model adapted from several refraction profiles in the region. The calculated hypocenters have been shown to be insensitive to details of the assumed layered model. All of the epicenters lie within the transform portion of the fracture zone. About half are aligned along a well defined topographic trough striking parallel to the spreading direction in the northern part of the transform. Most of the earthquakes were very shallow (<4 km) but no shallowing of activity is observed as the ridge-transform intersection is approached. In fact, the deepest hypocenters are obtained for a cluster of activity within 10 km of the ridge-transform intersection. The calculated depth difference is supported by the waveforms recorded by the MIT OBS. First motion polarities of almost all of these events are compatible with a fault mechanism of right-lateral strike-slip motion along a nearly vertical fault striking approximately N75°E. The second concentration of activity in the central part of the transform shows much more scatter for both epicenters and depths. The observed first motion polarities for groups of events in this region either defy interpretation in terms of a fault plane solution or provide inadequate coverage of the focal sphere. Several observations suggest that pronounced lateral velocity variations are biasing the locations and take off angles calculated assuming a laterally homogeneous velocity

structure. Moments of the earthquakes range over more than three orders of magnitude and no differences are observed between the stress drops and b values in regions 1 and 2.

TABLE 4.1 Characteristics of Ocean Bottom Seismometers and Hydrophones Used for This Study

Institution	Institution Abbreviation	Components*	Recording†	Reference
Univ. of California, Santa Barbara	SB	V,H,H	D,E	Prothero [1979]
Univ. of Hawaii	H	V,H,P	A,C	Sutton et al. [1977]
Lamont-Doherty Geol. Observ.	L	V,P	A,C	Bookbinder et al. [1978]
Mass. Inst. of Tech.	M	V,H,H	D,E	Mattaboni and Solomon [1977] Duschenes et al. [1981]
Oregon State Univ.	O	V,P	A,C	S.H. Johnson et al. [1977]
Scripps Inst. of Oceanography	SC	V	D,E	Prothero [1974]
Univ. of Texas Galveston	T	V	A,E	Latham et al. [1978]
Univ. of Washington	W	V,H,H	A,C	R.V. Johnson et al. [1977]
Woods Hole Ocean. Instit.	WH	P	A,C	Koelsch and Purdy [1979]

*V, vertical geophone; H, horizontal geophone; P, hydrophone.
†D, digital; A, analog; E, event detection; C, continuous.

note: The range of instrument types reflects in part the broad range of scientific objectives of their creators. Some were designed primarily for refraction work whereas others were designed to moniter microearthquake activity.

TABLE 4.2 Geographic Coordinates of Instruments During Phase II of ROSE

Instrument	Latitude		Longitude		Depth Corrected
	Degrees	Minutes	Degrees	Minutes	Meters
L1	15	30.30	105	25.98	2800
H516	15	29.60	105	5.30	2842
SB1	15	26.20	105	4.40	2801
H517	15	25.40	104	56.60	3883
T2	15	25.20	105	15.10	3010
SC2	15	24.50	105	10.10	3288
SC1'	15	22.60	105	6.10	3366
SC1	15	22.10	105	7.50	3319
SB2	15	21.70	105	2.00	3032
T3	15	18.16	105	12.76	3041
WH1	15	13.98	104	54.72	2678
WH7'	15	13.98	104	54.48	2740
H520	15	12.70	104	55.10	2725
W2	15	10.50	105	18.50	3388
M3	15	9.30	104	55.32	2855
WH7	15	9.18	104	50.58	2863
WH1'	15	9.12	104	52.38	2890
T5	15	8.70	105	11.30	3572
T13	15	6.92	104	38.73	3214
T14	15	6.67	104	31.27	2791
T4	15	6.10	105	27.10	3090
M2	15	5.58	104	56.22	2856
WH6'	15	3.42	104	45.18	2203
WH5	15	1.98	104	44.88	2517
WH3'	14	59.88	105	16.50	3013
WH2	14	59.10	105	16.98	2996
03	14	58.43	104	50.14	4068
WH4	14	54.90	105	8.52	3098
WH4'	14	53.82	105	8.01	3090
L6	14	52.38	104	30.00	2966
WH5'	14	51.00	104	44.40	2678
WH6	14	50.52	104	44.40	2715
WH8	14	49.68	105	22.62	3184
T10	14	48.43	104	59.43	3347
WH2'	14	40.80	105	15.00	3311
WH3	14	40.38	105	15.72	3329
L4	14	31.32	105	15.35	3203

In the instrument identifications the letters refer to the institution abbreviations of Table 4.1, and the numbers to each institution's numbering scheme. The 'primed' WHOI identifications correspond to the position of each instrument after being redeployed. Because the tape capacity of the WHOI instruments is about 8 days, most were retrieved and redeployed midway through phase II.

TABLE 4.3 Layered P-Wave Velocity Model Used for Earthquake Locations

Layer	Velocity, km/s	Depth, km	Thickness, km
1	4.38	0.00	0.40
2	5.00	0.40	0.40
3	5.62	0.80	0.40
4	6.05	1.20	0.80
5	6.39	2.00	1.00
6	6.73	3.00	1.00
7	7.07	4.00	1.00
8	7.42	5.00	1.00
9	7.72	6.00	0.65
10	7.84	6.65	

TABLE 4.4 Slopes and Intercepts for Data Displayed in Figure 4.4

	data set	slope	intercept	# of pts.
a)	1 (M2-M3)	1.78±0.22	-0.10±0.16	11
	2 (SB1-SC2; SB2-SC3)	1.76±0.10	-0.02±0.13	15
	3 (T14-M2, M3)	1.77±0.20	-0.14±0.40	10
	4 (T5-M2, M3)	1.43±0.07	0.37±0.14	13
	5 (T5-SB1, SB2, SC2, SC3)	1.05±0.24	1.00±0.61	22
b)	4 ($\Delta P<2.1S$)	1.72±0.13	0.06±0.18	9
	4 ($\Delta P>2.1S$)	1.54±0.18	-0.18±0.61	4
	5 ($\Delta P<2.1S$)	1.80±0.23	-0.39±0.35	8
	5 ($\Delta P>2.1S$)	1.83±0.12	-0.74±0.44	14

TABLE 4.5

Hypocentral Parameters of Earthquakes Located in the Orozco Transform Fault*

	origin time				latitude		longitude		depth	nor		mag	dcs	rms	erh	erz
m	d	h	m	sec	deg	min	deg	min	km	p	s	deg	km	sec	km	km
2	27	22	38	36.31	15	13.17	104	47.71	0.85	7	1	147	13.3	0.24	0.9	3.0
3	1	11	50	7.13	15	4.69	104	38.14	3.64	4	1	191	12.8	0.04	1.4	pdc
3	1	12	16	23.12	15	21.54	105	17.84	5.20	2	3	271	8.3	0.02	1.6	2.4
3	1	14	57	51.02	15	22.41	105	14.20	0.05	7	3	87	5.4	0.21	0.4	1.3
3	1	15	6	34.76	15	21.84	105	16.59	3.82	4	3	180	6.8	0.10	0.8	1.1
3	1	21	48	23.33	15	8.97	104	39.32	2.65	3	1	241	15.0	0.06	2.9	2.9
3	2	5	23	10.72	15	14.81	104	44.10	11.43	20	2	191	15.6	0.15	0.9	1.9
3	2	7	18	4.84	15	25.02	104	57.70	3.08	14	2	150	2.0	0.07	1.6	1.8
3	2	8	54	5.75	15	6.85	104	49.17	9.92	3	1	323	5.0	0.00	5.3	3.1
3	2	13	0	21.18	15	23.22	105	12.70	3.96	14	1	124	5.3	0.09	0.6	1.3
3	2	13	35	1.61	15	6.77	104	48.93	10.44	3	1	327	5.3	0.09	5.5	3.1
3	2	16	45	8.66	15	23.55	105	12.51	1.70	9	1	130	4.6	0.12	0.7	1.5
3	2	17	21	9.63	15	23.59	105	12.09	4.64	16	2	128	3.9	0.10	0.6	1.2
3	2	17	59	42.24	15	24.68	105	12.30	8.89	2	2	343	4.0	0.01	plc	1.3
3	2	19	36	12.23	15	22.87	105	15.82	0.94	2	2	360	10.6	0.02	plc	3.1
3	3	3	59	31.23	15	24.76	105	9.40	4.58	4	3	143	1.3	0.07	0.8	0.4
3	3	10	17	56.79	15	22.62	105	16.21	0.26	2	2	360	11.5	0.09	plc	3.8
3	3	10	52	25.27	15	22.58	105	16.26	0.63	2	2	360	11.6	0.12	plc	3.7
3	3	17	24	58.13	15	24.52	105	13.31	7.31	17	2	222	5.8	0.11	0.9	2.2
3	3	22	38	51.87	15	22.31	105	17.91	0.22	2	2	360	14.5	0.14	plc	5.1
3	3	23	3	15.25	15	23.23	105	14.80	3.10	2	2	359	8.8	0.01	plc	2.4
3	3	23	11	59.87	15	10.30	104	49.15	6.72	4	2	298	3.3	0.12	1.5	1.9
3	4	9	19	23.80	15	12.38	104	47.00	3.18	19	3	145	8.8	0.15	0.5	1.0
3	4	9	37	47.56	15	12.98	104	47.47	7.32	4	1	226	13.6	0.14	1.4	pdc
3	4	9	42	18.15	15	12.72	104	46.44	6.41	19	1	179	9.9	0.13	0.8	2.1
3	4	10	1	7.86	15	12.00	104	47.30	6.15	4	1	225	14.0	0.13	1.2	pdc
3	4	10	12	53.65	15	12.54	104	47.57	7.01	4	1	224	13.5	0.12	1.3	pdc
3	4	10	37	12.11	15	9.40	104	50.97	5.63	4	0	173	0.8	0.00	2.7	1.6
3	4	10	53	8.28	15	9.49	104	49.80	11.37	4	1	204	9.9	0.05	1.0	pdc
3	4	11	21	16.95	15	25.69	104	59.06	0.17	8	1	176	4.4	0.13	1.0	3.6
3	4	11	30	37.96	15	29.44	104	59.86	1.61	3	2	268	9.5	0.15	4.0	3.5
3	4	14	59	46.01	15	18.65	104	46.63	2.93	7	1	229	16.8	0.11	1.3	3.1
3	4	18	56	5.15	15	25.54	105	0.00	2.66	16	2	171	6.0	0.11	1.3	1.6
3	4	20	10	37.26	15	23.84	105	12.45	15.11	7	1	136	15.0	0.07	1.0	2.6
3	5	0	58	15.77	15	39.52	104	47.44	23.01	7	0	287	30.9	0.20	1.3	4.8
3	5	2	19	4.29	15	13.07	104	47.68	6.70	9	2	147	13.3	0.10	0.8	pdc
3	5	10	10	27.31	15	18.56	104	44.45	17.38	9	1	192	20.3	0.10	1.2	4.6
3	5	21	4	42.83	15	8.78	104	38.99	0.56	3	1	180	14.3	0.06	1.8	3.0
3	6	15	10	41.65	15	28.21	104	59.48	1.47	3	3	332	12.9	0.08	1.5	1.6
3	6	21	33	34.24	15	25.18	105	13.95	5.01	3	2	281	14.8	0.16	1.8	0.5
3	6	23	5	12.84	15	25.95	105	4.30	3.16	4	3	304	6.9	0.10	1.3	1.0
3	7	0	7	35.77	15	25.39	105	16.05	1.32	3	3	283	18.5	0.10	3.6	4.0
3	7	16	43	31.60	15	26.43	105	12.31	0.30	9	2	257	13.2	0.07	2.2	2.3
3	8	0	2	35.97	15	13.01	104	47.70	8.82	6	1	145	8.8	0.09	0.9	3.7
3	8	0	23	55.42	15	13.14	104	48.29	1.61	4	1	280	8.4	0.14	1.7	1.9
3	8	0	58	5.37	15	13.33	104	47.21	3.77	14	2	149	9.8	0.14	0.6	1.5
3	8	1	31	55.01	15	13.79	104	47.55	0.00	4	1	151	16.2	0.04	0.8	2.4
3	8	12	14	26.51	15	24.09	105	7.03	0.50	19	1	88	3.3	0.08	0.5	0.8
3	8	12	19	0.61	15	24.12	105	6.40	0.18	17	2	82	2.8	0.09	0.5	0.9
3	8	12	26	38.66	15	24.19	105	6.11	0.20	8	0	146	2.9	0.10	0.9	2.3
3	8	12	38	22.70	15	24.11	105	6.86	0.84	18	2	147	3.1	0.10	0.5	0.9
3	8	12	50	16.74	15	24.20	105	7.17	0.06	5	2	177	3.5	0.10	0.6	1.5
3	8	13	21	35.19	15	24.49	105	7.01	2.40	4	2	183	3.9	0.13	1.2	0.9
3	8	13	39	26.74	15	24.19	105	5.81	1.87	7	2	84	3.0	0.13	0.6	0.7
3	8	14	32	18.29	15	24.26	105	5.53	0.04	8	1	80	3.2	0.18	0.6	1.3
3	8	14	45	54.61	15	24.33	105	5.51	0.39	7	2	87	3.3	0.04	0.6	1.2
3	8	14	51	59.96	15	24.34	105	6.13	1.08	8	2	90	3.3	0.09	0.6	0.9
3	8	14	52	16.87	15	24.69	105	6.43	3.72	9	2	208	30.9	0.09	1.0	3.7
3	8	15	14	9.50	15	24.34	105	5.31	0.04	5	3	156	3.5	0.10	0.6	1.1
3	8	16	1	29.95	15	24.49	105	5.79	0.95	17	2	79	3.5	0.13	0.5	0.8

TABLE 4.5 (cont'd.)

3	8	18	32	44.65	15	16.68	104	31.38	5.01	7	0	276	36.4	0.08	5.5	pdc
3	8	20	31	35.17	15	23.90	105	15.97	0.16	5	2	209	17.8	0.14	1.5	2.1
3	8	20	44	38.88	15	25.12	105	16.57	0.11	7	3	240	19.3	0.10	2.1	1.7
3	9	3	8	37.94	15	24.62	105	4.77	0.25	4	1	143	4.4	0.12	1.0	2.7
3	9	20	29	30.26	15	24.46	105	11.63	1.20	4	2	226	10.5	0.24	1.0	2.5
3	12	8	53	15.65	15	24.24	104	59.07	3.38	3	1	193	4.8	0.03	1.6	pdc
3	12	11	1	54.14	15	11.57	104	45.80	4.14	13	1	212	12.6	0.08	1.0	1.7
3	13	18	49	17.85	15	8.27	104	40.90	4.84	6	0	287	11.8	0.01	5.9	2.1
3	13	23	42	10.60	15	9.84	104	46.03	6.24	4	1	243	22.3	0.08	1.6	pdc

*Latitudes and longitudes are in degrees and minutes N and W, respectively; nor = number of readings; mag = maximum azimuthal gap; dcs = distance to the closest station; rms = root mean squared travel time residual; erh = horizontal error (from projection of error ellipse onto horizontal plane); erd =depth error; pdc = poor depth control (as indicated by an eigenvalue of [A] less than 0.016, corresponding primarily to the hypocentral adjustment in depth); plc = poor latitude control.

TABLE 4.6a. Average Station Residuals for Earthquakes Located in the Orozco Transform Fault (x 10^{-2} seconds)

station		REGION 1						REGION 2					
		>10 readings			<10 readings			>10 readings			<10 readings		
		a*	b**	c***	a	b	c	a	b	c	a	b	c
L1	P	1	6	9	4	7	8	32	10	2			0
H516	P	7	2	4	7	8	10			0			0
SB1	P(a)	13	10	5	2	7	10	8		1			0
	P(b)	-7		1			0			0			0
	S	83	1	2	9	11	10			0			0
H517	P	-9	11	11	6	13	15	-7	6	6	1	7	9
T2	P			0	-1	1	2			0			0
	S			0	4	1	2			0			0
SC2	P	0	6	6	-6		1	6	6	3			0
	S			0	6		1			0			0
SC1'	P	0	3	5	-9	7	16			0			0
	S	8	6	2	14	10	14			0			0
SC1	P			0	-17		1			0			0
	S			0	15		1			0			0
SB2	P	-9	4	5	1	7	7	7		1			0
	S			0	6	16	7			0			0
T3	P			0	0	2	2			0			0
	S			0	-7	3	2			0			0
WH1	P	2	3	11	-6	10	5	-12	3	5	-14	1	2
WH7'	P			0			0			0			0
H520	P	-4	6	8	6	13	3	16	1	6	9	7	13
W2	P			0	3		1			0			0
M3	P	3	4	9	0	9	2	-19	4	5	-13	8	13
	S	9	10	8	25	8	2	3	6	5	2	7	12
WH7	P	4	5	11	-4	10	3	5	8	5	1	6	17
WH1'	P			0			0			0	2		1
T5	P	9	8	8	8	9	17	4	6	6	14		1
	S	7	11	4	6	20	16	-21	30	3	-6	20	16
T14	P			0			0	22	18	6	-6	11	5
	S			0			0	57	30	5	13	19	5
T4	P	-6	4	7	6	3	2	-5	35	4			0
M2	P	-5	6	9			0	-12	5	6	-2		1
	S	-3	7	9			0	9	10	6	17		1
WH6'	P			0			0	-7		1			0
WH5	P	8	6	9			0	-12	4	3			0
WH3'	P			0			0	5		1			0
WH2	P	-14	3	10	-9	8	7	-12	9	5	23		1
03	P	9	3	6			0	4	6	7			0
WH4	P	-6	1	4			0	16	10	4	-4		1
WH4'	P	14	6	6			0	12		1			0
L6	P			0			0	-19	13	4	-6		1

WH5'	P			0			0		8		1		0
WH6	P	4	8	3			0	-9	10	4	-1		1
WH8	P	-7	3	9	8	9	3	2	7	4			0
T10	P	7	11	7			0	8	9	5	-7	14	3
WH2'	P			0			0	-14		1			0
WH3	P	14	6	4			0	-3	8	3			0
L4	P	34	8	5			0	32	11	2			0

*mean residual (x10^{-2} seconds)
**rms deviation from mean residual (x10^{-2} seconds)
***number of earthquakes

Table 4.6b Mean of RMS Deviation of Average Station Residuals in Table 4.6b (x 10^{-2} seconds).

	P	S
region 1 (≥10)	6±3	7±4
region 1 (<10)	7±3	10±6
region 2 (≥10)a*	10±8	15±11
	7±3	19±11
region 2 (<10)b**	7±3	13±6

*mean of rms deviation with T4 and T14
**without T4 and T14

TABLE 4.7 Moments and Corner Frequencies for Earthquakes Recorded on OBS M2. $M_0(P)$ determined from P waves; $M_0(S)$ and f_c determined from S waves. Q=500, V_p=6.5, km/sec, V_s=3.7 km/sec assumed. Moment values in parentheses found from OBS M3 or SB2 as described in text.

a. Region 1

event	$M_0(P)$ dyne-cm	$M_0(S)$ dyne-cm	f_c
02 0718	1.4×10^{18}	2.2×10^{18}	20
02 1300		(1.7×10^{18})	
02 1645		(6.2×10^{17})	
02 1721	3.4×10^{18}	5.3×10^{18}	14
03 1724	4.5×10^{18}	6.9×10^{18}	9
04 1856	2.1×10^{18}	2.2×10^{18}	15
08 1214	$>3.6 \times 10^{20}$	$>2.3 \times 10^{20}$	<2
08 1219	4.5×10^{19}	7.2×10^{19}	9
08 1238		8.2×10^{18}	15
08 1339		(8.0×10^{17})	
08 1432		(1.3×10^{18})	
08 1445		(1.1×10^{18})	
08 1451		(6.8×10^{17})	
08 1452		7.2×10^{18}	15
08 1514		(6.6×10^{17})	
08 1601		4.0×10^{18}	8

b. Region 2

02 0523	2.8×10^{19}	2.7×10^{19}	13
03 2311	3.8×10^{17}	1.8×10^{17}	25
04 0919		5.7×10^{18}	16
04 0938		(7.5×10^{17})	
04 0942		2.4×10^{19}	15
04 1001		(7.5×10^{17})	
04 1012		(1.2×10^{18})	
05 0219	7.4×10^{18}	2.0×10^{18}	17
08 0002		(8.5×10^{17})	
08 0023		(9.2×10^{17})	
08 0058	5.5×10^{18}	2.6×10^{18}	15
08 0131		(8.9×10^{17})	
08 1257		1.1×10^{18}	13
12 1101		2.4×10^{18}	17

FIGURE CAPTIONS

4.1 Location of instruments in the ROSE microseismic network. Geographic coordinates of the instruments are listed in Table 4.2. Instrument identification codes are given in Table 4.1.

4.2 Histograms of earthquake activity per half-day observed during Phase II of ROSE. The instrument identification codes are given in Table 4.1. For further discussion, see text.

4.3 Examples of seismograms recorded by the three component MIT OBS which illustrate pitfalls of picking S wave arrival times from a single vertical component (discussed in text).
a. Event of March 3 at 23h11m recorded by M3.
b. Event of March 2 at 17h21m recorded by M2.
c. Event of March 8 at 00h58m recorded by M2.

4.4 (S_2-S_1) v.s. (P_2-P_1) where P_1, S_1 and P_2, S_2 are arrival times of P and S waves recorded at stations 1 and 2, respectively. Symbols indicate different groupings of station pairs as identified in the legend. Notation T14-M2, M3 is abbreviated from T14-M2, T14-M3, etc. Slopes and intercepts of lines fit through the data are given in Table 4.4.

4.5 Epicenters of earthquakes located in the Orozco Fracture Zone during ROSE II.

4.6 Effect on the locations of changing parameters of the assumed velocity model. Results are presented in the form of histograms of latitude, longitude and depth calculated with respect to the model of Table 3.3 with V_p/V_s = 1.75 (crust A) minus latitude, longitude and depth for the perturbed model. The perturbed models are:

a. velocity model of Table 4.3 with V_p/V_s = 1.78

b. a 6 km thick crust with a velocity of 6 km/sec over a half-space with a velocity of 8 km/sec (crust B).

c. velocity model of Table 4.3 except that the thickness of the 7.2 km/sec layer is decreased to 0.5 km and the half-space velocity is increased to 8 km/sec (crust C).

4.7 Seismic activity in region 1 displayed in three time periods. No activity was located in this region on February 27 and 28 or March 10 and 11. Open triangles represent stations operating during the given time period. Squares represent locations calculated from at least 10 arrival time readings, circles from fewer than 10 readings. The axis of the East Pacific Rise intersects the transform fault near 105°18'W. Bathymetric contours are labeled in meters; contour interval is 200m.

4.8 Latitude and longitude of the March 8 earthquake at 12h14m and its aftershocks plotted versus time showing the eastward migration of activity. Large dots represent locations calculated from at least 10 arrival time readings; small dots, fewer than 10 readings. Error bars indicate the 95% confidence limits of the solution.

4.9 Depth of earthquakes in region 1 projected onto a vertical east-west plane. Large dots represent locations calculated from at least 10 arrival time readings; small dots, fewer than ten readings. Open circles indicate that the geometry of the network with respect to the earthquake provided poor depth control. Error bars indicate 95% confidence interval of the solution.

4.10 Rms travel time residual for events near 105°12'W vs. depth. Squares represent solutions with data from station SC2 included; dots represent solutions without SC2. Automatic weighting of the readings as a function of residual was suppressed so that locations at each depth were calculated from the same dataset.

4.11 Same as figure 4.10 for events in the March 8 sequence with and without readings from station SC1'.

4.12 Effect on the calculated hypocenter of perturbing the geographic coordinates of station SC2 by 0.5' minutes (approximately 1 km) to the N, S, E and W. Dots indicate location in table 3.5; open circles indicate only station coordinates perturbed; open triangles indicate both station coordinates and velocity model (see Figure 4.6b) perturbed.

4.13 Vertical component P-wave seismograms recorded on the MIT OBS.
a. Sources near 105°12'W
b. Sources near 105°6'W. A record from a shot of 500 lbs. of TNT (#3426) is shown for comparison.

4.14 (S-P) arrival time difference as a function of time for stations near trough A. Filled circles represent earthquakes which were located; open circles represent events with too few arrival time readings to locate. The dashed line represents the minimum travel time for a surface event located along the line of activity defined by the epicenters, assuming V_p = 6.0 km/sec and V_p/V_s = 1.75. See text for further discussion.

4.15 Seismic activity in region 2. No activity was located on February 28 or March 6,7,9,10 and 11. Squares represent locations calculated from at least 10 arrival time readings, circles from fewer than 10 readings. Bathymetric contours are labeled in meters; contour interval is 200m.

4.16 Depth of earthquakes in region 2 projected onto a vertical north-south plane. Symbols are as in figure 4.9.

4.17 Examples of rms travel time residuals for events in region 2 as a function of depth. As for figures 4.10 and 4.11, automatic weighting of the residuals was suppressed.

4.18 Locations of earthquakes in region 2 calculated relative to the March 4 event at 09h19m assuming V_p = 6.0 km/sec, V_p/V_s = 1.75.

4.19 Histograms of observed S-P arrival time differences at University of Texas OBS which were deployed in the central region of the Orozco transform fault (from Ouchi et al., 1982). ST10, 13 and 14 are T10, T13, T14 in Figure 4.1.

4.20 Effect on the locations of perturbing the geographical coordinates of stations H520 and WH1 as described in the text.

4.21 Composite fault plane solutions for events in region 1. Dots represent compressional first arrivals; open circles indicate dilitations.

4.22 Composite fault plane solutions for events in region 2.

4.23 Vertical component seismograms recorded at OBS M3 from a sequence of earthquakes near 15°12'N, 104°47'W. The moment of the 0058 event is about 3 times larger than that of the other events.

4.24 Examples of P and S waveforms and spectra recorded on the vertical component of OBS M2. The portion of the waveform used to calculate the spectrum is indicated by arrows above the seismogram. The spectra are not very sensitive to the length of record transformed.

4.25 a. Log(Moment) vs. corner frequency for earthquakes in the Orozco Transform Fault. Lines of constant stress drop (Brune, 1970) are also shown.

b. Log(Moment) vs. cumulative number of earthquakes with moment $<M_0$ for earthquakes in the Orozco Transform Fault. A B value of 0.5 is indicated in both regions.

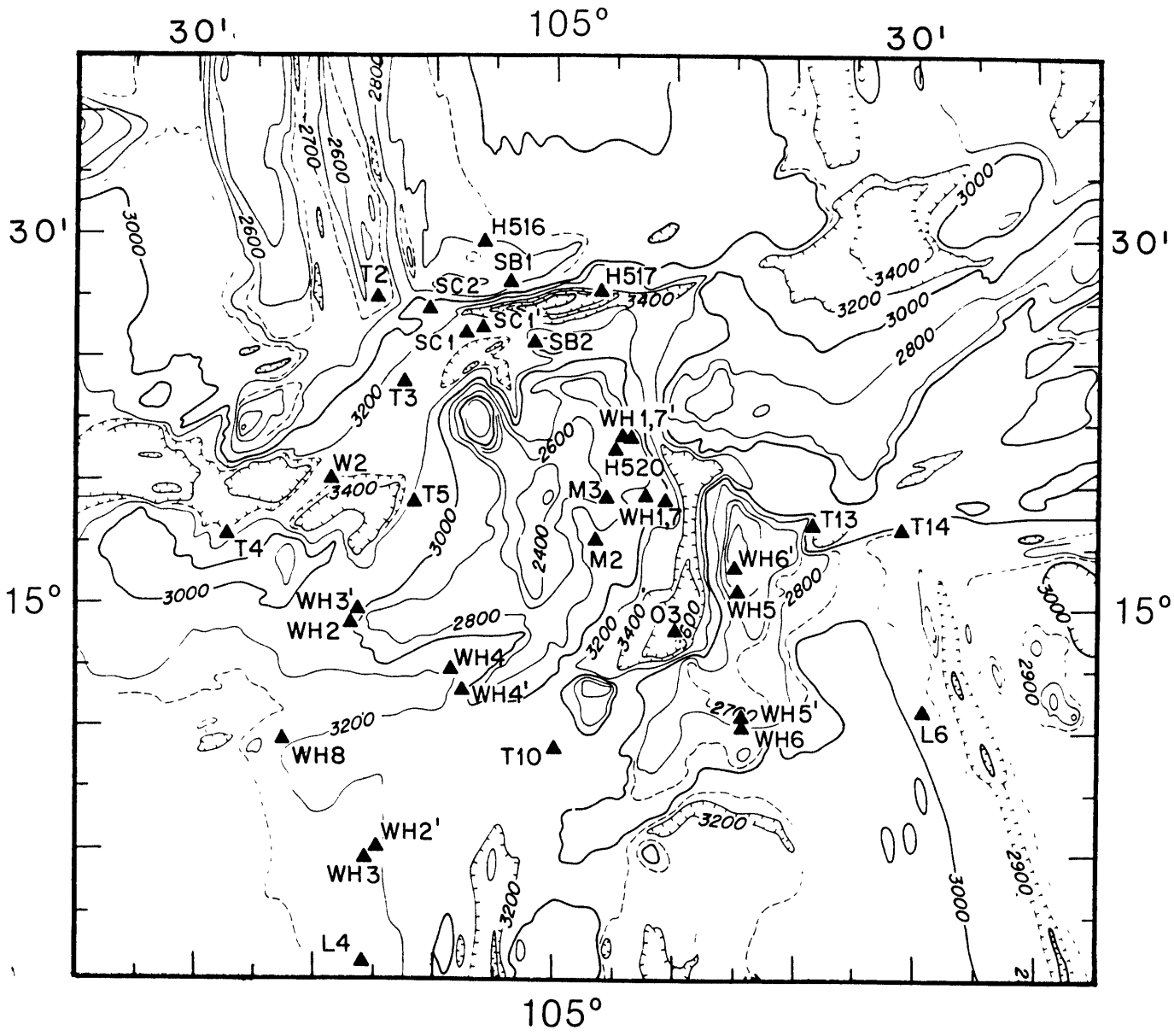
30'
105°
30'
30'
15°
15°
105°
H516
SB1
T2
SC2
H517
SC1'
SC1
SB2
T3
WH1,7'
H520
W2
T5
M3
WH1,7
T13
T14
T4
M2
WH6'
WH3'
WH5
WH2
O3
WH4
WH4'
WH5'
WH6
WH8
T10
L6
WH2'
WH3
L4
2800
2700
2600
3000
3400
3200
2900
2400

figure 4.1

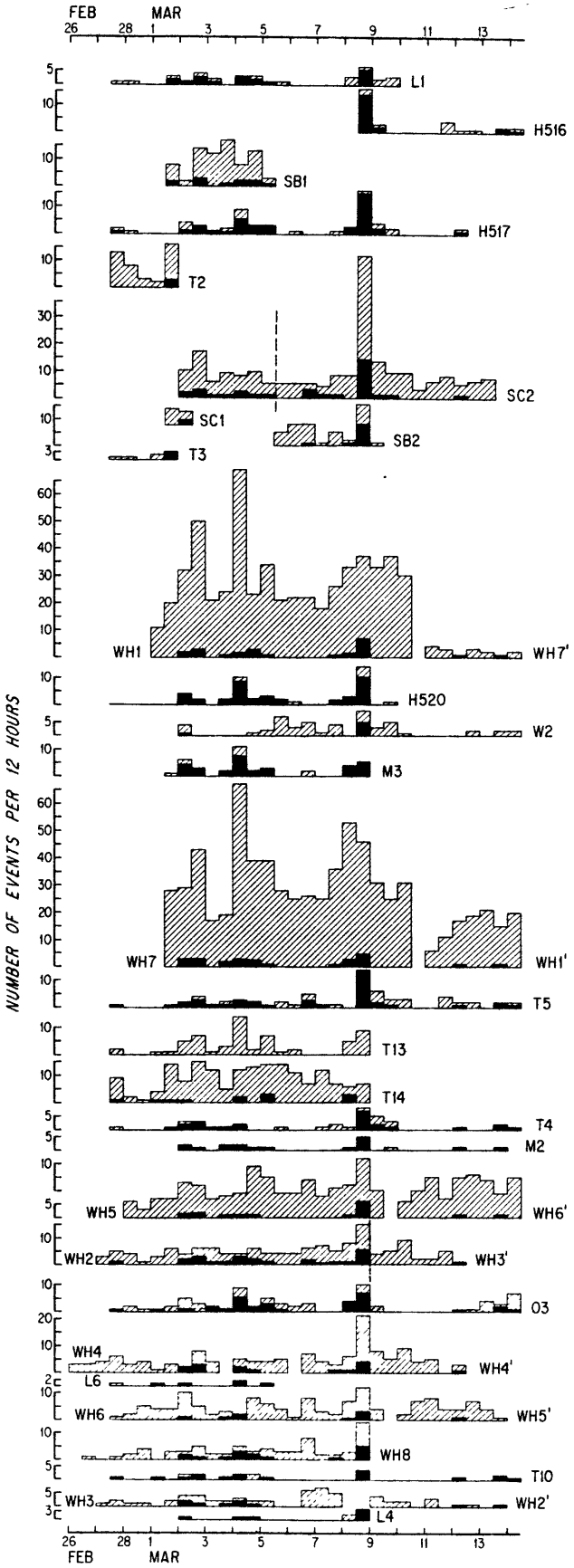
FEB
MAR
26
28
1
3
5
7
9
11
13
NUMBER OF EVENTS PER 12 HOURS
L1
H516
SB1
H517
T2
SC2
SC1
SB2
T3
WH1
WH7'
H520
W2
M3
WH7
WH1'
T5
T13
T14
T4
M2
WH5
WH6'
WH2
WH3'
03
WH4
WH4'
L6
WH6
WH5'
WH8
T10
WH3
WH2'
L4

figure 4.2

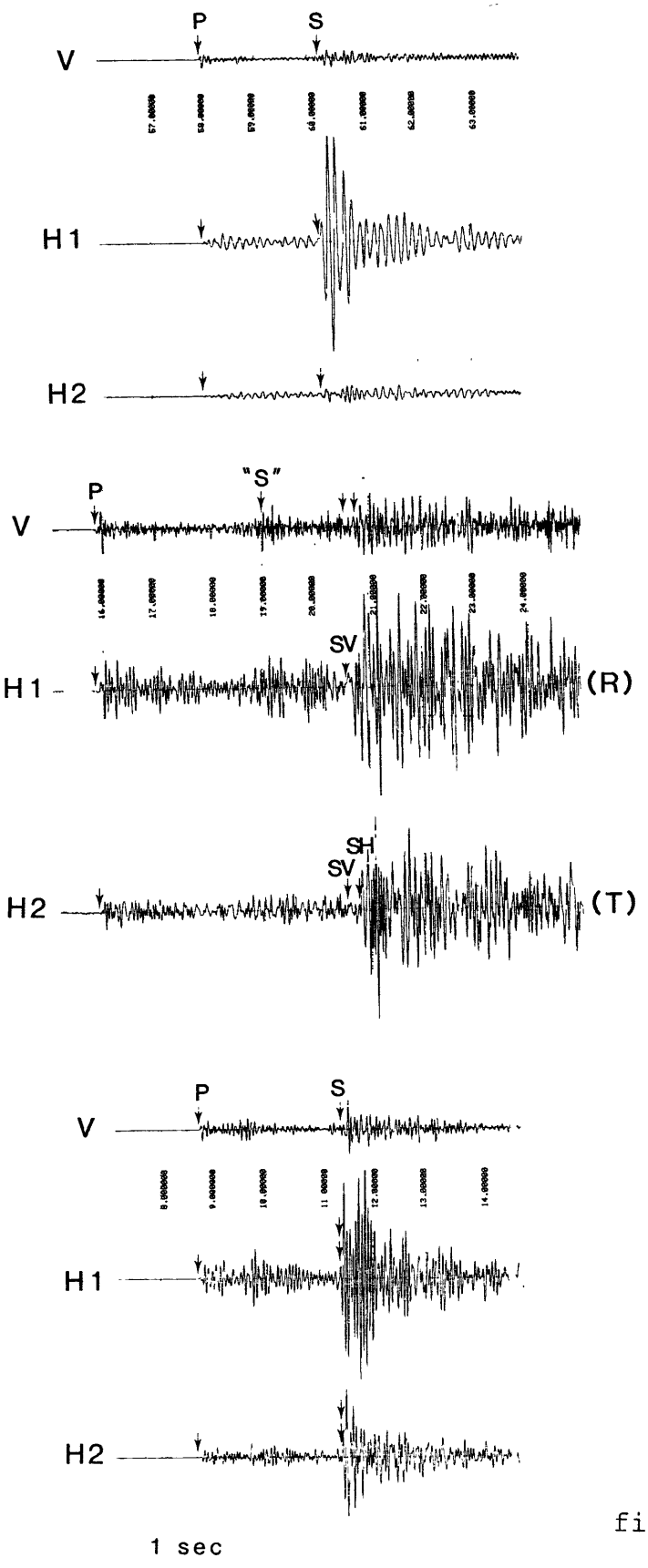

figure 4.3

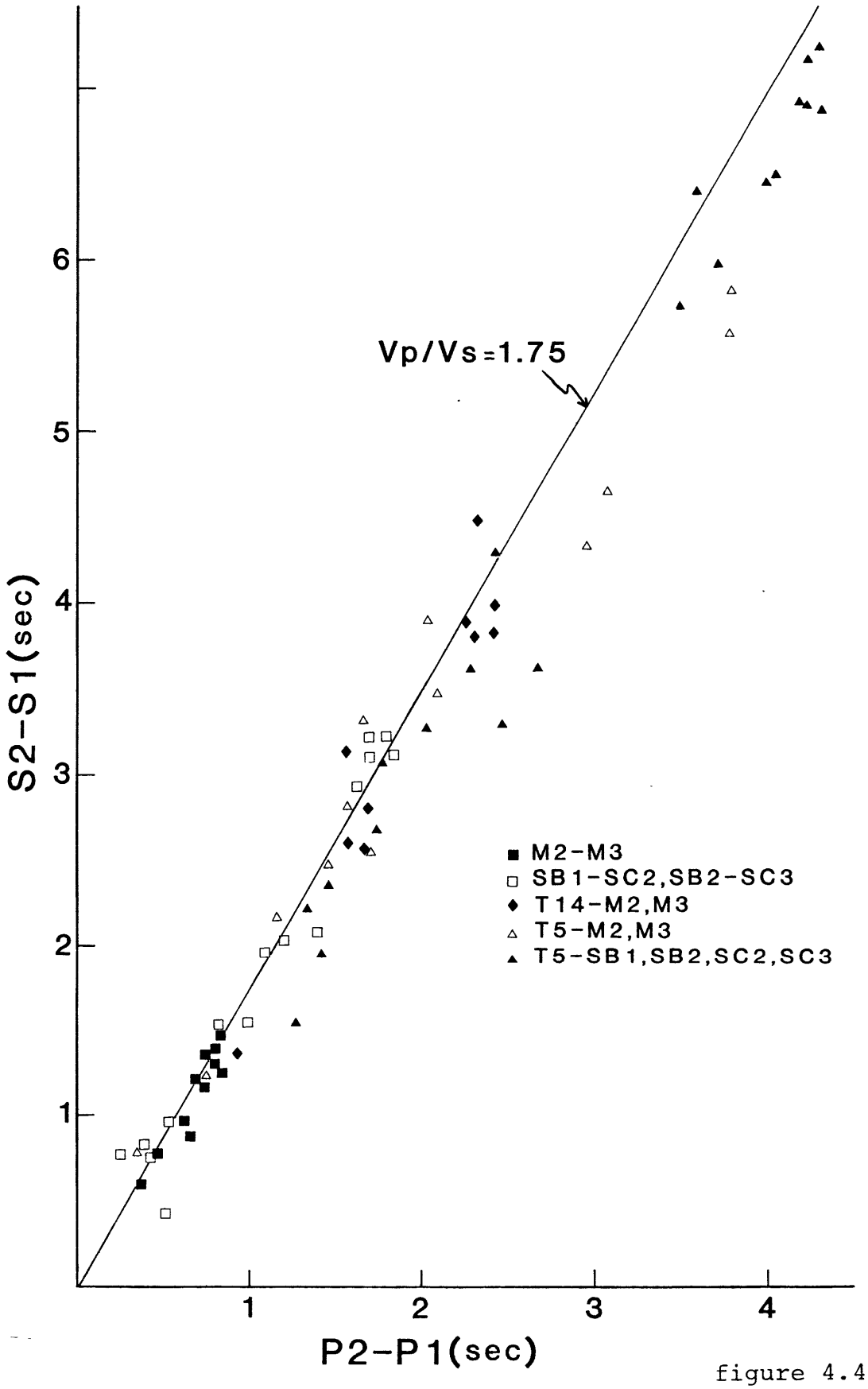
Vp/Vs=1.75
S2-S1(sec)
P2-P1(sec)
1
2
3
4
5
6
M2-M3
SB1-SC2,SB2-SC3
T14-M2,M3
T5-M2,M3
T5-SB1,SB2,SC2,SC3

figure 4.4

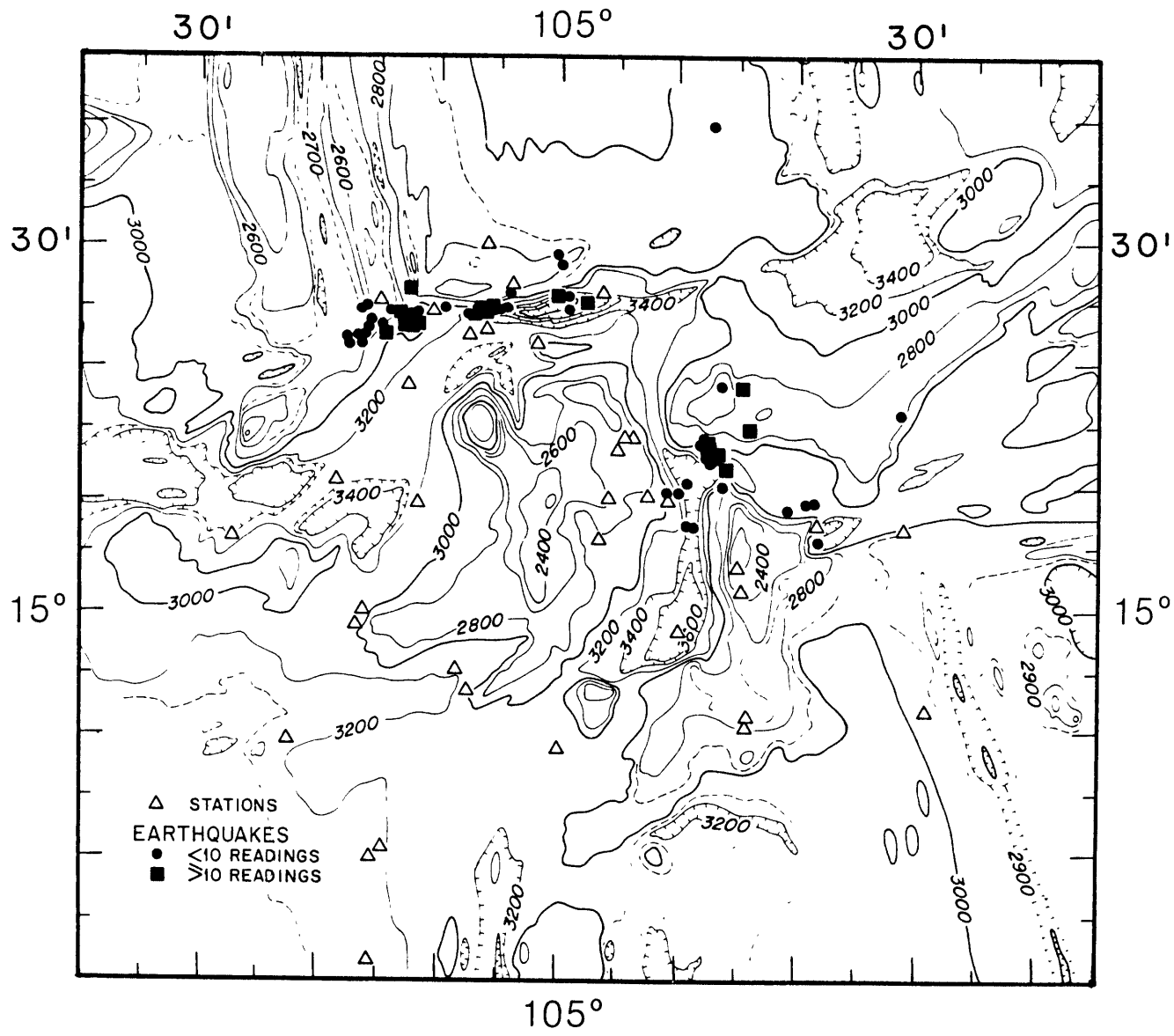
30'
105°
30'
30'
15°
15°
105°
2800
2700
2600
3000
3400
3200
2400
2900
STATIONS
EARTHQUAKES
≤10 READINGS
≥10 READINGS

Figure 4.5

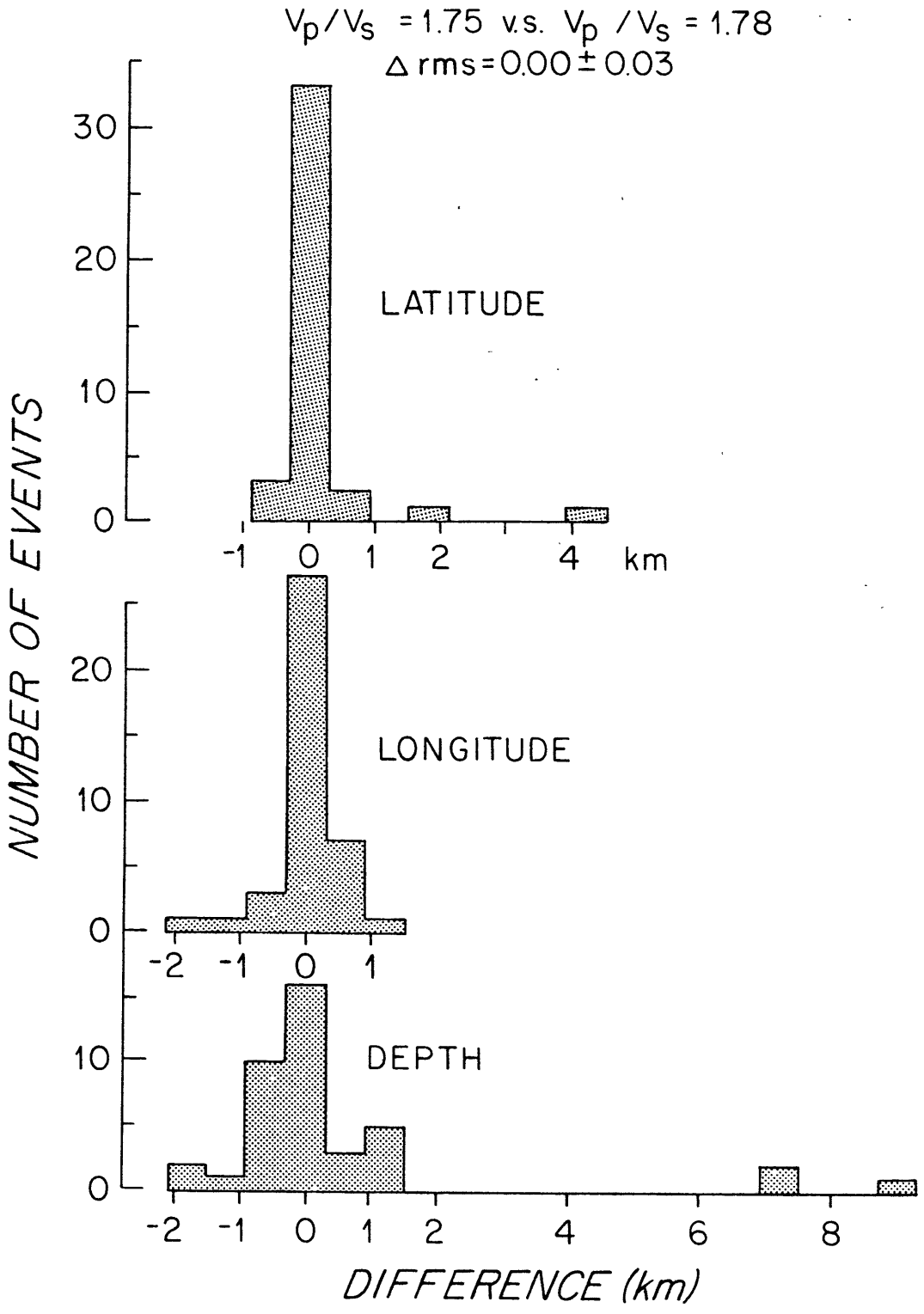
V_p/V_s = 1.75 v.s. V_p/V_s = 1.78
Δ rms = 0.00 ± 0.03
LATITUDE
LONGITUDE
DEPTH
km
NUMBER OF EVENTS
DIFFERENCE (km)

figure 4.6a

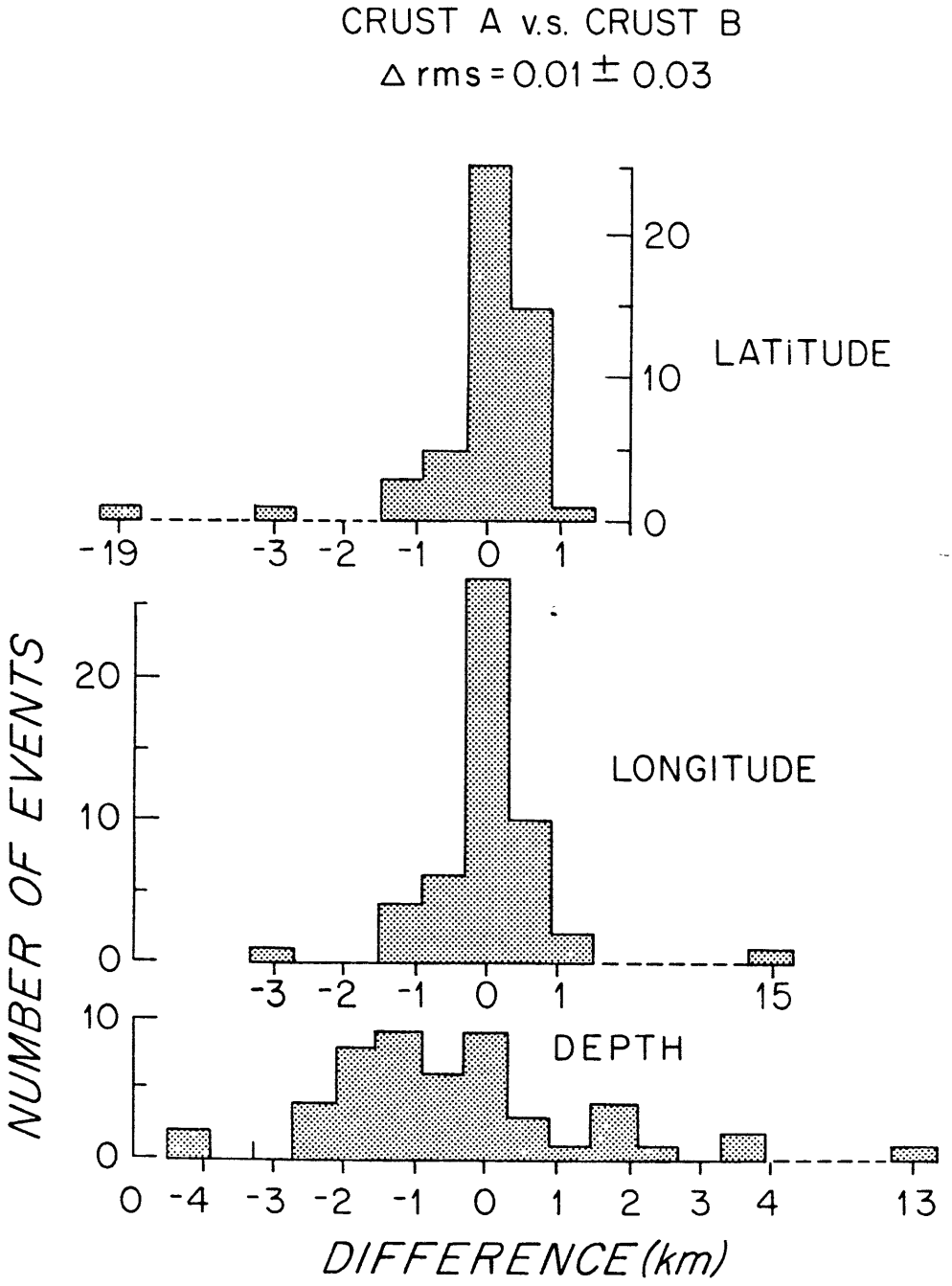
CRUST A v.s. CRUST B
Δ rms = 0.01 ± 0.03
LATITUDE
LONGITUDE
DEPTH
NUMBER OF EVENTS
DIFFERENCE(km)
20
10
0
-19
-3
-2
-1
0
1
15
-4
2
3
4
13

figure 4.6b

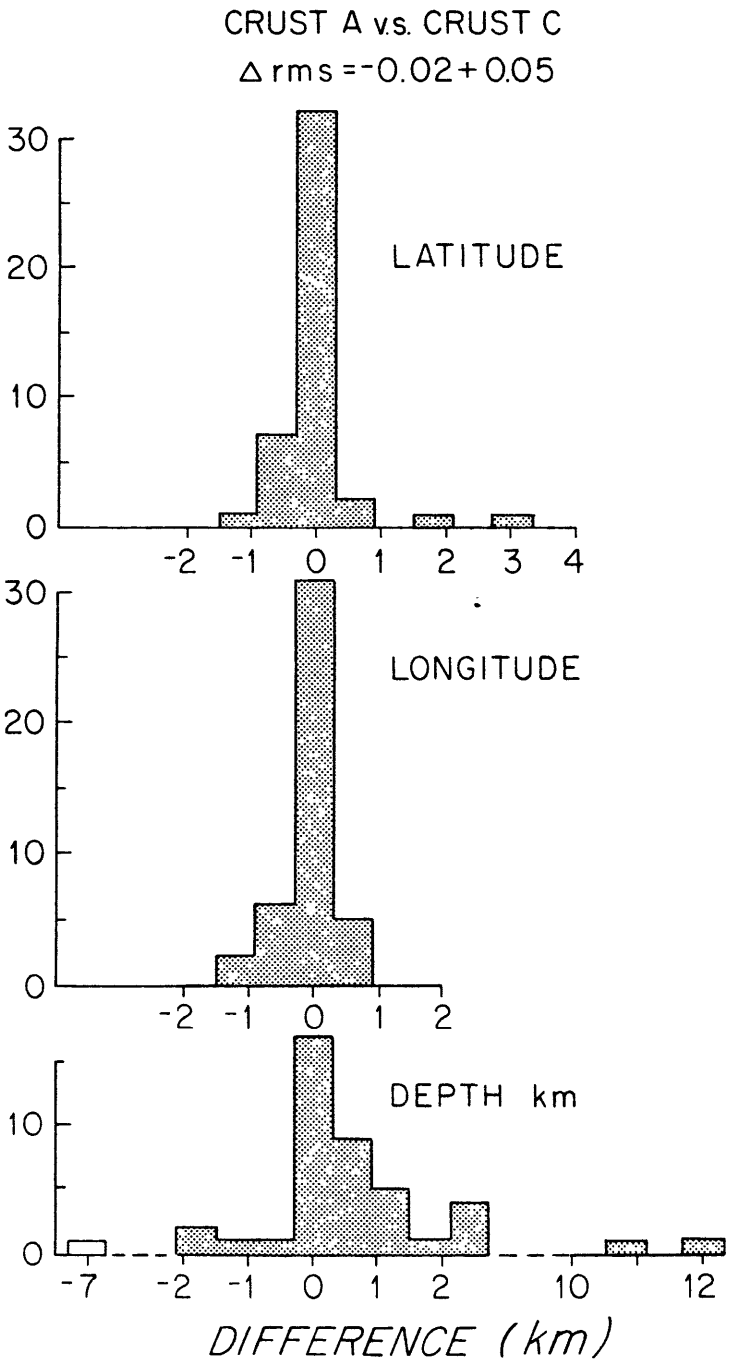
CRUST A v.s. CRUST C
Δ rms =-0.02+0.05
LATITUDE
LONGITUDE
DEPTH km
DIFFERENCE (km)

figure 4.6c

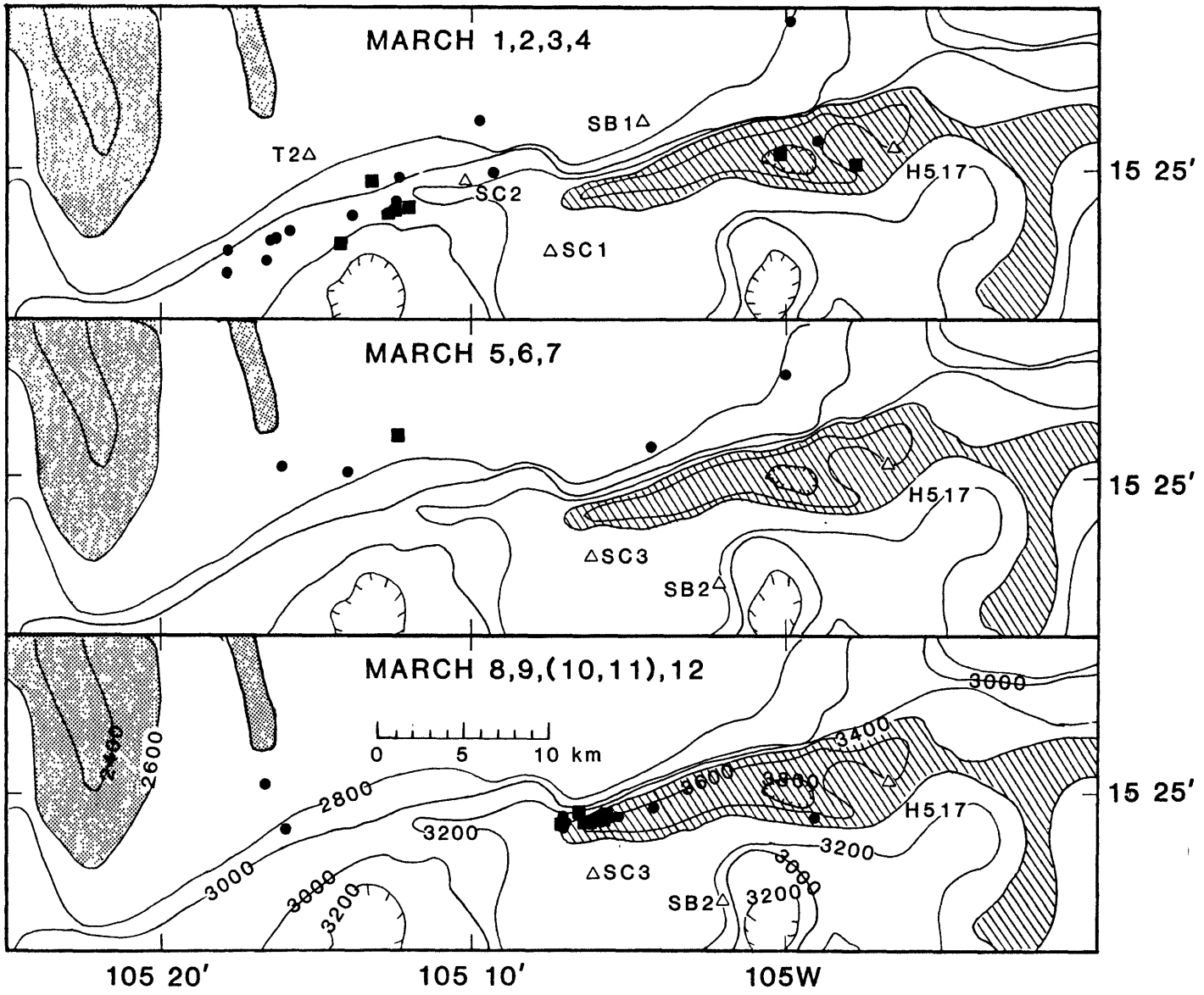
MARCH 1,2,3,4
SB1△
T2△
SC2
△SC1
H5 17
15 25′
MARCH 5,6,7
△SC3
SB2△
H5 17
15 25′
MARCH 8,9,(10,11),12
0 5 10 km
2600
2800
3000
3200
3400
3600
H5 17
△SC3
SB2△
15 25′
105 20′
105 10′
105W

Figure 4.7

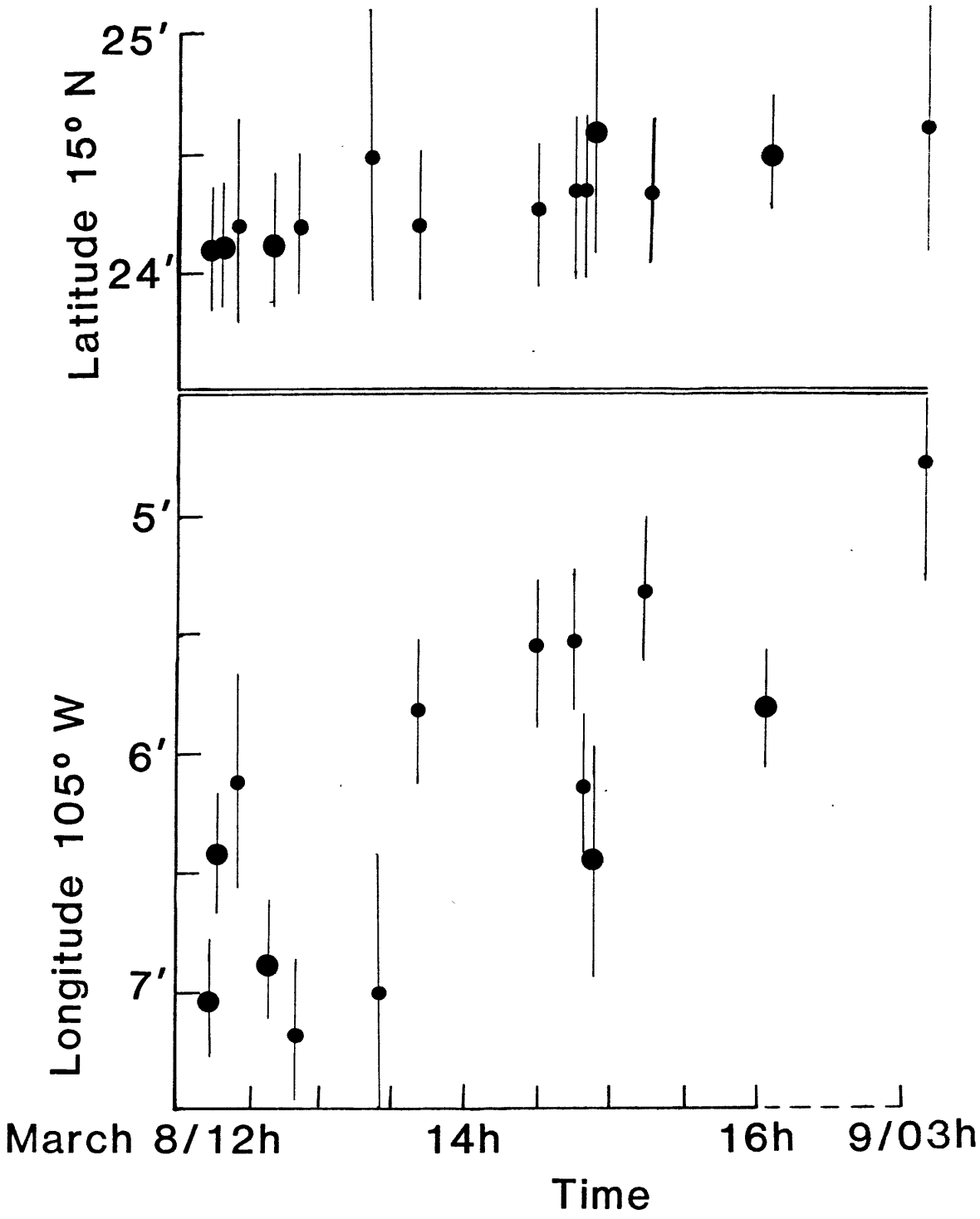
25′
24′
Latitude 15° N
5′
6′
7′
Longitude 105° W
March 8/12h
14h
16h
9/03h
Time

figure 4.8

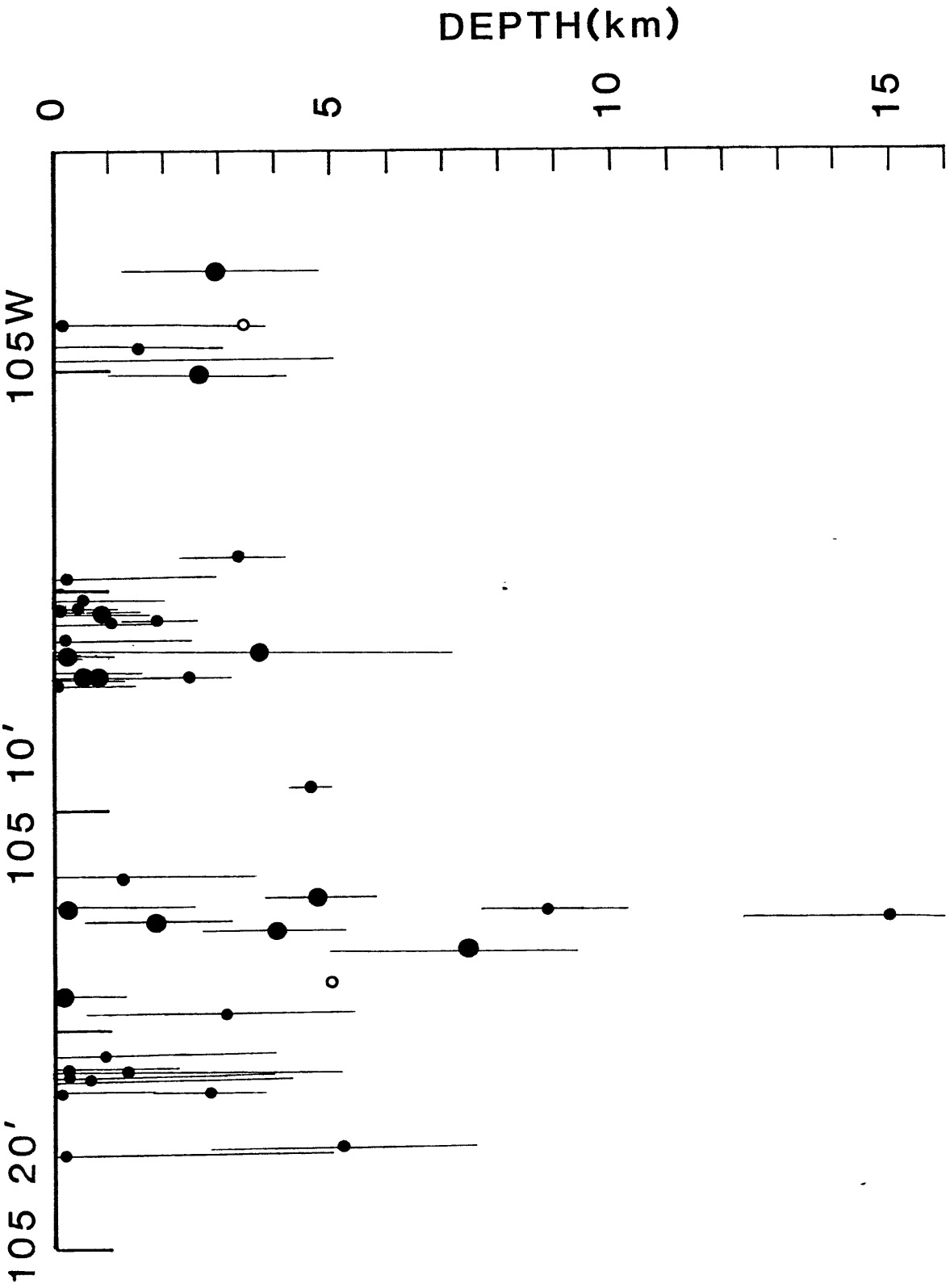

figure 4.9

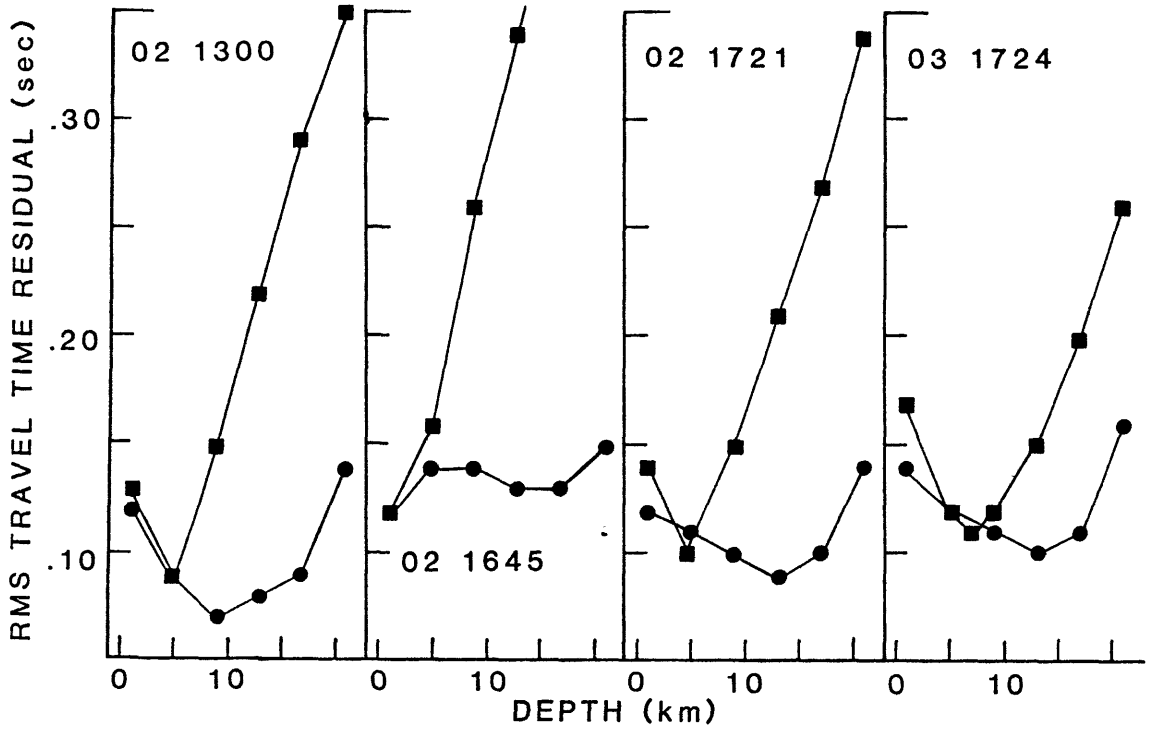
RMS TRAVEL TIME RESIDUAL (sec)
.30
.20
.10
02 1300
02 1645
02 1721
03 1724
0
10
DEPTH (km)

figure 4.10

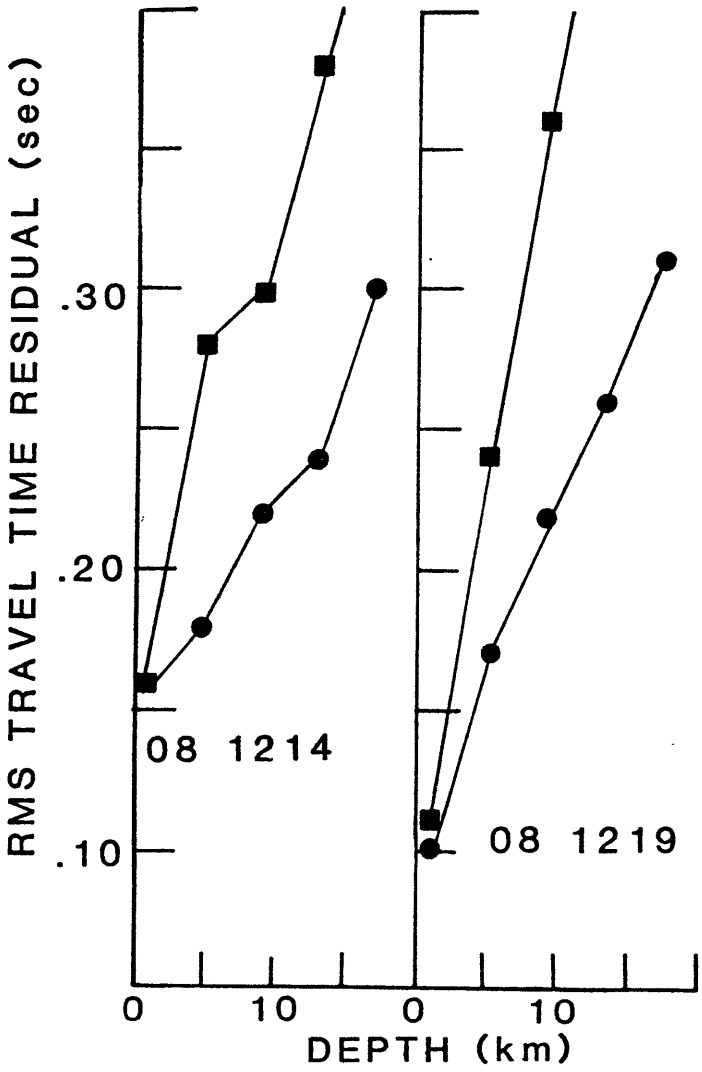
RMS TRAVEL TIME RESIDUAL (sec)
.30
.20
.10
08 1214
08 1219
0
10
0
10
DEPTH (km)

figure 4.11

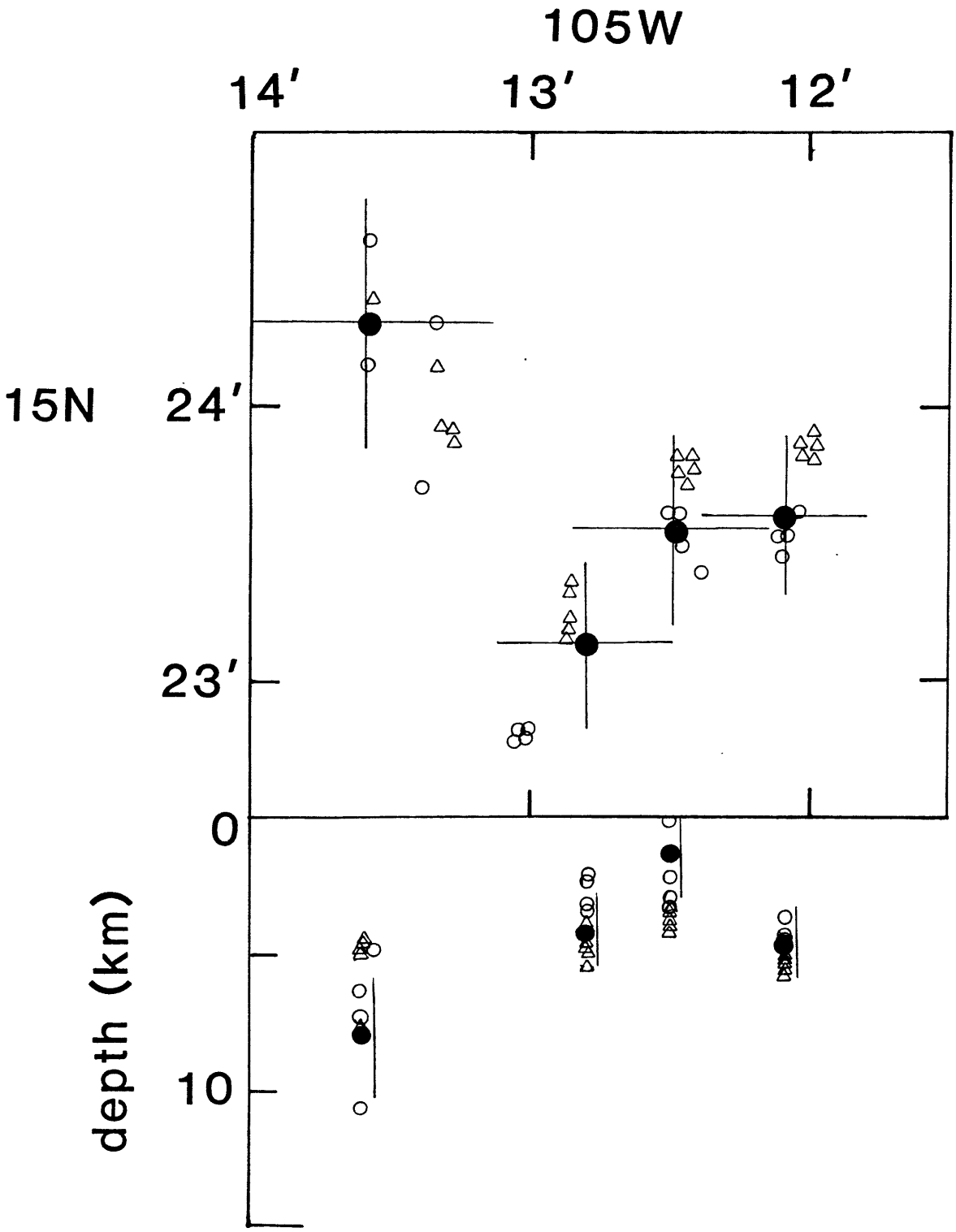

figure 4.12

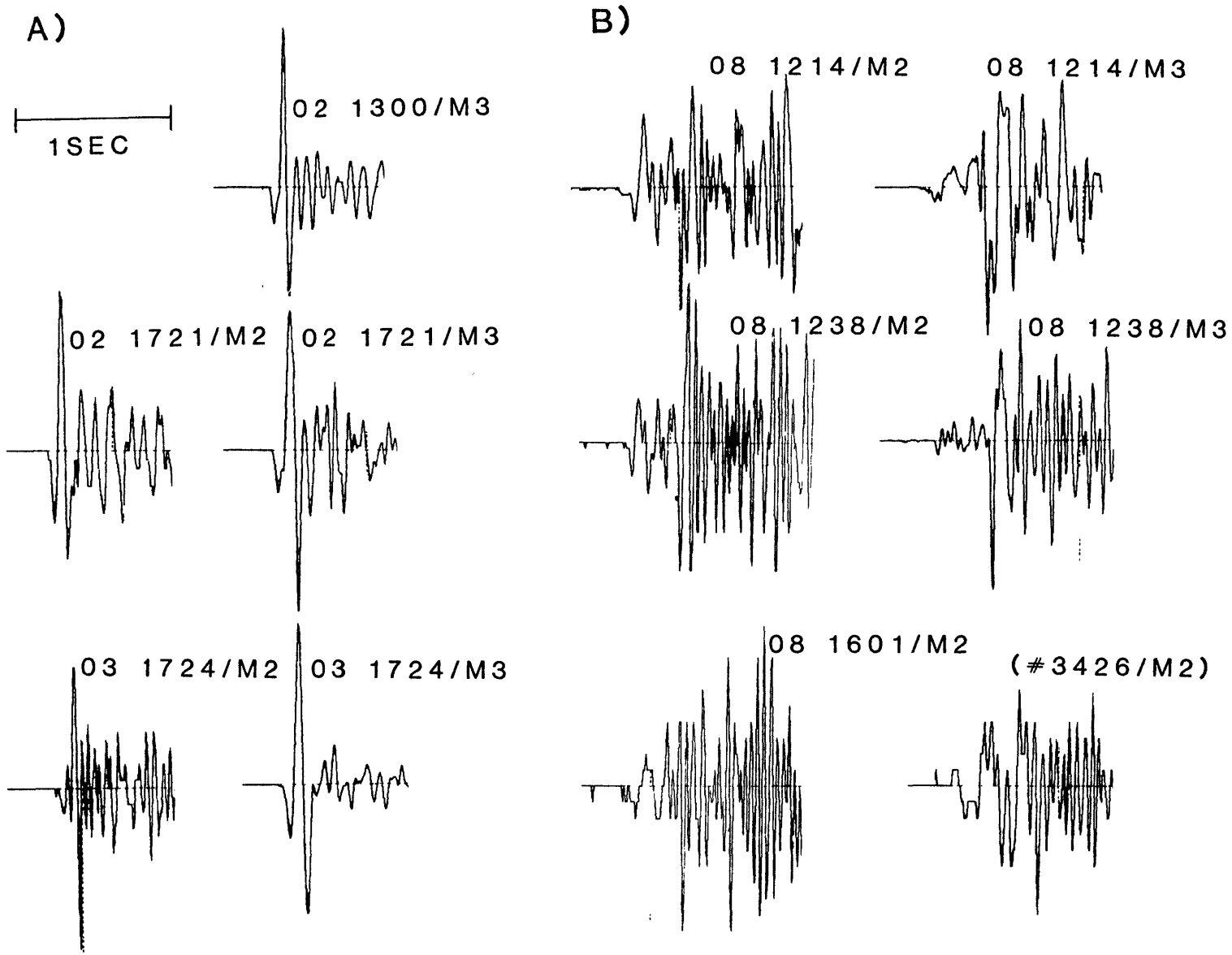
A)
1SEC
02 1300/M3
02 1721/M2
02 1721/M3
03 1724/M2
03 1724/M3
B)
08 1214/M2
08 1214/M3
08 1238/M2
08 1238/M3
08 1601/M2
(#3426/M2)

figure 4.13

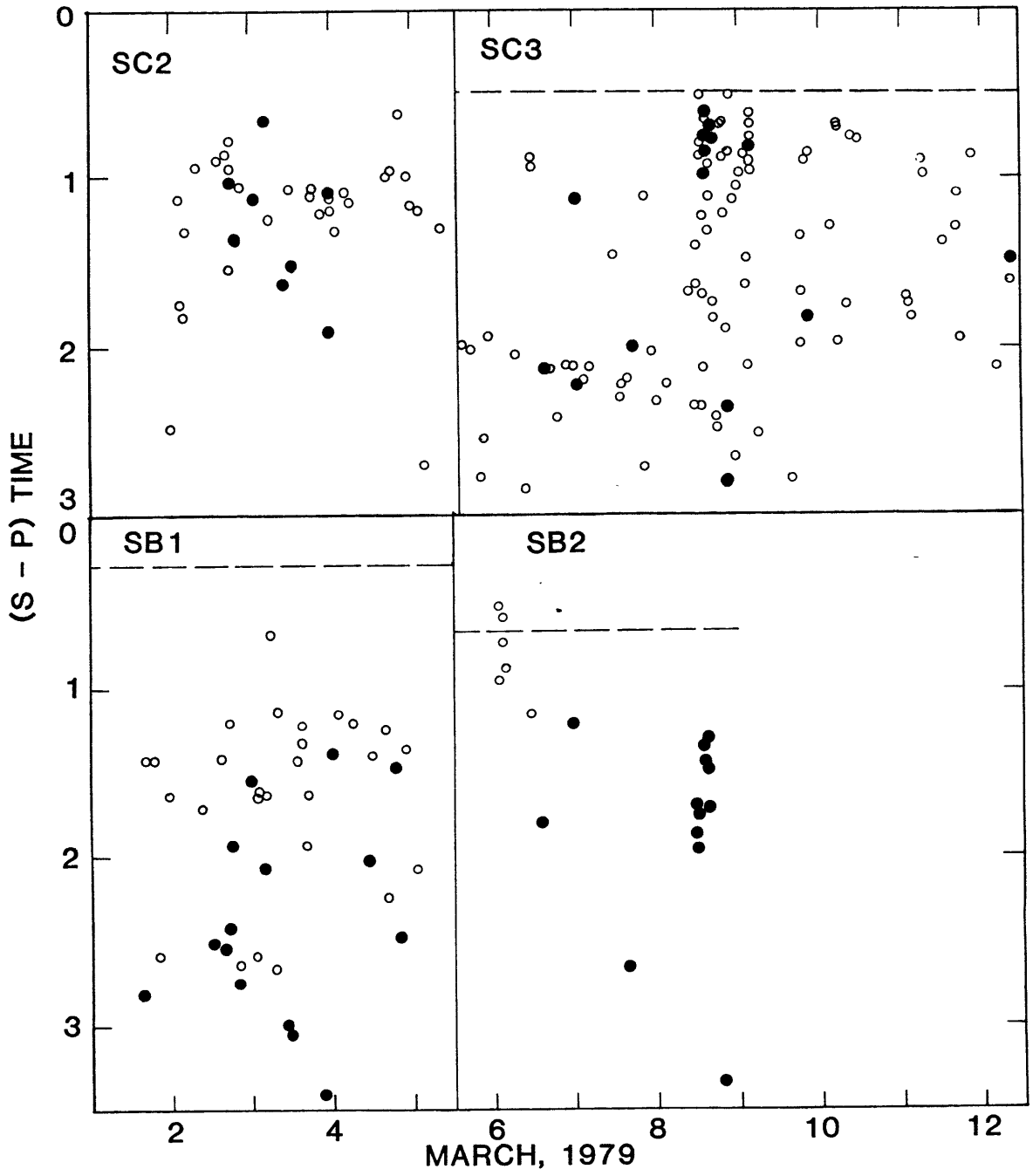

figure 4.14

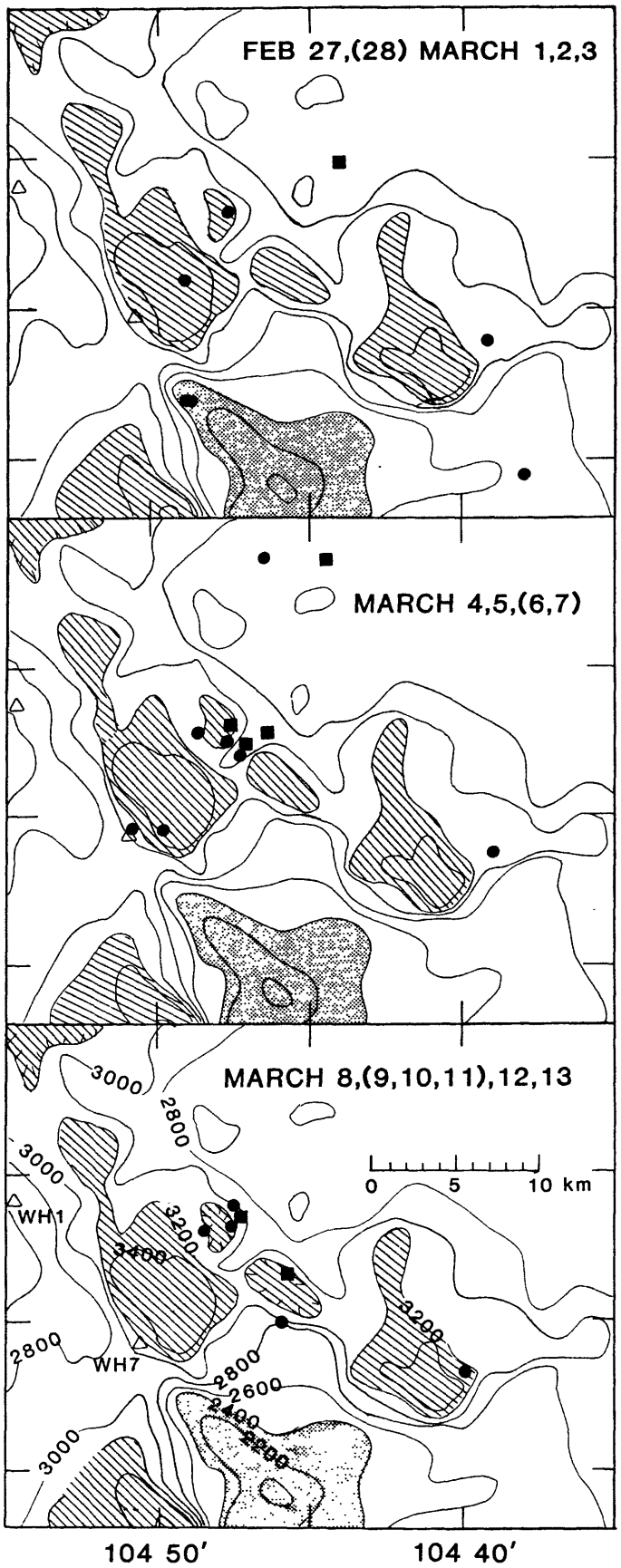
FEB 27,(28) MARCH 1,2,3
MARCH 4,5,(6,7)
MARCH 8,(9,10,11),12,13
15 15′
15 5′
0 5 10 km
WH1
WH7
3000
2800
3200
3400
2600
2400
2200
104 50′
104 40′

figure 4.15

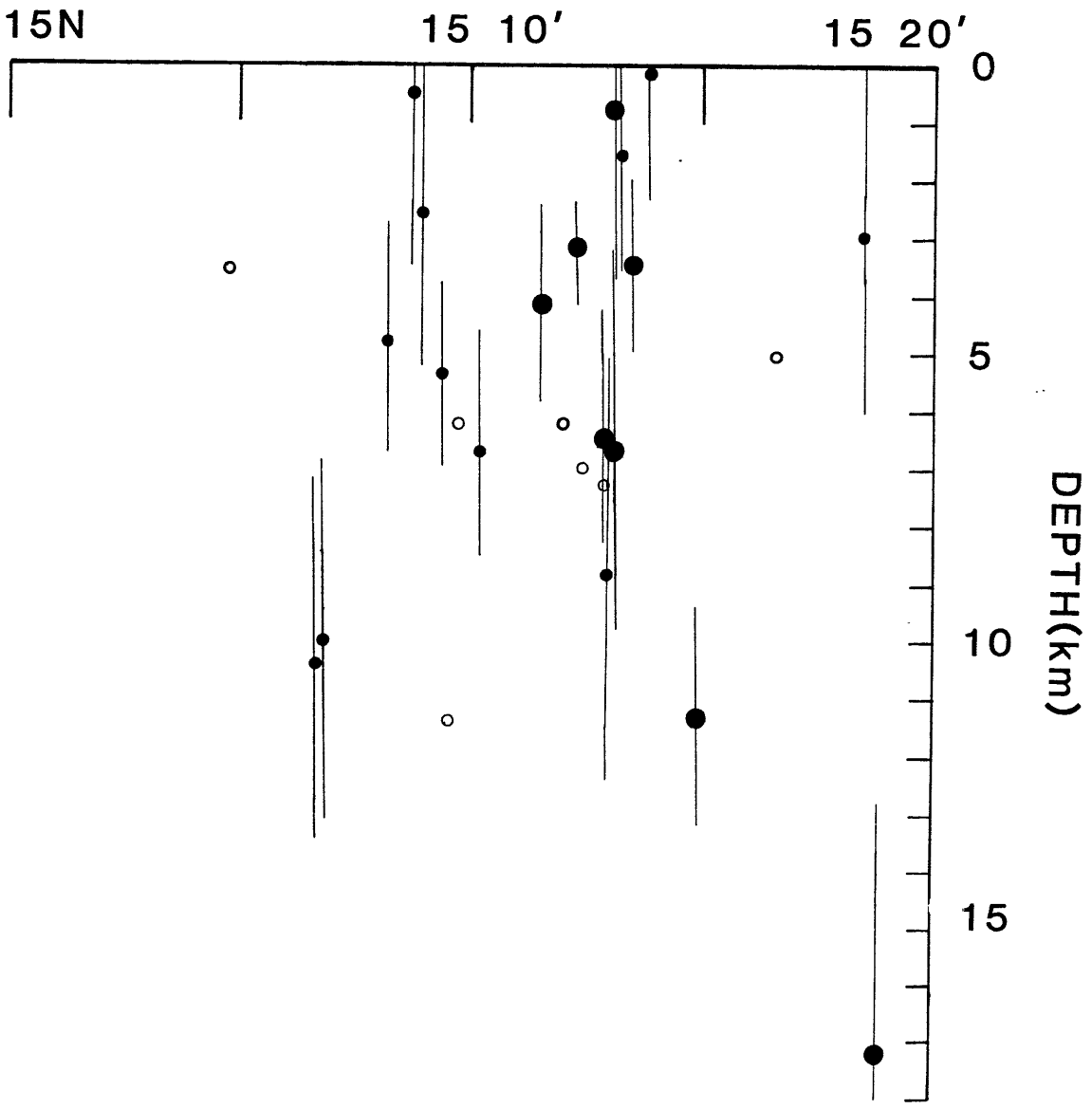

figure 4.16

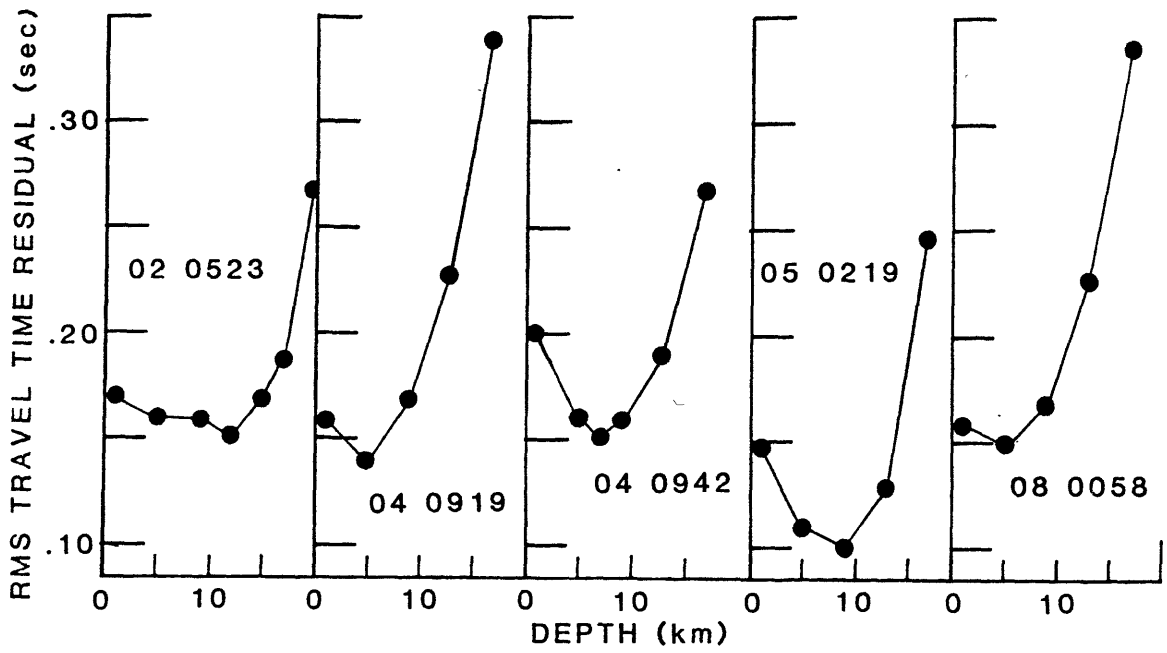
RMS TRAVEL TIME RESIDUAL (sec)
.30
.20
.10
02 0523
04 0919
04 0942
05 0219
08 0058
0
10
DEPTH (km)

figure 4.17

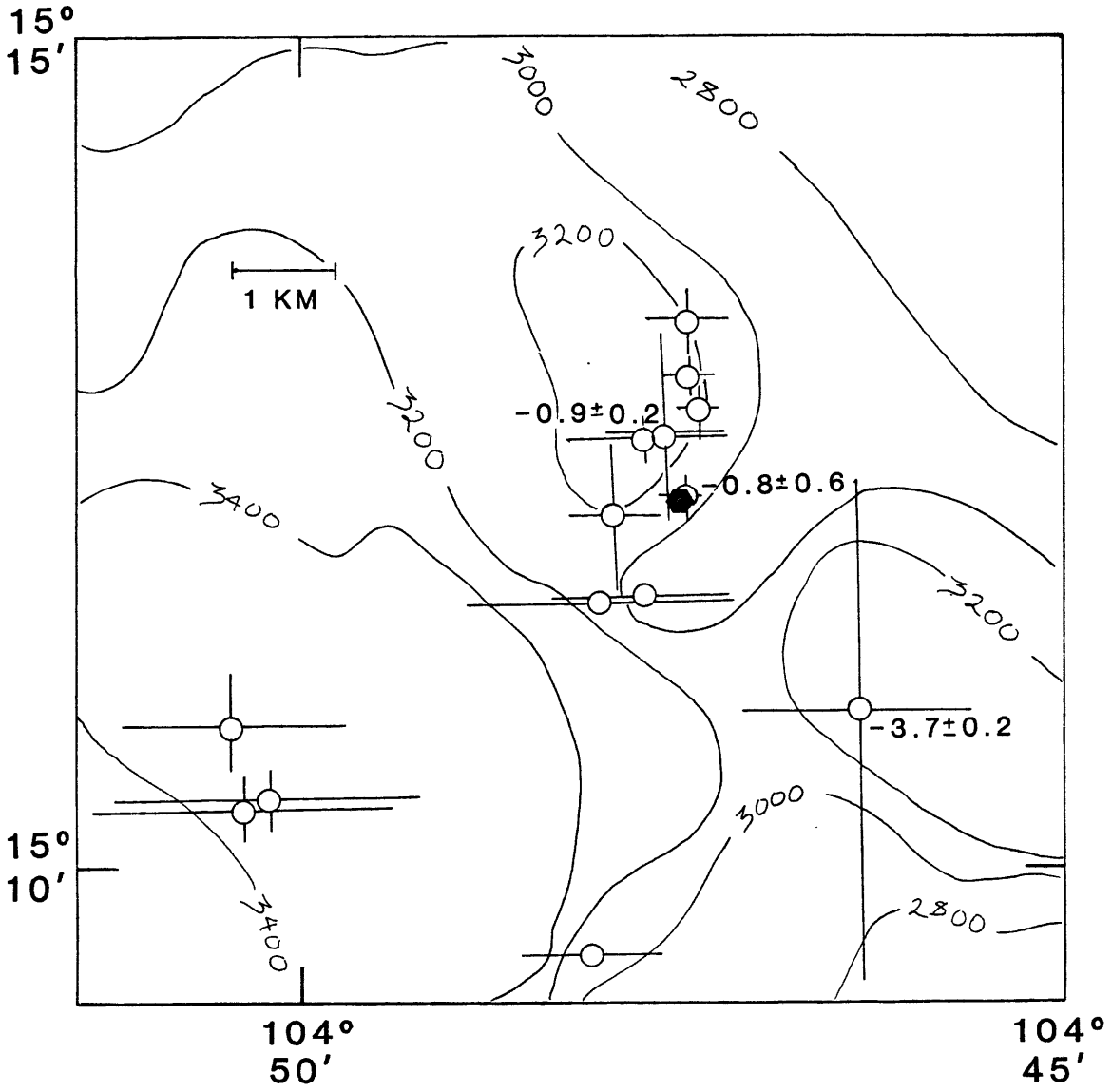
15°
15′
3000
2800
3200
1 KM
-0.9±0.2
-0.8±0.6
3400
3200
3200
-3.7±0.2
3000
15°
10′
3400
2800
104°
50′
104°
45′

figure 4.18

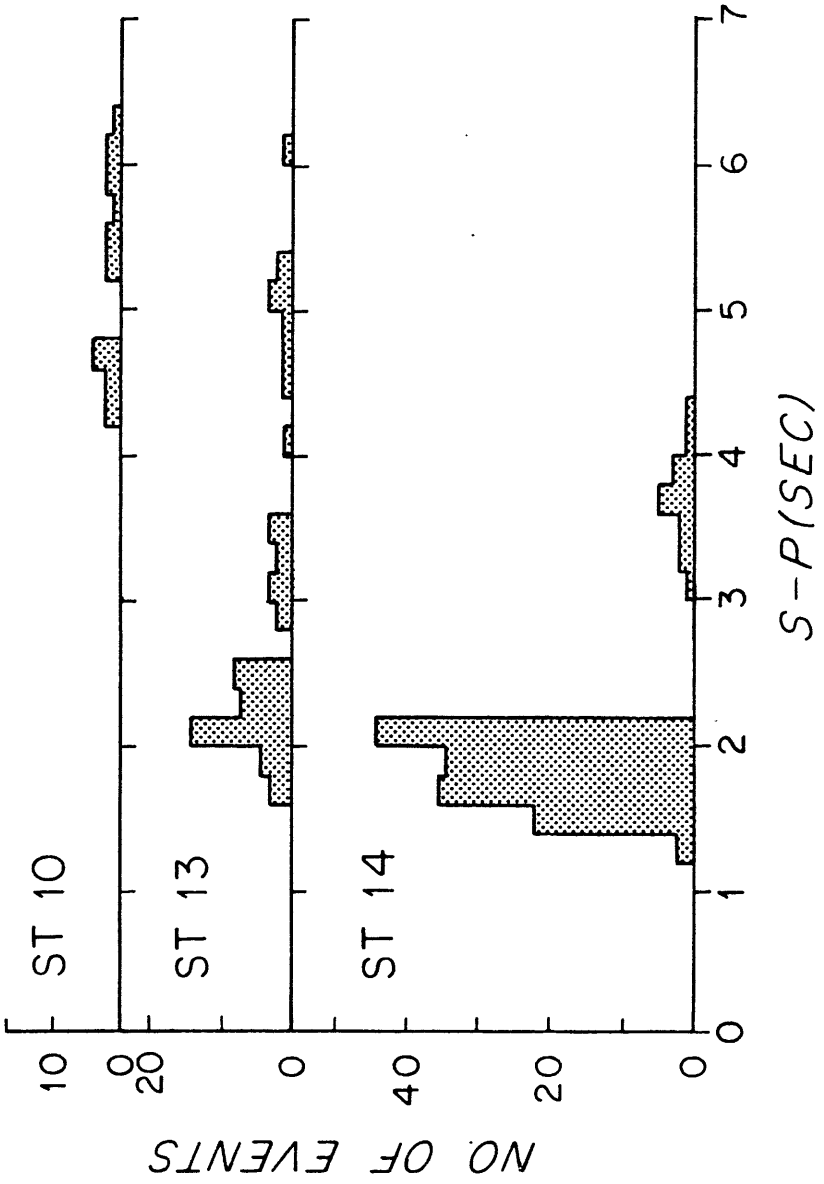

figure 4.19

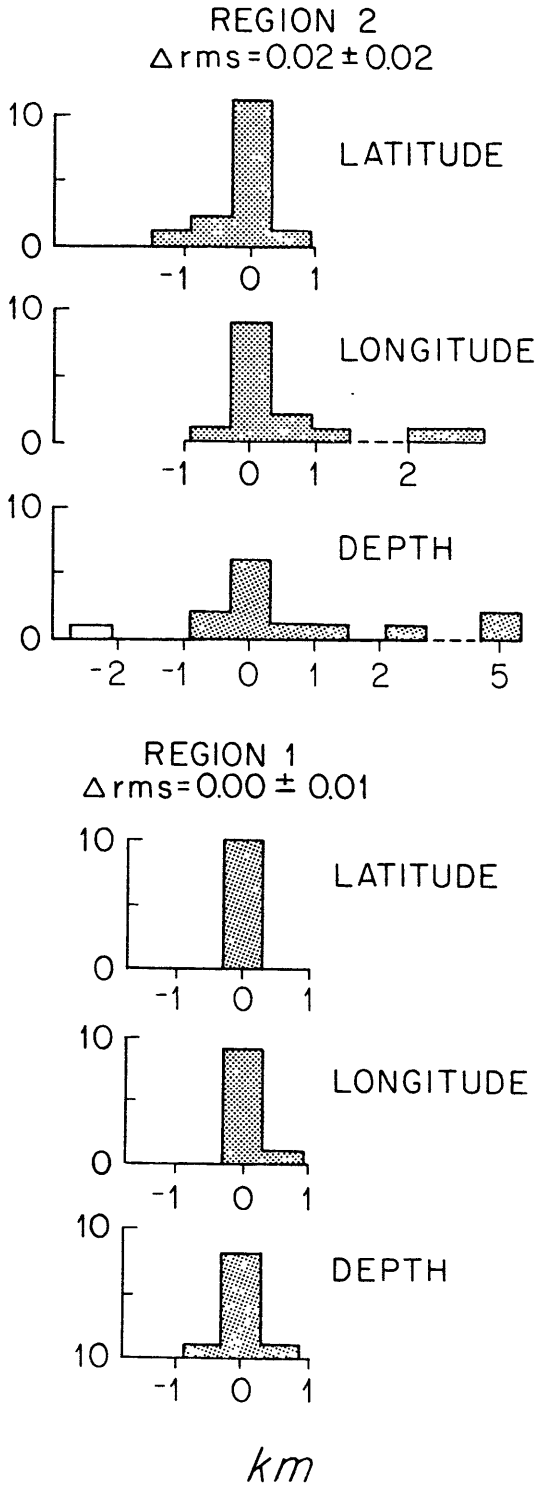
REGION 2
Δrms=0.02±0.02
10
0
LATITUDE
-1 0 1
10
0
LONGITUDE
-1 0 1 2
10
0
DEPTH
-2 -1 0 1 2 5
REGION 1
Δrms=0.00±0.01
10
0
LATITUDE
-1 0 1
10
0
LONGITUDE
-1 0 1
10
10
DEPTH
-1 0 1
km

figure 4.20

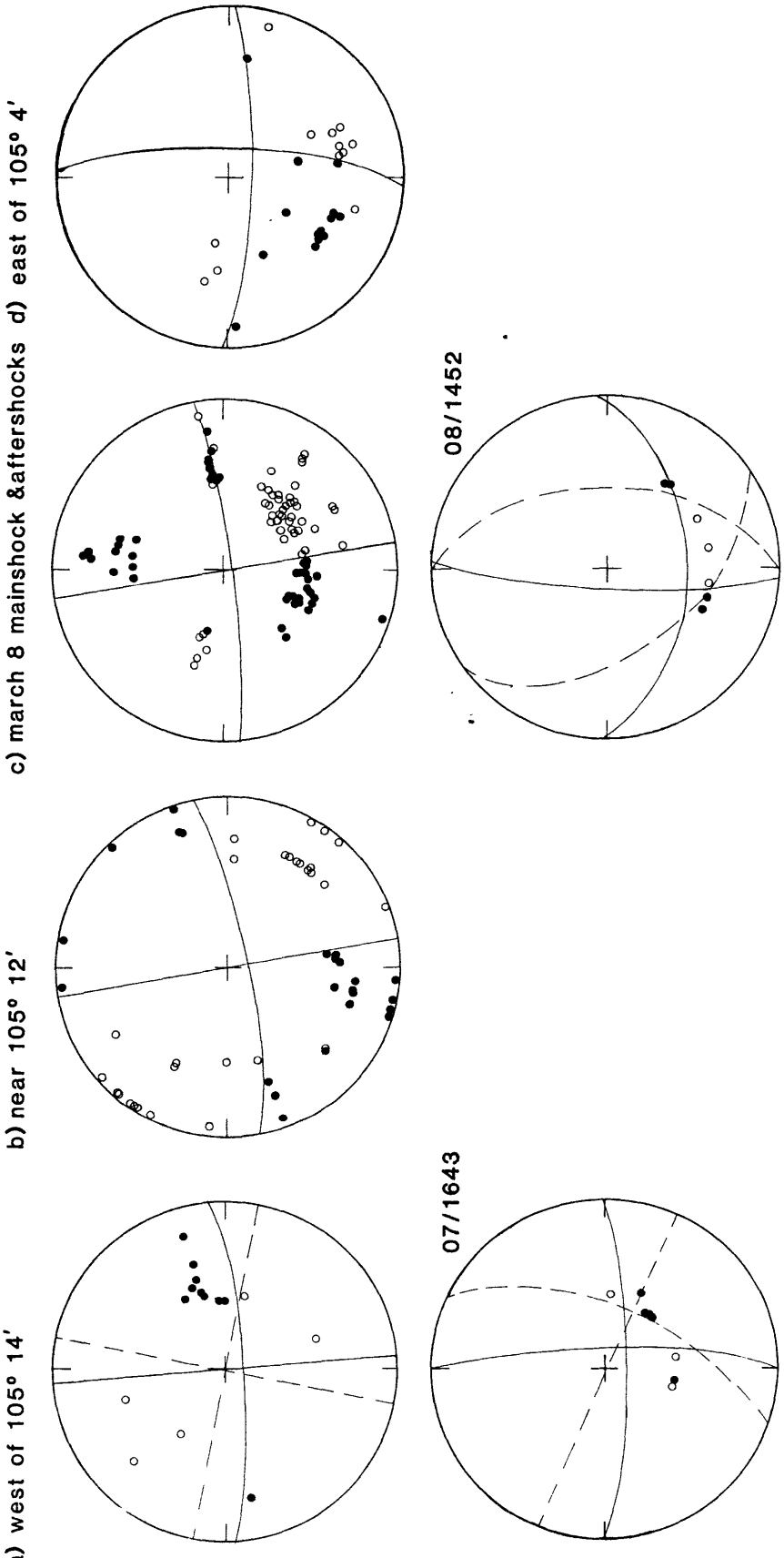
a) west of 105° 14'
b) near 105° 12'
c) march 8 mainshock &aftershocks
d) east of 105° 4'
07/1643
08/1452

figure 4.21

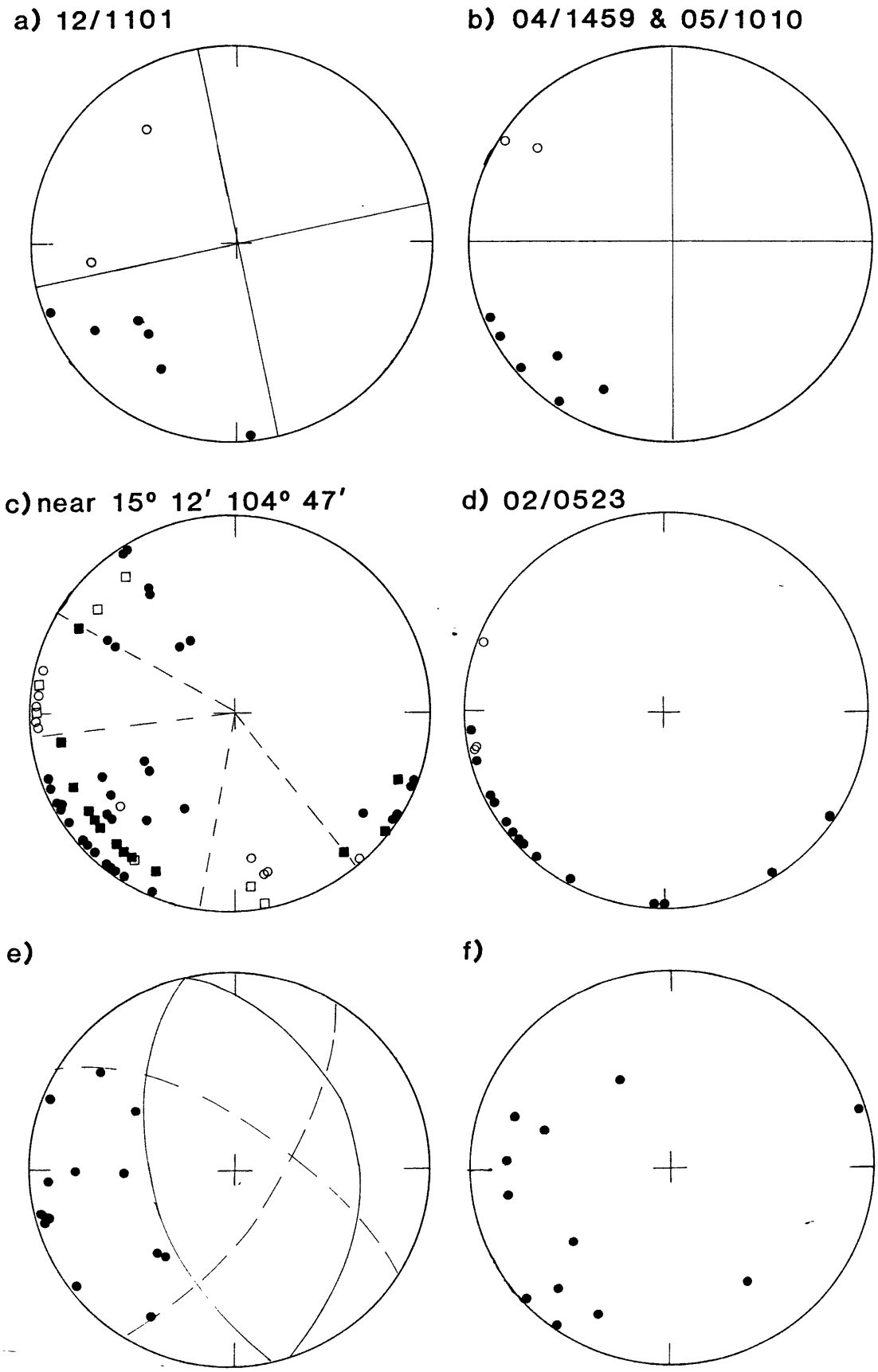

figure 4.22

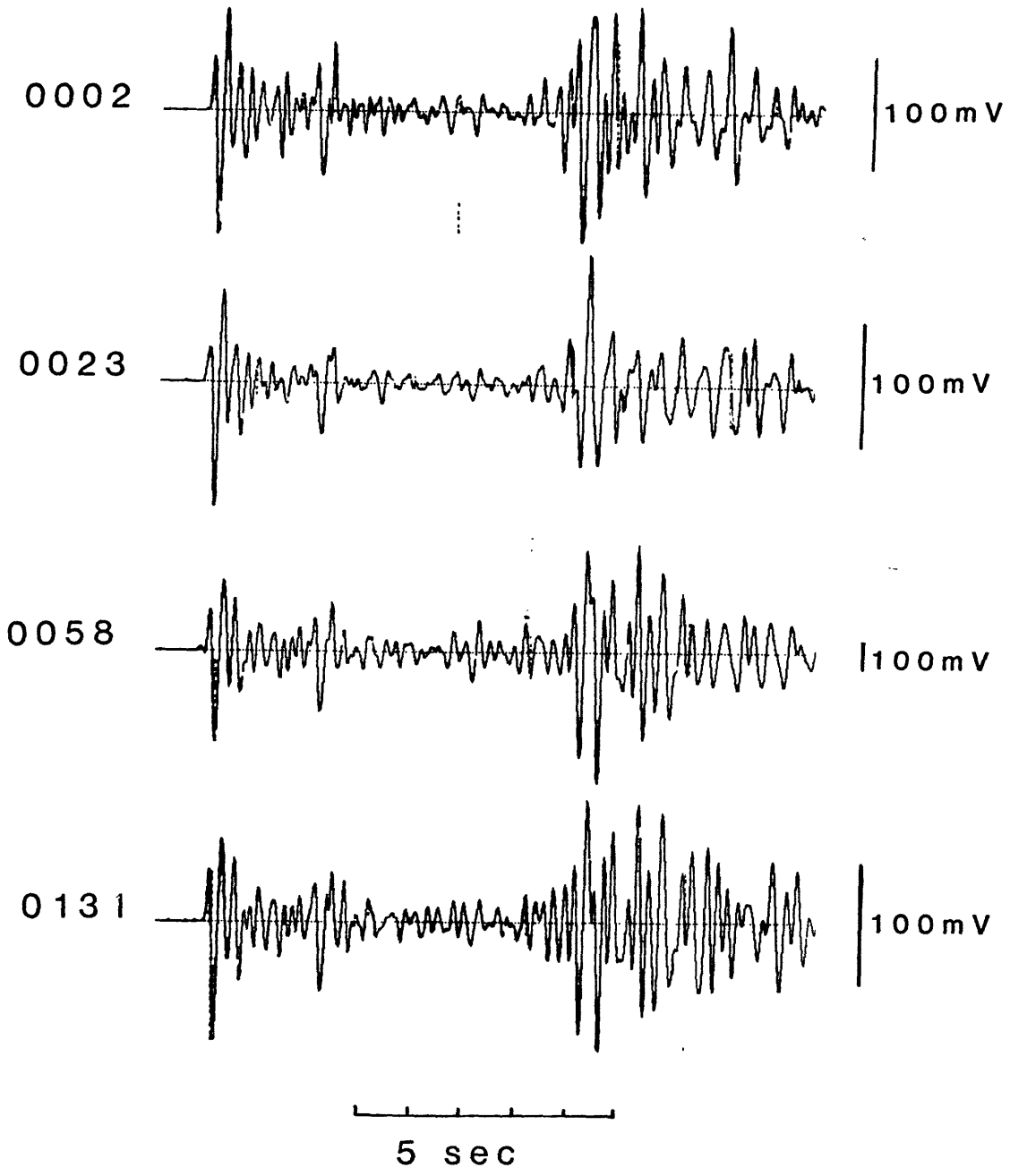

figure 4.23

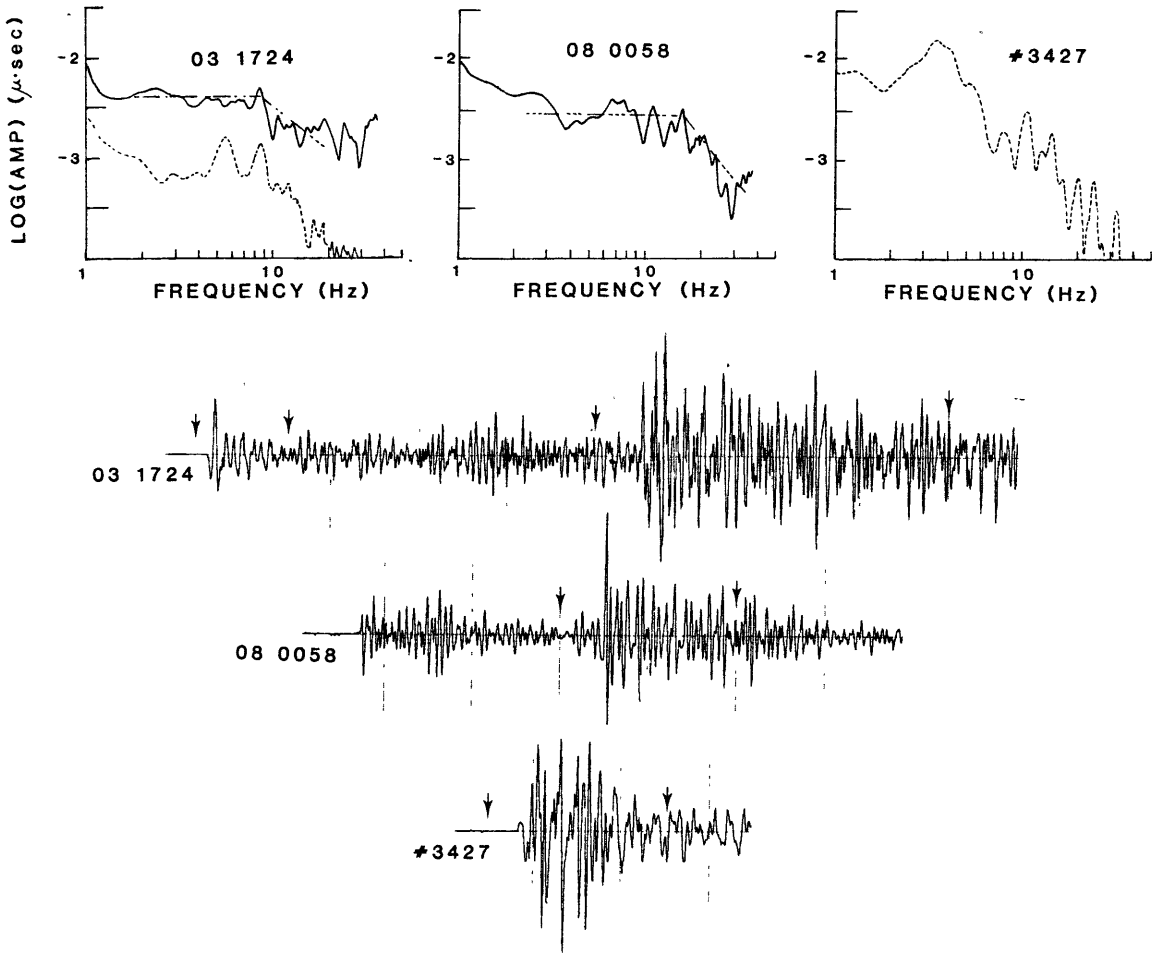
LOG(AMP) (μ·sec)
-2
-3
03 1724
1
10
FREQUENCY (Hz)
08 0058
#3427
03 1724
08 0058
#3427

figure 4.24

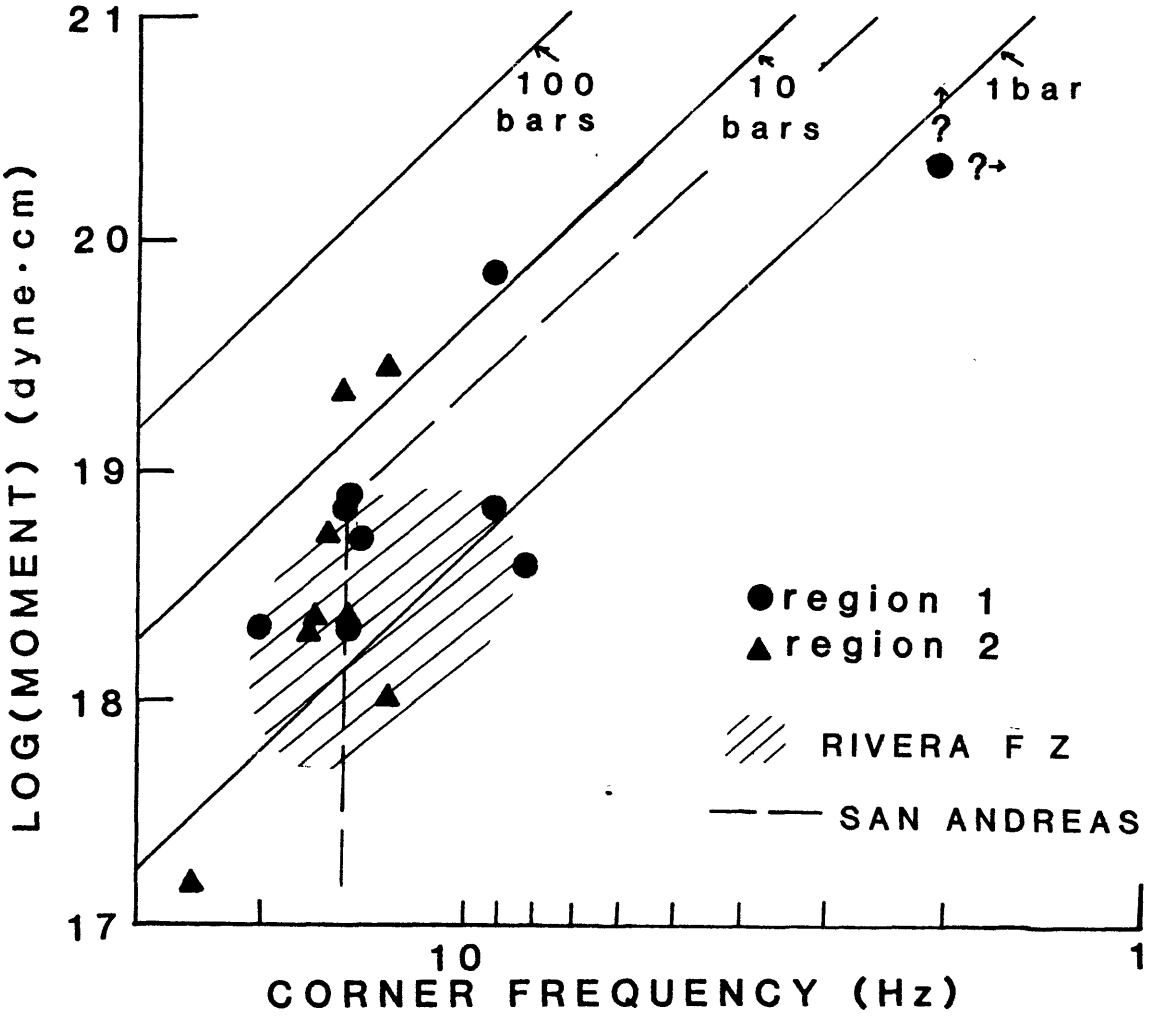
21
20
19
18
17
LOG(MOMENT) (dyne·cm)
100 bars
10 bars
1 bar
?
?
region 1
region 2
RIVERA F Z
SAN ANDREAS
10
1
CORNER FREQUENCY (Hz)

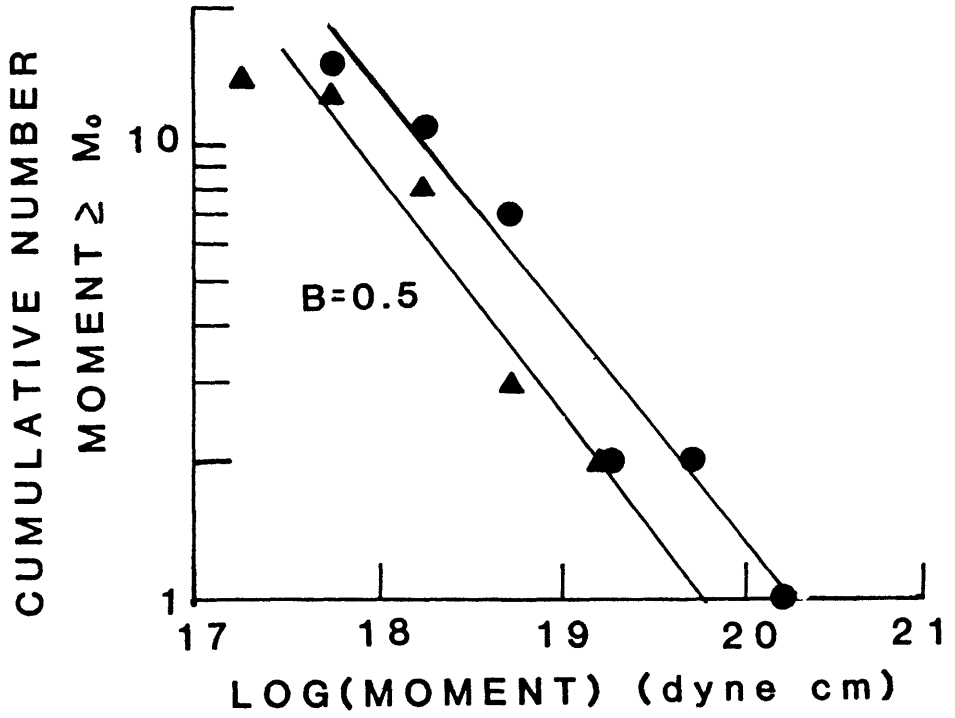
CUMULATIVE NUMBER
MOMENT ≥ M₀
10
1
B=0.5
17
18
19
20
21
LOG(MOMENT) (dyne cm)

figure 4.25

CHAPTER V

CRUSTAL STRUCTURE OF THE OROZCO TRANSFORM FAULT

In this chapter, the crustal structure of the transform zone is examined. In the first section, the incident angles and azimuths of body waves from both shots and earthquakes observed at station M2 are discussed. These angles, measured from particle motion plots of the three orthogonal components, show pronounced systematic deviations from those expected for a laterally homogeneous velocity structure. Three dimensional ray tracing is used to examine possible models which might explain the observations. A velocity structure is found which adequately reproduces the observations and the effect of this structure on the earthquake hypocenters and source parameters presented in the previous chapter is discussed.

In the second part of the chapter, refraction data from ROSE II are analyzed in an attempt to confirm the existence of the structures inferred from the incidence angles. Figure 5.1 shows the location of refraction data collected during ROSE II. The lines represent profiles of closely spaced shots. The dots represent individual large shots. Geographic coordinates of the large shots are given in Table 5.1. Many of the large shots also provided data for the particle motion study.

5.1 INCIDENT ANGLES AND AZIMUTHS

The particle motion plots were initially calculated as part of the coupling study presented in Chapter III in order to see if the body waveforms showed simple rectilinear motion. When large systematic deflections of the incident azimuths were observed, we decided to use these data to examine the possibility of lateral velocity variations in the transform zone.

5.1.1 ORIENTATION OF THE HORIZONTAL COMPONENTS

The orientation of the horizontal components relative to north was determined from the motion of the OBS in response to the water wave from large shots. Although a reliable orientation device, of course, provides a simpler means of orienting the components, laboratory tests indicated that the MIT OBS compass was not reliable*. The water waves were examined to provide an independent determination. Since other attempts to orient horizontal components by this method are not documented in the readily accessible literature, several potential sources of error will be discussed in detail. This discussion also applies to the body wave observations presented in section 5.1.2.

Use of the water wave to orient the components was originally suggested by the observations shown in Figure 5.2 from ROSE I, when OBS M1 was deployed near the intersection of two shot lines. One would expect the first motion to be

---

*The compass has since been replaced by a new system.

down on the vertical component and away from the azimuth of approach on the horizontal components. At ranges greater than about 10 km, the first few cycles of the water wave are clearly observed on H1 and not on H2 for shots along the east-west line; for shots along the north-south line, the water wave is observed on H2 and not on H1. This suggests that the horizontal components were oriented approximately along the direction of the shot lines. The change in amplitude and sign of the first cycle on the horizontal components when the north-south line passes within a few kilometers of the OBS also supports this conclusion.

For M2 and M3 during ROSE II, the water waves from large shots were used to orient the components. Unlike the case described above, a wide range of shot to receiver azimuths was available and the orientation was measured from the particle motion in the X-Y, X-Z and Y-Z planes during the first cycle of the water wave. Examples are shown in Figure 5.3. As expected for a water wave arriving obliquely from above, a sharp rectilinear motion is observed in X-Y and a rolling motion observed in X-Z and Y-Z. In most cases the observed first motion on the vertical component is down (e.g., shot 3427). For a few shots at long ranges, however, the first motion is up (e.g., shot 3430). Assuming that these observations represent a phase reflected at the air-sea interface (which is the first water wave arrival because of the local velocity structure of the water column), the first motion should be towards the direction of the incident water

wave; the apparent polarity of the horizontal components was adjusted accordingly.

Figure 5.4 shows the apparent orientation of the Y axis (component H1) as a function of azimuth from the OBS to the shot. The mean azimuth of the Y axis is 57±13°NE for M2 and 32±8° NE for M3. The corresponding X axis orientations (component H2) are 147° SE and 122° SE, respectively.

Several effects which can bias the apparent orientation are illustrated in Figure 5.5 for Y and X components oriented north and east. An instrument mislocation where the true location is 1 km to the north of that assumed is shown in 5.5a for assumed source-receiver ranges of 10 and 20 km. The maximum difference between the apparent azimuth and the true azimuth increases with decreasing range and is almost 6° for a range of 10 km; the observed incident angle is not affected by instrument mislocation. In chapter 4.6, patterns in the average station residuals were noted which suggested errors in the geographical coordinates of the instruments of about 1 km. The scatter in figure 5.4 for station M2 can be decreased slightly by perturbing the coordinates of M2 by 1 km to the northeast, giving an orientation for Y of 56±11° NE. Instrument mislocation may contribute to but cannot entirely explain the observed scatter.

Figure 5.5b shows the effect of a 5° tilt towards the west of the east-west geophone. The gimbaled geophone mount in the MIT OBS should compensate for tilt of the package to within at least 5°; moreover, the horizontal geophones would

not function properly for greater tilts and would probably yield seismograms that were clearly "anomalous". The azimuthal pattern is the same as for an instrument mislocation and the maximum deflection depends strongly on the angle of incidence. For the direct wave at long ranges, we expect the incident angle to be large. This effect does not depend on range.

Figure 5.5c shows the effect of a consistently greater amplification on the east-west component. The predicted azimuthal variation of the apparent azimuth of Y is different from the cases discussed above. In Figure 3.17, a consistently greater amplification of up to an order of magnitude was observed for component H1 on M3. The apparent azimuth of water waves at M3, however, does not show the pronounced azimuthal deflection predicted by Figure 5.5c. This supports the conclusion of Chapter 3.2.3 that the amplification of H1 is caused by a geologic feature of the deployment site rather than by the geophones or recording hardware. Figure 3.17 did not indicate any systematically greater amplification for either of the horizontal components of M2.

Combinations of the factors discussed above could lead to a complicated pattern of apparent orientation of Y. Additional scatter could be due to the presence of topographic obstacles along the path or to interaction of the water wave with the seafloor close to the instrument. For both M2 and M3, the main package was aligned along the X axis

and this may explain the scatter for M2 at azimuths of -5 to -30° and for M3 at -60°.

Considering the various factors discussed above, the orientation of the horizontal components determined from the water waves is probably accurate to within ±10°.

5.1.2 BODY WAVE INCIDENT ANGLES AND AZIMUTHS

The incident angles and azimuths of body waves from both shots and earthquakes were measured from plots of the particle motion in the X-Y, X-Z and Y-Z planes. Several examples are shown in Figures 5.6 and 5.7.

At station M2, the incident angles and azimuths can be measured to within a few degrees. In the examples of Figure 5.6, the horizontal components have been rotated so that the positive Y axis corresponds to the radial direction away from the source, assuming a laterally homogeneous velocity structure and an orientation of 57° NE for component H1. The P wave from the March 2 earthquake at 17h21m shows a dilatational first arrival deflected 20-24° counterclockwise from the expected radial direction. The angle of incidence, measured after rotating the Y axis to the apparent azimuth, is 39-45°. The neighboring shot 3437 shows a similar pattern for a compressional first arrival. The first S wave arrival (Figure 5.6b) for the 17h21m event represents SV motion (also see Figure 4.4) and shows the same azimuthal deflection as the P wave. The March 2 earthquake at 05h23m also represents a compressional first arrival. For this event, the apparent

azimuth is deflected by more than 90° from the radial direction and the incident angle is small. The S wave arrival is polarized along the transverse component.

Figure 5.7 shows examples of particle motions at station M3 for the same events as in Figure 5.6. The first cycle of motion is nearly vertical (0°-15°) followed by nearly horizontal motion along Y(H1). S waves observed at M3 from earthquakes in regions 1 and 2 are polarized along Y, regardless of the azimuth of approach, reflecting the same coupling problem as that causing the high spectral amplitudes on H1 in Figure 3.17. Unfortunately, this masks any information on regional velocity structure which might be contained in the incident angles and azimuths recorded by M3.

The measured incident angles and azimuths of P waves and the apparent polarization of S waves at M2 are compiled in Table 5.2; the P wave angles are illustrated in Figure 5.8. Pronounced systematic deviations from angles expected for a laterally homogeneous structure can be observed. For earthquakes and shots to the north, south, and west of the OBS, the observed incident angles are consistently between 38° and 47° and the apparent azimuths show a deflection that varies with geographic azimuth; the maximum deflection is observed for sources to the north and south of the OBS and the maximum amplitude of the deflection is greater than the uncertainty in the orientation determined from the water waves. The first cycle of the S wave from earthquakes in

region 1 is polarized as SV and shows a deflection from the radial direction similar to that observed for P waves. For earthquakes and shots from the central part of the transform, the incident angles are small and the apparent azimuth of approach is deflected by more than 90°; the apparent S wave polarization directions are scattered.

Before discussing the observations in Table 5.2 in terms of lateral velocity heterogeneities, we must first examine other factors which may contribute to the observed anomalies in propagation direction. The azimuthal effects of instrument mislocation (Figure 5.5a) or of consistently greater amplification of one channel (Figure 5.5c) do not depend on the incidence angle and are the same for the P waves as for water waves. The effect of tilt (Figure 5.5b), however, depends strongly on the incidence angle. The effect of a 5° tilt of the east-west component towards the west is illustrated in Figure 5.9 for incident angles of 45°, 20° and 5°. Note that the azimuthal pattern for a wave incident from below is the opposite of that for the water wave which impinges from above. For a small angle of incidence, the apparent azimuthal deflection can be as great as ±45°.

The observed incident angle i is also affected by waves reflected and transmitted at the seafloor-water interface. If the amplitude of the incident P wave is 1 and the angle of incidence is i, the apparent incident angle $\bar{i}$ is:

$$\tan \bar{i} = D_H/D_V = \frac{\sin i + \acute{\grave{P}}\acute{P} \sin i + \acute{\grave{P}}\grave{S} \cos j + \acute{\acute{P}}\acute{P} \sin i'}{\cos i - \acute{\grave{P}}\acute{P} \cos i + \acute{\grave{P}}\grave{S} \sin j + \acute{\acute{P}}\grave{P} \cos i'} \quad (5.1)$$

where D_H and D_V are the total horizontal and vertical displacements, $\acute{\grave{P}}\acute{P}$ and $\acute{\grave{P}}\grave{S}$ are the reflection coefficients for the reflected P and S wave displacements, $\acute{\acute{P}}\acute{P}$ is the transmission coefficient for the P wave transmitted into the water, and j and i' are the angles of the reflected S and transmitted P waves, respectively. Ergin (1952) calculated the square root of energy ratios of the reflected and transmitted waves for the case of a P wave in a solid half-space incident on a solid-liquid interface. Modifying these energy ratios to correspond to displacements (Aki and Richards, 1980), the appropriate coefficients are:

$$\acute{\grave{P}}\acute{P} = -\left[\cos i'\left(\frac{\alpha_1}{\beta_1}\cos^2 2j - \frac{\beta_1}{\alpha_1}\sin 2i \sin 2j\right) - \frac{\alpha_2}{\beta_1}\frac{\rho_2}{\rho_1}\cos i\right]/D \quad (5.2a)$$

$$\acute{\grave{P}}\grave{S} = \left[2\left(\frac{\alpha_1 \cos i}{\beta_1 \cos j}\right)^{1/2}(\sin 2i \sin 2j)^{1/2}\cos 2j \cos i'\right]/D \quad (5.2b)$$

$$\acute{\acute{P}}\acute{P} = \left[2\left(\frac{\rho_1 \alpha_1 \cos i}{\rho_2 \alpha_2 \cos i'}\right)^{1/2}\left(\frac{\alpha_1 \alpha_2}{\beta_1^2}\frac{\rho_2}{\rho_1}\cos i \cos i'\right)^{1/2}\cos 2j\right]/D \quad (5.2c)$$

$$D = \cos i'\left(\frac{\alpha_1}{\beta_1}\cos^2 2j + \frac{\beta_1}{\alpha_1}\sin 2i \sin 2j\right) + \frac{\alpha_2}{\beta_1}\frac{\rho_2}{\rho_1}\cos i \quad (5.2d)$$

where α_1, β_1 and ρ_1 are the P wave velocity, S wave velocity and density in the basement, and α_2 and ρ_2 are the velocity and density in the water.

In Figure 5.10, the apparent and true angles of incidence are compared for a range of values for α_1, σ and ρ, where σ is the Poisson's ratio ($\sigma = 1/2(1-[(V_p/V_s)^2-1]^{-1})$). For all cases, the apparent angle is less than the true angle because of the P wave which is transmitted into the water; the effect increases with increasing velocity contrast between the basement and the water and with increasing Poisson's ratio.

For a Poisson's ratio between 0.25 and 0.30 (reasonable values for upper oceanic crustal rocks; Hyndman, 1979), the observed incident angles of 39 to 45^o correspond to true angles of 50 to 65^o. Assuming that the arrivals have a phase velocity of about 8 km/sec (see section 5.3), these incident angles correspond to a velocity of about 6 km/sec below the OBS. Although the angles of incidence may be systematically overestimated because of a possible difference in the horizontal and vertical coupling responses (note higher spectral levels on the horizontal components in figures 3.17 and 4.24), this observation suggests that the low velocity, high gradient layer which generally constitutes the upper one to two kilometers of the oceanic crust may be unusually thin beneath M2 (i.e. invisible to a seismic wavelength of hundreds of meters). The observed incident angles of 22 to 27^o correspond to true angles of about 28 to 38^o.

The effect illustrated in figure 5.10 also provides an explanation for the nearly vertical incident angles observed for all P wave arrivals at instruments which we suspect were sited on low velocity, low strength sediment (see chapter 3.2.3). For a P wave velocity beneath the instrument of 2.5 km/sec, arrivals with a phase velocity of 8 km/sec should have an incident angle of 18^{o}. If σ is greater than 0.40, however, the apparent incident angle will be less than 10^{o}; in the ocean, σ of the surface sediments may be as low as 0.498 (Hamilton et al., 1970).

Applying the above discussion to the observations in Table 5.2 and Figure 5.8, we note that the pattern of azimuthal deflection for events to the north, west and south of M2 is similar to that observed for the water waves and may be due in part to instrument mislocation (Figure 5.5a). At a given station, however, the amplitude of the P wave deflection is greater than that of the water waves. The effect of tilt (Figures 5.5b and 5.9) depends strongly on incident angle but the azimuthal pattern for the water wave should be the opposite of that for the P waves. The observed pattern also does not match the pattern of Figure 5.5c for a systematically greater amplification on one horizontal channel. The deflection of body wave incident angles for sources to the north, west and south of M2, therefore, probably does reflect, at least in part, a regional geologic effect.

Because of the large influence of geophone tilt on the apparent azimuth when the incident angle is small, the numerical value of the observed angles from sources in the central part of the transform should be interpreted rather loosely. The "steep" angles of incidence and "large" azimuthal deflection, however, probably do reflect regional lateral velocity heterogeneity.

5.1.3 RAY TRACING THROUGH LATERALLY HETEROGENEOUS VELOCITY STRUCTURES

A number of geologic scenarios can be invoked to explain these observed incident angles and azimuths. For example, the systematic deflection with azimuth might be caused by high velocity material beneath the topographic ridge to the west of M2 and the steep incident angles from sources in the central part of the transform might result from a low velocity zone in the crust between the sources and M2. To test whether such structures could result in the observed deflections for geologically reasonable velocity gradients, rays were traced through laterally heterogeneous velocity models and the incident and takeoff angles compared to those expected for a layered structure.

The problem of tracing rays in a laterally heterogeneous structure can be approached either as a boundary value problem where the two endpoints of the ray are fixed or as an initial value problem where the initial point and takeoff angle and azimuth are specified. These two approaches have been discussed and compared by Julian and Gubbins (1977).

Several other papers which discuss the principals and practice of ray tracing are Jacob (1970), Julian (1970), Wesson (1971), Pereyra et al. (1980), Thurber (1981) and Luk et al. (1982).

The boundary value approach is generally referred to as the "bending" method because an initial path between the two endpoints is mathematically perturbed or "bent" until it converges to a minimum time path satisfying the ray equation. The velocity and first and second derivatives must be known at each point along the ray. The initial value approach is known as the "shooting" method because the ray is shot from an initial point and follows a trajectory directed at each increment by the local velocity and first derivative.

For this study, a bending program developed by Pereyra et al. (1980) was used to calculate the ray path between M2 and sources for which incident angles and azimuths had been observed. To qualitatively evaluate whether the rays obtained by the bending program represent significant arrivals, the program of Luk et al. (1982) was used to "shoot" a cone of rays around the takeoff angle and azimuth determined by the "bending" program and determine whether the receiver was in a shadow zone or at a focus with respect to the model. For both programs, the velocity model was described by a three dimensional grid. A cubic spline under tension (Cline, 1974) was used to interpolate the velocity and first and second derivatives between the nodes of the grid.

Because several rays representing local travel time minima may exist between a given source-receiver pair, the initial ray path for the bending method must be close to the path for the arrival under consideration. For a deep source, an initial estimate of a straight line between the endpoints will probably converge to the first arrival. If both endpoints are on the seafloor, however, a straight line initial estimate will, in most cases, converge to an arrival which is not the first arrival. To avoid explicitly specifying each initial path, the source locations for shots and very shallow earthquakes were projected onto the Moho along the raypath for a laterally homogeneous model; the initial ray was then the straight line between this point and M2. Because the sources were well outside of the zone of lateral heterogeneity in the model and were at source-receiver distances much longer than the critical distance for Moho arrivals, this should not significantly affect the calculated incidence angles and azimuths at M2.

A velocity model which reproduces the general features of the observed pattern of incident angles and azimuthal deflections while remaining geologically reasonable was found by trial and error. Initial models were constructed to simulate the type of structures mentioned at the beginning of this section. The initial models were then perturbed by changing either the velocity values at the grid points or the grid spacing. Because of the large uncertainty in the

determination of incident angles and azimuths, no quantitative measures of fit were applied.

The lateral distribution of sources and grid points for the final model is illustrated in Figure 5.11a. The 3000m contour from the map of Mammerickx (1980) is also shown. The velocity values at the grid points and velocity-depth profiles at several points in the model are shown in Figures 5.11b and 5.11c, respectively. The major features of the model are high velocities beneath the north-south ridge to the west of M2 and low velocities between M2 and sources in the central transform region. Outside of these anomalous zones, the grid describes a laterally homogeneous structure similar to that used for the hypocenter locations in Chapter IV. The calculated incident angles and azimuths at M2 are compared to the observations in Table 5.3.

For azimuths affected by the high velocities beneath the north-south ridge to the west of M2, the angles of incidence can be matched quite well and, although the amplitudes of the calculated azimuthal deflections are smaller than those observed, the signs and relative amplitudes are reproduced (rays 1-6; Table 5.3). The azimuthal deflection depends primarily on the horizontal velocity gradient in the upper mantle and is not changed significantly by changing the depth distribution of the grid to model a narrower Moho transition zone (dotted line in Figure 5.11c). The numerical value of the calculated deflection is sensitive to small changes in the lateral position of the grid points; the general pattern,

however, is quite stable. The magnitude of the azimuthal deflection could be increased by increasing the number of horizontal grid points and adjusting the local horizontal velocity gradients. Because of the uncertainty in the orientation of the horizontal components and the oversimplification of modeling a complex structure by a coarse grid, a numerical improvement of the fit would not necessarily imply a more "accurate" geologic model.

To interpret these results geologically, note that the amplitude of the topography in this region is similar to the uplift of isovelocity surfaces in the model. This suggests that the velocity increase beneath the north-south ridges in the transform zone may reflect an approximately constant crustal thickness with the Moho being parallel to topography; very little actual crustal thinning need be invoked. In the next section, we shall examine refraction data from ROSE II to see if we can determine the crustal structure and thickness.

The SV wave deflection for earthquake sources in region 1 can be explained by the same model. The observation that SH is delayed relative to SV may reflect anisotropy of the S wave velocity in the crust or upper mantle with the vertical velocity being higher than the horizontal velocity. A system of vertical cracks, for example, would have such an effect. Stephen (1981) observed similar SV-SH polarization for data recorded by a three component borehole seismometer emplaced in the upper crust. Because the anisotropy may occur over any

portion of the earthquake-station path, however, more data is required before any significance can be attributed to this observation.

In the central part of the transform, the model of Figure 5.11 simulates a crustal magma chamber. The lowest velocity, of 3 km/sec at a depth of 2 km is appropriate for molten basalt as determined in laboratory experiments (Murase and McBirney, 1973). The low velocity in the model increases to a "normal" crustal velocity over a radius of approximately 10 km. When the low velocity zone is between the source and the receiver, the rays are bent down and around the low velocity zone resulting in small angles of incidence and large azimuthal deflections at M2.

The incident angles and the sign of the azimuthal deflections are matched quite well (rays 7-14, Table 5.3). The amplitudes of the deflections, however, are much smaller than those observed, and no rays have been calculated with deflections so great that they actually appear to arrive from the west. For several reasons discussed below, the fit to the data is nevertheless considered to be adequate.

In Figure 5.9, we saw that large deflections in the apparent azimuth are caused by a small tilt of the geophones if the angle of incidence is small. In the central region of the transform (rays 9-14), the source locations are within a narrow azimuthal range from M2; this azimuth also approximately corresponds to the orientation of the Y component. If the Y axis were tilted away from the sources,

both the positive and negative "apparent" deflections would increase by tens of degrees for "true" azimuthal deflections like those calculated for the model.

Rays could also be made to bend back on themselves by adjusting the velocity model of Figure 5.11 in the vicinity of M2. The velocity gradients required, however, are very large with respect to the wavelength of the data being modeled (400-500m) so that the results would be inappropriate for explaining the observations. What is effectively suggested is a steeply dipping reflector below M2 to the west. This scenario is illustrated schematically in Figure 5.12. A nearly vertical boundary would not seriously affect rays 1-6 in Table 5.3 (ray A in Figure 5.11) but might reflect arrivals near grazing incidence (ray B). For the reflected arrivals to be first arrivals, M2 must be in a shadow zone for rays leaving the source (ray C). Any geologic inferences about the geometry or nature of such an "interface" are purely speculative; for example, the "interface" might represent a dike of a composition or fabric different from that of the surrounding rock.

Both of the effects discussed above require small angles of incidence below M2 and are essentially variations of the model of Figure 5.11. We were not able to construct geologically reasonable models which would result in small incident angles at M2 that did not have a low velocity region between the sources and M2. Although we conclude that the incident angles observed at M2 suggest the presence of a low

velocity body in the central transform region, we are not able to constrain details of the geometry. For example, the vertical extent of the low velocity zone in Figure 5.11 is required in order for rays to converge at M2; shooting a cone of rays from the source point indicates that M2 is in a shadow zone for a purely crustal low velocity zone. Although the root is "required" by our method of modeling the situation through ray tracing, the discussion of the previous paragraph suggests that it is not necessarily required geologically. Unsupported by additional information, these observations would not provide an irrefutable case for a magma chamber; that the model described here can tentatively answer several questions raised in the previous chapter, however, is circumstantial evidence for its general validity.

5.1.4 EFFECT ON HYPOCENTER LOCATIONS AND FAULT PLANE SOLUTIONS

The lateral heterogeneities invoked to explain the observed incident angles and azimuths at M2 also affect the travel time and take-off angle and azimuth at the source, thus inducing errors into the hypocenter locations and fault plane solutions determined in Chapter IV. To examine these effects, synthetic travel time data were generated by tracing rays through the structure of Figure 5.11 from source points corresponding to earthquake hypocenters to points corresponding to stations in the array. These travel times were then inverted for the apparent hypocentral parameters

using HYPOINVERSE and the velocity structure of Table 4.3. The results of the locations are shown in Table 5.4 and Figure 5.13.

In region 2, the structure for Figure 5.11 leads to epicentral mislocations of up to 10 km, much larger than the errors indicated by the 95% confidence ellipse of the solution as defined in Chapter 4.2. Although the true depths are all 8 km, the apparent depths range from 4 to 17 km. The location of event 6, in region 1, is not affected.

Because we do not know the detailed geometry of the low velocity region, particularly its extension into the topographic troughs to the north and east, we cannot apply these results to quantitatively correct the hypocentral parameters determined in Chapter IV. These results do, however, provide tentative answers to some of the questions raised in Chapter IV. In particular, the earthquakes which appear to be located beneath ridge β' (Figs. 2.4 and 4.5) may actually have occurred within trough B, and the discrepancy between calculated locations near the site of instrument T13 and the arrival time difference between S and P waves at T13 may be due to hypocentral mislocation. Events in the cluster near 15°12'N, 104°47'W do not appear to be severely mislocated. The ray tracing model, which results in ray paths to stations M2 and M3 which are 8-15% longer than those for a laterally homogeneous structure, is also compatible with the apparent delay of S relative to P observed at M2 and M3, from events in region 2 (see Chapter 4.6).

The difference between the "true" take off angles and azimuths at the source and the "apparent" angles calculated from the locations with respect to a laterally homogeneous structure are shown in Figure 5.14a. We see that the "apparent" angles differ from the "true" angles by tens of degrees. The error in the take-off angles is due to the uncertainty in the hypocentral depth as well as to the effect of the laterally heterogeneous velocity model and is a common problem for fault plane solutions from local events. The azimuthal error, however, is due primarily to the effect of deflection of the ray paths by the laterally heterogeneous velocity structure; at most ±5° are contributed by the epicentral mislocation. For event 6, the azimuthal deflections are all less than 5°.

In Figure 5.14b, the results for source location 1 are used to compare "true" and "apparent" fault plane solutions for several possible mechanisms. Comparing solutions a', b' and c' to the fault plane solutions in Figure 4.22, we see that the perplexing four-quadrant pattern in Figure 4.22c, which represents a composite solution for the cluster of events near 15°12'N, 104°47'W, may be compatible with normal faulting along a north-west striking plane; the component of strike-slip motion is also compatible with the expected sense of transform motion. The entire range of solutions observed in Figure 4.22 can be modeled by small changes in strike and dip. The observed fault plane solutions for events in region 2, therefore, may suggest a "leaky" transform fault with

either an en echelon system of ridges and transforms or an obliquely spreading segment.

5.1.5 SUMMARY OF RESULTS FROM INCIDENT ANGLES AND AZIMUTHS

The orientation of the MIT OBS can be determined to within about ±10° from the observed particle motion of water waves from shots. Incident angles and azimuths at OBS M2 from earthquake and explosive sources throughout the transform show systematic deflections from the angles expected for a laterally homogeneous velocity structure which are much larger than the uncertainty in the orientation of the components. P wave arrivals from sources to the north, west and south have incident angles of about 45° and azimuthal deflections which vary with geographic azimuth; arrivals from the east have incident angles of about 25° (measured from vertical) and azimuthal deflections greater than 90°.

Rays traced through three dimensional P wave velocity grids using a "bending" method with endpoints fixed at the source and receiver positions suggest a positive velocity gradient in the upper mantle to the west of M2. Geologically, this might correspond to a positive (downward) velocity gradient in the upper mantle and a constant thickness crust so that the Moho would follow the surface topography beneath ridge α (Fig. 2.4).

For P waves from sources in the central transform, we observe small angles of incidence (measured from vertical)

and the azimuthal deflections are so large that the P waves actually appear to arrive from the west. Low velocities in the model, simulating a magma chamber in the central transform between the sources and the receivers, bend rays down and around the low velocity zone resulting in small incident angles and large azimuthal deflections at station M2. We are not able to constrain the detailed geometry and lateral extent of the proposed low velocity body with the data available from ROSE.

The effect of this velocity structure on the hypocentral parameters and fault plane solutions determined in Chapter IV is studied by tracing rays to calculate synthetic travel time data and then relocating the events relative to the laterally homogeneous model of Chapter IV. Possible mislocations of up to 10 km and large distortions of the take off angles and azimuths are indicated. These results tentatively answer several of the questions raised in the previous chapter. In particular, the hypocenters under ridge β' may actually have been within trough B and the contradiction between calculated hypocenters near station T13 and the observed arrival time difference between P and S waves from these events at T13 may have been due to mislocation. The ray paths in the model are 8-15% longer than those expected for a laterally homogeneous model and provide an explanation for the apparent delay of S waves relative to P waves which was observed at stations M2 and M3 for sources in region 2.

5.2 SEISMIC REFRACTION DATA: SMALL SHOTS

Figure 5.16 (a-g) shows record sections of the data recorded from lines 1, 2 and 4 (Fig. 5.1) at OBH WH4, WH5, and WH6 (Fig. 4.1), and Figure 5.15, illustrates the location of these profiles. For lines 1 and 2, sources were 2.73 kg. charges of TNT; for line 4, sources were 0.82 kg. SUS charges. Shot-receiver ranges were calculated from the arrival time of the direct water wave as described by Detrick and Purdy (1980) for a regional water column sounding velocity 1.4944 km/sec. Errors in the range determination are less than 20 meters. The topography beneath the shots is shown below the record sections and the travel time through the water column has been removed from the seismograms. A range dependent amplification of $(R/R_0)^{\alpha}$ has also been applied for $R>R_0$ where R is range, R_0 = 5 km and α = 1.

Travel times were picked from traces plotted at a scale of 5 in/sec (uncorrected for topography) and could be picked to within 0.02 seconds in most cases. The smoothed apparent slowness (1/velocity) and depth beneath the shot were used to correct the travel times (T) and ranges (X) for the effect of topography using the "water path" correction method (Purdy 1982b). This correction removes the water column portion of the ray path and projects the shot point onto the seafloor. It is calculated by:

$$\Delta T = \int_0^h [c(z)\cdot(1-u^2\cdot c^2(z))]^{-1/2}dz \qquad (5.2a)$$

$$\Delta X = \int_0^h u\cdot c(z)[1-u^2\cdot c^2(z)]^{-1/2}dz \qquad (5.2b)$$

where ΔT and ΔX are the corrections to the travel time and range; h is the water depth; u is the apparent slowness; and c(z) is the P wave velocity in the water column as a function of depth. Because of the large topographic variation along most of the lines, this correction is the major source of error in the data. The appropriate depth for the correction is the depth at the ray entry point which may be several hundred meters from the point below the shot. These corrections will be discussed further with respect to individual profiles.

A spline curve was then fit to the topographically corrected data. The assumed errors on the travel time data were adjusted so that slowness decreased with range. Differences in the minimum acceptable error among the lines probably reflect variations in topographic roughness on the scale of several hundred meters.

The intercept time (τ)-slowness (p) relationship was derived from the smoothly increasing curve fit to the travel time data. Slowness at point (X_1,T_1) on the T-X curve is equal to the slope of the curve at this point; the intercept time is related to T,X and p through the equation $\tau(p) = T(p)-pX(p)$. The τ-p curve was then inverted to find velocity as a function of depth through:

$$z(p) = 1/\pi \int_0^{\tau(p)} d\tau[v^2(\tau)-p^2]^{-1/2} \qquad (5.3)$$

where v is the inverse function to $\tau(p)$ and $z(p)$ is the depth at which the velocity is $1/p$ (Johnson and Gilbert, 1972, Bessonova, 1974). The velocity in the uppermost crust, from which no arrivals are observed for surface shots, was determined as described by Ewing and Purdy (1982).

Although the propagation of seismic energy through the crust in this region is very good (noted also by Ouchi et al., 1982) and arrivals are clear out to relatively long ranges for 2.73 kg. shots, P_n arrivals are not observed and the Moho velocity and crustal thickness cannot be determined from the travel time data alone. The high amplitude region at the triplication in the travel time curve where the layer 3 refraction and the Moho refraction and wide angle reflection interfere, however, is well developed and the crustal thickness can be constrained by comparing the observations to synthetic seismograms. Seismograms were calculated for this purpose using the WKBJ method developed by Chapman (1978).

5.2.1 LINE 1-WH5-S and LINE 1-WH6-N

The travel times from line 1 to the south of WH5 (Fig. 5.16b) and line 1 to the north of WH6 (Fig. 5.16c) are shown in Figure 5.17a. For a range of 0 to 20 km, these data represent a reversed profile along ridge β in the central transform; the topography is also quite smooth along this portion of line 1. The similarity of the travel time-distance

relationships for the two profiles indicates a flat-lying, laterally homogeneous crust. The curvature of the travel time-distance curve suggests a velocity gradient rather than a stack of homogeneous layers.

The travel times in Figure 5.17a differ for ranges greater than 20 km. Both profiles also show a sharp change in topography at this range with line 1-WH5-S becoming deeper and line 1-WH6-N becoming shallower. That the apparent difference in travel time may be entirely due to errors in the topographic corrections is shown in Figure 5.18 where the corrected and uncorrected data are compared.

The τ-p curves derived from the spline curves fit to the travel time data were inverted to obtain velocity as a function of depth. These results are shown in Figure 5.19a. Approximate error bounds were determined qualitatively by perturbing the data several times and reinverting. The most important aspect of the solution is the approximately constant gradient of 0.5 $(sec)^{-1}$ throughout most of the crust. The surface velocity and gradient in the upper kilometer of the crust is poorly determined and may vary along the line. As previously mentioned, the crustal thickness and Moho velocity cannot be constrained by the travel time data alone and the velocity-depth profiles in Figure 5.19a will serve as initial crustal models for the synthetic seismogram calculations of Chapter 5.2.4.

A second arrival can be observed on line 1-WH5-S (Figure 5.16b). This arrival is not observed on the other profiles and probably represents energy traveling as S in the crust.

Spudich (1979) and White and Stephen (1981) have discussed the conditions required for efficient P to S conversion in oceanic crust and have concluded that most conversion must take place at the sediment-basement or water-basement interface and that conversion efficiency is enhanced by an interface that is sharp relative to a shear wavelength (a few hundred meters). The observation of this arrival on line 1-WH5-S but not on the other lines probably reflects variability in the basement-water interface. The travel time of this arrival is appropriate for an S wave converted from P at the seafloor. The corresponding velocity-depth profile is also shown in Figure 5.19a; a continuous gradient of 0.28 to 0.3 sec^{-1} is observed. Because of the lack of data at ranges less than 10 km, the upper crustal velocity, and consequently the depth to an observed velocity, is poorly determined, and we cannot constrain the the Poisson's ratio of the crust. The observed gradient is consistant with a Poisson's ratio of 0.22 to 0.27.

5.2.2 LINE 1-WH6-S, LINE 2-WH4-S, LINE 4-WH4-W

Figure 5.17b shows the travel times along line 1 to the south of WH6 (Fig. 5.16d), line 2 to the south of WH4 (Fig. 5.16e), and line 4 to the west of WH4 (Fig. 5.16f). These three lines are on topographically "normal" crust of age 0.8 my, 1.5 my and 2 my, respectively. Lines 1-WH6-S and 2-WH4-S are oriented parallel to the spreading center and line 4-WH4-W is perpendicular to the spreading center. The travel time-distance relationships are similar for the three

profiles. Although differences among the three lines might reflect changes in the crustal structure with age, these differences may also reflect errors in the topographic corrections. For example, the travel time-distance data along line 1-WH6-S and line 2-WH4-S can be fit by a smooth spline curve with slowness decreasing with increasing range for an assumed travel time error of 0.015 seconds whereas observed oscillations in the data for line 4-WH4-W require an assumed error of 0.025 seconds. The oscillations along line 4 may result from the fact that the topography is strongly lineated parallel to the spreading axis and appears as a series of steps spaced approximately 1-2 km apart along profiles perpendicular to the spreading axis (Fig. 2.6).

The travel times along these three profiles are significantly different from those in Figure 5.17a and resemble those typically observed for oceanic crust. Figure 5.19b shows the corresponding velocity depth functions. Although the gradient and thickness of the upper layer are poorly constrained, the range of values is typical for oceanic layer 2. A thick layer with a nearly constant velocity of about 6.8 km/sec is well resolved for all three profiles. The increase in the velocity at the base of this layer is at least partly an artifact of the smoothing induced by fitting a continuous spline curve rather than straight line segments to the data. Again, the crustal thickness cannot be resolved from the travel time data alone and will be examined in section 5.2.4.

5.2.3 LINE 1-WH5-N AND LINE 2-WH4-N

Line 1-WH5-N (Fig. 5.16a) crosses the seismically active east-west trough in the central transform and might be useful for discriminating between a transform and a spreading environment. Unfortunately, the topography along the line precludes any serious interpretation of the travel time data. Figure 5.20 shows the corrected and uncorrected travel time data. The corrected data define an apparent velocity of approximately 6 km/sec at a depth of 1 to 3 km, assuming an error of 0.03 seconds on the travel time data. Whether or not shots over the trough are delayed during their passage through the crust cannot be resolved, given the error on the appropriate depth for the topographic correction. The amplitude variation, moreover, might be due to the focussing and defocussing effect of topography (Purdy, 1982b) as well as to attenuation within the crust.

Line 2 to the north of WH4 (Fig. 5.16g) follows the crest of the topographic ridge under which the "high velocities" were inferred in the first part of this chapter. The absence of shots at ranges less than 10 km and the topographic variation along this line, however, also do not permit a structural interpretation. Figure 5.21 shows the travel times both uncorrected and corrected for the depth below the shot. The corrected time-distance curve does not correspond to any laterally homogeneous velocity model. Comparing the topography along the shot line to the regional bathymetry shown in Figure 5.1, one notes that the shot line

seems to have drifted on and off of the crest of the topographic ridge, and the appropriate depth for the topographic correction might be along the crest. Corrections made assuming two different profiles for the ridge are also shown in Figure 5.21. Profile A results in the smoothest travel time-distance curve and indicates an apparent velocity of approximately 6 km/sec assuming an error on the travel times of 0.03 seconds. Given the uncertainty in the correction, however, not much significance is attributed to this observation.

It should be noted here that Ouchi et al. (1982) have published an interpretation of this line as recorded on instruments T10 and T5. At T5, they observe an apparent velocity of 7.0 km/sec for a range of 13 to 29 km. At T10, which was on the shot line, they found a 0.75 km thick layer with a velocity of 4.4 km/sec, 1.8 km with a velocity of 5.5 km/sec, 3.7 km with a velocity of 6.9 km/sec and a Moho velocity of 7.8 km/sec from a classic slope-intercept analysis (e.g. Ewing, 1963). A similar structure was observed along this line to the south of T10, although the Moho depth and layer 3 thickness were not determined. They do not however, discuss how topographic corrections were applied.

5.2.4 SYNTHETIC SEISMOGRAMS

In the record sections in Figure 5.16, an increase in amplitude resulting from interference between the crustal refraction and the Moho refraction and wide angle reflection at the triplication in the travel time curve is seen clearly on most of the profiles. On line 1-WH5-S and line 1-WH6-N (Figs. 5.16b and c), the maximum amplitude is observed for a range of approximately 22 to 25 km; for line 1-WH6-S, line 2-WH4-S and line 4-WH4-W, (Fig. 5.16d,e,f), the maximum amplitude occurs near 30 km range. The amplitude patterns, moreover, can be related to the two different types of crustal structure shown in Figure 5.19. The structures in Figures 5.19a and 5.19b will subsequently be referred to as Crust A and Crust B, respectively.

For the profiles indicating Crust B, the Moho reflection can be seen as a second arrival for ranges of 24 to 30 km and the amplitudes of arrivals from the 6.8 km/sec layer are very small, as expected for arrivals from a homogeneous layer. On line 1-WH6-S, large amplitudes are observed for ranges less than 12 km, supporting the interpretation of a strong velocity gradient in the upper crust. Variability in the amplitudes for shots along line 4-WH4-W at close ranges is probably due to the rough topography.

In contrast to the amplitude pattern described above, no second arrival corresponding to a Moho reflection can be observed on line 1-WH5-S and line 1-WH6-N; moreover, the amplitude of crustal arrivals is relatively large at all

ranges, supporting the interpretation from the travel times of a continuous gradient through the crust. For both sets of profiles, the arrival interpreted to be the wide angle reflection from the Moho is well developed, indicating that the Moho exists as relatively a sharp boundary beneath both types of crust.

To quantify these observations and constrain the crustal thickness, synthetic seismograms were calculated by the WKBJ method developed by Chapman (1978) and implemented at WHOI by R. Stephen (personal communication, 1981) for velocity models derived from the results in Figure 5.19. The main advantage of the WKBJ method is that the computation is very rapid because integration over both ray parameter and frequency is performed analytically. The disadvantage is that the method is not exact and the WKBJ approximation breaks down in the vicinity of turning points. Chapman (1978) has modified the method to include head waves, but the complexities of "interface head waves" and "whispering gallery" phases are not modelled. For waves propagating along discontinuities in the earth, such effects are important and the WKBJ method is therefore not appropriate for modelling the detailed structure of the Moho transition zone.

In this study our objective was to examine the gross effect of the crustal thickness and velocity gradient on the arrivals which interfere at the triplication point in the travel time curve. No attempt was made to model waveforms exactly. In the models presented here, the Moho transition

zone was represented by a velocity gradient which was the same for all models. The source pulse was defined by:

$$S(t) = \cos(2\pi ft)\exp[-((2\pi ft)/\gamma)^2] \qquad (5.4)$$

where f = 10 Hz and γ = 5. The amplitudes in the plotted recorded sections were normalized and amplified with range to correspond to the record sections of observed data.

Seismograms calculated for three models compatible with Crust A are shown in Figure 5.22a. The corresponding velocity-depth profiles are shown in Figure 5.22b and the predicted travel times compared to the data in Figure 5.22c. Model C, which includes a decrease in the velocity gradient at the base of the crust and has a total crustal thickness of 5.4 km, best reproduces the major features of the data Fig. 5.21d). The decrease in gradient at the base of the crust is required to simultaneously match the travel times and the range at which the maximum amplitude is observed. The appearance of a prominent phase representing a wide angle reflection from the Moho also requires a low gradient just above the Moho. This decrease in gradient causes a small triplication point at a range of approximately 16 km resulting in an increased amplitudes. Such an increase can be observed along line 1-WH6-N at about 14 to 15 km range and, less clearly, on line 1-WH5-S from about 14 to 18 km. That no P_n arrival is observed in the data beyond the triplication point may be related to both the small shot size and to the nature of the Moho transition zone which we cannot

model accurately with this method.

The crustal structure under the northern part of line 2 cannot be determined from the travel times because of uncertainties in the appropriate depth to use for topographic corrections. Assuming the structure under the northern part of line 1 and increasing the thickness of the basal layer, a total crustal thickness of about 5.8 km is required to match the range at which the Moho triplication is observed. This estimate is very uncertain, however, because the amplitudes may also be significantly affected by the topographic roughness with a wavelength of a few hundred meters along the line.

Seismograms calculated for models compatible with Crust B are shown in Figure 5.23a and the corresponding velocity-depth profiles and travel times are shown in Figures 5.23b and 5.23c, respectively. Profiles A and B demonstrate that we cannot resolve the gradient and thickness of the upper layer, given the apparent errors on travel times from line 4-WH4-W. A crustal thickness of about 6 km is required to fit the observed range for the triplication point (Model C). We see, moreover, the pronounced effect of the thick, nearly homogeneous layer on the amplitudes in the range of 15 to 25 km. The Moho reflection can be seen as a second arrival in both the synthetic and the real data from 25 to 30 km range, and the wide angle reflection is prominent at ranges beyond 30 km. On line 4-WH4-S, the "first" arrivals picked for ranges greater than 30 km probably represent the

wide angle reflection; along line 1-WH4-W, P_n arrivals may possibly be observed. Differences in the relative amplitude of the Moho reflection and refraction corresponding to paths perpendicular and parallel to the spreading direction have also been observed by G. M. Purdy (personal communication, 1981) from the ROSE I data. Further examination of this question is beyond the scope of this study.

5.2.5 SUMMARY OF RESULTS FROM SMALL SHOTS

The velocity structure of the crust beneath ridges α and β in the central transform zone (Fig. 2.4) is anomalous, showing a fairly constant P wave velocity gradient of about 0.5 $(sec)^{-1}$ and an S wave velocity gradient of about 0.29 $(sec)^{-1}$ throughout most of the crust (lines 1-WH5-S and WH6-N). The value of a steeper gradient in the top few hundred meters is poorly resolved. A 1.4 km thick layer with a velocity of about 7.1 km/sec is required at the base of the crust in order to simultaneously fit both the travel time and amplitude data and the total crustal thickness along line 1 between WH5 and WH6 is about 5.4 km.

Lines 1-WH6-S, 2-WH4-S and 4-WH4-W all reveal the two layer crustal structure commonly found throughout the world's oceans: a 1.5 km thick layer with a gradient of about 2.5 sec^{-1} overlying a 4.5 thick layer with a low gradient of 0.1 to 0.2 sec^{-1} and a velocity of about 6.9 km/sec. The range at which the amplitude signature of the Moho triplication point is observed constrains the crustal thickness to be approximately 6 km. Differences in the amplitudes for

crustal arrivals also support the differences in crustal structure obtained from inversion of the travel times.

The upper mantle velocity can not be determined from this dataset. Clear arrivals interpreted to be wide angle reflections from the Moho, however, indicate that it exists beneath both types of crust as a sharp interface on the scale of a seismic wavelength.

5.3 LARGE SHOTS

Travel times from the large shots (Fig. 5.1 and Table 5.1) to the MIT and WHOI instruments were also examined in the hope of determining the upper mantle velocity and further constraining the crustal structure. The shots were also "relocated" using HYPOINVERSE and the velocity structure of Table 4.3 to obtain additional information for evaluating the effect of lateral heterogeneities on the earthquake locations.

5.3.1 TRAVEL TIMES

The travel times observed at MIT and WHOI instruments are plotted against range in Figure 5.24a. When the water wave arrival time could be picked, the ranges were calculated from the water wave travel time assuming a P wave velocity in water of 1.5 km/sec. For a few shots, indicated by crosses in Figure 5.20a, the range was determined from the navigation. In general, ranges determined from the water wave travel time are one or two kilometers less than those

determined from the navigation and show less scatter in Figure 5.24.

Corrections were applied to the travel times to normalize all stations and shots to a depth of 3 km. Topographic corrections under the shot points were calculated by the method of Whitmarsh (1975) for an assumed crustal velocity of 5.0 km/sec:

$$\frac{\Delta T}{\Delta h} = [(1-V_0^2p^2)^{1/2}/V_0]-[(1-V_c^2p^2)^{1/2}/V_c] \qquad (5.5)$$

where V_0 is the water column sounding velocity, V_c is the crustal velocity, p is the slowness, and Δh is the difference between the depth below the shot and the normalization depth. This method assumes that all topography is in the top "layer" and that underlying refractors are horizontal. Because it is less sensitive than the "water path" correction to errors in p, it is more appropriate for sparse data (Purdy, 1982b). Phase velocities (1/p) of 6.8 km/sec and 8 km/sec were assumed for ranges less than and greater than 30 km, respectively. The error induced by errors in the assumed crustal and phase velocities have been discussed by Purdy (1982b) and are on the order of a few hundredths of a second. More serious sources of error are the uncertainty in the depth of the ray entry point and the assumption inherent in the correction that the topography is entirely due to variations in the thickness of the upper crust. From the results in section 5.2, we have seen that this assumption is certainly not valid.

To determine whether some of the scatter in Figure 5.24a might be due to structural variations which could potentially be localized to either the shot or station regions, the data were separated into groups of neighboring stations (Fig. 5.24b-e) and the average travel time to all stations from individual shots with ranges greater than 30 km (calculated from water wave arrivals) were plotted (Fig. 5.25). Although the differences are within the errors, shots 3425, 3436, 3438, 3441 and 3442 are delayed by 0.1 to 0.4 seconds relative to most of the shots. The data are too sparse to quantify the extent of the velocity anomalies responsible for these delays. We can, however, make a few general inferences. Shots 3436 and 3438 cross presently inactive and active parts of the northern east-west trending transform trough and shot 3442 is within the central transform region. Shot 3441 passes through the southern branch of the East Pacific Rise but is only slightly delayed along paths to the west (Fig. 5.25b and c); for paths crossing the central transform trough (Fig. 5.25d), the delay is larger. These observations suggest the presence of low velocity material within the transform troughs. The anomaly can be localized to the region between the shot and the closest station because the delay from these shots (travel times plotted as open circles in Figure 5.24) is approximately constant with range. Paths from 3425 do not uniquely cross any obvious topographic features, but again the anomaly must be local

since similar paths from 3426, 3428, and 3429 do not consistently show this delay.

Returning to figure 5.24 and ignoring data from shots 3425, 3426, 3438, 3441 and 3442 and from shot-receiver pairs for which range cannot be determined from the water wave, apparent velocities and intercept times were calculated and are shown in Table 5.5. Because the Moho triplication point is observed for ranges of about 25 to 30 km in section 5.2, the data were arbitrarily divided into two groups with ranges less than and greater than 30 km. When all data are combined, the results are typical of oceanic crust throughout the world (eg. Trehu et al., 1976): a crustal layer with a velocity of 6.9 km/sec and an intercept time of 0.4 seconds and an upper mantle velocity of 8 km/sec with an intercept time of 1.0 seconds. Comparing the results from individual groups of stations, an upper mantle velocity of 8.00 to 8.13 km/sec is determined for all groups and differences among the intercept times are observed. The longest intercept time is for stations WH2, WH3, WH8 and WH4', located on "normal" oceanic crust as defined by figure 5.23-model C; the shortest intercept times are observed for M2, M3, W1 and W7. This supports the inference from sections 5.1 and 5.2 that the shallow crust of ridges α and β is at least no thicker and may be thinner than the "normal" oceanic crust in the region. The relatively high upper mantle velocity, moreover argues against a thermal origin for the topography. Possible upper

mantle P wave velocity anisotropy (Raitt et al., 1969) cannot be resolved from this data set.

5.3.2 RELOCATIONS

In order to test whether the velocity model assumed in Chapter IV was biasing the locations, travel times from the shots to the MIT and WHOI instruments were used to "locate" the shots relative to this model. In Figure 5.26, the structure from Chapter IV is compared to the two models found in section 5.2 and we see that it represents a compromise between the two models. The upper mantle velocity of 7.8 km/sec, however, is lower than that indicated by the large shots. Tests discussed in Chapter IV demonstrate that an increase in the upper mantle velocity to 8 km/sec does not significantly bias the hypocenters (Fig. 4.6c) and we would expect the calculated origin times to be early by a few tenths of a second.

For the "locations" of the shots depth was fixed at 0.05 km and the data were inverted to obtain origin time and "epicenter." The results are shown in Figure 5.27 and Table 5.6. Most of the shots are "located" at their true source to within the 95% confidence ellipse of the solution. Generally "early" origin times support the conclusion that the 7.8 km/sec upper mantle velocity is too low. Exceptions are shots 3425, 3441 and 3442. Shots 3425 and 3441 are well outside of the array and, moreover, are not in a region from which earthquakes were detected. Shot 3442, however, was within the central transform and shows a direction of mislocation

similar to those discussed in 5.1.4. "Locations" of shots near the northern transform trough (3434, 3437, and 3438) have large latitude uncertainties because of the station distribution for this data set, but do not show any systematic bias.

The station distribution does not provide adequate depth resolution for many of the shots and the depth remains near the initial depth when it is a free parameter in the damped inversion. For those shots for which depth can be resolved, the solution converges to a very shallow depth in all cases for initial depths of 0.05 and 5.0 km.

In Figure 5.28, the residuals at individual stations are plotted as a function of azimuth and compared to the residuals from earthquakes in region 1 and region 2 (Table 4.6). In general, the residuals from the two datasets agree. The wide azimuthal distribution of the shots clearly shows the effect of possible errors in instrument coordinates and confirms the suspicion that a formal inversion to jointly determine velocity and hypocenters (Thurber, 1981) would not provide additional information because of errors in the data.

5.3.3 SUMMARY OF RESULTS FROM LARGE SHOTS

Arrival times from shots with paths which cross troughs A and B (Fig. 2.4) appear to be delayed by 0.1 to 0.4 seconds compared to most of the shots. When these shots are removed from the data set and data from all MIT and WHOI instruments is combined, a velocity of 6.9 km/sec with an intercept time

of 0.4 seconds and a velocity of 8.0 km/sec with an intercept time of 1.0 seconds are obtained for ranges less than and greater than 30 km, respectively. These values are typical of oceanic crust throughout the oceans. For different station groups on topographically distinct structures, upper mantle velocities of 8.00-8.13 km/sec are determined and small differences are observed in the intercept times. The largest intercept time is for stations located on the local "normal" oceanic crust as defined by Figure 5.19b and the smallest intercept time is for stations on the eastern flank of ridge α.

Relocating the shots with HYPOINVERSE and the velocity model of Table 4.3 indicates that the assumed model does not significantly bias the locations throughout most of the transform zone. Systematically early origin times support the conclusion that the 7.8 km/sec upper mantle velocity in Table 4.3 is too low. Shot 3442, located in trough B in the central transform, shows a mislocation similar to those obtained from synthetic data in section 5.1.4. Station residuals from these "locations" support the conclusion in Chapter IV that the geographic coordinates of the stations may be in error by as much as a kilometer.

5.4 SUMMARY

Several independent data sets provide information on the crustal structure in the transform region of the Orozco Fracture Zone. The results have been summarized in sections

5.1.5, 5.2.5 and 5.3.3. These results, if not directly supportive of each other, are at least mutually consistent. Two distinct crustal types which are associated with topographic features can be distinguished (section 5.2). On relatively smooth crust characteristic of that formed at fast spreading ridges, a structure typical of oceanic crust is determined from 3 different, unreversed profiles. A 1.5 km thick layer in which the velocity increases from 3 to 6.7 km/sec overlies a 4.5 km thick layer with a low gradient of about 0.1 sec^{-1}. No differences between crust of ages from 0.8 to 2 m.y. can be resolved.

In the central part of the transform, the shallow, north-south trending ridges (ridges α and β in Figure 2.4) appear to be constructed from anomalous crust. A reversed refraction profile along ridge β indicates a velocity gradient of 0.5 sec^{-1} throughout most of the crust (from 5.25 km/sec to 7.15 km/sec over 3.5 km). This gradient decreases to about 0.1 $(sec)^{-1}$ at the base of the crust. A thin (~800m) high gradient layer in the upper few hundred meters must exist to satisfy the travel time data. The total crustal thickness is about 5.4 km. Although the crustal thickness under ridge α cannot be determined directly because of large uncertainties in the topographic corrections, the results of the ray tracing analysis and the intercept times from large shots and receivers on the ridge also suggest a thin crust. Speculations on the geologic implications of these observations are reserved for the next chapter.

The upper mantle velocity, determined from large shots at ranges from 30 to 100 km (section 5.3.1) is 8.00 to 8.13 km/sec throughout most of the region; no difference is observed between the velocity beneath the two types of crust. That the Moho exists as a well-defined velocity contrast with respect to a wavelength of about 1 km is indicated by the large amplitude of the wide angle reflection observed on the refraction profiles (section 5.2.4).

Incident angles and azimuths observed at station M2 from sources in the central transform suggest the presence of a low velocity zone, perhaps a magma chamber, at the western end of trough B (section 5.1.3). That the presence of such a body provides an explanation for several of the questions raised in Chapter IV about earthquake locations and fault plane solutions from region 2 is circumstantial evidence supporting this possibly controversial interpretation. The detailed geometry and lateral extent of the proposed body cannot be resolved by the data currently available.

The crustal structure in the northern transform trough, where the earthquake epicenters and bathymetry clearly delineate the active transform fault, cannot be determined from the data presented in this chapter. Waveforms from earthquakes along the trough (Chapter IV), however, suggest that near the intersection of the transform with the East Pacific Rise (near 105°12'W), the Moho may be shallower than about 3 or 4 km. Further to the east (near 105°7'W), the Moho exists within the transform at a depth of several km.

In the next chapter, this information on the crustal structure of the transform zone will be combined with the results of Chapters II and IV in an attempt to deduce the present tectonic regime of the Orozco transform fault.

TABLE 5.1 Large Shots During ROSE II

Shot no.	time					latitude		longitude		depth	shot size	bubble pulse period
	m	d	hr	min	sec	deg	min	deg	min	m	kg	sec
3425	3	4	17	20	37.66	14	33.9	104	46.0	3161	218	.250
3426	3	4	20	15	1.84	14	50.3	104	43.4	2683	218	.240
3427	3	4	22	15	38.59	15	2.3	104	44.2	2303	218	.245
3428	3	5	1	14	17.12	14	49.4	104	57.6	3144	218	.240
3429	3	5	3	19	19.72	14	38.4	105	0.3	3233	218	.250
3430	3	5	15	44	11.23	14	31.3	105	15.1	3214	218	.250
3431	3	5	19	21	1.38	14	50.2	105	23.2	3195	218	.245
3432	3	6	22	46	58.76	15	3.5	105	9.1	2846	218	.245
3433	3	6	1	26	46.09	15	10.3	104	55.2	2762	218	.245
3434	3	6	3	25	54.18	15	18.4	104	58.3	2655	218	.240
3435	3	6	15	44	10.75	15	5.4	105	26.1	3225	218	.245
3436	3	6	18	26	1.62	15	21.0	105	29.4	2841	218	.250
3437	3	6	21	37	26.77	15	19.2	105	8.1	6227	218	.245
3438	3	6	23	37	52.22	15	29.6	105	5.8	2711	218	.245
3440	3	7	17	20	4.33	14	53.5	103	58.4	3107	907	.400
3441	3	7	20	12	16.49	14	55.8	104	21.5	2901	907	.410
3442	3	7	22	45	3.91	15	9.9	104	34.2	2978	218	.260

TABLE 5.2a Incidence Angles and Azimuths of P Waves

Observed at M2

Origin time (d-hr-min) shot no.	distance (km)	azimuth OBS to source	azimuth source to OBS	P waves a*	b**	c***
02-05-23	28	52	232	27	100-104	-(128-132)
02-17-21	44	319	139	39-44	115-119	-(20-24)
03-17-24	47	318	138	39-44	109-113	-(25-29)
04-09-19	21	53	233	22	80-95	-(139-153)
04-09-42	22	53	233	23-30	99-103	-(130-134)
05-02-19	21	48	228	28	105-109	-(119-123)
05-00-58	22	49	229	28	99-105	-(124-130)
08-12-14	39	330	150	35-41	117-121	-(29-33)
08-12-19	39	332	152	41-45	109-113	-(39-43)
08-12-38	39	331	151	37-45	116-120	-(31-35)
12-11-01	22	60	240	17	37-57	+(157-177)
3426	34	141	321	33	34-40	+(73-79)
3427	20	107	287	19	77-81	+(150-154)
3428	30	185	5	40-45	44-48	+(39-43)
3432	26	259	79	45-50	77-81	-2-+2
3433	7	12	192	45-50	129-133	-(59-63)
3439	23	351	171	40-42	123-127	-(44-48)
3437	35	320	140	43-45	106-110	-(30-34)

*a - incidence angle, in degrees, measured from vertical

**b - azimuth, in degrees, measured clockwise from north, assuming positive Y axis oriented 57°NE

***c - deflection, in degrees; from azimuth expected for a laterally homogeneous structure

TABLE 5.2b Incidence Angles and Azimuths of S Waves Observed at M2

Origin time (d-hr-min) shot no.	distance (km)	azimuth OBS to source	azimuth source to OBS	S waves a	b	c
02-05-23	28	52	232	78-85	142-162	-(70-90)
02-17-21	44	319	139	82	113	-26
03-17-24	47	318	138	82	118-128	-(10-20)
03-23-12	15	56	236	90	186-201	-(35-50)
04-18-56	38	349	169	75-85	139	-30
05-02-19	21	48	228	80	139-159	-(70-90)
05-00-58	22	49	229	80-85	159-164	-(65-70)
08-12-14	39	330	150	82	130-140	-(10-20)
08-12-19	39	332	152	90	132-142	-(10-20)
08-12-38	39	331	151	82	131-150	-(0-20)
08-14-52	40	332	152	75-80	127-132	-(20-25)
12-11-01	22	60	240	72	212	-28
13-18-49	28	80	260	77	200-222	-(38-60)

*a - incidence angle, in degrees, measured from vertical

**b - azimuth, in degrees, measured clockwise from north, assuming positive Y axis oriented 57°NE

***c - deflection, in degrees; from azimuth expected for a laterally homogeneous structure

TABLE 5.3 Deflections of the Incidence Angle and Azimuth For the Model of Figure 5.11

Number on Figure 5.10	Source	incidence azimuth		incidence angle	
		model	observed	model	observed
1	3428	+14	+(39-43)	43	40-45
2	3432	-2	-2-+2	48	45-50
3	3437	-10	-(30-34)	48	43-45
4	A*	-10	-(20-29)	47	39-45
5	B**	-14	-(29-43)	46	35-45
6	3434	-19	-(44-48)	46	40-42
7	3426	+16	+(73-78)	32	33
8	3427	+42	+(150-154)	31	19
9		+30		17	
10		+27		17	
11	March 11,11h01m	+22	+(157-177)	18	17
12		-35		22	
13	C***	-24	-(119-153)	18	22-30
14	March 2,05h23m	-44	-(128-132)	18	27

*A - March 2, 17h21m and March 3, 17h24m

**B - March 8, 12h14m, 12h19m and 12h38m

***C - March 4, 09h19m and 09h42m; March 5 02h19m; March 8, 00h58m

TABLE 5.4 Effect of the Model in Figure 5.10

on Hypocenter Determinations*

Event No.	Source Coordinates (km)			"location" calculated with HYPOINVERSE* coordinates (km)			origin time (sec)	nor	dcs	mag	rms	erh	erz
	X	Y	Z	X	Y	Z							
1	56	81	8	50.1	85.7	17.3	-0.04	11	17.6	182	0.16	0.9	2.3
2	50	78	8	46/6	65.4	13.9	0.85	9	12.3	154	0.16	1.2	2.5
3	54	74	8	50.4	69.2	5.4	0.85	8	13.0	162	0.17	1.0	2.6
4	46	74	8	41.4	73.3	3.7	0.52	9	14.0	178	0.43	1.1	pdc
5	61	77	8	58.7	76.0	12.3	0.68	8	7.8	170	0.09	1.3	2.1
6	85	105.5	6	84.6	106.1	4.6	0.19	9	5.1	153	0.09	1.1	1.5

*Although the hypocentral coordinates are given in kilometers corresponding to the grid of Fig. 5.11, for calculations with HYPOINVERSE station and source coordinates were given as latitude minutes = Y/2, longitude (minutes) = X/2 and depth = Z. The origin time is given relative to a "true" origin time of 0. The other parameters are as described in Table 4.5.

TABLE 5.5 Slope and Intercept for Travel Times of Large Shots. Only shots for which range was calculated from water wave travel times are included. Shots 3425, 3436, 3438, 3441 and 3442 not included.

a. Range less than 30 km

data set	no. of readings	slope	intercept	velocity
all	20	0.145±0.007	0.414±0.146	6.90±0.34
W2, W3, W4, W8	4	0.174±0.034	-0.231±0.828	5.75±1.17
W5, W6	5	0.148±0.023	0.479±0.538	6.76±1.20
M2, M3, W1, W7	11	0.139±0.007	0.473±0.140	7.19±0.37

b. Range greater than 30 km

data set	no. of readings	slope	intercept	velocity
all	49	0.125±0.001	1.000±0.104	8.00±0.06
W2, W3, W4, W8	19	0.123±0.002	1.233±0.118	8.13±0.13
W5, W6	14	0.123±0.002	1.129±0.130	8.13±0.13
M2, M3, W1, W7	16	0.129±0.002	0.747±0.126	7.75±0.12
W1, W7	9	0.125±0.002	1.083±0.134	8.00±0.13
M2, M3	7	0.123±0.006	0.869±0.236	8.13±0.40

TABLE 5.6 Relocations of Large Shots Relative to the Velocity Structure of Chapter IV.

Depth fixed at 0.05 km for all events.

shot number	origin time*		sec	latitude		longitude		nor	mag	dcs	rms	erh**
3425	23	59	59.82	14	33.16	104	45.40	7	281	32.3	0.31	6.3
3426	23	59	59.89	14	50.87	104	43.50	9	258	20.7	0.11	4.3
3427	0	0	0.07	15	2.64	104	45.23	10	192	1.4	0.11	1.2
3428	23	59	59.85	14	49.48	104	57.24	9	159	20.9	0.07	1.0
3429	23	59	59.82	14	38.44	104	59.61	8	228	29.1	0.08	2.2
3430	23	59	59.73	14	30.33	105	14.95	8	285	18.6	0.04	4.1
3431	23	59	59.88	14	49.91	105	22.05	8	141	1.0	0.11	0.9
3432	23	59	59.98	15	3.28	105	8.64	9	168	16.8	0.10	1.1
3433	23	59	59.99	15	9.71	104	55.56	9	127	7.8	0.13	0.7
3434	23	59	59.82	15	18.46	104	58.22	9	277	10.4	0.11	3.7
3435	23	59	59.57	15	5.95	105	27.66	7	272	22.9	0.10	3.2
3437	23	59	59.83	15	18.87	105	8.63	8	265	26.4	0.07	4.7
3438	0	0	0.12	15	29.24	105	6.61	7	300	35.3	0.11	1.1
3441	0	0	0.86	15	0.53	104	21.36	6	313	42.2	0.31	1.7
3442	23	59	59.16	15	12.10	104	29.59	8	299	33.2	0.15	8.0

* Origin time of 0h0m0sec corresponds to the true shot time

** See Table 4.5 for explanation of column headings

FIGURE CAPTIONS

5.1 Location of refraction shots during ROSE II. The lines represent small charges spaced approximately 1 km apart; the dots represent large shots (Table 5.1). Topography is from Mammerickx (1980).

5.2 Orientation of OBS M1, deployed during ROSE I. The seismograms show the water wave recorded on the three components of the OBS. The insert shows the orientation and polarity of the horizontal components as determined from a visual examination of the relative amplitudes and polarities on the two horizontal components.

5.3 Examples of particle motions of water waves observed on OBS M2. The Z axis is positive upwards. Records were high-pass filtered with a cutoff frequency of 10 Hz before calculating particle motions. The heavy line emphasizes the first cycle of motion. A total of 0.15 seconds is shown.

5.4 Apparent azimuth of the Y axis relative to north as a function of azimuth from the OBS to the shot. The mean orientation is indicated by a straight line.

5.5 Examples of effects which might bias the determination of the orientation of horizontal components obtained from observations of water waves. Examples were calculated for a true azimuth of 0° for the Y axis. The difference between the apparent azimuth and the true azimuth is plotted as a function of azimuth from the OBS to the source. The situations modeled are:

a. a mislocation of the OBS with the true location being 1 km to the north of that assumed. The effect is calculated for source-receiver ranges (relative to the assumed OBS location) of 10 and 20 km.

b. a tilt of the X component 5° to the west. The effect is calculated for incident angles of 80° and 45°, measured from the upward vertical.

c. a systematic amplification of the X component relative to the Y component of 110% and 150%.

5.6 Particle motion of the first cycle of body waves from earthquakes and shots observed at instrument M2. Incidence angles and azimuths were measured from these plots. Records were low pass filtered with a cutoff frequency of 10 Hz before calculating particle motions. The heavy line emphasizes the first cycle of motion. A total of approximately 0.5 seconds is shown. The horizontal components have been rotated to the radial (R) and transverse (T) directions.

a. P waves

b. S waves

5.7 Particle motions of P waves observed at M3 (see figure caption 5.6). Horizontal components have not been rotated.

5.8 Incident angles and azimuths of P waves observed at OBS M2. The arrows represent the apparent azimuth of propagation as seen at M2, assuming an orientation for H1 of 57°NE. The number represents the observed incidence angle, in degrees, measured from the downward vertical. The straight line at the shots shows the straight line azimuth from source to receiver and the dashed line shows the difference between the orientation of Y determined from the water wave from that particular shot and the average orientation. The amplitude of the azimuthal deflection of the P wave is much larger than the scatter in the orientation determined from the water waves. The 3000 m contour from the Mammerickx (1980) map of the Orozco Fracture Zone is shown for geographic reference.

5.9 Effect of 5° westward tilt of the geophones on the apparent incident angle and azimuth. Curves are shown for incident angles of 5°, 20° and 45°, measured from vertical and an incident azimuth towards the west.

5.10 Apparent vs. true incident angle for P waves as a function of the P wave velocity, Poisson's ratio and density beneath the OBS.

5.11 Model for tracing rays to match the observed incident angles and azimuths at M2.

a. Horizontal distribution of the grid. Longitude 105°W, latitude 15°N and the 3000m contour from the Mammerickx (1980) map are shown for reference. The star represents the position of OBS M2 and the circles represent the position of source points. The open circles are the source position projected to a depth of 6 km. The shaded areas delimit the zones of lateral velocity gradients and the letters show the position of the velocity-depth profiles in Figure 5.11c.

b. Values of P-wave velocity at the grid points.

c. Velocity-depth profiles at points A,B,C and D marked on Figure 5.11a.

5.12 Schematic illustration of a structure which could result in apparent azimuthal deflections of more than 90°.

5.13 Effect of the velocity model of Figure 5.11 on earthquake locations. The numbers identify source locations. The "true" and "apparent" hypocentral parameters are given in Table 5.4. For further explanation, see the text of figure caption 5.11a.

5.14 a. Effect of the velocity model of Figure 5.11 on the takeoff angles and azimuths for sources in region 2. Events 1, 3 and 5 from Figure 5.13 and Table 5.4 are shown. The "true" takeoff angles are plotted on the lower hemisphere of the focal sphere for all events; the "apparent" angles for events 1 and 3 are plotted on the upper hemisphere.

b. Examples of "true" (a,b,c) and "apparent" (a',b',c') fault plane solutions from event 1. Compare to the fault plane solutions in Figure 4.22.

5.15 Location of the refraction profiles analyzed in this chapter. The nomenclature used to refer to these profiles is shown.

5.16 Record sections discussed in this chapter. Travel times in this, and in all subsequent travel time-range plots, have been reduced by $\Delta/(8.0$ km/sec), where Δ is range (km). Travel times have been corrected for topography and a range dependent amplification has been applied (see text).

a. Line 1-WH5-N
b. Line 1-WH5-S
c. Line 1-WH6-N
d. Line 1-WH6-S
e. Line 2-WH4-S
f. Line 4-WH4-W
g. Line 2-WH4-N

5.17 P-wave travel time-distance data for refraction lines from ROSE II. The data have been corrected for topography as described in the text.

a) Line 1-WH5-S and Line 1-WH6-N

b) Line 1-WH6-S, Line 2-WH4-S and Line 4-WH4-W

5.18 Travel times uncorrected for topography for lines shown in Figure 5.17a. For ranges less than 20 km, the shape of the T-X curve is not affected by the correction. The effect for ranges greater than 20 km is shown by the arrows.

5.19 Velocity-depth profiles derived from the travel time data in Figure 5.17a.

5.20 a) Corrected and uncorrected travel time data for line 1-WH5-N. The label in parentheses on the time axis corresponds to the uncorrected travel times.

b) Corresponding P-wave velocity-depth profile.

5.21 Corrected and uncorrected travel time data for line 2-WH4-N. The effect of modifying the topographic profile used for the correction is illustrated. The data corrected using the depth beneath the shot and two alternate models (A and B) are shown.

5.22 Figure 5.22a shows synthetic seismograms calculated for the velocity models of Figure 5.22b in order to model the amplitude-range pattern observed on line 1-WH5-S and line 1-WH6-N. Figure 5.22c shows the corresponding travel time curves compared to the data. See text for further discussion.

5.23 Same as Figure 5.22 for line 1-WH6-S, line 2-WH4-S, and line 4-WH4-W.

5.24 Travel time-distance data for the large shots recorded during ROSE II at WHOI and MIT instruments.

5.25 Average travel times at groups of stations for individual large shots with ranges greater than 30 km.

5.26 Velocity structure used to calculate the locations in Chapter IV compared to the results from the refraction data.

5.27 "Locations" of shots relative to the velocity model of Chapter IV. The open circles represent the shot locations determined from the navigation and the dots are the calculated locations. The axes of the 95% confidence ellipse of the solution are also shown. Open triangles represent the station locations.

5.28 Station residuals from the shot locations as a function of azimuth. The shaded rectangles show the results from the earthquake locations presented in Table 4.6 for region 1 and the diagonal lines indicate residuals from region 2. The mean residual at the station is also shown.

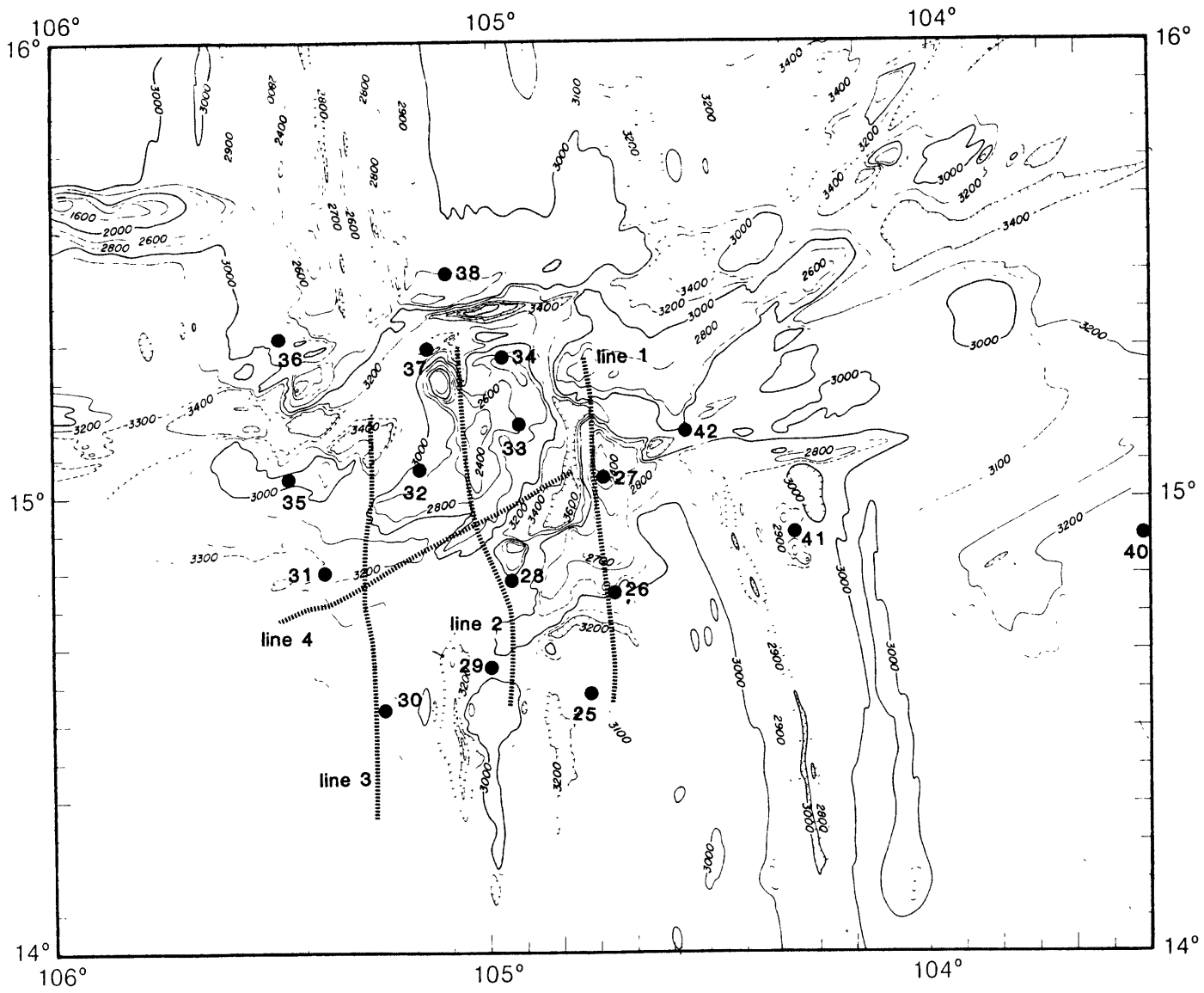
106°
105°
104°
16°
15°
14°
38
36
37
34
33
42
32
35
27
41
40
31
28
26
29
30
25
line 1
line 2
line 3
line 4

figure 5.1

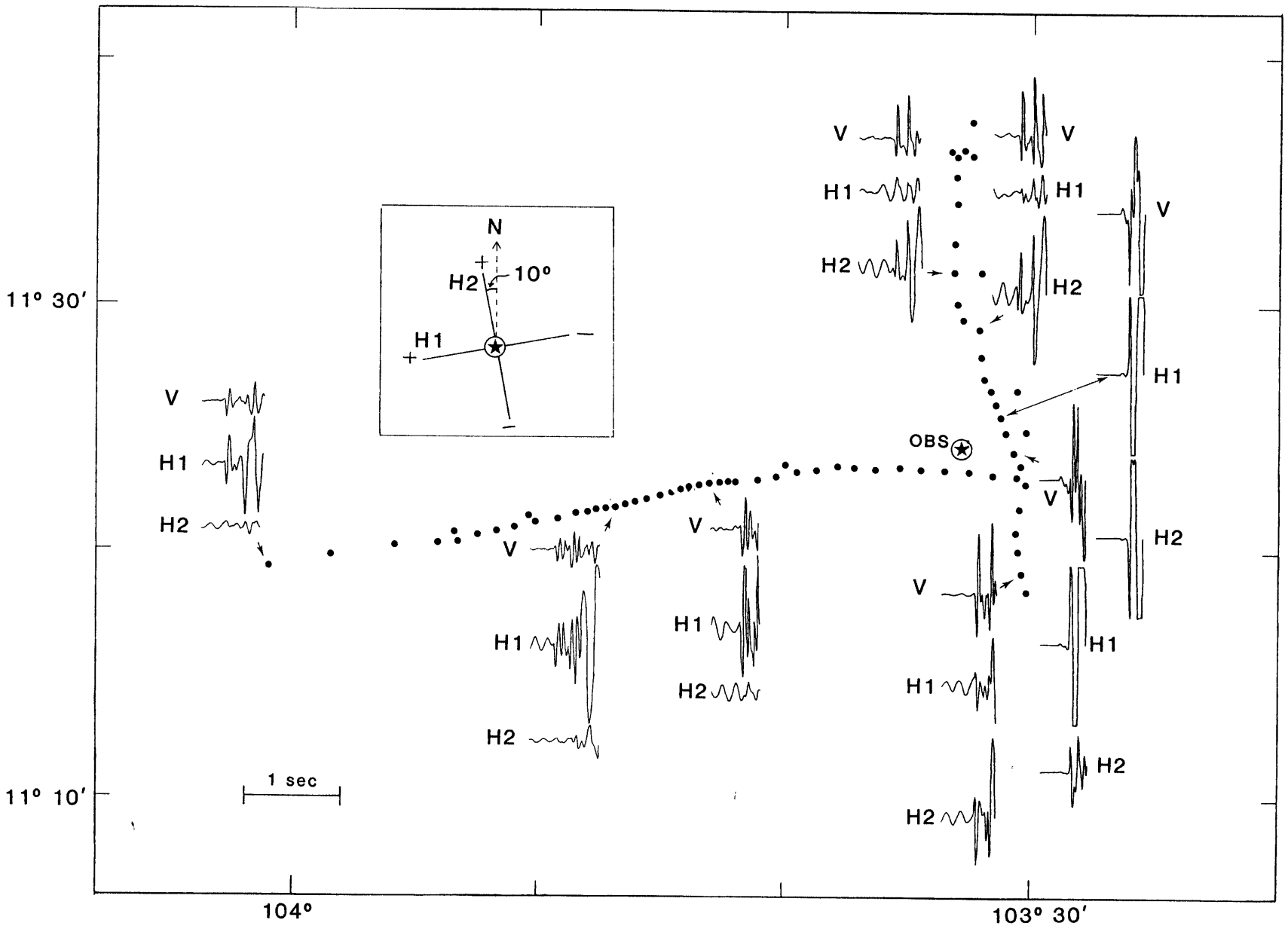

figure 5.2

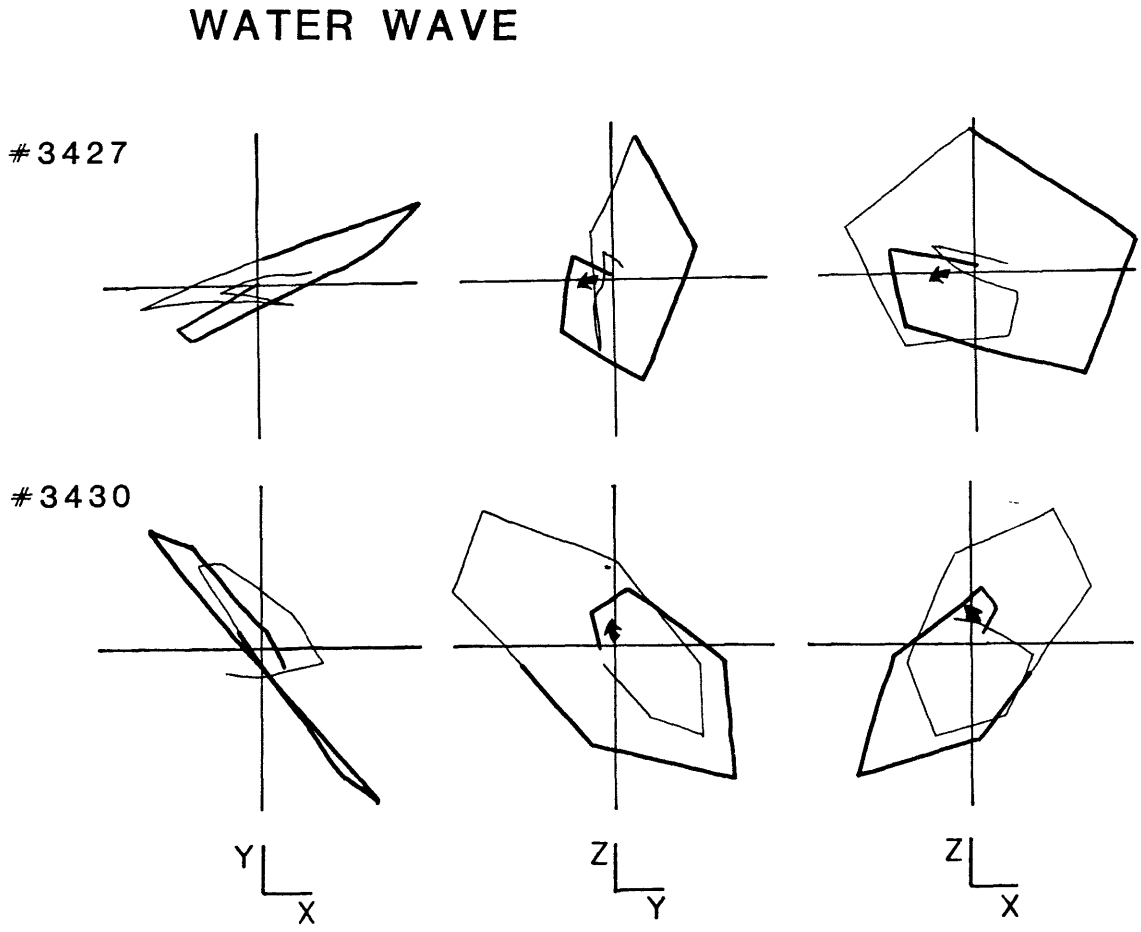

figure 5.3

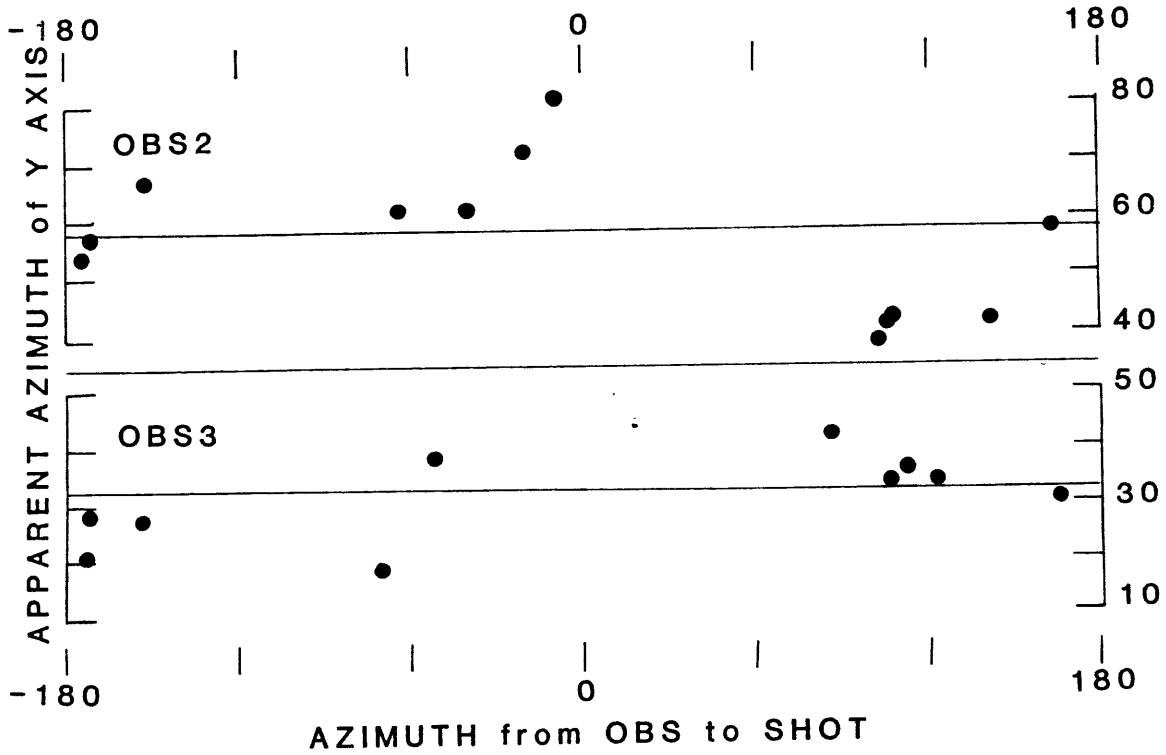
-180
0
180
APPARENT AZIMUTH of Y AXIS
OBS2
80
60
40
OBS3
50
30
10
-180
0
180
AZIMUTH from OBS to SHOT

figure 5.4

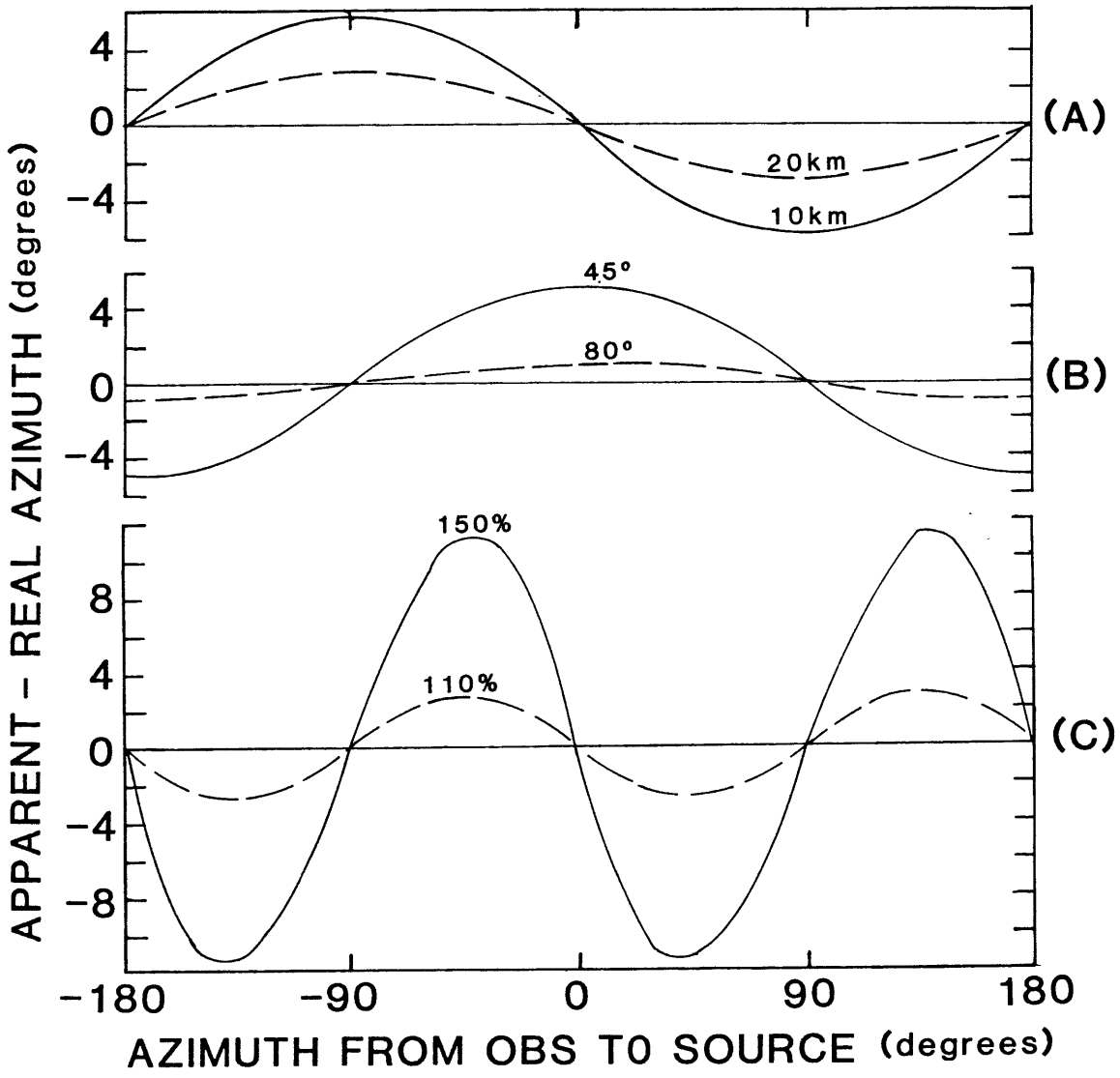
4
0
-4
(A)
20km
10km
45°
4
80°
0
-4
(B)
150%
8
4
110%
0
-4
-8
(C)
APPARENT - REAL AZIMUTH (degrees)
-180
-90
0
90
180
AZIMUTH FROM OBS TO SOURCE (degrees)

figure 5.5

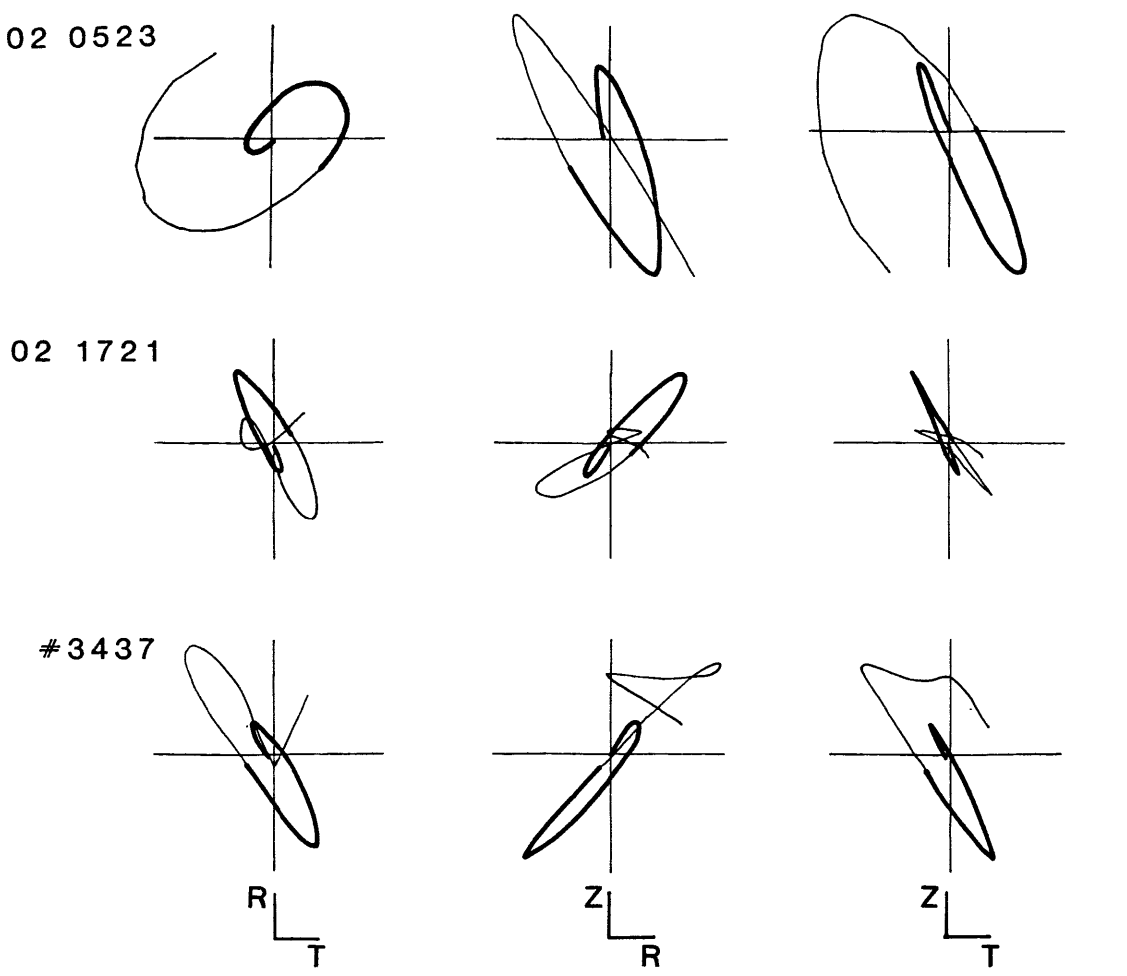
A) P WAVE - M2
02 0523
02 1721
#3437
R
T
Z
R
Z
T
B) S WAVE
02 0523
02 1721
R
T
Z
R
Z
T

figure 5.6

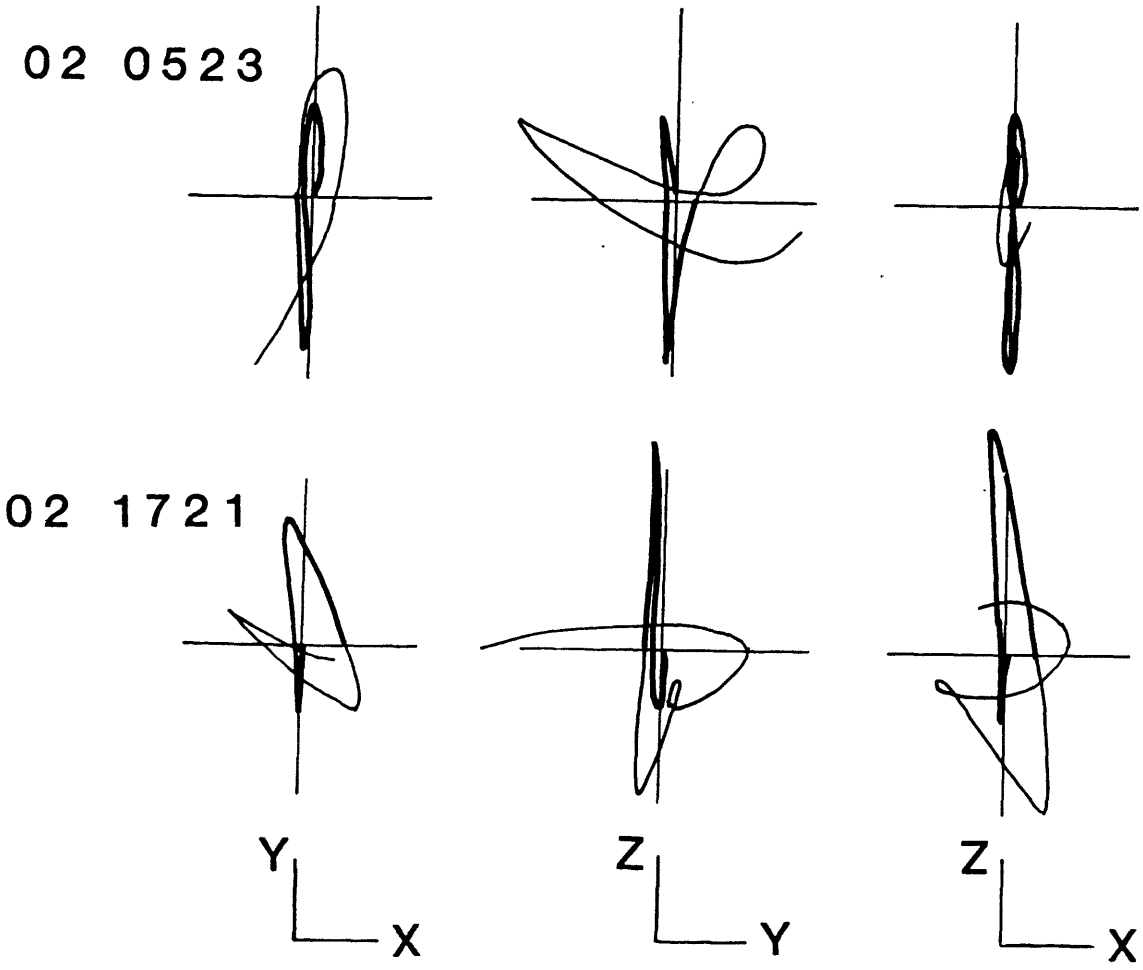

figure 5.7

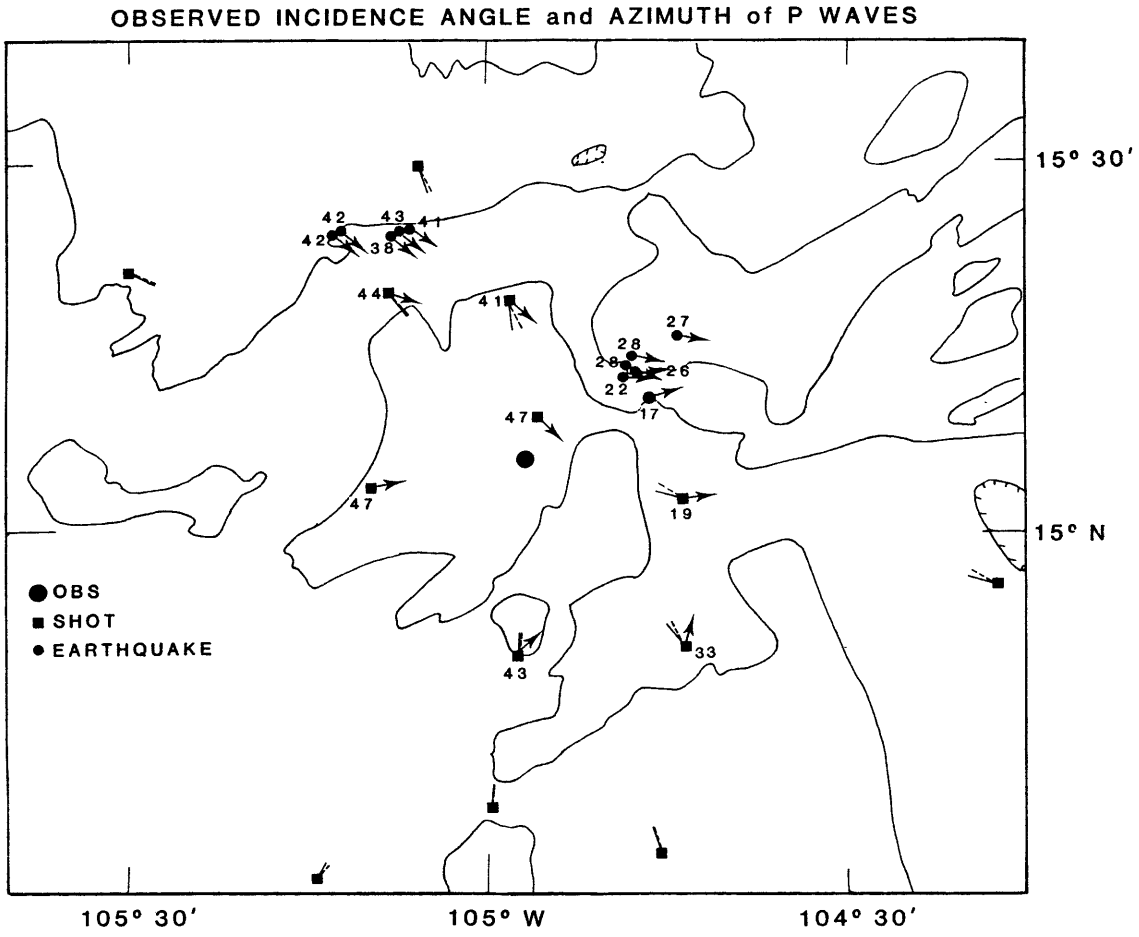
OBSERVED INCIDENCE ANGLE and AZIMUTH of P WAVES
15° 30'
15° N
105° 30'
105° W
104° 30'
OBS
SHOT
EARTHQUAKE
42
43
41
42
38
44
41
27
28
28
26
22
17
47
47
19
43
33

figure 5.8

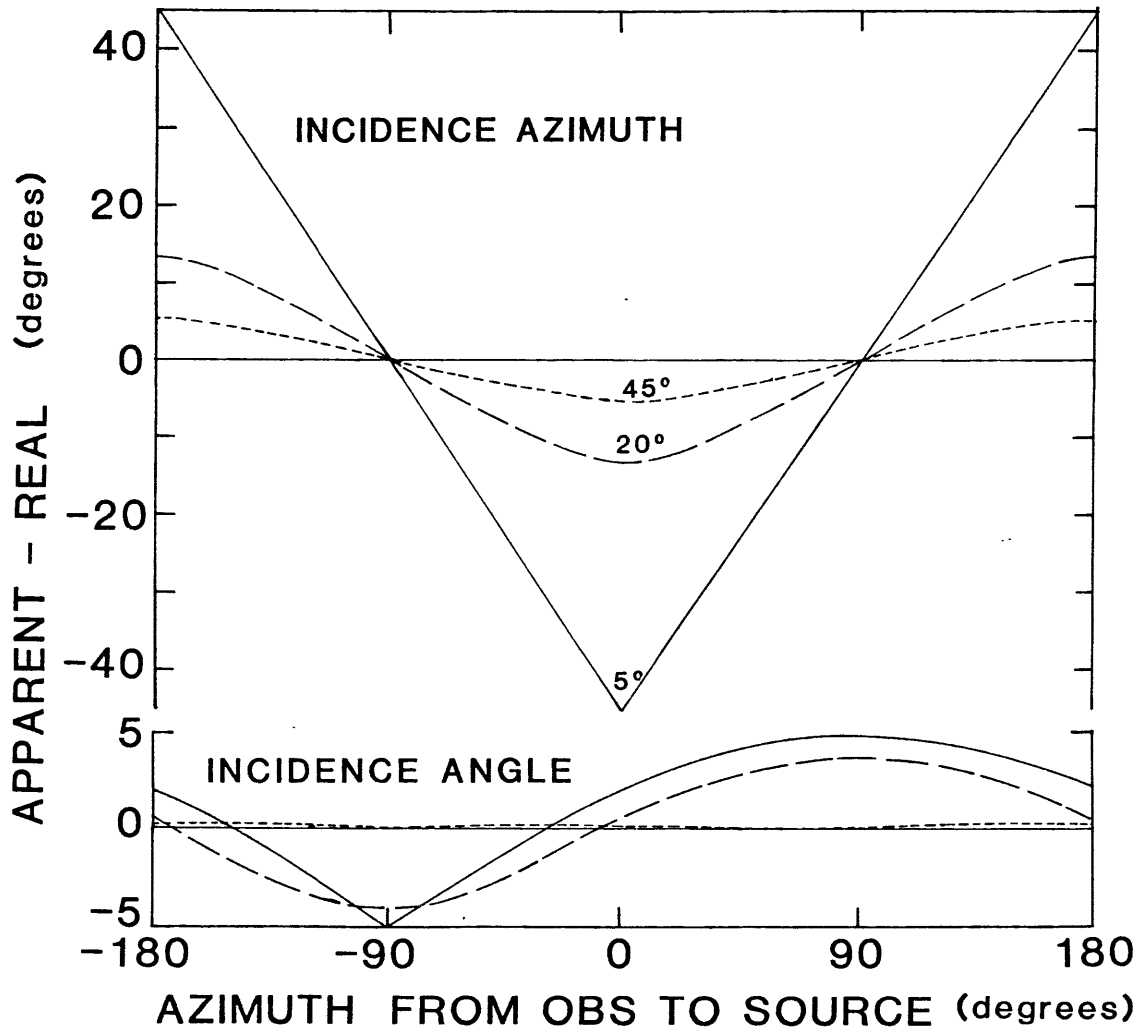
INCIDENCE AZIMUTH
INCIDENCE ANGLE
45°
20°
5°
40
20
0
-20
-40
5
0
-5
-180
-90
0
90
180
APPARENT - REAL (degrees)
AZIMUTH FROM OBS TO SOURCE (degrees)

figure 5.9

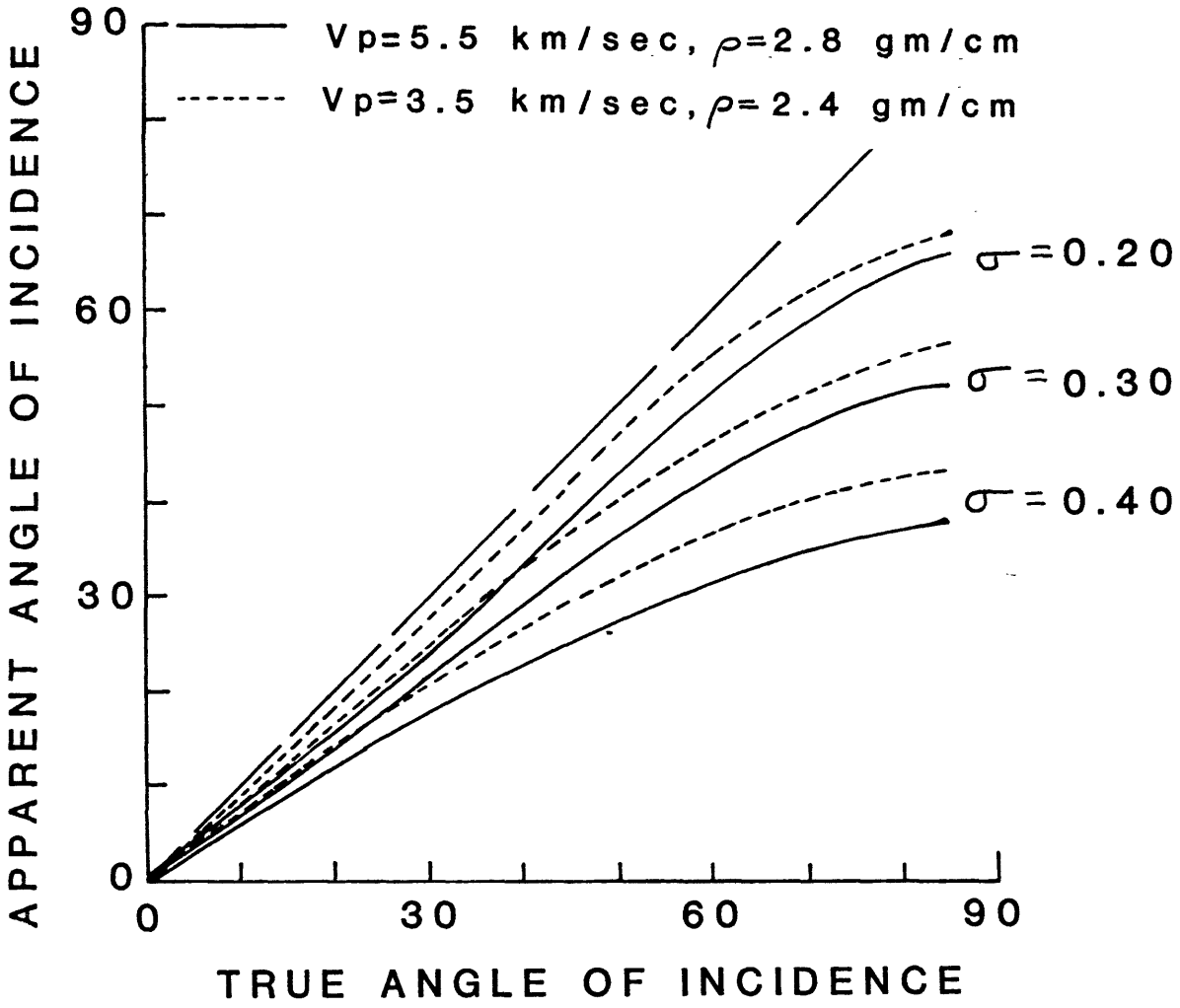
Vp=5.5 km/sec, ρ=2.8 gm/cm
Vp=3.5 km/sec, ρ=2.4 gm/cm
σ=0.20
σ=0.30
σ=0.40
APPARENT ANGLE OF INCIDENCE
TRUE ANGLE OF INCIDENCE
0
30
60
90

figure 5.10

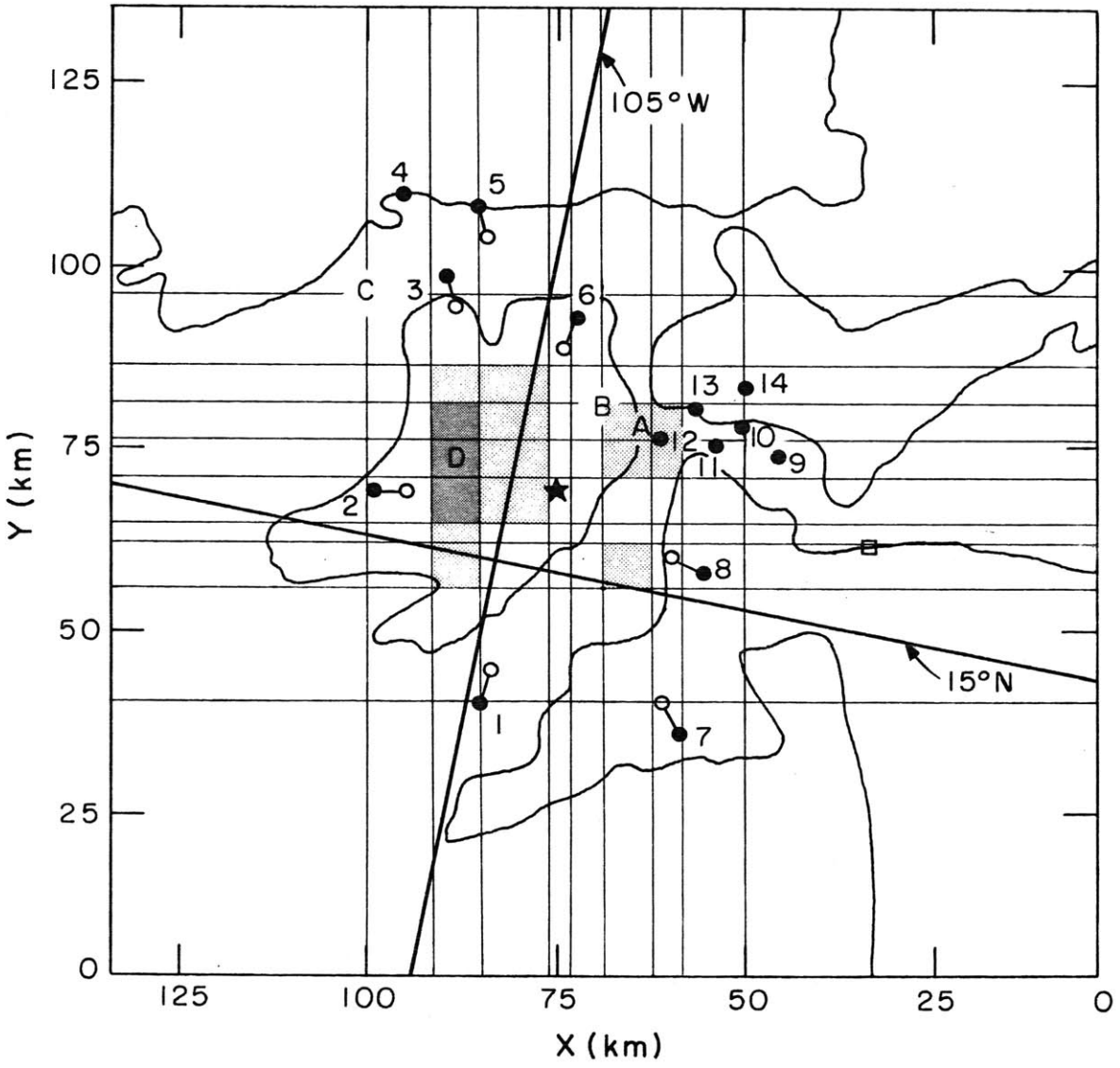
125
100
75
50
25
0
Y (km)
125
100
75
50
25
0
X (km)
105°W
15°N
1
2
3
4
5
6
7
8
9
10
11
12
13
14
A
B
C
D

figure 5.11a

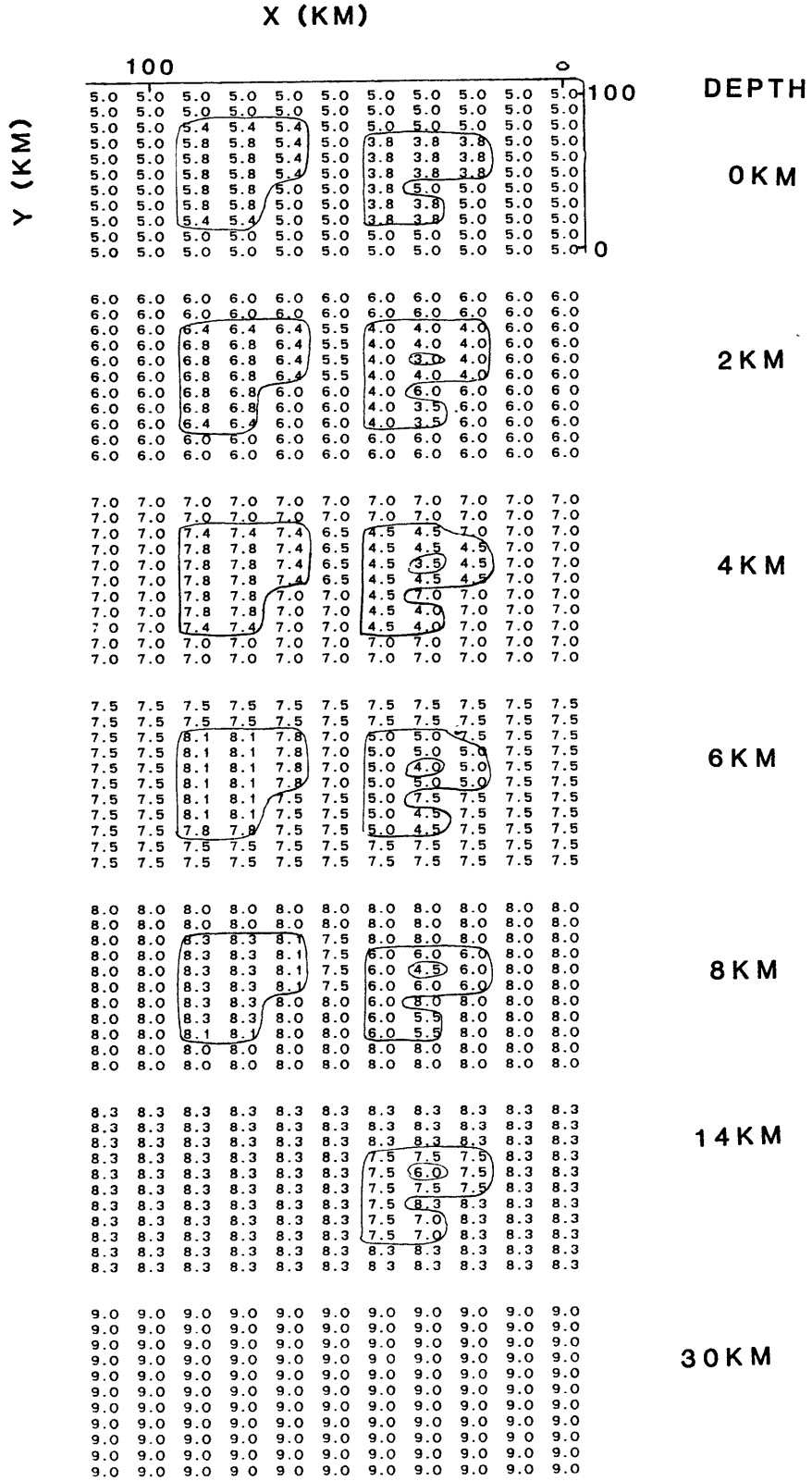

X grid - 0 50 58 63 70 74 76 84 92 100 138KM

Y grid - 0 40 55 60 62 71 76 81 87 97 100 KM

figure 5.11b

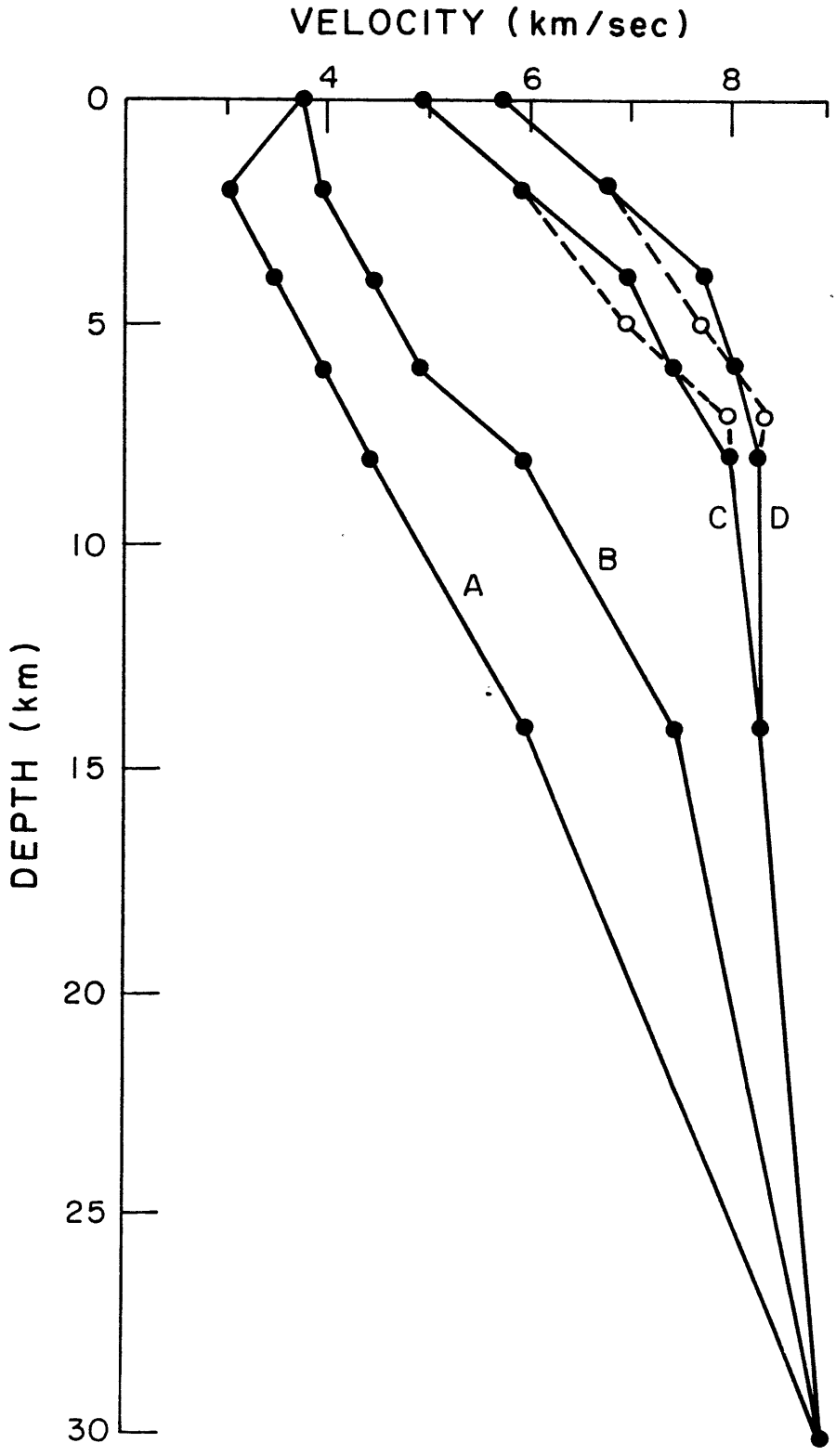

figure 5.11c

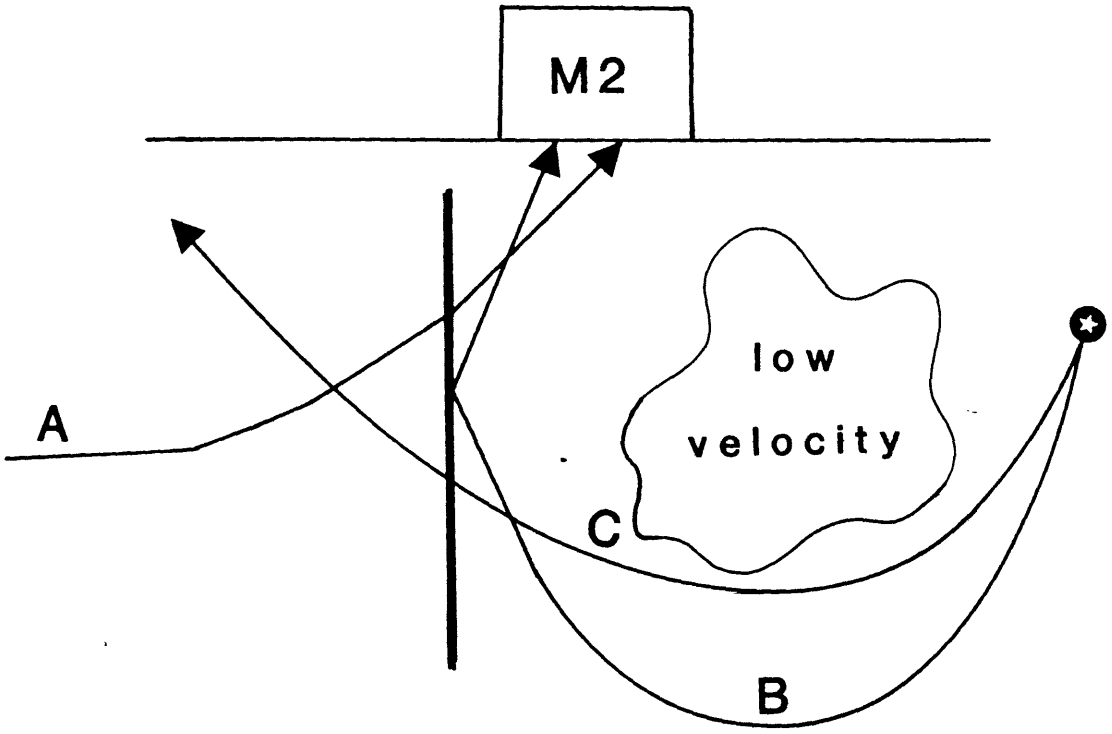

figure 5.12

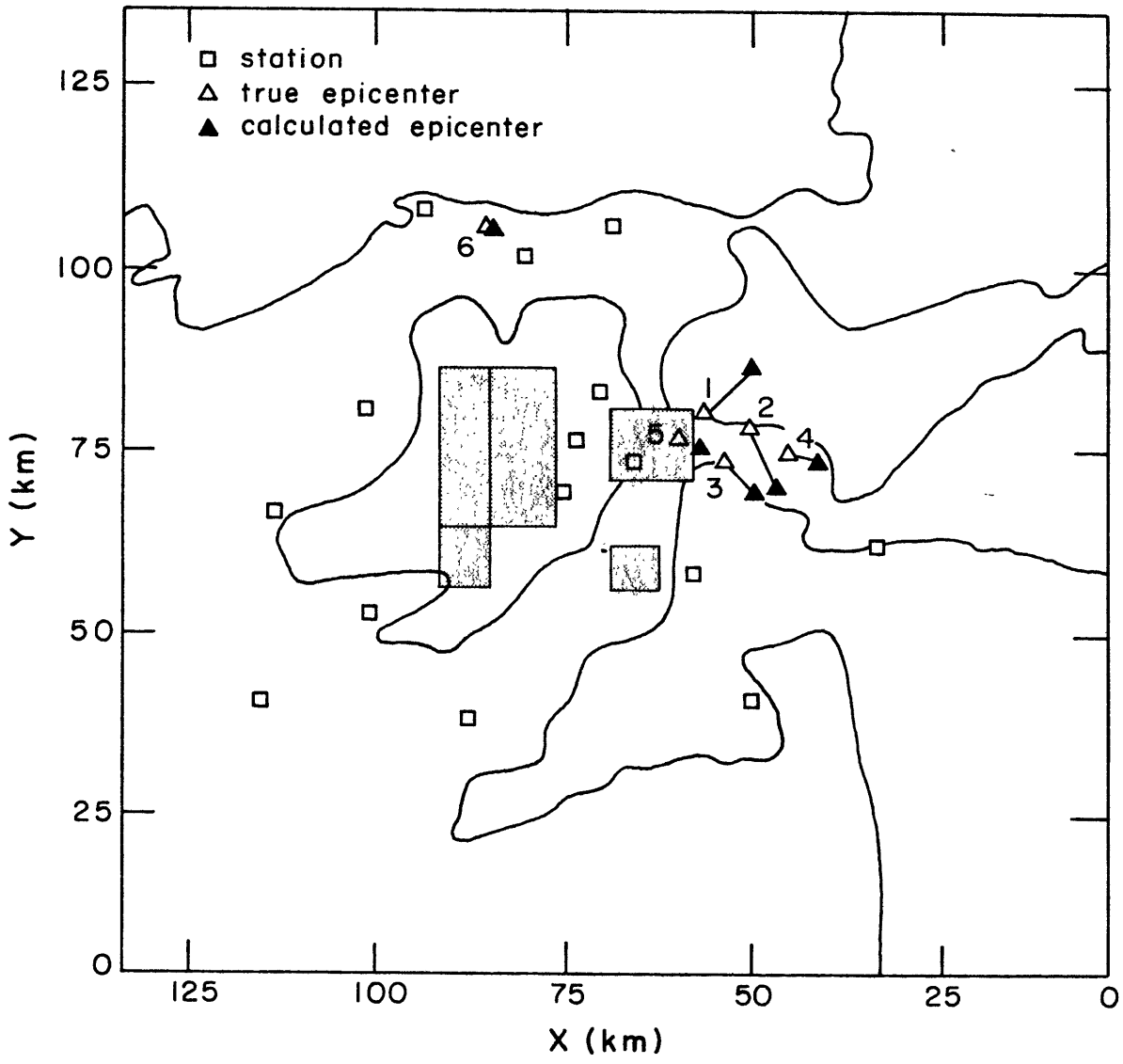
station
true epicenter
calculated epicenter
125
100
75
50
25
0
Y (km)
125
100
75
50
25
0
X (km)
1
2
3
4
5
6

figure 5.13

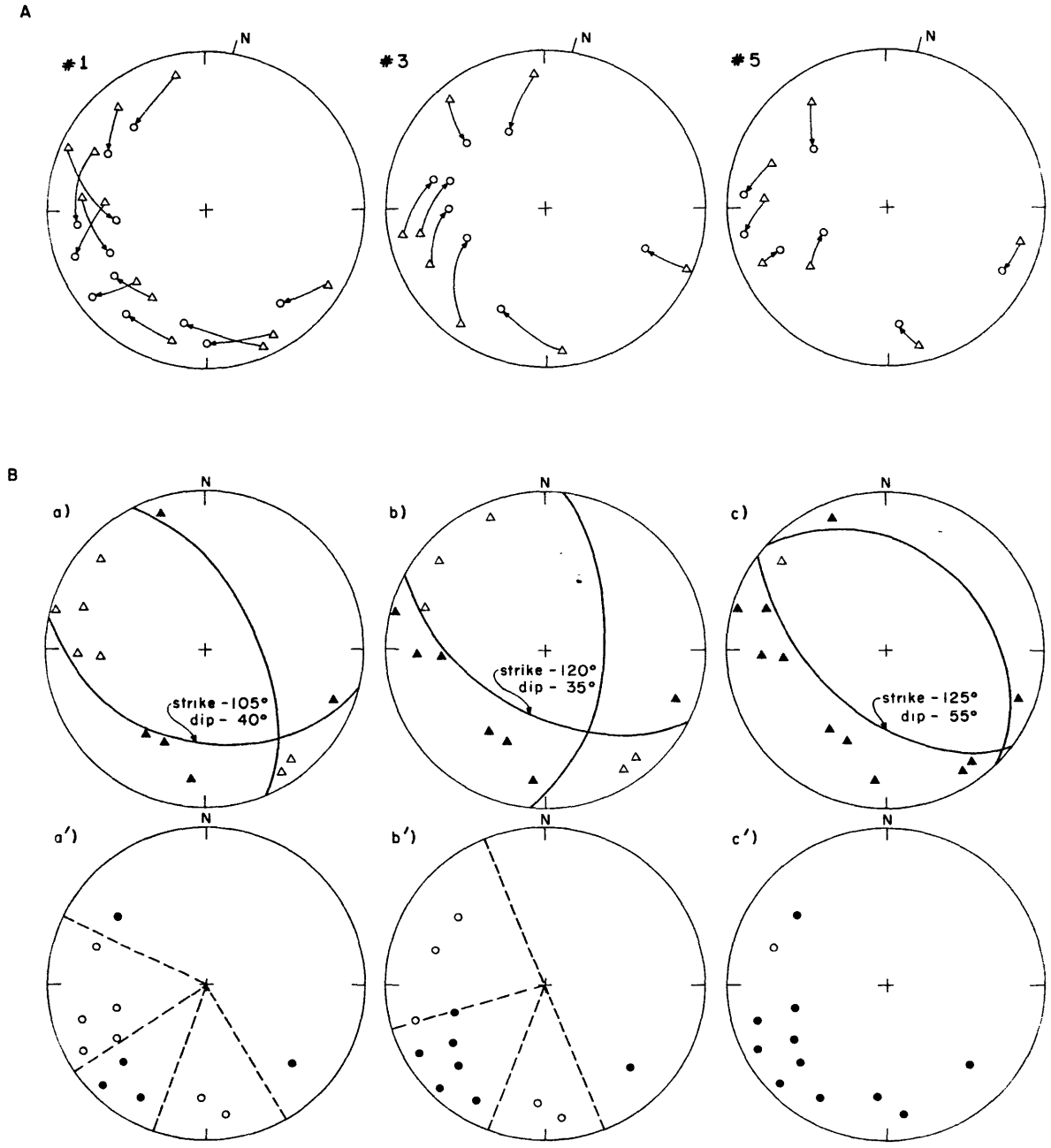
A
#1
#3
#5
N
B
a)
b)
c)
strike - 105°
dip - 40°
strike - 120°
dip - 35°
strike - 125°
dip - 55°
a')
b')
c')

figure 5.14

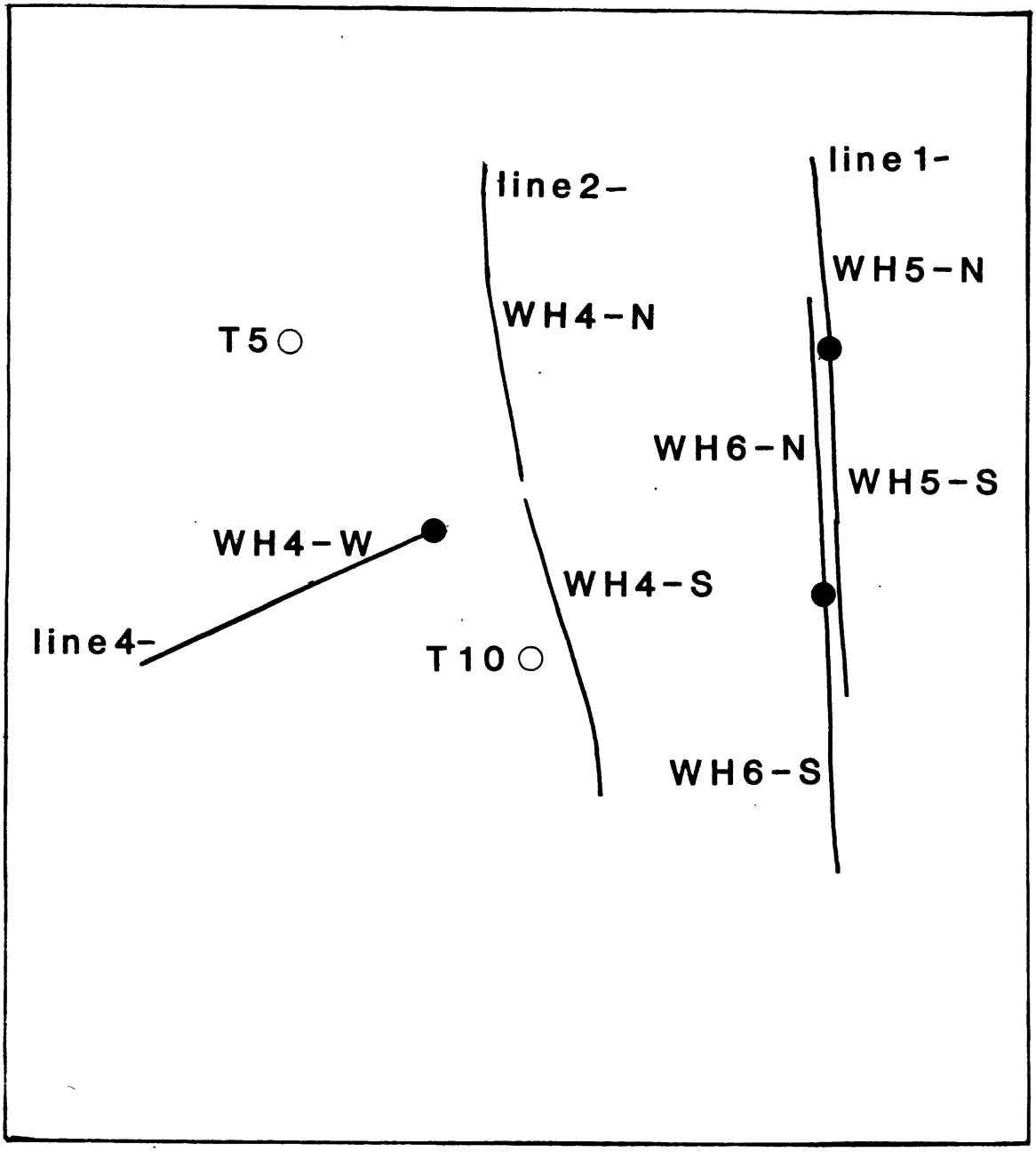

figure 5.15

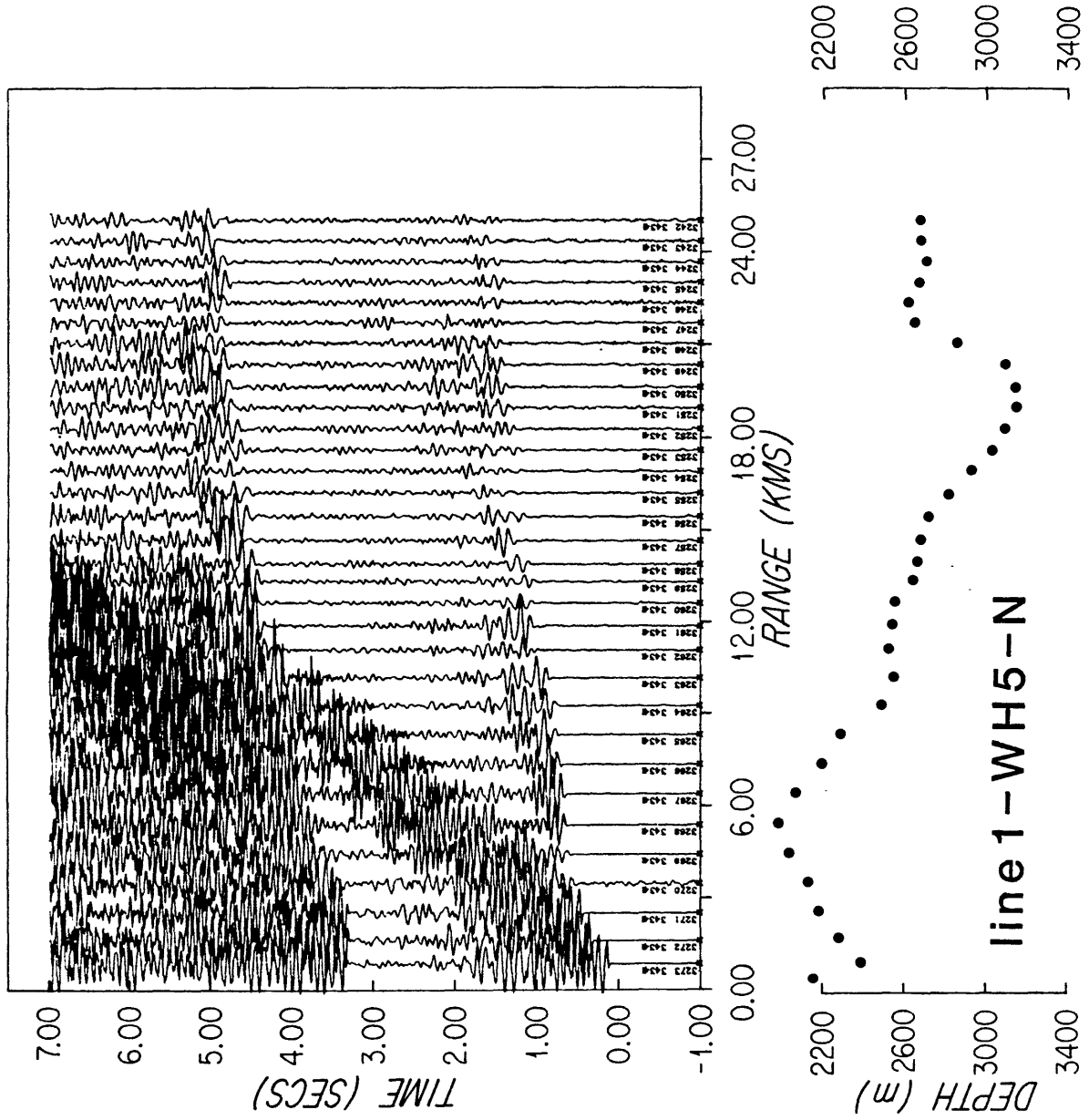
line1-WH5-N
RANGE (KMS)
0.00
6.00
12.00
18.00
24.00
27.00
DEPTH (m)
2200
2600
3000
3400
TIME (SECS)
7.00
6.00
5.00
4.00
3.00
2.00
1.00
0.00
-1.00

figure 5.16a

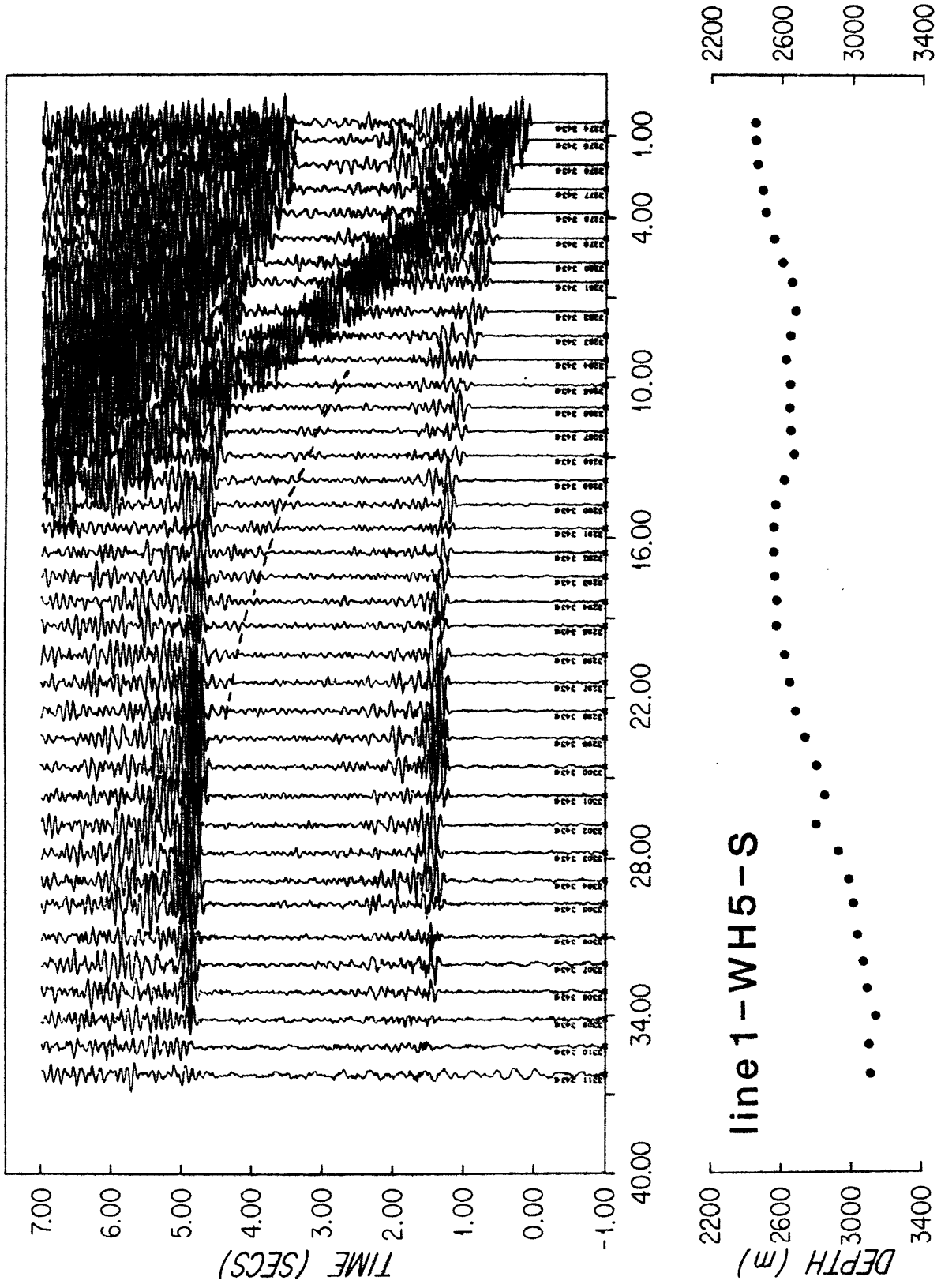
7.00
6.00
5.00
4.00
3.00
2.00
1.00
0.00
-1.00
TIME (SECS)
1.00
4.00
10.00
16.00
22.00
28.00
34.00
40.00
2200
2600
3000
3400
line1-WH5-S
DEPTH (m)

figure 5.16b

7.00
6.00
5.00
4.00
3.00
2.00
1.00
0.00
-1.00
TIME (SECS)
0.00
6.00
12.00
18.00
24.00
30.00
36.00
RANGE (KMS)
DEPTH (m)
2200
2600
3000
3400
line1-WH6-N

figure 5.16c

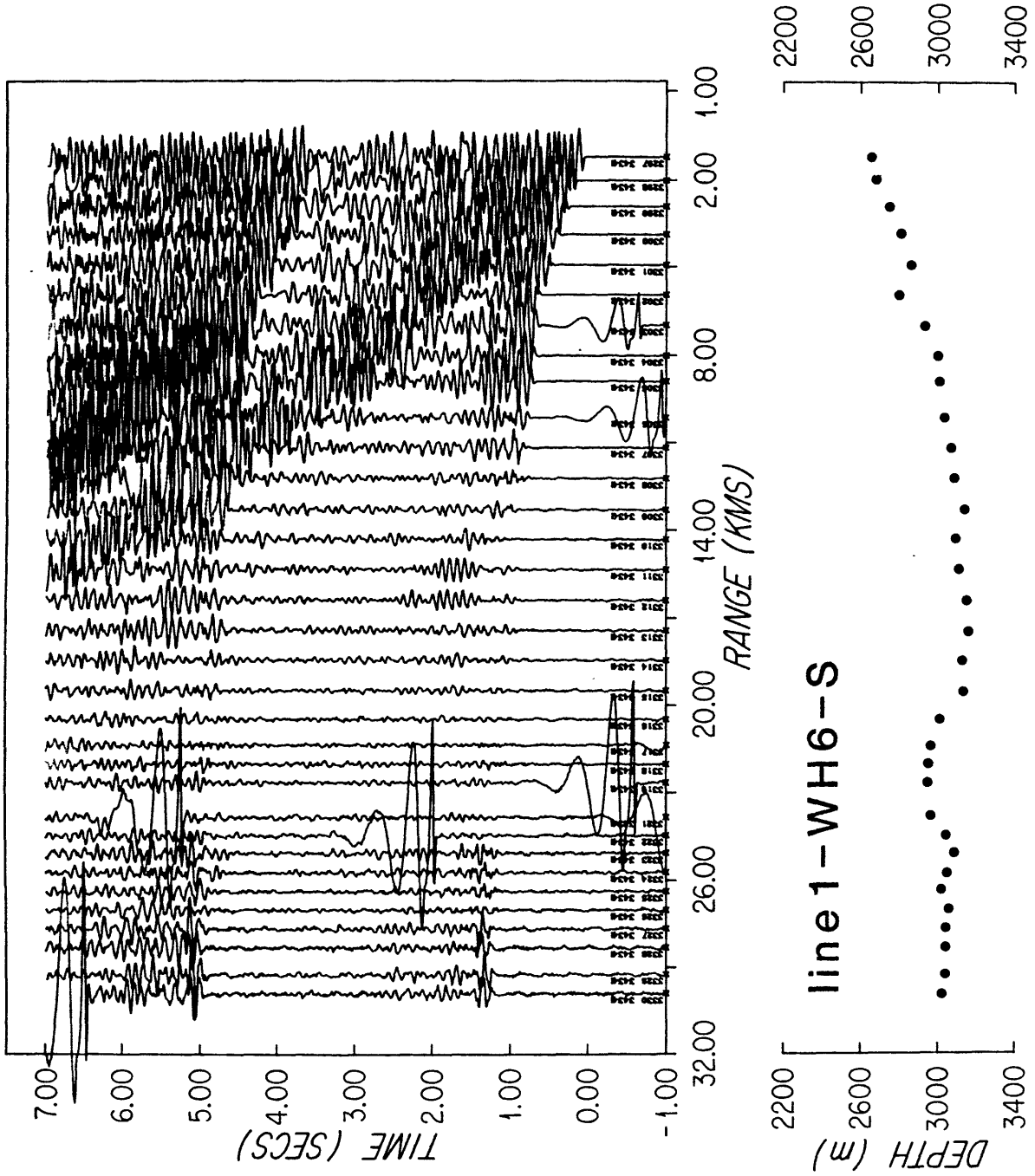
line1-WH6-S
TIME (SECS)
7.00
6.00
5.00
4.00
3.00
2.00
1.00
0.00
-1.00
RANGE (KMS)
1.00
2.00
8.00
14.00
20.00
26.00
32.00
DEPTH (m)
2200
2600
3000
3400

figure 5.16d

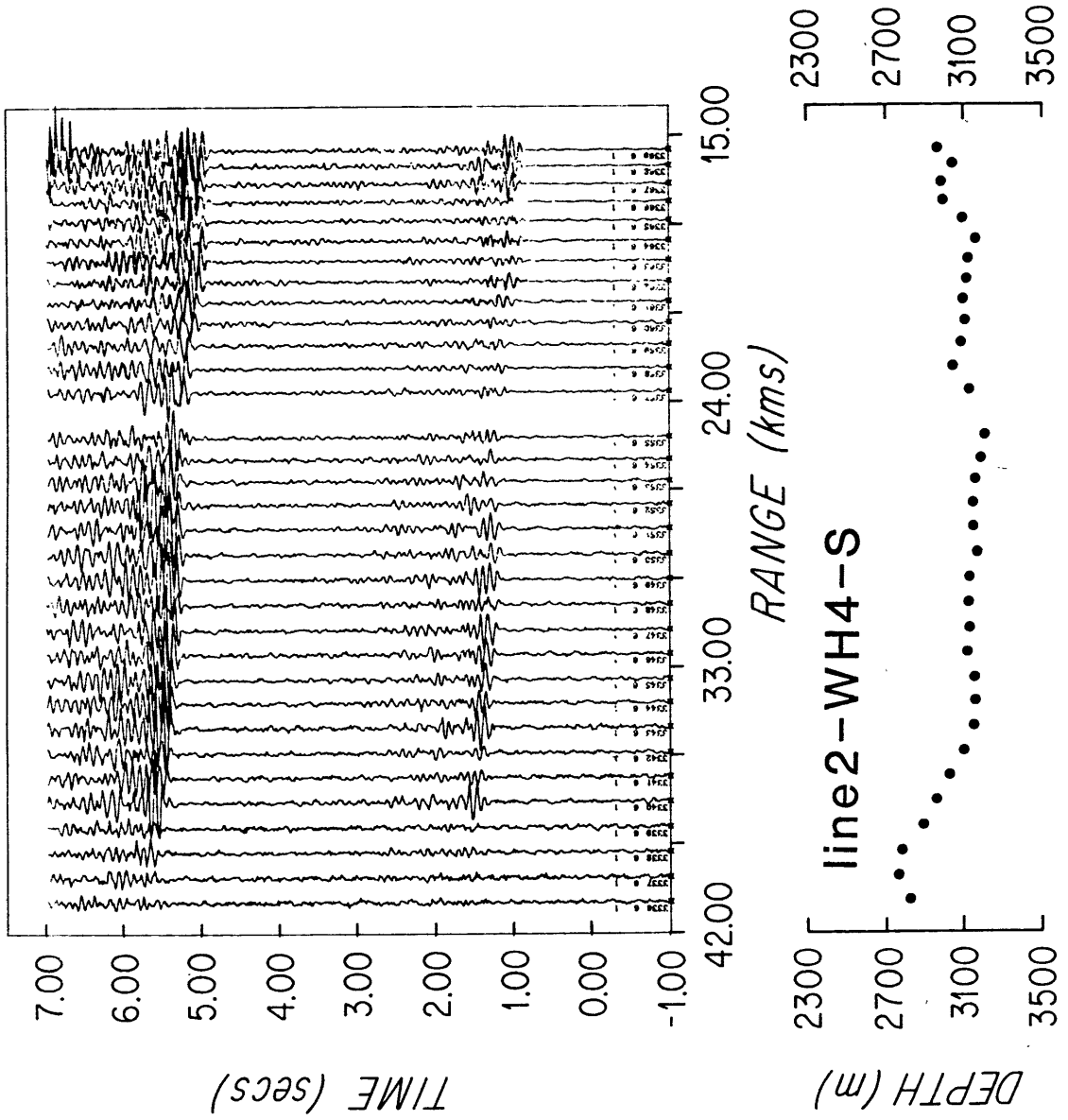
7.00
6.00
5.00
4.00
3.00
2.00
1.00
0.00
-1.00
TIME (secs)
15.00
24.00
33.00
42.00
RANGE (kms)
2300
2700
3100
3500
line2-WH4-S
2300
2700
3100
3500
DEPTH (m)

figure 5.16e

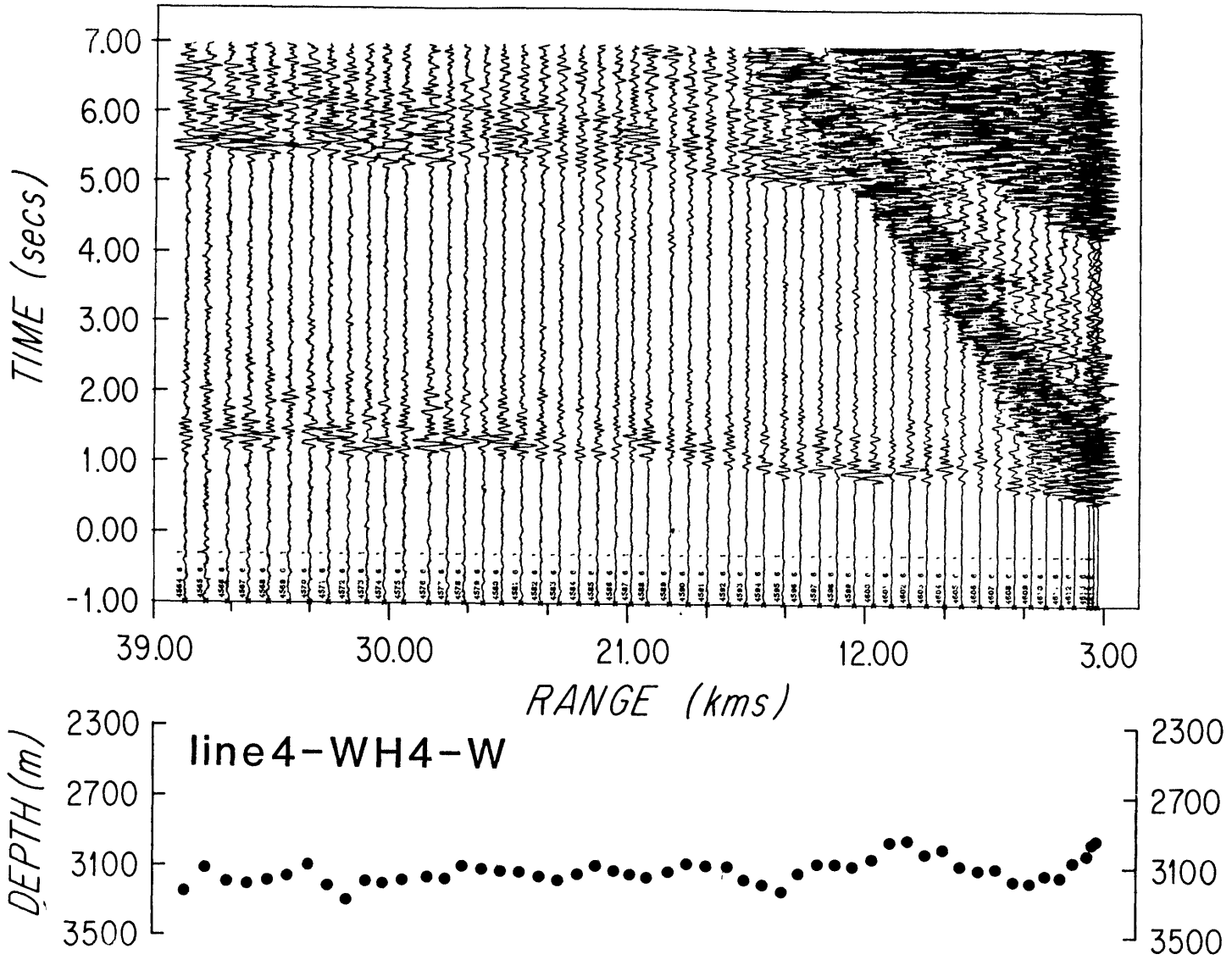
7.00
6.00
5.00
4.00
3.00
2.00
1.00
0.00
-1.00
TIME (secs)
39.00
30.00
21.00
12.00
3.00
RANGE (kms)
line4-WH4-W
2300
2700
3100
3500
DEPTH (m)

figure 5.16f

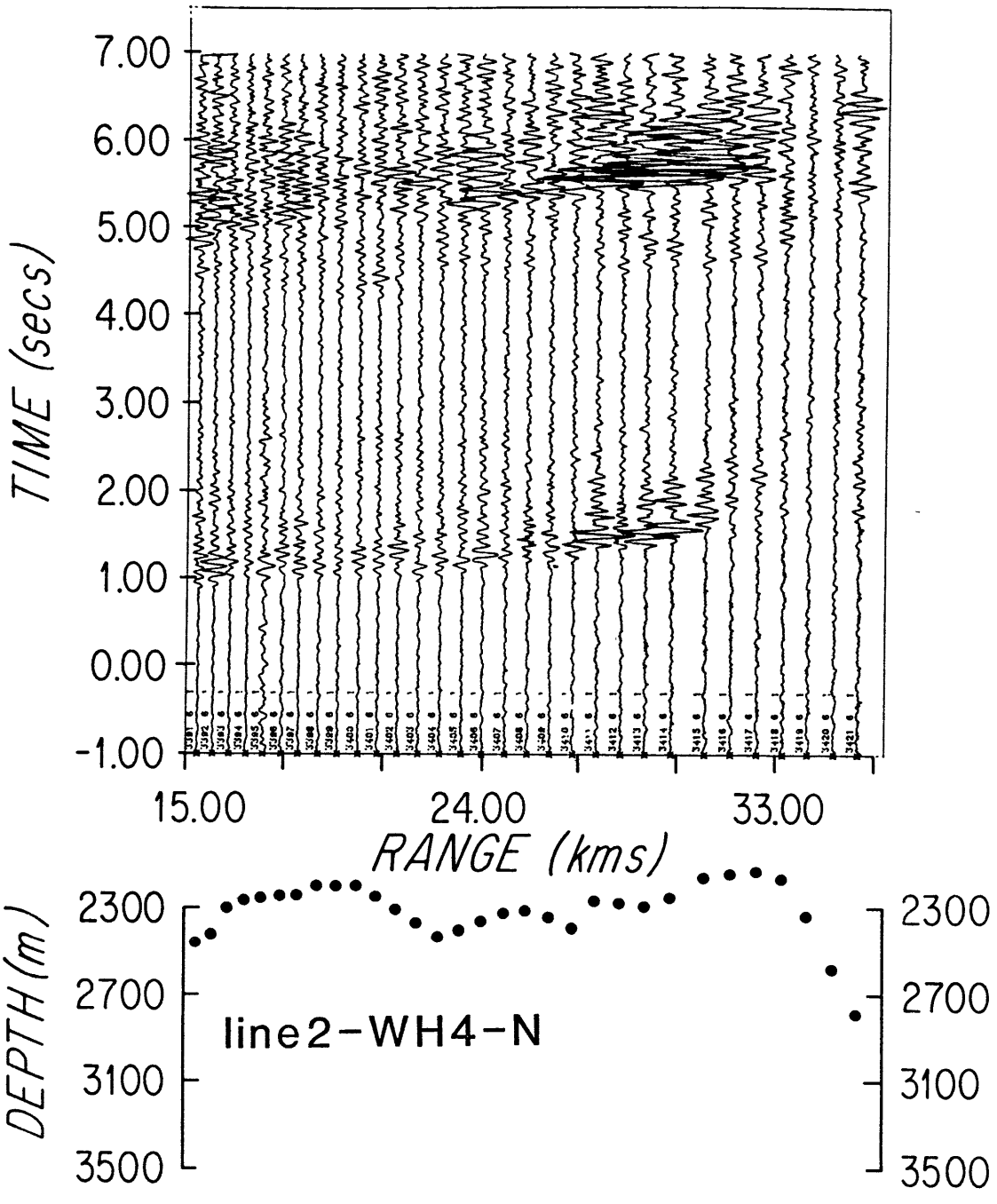
7.00
6.00
5.00
4.00
3.00
2.00
1.00
0.00
-1.00
TIME (secs)
15.00
24.00
33.00
RANGE (kms)
2300
2700
3100
3500
DEPTH (m)
line2-WH4-N

Figure 5.16g

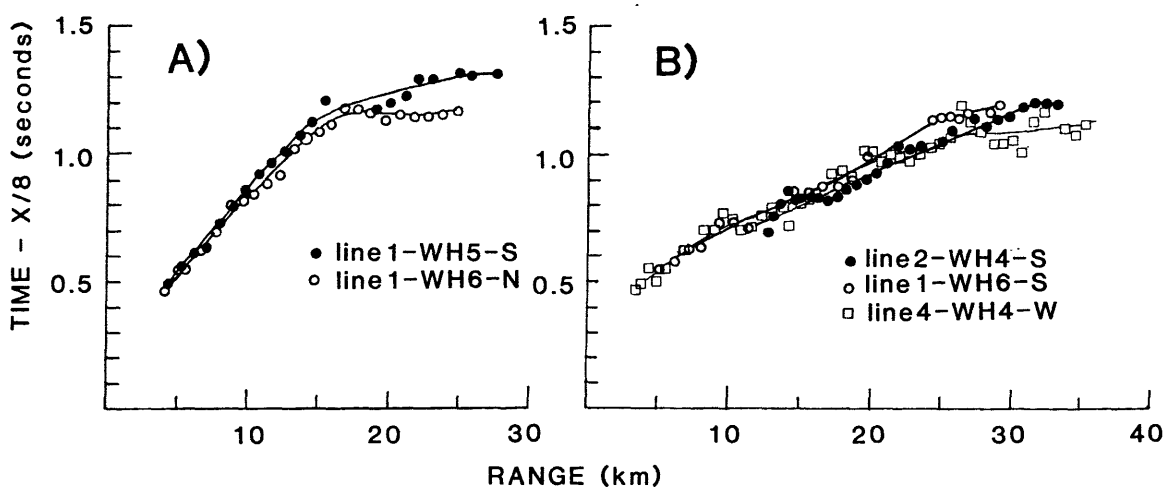
A)
B)
TIME - X/8 (seconds)
1.5
1.0
0.5
10
20
30
40
RANGE (km)
• line1-WH5-S
o line1-WH6-N
• line2-WH4-S
o line1-WH6-S
□ line4-WH4-W

figure 5.17

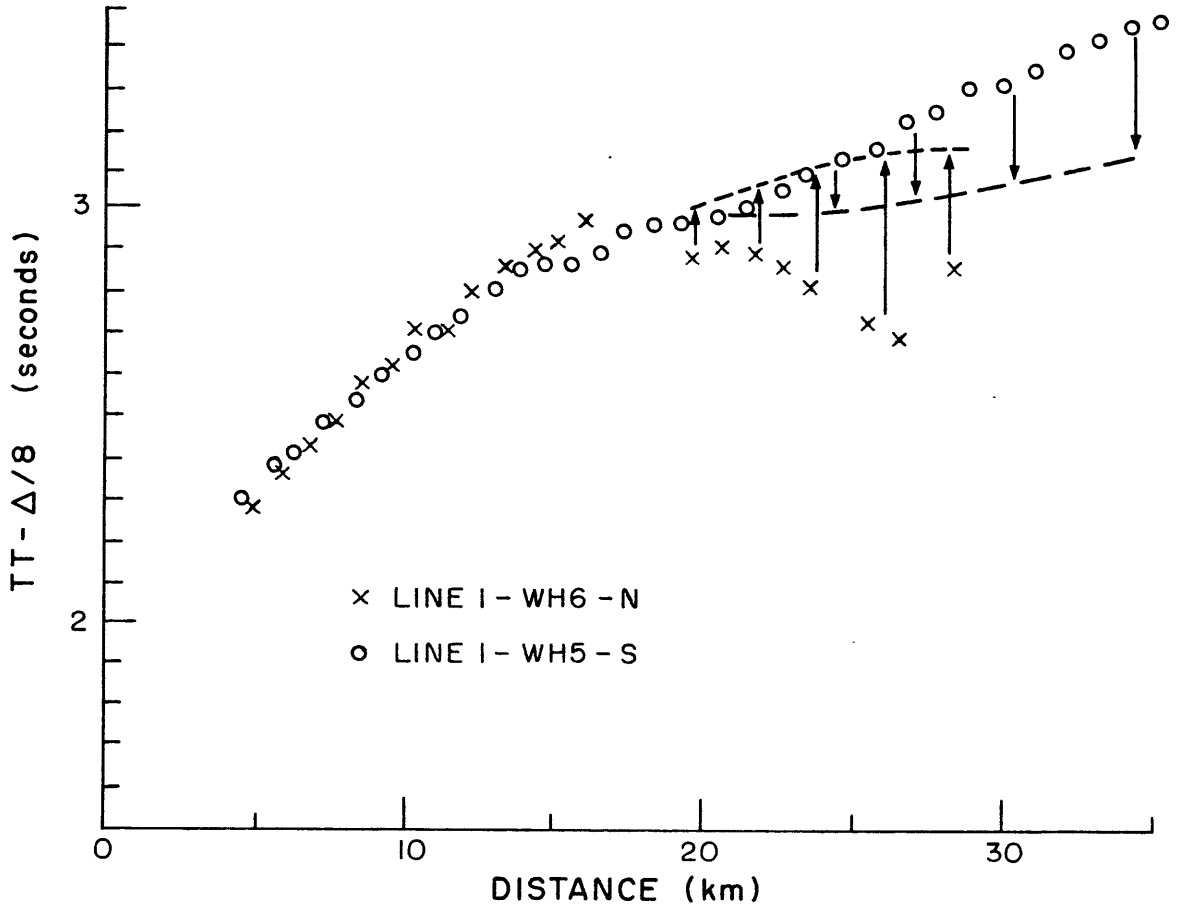

figure 5.18

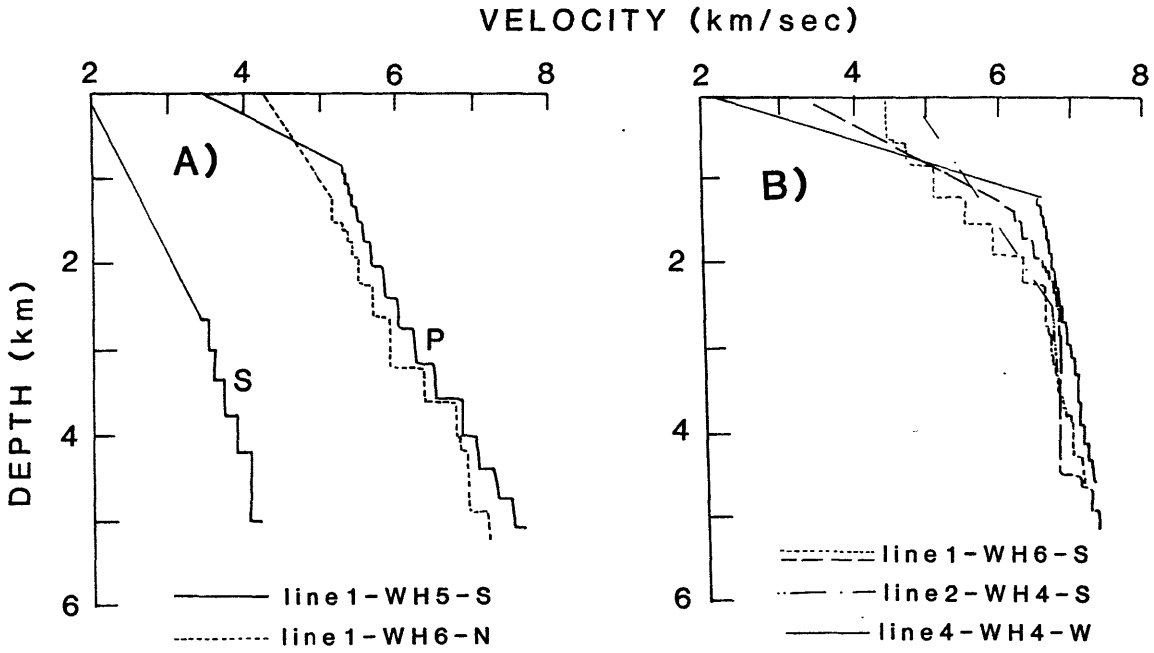
VELOCITY (km/sec)
2
4
6
8
A)
B)
DEPTH (km)
2
4
6
P
S
line1-WH5-S
line1-WH6-N
line1-WH6-S
line2-WH4-S
line4-WH4-W

figure 5.19

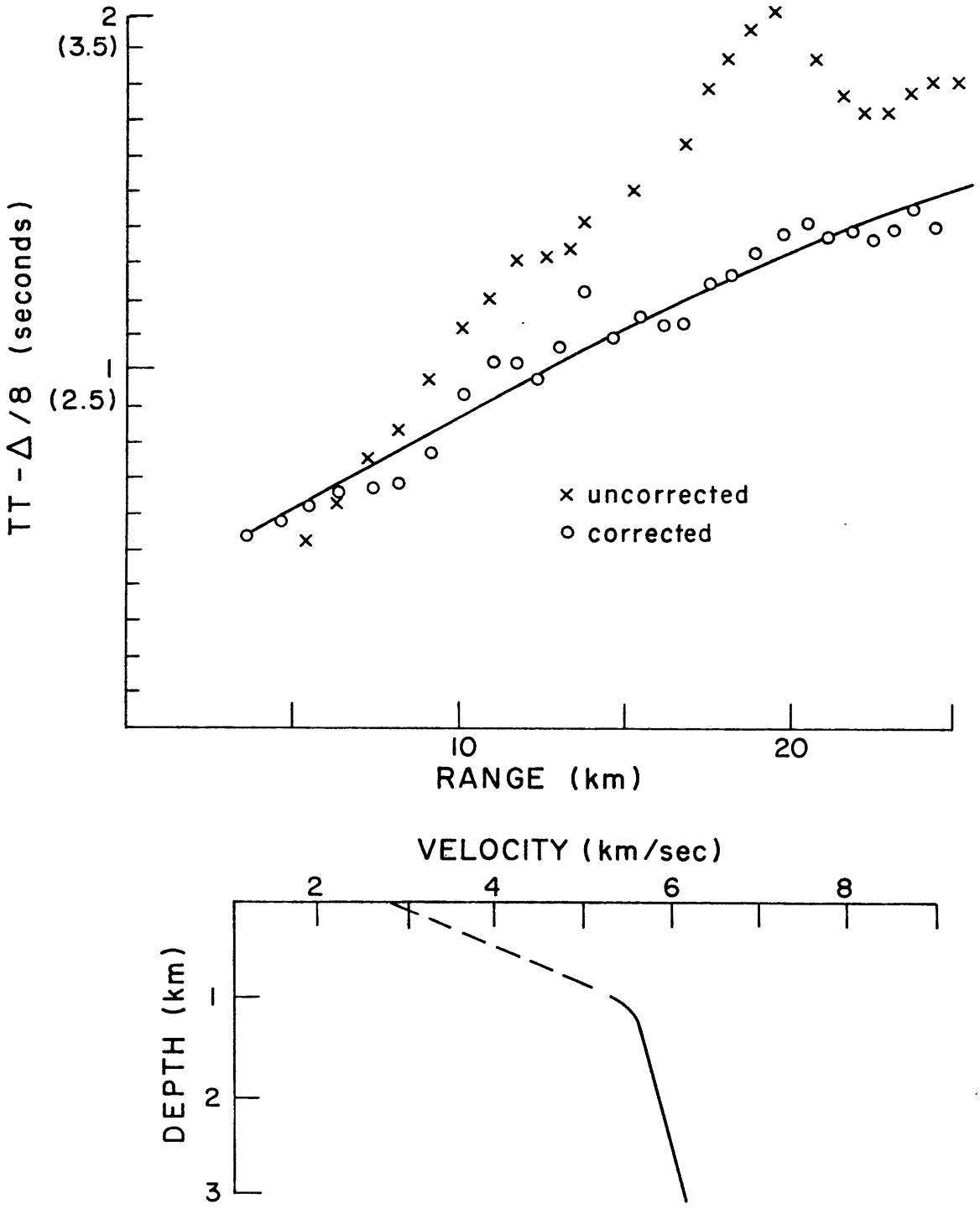
2
(3.5)
1
(2.5)
TT - Δ/8 (seconds)
× uncorrected
o corrected
10
20
RANGE (km)
VELOCITY (km/sec)
2
4
6
8
DEPTH (km)
1
2
3

figure 5.20

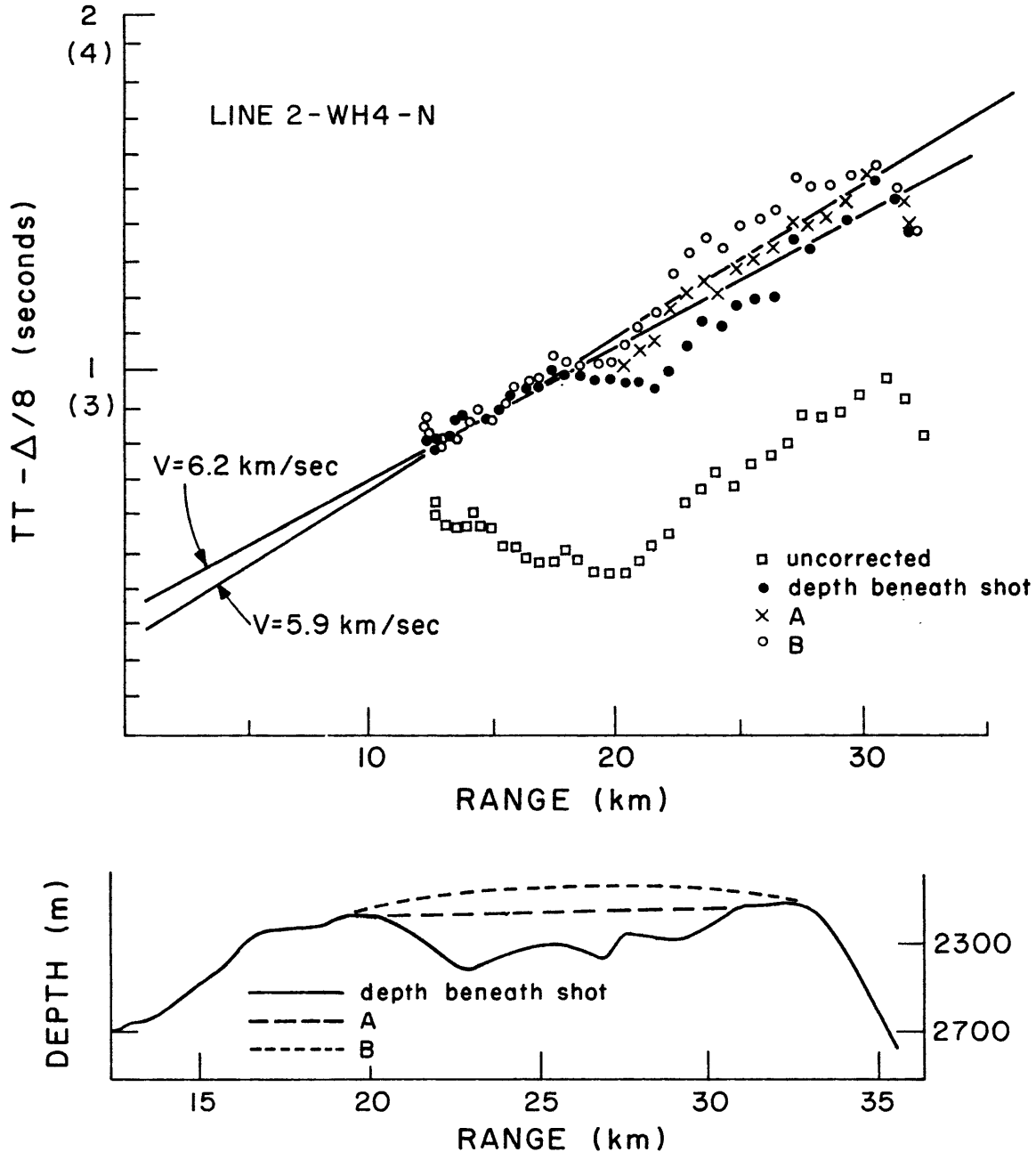
LINE 2-WH4-N
TT - Δ/8 (seconds)
2
(4)
1
(3)
V=6.2 km/sec
V=5.9 km/sec
uncorrected
depth beneath shot
A
B
10
20
30
RANGE (km)
DEPTH (m)
depth beneath shot
A
B
2300
2700
15
20
25
30
35
RANGE (km)

figure 5.21

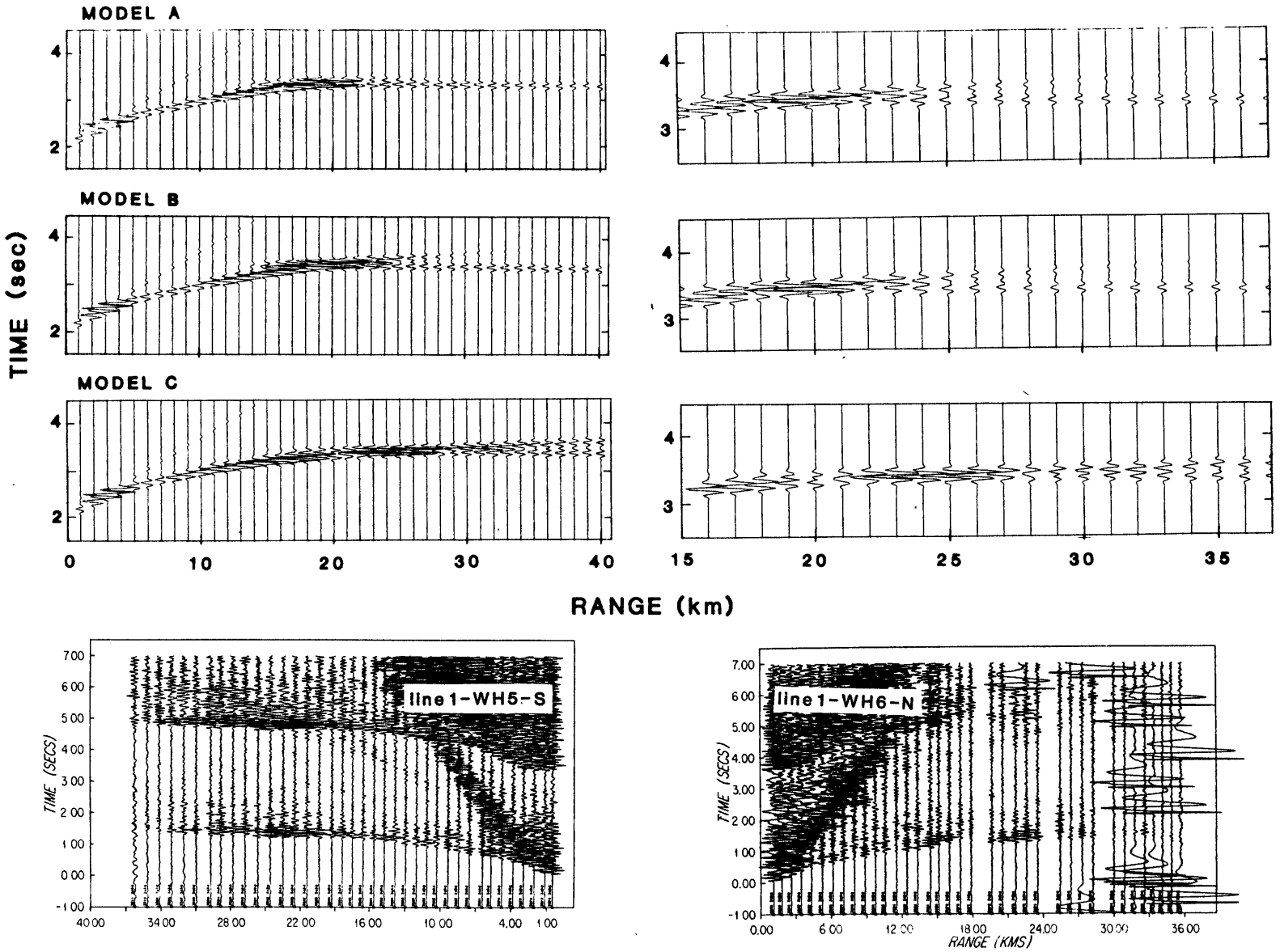
MODEL A
MODEL B
MODEL C
TIME (sec)
RANGE (km)
0
10
20
30
40
15
20
25
30
35
line 1-WH5-S
TIME (SECS)
line 1-WH6-N
TIME (SECS)
RANGE (KMS)

figure 5.22a

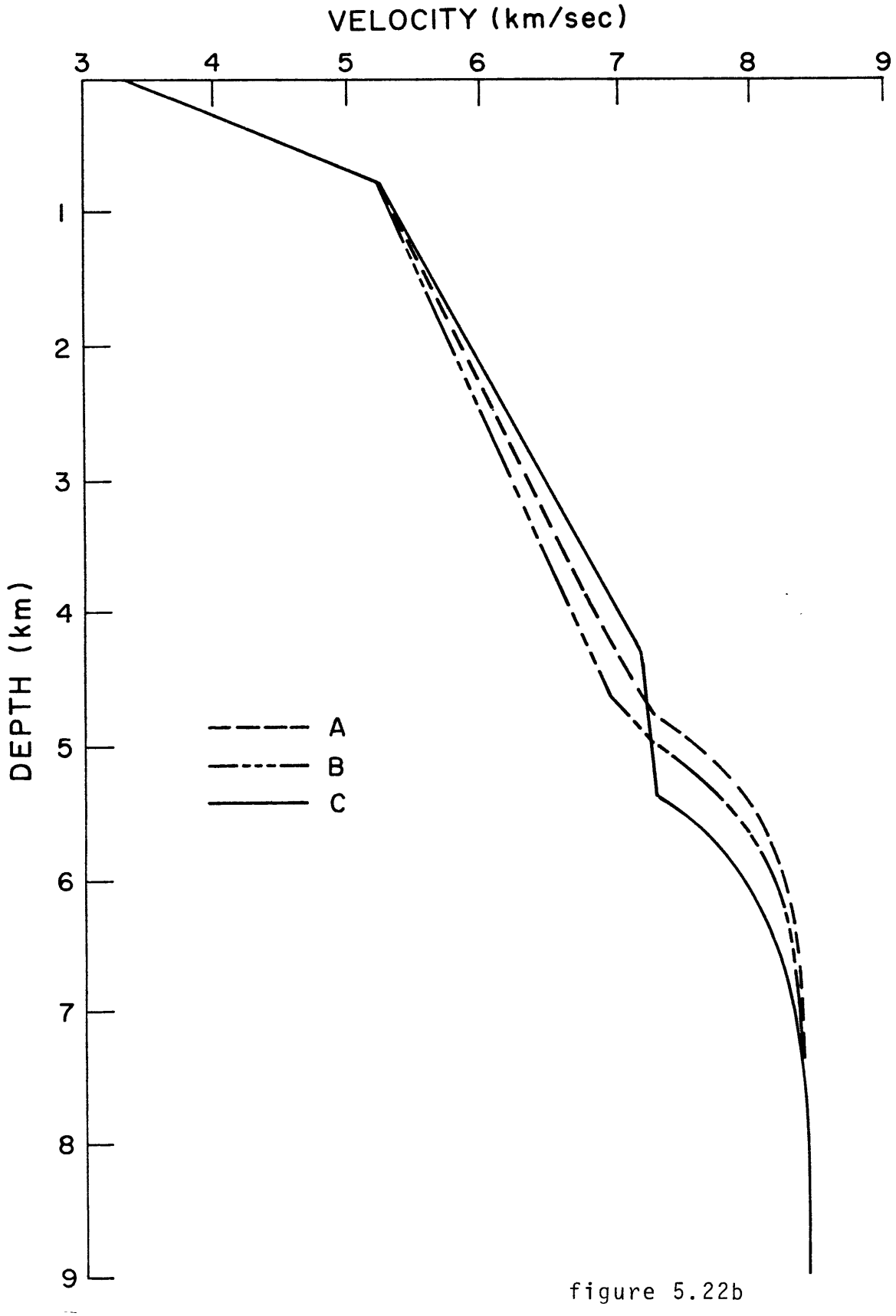

figure 5.22b

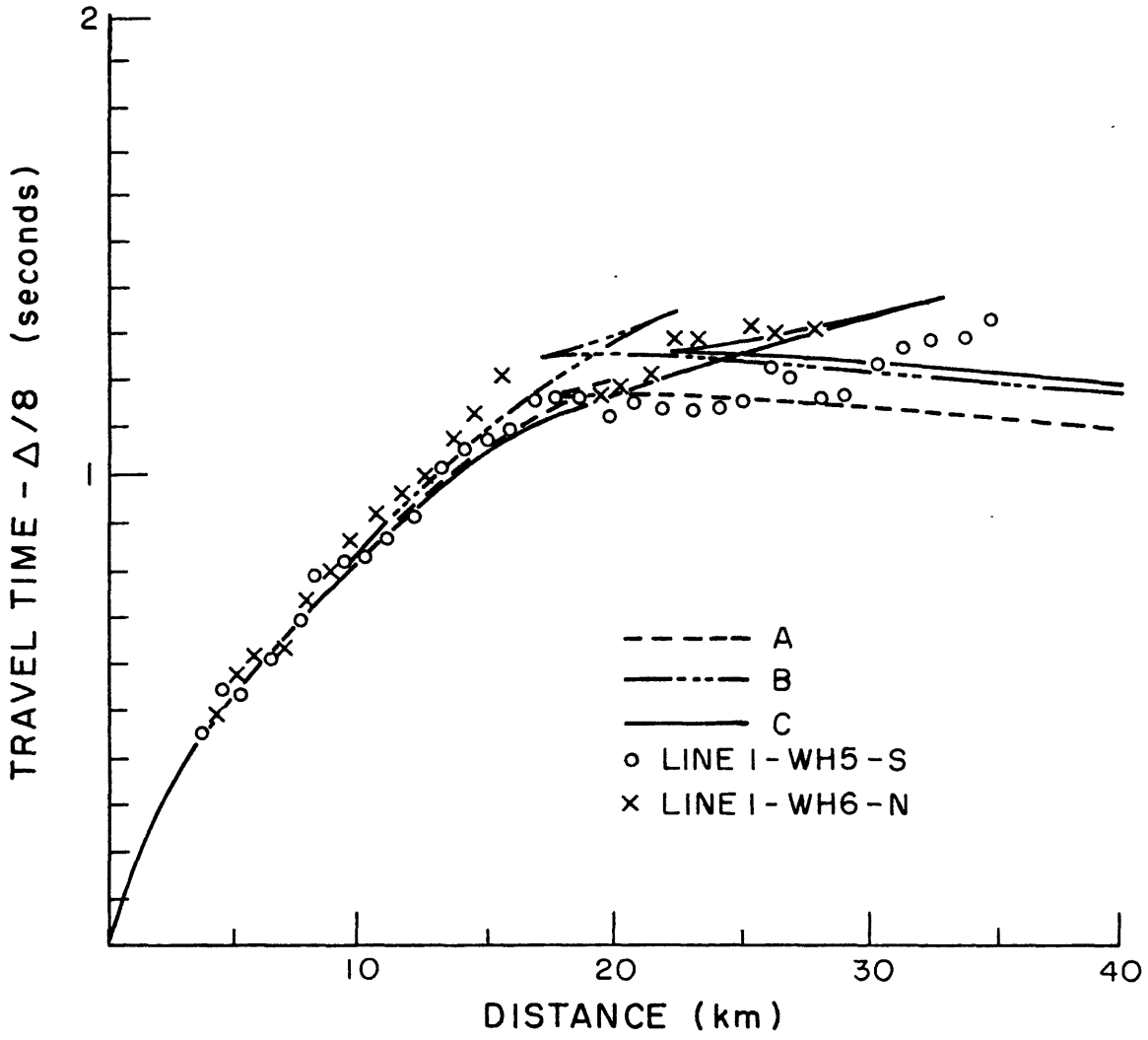
TRAVEL TIME - Δ/8 (seconds)
2
1
10
20
30
40
DISTANCE (km)
A
B
C
LINE I - WH5 - S
LINE I - WH6 - N

figure 5.22c

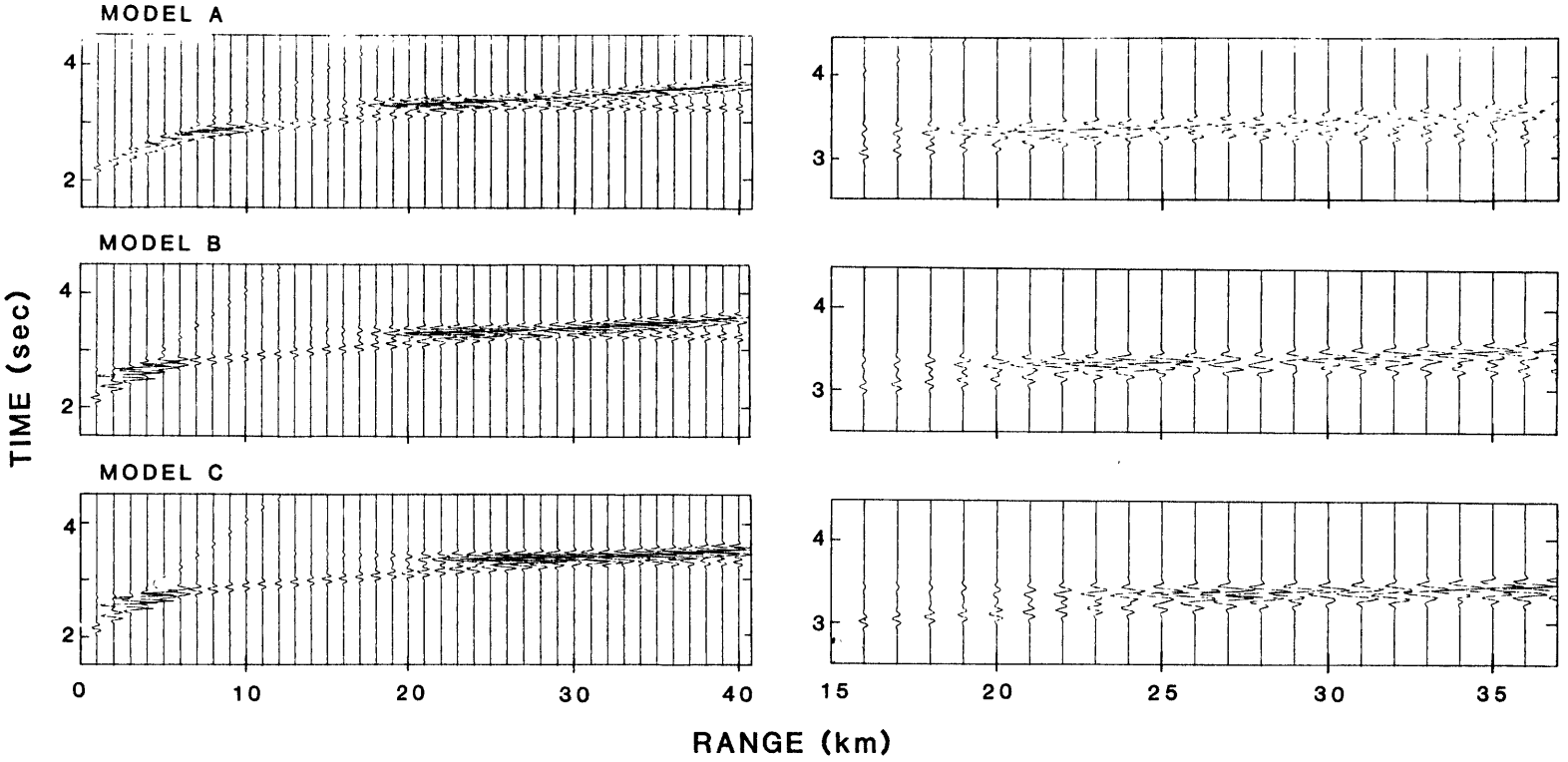
MODEL A
MODEL B
MODEL C
TIME (sec)
RANGE (km)
0
10
20
30
40
15
20
25
30
35

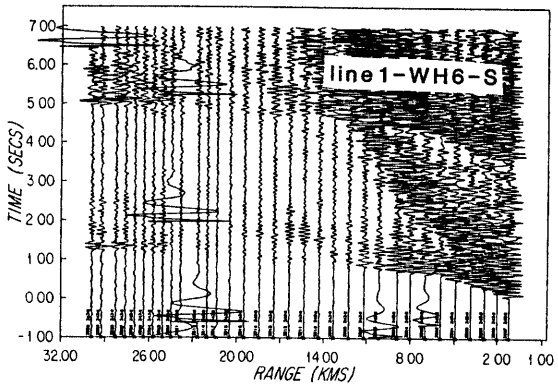
line1-WH6-S
TIME (SECS)
RANGE (KMS)

figure 5.23a

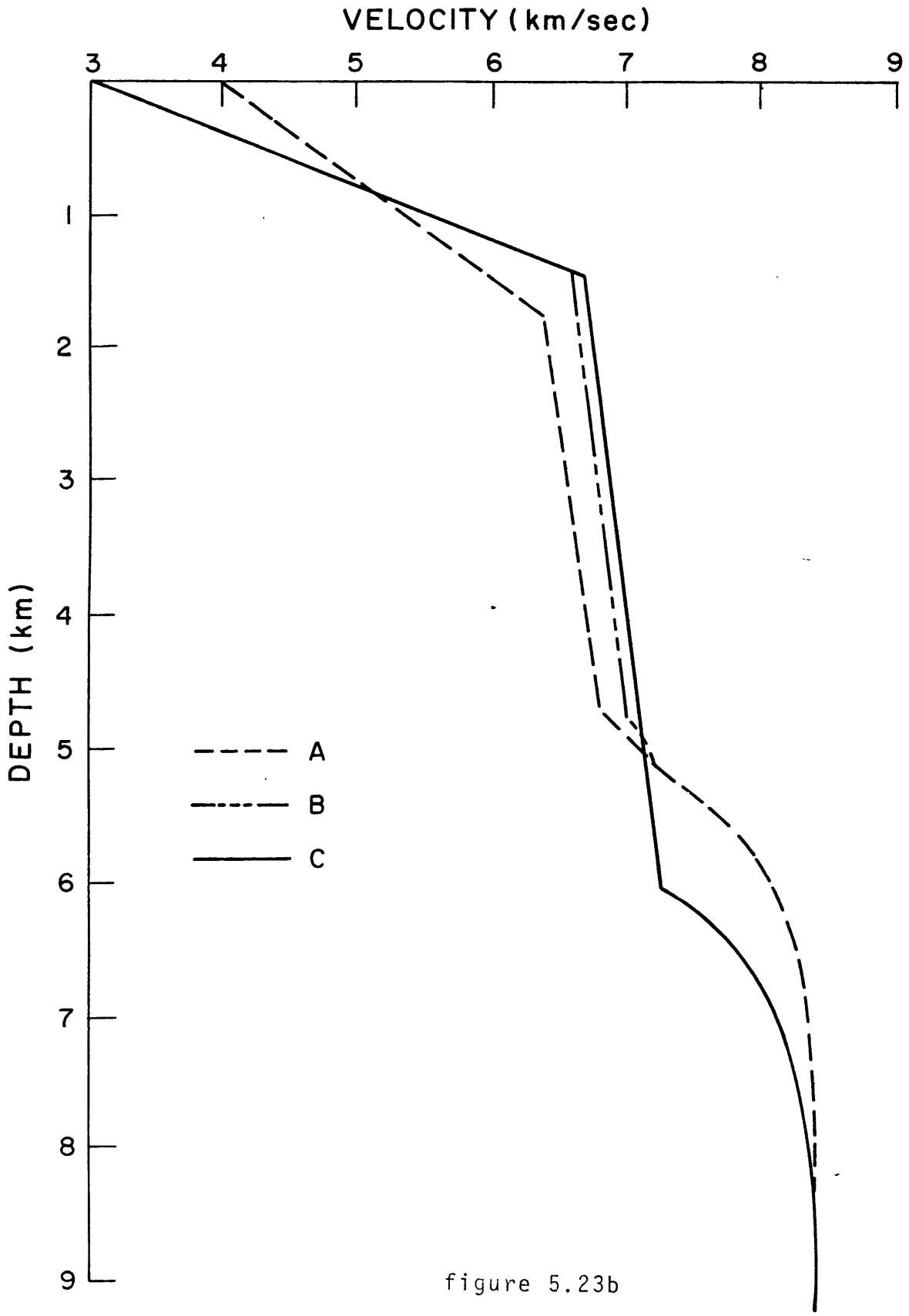

figure 5.23b

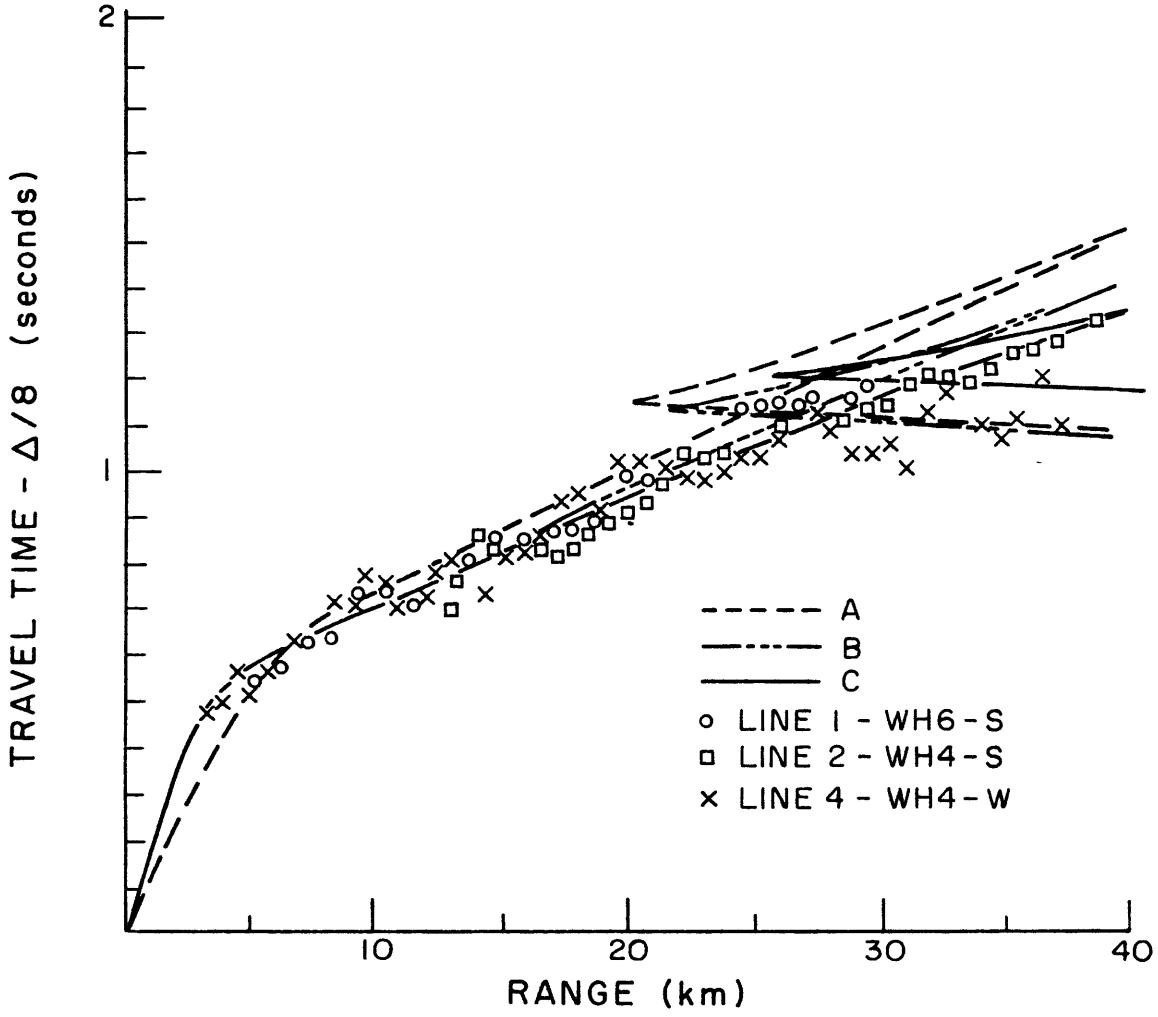
TRAVEL TIME - Δ/8 (seconds)
2
1
10
20
30
40
RANGE (km)
A
B
C
LINE 1 - WH6-S
LINE 2 - WH4-S
LINE 4 - WH4-W

figure 5.23c

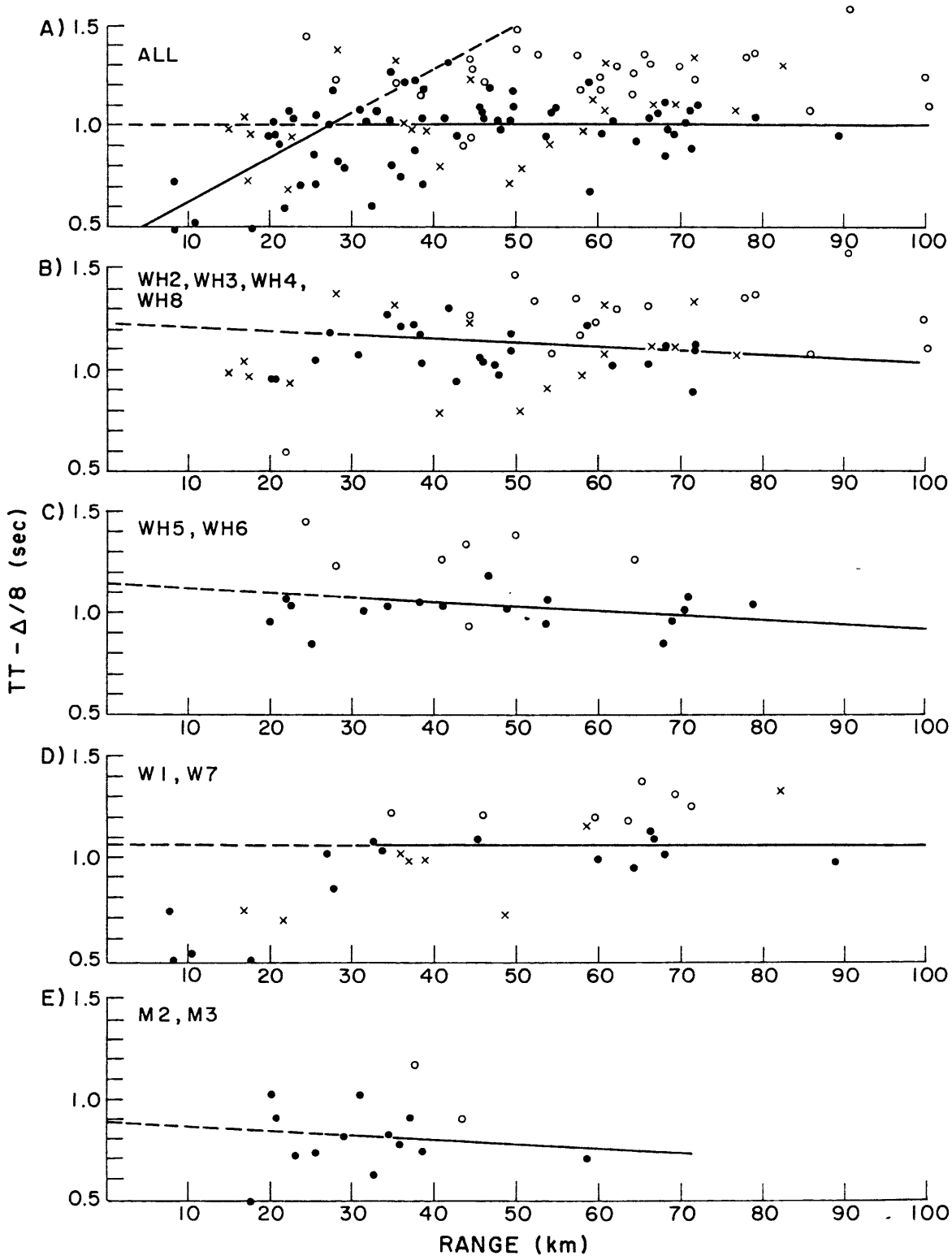
A) 1.5
ALL
1.0
0.5
10 20 30 40 50 60 70 80 90 100
B) 1.5
WH2, WH3, WH4,
WH8
1.0
0.5
10 20 30 40 50 60 70 80 90 100
C) 1.5
WH5, WH6
1.0
0.5
10 20 30 40 50 60 70 80 90 100
D) 1.5
W1, W7
1.0
0.5
10 20 30 40 50 60 70 80 90 100
E) 1.5
M2, M3
1.0
0.5
10 20 30 40 50 60 70 80 90 100
TT - Δ/8 (sec)
RANGE (km)

figure 5.24

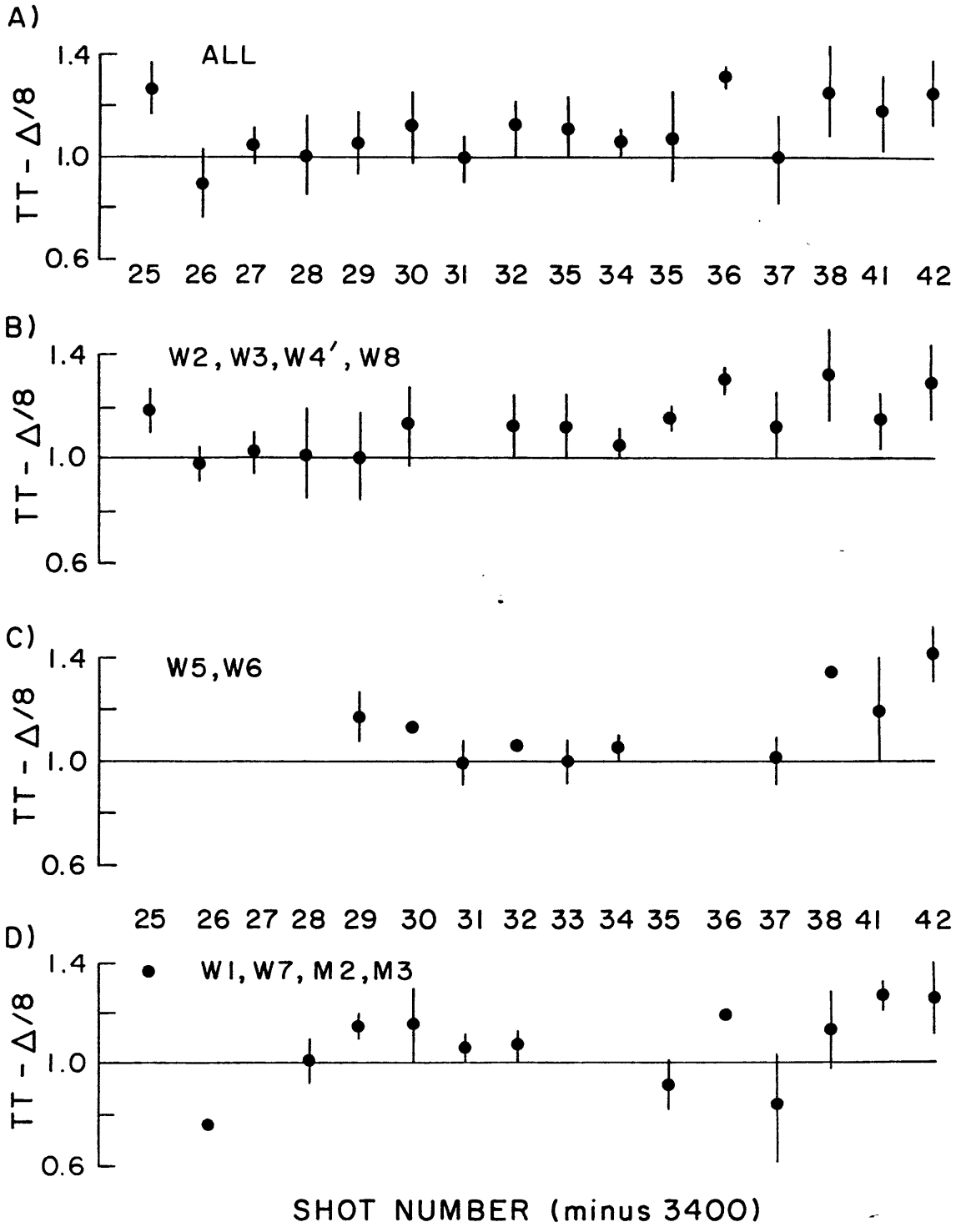
A)
ALL
B)
W2, W3, W4′, W8
C)
W5, W6
D)
W1, W7, M2, M3
TT - Δ/8
1.4
1.0
0.6
25 26 27 28 29 30 31 32 33 34 35 36 37 38 41 42
SHOT NUMBER (minus 3400)

figure 5.25

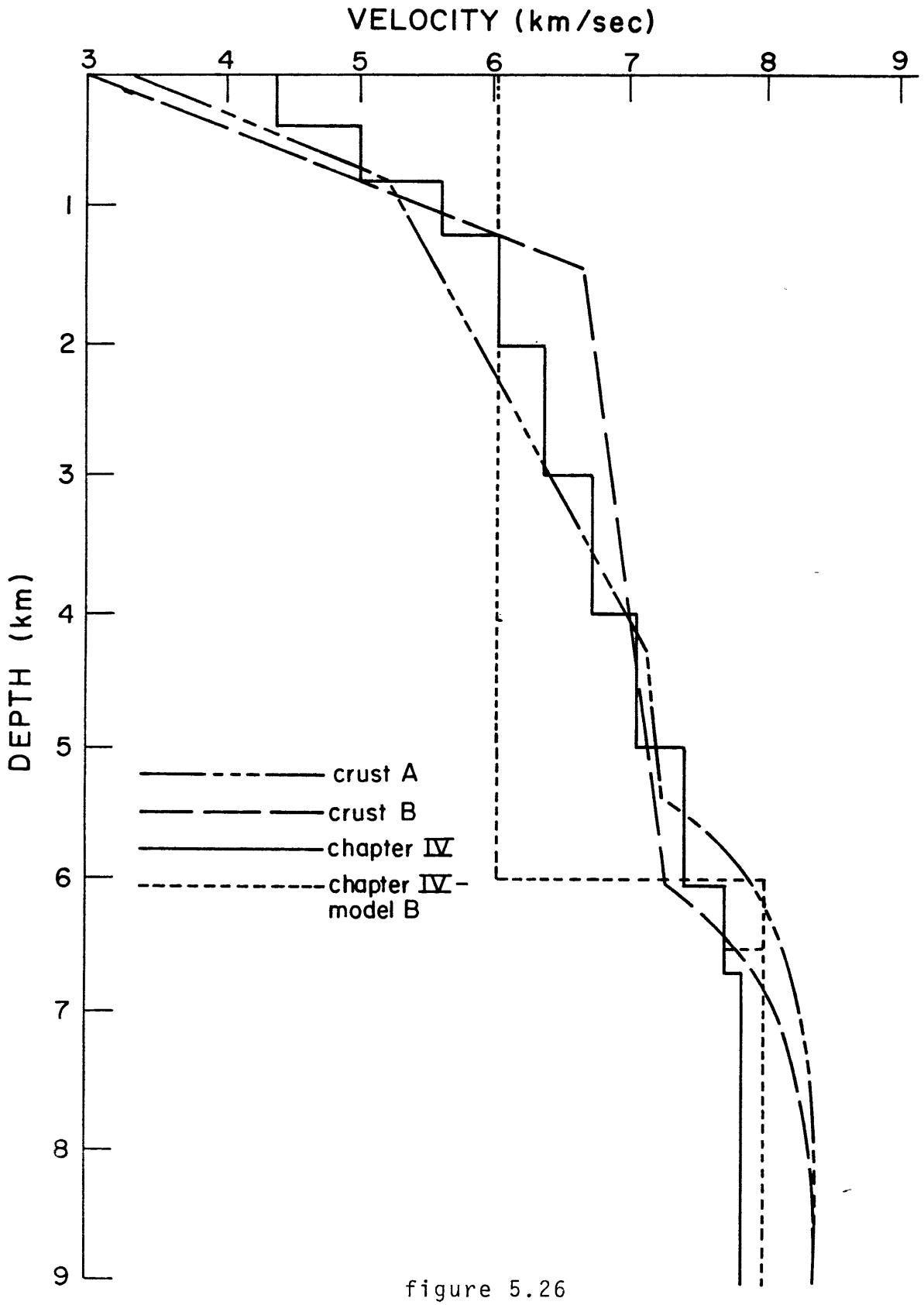
VELOCITY (km/sec)
3
4
5
6
7
8
9
DEPTH (km)
1
2
3
4
5
6
7
8
9
crust A
crust B
chapter IV
chapter IV - model B

figure 5.26

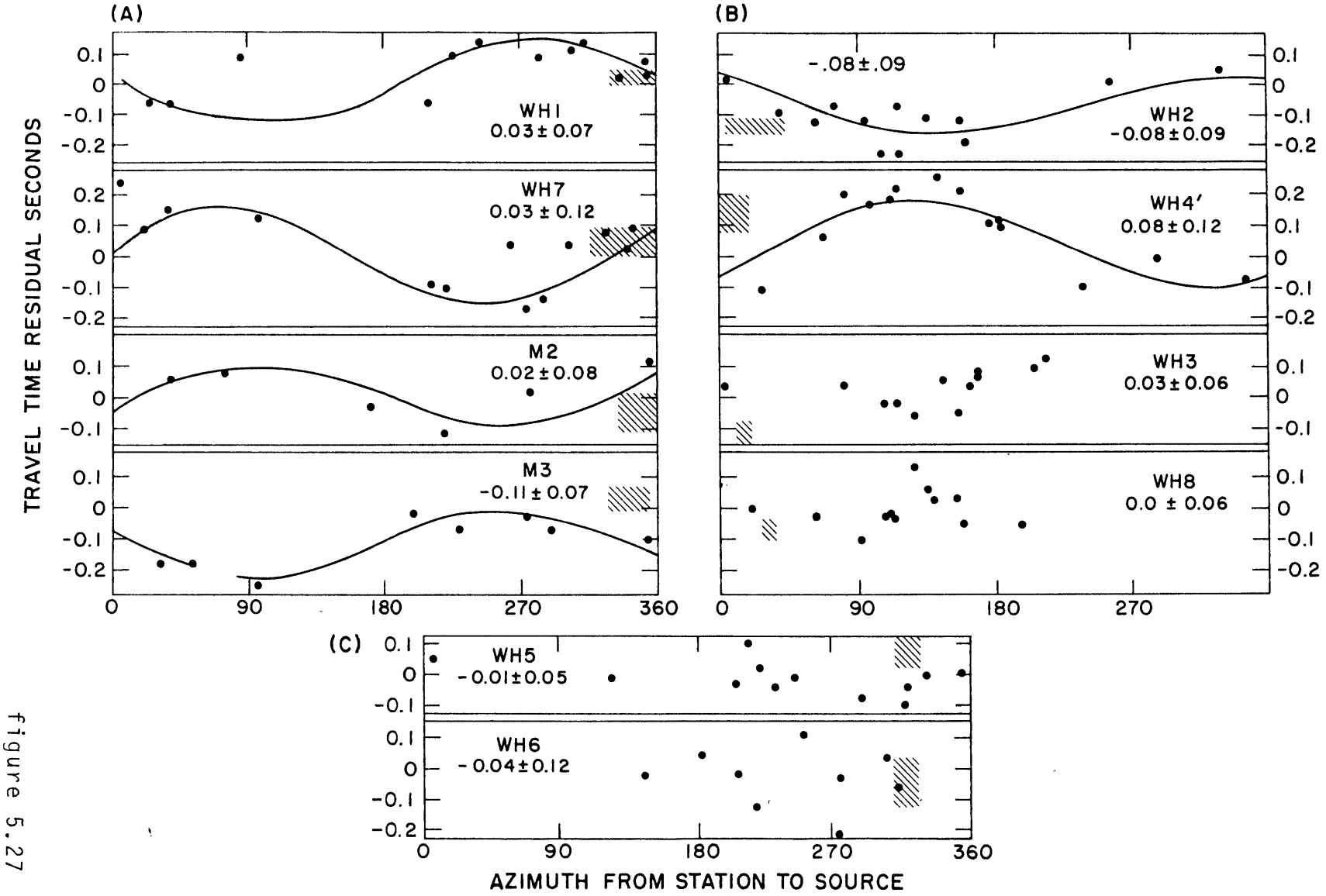
(A)
(B)
(C)
TRAVEL TIME RESIDUAL SECONDS
AZIMUTH FROM STATION TO SOURCE
WH1
0.03 ± 0.07
WH7
0.03 ± 0.12
M2
0.02 ± 0.08
M3
-0.11 ± 0.07
-.08 ± .09
WH2
-0.08 ± 0.09
WH4'
0.08 ± 0.12
WH3
0.03 ± 0.06
WH8
0.0 ± 0.06
WH5
-0.01 ± 0.05
WH6
-0.04 ± 0.12
0
90
180
270
360

figure 5.27

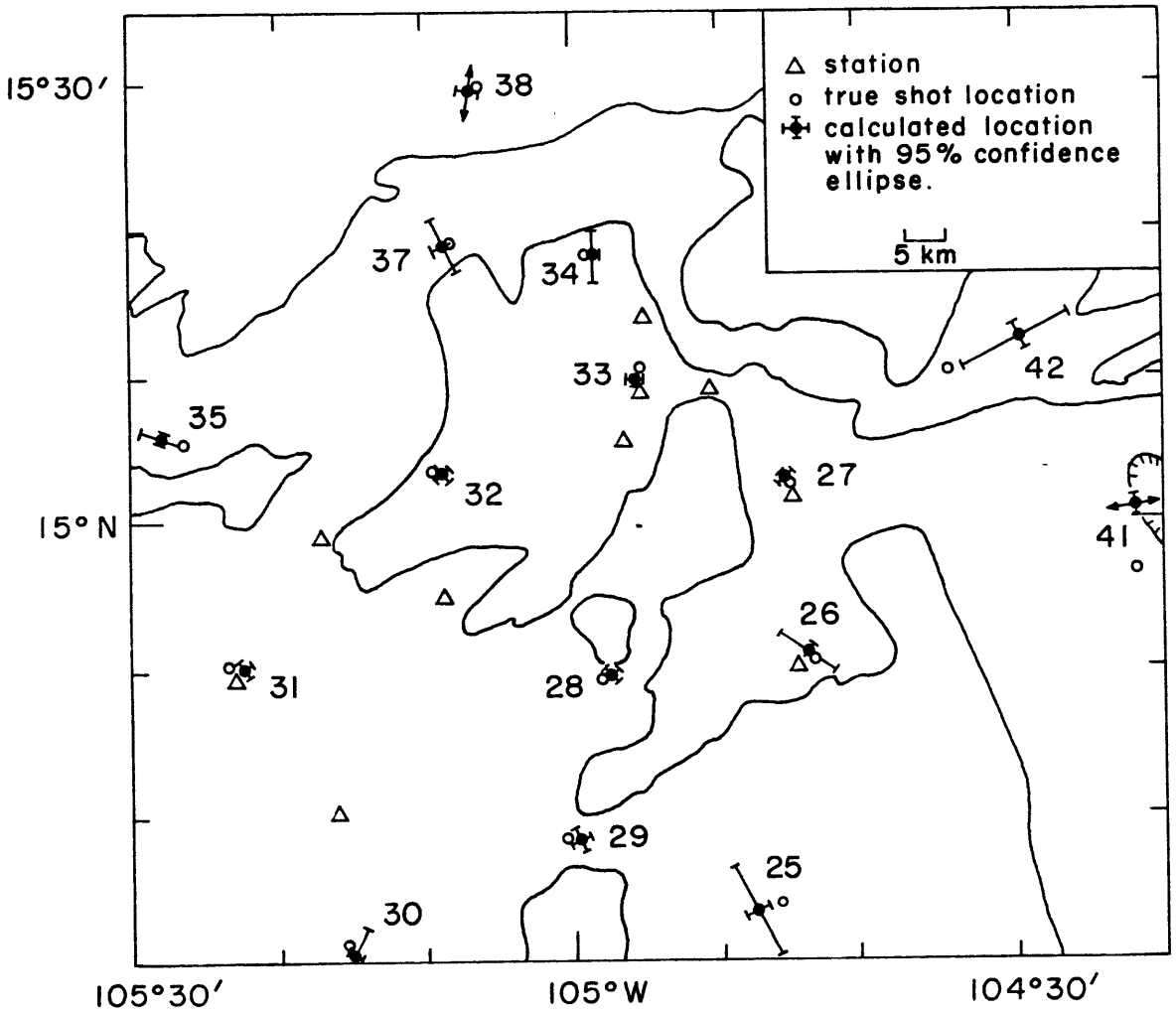
station
true shot location
calculated location with 95% confidence ellipse.
5 km
15°30′
15° N
105°30′
105°W
104°30′
38
37
34
33
42
35
32
27
41
26
31
28
29
25
30

figure 5.28

CHAPTER VI

SUMMARY, SYNTHESIS & SPECULATIONS

In this thesis, seismic waves generated by sources ranging from 2.7 kg. shots of TNT to magnitude 5 earthquakes (approximately equivalent in energy release to the 1946 atomic blast at Bikini Island; Bolt, 1978) have been studied to determine the seismic activity and crustal structure of the Orozco transform fault. The purpose of this chapter is to summarize and synthesize these diverse results into a picture of the current tectonic activity and to speculate on the history that has resulted in the present configuration.

The tectonic history of the central eastern Pacific Ocean and the bathymetric and magnetic anomaly data from the transform zone were summarized in Chapter II; the teleseismic history, as recorded by the World Wide Standard Seismograph Network (WWSSN) was also studied. That the plate tectonic configuration of the central eastern Pacific has undergone a major reorganization during the past several million years is well documented in the bathymetry and magnetic anomalies to the west of the present axis of the East Pacific Rise (Klitgord and Mammerickx, 1982). Portions of the East Pacific Rise have jumped to the east, and the Rivera-Cocos plate boundary has migrated northward. The tectonic role of the Orozco Fracture Zone has changed during this evolution. From the time of anomaly 5 to anomaly 3, it was the boundary between the Rivera and Cocos plates and offset the East Pacific Rise by hundreds of kilometers. This role is

now played by the Rivera Fracture Zone to the north, and the Orozco Fracture Zone offsets the East Pacific Rise by only 90 km.

The bathymetry of the transform portion of the Orozco Fracture Zone does not resemble that of other transform faults which have been studied in detail. Most transform faults are represented by a zone about 10 to 30 km wide containing one or two well-defined troughs oriented parallel to the spreading direction. The Orozco transform fault, on the other hand, covers an area of 90 x 90 km which includes ridges and troughs trending both parallel and perpendicular to the present regional spreading direction. The zone of disturbed topography, moreover, extends to the south parallel to the axis of the East Pacific Rise. Magnetic anomalies indicate a recent eastward shift of the spreading axis. The details of this evolution, however, cannot be resolved from the available magnetic anomaly data. The main physiographic features of the transform zone are illustrated in Figure 6.1. Questions posed are: Where is the trace of the active plate boundary as defined by the seismicity? What are the lateral and vertical dimensions of the seismic zone and what are the source mechanisms of the earthquakes? What is the origin of ridges α and β and do they represent current or relict tectonic features?

The results of the teleseismic study are consistent with those of similar studies of teleseismic earthquakes from transform faults but are not precise enough to answer the

above questions. The epicenters of teleseismic earthquakes are too scattered to delineate the active plate boundary. The average fault width, determined from the seismic moment sum, is 0.5 km but this estimate may be in error by up to an order of magnitude. A detailed study of one of the largest earthquakes (m_b = 5.1) indicates right lateral strike slip motion along a fault with a strike parallel to the spreading direction and constrains the source depth to be less than 5 km.

The transfer function between ground motion and the data recorded by the MIT OBS, including the response of the recording electronics and the coupling of the instrument to the seafloor, was determined in Chapter III. This information is required for further study of the waveforms recorded by these instruments.

Hypocentral coordinates of 70 microearthquakes recorded by the 29 station ROSE network in the Orozco Fracture Zone were determined in Chapter IV. This represents 85% of the events for which 4 or more arrival time readings were available. The locations were calculated on the basis of an assumed laterally homogeneous velocity structure which was adapted from the results of several seismic refraction profiles obtained during previous experiments in the region. The 95% confidence ellipsoids of the solutions indicate that most of the epicenters are precise to within at least 2 km given the assumed velocity model; the error on the depths are slightly larger. The effect on the locations of changes in

the layered velocity model are, in general, less than 1 km.

The epicenters are shown superimposed on the bathymetry in Figure 6.2 and clearly define the active plate boundary. Squares denote earthquakes located with at least 10 readings; dots denote fewer than 10 readings. This provides a rough estimate of relative size. Moments of the larger events, derived from the spectra of waveforms recorded by the MIT OBS, range over more than three orders of magnitude with largest being at least 2.3×10^{20} dyne cm.

All but one of the earthquakes lie within the transform portion of Orozco Fracture Zone. About half are aligned along trough A which is a narrow, deep trough striking parallel to the spreading direction and defines the northern boundary of the transform zone (referred to as region 1). The other epicenters, along trough B and ridge β' (region 2), are not obviously related to topographic features. No activity was located in trough C; the apparent absence of seismic activity in this region is supported by the observation at stations in or near the trough that the arrival time difference between P and S waves for the closest events recorded corresponds to sources in region B. No earthquakes were located at the eastern end of trough B near the intersection with East Pacific Rise; a station located in this region, however, detected many close events which were probably too small to be detected throughout the network.

The temporal-spatial sequence of activity in region 1 is shown in Figure 6.3. During the first few days, activity

occurred at both ends of the trough. This was followed by several days with very little activity which was terminated on March 8 by a mainshock-aftershock sequence near 105°6'W which broke a portion of the fault which had previously been quiet. The mainshock of this sequence is the largest earthquake of the experiment and represents over half of the total moment. An eastward migration of the aftershocks with time along what may be a single fault plane can be resolved. A "seismic gap" preceeding this sequence is observed even for earthquakes so small that they were recorded at only a single station and for which locations were estimated from the P-S arrival time difference. All but three of the earthquakes in region 1 show first motion radiation patterns compatible with right lateral strike slip motion along a steeply dipping fault parallel to trough A.

Most of the earthquakes in region 1 were very shallow (<4 km). The decrease in depth as the rise-transform intersection is approached which is predicted by simple thermal models of spreading centers, however, is not observed. In fact, the deepest hypocenters, observed for a sequence of events near 105°12'W, are within 10 km of the rise-transform intersection and the focal depths of 4 to 7 km appear to be well determined. This contrasts with depths of less than 2 km for most of the earthquakes in the mainshock-aftershock sequence. The apparent depth difference is supported by the waveforms observed at the MIT OBS M2 and M3. For events near 105°6'W, a clear P_n arrival is observed

as the first arrival, and the arrival time difference between P_n and the direct arrival constrains the mainshock and the four largest aftershocks to be at essentially the same depth. First arrivals from events near 105°0'W also show P_n character. P waves from earthquakes near 105°12'W, however, have simple, impulsive waveforms indicating a source below the Moho. This observation suggests that the Moho is shallower than about 4 km near the rise-transform intersection; moreover, it requires that the rock at this depth be cool enough to generate earthquakes with moments of about 10^{19} dyne cm.

These results on the seismicity in region 1 are not affected by the lateral velocity heterogeneities found in Chapter V.

In Figure 6.4, the temporal-spatial sequence of activity in region 2 is shown. Except for recurrent activity near 15°12'N, 104°47'W, no systematic pattern is observed and apparent depths are scattered from 0 to 15 km. Also note the marked difference in topographic character between trough A and trough B. The first motion radiation patterns for these events plotted relative to a laterally homogeneous model cannot be interpreted in terms of double couple fault plane solutions. Inconsistencies are also observed between locations calculated primarily from P wave arrivals and S-P arrival time differences observed at stations M2, M3 and T13. The questions that arise are: What is the nature of earthquakes beneath ridge β'? Are the source mechanisms

truly anomalous or is our assumption of lateral homogeneity at fault? What is the cause of the apparent S wave delays? These questions can be tentatively answered by the results of Chapter V.

Various aspects of the crustal structure in the tranform were determined in Chapter V. Incident angles and azimuths observed at station M2 from natural and explosive sources, lines of small charges shot to WHOI OBH, and 500 lb shots of TNT recorded by WHOI and MIT instruments provided data for this study. The results from the three data sets are mutually consistent and are summarized in Figure 6.5. The upper mantle velocity is 8 to 8.13 km/sec throughout much of the transform region; the crust under ridge β (and inferred, by symmetry, under ridge α) is anomalous compared to the "normal oceanic crust" in the region; and a low velocity zone, perhaps a magma chamber, is suggested near the western end of trough B.

Wave propagation directions observed at station M2 from both earthquake and explosive sources to the north, west and south show a systematic deflection relative to the angles expected for a laterally homogeneous crust. The azimuthal deflection varies with geographic azimuth while the angles of incidence are consistently around 40°. Sources in the central transform (region 2) have small incident angles and the azimuths are deflected to such a degree that they actually appear to arrive from the west. Several factors affecting the observed angles are discussed and we conclude

that at least some of the deflection must be caused by lateral velocity gradients in the transform region. Geologically reasonable structures which might explain the observations are examined by tracing rays with endpoints fixed at the source and receiver through three dimensional velocity grids.

To explain the observations from the north, west, and south, the final model has high velocities in the upper mantle below ridge α to the west of M2. Geologically, this model is compatible with a Moho which approximately follows the topographic contours. To model the general features of the observations from the central transform, a region of low velocities simulating a magma chamber is required between the sources and the receivers. We cannot, however, resolve the detailed geometry and lateral extent of this proposed body from the available data.

By calculating synthetic travel time data from sources in regions 1 and 2 to points corresponding to stations in the ROSE network, we can qualitatively evaluate the effect of the proposed structures on the hypocenter and fault plane solutions calculated relative to a laterally homogeneous structure. Results from region 1 are not significantly affected. In region 2, however, hypocentral mislocations of up to 10 km are induced. In particular, an 8 km deep "source" along the northern edge of trough B appears to be under ridge β' at a depth of 17 km, near the apparent hypocenter of one of the largest events from ROSE. The

"relocation" of a 500 lb shot in trough B from travel times recorded by MIT and WHOI instruments also shows a similar mislocation. Because the ray paths are 8 to 15% longer than for a laterally homogeneous model, this structure is consistent with the observed delay of S waves relative to P waves observed at M2 and M3. Model fault plane solutions, corrected for the distortions of the azimuths and take-off angles induced by the low velocity zone, suggest that the perplexing observations from earthquakes in region 2 might actually represent normal faulting with a component of right lateral strike slip along NW striking planes. That the low velocity region deduced from the observed incident angles and azimuths provides answers to the questions posed by the locations calculated with a laterally homogeneous model is circumstantial evidence supporting the validity of the model.

Two distinct crustal types were determined from the refraction profiles recorded on the WHOI OBH. For the relatively smooth crust characteristic of that formed at fast spreading rises, a structure typical of oceanic crust throughout the world's oceans is found from 3 different, unreversed profiles. A 1.5 km thick layer in which velocity increases from 3 to 6.7 km/sec overlies a thick layer with nearly constant velocity of about 6.8 km/sec. Modeling of the amplitude pattern of the Moho triplication point constrains this layer to be about 4.5 km thick with a total crustal thickness of 6 km.

A reversed profile under ridge β, on the other hand, indicates a velocity gradient of 0.5 sec^{-1} throughout most of the crust (from 5.25 km/sec to 7.15 km/sec over 3.5 km). This gradient decreases to about 0.1 km/sec at the base of the crust. A thin, high gradient layer must exist in the upper few hundred meters to satisfy the travel time data. Modeling of the amplitudes at the Moho triplication point constrains the crustal thickness to be about 5.4 km. Because of the topographic similarity of ridges α and β, this anomalous structure is also inferred for ridge α.

The upper mantle velocity of 8 to 8.13 km/sec is determined from the travel times of large shots to MIT and WHOI instruments. No difference can be resolved between the upper mantle velocity beneath the "anomalous" crust of ridges α and β and that beneath "normal oceanic crust". Delays are observed for shots crossing troughs A and B but the data are too sparse to provide quantitative constraints on the structure. No delays are observed for shots crossing beneath trough C. The intercept times support the inference from the other two data sets that the crust under ridges α and β is no thicker, and is possibly thinner, than that beneath "normal oceanic crust".

Although we must remember that a mere two week sample of seismicity may be significantly biased, we conclude from the results presented above that the actual plate boundary in the Orozco transform fault extends along trough A from the East Pacific Rise to 15°25'N, 104°55'W with a strike of 080°,

changes to a north-south strike until 15°15'N, 104°50'W, and then continues along trough B with a strike of 290° until it reaches the East Pacific Rise at 15°7'N, 105°30'W. The band of seismicity along trough A indicates that the instantaneous plate boundary is less than 3 km wide. In contrast to results from other studies of seismicity at ridge-transform intersections, the seismic zone does not appear to widen near the intersection; nor does the depth of the trough increase. No earthquakes were detected along the north-south section which must, by this interpretation, be a 20 km long spreading center. This is consistent with results from other studies which find that transform faults are more active seismically than spreading centers, particularly at intermediate to fast spreading rates. Seismicity resumes along trough B which must be either a series of short ridge and transform sections or an oblique spreading center. The tentative interpretation of normal faulting with a component of right lateral strike-slip motion suggests a configuration intermediate between these two extremes. For example, the narrow section of trough B near 15°11'N, 104°46'W may be a zone of oblique shear which joins two small spreading basins and along which earthquakes are concentrated. The absence of seismicity, even to the lowest level detectable by a single instrument, associated with trough C and ridges α and β over the two-week period of ROSE is insufficient evidence to justify discounting this system as an active tectonic element. The absence of any upper mantle velocity anomaly below C, however, supports the

inference that these are relict features.

The present configuration, however, cannot have existed for more than a few hundred thousand years because, closing the seafloor along this boundary, one soon encounters topographic obstacles. Figure 6.6a shows an estimate of the extent of crust formed at the present boundary in the past 700,000 years (the width of the central anomaly). This figure suggests that before this time trough C represented the axial valley of the spreading center (Figure 6.6b). The apparent rotation of trough C and ridges α and β and the pinching out of anomalies J and 2 (and perhaps also the central anomaly) on the east flank of the present rise axis from 12 to 15^{o}N suggest a "propagating rift" (Hey et al., 1980) mode of transferring the locus of spreading. More detailed bathymetric and magnetic anomaly data are required before the timing of the process can be resolved.

A possible explanation for the anomalous velocity structure under ridge β is that hydrothermal circulation penetrated more deeply into the crust as spreading became slower, and that the continuous velocity gradient reflects cracking and hydrothermal alteration which extend through almost the entire crust. Alternatively, the similarity of topographic profiles across ridges α and β to those across the East Pacific Rise from 15^{o}30'N to 16^{o}N, where the rise is anomalously shallow and rough (for a topographic wavelength of several kilometers) for a moderately fast spreading center, suggests that the topography may at least partly

reflect a regional chemical anomaly in the upper mantle. More data, measuring a range of geological, geophysical and geochemical parameters, are required before this hypothesis can be evaluated.

The northern part of the Orozco Fracture Zone shows a topographic pattern characteristic of the "finite width" transform faults described by Schouten et al. (1980). The features of their model are summarized in Figure 6.7. Although the active transform fault is only a few kilometers wide on a human time scale, in a "steady state" time frame of thousands of years, the transform migrates back and forth across a zone 10 to 30 kilometers wide.

In conclusion, the second phase of project ROSE has provided a data set which is valuable for a number of reasons. The size of the ROSE network has permitted hypocentral parameters and source mechanisms of microearthquakes to be determined with a precision unprecedented in marine microseismic work. Because of the complexity of the Orozco transform fault, a variety of tectonic elements within the general spreading center-transform fault environment has been sampled. The refraction data collected in the region have complemented the study of the microearthquakes by providing additional control on the crustal and upper mantle velocity structure. Comparison of different instruments, both during ROSE and during preliminary tests, has led to a better understanding of some of the problems which have plagued OBS studies in the past.

FIGURE CAPTIONS

6.1 Physiographic features of the Orozco Fracture Zone (see figure caption 2.4).

6.2 Epicenters of earthquakes located in the Orozco Fracture Zone during project ROSE.

6.3 Seismic activity in region 1 (see figure caption 4.7).

6.4 Seismic activity in region 2 (see figure caption 4.17).

6.5 Summary of the information on crustal structure in the Orozco transform fault region determined in Chapter V.

6.6 a. Present location of the Pacific-Cocos plate boundary in the region of the Orozco transform fault.

b. Proposed plate boundary 700,000 years ago.

6.7 "Steady-state" geometry of a finite width transform zone that offsets two spreading centers (heavy double lines). This geometry has been calculated for strike-slip transform fault activity that is normally distributed about the median axis of the transform zone with standard deviation σ. The numbered ioschrons illustrate the asymmetric evolution of the seafloor in a finite-width transform zone. Note the mixed-age isochrons in the inactive parts of the transform. Hachures indicate seafloor with transform deformation history (from Schouten et al., 1980).

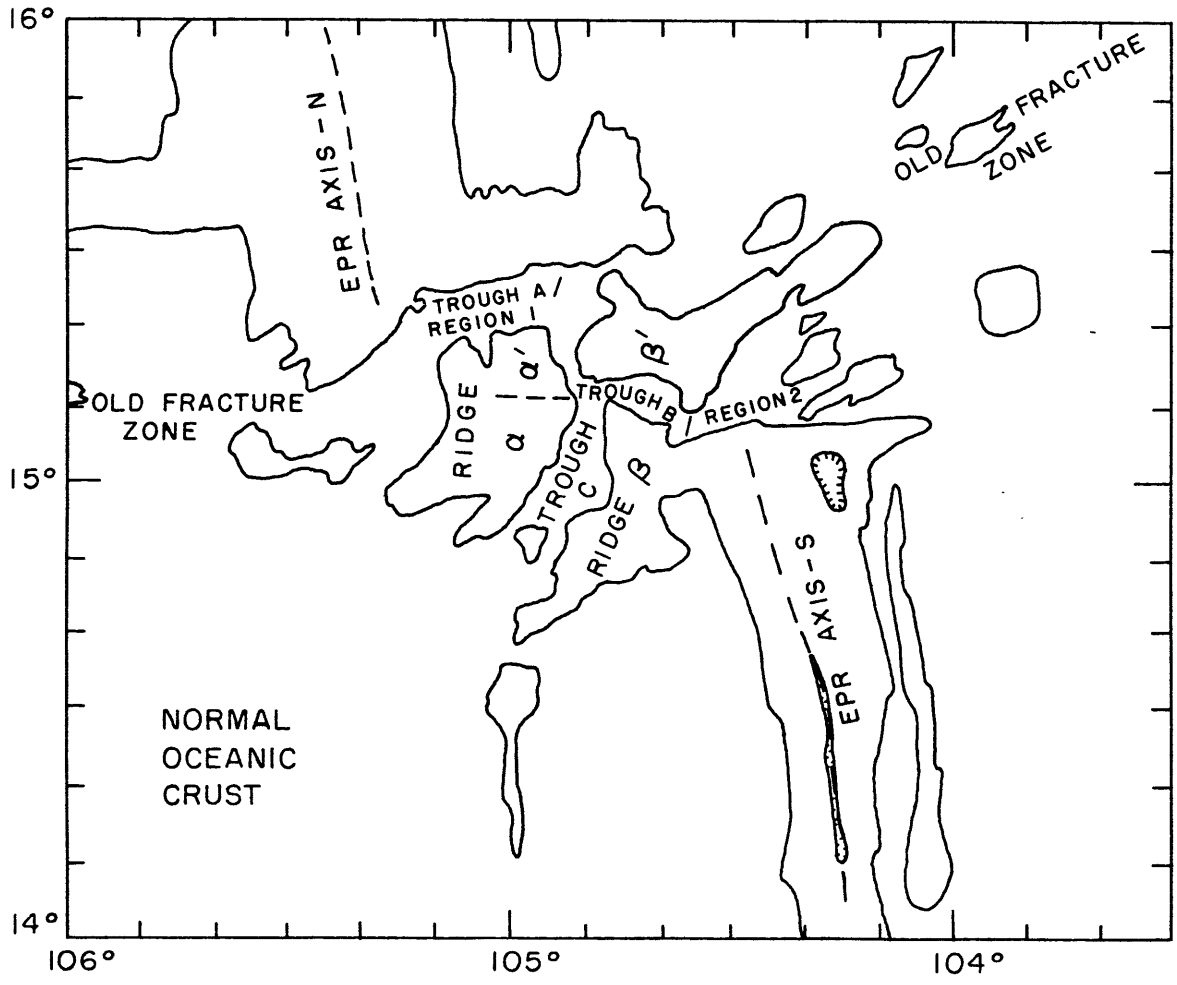
16°
15°
14°
106°
105°
104°
EPR AXIS-N
OLD FRACTURE ZONE
TROUGH A / REGION 1
RIDGE α
α'
β'
TROUGH B / REGION 2
TROUGH C
RIDGE β
EPR AXIS-S
OLD FRACTURE ZONE
NORMAL OCEANIC CRUST

figure 6.1

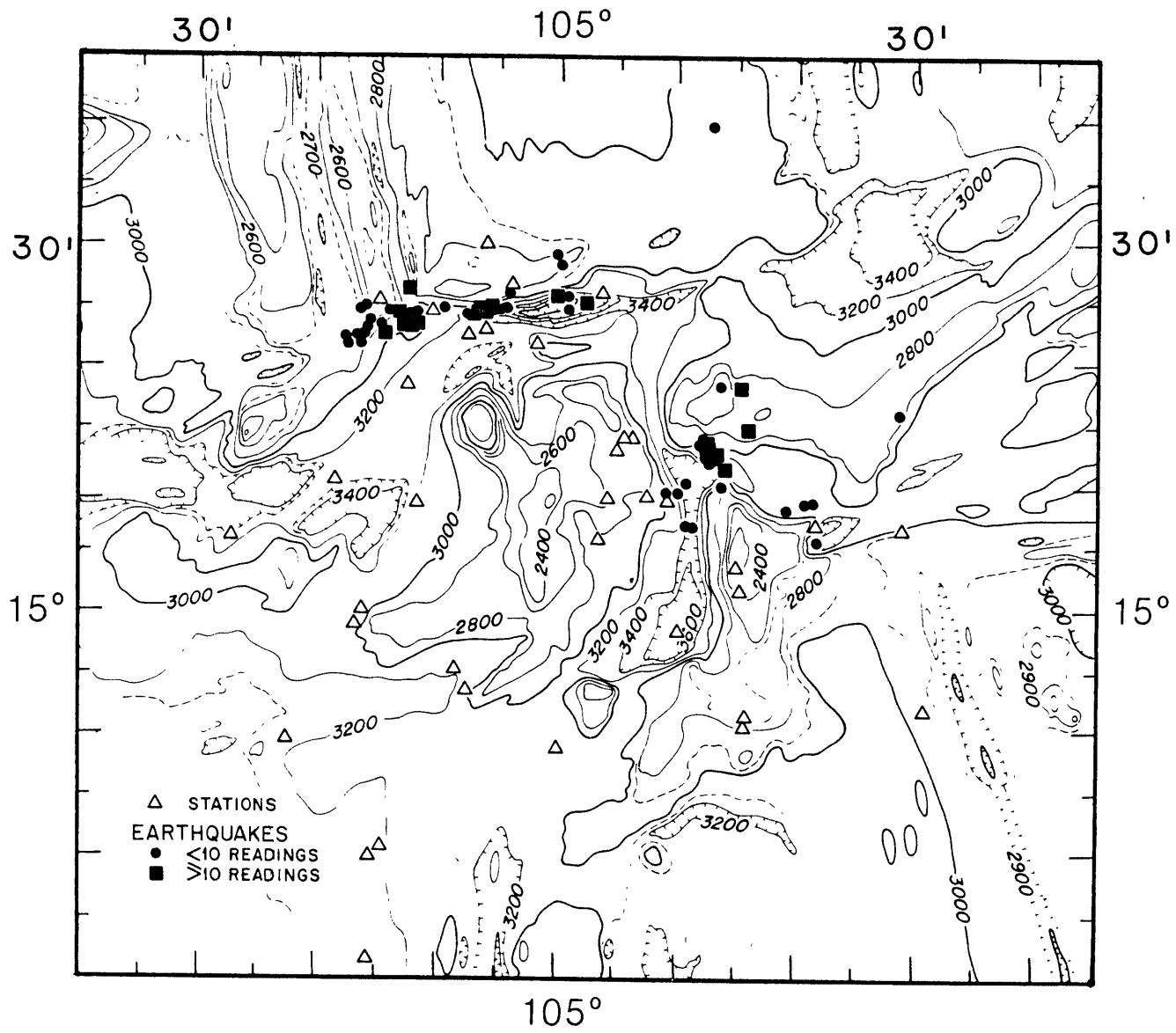
30'
105°
30'
30'
15°
15°
105°
STATIONS
EARTHQUAKES
≤10 READINGS
≥10 READINGS

figure 6.2

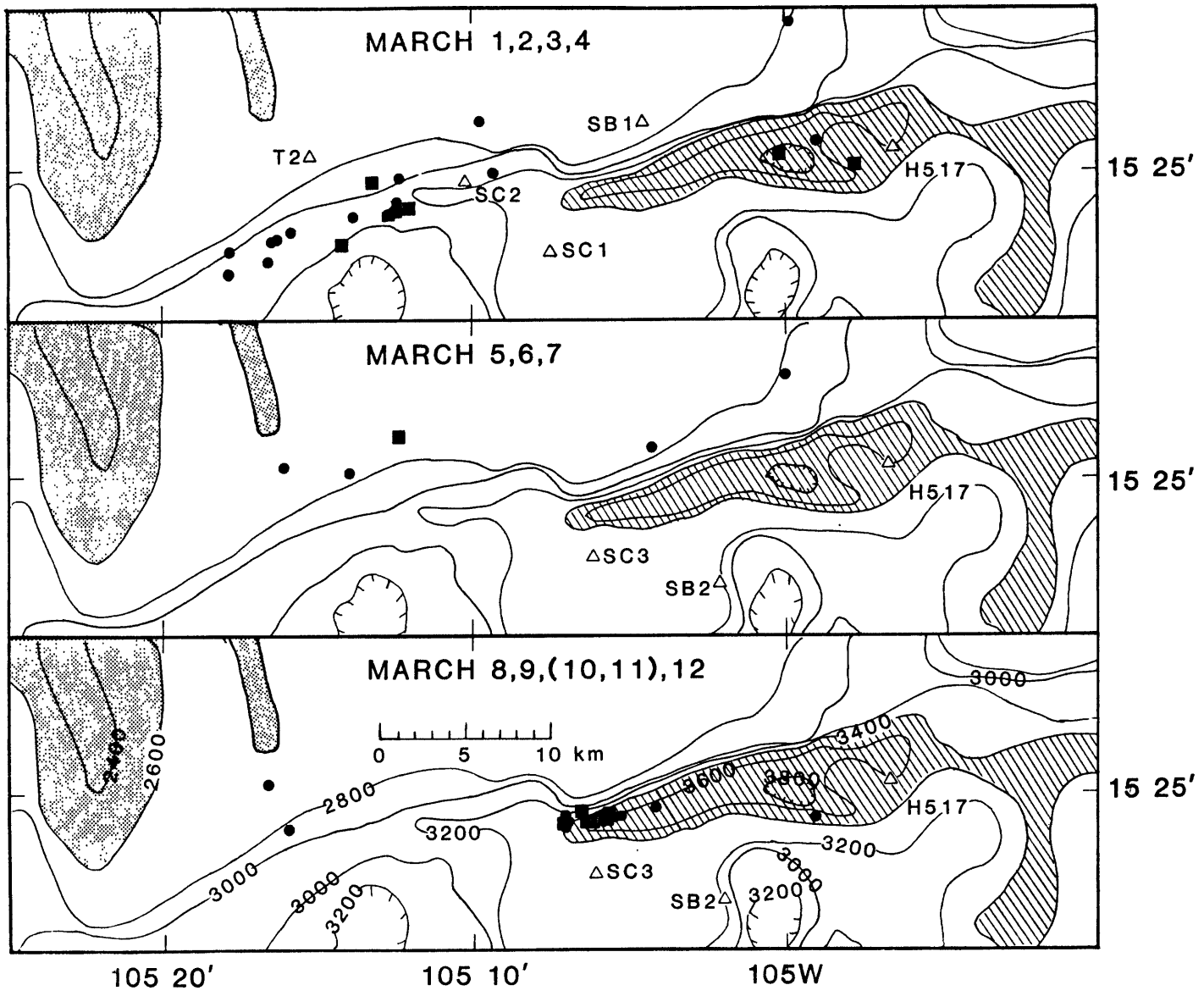
MARCH 1,2,3,4
SB1
T2
SC2
SC1
H5.17
15 25′
MARCH 5,6,7
H5.17
SC3
SB2
15 25′
MARCH 8,9,(10,11),12
3000
0
5
10 km
2400
2600
2800
3000
3200
3400
3600
H5.17
SC3
SB2
15 25′
105 20′
105 10′
105W

figure 6.3

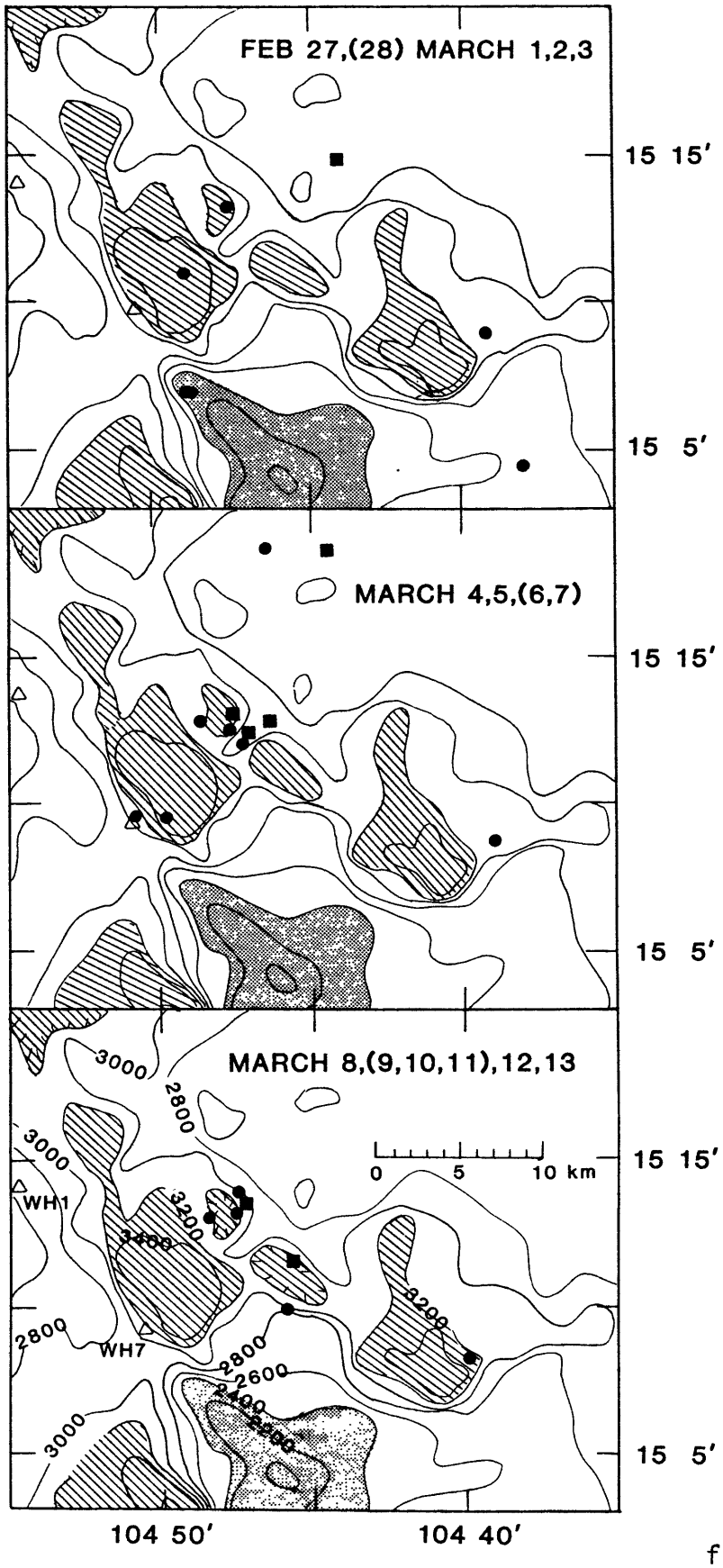
FEB 27,(28) MARCH 1,2,3
MARCH 4,5,(6,7)
MARCH 8,(9,10,11),12,13
15 15′
15 5′
0 5 10 km
3000
2800
3200
3400
WH1
WH7
2600
104 50′
104 40′

figure 6.4

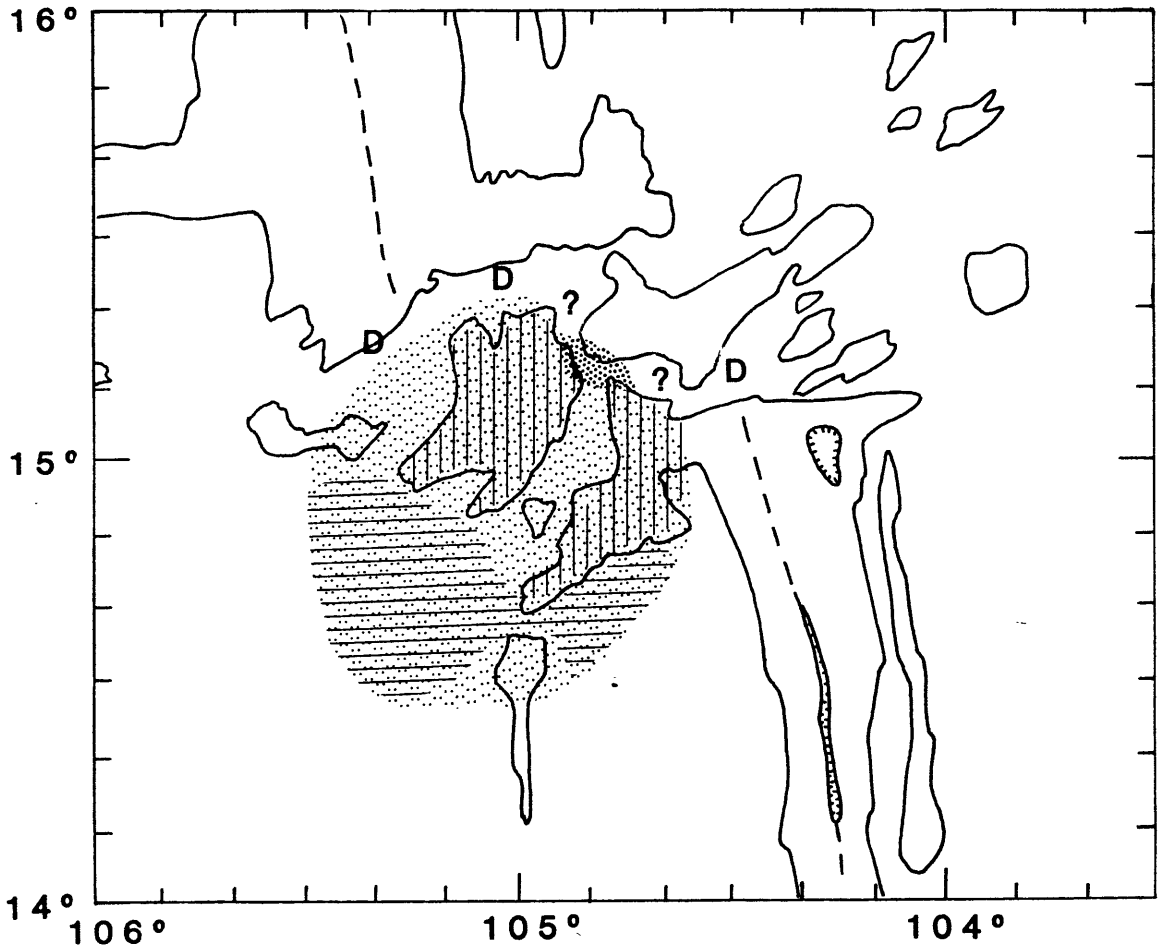
16°
15°
14°
106°
105°
104°
D
D
?
?
D
low velocity body
crustal type B
crustal type A
upper mantle velocity - 8-8.13 km/sec
D travel time delay

figure 6.5

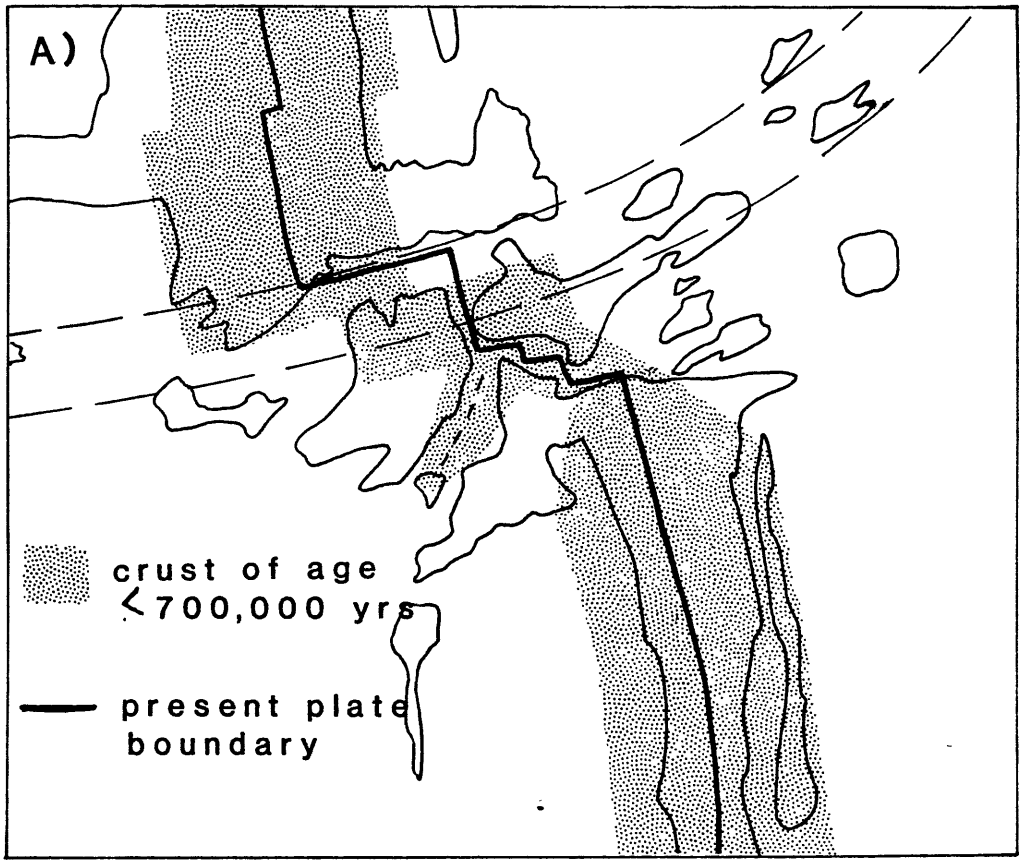
A)
crust of age
< 700,000 yrs
present plate
boundary

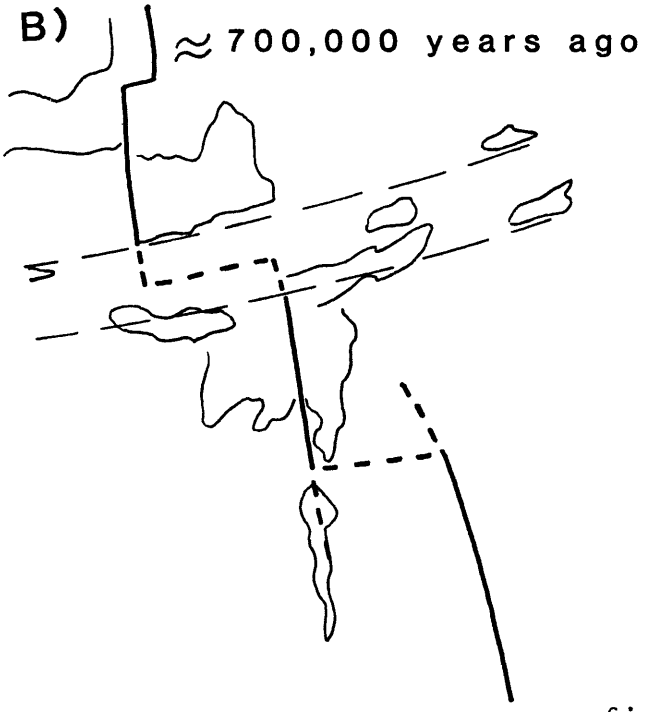
B)
≈ 700,000 years ago

figure 6.6

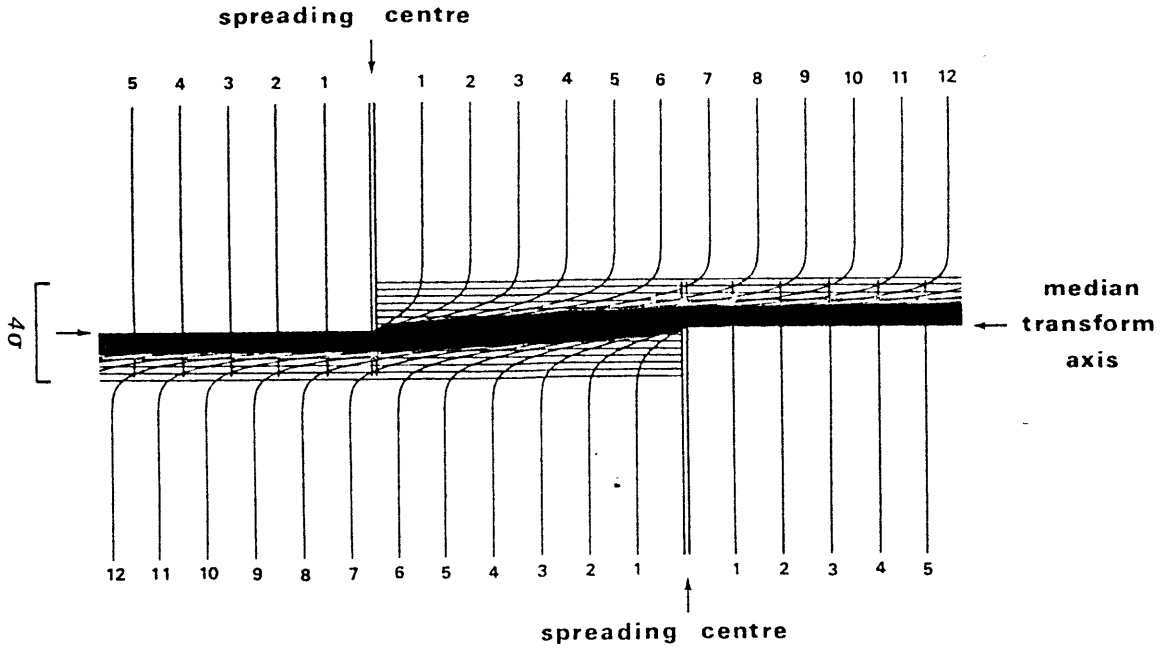
spreading centre
5 4 3 2 1
1 2 3 4 5 6 7 8 9 10 11 12
4σ
median
transform
axis
12 11 10 9 8 7 6 5 4 3 2 1
1 2 3 4 5
spreading centre

figure 6.7

REFERENCES

Aki, K., Generation and propagation of G waves from the Niigata earthquake of June 16, 1964, Bull. Earthquake Res. Inst., Tokyo Univ., 44, 23-88, 1966.

Aki, K., Scaling law of seismic spectrum, J. Geophys. Res., 72, 1217-1231, 1967.

Aki, K., Scaling law of earthquake source time-function, Geophys. J., 31, 3-25, 1972.

Aki, K., Attenuation of shear waves in the lithosphere for frequencies from 0.05 to 25 Hz., Phys. Earth Plan. Int., 21, 50-60, 1980.

Aki, K. and P.G. Richards, Quantitative Seismology: Theory and Methods, W.H. Freeman and Co., San Francisco, CA, 1980.

Barash, T., A dissolvable link release mechanism, Exposure: a newsletter for ocean technologists, 8, 1-5, 1980.

Bessonova, E.N., V.M. Fishman, V.Z. Ryaboyi and G.A. Sitnikova, The tau method for inversion of travel times - I, deep seismic sounding data, Geophys. J.R. astr. Soc., 36, 377-398, 1974.

Bibee, L.D., Crustal structure beneath mid-ocean ridges, paper presented at A.G.U. Chapman conference on the generation of the oceanic lithosphere, April, 1981.

Bolt, B.A., Earthquakes: A Primer, W.H. Freeman and Co., San Francisco, CA, 241 pp., 1978.

Bookbinder, R.G., A.C. Hubbard, W.G. MacDonald, and P.W. Pomeroy, Design of an ocean bottom seismometer with response from 25 Hz to 100 sec, Proc. 4th Ann. Conf.: Oceans 78, Marine Technology/IEEE, 510-515, 1978.

Brune, J.N., Seismic moment, seismicity and rate of slip along major fault zones, J. Geophys. Res., 73, 777-784, 1968.

Brune, J.N., Tectonic stress and the spectra of seismic shear waves from earthquakes, J. Geophys. Res., 75, 4997-5009, 1970; correction: J. Geophys. Res., 76, 5002, 1971.

Brune, J.N., R.J. Archuleta and S. Hartzell, Far-field S-wave spectra, corner frequencies and pulse shapes, J. Geophys. Res., 84, 2262-2272, 1979.

Burr, N.C. and S.C. Solomon, The relationship of source parameters of oceanic transform earthquakes to plate velocity and transform length, J. Geophys. Res., 83, 1193-1205, 1978.

Buskirk, R.E., C. Frohlich, G.V. Latham, and J. Lawton, Evidence that biological activity affects ocean bottom seismograph recordings (abstract), Trans. Am. Geophys. Un., 61, 309, 1980.

Byrd, R.C., A laboratory study of the fluid-structure interaction of submerged tanks and caissons in earthquakes, NOAA, Office of Sea Grant Report Number UCB/EERC-78/08, 150 pp., 1978.

Chapman, C.H., A new method for computing seismograms, Geophys. J.R. astr. Soc., 54, 481-518, 1978.

Chouet, B., K. Aki, and M. Tsujiura, Regional variation of the scaling law of earthquake source spectra, Bull. Seis. Soc. Am., 68, 49-79, 1978.

Christensen, N.I., The abundance of serpentinites in the oceanic crust, J. Geol., 80, 709-719, 1972.

Christensen, N.I., and M.H. Salisbury, Velocities, elastic moduli and weathering-age relations for Pacific Layer 2 basalts, Earth Planet. Sci. Lett., 19, 461-470, 1973.

Christensen, N.I. and M.H. Salisbury, Structure and constitution of the lower oceanic crust, Rev. Geophys. Space Phys., 13, 57-86, 1975.

Cline, A.K., Scalar- and planar-valued curve fitting using splines under tension, Numer. Math., 17, 218-220,1974.

Crane, K., The intersection of the Siqueiros transform fault and the East Pacific Rise, Mar. Geol., 21, 25-46, 1976.

Creager, K.C. and L.M. Dorman, Accurate location of ocean bottom seismograph arrays using acoustic ranging when ship position errors are covariant (abstract), Trans. Am. Geophys. Un., 61, 1048, 1980.

CYAMEX scientific team and L. Pastouret, Submersible structural study of Tamayo transform fault: East Pacific Rise, 23°N (project RITA), Mar. Geophys. Res., 4, 381-401, 1981.

Detrick, R.S. and G.M. Purdy, The crustal structure of the Kane Fracture Zone from seismic refraction studies, J. Geophys. Res., 85, 3759-3777, 1980.

Duennebier, F.K., G. Blackington and G.H. Sutton, Current-generated noise recorded on ocean bottom seismometers, Mar. Geophys. Res., 5, 109-115, 1981.

Duschenes, J.D., T.W. Barash, P.J. Mattaboni, and S.C. Solomon, On the use of an externally deployed geophone package on an ocean bottom seismometer, Mar. Geophys. Res., 4, 437-450, 1981.

Eittreim, S. and J.I. Ewing, Vema Fracture Zone transform fault, Geology, 3, 555-558, 1975.

Ergin, K., Energy ratio of the seismic waves reflected and refracted at a rock-water boundary, Bull. Seis. Soc. Am., 42, 349-372, 1952.

Ewing, J.I., Elementary theory of seismic refraction and reflection measurements, in The Sea, vol. 3, M.N. Hill, ed., Wiley-Interscience, N.J., 3-19, 1963.

Ewing, J.I., Rivera ocean seismic experiment (ROSE) overview, J. Geophys. Res., in press, 1982.

Ewing, J.I., and G.M. Purdy, Upper crustal velocity structure in the ROSE area of the East Pacific Rise, J. Geophys. Res., in press, 1982.

Fox, P.J., E. Schreiber, H. Rowlett, and K. McCamy, The geology of the oceanographer fracture zone: a model for fracture zones, J. Geophys. Res., 81, 4117-4128, 1976.

Francis, T.J.G., The detailed seismicity of mid-ocean ridges, Earth Plan. Sci. Lett., 4, 39-46, 1968.

Francis, T.J.G., The ratio of compressional to shear velocity and rock porosity on the axis of the Mid-Atlantic Ridge, J. Geophys. Res., 81, 4361-4364, 1976.

Francis, T.J.G., and I.T. Porter, Median valley seismology: the mid-Atlantic ridge near 45°N, Geophys. J.R. astr. Soc., 34, 279-311, 1973.

Francis, T.J.G., I.T. Porter and J.R. McGrath, Ocean-bottom seismograph observations on the mid-Atlantic ridge near latitude 37°N, Geol. Soc. Amer. Bull., 88, 664-677, 1977.

Francis, T.J.G., I.T. Porter, and R.C. Lilwall, Microearthquakes near the eastern end of St. Paul's Fracture Zone, Geophys. J.R. astr. Soc., 53, 201-217, 1978.

Geller, R.J. and H. Kanamori, Magnitudes of great shallow earthquakes from 1904 to 1952, Bull. Seis. Soc. Am., 67, 587-598, 1977.

Gilbert, F., Excitation of the normal modes of the earth by earthquake sources, Geophys. J.R. astr. Soc., 22, 223-226, 1970.

Gutenberg, B. and C.F. Richter, Seismicity of the Earth and Associated Phenomena, Princeton Univ. Press, Princeton, N.J., 310 pp., 1954.

Hamilton, E.L., H.P. Bucker, D.L. Keir, and J.A. Whitney, Velocities of compressional and shear waves in marine sediments determined in situ from a research submersible, J. Geophys. Res., 75, 4039-4049, 1970.

Handschumacher, D.W., Post-Eocene plate tectonics of the eastern Pacific, in The Geophysics of the Pacific Ocean Basin and its Margin, Geophys. Monogr. Ser., Vol. 19, G.H. Sutton, ed., AGU, Washington, D.C., 177-202, 1976.

Hey, R., F.K. Duennebier, and W.J. Morgan, Propagating rifts on mid-ocean ridges, J. Geophys. Res., 85, 3647-3658, 1980.

Hoover, G.M. and J.T. O'Brien, The influence of the planted geophone on seismic land data, Geophysics, 45, 1239-1253, 1980.

Houtz, R. and J.I. Ewing, Upper crustal structure as a function of plate age, J. Geophys. Res., 81, 2490-2498, 1976.

Hyndman, R.D., Poisson's ratio in the oceanic crust - A review, Tectonophysics, 59, 321-333, 1979.

Jacob, K.H., Three-dimensional seismic ray tracing in a laterally heterogeneous spherical earth, J. Geophys. Res., 75, 6675-6689, 1970.

Johnson, L.E. and F. Gilbert, Inversion and inference for teleseismic ray data, in Methods in Computational Physics, v. 12: B.A. Bolt, ed., Academic Press, N.Y., 231-266, 1972.

Johnson, S.H., M.D. Cranford, B.T. Brown, J.E. Bowers, and R.E. McAllister, A free-fall direct recording ocean-bottom seismograph, Mar. Geophys. Res., 3, 103-117, 1977.

Johnson, S.H., and P.R. Jones, Microearthquakes located on the Blanco fracture zone with sonobuoy arrays, J. Geophys. Res., 83, 255-261, 1978.

Johnson, S.H. and R.E. Alister, Bottom seismometer observations of airgun signals at Lopez Island, Mar. Geophys. Res., 5, 87-94, 1981.

Johnson, R.V., II, C.R.B. Lister, and B.T.R. Lewis, A direct recording ocean bottom seismometer, Mar. Geophys. Res., 3, 65-85, 1977.

Jones, P.R., and S.H. Johnson, Sonobuoy array measurements of active faulting on the Gorda Ridge, J. Geophys. Res., 83, 3435-3440, 1978.

Julian, B.R. and D. Gubbins, Three-dimensional seismic ray tracing, J. Geophys., 43, 95-114, 1977.

Kanasewich, E.R., T. Alpaslan, and F. Hron, The importance of S-wave precursors in shear-wave studies, Bull. Seis. Soc. Amer., 63, 2167-2176, 1973.

Kastens, K.A., K.C. Macdonald, K. Becker, and K. Crane, The Tamayo transform fault in the Gulf of California, Mar. Geophys. Res., 4, 129-151, 1979.

Klein, F.W., Hypocenter location program HYPOINVERSE; Part 1: User's guide to versions 1, 2, 3, 4, U.S.G.S. Open File Report 78-694, 1978.

Klitgord, K.D. And J. Mammerickx, East Pacific Rise: Magnetic anomaly and bathymetric framework, J. Geophys. Res., in press, 1982.

Koelsch, D.E., and G.M. Purdy, An ocean bottom hydrophone instrument for seismic refraction experiments in the deep ocean, Mar. Geophys. Res., 4, 115-125, 1979.

Lamer, A., Couplage sol-geophone, Geophys. Prosp., 18, 300-319, 1969.

Landisman, M., A. Dziewonski, and Y. Sato, Recent improvements in the analysis of surface wave observations, Geophys. J.R. astr. Soc., 17, 359-403, 1969.

Latham, G., P. Donoho, K. Griffiths, A. Roberts, and A.K. Ibrahim, The Texas ocean bottom seismograph, paper presented at the Offshore Technology Conference, Soc. of Explor. Geophys., Houston, TX, 1978.

LaTraille, S.L., J.F. Gettrust, and M. Simpson, The ROSE seismic data archive data archive system, J. Geophys. Res., in press, 1982.

Lewis, B.T.R. and W.E. Syndsman, Fine structure of the lower oceanic crust on the Cocos plate, Tectonophysics, 55, 87-105, 1979.

Lieberman, R.C. and P.W. Pomeroy, Relative excitation of surface waves by earthquakes and underground explosions, J. Geophys. Res., 74, 1575-1590, 1969.

Lilwall, R.C., T.J.G. Francis, and I.T. Porter, Ocean-bottom seismograph observations on the mid-Atlantic ridge near 45°N, Geophys. J.R. astr. Soc., 51, 357-370, 1977.

Lilwall, R.C. and T.J.G. Francis, Hypocentral resolution of small ocean bottom seismic networks, Geophys. J.R. astr. Soc., 54, 721-728, 1978.

Lilwall, R.C., T.J.G. Francis, and I.T. Porter, Ocean-bottom seismograph observations on the mid-Atlantic ridge near 45°N - further results, Geophys. J.R. astr. Soc., 55, 255-262, 1978.

Lilwall, R.C., T.J.G. Francis, and I.T. Porter, A microearthquake survey at the junction of the East Pacific Rise and the Wilkes (9°S) fracture zone, Geophys. J. R. astr. Soc., 66, 407-416, 1981.

Lilwall, R.C., T.J.G. Francis, and I.T. Porter, Some ocean-bottom seismograph observations on the Reykjanes Ridge at 59°N, Geophys. J.R. astr. Soc., 62, 321-327, 1980.

Luk, F., R. Comer, and W.H.K. Lee, Solving seismic ray tracing problems in a heterogeneous medium by a general shooting method, in preparation, 1982.

Macdonald, K.C. and J.D. Mudie, Microearthquakes on the Galapagos spreading center and the seismicity of fast-spreading ridges, Geophys. J.R. astr. Soc., 36, 245-257, 1974.

Madariaga, R., Dynamics of an expanding circular fault, Bull. Seis. Soc. Am., 66, 639-666, 1976.

Mammerickx, J., The bathymetry of the Orozco Fracture Zone, unpublished map, Scripps Institute of Oceanography, 1980.

Mattaboni, P.J. and S.C. Solomon, MITOBS: A seismometer system for ocean-bottom earthquake studies, Mar. Geophys. Res., 3, 87-102, 1977.

McClain, J.S. and B.T.R. Lewis, A seismic experiment at the axis of the East Pacific Rise, Mar. Geol., 35, 147-169, 1980.

McCowan, D.W., Moment tensor representation of surface wave sources, Geophys. J.R. astr. Soc., 44, 595-599, 1976.

Mendiguren, J.A., Inversion of surface wave data in source mechanism studies, J. Geophys. Res., 82, 899-894, 1977.

Minster, J.B. and T.H. Jordan, Present-day plate motions, J. Geophys. Res., 83, 5331-5354, 1978.

Murase, T. and A.R. McBirney, Properties of some common igneous rocks and their melts at high temperatures, Geol. Soc. Am. Bull., 84, 3563-3592, 1973.

Orcutt, J.A., B.L.N. Kennett, and L.M. Dorman, Structure of the East Pacific Rise from an ocean bottom seismometer survey, Geophys. J.R. astr. Soc., 45, 305-320, 1976.

Ouchi, T., A.K. Ibrahim, and G.V. Latham, Seismicity and crustal structure in the Orozco fracture zone Project ROSE phase II, J. Geophys. Res., in press, 1982.

Patton, H., Reference point method for determining the source and path effects of surface waves, J. Geophys. Res., 85, 821-848, 1980.

Pereyra, V., W.H.K. Lee, and H.B. Keller, Solving two-point seismic ray tracing problems in a heterogeneous medium, Bull. Seis. Soc. Amer., 70, 79-99, 1980.

Project ROSE Scientists, Microearthquake activity on the Orozco Fracture Zone: preliminary results from Project ROSE, J. Geophys. Res., 86, 3783-3790, 1981.

Prothero, W.A., Jr., An ocean bottom seismometer capsule, Bull. Seis. Soc. Am., 65, 1251-1262, 1974.

Prothero, W.A., Jr., An operationally optimized ocean-bottom seismometer capsule, Phys. Earth Plan. Inst., 18, 71-77, 1979.

Prothero, W.A., I. Reid, M.S. Reichle, and J.N. Brune, Ocean bottom seismic measurements on the East Pacific Rise and Rivera Fracture Zone, Nature, 262, 121-124, 1976.

Prothero, W.A., Jr., and I. Reid, Microearthquakes on the East Pacific Rise at 21°N and the Rivera Fracture Zone, in preparation, 1982.

Purdy, G.M., The variability in seismic structure of layer 2 near the East Pacific Rise at 12°N, J. Geophys. Res., in press, 1982a.

Purdy, G.M., The correction for the travel time effects of seafloor topography in the interpretation of marine seismic data, J. Geophys. Res., in press, 1982b.

Raitt, R.W., G.G. Shor, Jr., T.J.G. Francis, and G.B. Morris, Anisotropy of the Pacific upper mantle, J. Geophys. Res., 74, 3095-3109, 1969.

Rautian, T.G. and V.I. Khalturin, The use of the coda for determination of the earthquake source spectrum, Bull. Seis. Soc. Am., 68, 923-948, 1978.

Reichle, M.S., A seismological study of the Gulf of California: Sonobuoy and teleseismic observations and tectonic implications, Ph.D. Thesis, Univ. of California, San Diego, 1975.

Reichle, M.S., G.F. Sharman, and J.N. Brune, Sonobuoy and telesismic study of Gulf of California transform fault earthquake sequences, Bull. Seismol. Soc. Amer., 66, 1623-1641, 1976.

Reichle, M.S. and I. Reid, Detailed study of earthquake swarms from the Gulf of California, Bull. Seismol. Soc. Amer., 67, 159-171, 1977.

Reid, I.D., The Rivera plate: a study in seismology and plate tectonics, Ph.D. Thesis, Univ. of California, San Diego, 288 pp., 1976.

Reid, I. and K. Macdonald, Microearthquake study of the mid-Atlantic ridge near 37°N, using sonobuoys, Nature, 246, 88-89, 1973.

Reid, I., M. Reichle, J. Brune, and H. Bradner, Microearthquake studies using sonobuoys, preliminary results from the Gulf of California, Geophys. J. R. astr. Soc., 34, 365-379, 1973.

Reid, I., J.A. Orcutt, and W.A. Prothero, Seismic evidence for a narrow zone of partial melting underlying the East Pacific rise at 21°N, Geol. Soc. Amer. Bull., 88, 678-682, 1977.

Reid, I. and W.A. Prothero, Jr., An earthquake sequence studied with ocean-bottom seismometers, Geophys. J. R. astr. Soc., 64, 381-391, 1981.

Richart, R.E., Jr., Hall, J.R., Jr., and R.D. Woods, Vibrations of Soils and Foundations, Prentiss-Hall International Series in Theoretical and Applied Mechanics, Prentice-Hall, Inc., Englewood Cliffs, NJ, 414 pp., 1970.

Roecker, S.W., Seismicity and tectonics of the Pamir-Hindu Kush region of central Asia, Ph.D. Thesis, M.I.T., Cambridge, MA, 297 pp., 1981.

Romanowicz, B.A., Moment tensor inversion of long period Rayleigh waves: a new approach, J. Geophys. Res., in press, 1982.

Rothe, J.P., The Seismicity of the Earth, UNESCO, 336 pp., 1969.

Rowlett, H., Seismicity at intersections of spreading centers and transform faults, J. Geophys. Res., 86, 3815-3820, 1981.

Schouten, H., J. Karson, and H. Dick, Geometry of transform zones, Nature, 288, 470-473, 1980.

Sclater, J.G., R.N. Anderson, and M.L. Bell, Elevation of ridges and evolution of the central eastern Pacific, J. Geophys. Res., 76, 7888-7915, 1971.

Searle, R., The active part of the Charlie-Gibbs Fracture zone: a study using sonar and other geophysical techniques, J. Geophys. Res., 86, 243-262, 1981.

Shih, J.S., The nature and origin of fine-scale sea-floor relief, Ph.D. Thesis, M.I.T., 222 pp., 1979.

Sleep, N.H., Formation of oceanic crust: some thermal constraints, J. Geophys. Res., 80, 4037-4042, 1975.

Solomon, S.C., P.J. Mattaboni, and R.L. Hester, Microseismicity near the Indian Ocean triple junction, Geophys. Res. Lett., 4, 597-600, 1977.

Spindel, R.C., S.B. Davis, K.C. Macdonald, R.P. Porter, and J.D. Phillips, Microearthquake survey of median valley of the mid-Atlantic ridge at 36°30'N, Nature, 248, 577-579, 1974.

Spudich, P.A., Oceanic crustal studies using waveform analysis and shear waves, Ph.D. Thesis, Univ. of California, San Diego, 125 pp., 1979.

Spudich, P.A. and J. Orcutt, Petrology and porosity of an oceanic crustal site: results from waveform modeling of seismic refraction data, J. Geophys. Res., 85, 1409-1433, 1980.

Stephen, R.A., Seismic aniostropy observed in the upper oceanic crust, Geophys. Res. Let., 8, 865-868, 1981.

Sutton, G.H., J. Kasahara, W.N. Ichinose, and D.A. Byrne, Ocean bottom seismograph development at Hawaii Institute of Geophysics, Mar. Geophys. Res., 3, 153-177, 1977.

Sutton, G.H., F.K. Duennebier, and B. Iwatake, Coupling of ocean bottom seismometers to soft bottoms, Mar. Geophys. Res., 5, 35-52, 1981.

Thurber, C.H., Earth structure and earthquake locations in the Coyote Lake area, central California, Ph.D. Thesis, M.I.T., 332 pp., 1981.

Trehu, A.M., J.G. Sclater, and J.L. Nabelek, The depth and thickness of the ocean crust and its dependence upon age, Bull. Soc. Geol. France, 7, 917-930, 1976.

Trehu, A.M., J.L. Nabelek, and S.C. Solomon, Source characterization of two Reykjanes Ridge earthquakes: surface waves and moment tensors; P waveforms and non-orthogonal nodal planes, J. Geophys. Res., 86, 1701-1724, 1981.

Tsai, Y.B., Determination of focal depths of earthquakes in the mid-oceanic ridges from amplitude spectra of surface waves, Ph.D. Thesis, M.I.T., 1969.

Tuthill, J.D., B.T.R. Lewis, and J.O. Garmany, Stonely waves, Lopez Island noise, and deep sea noise from 1 to 5 Hz., Mar. Geophys. Res., 5, 95-108, 1981.

Weidner, D.J. and K. Aki, Focal depth and mechanism of mid-ocean ridge earthquakes, J. Geophys. Res., 78, 1818-1831, 1973.

Wesson, R.L., Travel time inversion for laterally inhomogeneous crustal velocity models, Bull. Seis. Soc. Amer., 61, 729-746, 1971.

White, R.S. and R.A. Stephen, Compressional to shear wave conversion in oceanic crust, Geophys. J. R. astr. Soc., 63, 547-565, 1980.

Whitmarsh, R.B., Axial intrusion zone beneath the median valley of the Mid-Atlantic Ridge at 37°N detected by explosion seismology, Geophys. J. R. astr. Soc., 42, 189-215, 1975.

Wyss, M., Towards a physical understanding of the earthquake frequency distribution, Geophys. J. R. astr. Soc., 31, 341-359, 1973.

Zelikovitz, S.J. and W.A. Prothero, Jr., The vertical response of an ocean bottom seismometer: analysis of the Lopez Island vertical transient tests, Mar. Geophys. Res., 5, 53-68, 1981.

BIOGRAPHICAL NOTE

The author was born on January 7, 1955, in Princeton, N.J., while her parents were graduate students starving in a garrett. She left Princeton at the age of 5 months for a summer in Wilmington, De., followed by three years under the Eiffel Tower in Paris, France. Most of her childhood was spent in the Mt. Pleasant school district in Wilmington, with several interludes in "gay Paree" and summer vacations on Cape Cod. For college, she returned to Princeton, which no longer maintained the "monastic" atmosphere that had forced her mother to commute to Columbia with a cranky infant. She graduated with a B.A. in geology and geophysics in 1975 and went to work for a summer in Woods Hole. This was followed by a year at the University of Paris VII with a fellowship from the French government; there the university was on strike for most of the spring semester, providing time for sun, ski and sights. "Serious" studies resumed in the MIT/WHOI joint program and resulted in this thesis. That she now chooses to continue as a post-doc at the USGS in Woods Hole implicitly implies that this life has been interesting and fun.

Publications resulting from these pelegrinations are:

Trehu, A.M., Depth vs. age: A perspective on mid-ocean ridges, Earth and Plan. Sci. Let., 27, 287-304, 1975.

Anderson, R.N., G.F. Moore, S.S. Schilt, R.C. Cardwell, A.M. Trehu and V. Vacquier, Heat flow near a fossil ridge on the north flank of the Galapagos Spreading Center, J. Geophys. Res., 81, 1828-1838, 1976.

Trehu, A.M., J.G. Sclater and J.L. Náběl ek, The depth and thickness of the oceanic crust and its dependence upon age, Bull. Soc. Geol. France, 18, 917-930, 1976.

Trehu, A.M., J.L. Náběl ek and S.C. Solomon, Source characterization of two earthquakes on the Reykjanes Ridge: Surface waves and moment tensors; P waves and non-orthogonal nodal planes, J. Geophys. Res., 86, 1701-1724, 1981.

Project ROSE scientists, Microearthquakes of the Orozco Fracture Zone: Preliminary results from project ROSE, J. Geophys. Res., 86, 3783-3790, 1981.

Trehu, A.M. and S.C. Solomon, The coupling parameters of the MIT OBS at two nearshore sites, Marine Geophys. Res., 5, 69-78, 1981.

APPENDIX I

Source characterization of two Reykjanes Ridge earthquakes : Surface waves and moment tensors; P waveforms and nonorthogonal nodal planes.

by

A.M. Tréhu, J.L. Nábělek and S.C. Solomon

JOURNAL OF GEOPHYSICAL RESEARCH, VOL. 86, NO. B3, PAGES 1701–1724, MARCH 10, 1981

Source Characterization of Two Reykjanes Ridge Earthquakes: Surface Waves and Moment Tensors; *P* Waveforms and Nonorthogonal Nodal Planes

ANNE M. TRÉHU

MIT/WHOI Joint Program in Oceanography, Massachusetts Institute of Technology, Cambridge, Massachusetts 02139

JOHN L. NÁBĚLEK AND SEAN C. SOLOMON

Department of Earth and Planetary Sciences, Massachusetts Institute of Technology, Cambridge, Massachusetts 02139

Well-constrained fault plane solutions from *P* wave first motions for mid-ocean ridge normal faulting earthquakes usually require nonorthogonal nodal planes. Local structural effects and/or departures from a double-couple source mechanism have been invoked to explain this phenomenon. In order to obtain an independent determination of the source mechanisms for the April 24, 1970, and April 3, 1972, events on the southern Reykjanes Ridge, we invert the Rayleigh wave radiation pattern to obtain the source moment tensor. The moment tensor formulation should be particularly well suited to this problem because it is not restricted a priori to a double-couple source mechanism. A potential drawback of the technique, however, is the requirement that phase velocities along the earthquake-station paths be known very accurately in order to obtain the source phase from the observed phase, and an objective of this study was to determine whether a regionalized phase velocity model compiled from published dispersion curves is adequate. The results of the moment tensor inversion for both events indicate shallow normal faulting with the tension axis approximately horizontal and perpendicular to the local strike of the ridge. Apparent departures from a pure double-couple source seem to result from errors in the data and the poor resolution of the M_{xz} and M_{yz} components of the moment tensor for shallow sources. After performing the inversion under a series of increasingly more stringent constraints we conclude that the data for both events are compatible with pure double-couple sources with moments of 4.8 and 7.5 $\times 10^{24}$ dyn cm, respectively. We then show that interference between *P*, *pP*, and *sP* due to shallowness of the source can account for the observed nonorthogonality and match the observed *P* waveforms for the April 3, 1972, event with theoretical seismograms calculated for a shear fault whose orientation is consistent with the surface wave solution. The best fit to the data is obtained for a long, narrow fault (13 km by 3 km), with rupture initiating near the seafloor. The moment indicated by the *P* waves is 7.5 $\times$ 10^{24} dyn cm. These source parameters give an average displacement of about 60 cm and a stress drop of 30–60 bars, taking into account various uncertainties. Although we might expect attentuation to be high in the mid-ocean ridge environment, the average attenuation required to fit the teleseismic data is not higher than normal ($t^* = 1$ s). The *P* waves from the April 24, 1970, earthquake were too small to be suitable for quantitative modeling by synthetic seismograms but are qualitatively consistent with a shallow fault model similar to that for the larger event. We conclude that the faulting process described by these two earthquake mechanisms is directly related to the formation of rift valley topography.

INTRODUCTION

Fault plane solutions of ridge crest earthquakes regularly indicate nonorthogonal nodal planes for normal faulting events [*Sykes*, 1967, 1970; *Solomon and Julian*, 1974]. Because orthogonal nodal planes are implicitly required by the double-couple faulting mechanism from which the fault plane solution is derived, either a process must be found whereby the true body wave radiation pattern is distorted to yield an apparent nonorthogonality, or an alternative faulting mechanism must be found. Several explanations for this phenomenon have been proposed. *Solomon and Julian* [1974] demonstrated that a low-velocity wedge below the ridge, the existence of which is predicted by thermal models and confirmed by surface wave and refraction studies, can focus rays from a source on the ridge, thus collapsing the apparent dilatational quadrant. Other explanations include (1) an explosive volcanic component superimposed upon the double couple [*Solomon and Julian*, 1974], (2) a mechanism of extensional failure in a porous, fluid-saturated medium [*Robson et al.*, 1968], and (3) interference between *P*, *pP*, and *sP* resulting from the shallowness of the source [*Hart*, 1978].

Focusing of rays below the source and interference at the surface are explanations invoking structural effects which would distort the apparent body wave radiation pattern of a double-couple fault but which should not strongly affect the surface wave radiation pattern. A true source mechanism of an explosion or of tensional cracking, on the other hand, should be manifested in the surface waves as well as in the body waves. An independent source mechanism determination obtained from the surface waves should therefore help to distinguish the cause of the nonorthogonality. The recently developed technique of inverting surface wave data to obtain the source moment tensor should be especially suited to this problem, since the moment tensor is not restricted a priori to correspond to a double couple. The surface wave solution can then provide a base from which the body wave problem can be reexamined.

The frequency of teleseismically observable events combined with a fortuitous location with respect to azimuthal coverage by the World-Wide Standard Seismograph Network (WWSSN) makes the southern Reykjanes Ridge an excellent laboratory for studying the mechanism of faulting on a slowly

Paper number 80B1369.
0148-0227/81/080B-1369$01.00

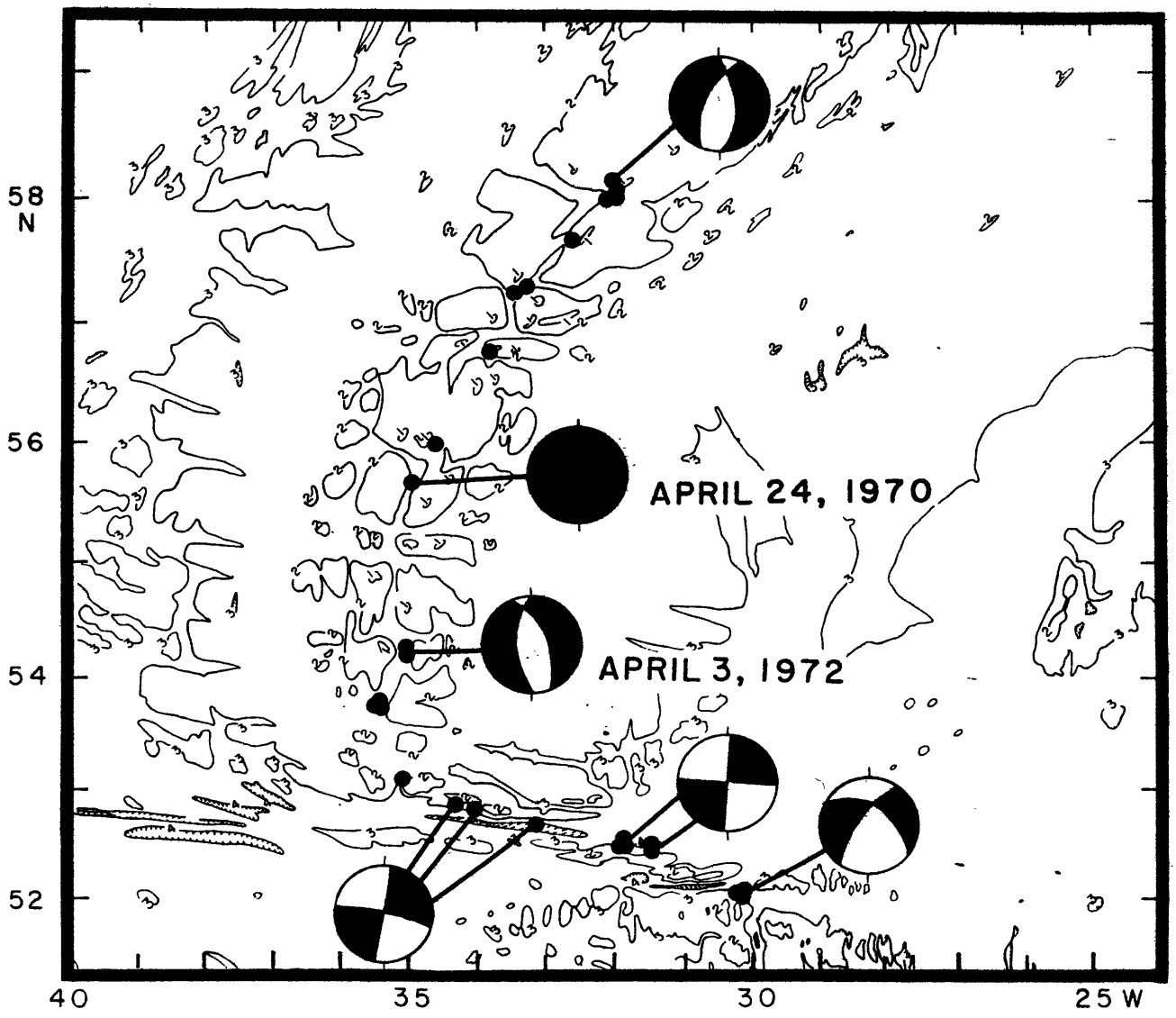

Fig. 1. Bathymetric map of the southern Reykjanes Ridge and Gibbs Fracture Zone. Contours are at 1-km intervals. Earthquakes of m_b greater than 5.0 recorded by the WWSSN from 1962 to 1978 are shown by dots. Fault plane solutions are from *Einarsson* [1979]. Bathymetry from NAVOCEANO World Relief Map, NA-4, May 1977.

spreading ridge and the phenomenon of nonorthogonal nodal planes. Although one could argue that the area might be anomalous owing to proximity to the Iceland hot spot, topographically and geochemically, the ridge south of about 59°N appears to be beyond the hot spot's direct influence [*Vogt and Johnson*, 1975]. Spreading direction is approximately perpendicular to the ridge, and the axis is broken by an axial valley characteristic of its spreading rate. This contrasts with the obliquely spreading, smooth, shallow ridge to the north. The seismicity south of 59°N is also much more characteristic of that of the 'average' Mid-Atlantic Ridge [*Francis*, 1973]. North of 59°N the Reykjanes Ridge is nearly aseismic, resembling in this respect a fast spreading rise. The southern Reykjanes Ridge, on the other hand, has experienced several earthquakes with body wave magnitude m_b up to 5.5 since the inception of the WWSSN. Detailed bathymetric studies show that the transition between the two regimes is marked by a several-fold increase in offset across the fault scarps which border the axial constructional volcanic pile [*Laughton et al.*, 1979].

Figure 1 is a topographic map of the area showing earthquakes with m_b greater than 5 which were recorded between 1962 and 1978. Most of the ridge earthquakes display the pronounced distortion of the body wave radiation pattern characteristic of mid-ocean ridge events. Note, however, that for the April 24, 1970, earthquake at 56°N, compressional first arrivals appear nearly to cover the focal sphere. This mechanism, determined by *Einarsson* [1979], originally inspired our interest in the area. Einarsson suggested that this event might be an extreme manifestation of the nonorthogonality. An analysis of the surface wave radiation pattern was undertaken to determine whether this event might perhaps be an explosion.

In this paper the Rayleigh wave displacement spectra from the April 24, 1970, Reykjanes Ridge earthquake are inverted to obtain the source moment tensor. A moment tensor solution was also obtained for the April 3, 1972, event (Figure 1),

TABLE 1. Locations of Reykjanes Ridge Earthquakes Studied in This Paper (From the International Seismological Centre)

Date	Time, UT	Location, deg	Magnitude* m_b	Magnitude* M_S†
April 24, 1970	0123:17	55.64°N, 35.03°W	5.3	5.4
April 3, 1972‡	2036:20	54.33°N, 35.20°W	5.1	5.5

*Although the 1970 event is assigned a larger m_b by the ISC, an examination of seismograms recorded at the same station for the two events indicates that these values are erroneous, as *P* wave as well as surface wave arrivals are consistently of larger amplitude for the 1972 event.

†From USCGS and NEIC.

‡This event was the second of a pair of events at the same location and of approximately the same magnitude which were separated in time by 1 hour, 43 min. Seismograms for the two events are remarkably similar. The second event was chosen for study because clear *P* wave arrivals were observable for a greater range of azimuths and distances. These two events were not accompanied by any smaller teleseismically recorded events, unlike the 1970 earthquake, which was the largest event of a swarm sequence.

which yielded a well-constrained fault plane solution from *P* wave first motions requiring nodal planes separated by approximately 60°. The locations of these events are given in Table 1. The moment tensor solutions for both events indicate shallow normal faulting with the tension axis perpendicular to the strike of the spreading center.

We then show that the apparent nonorthogonality of the body wave solution for the April 3, 1972, event may be attributed to the interference effects between direct *P*, *pP*, and *sP* and that the body waveforms can be reconciled with the source mechanism obtained from the surface waves. We conclude that the April 24, 1970, event was too small to yield a reliable fault plane solution if the amplitude of the background noise and expected amplitude of the first arrival are considered. The observed body waves from the slightly larger April 3, 1972, event, however, are matched with synthetic seismograms calculated for a finite fault with an orientation corresponding to the moment tensor solution and suggest a narrow, long, shallow fault plane which reached the seafloor. This mechanism may correspond to faulting which breaks through the thin axial crust and contributes to the topography of rift valley and mountains.

SOURCE MECHANISM FROM SURFACE WAVES

Background

Surface waves are especially useful for studying oceanic earthquakes because such events are often too small to yield reliable fault plane solutions [*Kafka and Weidner*, 1979]; those fault plane solutions which have been obtained for spreading center events raise questions concerning the basic assumptions about the source mechanism. The radiation pattern of surface waves can be used to obtain an independent determination of the source mechanism. Moreover, because the surface waves used for this determination have a longer wavelength than the body waves used for the fault plane solution, they are less affected by structural anomalies immediately below the ridge axis.

The representation of the far-field displacement in terms of the moment tensor was first presented by *Gilbert* [1970] and *Gilbert and Dziewonski* [1975] for free oscillations and was extended to surface waves by *McCowan* [1976] and *Mendiguren* [1977] and to body waves by *Stump* [1976] and *McCowan* [1977]. Seismic waves radiated from a source at a given depth can be expressed as a linear combination of the moment tensor components. For surface waves, the inversion to obtain the moment tensor is much more rapid than the traditional trial and error method of calculating theoretical spectra for all possible combinations of strike, dip, and slip of a double-couple fault and matching the observed amplitude and phase spectra independently [e.g., *Ben-Menahem and Toksöz*, 1962, 1963; *Mitchell*, 1973; *Patton*, 1976]. Another advantage of the moment tensor representation is that it is not restricted to a double-couple source mechanism and should therefore provide insights into possible departures from this generally assumed faulting model. Other possible mechanisms contain isotropic and/or compensated linear vector dipole components [*Knopoff and Randall*, 1970]. For example, a tensional crack corresponds to the superposition of an explosion and a compensated linear vector dipole.

The formulation of the problem of retrieving the moment tensor from the vertical component of the Rayleigh wave is given in Appendix A. In summary, the moment tensor components can be retrieved from the real and imaginary parts of the observed source spectrum [*Mendiguren*, 1977; *Patton and Aki*, 1979]:

$$\text{real} = A_{ij}\cos\phi_{ij} = M_{zz}G_2(h, f_i) + (M_{xx} + M_{yy})G_1(h, f_i) - (M_{yy} - M_{xx})G_1(h, f_i)\cos 2\theta_j + 2M_{xy}G_1(h, f_i)\sin 2\theta_j + E_{ij}^R \quad (1a)$$

$$\text{imaginary} = A_{ij}\sin\phi_{ij} = M_{xz}G_3(h, f_i)\cos\theta_j + M_{yz}G_3(h, f_i)\sin\theta_j + E_{ij}^I \quad (1b)$$

In (1), A_{ij} and ϕ_{ij} are the amplitude and phase delay observed at station j and frequency f_i after having been corrected for the effects of propagation and the source time function, θ_j is the azimuth of station j with respect to the earthquake, and the E_{ij}^R and E_{ij}^I are error terms. The G_k are real functions of depth and frequency and are calculated for the appropriate source velocity and density structure using *Saito*'s [1967] al-

TABLE 2. Velocity Model for the Mid-Atlantic Ridge, From *Weidner* [1974]

Thickness, km	ρ, g/cm³	α, km/s	β, km/s
3	1.03	1.52	0.0
6	3.05	6.40	3.70
11	3.40	8.10	4.60
10	3.40	8.10	4.33
10	3.38	8.00	4.33
20	3.38	7.92	4.33
20	3.38	7.68	4.33
20	3.36	7.65	4.33
20	3.36	7.76	4.00
20	3.36	7.82	4.00
20	3.36	8.10	4.00
100	3.36	8.15	4.00
20	3.37	8.15	4.00
20	3.38	8.15	4.00
20	3.39	8.15	4.00
20	3.40	8.15	4.44
20	3.41	8.22	4.51
20	3.45	8.27	4.55
20	3.50	8.32	4.58
300	3.68	8.70	4.80

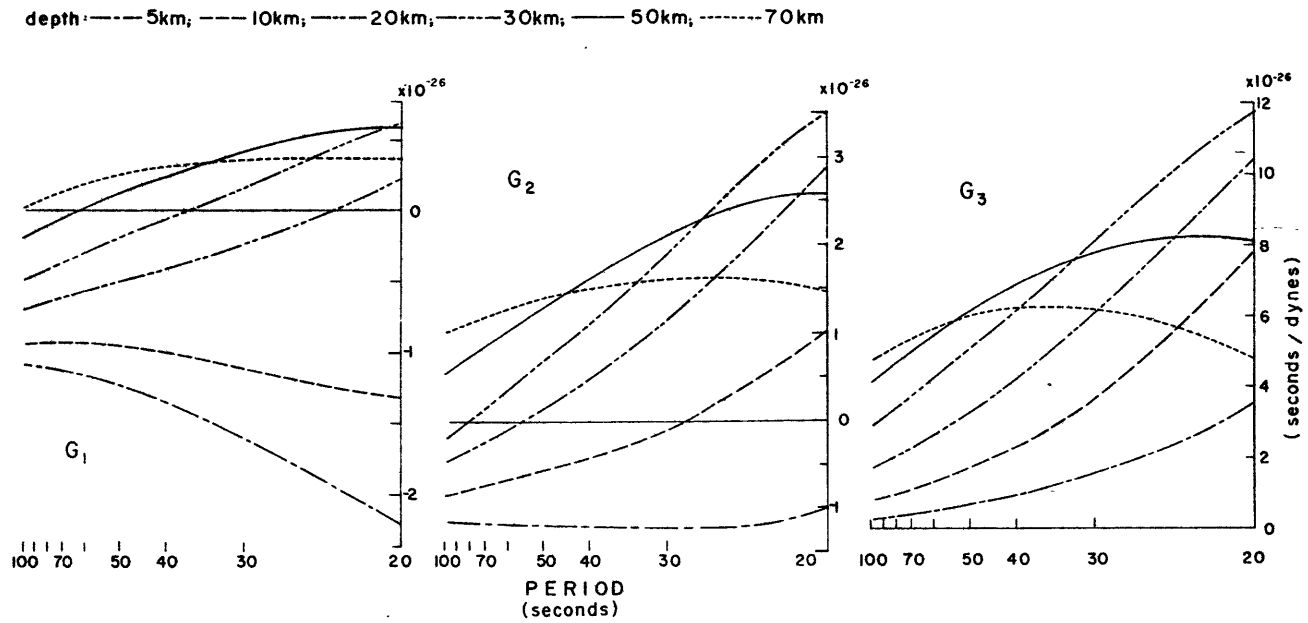

Fig. 2. Response curves calculated at different depths for the oceanic model of Table 2: $G_1 = AkY_3(h, \omega)/2$; $G_2 = A[-Y_2(h, \omega) - \lambda(h)kY_3(h, \omega)]/[\lambda(h) + 2\mu(h)]$; $G_3 = AY_4(h, \omega)/\mu h)$; $A = [Y_1(0, \omega)/4U\omega^2 I](2k/\pi r)^{1/2}$, where r is the data equalization distance of 4000 km. For definition of other terms, see Appendix A.

gorithm; G_k calculated for an oceanic model (Table 2) are displayed in Figure 2. For a given depth, the moment tensor components can be obtained from a one-step inversion of the real and imaginary parts of the spectrum. Depth can be determined by inverting for the moment tensor at a series of depths and choosing that depth which minimizes the residual $E^2 = \sum_{ij}\{(E_{ij}^R)^2 + (E_{ij}^I)^2\}$.

The resolving power of the inversion is determined by the behavior of the functions G_k over the period range of the data. We see from (1*a*) that with data from only a single frequency we cannot independently determine $(M_{xx} + M_{yy})$ and M_{zz}; even with data from a range of frequencies, G_1 and G_2 have too similar a frequency dependence over the frequency range of long-period surface wave data to permit independent resolution of the diagonal components for most source depths [*Mendiguren*, 1977]. The constraint $\sum_{i=1}^{3} M_{ii} = 0$, equivalent to no volume change, can be analytically imposed without destroying the linearity of the problem. Under this constraint, however, an explosive component in the source will masquerade as a vertically oriented compensated linear vector dipole. This effect will be examined further in the discussion of the surface wave results. We can also see that G_3 approaches zero as depth decreases because it is proportional to one of the stress eigenfunctions (Appendix A). This results in poor resolution of the M_{xz} and M_{yz} components for very shallow sources, and we may be forced to impose an additional constraint. If we have evidence indicating that the principal stress axes are approximately horizontal and vertical, we can assume that the imaginary part of the spectrum is due to noise in the data and solve for M_{xx}, M_{yy}, M_{zz}, and M_{xy} with M_{xz} and M_{yz} identically equal to zero. This constrains the corresponding double couple fault mechanism to be either dip slip with a dip of 45° or vertical strike slip.

A drawback of the moment tensor inversion method is the requirement that the phase velocity along the earthquake-station path be known very accurately [*Aki and Patton*, 1978] in order to correct the observed phase back to the source. In the moment tensor formulation, amplitude and phase cannot be decoupled without destroying the linearity of the problem (for an example of a nonlinear inversion using amplitude data alone, see *Kafka and Weidner* [1979]).

The relationship between the observed phase and the ϕ_{ij} of (1), in units of cycles, is

$$\phi_{ij} = \phi_{ij}^{\text{observed}} - \phi_{ij}^{\text{instr}} + [T_j - D_j/C_{ij}]f_i + 0.125 \pm n \quad (2)$$

where ϕ_{ij}^{instr} is the instrument phase response, T_j is the time between the origin time and the beginning of the digitized record, D_j is epicentral distance in kilometers, C_{ij} is the phase velocity, the constant 0.125 includes the effects of the source time function (assumed to be a step) and the asymptotic expansion of the Hankel function for the notation of equations (A5) and (1), and n is a constant which arises from the periodicity of the phase and is determined by C_{ij}. If we assume that T_j and D_j are known exactly, the error in ϕ_{ij} due to an error ΔC_{ij} in C_{ij} is $\Delta\phi_{ij} \simeq (f_i D_j \Delta C_{ij})/C_{ij}$. Numerical experiments [*Patton and Aki*, 1979] indicate that random errors on the phase of up to ±0.125 cycles lead to the introduction of an apparent non-double-couple component of 0 to 10%; an error of up to 0.25 cycles can lead to 36% non-double couple. The orientation of the principal axes of the moment tensor, however, remains very stable. For values typical of our data set, an epicentral distance of 2500 km and a velocity of 4 km/s, the phase change for a 50-s wave resulting from 0.25% error in the phase velocity is 0.13 cycles. For a given error in C, the error increases with increasing epicentral distance and decreasing period.

In his application of the method to a family of earthquakes in central Asia, *Patton* [1980] began by calculating phase velocities for the station-source paths by the method of *Weidner and Aki* [1973] using two neighboring earthquakes with different known source mechanisms to separate the path and source

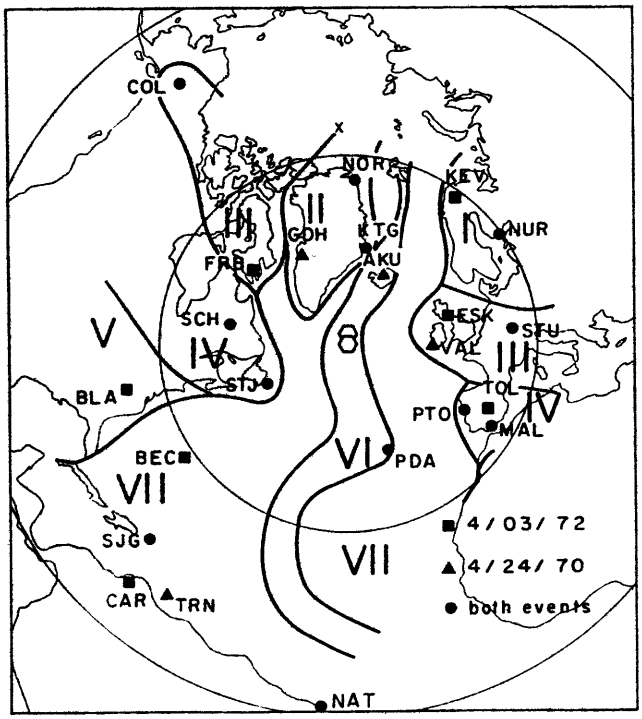

Fig. 3. Stations and regionalization used for the surface wave analysis plotted on an azimuthal equidistant projection centered on the April 3, 1972, event. Regions are labeled with Roman numerals, and the corresponding phase velocity dispersion curves are displayed in Figure 4. Circles mark distances of 30° and 60° from the epicenter of the 1972 event.

effects. The moment tensors of other earthquakes in the region were then calculated using these path parameters. An iterative scheme was adopted whereby once the mechanism of an earthquake had been determined, its 'known' mechanism was used to refine the values of the path parameters. A motivation for conducting the moment tensor inversions for the Reykjanes Ridge earthquakes was to see if reasonable results could be obtained simply by using a regionalized velocity model to correct for propagation and thus obtain a source mechanism solution for a single isolated event. An excellent azimuthal distribution of stations with short, structurally simple earthquake-station paths coupled with the availability of Rayleigh wave phase velocity studies in the North Atlantic Ocean and adjacent continental regions suggested that such an approach might be fruitful.

Data

For the April 24, 1970, event, vertical component Rayleigh waves from 23 stations of the WWSSN and Canadian network were digitized at an interval of 2 s. Each digitized time series was then Fourier-analyzed and corrected for instrument response, geometrical spreading, and attenuation. The Q model of *Tsai and Aki* [1969] was used. Amplitude spectra were equalized to a common distance of 4000 km. To decrease the effect of amplitude fluctuations due to multipathing, the amplitude spectra were smoothed by averaging over a frequency window of 0.04 Hz centered at each frequency.

The phase spectra were corrected for propagation effects using the regionalized phase velocity model of Figures 3 and 4. Regional boundaries were determined from geologic and bathymetric considerations. The oceanic domain was divided into young and old lithosphere roughly by the 20-m.y. isochron, and the continental margin was defined by the 4000-m isobath. For several necessary continental provinces, phase velocity dispersion curves were not available in the literature for the entire period range from 20 to 100 s, and an appropriate curve was extrapolated from curves published for geologically similar regions. The estimated errors on the phase velocities given by the authors of the regional studies range from about 0.2% (oceanic regions and recent studies of continental regions) to 1.0% (older continental studies). Table 3*a* shows the percentage of each earthquake-station path within a given region. These percentages were used to calculate an appropriate phase velocity for each period at each station.

The corrected source spectra were then sampled at 2-s intervals in period. Examples of seismograms and corrected source spectra are shown in Figure 5*a*. Only data for periods between 30 and 60 s were used in the inversion. The earthquake was too small to excite waves at periods much greater than 60 s, and data at periods shorter than 30 s were considered unreliable because of the effects of structural heterogeneities along the path and of phase velocity errors on the phase correction. The source spectra were then examined visually to see if phases were coherent. A few stations were dropped from the calculations at this stage, leaving 16 stations (256 data) for the final inversion. The rejected stations usually corresponded to long paths with sections parallel to structural discontinuities, and the incoherency of the phase was probably due to the interference effects of multipathing. Spurious phases or amplitudes at certain periods for otherwise coherent spectra were also noted and assigned zero weight (e.g., 52-s period at station VAL; see Figure 5*a*).

The vertical component of the Rayleigh wave for the April 3, 1972, event was treated similarly to that for the 1970 event except that amplitude spectra were not smoothed. The stations used for the analysis of this event are shown in Figure 3, the regionalization of the paths is given in Table 3*b*, and a

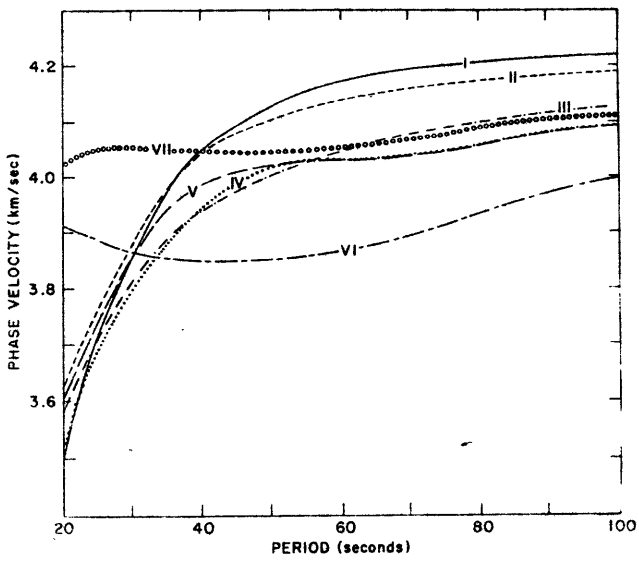

Fig. 4. Phase velocity dispersion curves for the regions shown in Figure 3. References are I, *Naponen* [1966] and *Calgagnile and Panza* [1978]; II, *Gregersen* [1971]; III and IV, *Wickens* [1971]; V, *Oliver et al.* [1961]; VI, *Forsyth* [1975] (5–10 m.y. normalized to water depth of 3.2 km); VII, *Weidner* [1974] (normal ocean basin).

TABLE 3*a*. Regionalization of Surface Wave Paths for the April 24, 1970, Event

Station	Distance, deg	Azimuth, deg	Fraction of Path by Region						
			I	II	III	IV	V	VI	VII
AKU	13.0	32.4	...	...	...		...	1.0	...
COL	49.2	328.8	...	0.20	0.66	...	...	0.03	0.11
GDH	16.0	335.8	...	0.56	...	...	...	0.16	0.28
KTG	15.9	16.1	...	0.20	...	...	...	0.48	0.32
MAL	28.0	119.5	...	...	...	0.25	...	0.15	0.60
NAT	60.6	180.0	...	...	...	...	...	0.44	0.56
NOR	26.6	5.9	...	0.60	...	...	...	0.20	0.20
NUR	30.9	56.1	0.36	...	...	...	...	0.18	0.46
PDA	19.0	156.6	...	...	...	...	...	1.0	...
PTO	22.6	118.9	...	...	...	0.08	...	0.18	0.74
SCH	18.0	280.6	...	...	...	0.30	...	0.06	0.64
SJG	44.3	224.8	...	...	...	...	...	0.09	0.91
STJ	13.6	241.0	...	...	...	0.22	...	0.16	0.62
STU	27.5	85.7	...	...	0.60	...	...	0.09	0.31
TRN	49.5	215.1	...	...	...	...	...	0.11	0.89
VAL	15.0	93.9	...	...	0.21	...	...	0.17	0.62

sample of the data is shown in Figure 5*b*. Periods from 32 to 78 s at 19 stations were used for a total of 456 data.

The data for the 1972 earthquake were filtered using the time variable filter technique of *Landisman et al.* [1969] to avoid potential interference from higher modes and multipathing. This time-variable filtering did not significantly change the source spectrum at most stations. Erratic phase values were not eliminated by the filtering, although they were sometimes shifted by up to ±4 s in period (Figure 5*b*). For one station, BLA, the analysis did suggest interference from a mode clearly separated in time from the fundamental mode. In this case, the filtering smoothed the source spectra significantly (Figure 5*b*), suggesting that the technique will be useful for treating the data from events less auspiciously located with respect to the WWSSN than those along the southern Reykjanes Ridge. Using filtered data did not improve the resolution of the inversion, and in the rest of this study, only results obtained from the unfiltered data will be presented.

Results

The inversions were performed under a series of increasingly more stringent constraints. With all six moment tensor components unconstrained (constraint 1 in Table 4) the diagonal components were poorly resolved. The no-volume-change constraint was therefore imposed (constraint 2). It then became apparent that the sources were very shallow and that large, poorly determined M_{xz} and M_{yz} components were dominating the solutions. As normal faulting with the tension axis approximately horizontal was indicated, the constraint that the imaginary part of the spectrum be zero was then imposed, both without and with the no-volume-change constraint (constraints 3 and 4, respectively).

The residuals of the inversions, normalized to the number of data minus the degrees of freedom, are plotted against depth in Figure 6. The behavior of the residuals with depth is similar for the two events. For the inversion of the real part,

TABLE 3*b*. Regionalization of Surface Wave Paths for the April 3, 1972, Event

Station	Distance, deg	Azimuth, deg	Fraction of Path by Region						
			I	II	III	IV	V	VI	VII
BEC	30.3	235.7	...	...	...	0.12	...	0.12	0.76
BLA	35.1	259.7	...	...	...	0.39	.32	0.08	0.21
CAR	50.5	222.2	...	...	...	...	...	0.09	0.91
COL	50.3	329.3	...	0.22	0.63	...	...	0.08	0.07
ESK	18.3	73.8	...	...	0.36	...	...	0.17	0.47
FRB	19.3	312.4	...	0.20	...	0.15	...	0.16	0.49
KEV	31.2	36.4	0.12	...	...	...	...	0.53	0.35
KTG	17.2	15.1	...	0.19	...	...	...	0.53	0.28
MAL	27.5	117.1	...	...	...	0.25	...	0.13	0.62
NAT	59.3	179.8	...	...	...	...	...	0.35	0.65
NOR	27.9	5.7	...	0.56	...	...	...	0.24	0.20
NUR	31.7	54.2	0.37	...	...	...	...	0.11	0.52
PDA	17.8	154.6	...	...	...	...	...	1.0	...
PTO	22.0	115.8	...	...	...	0.06	...	0.15	0.79
SCH	18.2	284.5	...	...	...	0.26	...	0.15	0.59
SJG	43.3	225.6	...	...	...	...	...	0.10	0.90
STJ	12.9	245.6	...	...	...	0.19	...	0.25	0.56
STU	27.7	83.0	...	...	0.59	...	...	0.11	0.30
TOL	25.4	111.8	...	...	...	0.23	...	0.13	0.64

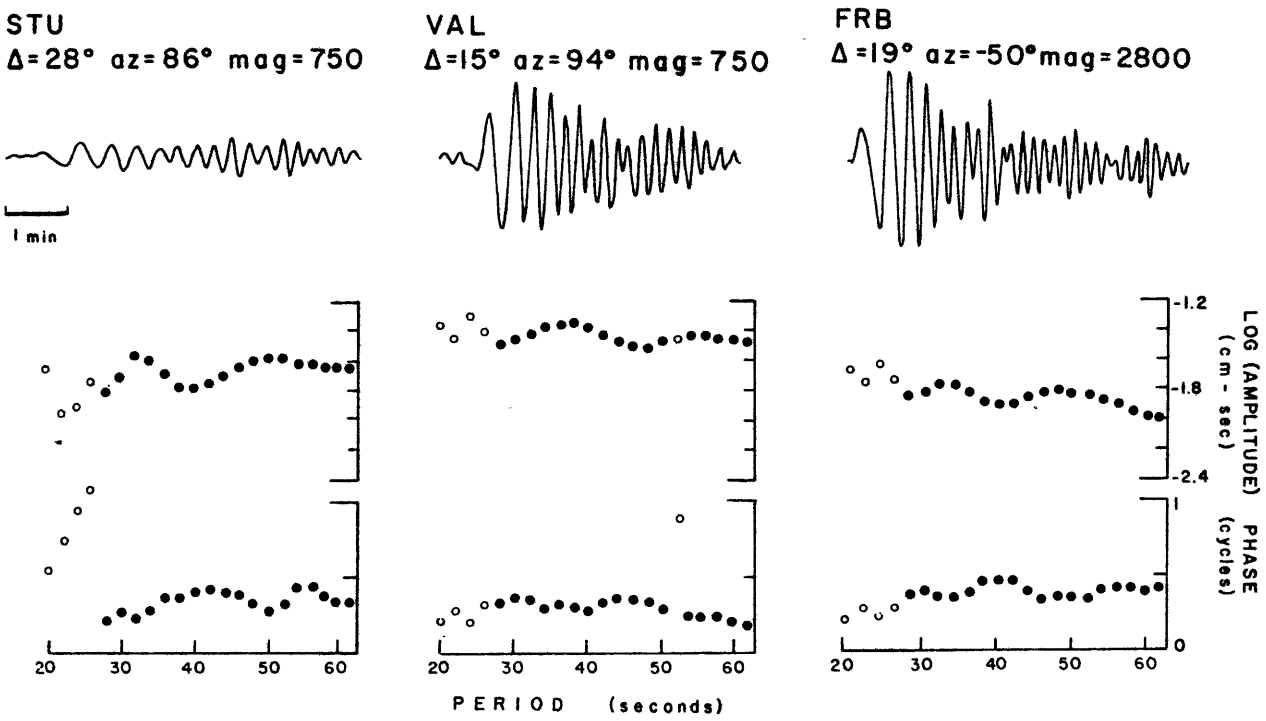

Fig. 5a. Examples of seismograms and corrected source spectra for the April 24, 1970, event. Displayed seismograms were traced directly from WWSSN records and are not equalized to a common epicentral distance and station magnification. Open circles in the source spectra indicate points which were eliminated from the data set for the inversion during the visual inspection of the data; Δ is epicentral distance in degrees, az is station azimuth in degrees from north, and mag is station magnification.

we observe minima for both shallow (4–10 km, or 1–7 km below seafloor) and deep (80–90 km) depths, regardless of the constraint imposed. This ambiguity is to be expected because over the period range of the data the behavior of G_1 and G_2 is similar for both shallow and deep events. The minima are more sharply defined when the constraint $\sum_{i=1}^{3} M_{ii} = 0$ is imposed. The inversion of the imaginary part provides no constraint on the depth. Imposing the constraint that the imaginary part of the spectrum is zero and that the observed amplitude reflects the real part decreases the residuals. Since one would expect to obtain larger residuals for the more highly constrained case, this behavior implies that by recasting the amplitude and phase spectra in terms of real and imaginary components, we are actually adding noise to the real part. This question will be discussed further when the results of the inversion under the various constraints are compared to the observations.

The results of the inversion for depths corresponding to minima in the residuals are given in Tables 4a and 4b. The errors for the eigenvalues and eigenvectors represent the first-order perturbation resulting from errors in the moment tensor components [*Mathews and Walker*, 1964; *Strelitz*, 1980]. First, note that although the calculated errors on the diagonal components are so large as to render the solution meaningless when the trace is not constrained to be zero (solutions for a depth of 4 km below seafloor, constraints 1 and 3), the orientation of the principal axes and the percentage of double-couple mechanism in the solution are similar to those for the corresponding solutions with the trace constrained (constraints 2 and 4, respectively). By imposing the no-volume-change constraint we are not suppressing any information which could otherwise be extracted from the data.

Next, let us discuss the results of the inversion under constraint 2. For shallow depths the solutions indicate normal faulting with tension approximately perpendicular to the spreading center. They do, however, contain important strike slip components and suggest significant departures from a pure double-couple source mechanism. We can also observe a marked rotation of the axes as depth increases from 1 to 7 km below the seafloor. Examination of the individual moment tensor components reveals that as depth decreases, the solution becomes increasingly dominated by the M_{xz} and M_{yz} components. The reason for the instability of the inversion of the imaginary part for shallow sources has been discussed above.

In order to avoid problems due to the poor resolution of M_{xz} and M_{yz} we tried performing the inversion under constraint 4, assuming a normal faulting mechanism ($\phi_{ij} = 0.5$ cycles for all i and j). For both events, the solution for a depth of 1 to 7 km below seafloor is very stable: double-couple normal faulting along a strike parallel to that of the spreading center. The moments increase regularly with depth; for a depth of 7 km (4 km below seafloor) the moments are 4.8 and 7.5×10^{24} dyn cm for the 1970 and 1972 events, respectively.

The solutions at 80 km under constraints 2 and 4 indicate primarily non-double-couple source mechanisms and do not bear any apparent relationship to the local geologic setting. The interchanging of the compression and tension axes relative to the shallow solutions (constraint 4) indicates that the ambiguity in determination of depth from the minimum in

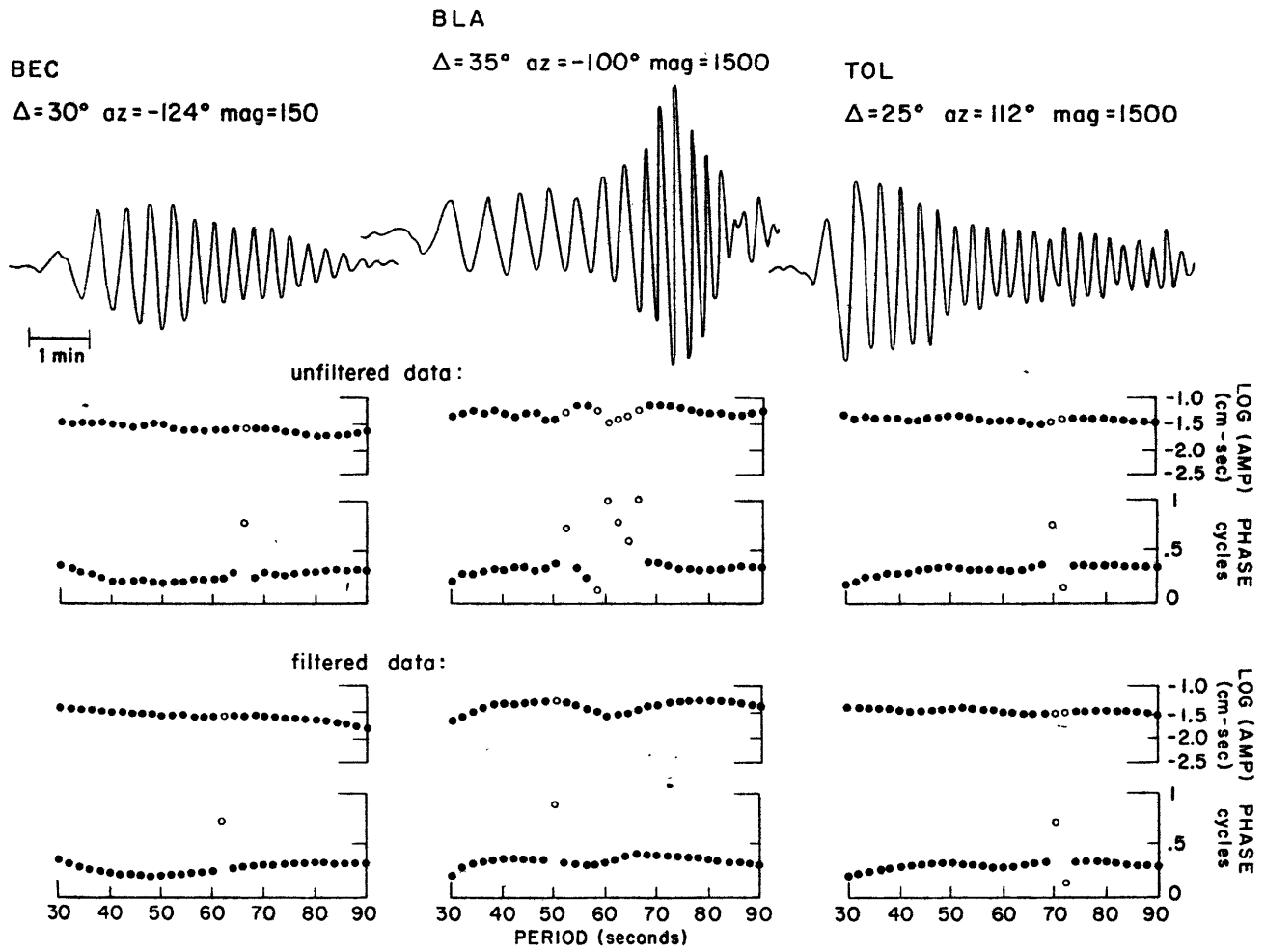

Fig. 5*b*. Examples of seismograms and corrected source spectra for the April 3, 1972, event. Source spectra obtained from filtered records are also shown.

the residuals of the surface wave inversion is a direct result of the similar behavior, with opposite sign, of G_1 and G_2 for both shallow and deep sources. In the next section we will see that the body waves are not compatible with a deep source and the solutions at 80 km will not be considered further.

Discussion

The fault plane solutions corresponding to the moment tensors obtained under constraints 2 and 4 for a depth of 7 km are superimposed on the observed *P* wave fault plane solutions in Figures 7*a* and 7*b*. We can see that the *P* wave first-motion pattern for the 1972 event displays the nonorthogonal nodal planes characteristic of mid-ocean ridge normal faulting events (Figure 7*b*). For the 1970 event, the data coverage is less complete, and the observed nodal planes are poorly constrained but are consistent with a normal faulting solution requiring nonorthogonal nodal planes. The large strike slip component in both moment tensor solutions under constraint 2 implies a pronounced asymmetry in the *P* wave radiation pattern which is not observed. Except for the observed nonorthogonality, the *P* wave first-motion patterns are consistent with the results of the surface wave inversion under constraint 4.

It has been noted that the residuals of the inversion are smaller under constraints 3 and 4 than under 1 and 2, implying that by separating the observed spectrum into its real and imaginary parts one is actually adding noise to the real part. An examination of the fit of the solution to the data, expressed both as real and imaginary part and as amplitude and phase, provides insights into this behavior. For the 1970 event (Figure 8), the observed value of the imaginary part is generally greater than that of the model (Figure 8*a*), and the phase is about 0.1 cycle less (Figure 8*b*). From (2) an origin time error of 5 s can result in a 0.1-cycle underestimation of the initial phase delay for a 50-s wave. If the true initial phase delay is 0 or 0.5 cycles, the result of such an error in the real part is to underestimate the amplitude and consequently the moment. That this is indeed happening is clear in Figure 8*b*, where the amplitude data are compared to the solutions calculated under constraints 2 and 4.

By comparing Figures 8*a* and 9*a* to Figures 8*b* and 9*b*, we see that the variation in the imaginary part of the spectrum with azimuth leading to large M_{xz} and M_{yz} components is primarily controlled by the variation in phase and that stations in the Caribbean (215° to 230° azimuth) are particularly important in defining this pattern. These stations have long earthquake-station paths relative to most of the other data used in this study and therefore have a greater potential error

TABLE 4*a*. Results of the Moment Tensor Inversion for the April 24, 1970, Event

	Depth Below Seafloor (Constraint)									
	4 km (4)	4 km (3)	4 km (2)	4 km (1)	1 km (4)	1 km (2)	7 km (4)	7 km (2)	77 km (4)	77 km (2)
					Moment Tensor Components, 10^{24} dyn cm					
M_{xx}	4.83 ± 0.10	4.94 ± 5.11	3.88 ± 0.17	4.74 ± 8.68	3.86 ± 0.08	3.14 ± 0.14	5.71 ± 0.12	4.58 ± 0.20	−13.9 ±0.4	−12.1 ± 0.7
M_{xy}	−1.03 ± 0.09	−1.03 ± 0.09	−0.46 ± 0.15	−0.46 ± 0.16	−0.87 ± 0.08	−0.39 ± 0.13	−1.22 ± 0.11	−0.55 ± 0.19	4.2 ± 0.4	1.9 ± 0.7
M_{yy}	0.47 ± 0.10	0.58 ± 5.13	−0.54 ± 0.17	0.33 ± 8.73	0.20 ± 0.08	−0.58 ± 0.14	0.45 ± 0.12	−0.70 ± 0.20	4.2 ± 0.4	6.1 ± 0.7
M_{xz}	...	...	2.67 ± 0.65	2.67 ± 0.65	...	10.3 ± 2.50	...	2.53 ± 0.61	...	0.7 ± 0.2
M_{yz}	...	...	−4.47 ± 0.66	−4.47 ± 0.66	...	−17.3 ± 2.56	...	−4.24 ± 0.62	...	−1.1 ± 0.2
M_{zz}	−5.30 ± 0.09	−4.81 ± 23.8	−3.34 ± 0.15	0.67 ± 40.40	−4.05 ± 0.07	−2.56 ± 0.12	−6.16 ± 0.10	−3.88 ± 0.18	9.6 ± 0.2	6.1 ± 0.3
					Eigenvalues, 10^{24} dyn cm					
Tension	5.06 ± 0.10	5.17 ± 4.87	5.53 ± 0.53	7.21 ± 14.11	4.05 ± 0.09	19.39 ± 2.53	5.98 ± 0.12	5.83 ± 0.46	9.6 ± 0.2	7.3 ± 0.4
Intermediate	0.24 ± 0.10	0.34 ± 4.89	1.43 ± 0.49	2.78 ± 8.35	0.00 ± 0.09	1.79 ± 0.48	0.18 ± 0.12	1.27 ± 0.51	5.2 ± 0.4	5.1 ± 0.4
Compression	−5.30 ± 0.09	−4.81 ± 23.80	−6.96 ± 0.63	−4.25 ± 20.95	−4.05 ± 0.07	−21.18 ± 2.54	−6.16 ± 0.10	−7.9 ± 0.59	−14.8 ± 0.4	−12.1 ± 0.7
					Eigenvectors (Strike°/Dip°)					
Tension	−77± 1/0	−77 ± 19/0	−64 ± 6/26 ± 2	−59 ± 218/35 ± 26	−77 ± 1/0	37 ± 8/42 ± 4	−78 ± 1/0	−70 ± 5/21 ± 1	0/90	4 ± 5/43 ± 8
Intermediate	13 ± 1/0	13 ± 19/0	37 ± 3/22 ± 6	49 ± 251/24 ± 82	13 ± 1/0	58 ± 3/5 ± 6	12 ± 1/0	30 ± 3/25 ± 5	12 ±1/0	−171 ± 2/48 ± 8
Compression	0/90	0/90	162 ± 2/54 ±4	165 ± 156/45 ± 81	0/90	154 ± 3/47 ± 5	0/90	164 ± 2/56 ± 4	−78 ± 1/0	96 ± 2/2 ± 2
					Percent					
Double couple	91	91	59	53	100	83	94	64	30	18
CLVD	9	4	41	21	0	17	6	36	70	82
Explosion	–	5	–	26	–	–	–	–	–	–
Double-couple scalar moment, 10^{24} dyn cm	4.8	4.7	4.1	3.8	4.1	17.6	5.8	4.5	4.4	2.2

TABLE 4*b*. Results of the Moment Tensor Inversion for the April 3, 1972, Event

	Depth Below Seafloor (Constraint)									
	4 km (4)	4 km (3)	4 km (2)	4 km (1)	1 km (4)	1 km (2)	7 km (4)	7 km (2)	77 km (4)	77 km (2)
					Moment Tensor Components, 10^{24} dyn cm					
M_{xx}	7.84 ± 0.16	7.99 ± 7.73	7.32 ± 0.18	7.12 ± 8.90	6.43 ± 0.14	6.08 ± 0.16	9.04 ± 0.19	8.46 ± 0.21	−23.3 ± 0.7	−24.3 ± 0.8
M_{xy}	−0.71 ± 0.12	−0.71 ± 0.12	−1.60 ± 0.14	−1.60 ± 0.14	−0.61 ± 0.11	−1.37 ± 0.12	−0.83 ± 0.15	−1.87 ± 0.17	3.1 ± 0.6	6.9 ± 0.6
M_{yy}	0.49 ± 0.16	0.64 ± 0.12	−1.28 ± 0.18	−1.48 ± 9.35	0.21 ± 0.14	−1.27 ± 0.16	0.35 ± 0.19	−1.64 ± 0.21	8.0 ± 0.7	12.7 ± 0.8
M_{xz}	...	...	−8.85 ± 0.81	−8.85 ± 0.81	...	−34.3 ± 3.15	...	−8.35 ± 0.76	...	−2.0 ± 0.2
M_{yz}	...	...	−5.96 ± 0.99	−5.96 ± 0.99	...	−23.2 ± 3.87	...	−5.59 ± 0.81	...	−1.3 ± 0.2
M_{zz}	−8.33 ± 0.13	−7.69 ± 33.6	−6.04 ± 0.15	−6.90 ± 38.6	−6.64 ± 0.11	−4.80 ± 0.13	−9.39 ± 0.15	−6.82 ± 0.17	15.4 ± 0.3	11.6 ± 0.3
					Eigenvalues, 10^{24} dyn cm					
Tension	7.91 ± 0.16	8.06 ± 7.66	11.86 ± 0.69	11.52 ± 10.67	6.49 ± 0.14	40.64 ± 3.31	9.12 ± 0.19	12.16 ± 0.60	15.4 ± 0.3	14.7 ± 0.6
Intermediate	0.42 ± 0.16	0.57 ± 8.05	1.60 ± 0.66	1.33 ± 8.85	0.15 ± 0.14	2.24 ± 0.71	0.27 ± 0.19	1.26 ± 0.61	8.3 ± 0.7	10.9 ± 0.3
Compression	−8.33 ± 0.13	−7.69 ± 33.60	−13.47 ± 0.88	−14.10 ± 26.01	−6.64 ± 0.11	−42.88 ± 3.44	−9.39 ± 0.15	−13.42 ± 0.75	−23.7 ± 0.7	−25.6 ± 0.8
					Eigenvectors (Strike°/Dip°)					
Tension	95 ± 1/0	95 ± 8/0	83 ± 3/28 ± 1	83 ± 67/27 ± 12	96 ± 1/0	62 ± 5/42 ± 2	95 ± 1/0	87 ± 3/24 ± 1	0/90	12 ± 1/27 ± 1
Intermediate	5 ± 1/0	5 ± 8/0	−18 ± 3/21 ± 3	−17 ± 45/20 ± 37	6 ± 1/0	−33 ± 3/5 ± 4	5 ± 1/0	−14 ± 3/23 ± 2	6 ± 1/0	−175 ± 1/62 ± 3
Compression	0/90	0/90	−140 ± 3/54 ± 3	−139 ± 89/55 ± 44	0/90	−129 ± 4/47 ± 3	0/90	−141 ± 3/55 ± 2	96 ± 1/0	−80 ± 2/3 ± 3
					Percent					
Double couple	90	90	76	75	95	90	94	81	30	15
CLVD	10	6	24	22	5	10	6	19	70	85
Explosion	–	4	–	3	–	–	–	–	–	–
Double-couple scalar moment, 10^{24} dyn cm	7.5	7.3	10.2	10.6	6.3	38.6	8.8	10.9	7.1	3.8

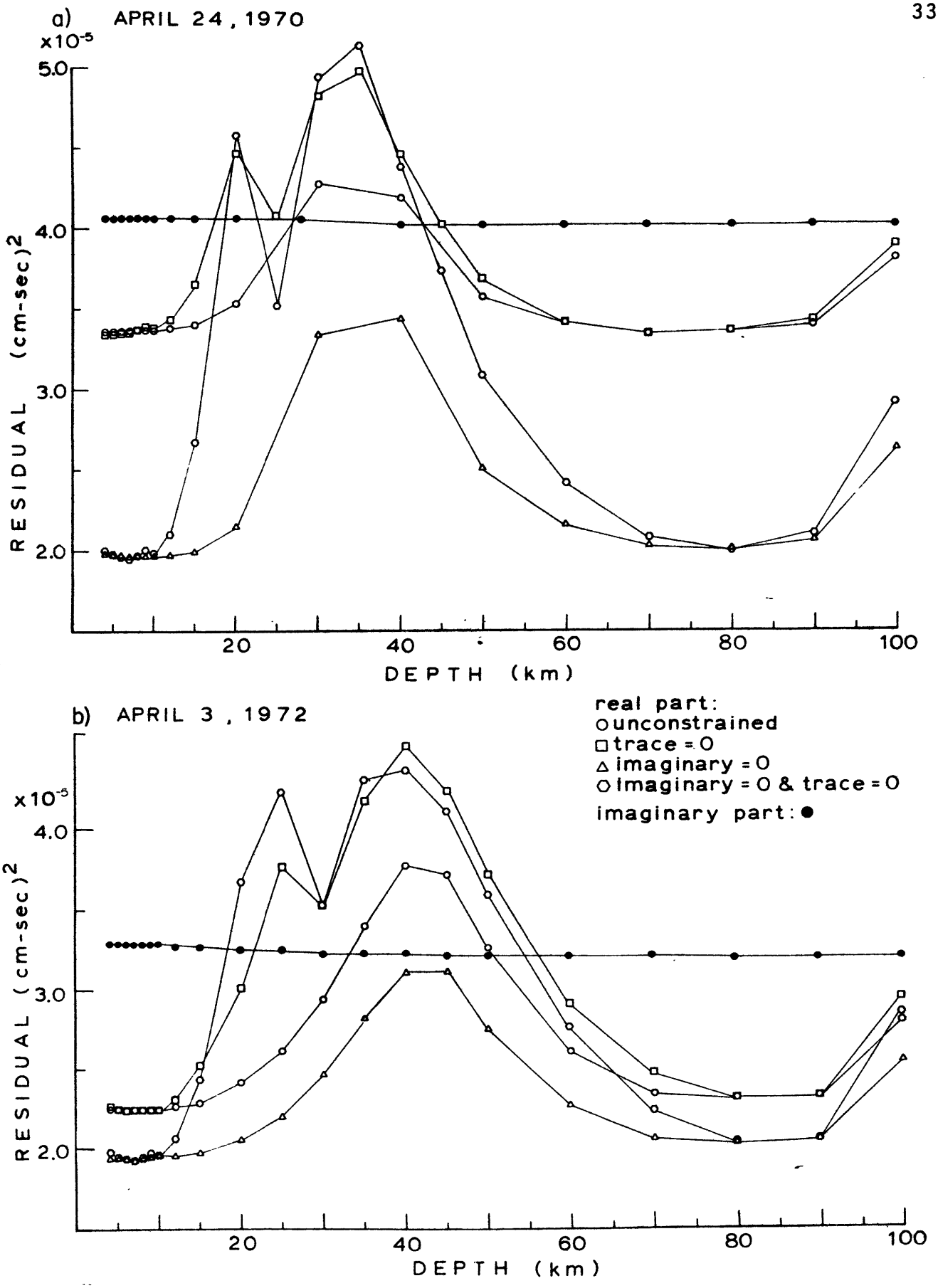

Fig. 6. (*a*) Residuals versus focal depth for the inversion of the Rayleigh wave radiation pattern to obtain the moment tensor for the April 24, 1970, event. (*b*) Residuals versus focal depth for the April 3, 1972, event.

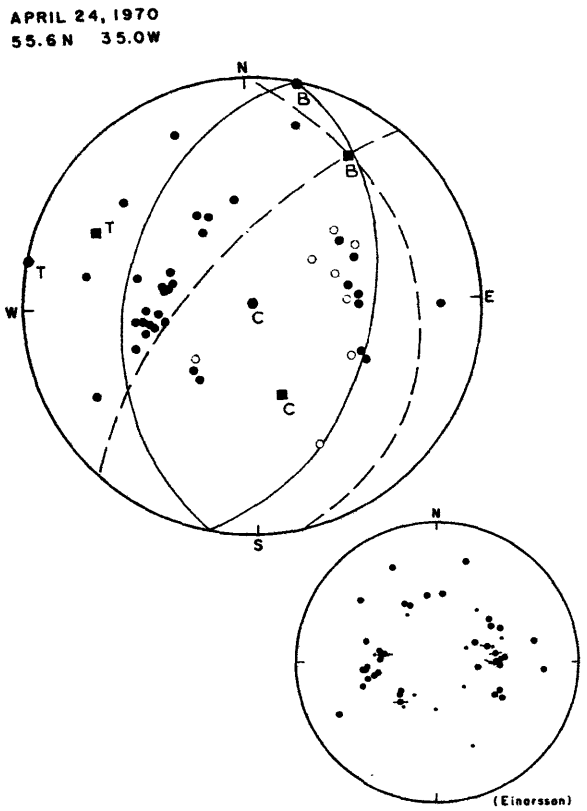

Fig. 7a. Fault plane solution for the April 24, 1970, event. Superimposed are the axes and double-couple fault plane solutions corresponding to the results of the moment tensor inversion under constraints 2 and 4 for a focal depth of 4 km below the seafloor. Dashed line and solid square, constraint 2; solid line and hexagon, constraint 4. T is tension; B is intermediate; C is compression. Closed circles indicate compressional first motion of the *P* wave. Open circles indicate stations for which the first motion was originally thought to be compressional but for which this interpretation was subsequently modified when considering the moment tensor solution and the expected amplitude of the first motion as predicted by synthetic seismograms. In the lower right-hand corner is the fault plane solution presented by *Einarsson* [1979]. Large dots signify clear arrivals, whereas small dots indicate less reliable picks. Arrows indicate *S* wave polarization angles.

due to phase velocity errors. Moreover, the phase velocity over the Caribbean portion of the path is poorly known. *Weidner* [1974] found anomalous phase velocities for paths to stations in the Caribbean from earthquakes along the Mid-Atlantic Ridge at 35°N and 15°N and attributed this to anomalously thick sediment cover. Inclusion of his model into the regionalization further decreases the initial phase at station CAR by about 0.23 cycles at 40 s, where the effect is maximum, and by 0.05 cycles at 80 s. Another possible source of error in the initial phase is epicentral mislocation; a mislocation of 12 km will impart a sinusoidal variation to the corrected initial phase with a maximum amplitude of about 0.1 cycles at 30 s and 0.04 cycles at 80 s.

If the true initial phase were close to 0.5 cycles at all azimuths, these errors would dominate the behavior of the imaginary part and induce additional noise on the real part. That the residuals decrease when the inversion is performed under constraints 3 and 4 suggests that this is indeed happening to some degree for the events studied in this paper. Although the sources for the two events studied may indeed contain minor M_{xz} and M_{yz} components, the values obtained from the inversion of the imaginary part seem to be overestimated, and we are unable to resolve their magnitude from our data.

Before proceeding to the body wave analysis, we should examine the effect on the inversion of the no-volume-change constraint when the source actually contains a volume change component, because this constraint must usually be imposed to resolve the diagonal components of the moment tensor. For a shallow explosive source with moment tensor

$$M_0 \begin{bmatrix} 1 & 0 & 0 \\ 0 & 1 & 0 \\ 0 & 0 & 1 \end{bmatrix},$$

the inversion should yield a solution of

$$b \cdot M_0 \begin{bmatrix} \frac{1}{2} & 0 & 0 \\ 0 & \frac{1}{2} & 0 \\ 0 & 0 & -1 \end{bmatrix}$$

which corresponds to a compensated linear vector dipole (CLVD) with compression along the *z* axis and tension along

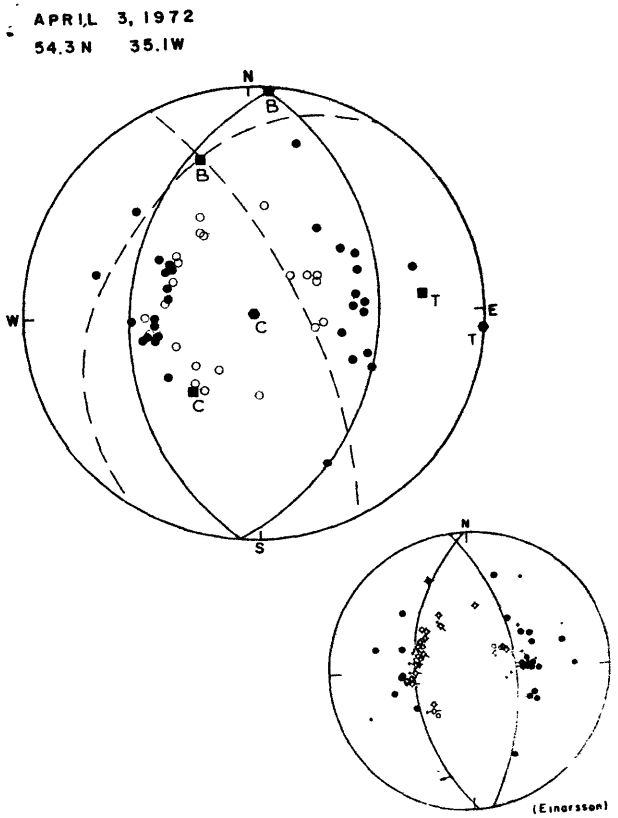

Fig. 7b. Fault plane solution for the April 3, 1972, event. Superimposed are the axes and nodal planes corresponding to the results of the moment tensor inversion for a focal depth of 4 km below the seafloor. Solid circles indicate compressional first motion of the *P* wave; open circles indicate dilatational first motion. Apparent nodal planes separated by approximately 60° are constrained by the data. In the lower right-hand corner is the fault plane solution presented by *Einarsson* [1979]: solid circles are compression; open circles are dilatation; crosses are nodal.

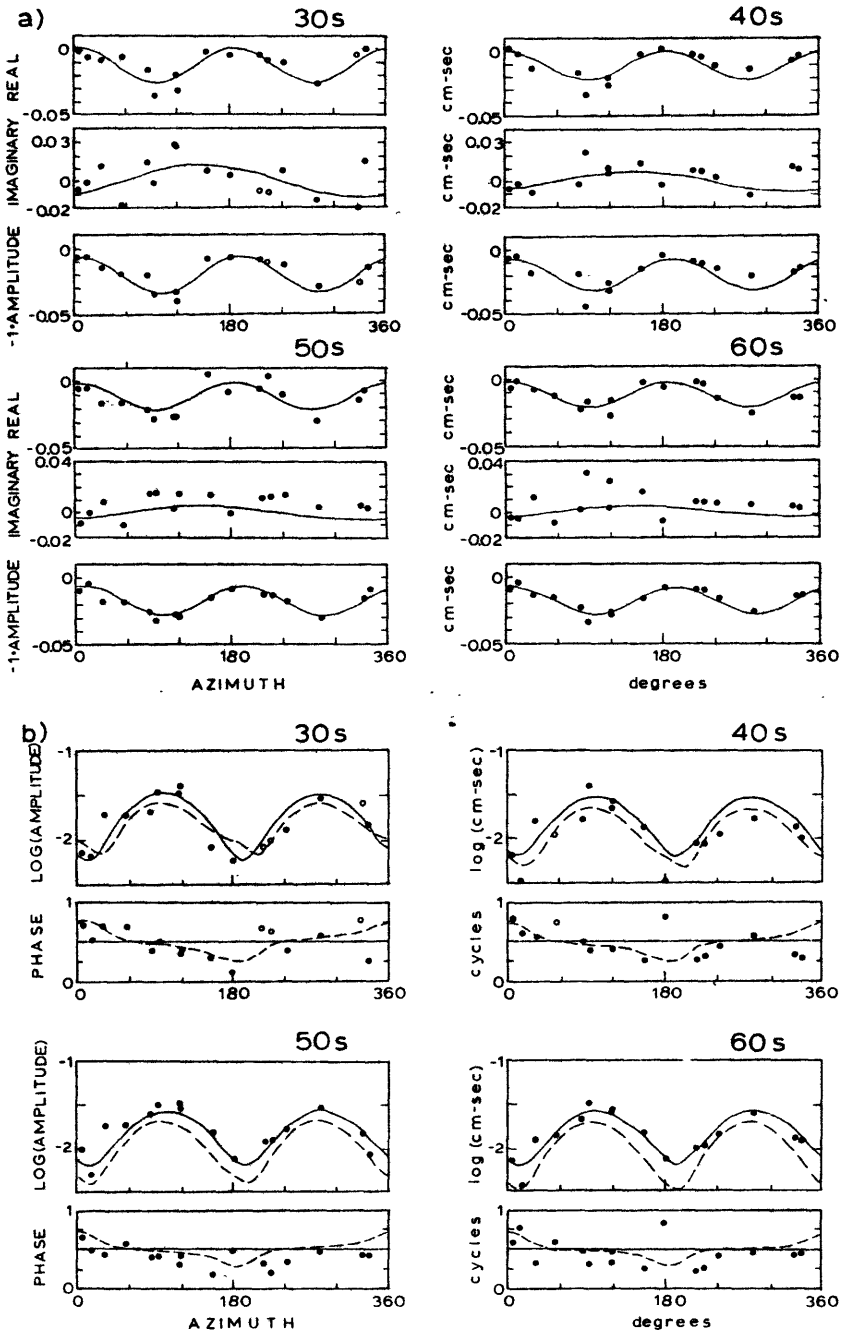

Fig. 8. (*a*) Examples at several periods of the fit of the moment tensor solution to the observed data for the April 24, 1970, event for a depth of 4 km below seafloor. Plots of the real and imaginary parts versus azimuth illustrate the fit when the inversion is performed under constraint 2; plots of negative amplitude versus azimuth show the result under constraint 4 (real part = amplitude, imaginary part = 0). Open circles indicate data that were weighted by zero during the visual inspection of the spectra. (*b*) Fit of the model to the data recast into the form of amplitude and phase: the solution under constraint 2 is given by dashed lines, the solution under constraint 4 is given by solid lines.

x and y. The factor b depends on depth and is close to 1 for a shallow source [*Patton*, 1978]. An explosion should be clearly distinguishable from a double-couple both with and without the no-volume-change constraint. A vertical tension crack in the y-z plane corresponds to the sum of a CLVD, with tension along x and compression along y and z, and an explosion. Under the $\sum_{i=1}^{3} M_{ii} = 0$ constraint, the explosive component will masquerade as a CLVD with compression along z; the sum of the two CLVD, assuming $b = 1$ and $\lambda = \mu$, is

$$M_0 \begin{bmatrix} 13/6 & 0 & 0 \\ 0 & 1/6 & 0 \\ 0 & 0 & -14/6 \end{bmatrix}$$

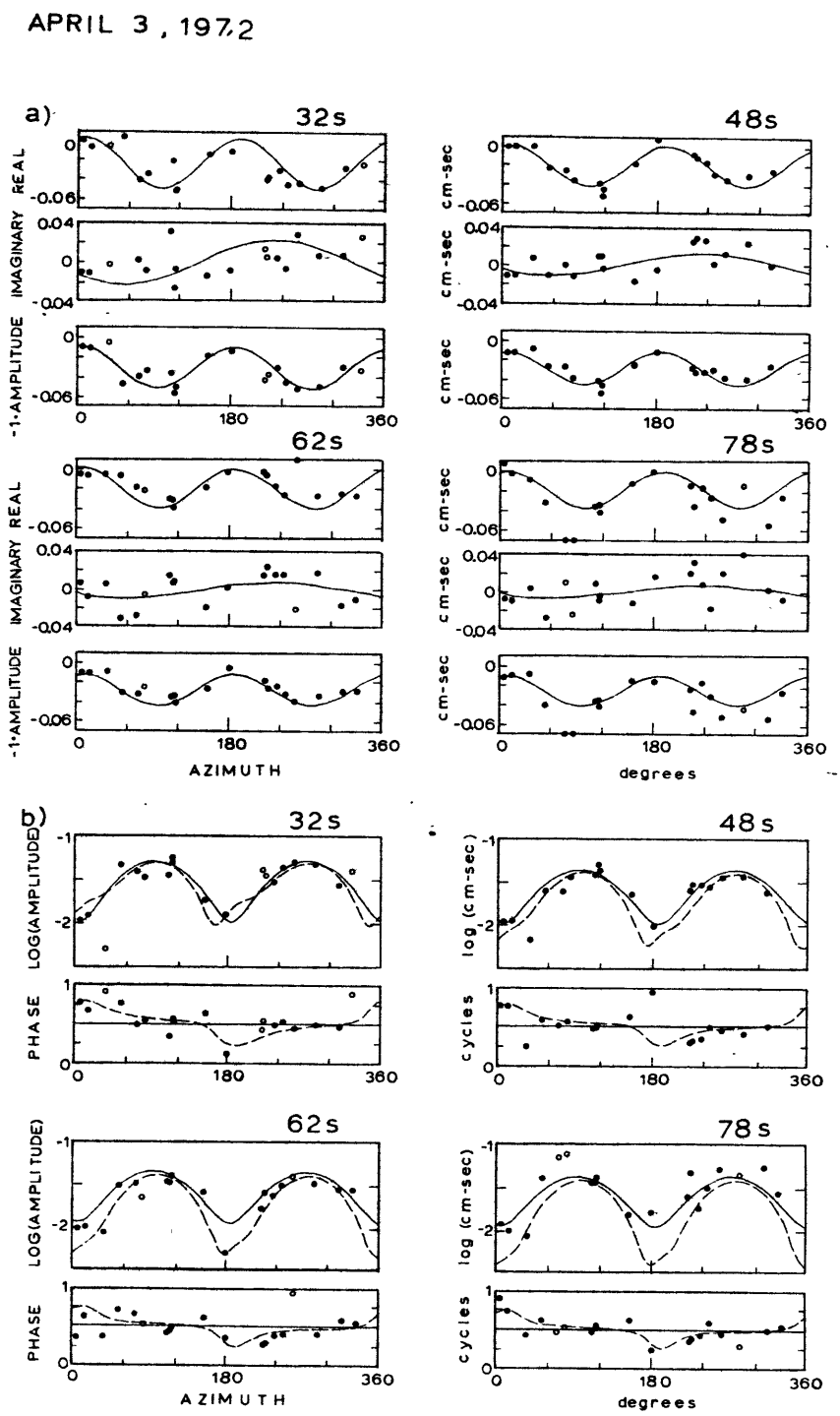

Fig. 9. Examples of the fit to the data of the moment tensor solution for the April 3, 1972, event for a depth of 4 km below seafloor (see caption to Figure 8).

resembling a source with 86% double-couple mechanism. For the events studied in this paper, the double-couple component of the source remains stable when the no-volume-change constraint is removed, and the CLVD component distributes itself between the new CLVD and the explosive components; moreover, the double-couple component increases as the residuals decrease. This suggests that the sources were primarily double couple and that noise in the data is appearing as apparent non-double-couple components.

In summary, the inversion of the surface waves to obtain the source moment tensor for two events on the Reykjanes Ridge indicates double-couple source mechanisms corresponding to normal faulting along planes with a dip of about 45° and strike parallel to the local strike of the spreading center. Both events appear to have been very shallow (1–7 km below seafloor). This study has demonstrated the difficulty in resolving M_{xz} and M_{yz} components of the moment tensor for very shallow events using data that are less than perfect. Be-

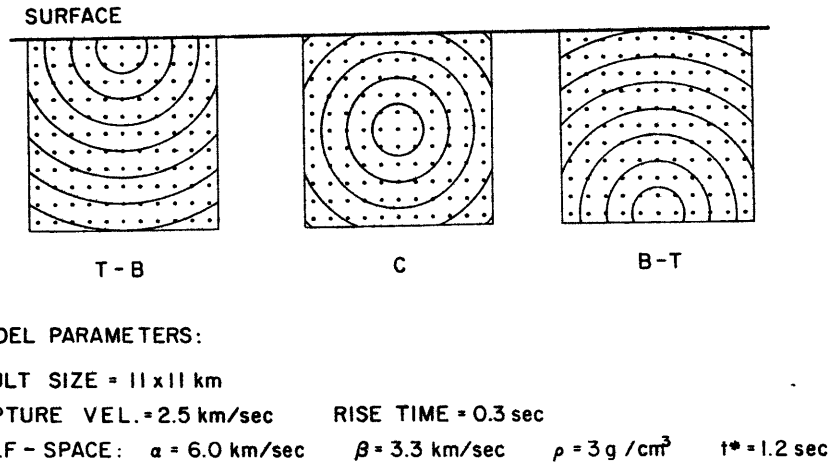

Fig. 10. Model parameters and fault geometry used in the example of *P* wave synthesis for a shallow, finite earthquake source. Circles are successive rupture fronts. Rupture propagates from top to bottom (T-B), from the center (C), and from bottom to top (B-T) in the three cases shown.

cause errors in the corrected initial phase due to mislocation and origin time errors alone are large enough to severely affect the determination of M_{xz} and M_{yz}, the corrected source phase obtained using a regionalized phase velocity model is not sufficiently accurate to resolve these two components of the moment tensor. We have not determined whether the regionalized model is adequate for slightly deeper events for which the inversion is not inherently plagued by this problem.

BODY WAVE ANALYSIS

Background

A striking feature discerned in the surface wave analysis of the two mid-ocean ridge events is the exceptionally shallow focal depth. This result suggests that interference between the direct and reflected body wave phases, as proposed by *Hart* [1978], might be responsible for the apparently nonorthogonal nodal planes. For a dip slip fault, arrivals reflected from the surface at the epicenter can have much larger amplitudes than and opposite polarities to the direct arrivals. If the source is shallow, the temporal separation of the arrivals is less than the pulse width of the impulse resonse of the long-period WWSSN seismometer convolved with the attenuation operator. The arrivals interfere destructively and the apparent nodal planes can be shifted well into the dilatational quadrant. *Langston* [1976] used such interference to constrain the depth of the 1967 Koyna, India, earthquake and cautioned that the interference could lead to errors when determining fault plane solutions from first-motion polarities for earthquakes with shallow focal depths.

We first present a simple hypothetical case of a shallow dip slip fault in a homogeneous half space and show that the interaction of surface reflections with the direct arrivals can indeed cause an apparent reversal of the first-motion polarity at certain take-off angles. We then demonstrate that the surface wave and the body wave observations can be reconciled for the April 3, 1972, earthquake if the event originated near the ocean floor. Although the April 24, 1970, event was too small to be suitable for quantitative modeling by synthetic seismograms, a qualitative inspection of the observed *P* waves suggests that interference could be reponsible for the apparent reversal of first-motion polarity.

The method used to calculate the synthetic seismograms is an extension of the point-source formulation of *Bouchon* [1976] to a finite fault. Seismograms are calculated by numerical integration of point sources distributed on a rectangular grid approximating the fault area. Rupture propagation is simulated by progressively firing individual point sources in a circular pattern radiating from the rupture origin with an appropriate rupture velocity. In order to approximate a smooth rupture, the grid spacing must be such that the firing intervals are smaller than the shortest period important to the problem. As attenuation and the response of the long-period WWSSN instrument effectively filter out periods shorter than 4s, a grid spacing of 1 km is appropriate for a rupture velocity between 2 and 3 km/s. The method incorporates the propagator matrix formulation [*Haskell*, 1953] for computation of the crustal response at the source and receiver and is particularly well

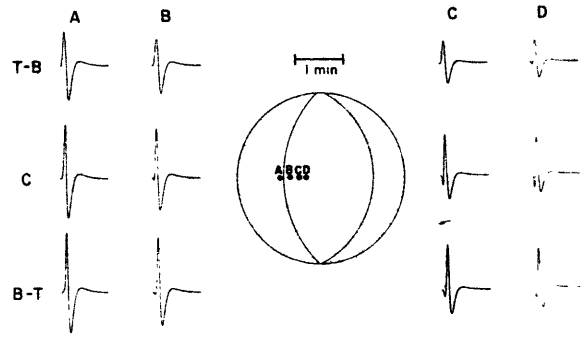

Fig. 11. Theoretical seismograms for models described in Figure 10. The dip of the fault is 55°. Also shown is the theoretical fault plane solution; points A, B, C, and D represent projections of ray paths for which seismograms were calculated. T-B, C, and B-T signify rupture propagation radiating from top-to-bottom, from the center, and from bottom-to-top, respectively.

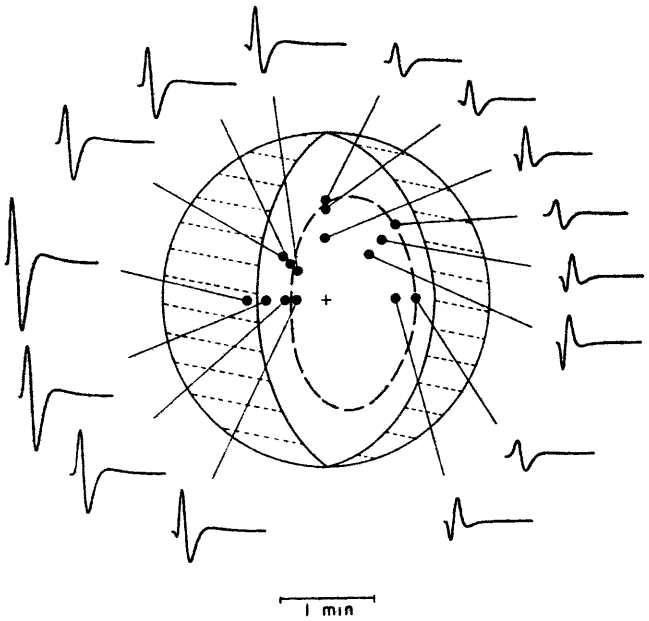

Fig. 12. Theoretical seismograms for case T-B in Figure 10 illustrating the apparent distortion of the fault plane solution due to interference between the direct and reflected phases. Solid line is the true fault plane solution, whereas dashed line delimits the apparent dilatational quadrant. The dip of the fault is 55°.

suited for crustal structures which cause extensive reverberation (e.g., structures with a water layer). A more detailed description of the method is presented in Appendix B.

The fault geometry and the medium parameters used in the example are shown in Figure 10. The fault is an 11 by 11 km rectangle which is located in a homogeneous half space and whose top edge reaches the surface. The rupture velocity is 2.5 km/s (0.8 times the shear velocity of the medium). Each point source has a rise time of 0.3 s. We have investigated three possible situations (Figure 10): rupture initiation (1) at the top, (2) in the center, and (3) at the bottom of the fault. Figure 11 shows synthetic P wave seismograms calculated for the three models depicted in Figure 10. Also shown are the theoretical nodal planes and the projections of the ray paths onto the focal sphere. The dip of the fault is 55°. In all figures the calculated seismograms begin at the time of the first expected arrival. No motion will be observed at that time if interference is canceling the first motion. In the examples, the seismograms are equalized to a common radius on the focal sphere, and the vertical-horizontal scale ratio is kept constant; the relative variations in amplitude for different ray paths are as shown.

Points B, C, and D lie within the theoretical dilatational quadrant, and we would therefore expect to observe downgoing first pulses. This is indeed what we observe when the rupture initiates at the center or at the bottom of the fault. An important aspect of the finite source model which influences the relative amplitude of the direct and reflected arrivals is vertical directivity; downward rupture propagation increases the amplitudes and shortens the effective time functions of the direct arrivals and decreases the amplitudes and lengthens the effective time functions of the reflected arrivals whereas upward propagation has the opposite effect. Because of directivity, the first motion has a larger amplitude if the rupture initiates at the center than at the bottom. Although directivity enhances direct arrivals most when rupture propagates from top to bottom, it plays a secondary role if the hypocenter is very shallow. In this case, destructive interference between the direct arrivals and surface reflections effectively masks the direct arrivals for certain take-off angles. First arrivals along ray paths B and C appear to be compressional, although they lie well within the theoretical dilatational quadrant. The nodal plane appears to be shifted into the dilatational quadrant by approximately 15°. Figure 12 illustrates the distortion of the fault plane solution for 55° dipping fault with rupture initiating near the free surface. If noise were superimposed on the signal, the observable dilatational quadrant would be further reduced.

The fault geometry and medium parameters affect the degree to which interference influences the waveform. For large faults, the finiteness and directivity strongly influence the radiation pattern. Because the vertical directivity for a rupture propagating from top to bottom increases the amplitude of the direct arrivals, decreasing the width of the fault will diminish this effect and increase the amount of observed nonorthogonality. Effects which increase the effective rise time will also cause an emergent direct P arrival and may further contribute to the distortion of the apparent dilatational quadrant (e.g., higher attenuation, lower rupture velocity, and longer rise time).

To apply the results for a normal fault to thrust faulting, only the polarity of the seismograms must be changed. These results can also be generalized to include earthquakes originating beneath low-velocity layers such as water or sediment, the base of which provides sufficient impedance contrast to produce large reflections. The predicted distortion of the apparent first motions, however, applies only to normal and thrust faults. For strike slip faults, the direct P and sP have the same polarity and, while pP has opposite polarity, its amplitude is too small to entirely cancel the direct arrival.

Data

The P wave fault plane solution based on long-period observations from the earthquake of April 3, 1972, is shown in

TABLE 5. Stations Used for the Body Wave Analysis of April 3, 1972, Earthquake

Station	Azimuth, deg	Distance, deg	Magnification
	WWSSN Network		
ATU	87.5	42.6	1500
BKS	−67.6	58.6	3000
CAR	−137.8	50.5	3000
COL	−30.7	50.3	1500
DUG	−71.9	51.8	3000
IST	80.2	43.6	1500
JER	84.5	53.6	3000
KBL	58.1	70.1	6000
NUR	54.2	31.7	1500
OXF	−95.1	42.2	3000
QUE	62.4	72.5	6000
QUI	−130.7	65.0	3000
SCP	−97.8	31.2	1500
TRI	85.1	32.0	3000
TUC	−80.2	56.2	1500
	Canadian Network		
EDM	−57.9	43.8	4500
FFC	−61.5	37.0	4200
FSJ	−51.3	48.3	3400

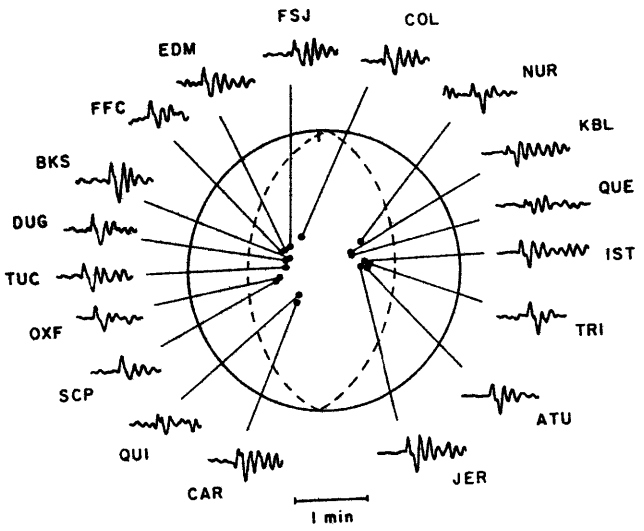

Fig. 13. Examples of long-period *P* wave seismograms (vertical component) observed for the April 3, 1972, event. Seismograms were equalized by correcting for geometrical spreading and for differences in the seismometer magnifications. Dots indicate projections of ray paths to the given stations. Also shown is the preferred fault plane solution.

Figure 7*b* and exhibits characteristically nonorthogonal nodal planes. Examples of the *P* waveforms used in the body wave analysis (Table 5) are shown in Figure 13. Several seconds of background noise preceding each *P* arrival are shown in order to illustrate the signal-to-noise ratio. This event is among the largest recorded on the Mid-Atlantic ridge and provides the best possible data from this tectonic region. In order to avoid complications due either to core or upper mantle structure, only stations at epicentral distances between 30° and 80° were used [*Burdick and Helmberger*, 1978]. Seismograms were equalized by correcting for differences in instrument magnification and for geometrical spreading. The correction for geometrical spreading was calculated using the formula of *Carpenter* [1966] and the *P* wave travel times of *Herrin* [1968]. The similarity in shape and amplitude of seismograms from neighboring stations indicates that background noise and crustal structure below the receivers do not significantly affect the observations. One nodal plane appears to pass through stations OXF and FFC; first motions at stations TUC, DUG, and EDM begin to show a dilatational character, whereas BKS, CAR, and COL are clearly dilatational. The other apparent nodal plane passes between stations KBL and JER. The monochromatic oscillations in the later portion of the seismogram are due to reverberation within the water layer.

Results

The synthesized seismograms are compared to the observations in Figure 14. The best overall match was obtained with a source mechanism compatible with that obtained from the surface wave inversion under constraint 4. The model parameters used in the synthesis are shown in Figure 15. The data do not enable us to determine which of the two nodal planes corresponds to the actual fault plane, and the westward dipping plane was arbitrarily chosen.

The match between the synthetic and observed waveforms is quite good. The fact that the observations tend to show a larger amplitude for the water reverberations than the theoretical seismograms indicates that the fault broke the seafloor. In the calculation of theoretical seismograms, the fault stops just below the surface of the seafloor; a finite displacement of the seafloor would enhance the amplitude of water arrivals. The period of the water reverberations constrains the water depth to be 2.8 km, in good agreement with the bathymetric data (Figure 1). The best overall match was obtained for a fault length of 13 km and a width of 3 km with rupture initiating near the seafloor and propagating bilaterally. We assumed a rupture velocity of 2.6 km/s (0.8 of the shear wave velocity). If the rupture propagation were not perfectly bilateral, the fault could be somewhat shorter. Unilateral rupture propagation, however, does not fit the observations, as it would require a noticeable directivity effect for stations with northern and southern azimuths. The width of the fault is constrained by the observed nonorthogonality. Keeping the other parameters unchanged, the width can be increased to 4 km without significant deterioration of the overall match. Lowering the rupture velocity may further slightly increase the maximum acceptable width and decrease the length. For a 44° dip this bound on width implies that the fault is confined to the upper 3 km or less of the crust.

Figure 16*a* illustrates the sensitivity of the solution to the fault geometry. For the 13 × 3 km fault, the effect of vertical directivity is negligible, and interference between the direct and reflected phases determines the apparent nonorthogonality. For a 6-km-wide fault with rupture propagation from top to bottom, however, the downward directivity enhances the amplitude of the direct arrival, so that it can be observed at take-off angles corresponding to the examples in Figure 16*a*. For bottom-to-top propagation, the direct and reflected arrivals from a 6-km-wide fault are sufficiently separated in time for the direct arrival to be observed. (Although top-to-bottom rupture propagation matches the observed seismograms better than bottom-to-top propagation for a 3 km wide fault, we do not ascribe any tectonic significance to this observation).

In Figure 16*a* we can also see that a model of a point source below the seafloor at a depth of 0.35 km matches the observed data as well as the 13 × 3 km finite fault model. This is not surprising, since for such a narrow fault the effect of vertical directivity is negligible. Although one might argue that extension of the point source model to a finite fault is therefore not justified, for this event we are able to constrain the fault geometry by using a finite fault model, and we feel that this added information is useful for understanding the tectonic processes involved.

The seismograms in Figure 16*b* were calculated for the moment tensor obtained from the surface wave inversion under constraint 2 for a depth of 4 km below seafloor (Table 4*b*). The overall match is worse than that for the solution under constraint 4, supporting the conclusion that the magnitude of the M_{xz} and M_{yz} components of the moment tensor is indeed an artifact of their poor resolution for shallow sources.

The average moment from the body wave analysis is 7.5×10^{24} dyn cm, the same as that obtained from the surface waves. This moment corresponds to about 60 cm of average displacement on the fault. The body wave moment was calculated by normalizing the amplitude of the synthetic seismograms to the first upgoing pulse of the observed *P* waves. The variation in the moment obtained from individual stations (Figure 14) indicates that the average value may be in error by as much as 50%.

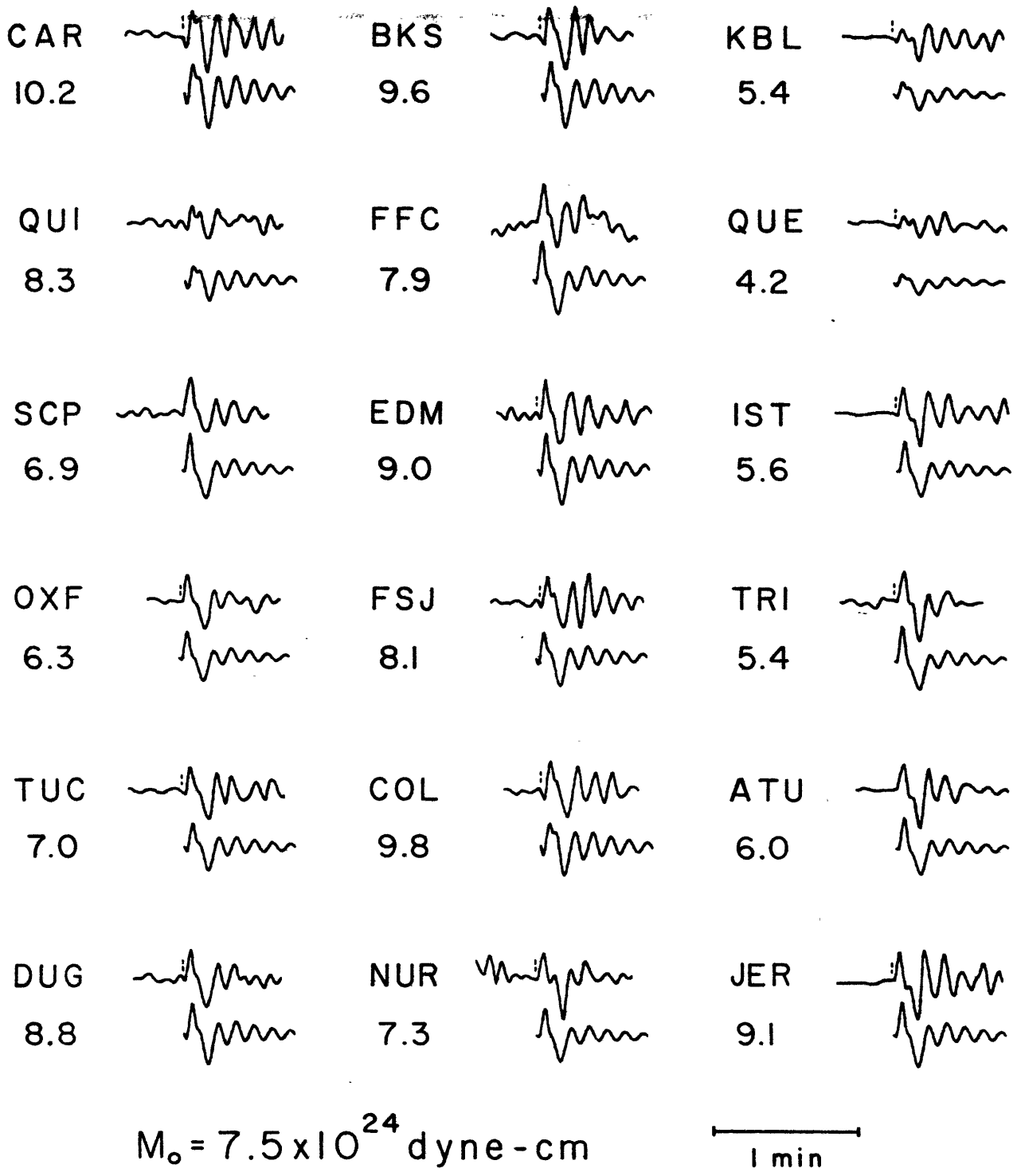

Fig. 14. Theoretical seismograms (vertical component) compared to observed *P* wave data for the April 3, 1972, event. Upper trace is observed; lower trace is calculated. Seismograms were equalized to a seismometer magnification of 3000. Numbers below the station names corresponded to moment (in units of 10^{24} dyn cm) at the given station, and M_0 is the average moment. Dotted lines on the observed seismograms indicate the time of the first motion observed on the short-period vertical component.

For a dip slip fault the stress drop can be expressed as

$$\Delta\sigma = \frac{4(\lambda + \mu)M_0}{\pi(\lambda + 2\mu)LW^2} \quad (3)$$

where λ and μ are the Lame's constants, M_0 is the scalar seismic moment of the double couple, and L and W are the length and width of the fault [*Knopoff*, 1958]. Allowing for the uncertainties discussed above, the stress drop is between 30 and 60 bars. This stress drop is similar to that found for other interplate events [*Kanamori and Anderson*, 1975].

The attenuation correction was applied by keeping a constant value of $t^* = T/Q$, where T is the travel time and Q is

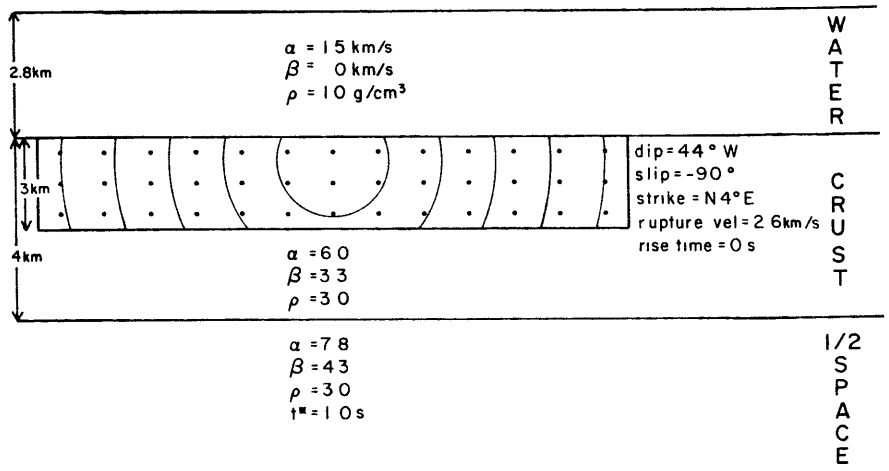

Fig. 15. Model parameters used for the calculation of the theoretical seismograms shown in Figure 14. The indicated fault width is measured downdip and the fault is projected onto a vertical plane parallel to the strike of the fault. Dots represent individual point sources. Fault length is 13 km. The medium structure below the receivers is a homogeneous halfspace with $\alpha = 6$ km/s, $\beta = 3.46$ km/s, and $\rho = 3$ g/cm^3.

the average quality factor along the path. A t^* of 1 s yielded a satisfactory match to the observed data, whereas a value larger than this produced overly smooth synthetic waveforms.

We have also examined the short-period seismograms. At most stations, a low-energy first arrival followed about 1.5 s later by a much stronger arrival was observed (Figure 17). The short-period first-motion arrival time corresponds well to the expected first-motion time indicated by the synthetic long-period records (Figure 14). In order to determine whether the larger arrival could be a depth phase, we calculated seismograms using the instrument response of the WWSSN short-period seismometer but were not able to match the observations by either a simple point source or a smoothly rupturing fault. A match could be obtained only if we assumed a discontinuous rupture process. Because of the large degree of nonuniqueness involved in modeling short-period seismograms, we did not pursue this analysis further.

A poor signal-to-noise ratio for the P waves from the April 24, 1970, earthquake made them unusable for quantitative waveform modeling. However, because of the similarity of the source mechanisms deduced from the source moment tensor inversions, we used the synthetic waveforms calculated for the April 3, 1972, event for a qualitative comparison. Examples of seismograms corresponding in distance and azimuth to those used to model the April 3, 1972, event are shown in Figure 18. If the amplitude of the background noise and expected ampli-

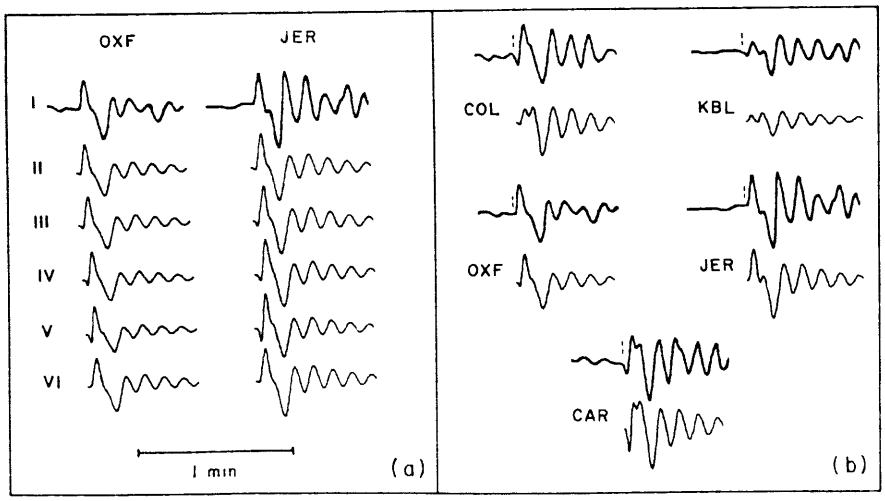

Fig. 16. (*a*) Theoretical P wave seismograms calculated for several fault geometries compared to the observed data (seismogram I). Fault dimensions are 13-km length by 3-km width for seismograms II and III and 7-km length by 6-km width for IV and V. Seismograms II and IV were calculated for rupture initiating at the top of the fault, whereas III and V were calculated for rupture initiating at the bottom. Other parameters are the same as in Figure 15. Seismogram VI was calculated for a point source at a depth of 0.35 km below seafloor and a triangular time function with a 0.8-s rise and 1.8-s roll-off. (*b*) Theoretical P wave seismograms (lower trace) calculated for the moment tensor obtained from the Rayleigh wave inversion under constraint 2 (Table 4*b*, 4 km below sea floor) compared to the observed data at several representative stations (upper trace). The seismograms were calculated for a point source with the same depth and time function as in Figure 16*a*. The fit is worse than that for constraint 4 (Figure 14). For example, constraint 2 requires that station CAR be further within the dilatational quadrant than is indicated by the data and that KBL have the wrong first-motion polarity.

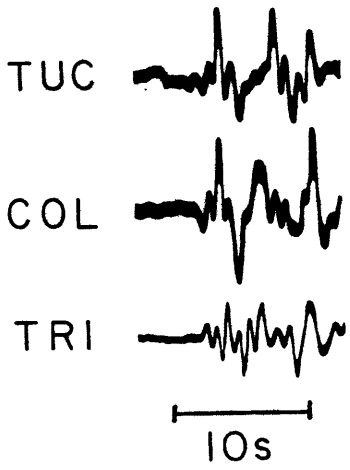

Fig. 17. Examples of short-period P wave seismograms (vertical component) for the April 3, 1972, event. Seismograms are direct copies of observed records.

tude of the first arrival are considered, it is not surprising that all the first motions were originally picked to be compressional. First motion polarity determinations at several stations were later revised to be 'possible' dilatations (e.g., KBL, TAB; Figure 18). The observed waveforms can qualitatively be explained by a shallow fault, similar to that deduced for the April 3, 1972 event.

Discussion

In summary, the body waveforms for the April 3, 1972, Mid-Atlantic ridge earthquake can be matched without invoking anomalous ray propagation if the source is confined to the upper 3 km or less of the crust. The nonorthogonality of the P wave fault plane solution can be entirely explained in terms of interference between the direct and reflected phases. Because of the trial-and-error technique used in the P wave analysis we must, however, admit the possibility of nonuniqueness in the solution.

The moment tensor inversion from the surface waves show that the source was consistent with a pure double-couple mechanism. Because of the long periods used in the surface wave inversion, however, one might argue that a small precursor with an explosive or tensile mechanism could cause the nonorthogonality of the P wave nodal planes and not be observable by the surface waves. Although this is a valid argument, it is not easy to prove because precursors of any mechanism would cause an emergent P wave which, especially for a shallow source, would be very difficult to pick. The agreement between the arrival time measured on the short-period records and that predicted by the synthetic seismograms argues against this explanation.

Thermal models of mid-ocean ridges and observed attentuation of teleseismic S waves passing under the southern Reykjanes Ridge [*Solomon*, 1973] suggest that we might also expect high attenuation of teleseismic P waves. The P wave attenuation ($t^* = 1$ s), however, does not appear to be larger than average. The results for P and S waves are not necessarily contradictory. If the low Q zone in the vicinity of the ridge crest is caused by partial melting, the compressional waves should be less affected than shear waves.

Our results do not exclude the possibility of a small amount of focusing contributing to the nonorthogonality. This would allow a slightly wider fault than that indicated by our analysis. We prefer that shallowness of the source be the explanation for the anomalous P wave fault plane solutions because of the simplicity of such a mechanism and because of the agreement between the results of the body wave synthesis and surface wave inversion.

CONCLUSIONS

The major conclusions of this study are the following:

1. The source moment tensor can be retrieved from the Rayleigh wave radiation pattern for a single isolated event. This method of obtaining the source mechanism is useful for small events for which the body wave fault plane solutions may be inconclusive and/or perplexing. For very shallow sources, however, the M_{xz} and M_{yz} components become poorly resolved and very sensitive to errors in the data; moreover, the three diagonal components cannot be independently determined. By comparing the results of the inversion performed under a series of increasingly more stringent constraints, we are able to qualitatively evaluate the validity of imposing constraints which lead to a stable solution.

2. The final moment tensor solutions for two events along the southern Reykjanes Ridge indicate double-couple, normal faulting mechanisms with the tension axis approximately horizontal and oriented perpendicular to the spreading center. For both events, the surface waves indicate a focal depth of 1–7 km below the seafloor.

3. The nonorthogonality of the nodal planes frequently observed in the body wave fault plane solutions for mid-ocean ridge normal faulting events can be attributed to extreme shallowness of the source which results in interference between the direct and reflected phases and effectively masks the first-motion recorded on long-period seismograms.

4. Comparison of observed P waveforms from the April 3, 1972, Reykjanes Ridge event to those calculated for a fault with an orientation obtained from the surface wave analysis indicates that the source was a long, narrow fault which broke the seafloor.

The faulting process implied by these results provides additional constraints on models of spreading center tectonics and thermal structure. The double-couple nature of the solutions relates these earthquakes to tectonic rather than volcanic processes and supports the evidence from seismicity and topography which associates teleseismically observable ridge-crest activity with rift valley formation. An important question about mid-ocean ridges concerns the depth of hydrothermal circulation and its effect on the thermal structure of the crust. The close agreement between observed ridge crest topography and that calculated for the simple model of a con-

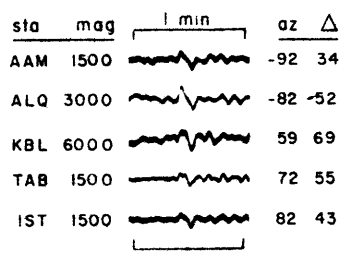

Fig. 18. Examples of long-period P wave seismograms recorded for the April 24, 1970, earthquake. Seismograms are direct copies of observed vertical component records. Mag is station magnification, az is station azimuth, and Δ is epicentral distance.

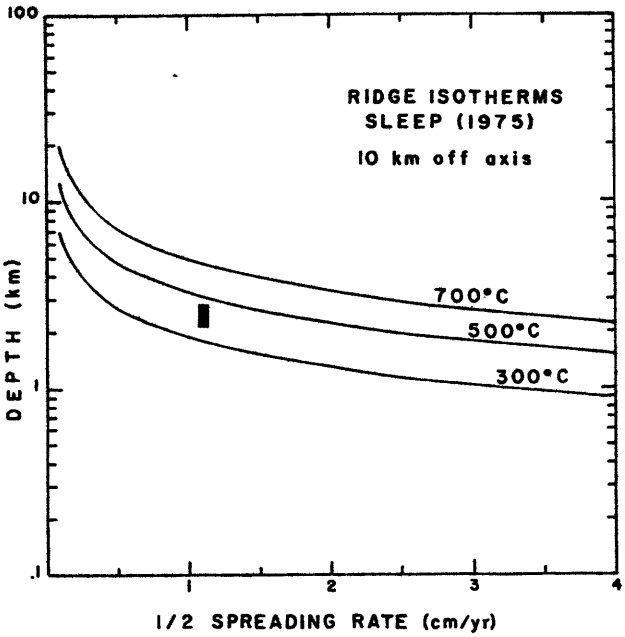

Fig. 19. Depth to various isotherms at a distance of 10 km from the ridge axis versus spreading rate, calculated for the thermal model of *Sleep* [1975]. Also indicated is the depth of faulting, 2.1–2.8 km, corresponding to the 3- to 4-km-wide fault obtained for the April 3, 1972, event. Figure modified from *Solomon and Burr* [1979].

ductively cooling slab suggests that extensive hydrothermal circulation is restricted to the top few kilometers of the crust [*Fehn and Cathles,* 1979]. On the other hand, deep (5–8 km) hydrothermal circulation has been invoked in order to depress the isotherms enough to produce a cold brittle layer of sufficient thickness to support faults with the dimensions implied by the moments of the largest spreading center events if it is assumed that length-width ratios and stress drops are similar to those observed for other plate boundary earthquakes [*Solomon,* 1979]. The long, narrow fault plane suggested by an analysis of the body waves from the earthquake on the Reykjanes Ridge, however, can be entirely accommodated within the brittle crust determined from the purely conductive model of *Sleep* [1975] if it is assumed that the earthquake occurred 10 km from the axis, along the rift valley walls (Figure 19). An as yet unanswered question is whether the length-width ratio will increase with increasing moment; the largest earthquake studied from this region had a moment of 2×10^{25} dyn cm [*Hart,* 1978], approximately twice that of the larger event studied here. Further studies of fault dimensions, stress drops, and recurrence intervals for ridge earthquakes in regions spanning a range of spreading rates should permit the incorporation of time-dependent faulting and stress release in models which simulate the spreading process and are used to explain the relationship between spreading rate, topography, and magma supply [e.g., *Sleep and Rosendahl,* 1979].

APPENDIX A: MOMENT TENSOR SOURCE REPRESENTATION AND SURFACE WAVE RADIATION

The displacement at y at time ζ in the direction $\hat{k}$ due to a seismic source at time t can be represented as

$$u_k(\mathbf{y}, \zeta) = \int_{-\infty}^{\infty} dt \left\{ \int_V dV_x G_{kj}(\mathbf{y}, \zeta; \mathbf{x}, t) \gamma_j^v(\mathbf{x}, t) + \int_S dS_x G_{kj}(\mathbf{y}, \zeta; \mathbf{x}, t) \gamma_j^s(\mathbf{x}, t) \right\} \quad \text{(A1)}$$

where V is the source volume, S is the surface of the source volume, γ_j^v and γ_j^s are the equivalent volume and surface forces corresponding to a physical mechanism, $G_{kj}(\mathbf{y}, \zeta; \mathbf{x}, t)$ is the impulse response or Green's function of the medium, and repeated indices imply summation [*Aki and Richards,* 1980]. If the 'moment density tensor' $\mathbf{m}$ is defined to be a symmetric tensor such that $m_{ij,i} = -\gamma_j^v$ in V and $n_i m_{ij} = \gamma_j^s$ on S ($\mathbf{n}$ being the unit normal to the surface), we can regroup the expression for displacement into one term using Gauss's theorem [*Backus and Mulcahy,* 1976]:

$$\begin{aligned} u_k(\mathbf{y}, \zeta) &= \int_{-\infty}^{\infty} \left\{ -\int_V dV_x G_{kj} m_{ij,i} + \int_S dS_x G_{kj} n_i m_{ij} \right\} dt \\ &= \int_{-\infty}^{\infty} \left\{ -\int_V dV_x G_{kj} m_{ij,i} + \int_V dV_x (G_{kj} m_{ij})_{,i} \right\} dt \\ &= \int_{-\infty}^{\infty} dt \int_V dV_x m_{ij} G_{kj,i} = \int_{-\infty}^{\infty} dt\, M_{ij} G_{kj,i} \end{aligned} \quad \text{(A2)}$$

For an effective point source, the 'moment tensor' M can be defined as the integral of the moment density tensor over the source volume and surface and can be retrieved from the far-field displacement radiation pattern (for free oscillations, see *Gilbert* [1970] and *Gilbert and Dziewonski* [1975]; for surface waves, see *McCowan* [1976] and *Mendiguren* [1977]; for body waves, see *McCowan* [1977] and *Strelitz* [1978]). The advantage of this representation is that the inversion of far-field displacements to obtain the moment tensor is linear and is not dependent on a presupposed source mechanism.

We can then relate observed moment tensors derived from data to phenomenological source models through the equivalent body forces. Although the total equivalent force is uniquely determined from the resulting motion, the interpretation in terms of a phenomenological source model, however, is not unique, as a given moment tensor can result from several different linear combinations of moment tensors. This ambiguity is inherent in any determination of source mechanism from the displacement field [*Aki and Richards,* 1980].

If we assume that the principal stress axes of the various components are coincident, the diagonalized moment tensor can be uniquely decomposed into isotropic, double-couple, and compensated linear vector dipole components. We first remove the isotropic part:

$$\begin{aligned} \mathbf{M}' &= \mathbf{M} - \tfrac{1}{3}(\text{trace } \mathbf{M})\mathbf{I} \\ &= M_0 \begin{bmatrix} 1 & 0 & 0 \\ 0 & f-1 & 0 \\ 0 & 0 & -f \end{bmatrix} \qquad 0 \le f \le \tfrac{1}{2} \end{aligned} \quad \text{(A3)}$$

where $\mathbf{I}$ is the identity matrix. We may then separate the double couple and compensated linear vector dipole components [*Knopoff and Randall,* 1970]:

$$M' = M_0 \left\{ (1-2f) \begin{bmatrix} 1 & 0 & 0 \\ 0 & -1 & 0 \\ 0 & 0 & 0 \end{bmatrix} + 2f \begin{bmatrix} 1 & 0 & 0 \\ 0 & -\frac{1}{2} & 0 \\ 0 & 0 & -\frac{1}{2} \end{bmatrix} \right\} \quad \text{(A4)}$$

The double-couple scalar moment M_{DC} is $(1-2f)M_0$, and the corresponding fault plane solution can be obtained from the principal axes of the moment tensor. M_{DC} can be related to the dimensions of a shear fault: $M_{DC} = \mu\bar{u}A$, where μ is the shear modulus, $\bar{u}$ is average displacement, and A is fault area [*Aki*, 1966].

In this study, the moment tensor is derived from the surface wave radiation pattern. For a vertically heterogeneous earth, the Fourier spectrum of the vertical component of the fundamental Rayleigh wave due to a point source with a step function source time function is

$$u(r, \theta, \omega) = Ae^{i\phi} = \frac{Y_1(0, \omega)}{4CUI\omega} [2/(\pi kr)]^{1/2} \exp[-i(\omega r/C - \pi/4)]$$

$$\cdot \left\{ (M_{xx} + M_{yy}) \frac{kY_3(h, \omega)}{2} + M_{zz} \frac{-Y_2(h, \omega) - \lambda(h)kY_3(h, \omega)}{\lambda(h) + 2\mu(h)} \right.$$

$$- (M_{yy} - M_{xx}) \frac{kY_3(h, \omega) \cos 2\theta}{2} + M_{xy}kY_3(h, \omega) \sin 2\theta$$

$$\left. -i \left[M_{xz} \frac{Y_4(h, \omega) \cos \theta}{\mu(h)} + M_{yz} \frac{Y_4(h, \omega) \sin \theta}{\mu(h)} \right] \right\} \quad \text{(A5)}$$

where A and ϕ are the observed amplitude and phase at the angular frequency ω and the M_{ij} are the moment tensor components in Cartesian coordinates with the x, y, and z axes pointed east, north, and up [*Mendiguren*, 1977]. The position of the receiver is expressed in polar coordinates, where r is distance and θ is azimuth measured counterclockwise from east. The $Y_i(h, \omega)$ are the eigenfunctions derived by *Saito* [1967] for the surface wave excitation problem and are functions of angular frequency and depth h; $\lambda(h)$ and $\mu(h)$ are the Lamé coefficients; $\omega^2 I$, k, C, and U are the kinetic energy, wave number, phase velocity, and group velocity. The moment tensor components can be retrieved through a linear inversion of the real and imaginary parts of the observed radiation pattern if a good azimuthal distribution of stations is available.

Appendix B: Method of *P* Wave Synthesis for Finite Sources

A fundamental assumption in calculations of teleseismic body waves from shallow sources is that only the free surface and the crustal and uppermost mantle structure at the source and receiver have a significant effect on the shape of the seismograms. Gradients within the mantle are considered to be too small to cause converted or reflected phases and travel time caustics, and the effect of the mantle portion of the propagation path is restricted to geometrical spreading and attenuation. For epicentral distances between 30° and 80° these assumptions are well justified [*Burdick and Helmberger*, 1978]. The synthetic seismogram is obtained by convolution of the response of the source $U(t)$ with the responses of the receiver $I(t)$, the crust below the receiver $R(t)$, attenuation $A(t)$, and geometrical spreading G.

Our technique for calculating source response is an extension of the formulation of *Bouchon* [1976] for a double-couple point source to a finite fault with circular rupture propagation. Contributions from point sources distributed along the fault surface on an equally spaced grid are numerically integrated. Rupture propagation is simulated by progressively firing individual point sources in a circular pattern radiating from the origin with a constant rupture velocity. In order to approximate a smooth rupture, the grid spacing must be such that the firing intervals are smaller than the shortest period important to the problem. The integration is performed in the frequency domain and then transformed back into the time domain. This enables efficient use of the propagator matrix algorithm of *Haskell* [1953] to obtain the response of the medium. This approach is particularly useful for the case examined in this paper because of the prolonged ringing of the P wave in the water layer. The ray-theoretical approach [e.g., *Langston and Helmberger*, 1974] is less efficient for such a large number of rays. Although we integrate in the frequency domain, we can separate individual phases by setting appropriate potentials to zero.

The problem configuration is the same as in the work of *Bouchon* [1976]. We assume that the dislocation has the same time dependence at any point on the fault surface and can be written in the form

$$D(\xi, t) = F(\xi)E(t - |\xi - \xi_0|/c) \quad \text{(B1)}$$

Its Fourier transform is

$$\hat{D}(\xi, \omega) = F(\xi)\hat{E}(\omega) \exp(-i\omega|\xi - \xi_0|/c) \quad \text{(B2)}$$

where $\xi = (\xi_1, \xi_2)$ is a point on the fault surface, ξ_0 is the point of origin of the rupture, c is the rupture velocity, and ω is the angular frequency. The fault is a rectangle of length $L = N\Delta\xi$, parallel to the surface, and of width $W = M\Delta\xi$, dipping at an arbitrary angle; $\Delta\xi$ is the grid spacing; and N and M are integers. The far-field P wave displacement spectrum due to this source can be expressed as

$$\hat{U}(\omega) = \Delta\xi^2 \sum_{n=1}^{N} \sum_{m=1}^{M} \mu_j \hat{D}(\xi, \omega)$$

$$\cdot \exp[ik(\xi_1 \cos\phi - \xi_2 \cos d \cdot \sin\phi)]$$

$$\cdot \sum_{i=1}^{4} g_{ij}(\omega) \exp[i\Delta_{ij}(z_0 + \xi_1 \sin d)] \quad \text{(B3)}$$

with

$$\xi_1 = (n - \tfrac{1}{2})\Delta\xi \qquad \xi_2 = (m - \tfrac{1}{2})\Delta\xi$$

where z_0 is the depth to the top of the fault; k is the horizontal wave number, which is determined by the take-off angle; ϕ and d are azimuth and dip of the fault; and μ_j is the shear modulus. The subscript j refers to the layer within the crustal model in which the point source is located. The terms g_{ij} and Δ_{ij} are as defined by *Bouchon* [1976] and are related to the upgoing and downgoing P and S waves excited by a source located within the layer j.

Following the same notation, the response of the crustal layers below the receiver to an incident P wave can be written in the form

$$\hat{R}(\omega) = [(A_{21} - A_{11})\nu_1 - (B_{11} + B_{21})k]\alpha_n/\omega \quad \text{(B4)}$$

where A_{ij} and B_{ij} represent upgoing and downgoing compres-

sional and rotational potentials in the layer immediately below the receiver; ν_1 is the corresponding vertical compressional wave number; and α_n is the compressional velocity of the medium below the crustal layers.

When calculated seismograms are to be compared to observed data, a correction must be made for geometrical spreading. This is a frequency-independent term which can be expressed in the form [*Carpenter*, 1966]

$$G = \frac{\alpha_S}{r_S r_R}\left(\frac{\rho_S \alpha_S}{\rho_R \alpha_R}\frac{1}{\sin\Delta\cos i_S \cos i_R}\frac{dT}{d\Delta}\left|\frac{d^2T}{d\Delta^2}\right|\right)^{1/2} \quad \text{(B5)}$$

with

$$\sin i_S = \frac{\alpha_S}{r_S}\frac{dT}{d\Delta} \qquad \sin i_R = \frac{\alpha_R}{r_R}\frac{dT}{d\Delta}$$

where α_S, ρ_S, α_R, and ρ_R are the velocity and density of the material below the crustal layers at the source and receiver, respectively, i_S is the angle the ray makes with the vertical at the base of the crust below the source and i_R is the corresponding angle below the receiver, r_S and r_R denote the distance from the base of the crust at the source and receiver to the center of the earth, T is the P wave travel time, and Δ is the angular distance between the source and receiver.

The effect of attenuation in the mantle is introduced by the causal Q operator of *Futterman* [1962]. In the frequency domain the operator is given by

$$A(\omega) = \exp\left[-\tfrac{1}{2}t^*\left(\frac{\omega}{1+\frac{1}{\pi}\ln\frac{\omega}{\omega_0}}\right)\right]$$

$$\cdot \exp\left[it^*\omega Q\left(\frac{1}{1+\frac{\pi}{Q}\ln\frac{\omega_1}{\omega_0}} - \frac{1}{1+\frac{\pi}{Q}\ln\frac{\omega}{\omega_0}}\right)\right] \quad \text{(B6)}$$

for the angular frequency ω in the range $\omega_0 \le \omega \le \omega_1$, ω_1 and ω_0 being the highest and lowest frequencies resolved in the data. The quantity t^* is defined as T/Q, where Q is the average quality factor along the path.

Finally, the seismogram must be convolved with the appropriate instrument response; for long-period WWSSN stations we use the formula by *Hagiwara* [1958].

Acknowledgments. We thank Pall Einarsson for first drawing our attention to the unusual earthquake of April 24, 1970, and for an early preprint of his paper. We also thank Kei Aki, Doug McCowan, Howard Patton, and Gerardo Suarez for assistance with the moment tensor analysis, and Michel Bouchon for advice on body wave synthesis. This research was supported by the Division of Earth Sciences, National Science Foundation, under NSF grant EAR77-09965; by the Advanced Research Projects Agency under contract F44620-75-C-0064 administered by the Air Force Office of Scientific Research; and by fellowships from the National Science Foundation (A.M.T.) and the Alfred P. Sloan Foundation (S.C.S.).

REFERENCES

Aki, K., Generation and propagation of G waves from the Niigata earthquake of June 16, 1964, *Bull. Earthquake Res. Inst. Tokyo Univ.*, *44*, 23–88, 1966.

Aki, K., and H. Patton, Determination of seismic moment tensor using surface waves, *Tectonophysics*, *43*, 213–222, 1978.

Aki, K., and P. Richards, *Methods of Quantitative Seismology*, vol. I, W. H. Freeman, San Francisco, Calif., 1980.

Backus, G., and M. Mulcahy, Moment tensors and other phenomenological descriptions of seismic sources, I, Continuous displacements, *Geophys. J. R. Astron. Soc.*, *46*, 341–361, 1976.

Ben-Menahem, A., and M. N. Toksöz, Source mechanism from spectra of long-period seismic surface waves, 1, Mongolian earthquake of December 4, 1957, *J. Geophys. Res.*, *67*, 1943–1955, 1962.

Ben-Menahem, A., and M. N. Toksöz, Source mechanism from spectra of long period seismic surface waves, 3, The Alaska earthquake of July 10, 1958, *Bull. Seismol. Soc. Am.*, *53*, 905–919, 1963.

Bouchon, M., Teleseismic body wave radiation from a seismic source in a layered medium, *Geophys. J. R. Astron. Soc.*, *47*, 515–530, 1976.

Burdick, L. J., and D. V. Helmberger, The upper mantle *P* velocity structure of the western United States, *J. Geophys. Res.*, *83*, 1699–1712, 1978.

Calganile, G., and G. F. Panza, Crust and upper mantle structure under the Baltic shield and Barents Sea from dispersion of surface waves, *Tectonophysics*, *47*, 59–71, 1978.

Carpenter, E. W., A qualitative evaluation of teleseismic explosion record, *Proc. R. Soc., Ser. A*, *290*, 396–407, 1966.

Einarsson, P., Seismicity and earthquake focal mechanisms along the mid-Atlantic plate boundary between Iceland and the Azores, *Tectonophysics*, *55*, 127–153, 1979.

Fehn, U., and L. M. Cathles, Hydrothermal convection at slow-spreading mid-ocean ridges, *Tectonophysics*, *55*, 239–260, 1979.

Forsyth, D. W., The early structural evolution and anisotropy of the oceanic upper mantle, *Geophys. J. R. Astron. Soc.*, *43*, 102–162, 1975.

Francis, T. J. G., The seismicity of the Reykjanes Ridge, *Earth Planet. Sci. Lett.*, *18*, 119–124, 1973.

Futterman, W. I., Dispersive body waves, *J. Geophys. Res.*, *67*, 5279–5291, 1962.

Gilbert, F., Excitation of the normal modes of the earth by earthquake sources, *Geophys. J. R. Astron. Soc.*, *22*, 223–226, 1970.

Gilbert, F., and A. M. Dziewonski, An application of normal mode theory to the retrieval of structural parameters and source mechanism from seismic spectra, *Phil. Trans. R. Soc. London, Ser. A*, *278*, 187–269, 1975.

Gregersen, S., Surface wave dispersion and crust structure in Greenland, *Geophys. J. R. Astron. Soc.*, *22*, 29–39, 1971.

Hagiwara, T., A note on the theory of the electromagnetic seismograph, *Bull. Earthquake Res. Inst. Tokyo Univ.*, *36*, 139–164, 1958.

Hart, R., Body wave studies of the September, 1969, North Atlantic Ridge earthquake (abstract), *Eos Trans. AGU*, *59*, 1135, 1978.

Haskell, N. A., The dispersion of surface waves in multilayered media, *Bull. Seismol. Soc. Am.*, *43*, 17–34, 1953.

Herrin, E., Introduction to '1968 Seismological tables for *P* phases,' *Bull. Seismol. Soc. Am.*, *58*, 1193–1241, 1968.

Kafka, A. L., and D. J. Weidner, The focal mechanisms and depths of small earthquakes as determined from Rayleigh wave radiation patterns, *Bull. Seismol. Soc. Am.*, *69*, 1379–1390, 1979.

Kanamori, H., and D. L. Anderson, Theoretical basis of some empirical relations in seismology, *Bull. Seismol. Soc. Am.*, *65*, 1073–1096, 1975.

Knopoff, L., Energy release in earthquakes, *Geophys. J. R. Astron. Soc.*, *1*, 44–52, 1958.

Knopoff, L., and J. Randall, The compensated linear vector dipole—A possible mechanism for deep earthquakes, *J. Geophys. Res.*, *75*, 4957–4963, 1970.

Landisman, M., A. Dziewonski, and Y. Sato, Recent improvements in the analysis of surface wave observations, *Geophys. J. R. Astron. Soc.*, *17*, 359–403, 1969.

Langston, C. A., Body wave inversion of the Koyna, India, earthquake of December 10, 1967, and some implications for body wave focal mechanisms, *J. Geophys. Res.*, *81*, 2571–2572, 1976.

Langston, C. A., and D. V. Helmberger, A procedure for modeling shallow dislocation sources, *Geophys. J. R. Astron. Soc.*, *42*, 117–130, 1975.

Laughton, A. S., R. C. Searle, and D. G. Roberts, The Reykjanes Ridge crest and the transition between its rifted and non-rifted regions, *Tectonophysics*, *55*, 173–177, 1979.

Mathews, J., and R. Walker, *Mathematical Methods of Physics*, pp. 273–275, W. A. Benjamin, New York, 1964.

McCowan, D. W., Moment tensor representation of surface wave sources, *Geophys. J. R. Astron. Soc.*, *44*, 595–599, 1976.

McCowan, D. W., A moment tensor representation of body-wave displacement vectors on the focal sphere, semi-annual technical summary, pp. 9–11, Lincoln Lab., Mass. Inst. of Technol., Cambridge, March 1977.

Mendiguren, J. A., Inversion of surface wave data in source mechanism studies, *J. Geophys. Res., 82,* 889–894, 1977.

Mitchell, B. J., Radiation and attenuation of Rayleigh waves from the southeastern Missouri earthquake of October 21, 1965, *J. Geophys. Res., 78,* 886–899, 1973.

Naponen, I., Surface wave phase velocities of Finland, *Bull. Seismol. Soc. Am., 56,* 1093–1104, 1966.

Oliver, J., R. Kovach, and J. Dorman, Crustal structure of the New York–Pennsylvania area, *J. Geophys. Res., 66,* 215–225, 1961.

Patton, H., A note on the source mechanism of the southeastern Missouri earthquake of October 21, 1965, *J. Geophys. Res., 81,* 1483–1486, 1976.

Patton, H. J., Source and propagation effects of Rayleigh waves from central Asian earthquakes, Ph.D. thesis, 342 pp., Mass. Inst. of Technol., Cambridge, 1978.

Patton, H., Reference point method for determining the source and path effects of surface waves, *J. Geophys. Res., 85,* 821–848, 1980.

Patton, H., and K. Aki, Bias in the estimate of seismic moment tensor by the linear inversion method, *Geophys. J. R. Astron. Soc., 59,* 479–495, 1979.

Robson, G. R., K. G. Barr, and L. C. Luna, Extension failure: An earthquake mechanism, *Nature, 218,* 28–32, 1968.

Saito, M., Excitation of free oscillations and surface waves by a point source in a vertically heterogeneous earth, *J. Geophys. Res., 72,* 3689–3699, 1967.

Sleep, N. H., Formation of oceanic crust: Some thermal constraints, *J. Geophys. Res., 80,* 4037–4042, 1975.

Sleep, N. H., and B. R. Rosendahl, Topography and tectonics of mid-ocean ridge axes, *J. Geophys. Res., 84,* 6831–6839, 1979.

Solomon, S. C., Shear wave attenuation and melting beneath the Mid-Atlantic Ridge, *J. Geophys. Res., 78,* 6044–6059, 1973.

Solomon, S. C., Earthquake source parameters, median valley faulting, and the depth of hydrothermal circulation for slow spreading ridges (abstract), *Eos Trans. AGU, 60,* 376, 1979.

Solomon, S. C., and N. C. Burr, The relationship of source parameters of ridge-crest and transform earthquakes to the thermal structure of oceanic lithosphere, *Tectonophysics, 55,* 107–126, 1979.

Solomon, S. C., and B. R. Julian, Seismic constraints on ocean-ridge mantle structure: Anomalous fault phane solutions from first motions, *Geophys. J. Roy, Astron. Soc., 38,* 265–285, 1974.

Strelitz, R. A., Moment tensor inversions and source models, *Geophys. J. R. Astron. Soc., 52,* 359–364, 1978.

Strelitz, R. A., The fate of the downgoing slab: A study of the moment tensors from body waves of complex deep focus earthquakes, *Phys. Earth Planet. Int., 21,* 83–96, 1980.

Stump, B. W., The determination of source mechanism by linear inversion of seismograms (abstract), *Eos Trans. AGU, 57,* 953, 1976.

Sykes, L. R., Mechanism of earthquakes and nature of faulting on the mid-ocean ridge, *J. Geophys. Res., 72,* 2131–2153, 1967.

Sykes, L. R., Focal mechanism solutions for earthquakes along the world rift system, *Bull. Seismol. Soc. Am., 60,* 1749–1752, 1970.

Tsai, Y. B., and K. Aki, Simultaneous determination of the seismic moment and attenuation of seismic surface waves, *Bull. Seismol. Soc. Am., 59,* 275–287, 1969.

Vogt, P. R., and G. L. Johnson, Transform faults and longitudinal flow below the mid-oceanic ridge, *J. Geophys. Res., 80,* 1399–1428, 1975.

Weidner, D. J., Rayleigh wave phase velocities in the Atlantic Ocean, *Geophys. J. R. Astron. Soc., 36,* 105–139, 1974.

Weidner, D. J., and K. Aki, Focal depth and mechanism of mid-ocean ridge earthquakes, *J. Geophys. Res., 78,* 1818–1831, 1973.

Wickens, A. J., Variations in lithospheric thickness in Canada, *Can. J. Earth Sci., 8,* 1154–1162, 1971.

(Received November 13, 1979;
revised September 9, 1980;
accepted September 23, 1980.)

APPENDIX II

Catalogue of waveforms recorded by the MIT OBS from earthquakes in the Orozco Fracture Zone.

For each event, the three components are, from top to bottom, H2, H1 and V.

The event time is given as day/hour/minutes. The vertical dotted lines indicate seconds.

The amplitude scale on the left is in units of millivolts and applies to the two horizontal components. The amplitude scale for the vertical component is twice that for the horizontals.

All data can be obtained in digital format from the ROSE data archive (see LaTraille et al., 1982).

REGION I

02/07/18

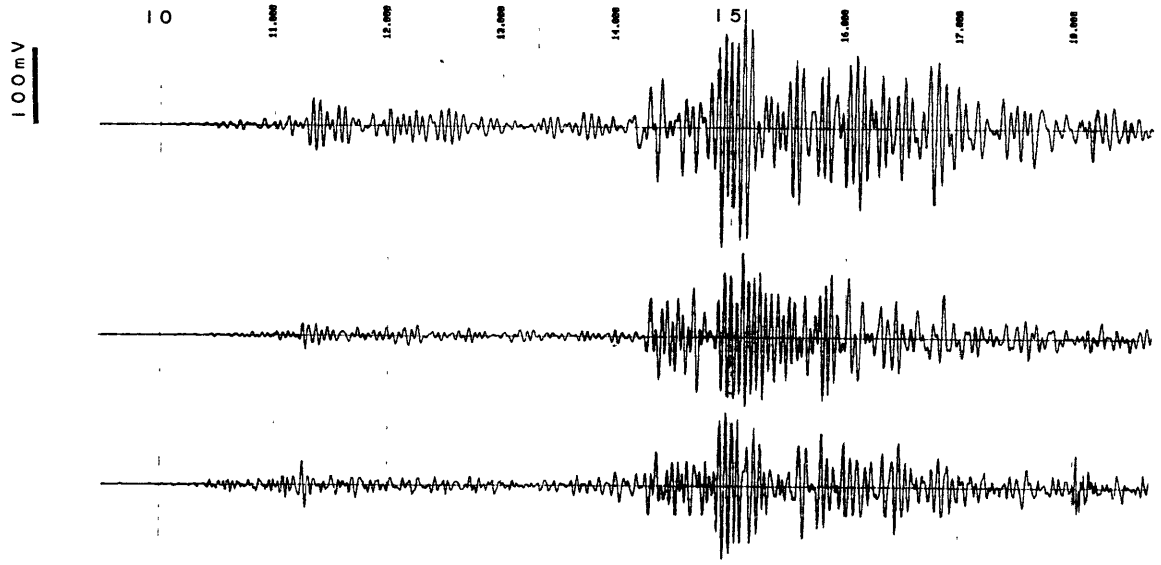

02/17/21

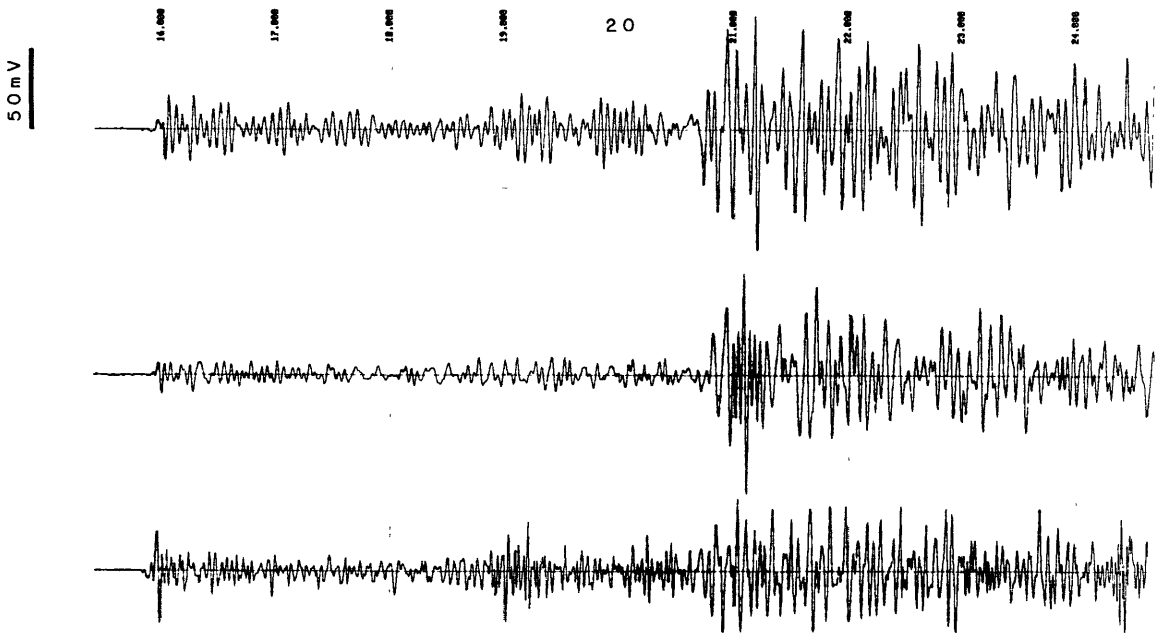

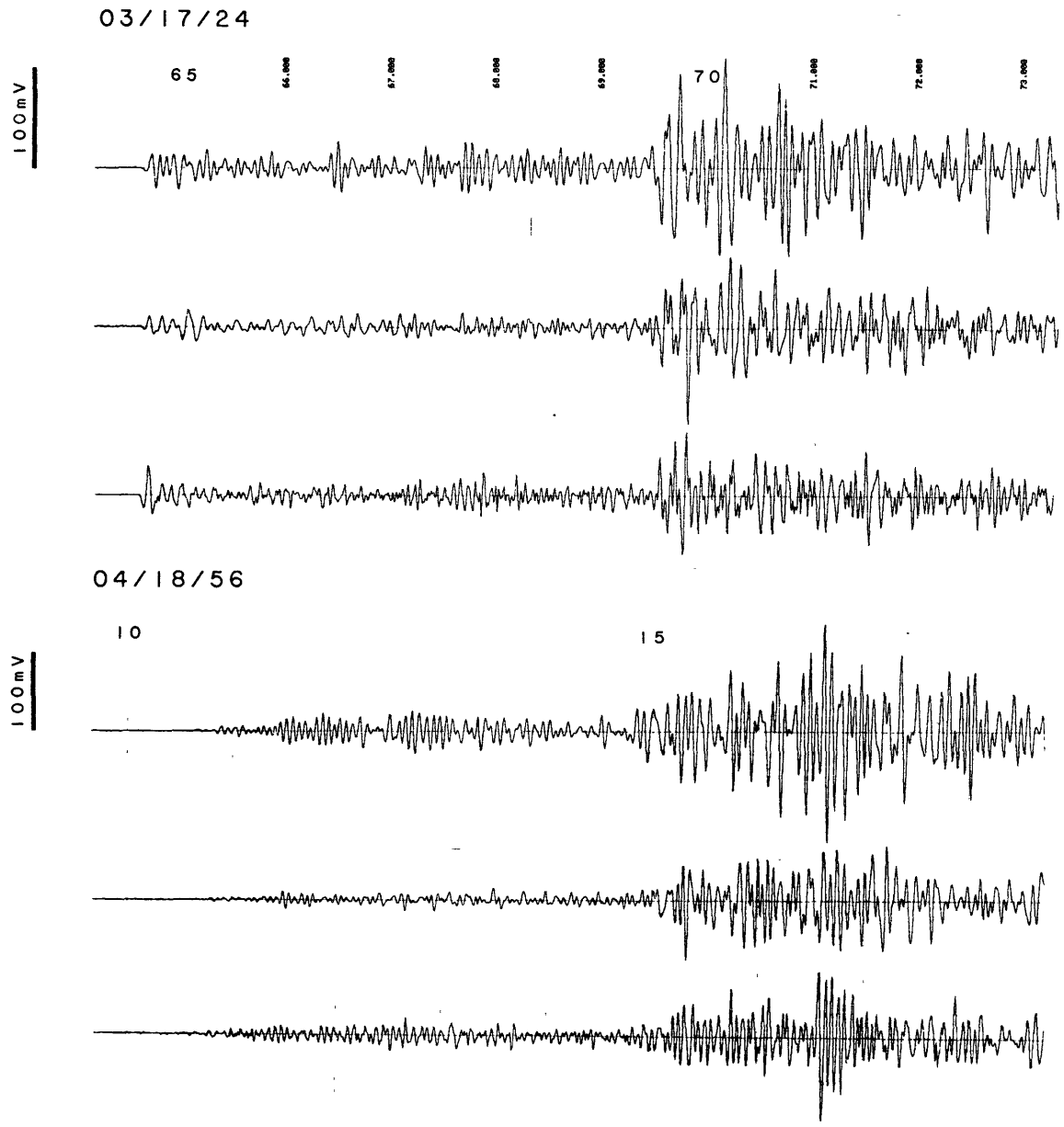
03/17/24
65
70
100mV
04/18/56
10
15
100mV

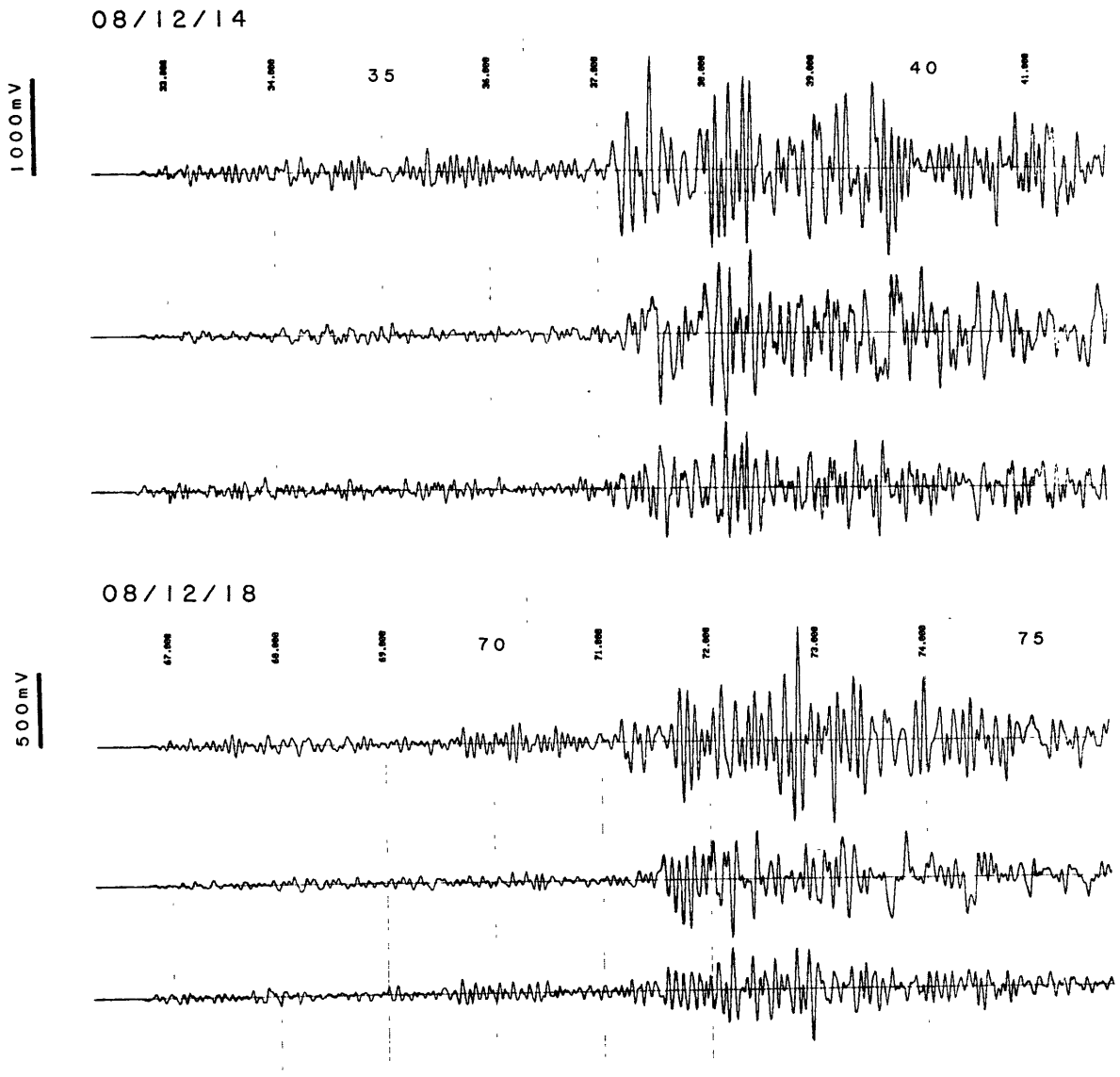
08/12/14
1000mV
35
40
08/12/18
500mV
70
75

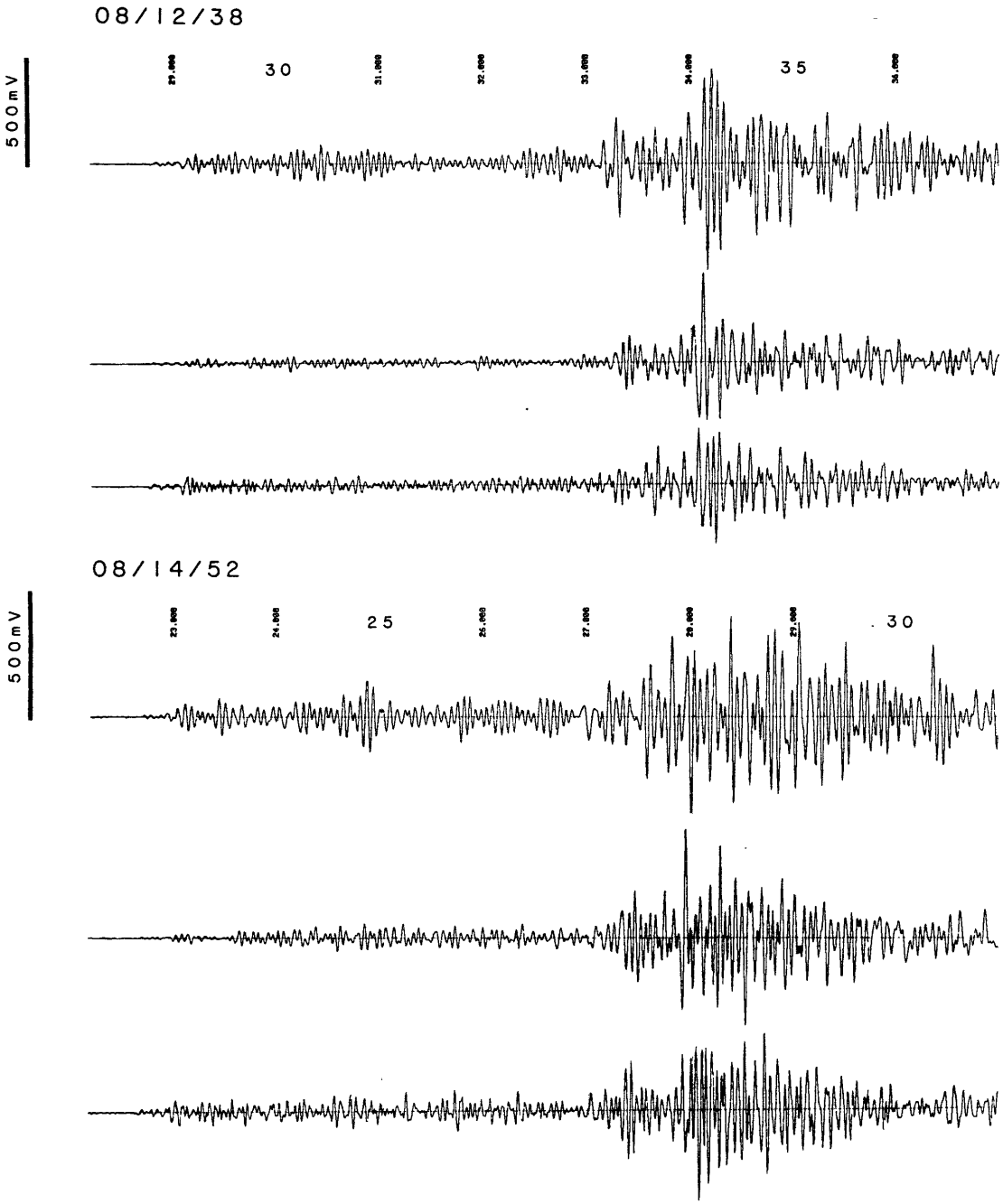
08/12/38
500mV
30
35
08/14/52
500mV
25
30

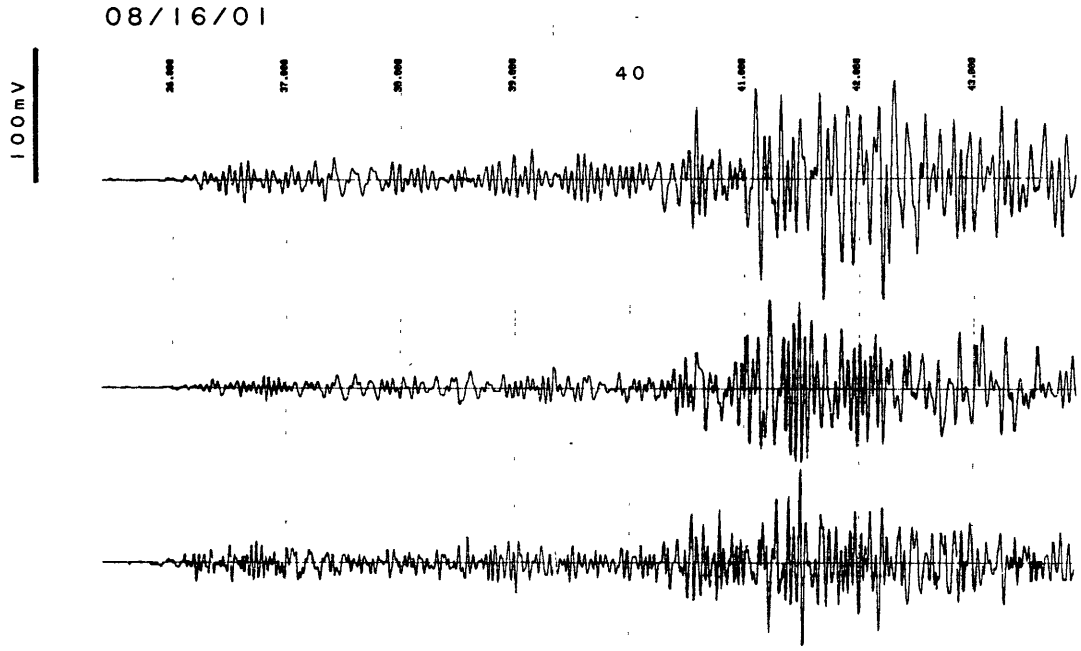
08/16/01
100mV
40

REGION 2

02/05/23

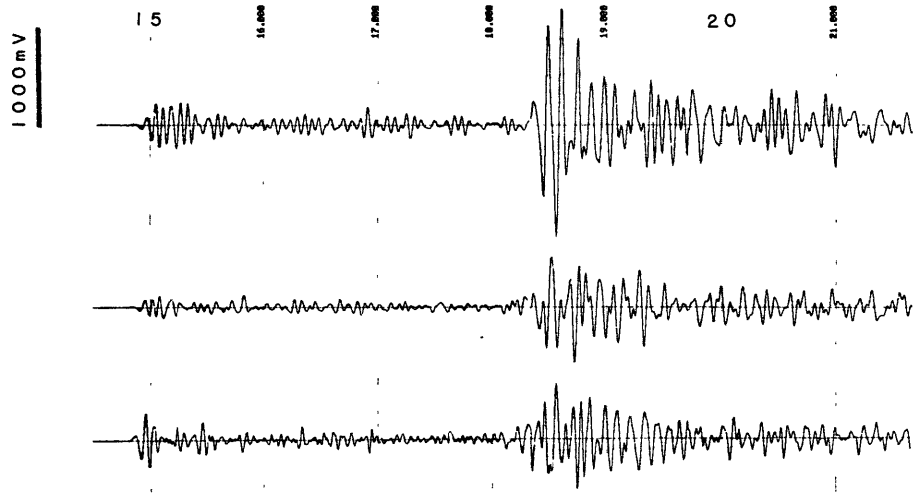

03/23/11

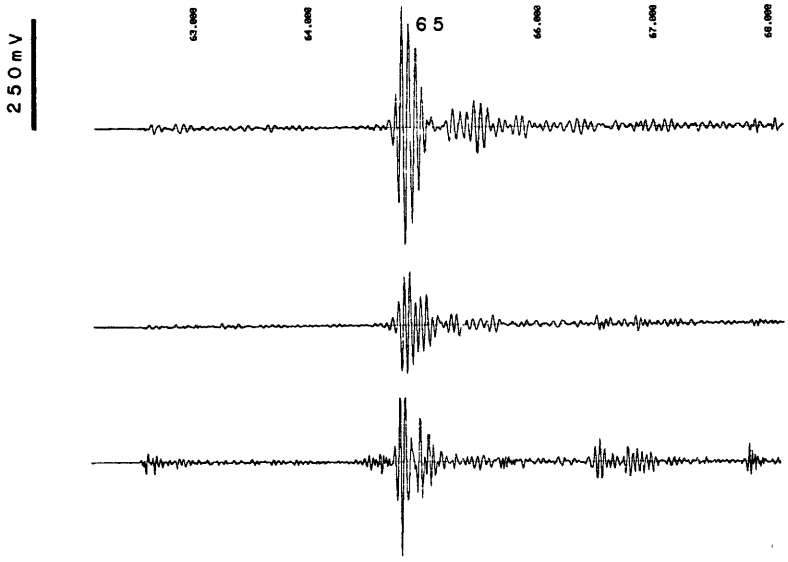

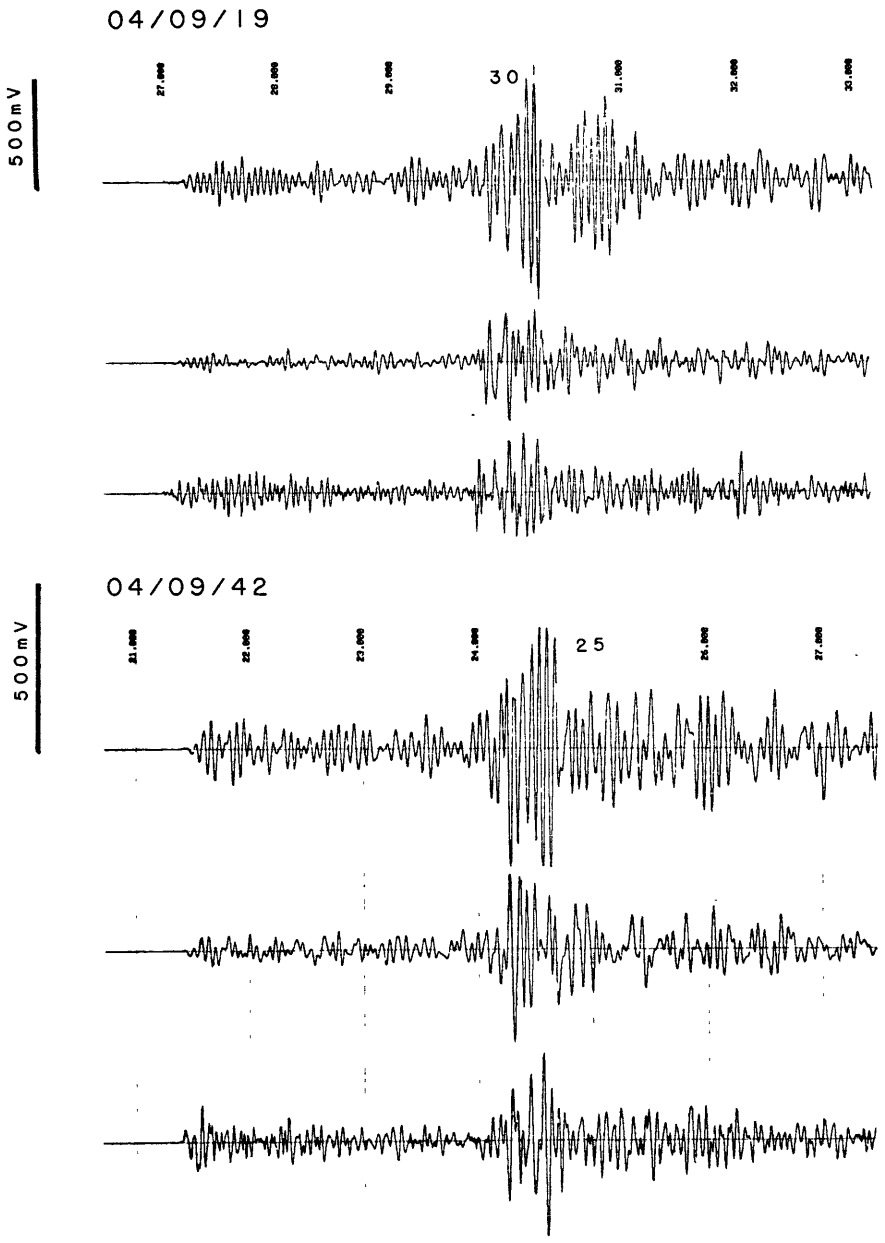
04/09/19
500mV
30
04/09/42
500mV
25

05/02/19

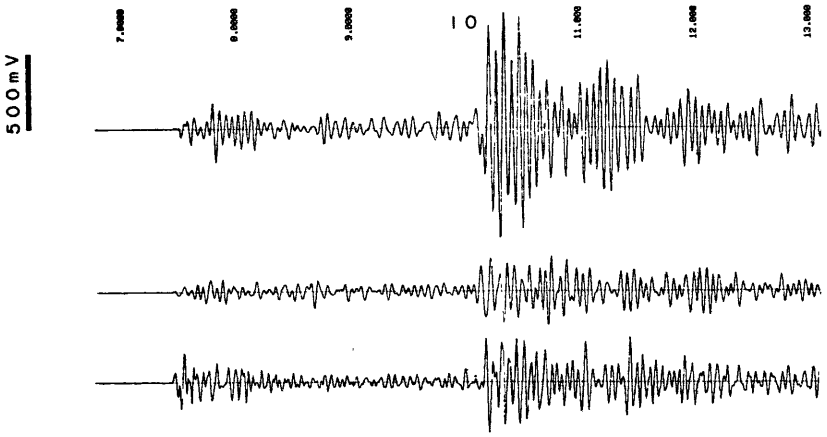

08/00/58

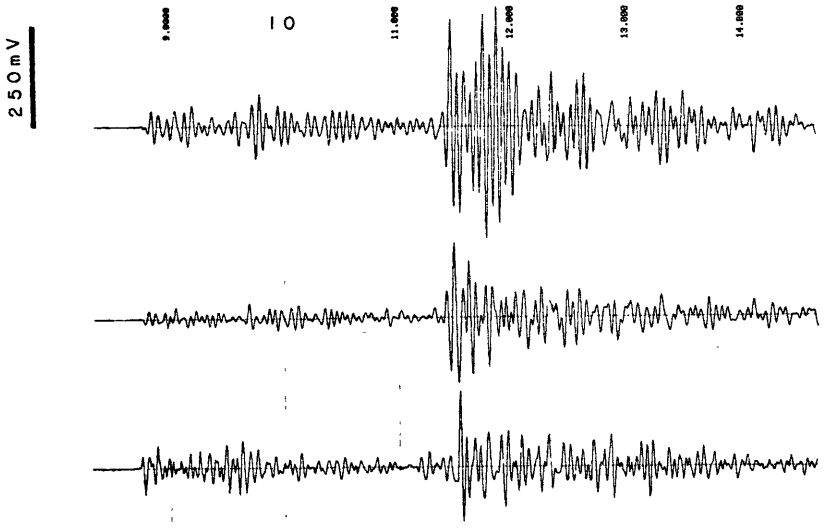

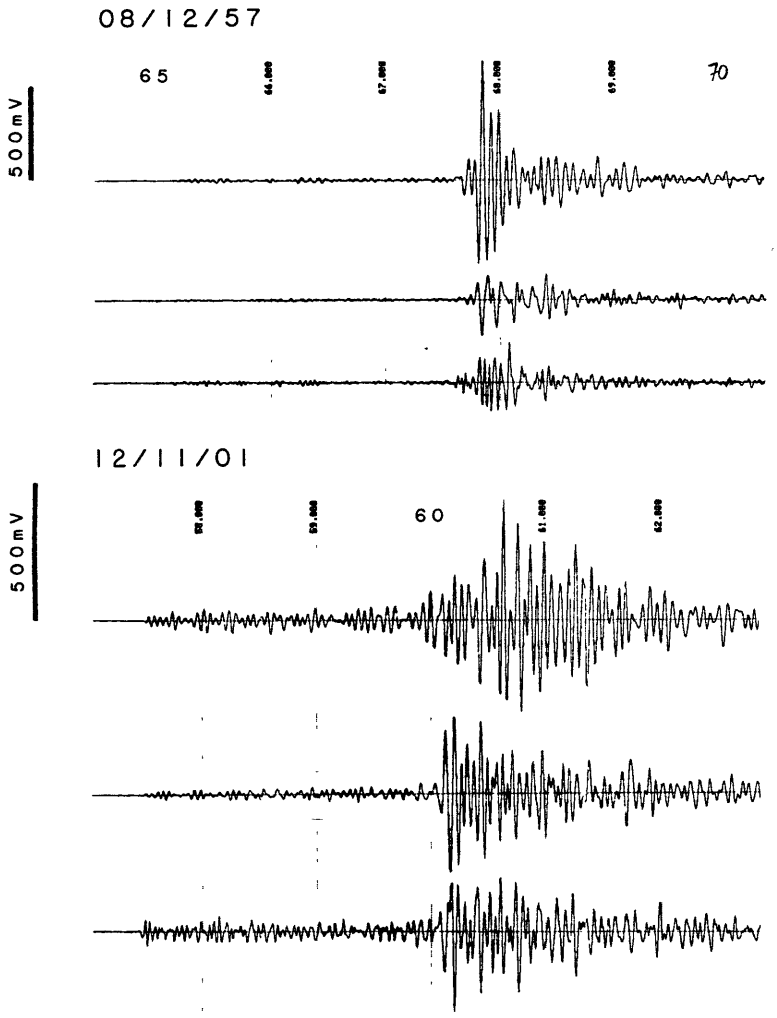
08/12/57
65
70
500mV
12/11/01
60
500mV

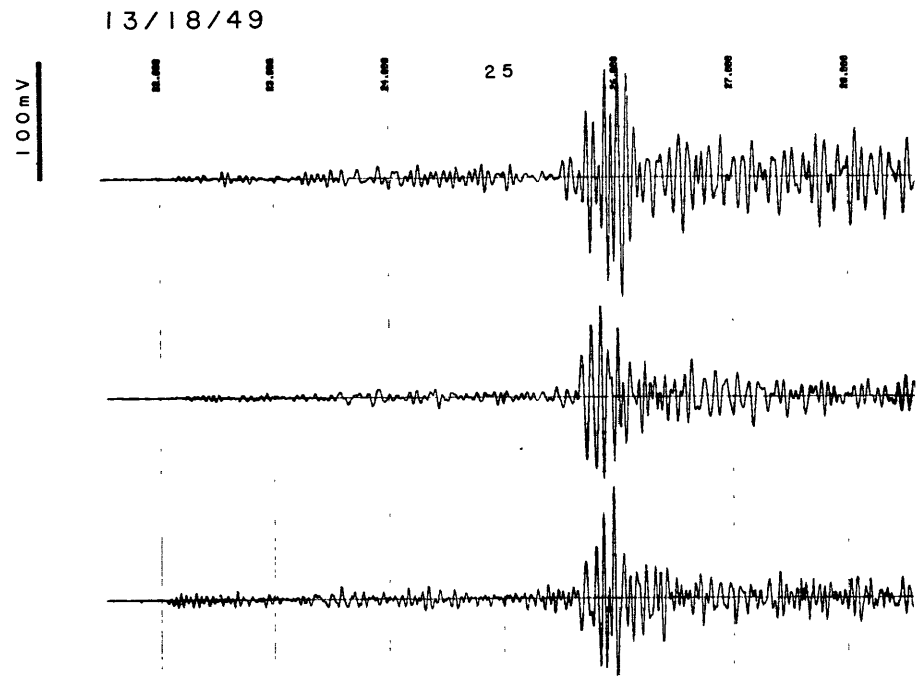
13/18/49
100mV
25

REGION I

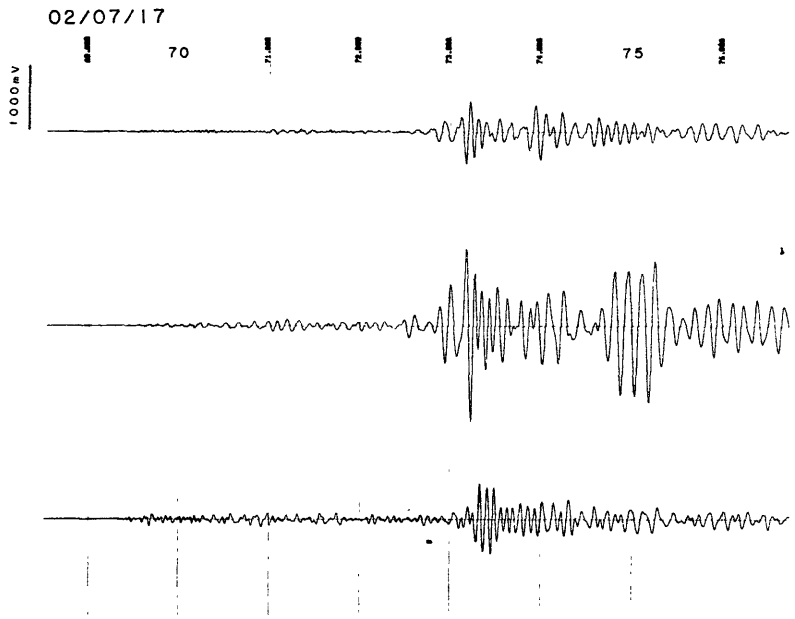

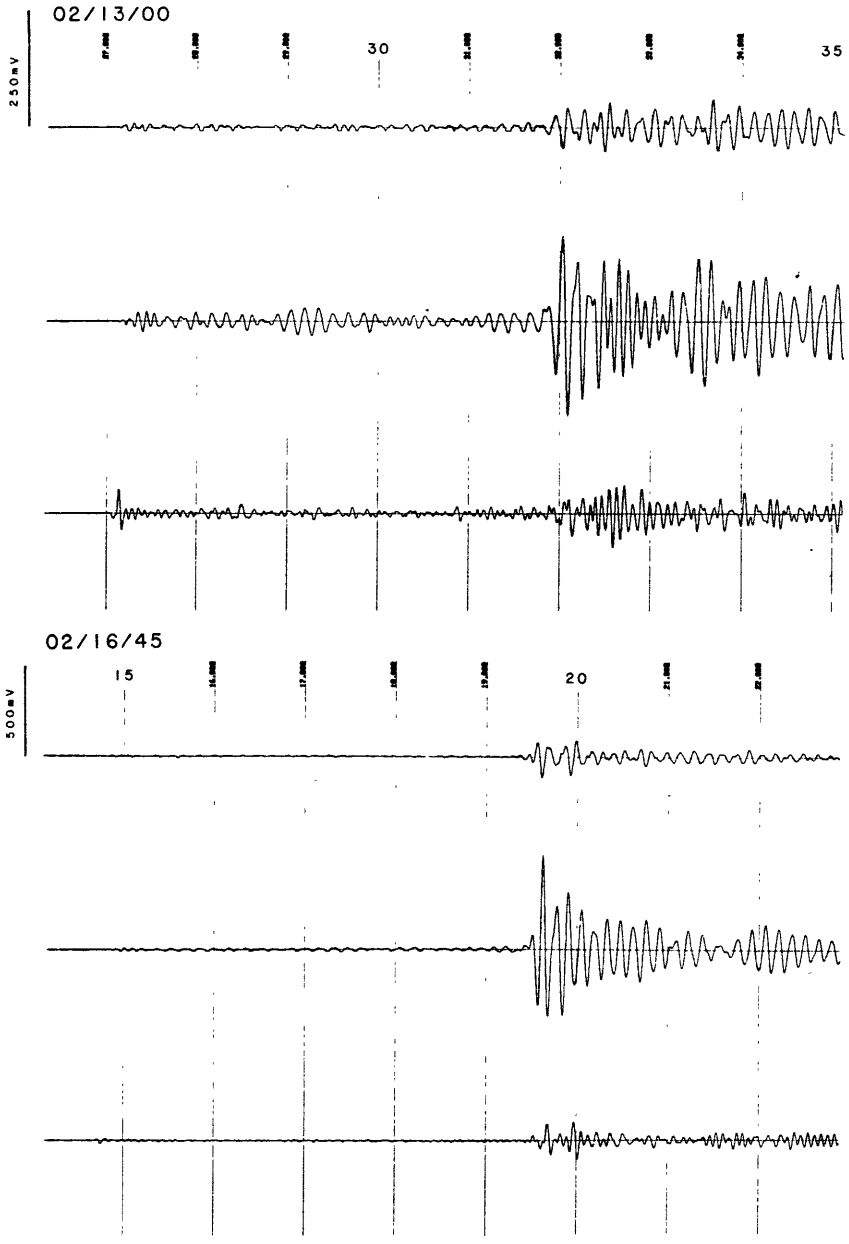
02/13/00
250mV
30
35
02/16/45
500mV
15
20

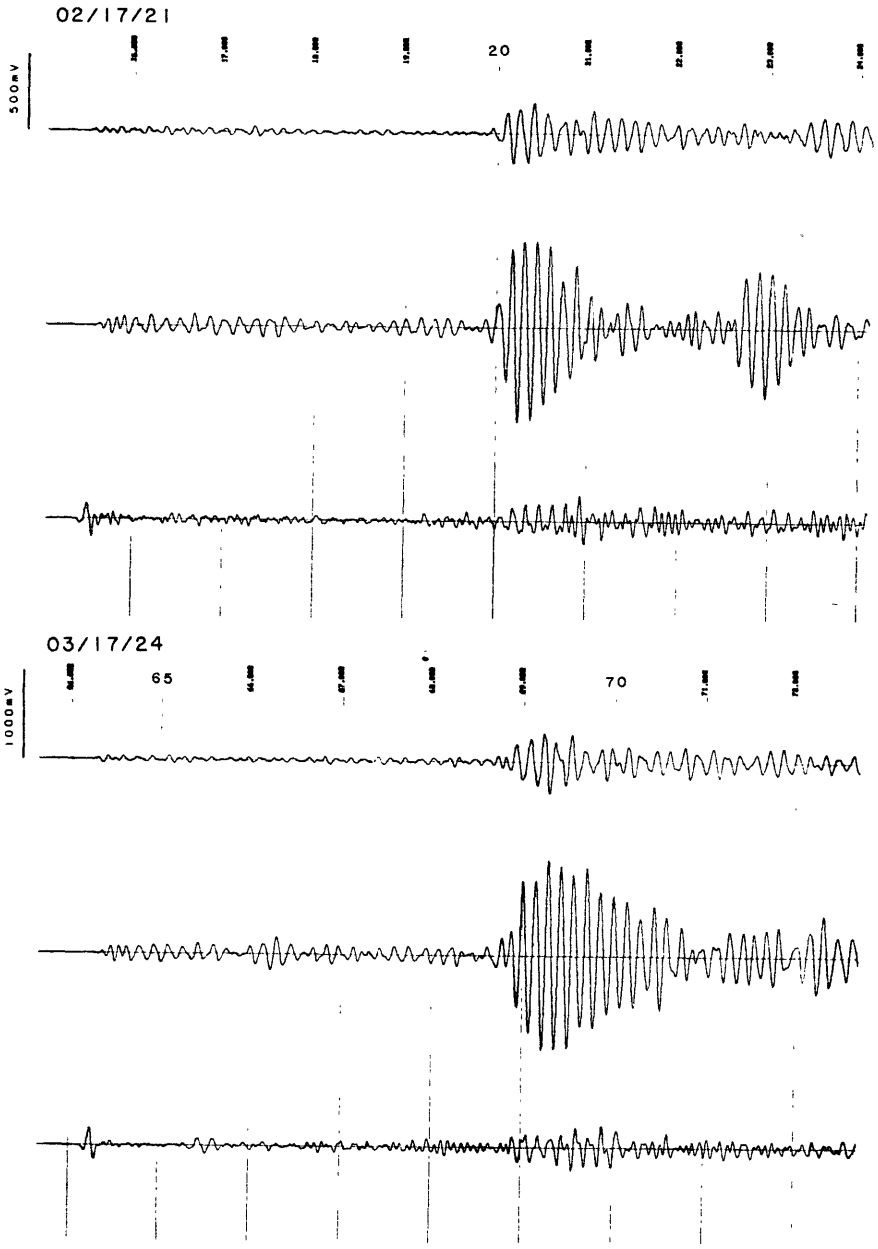
02/17/21
20
500mV
03/17/24
65
70
1000mV

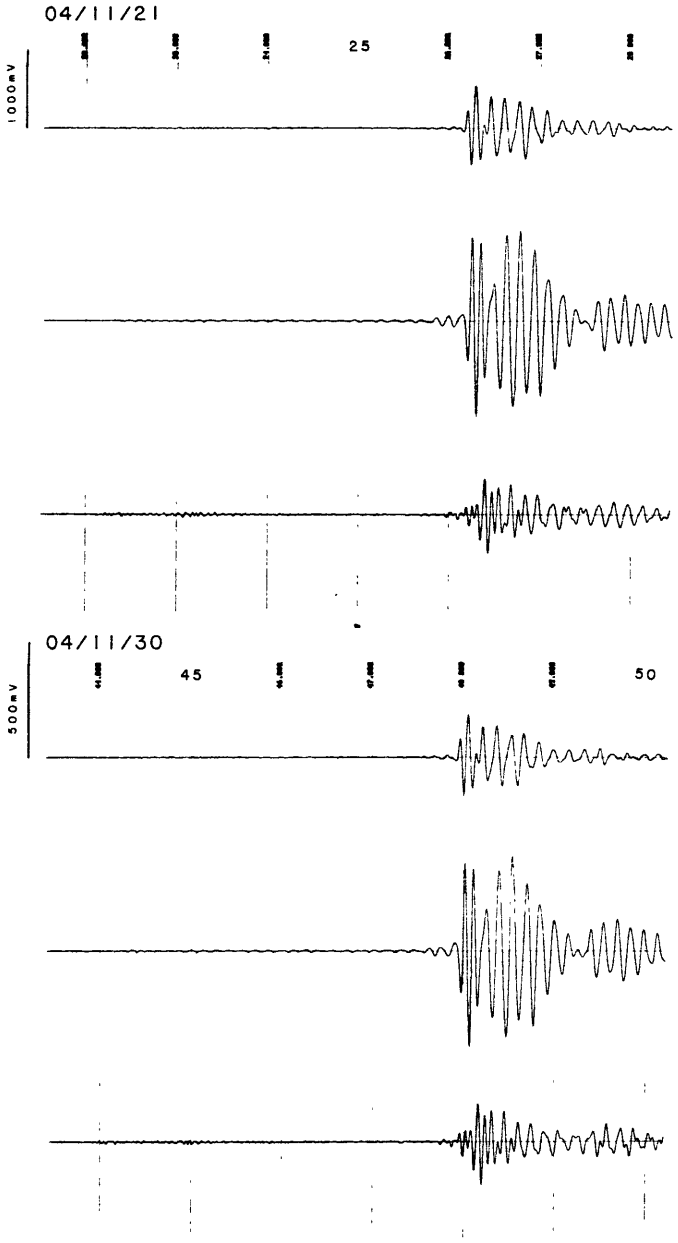
04/11/21
25
1000mV
04/11/30
45
50
500mV

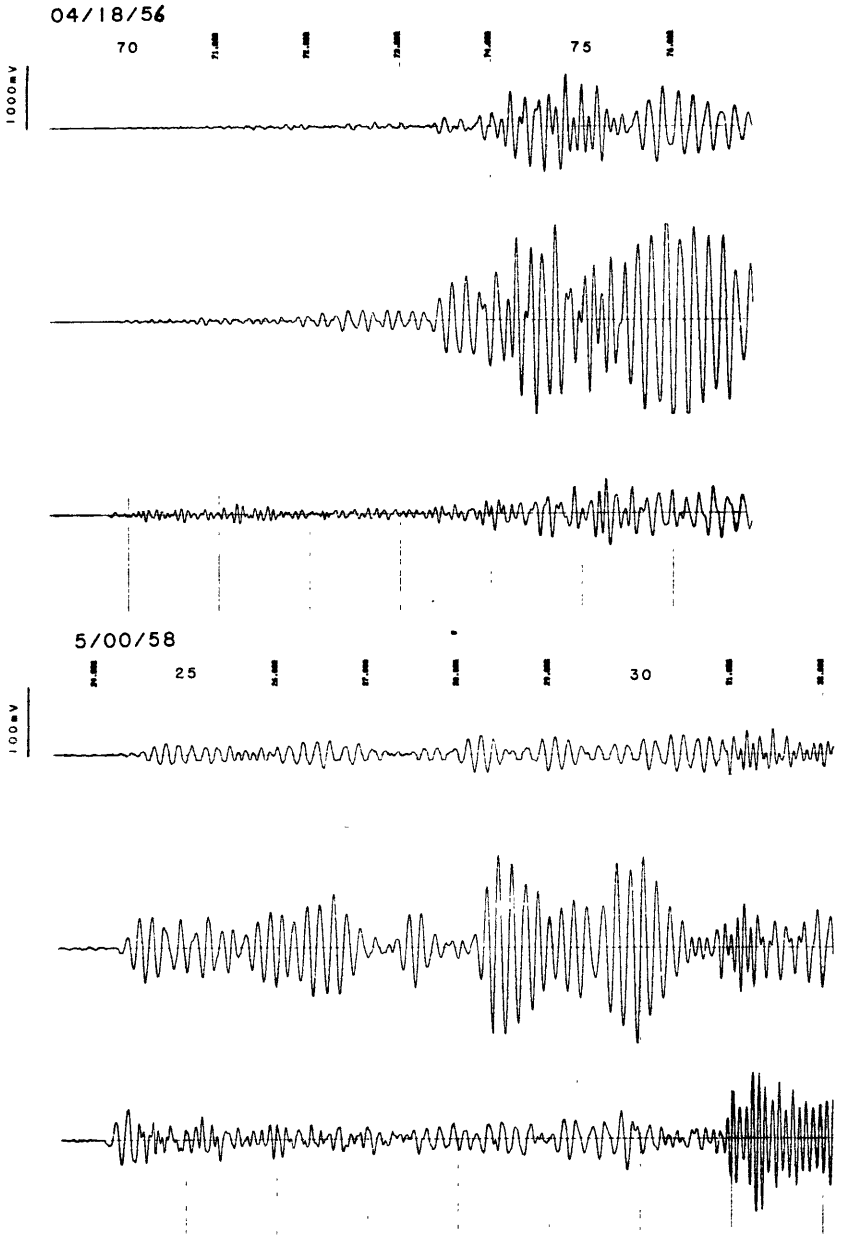
04/18/56
70
75
1000 a V
5/00/58
25
30
100 a V

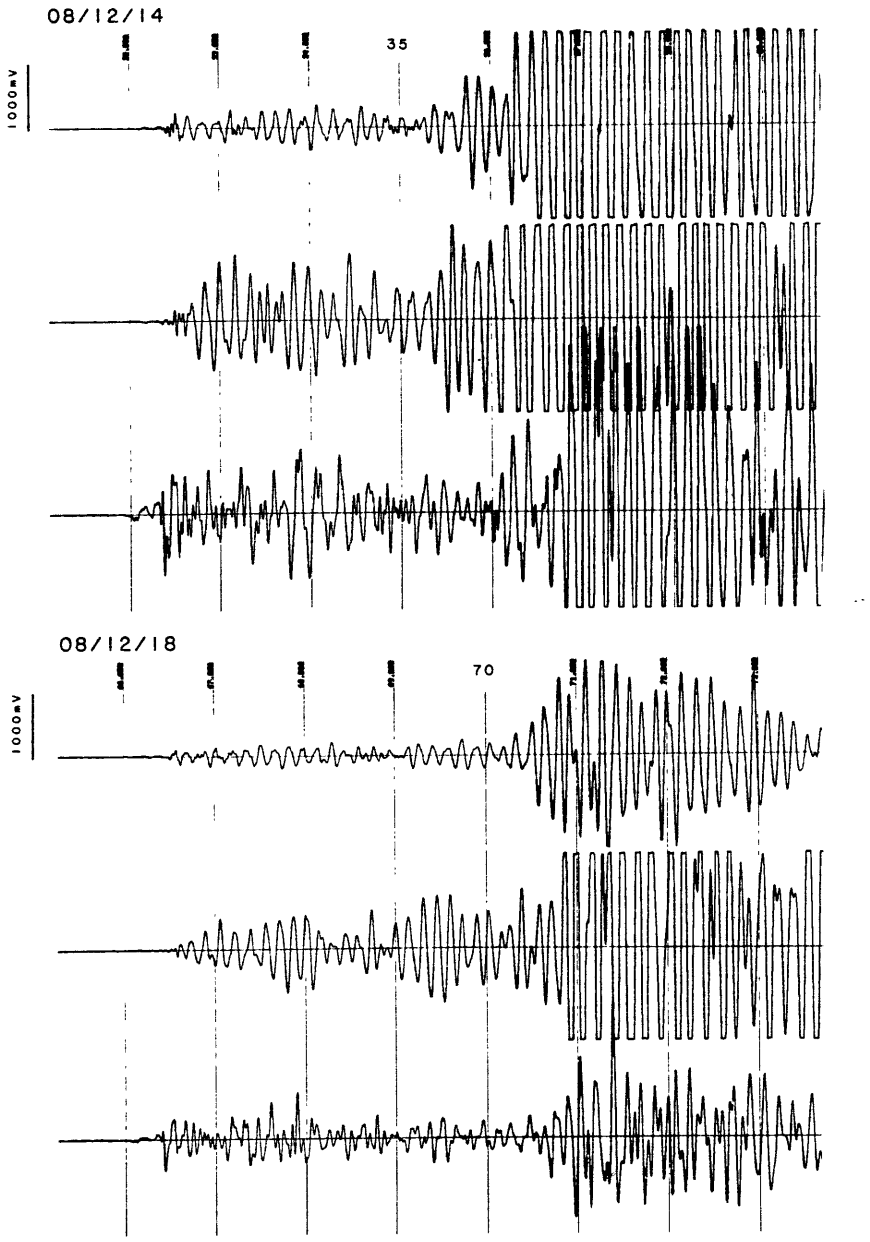
08/12/14
35
1000mV
08/12/18
70
1000mV

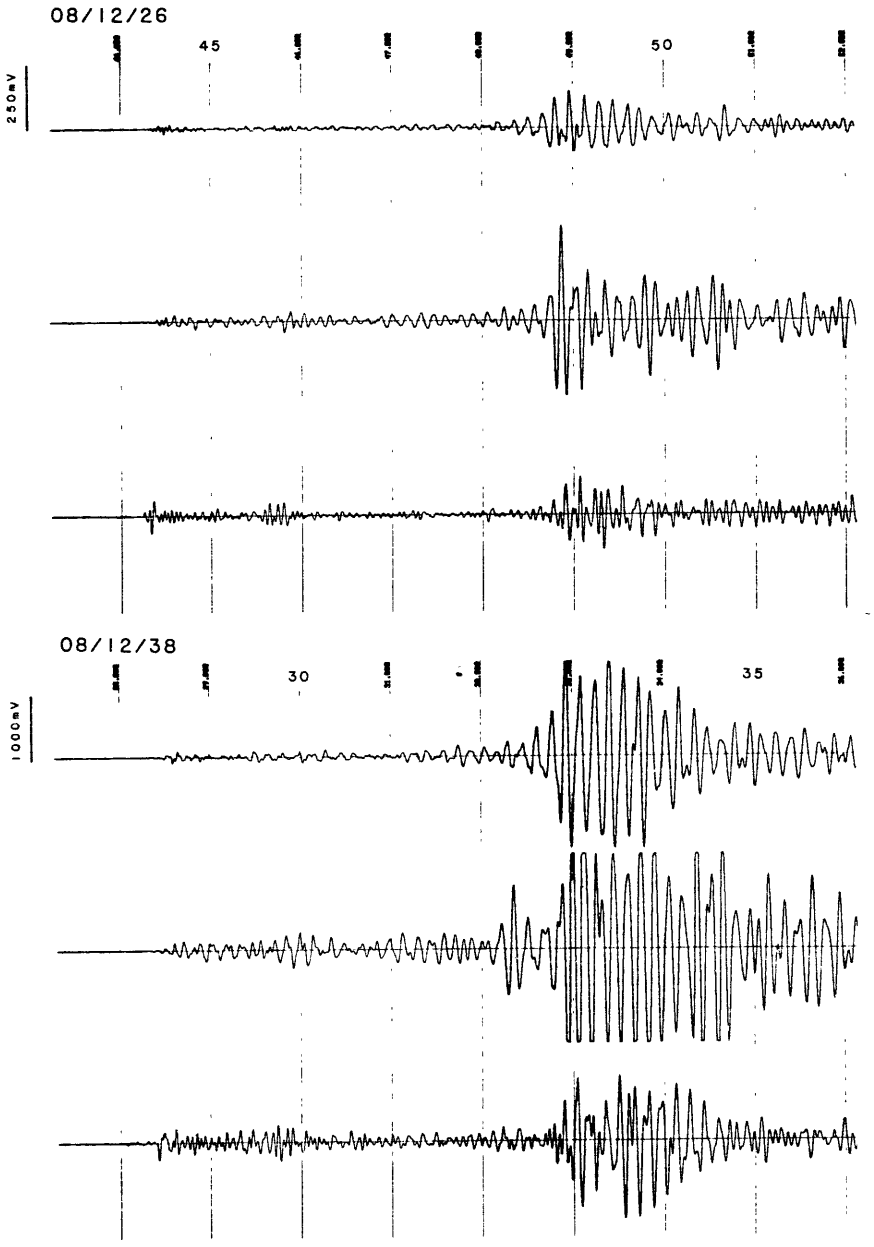
08/12/26
45
50
250mV
08/12/38
30
35
1000mV

REGION2

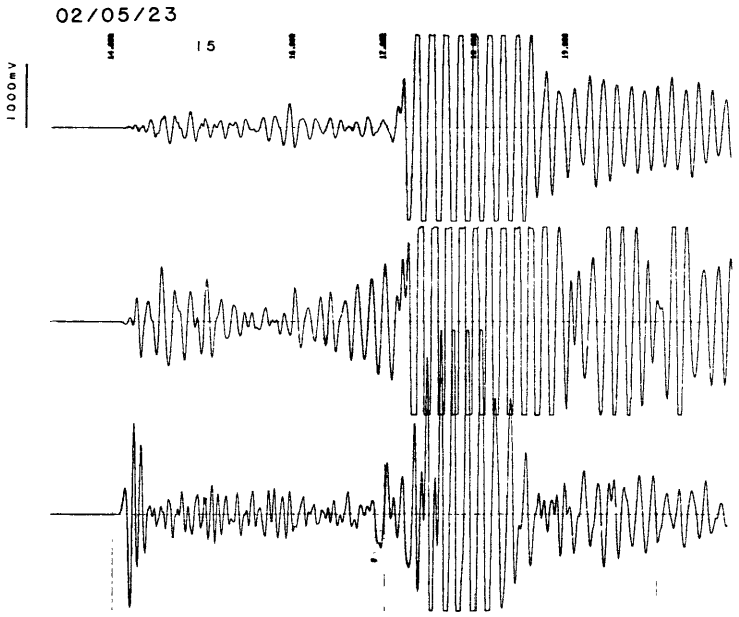

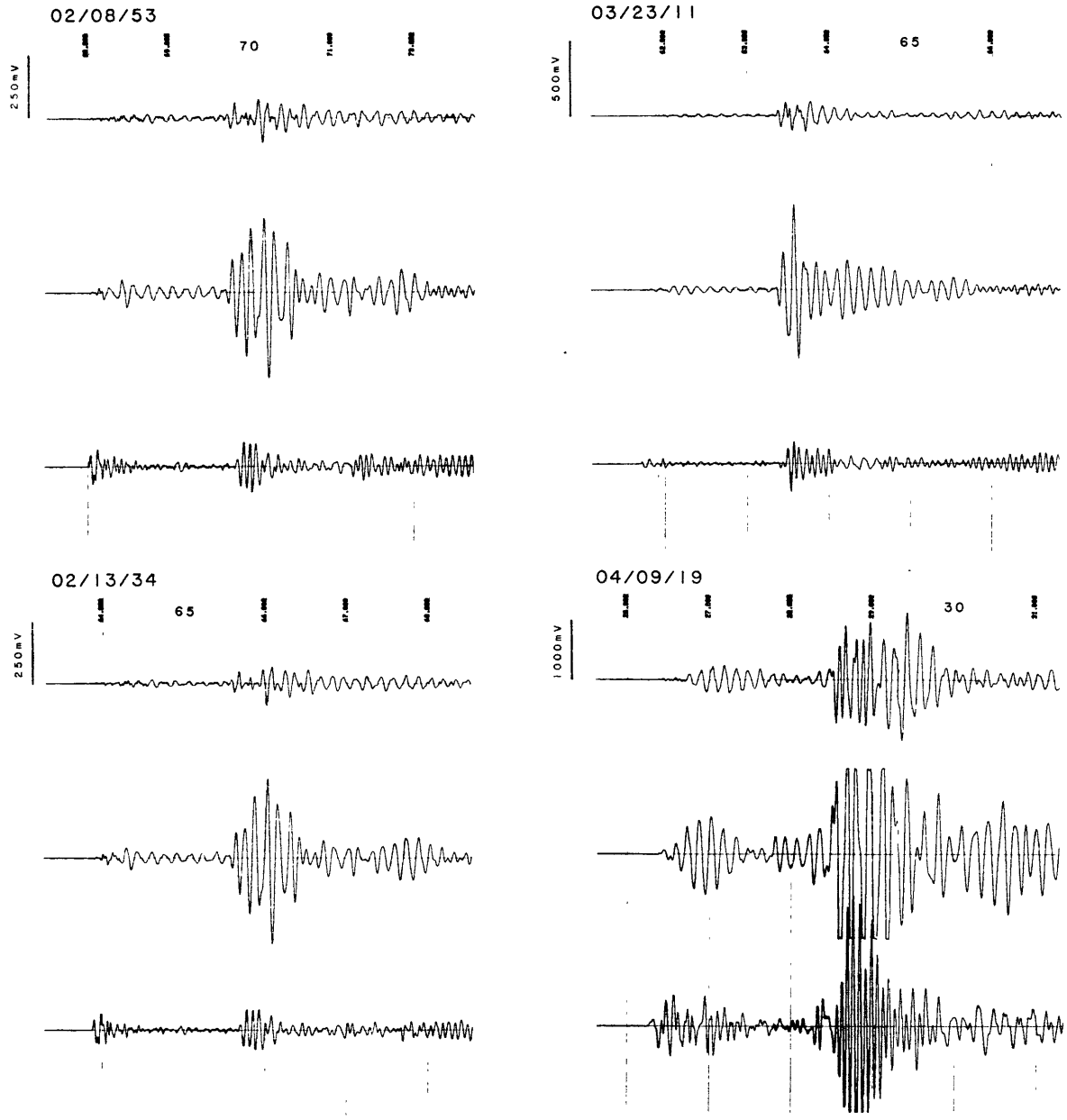
02/08/53
70
250mV
03/23/11
65
500mV
02/13/34
65
250mV
04/09/19
30
1000mV

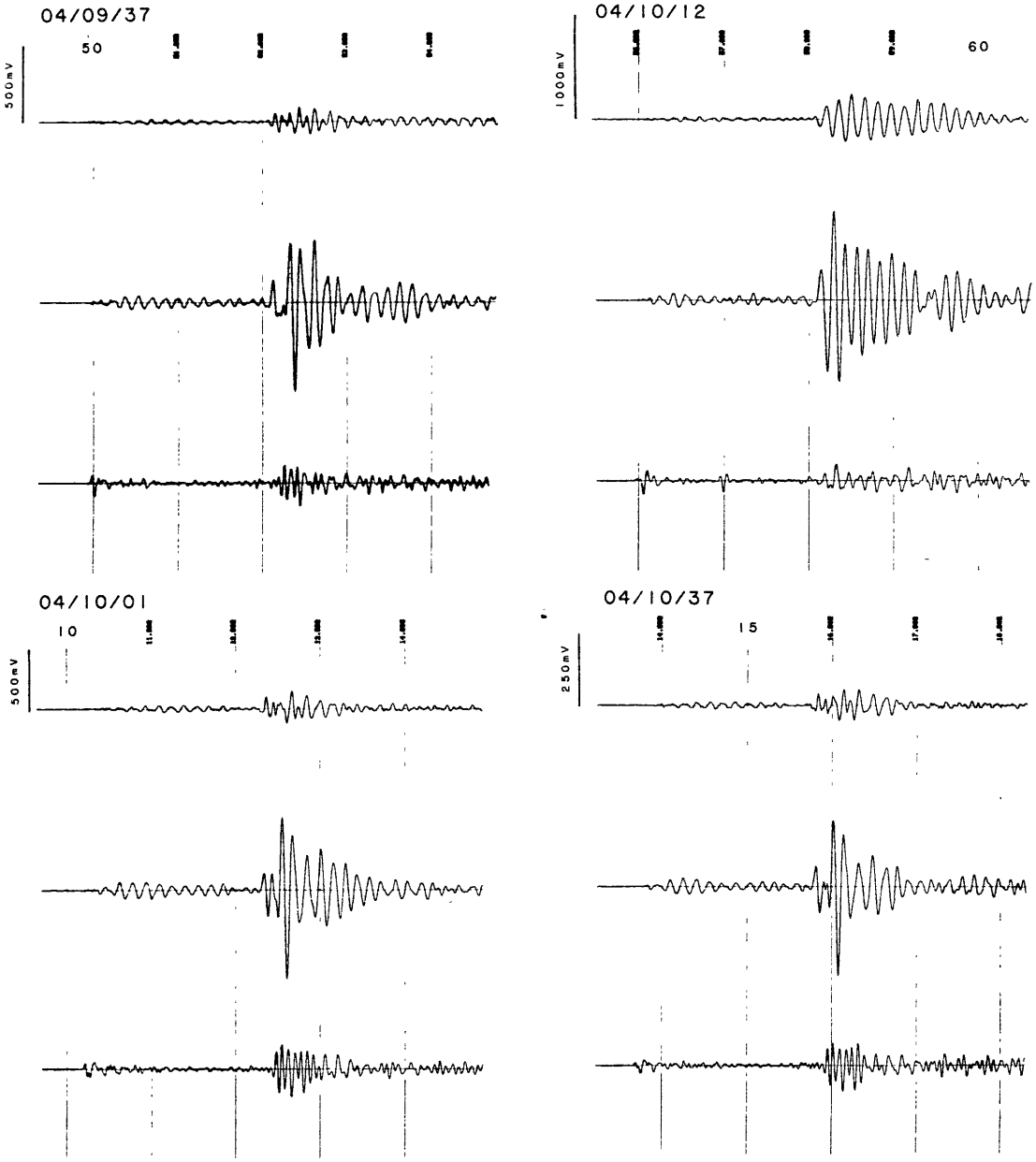
04/09/37
50
500mV
04/10/12
60
1000mV
04/10/01
10
500mV
04/10/37
15
250mV

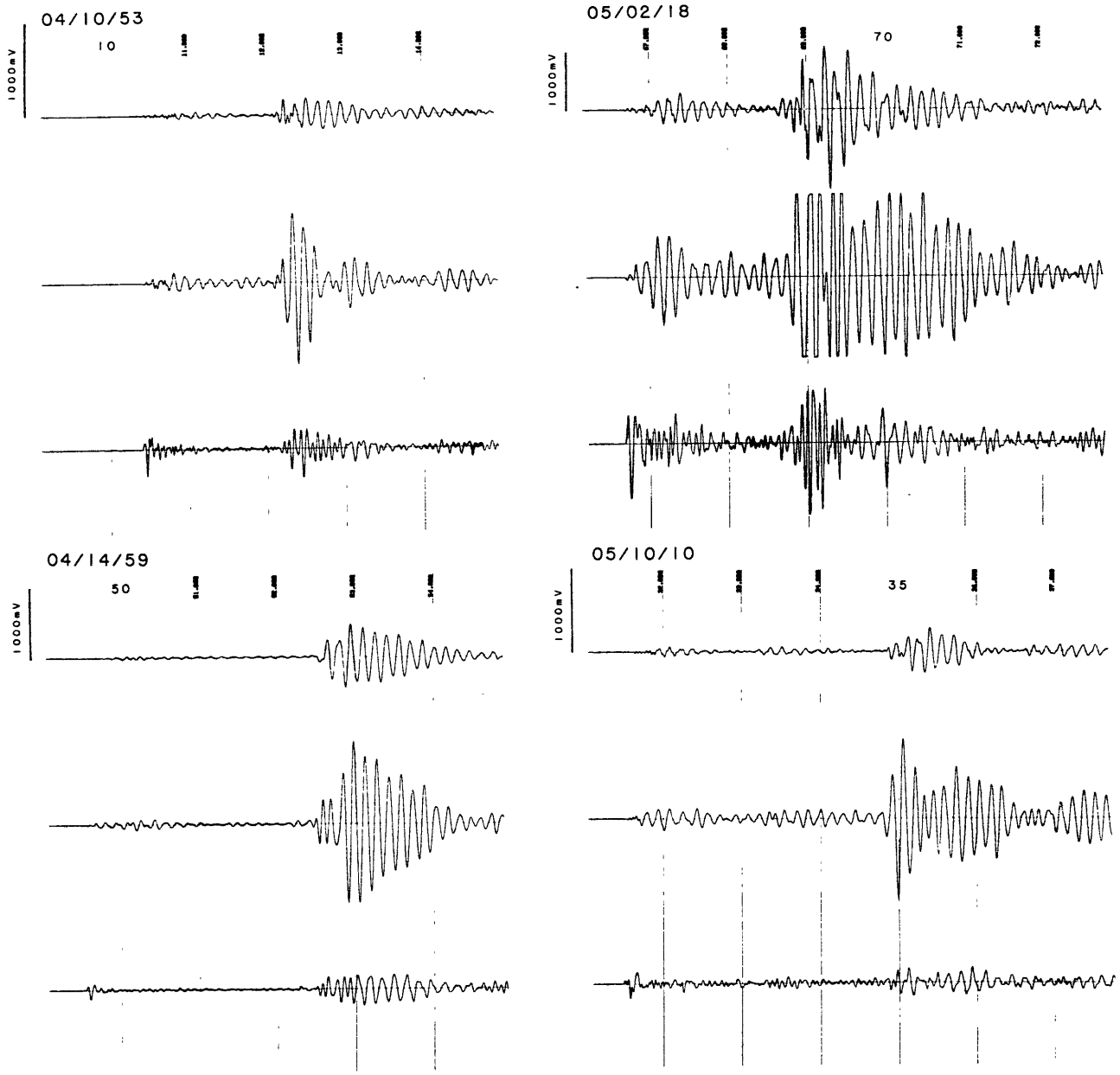
04/10/53
10
1000mV
05/02/18
70
1000mV
04/14/59
50
1000mV
05/10/10
35
1000mV

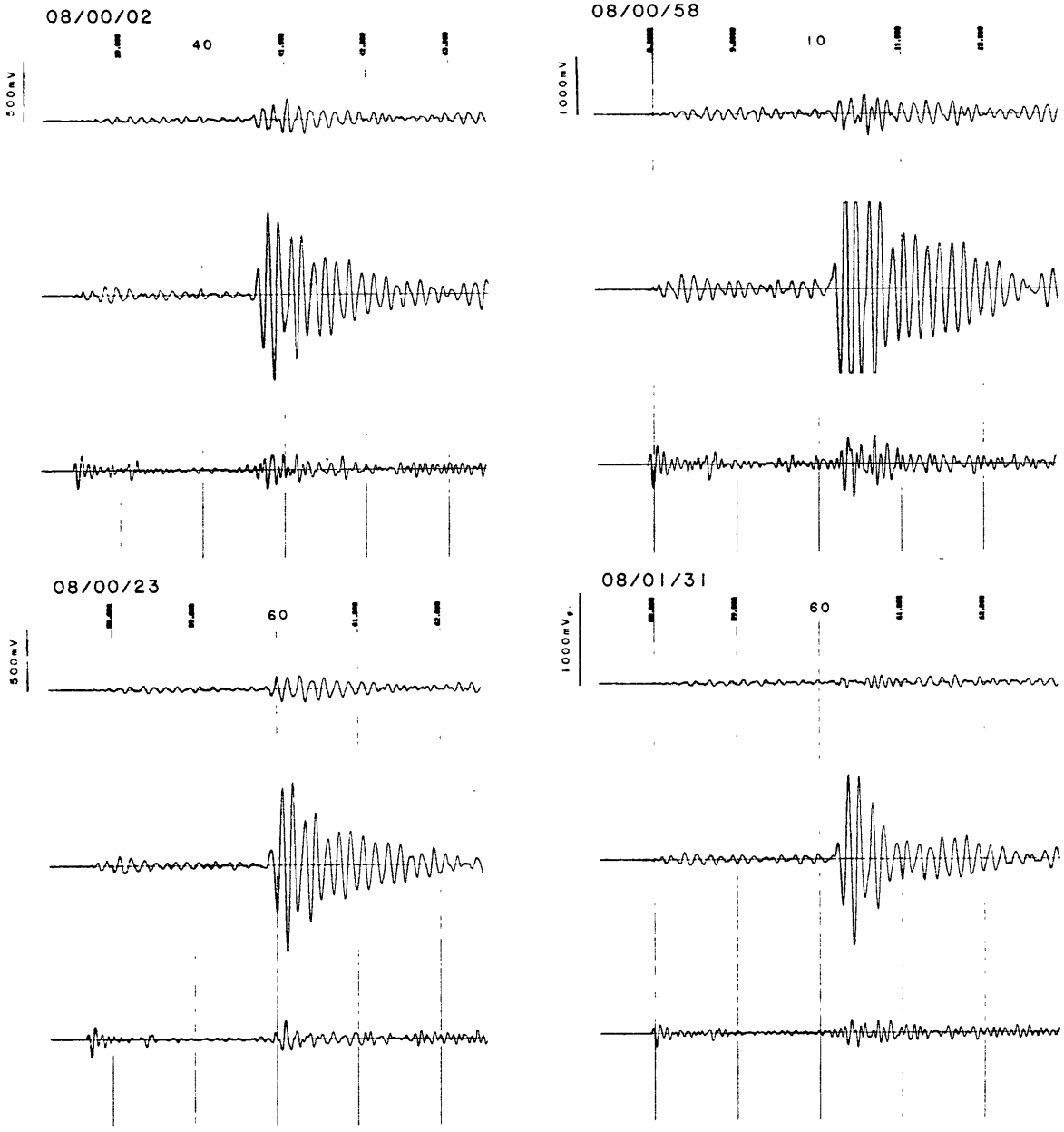
08/00/02
40
500mV
08/00/58
10
1000mV
08/00/23
60
500mV
08/01/31
60
1000mV